2016 Sensor Signal Processing for Defence (SSPD)

Edinburgh, UK
22 – 23 September 2016

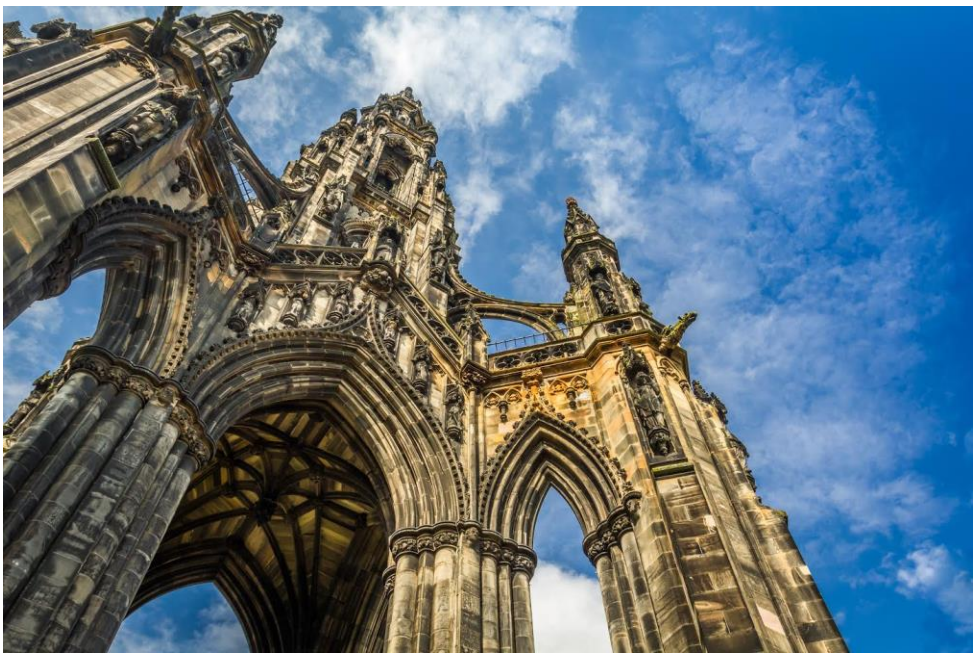

IEEE Catalog Number: CFP16SPD-ART (Xplore)
ISBN: 978-1-5090-0326-6 (Xplore)

IEEE Catalog Number: CFP16SPD-USB (USB)
ISBN: 978-1-5090-0325-9 (USB)

2016 Sensor Signal Processing for Defence (SSPD)

IEEE Catalog Number: CFP16SPD-ART
ISBN: 978-1-5090-0326-6

IEEE Catalog Number: CFP16SPD-USB
ISBN: 978-1-5090-0325-9

Printed copies of this publication are available from:

Curran Associates, Inc
57 Morehouse Lane
Red Hook, NY 12571 USA
Phone: (845) 758-0400
Fax: (845) 758-2633
E-mail: curran@proceedings.com

Produced by IEEE eXpress Conference Publishing

For information on producing a conference proceedings and receiving an estimate, contact conferencepublishing@ieee.org
http://www.ieee.org/conferencepublishing

SSPD 2016

Dear Colleagues,

We warmly welcome you to this year's SSPD Conference in the Royal College of Surgeons, Edinburgh. This event is the 6th conference of the Sensor Signal Processing for Defence series and provides a chance to present, listen to and discuss the latest scientific findings in signal processing for defence.

It is with great pleasure we welcome our two keynote speakers, Geert Leus from the Delft University of Technology, Netherlands, and Philip Perconti from the U.S Army Research Laboratory, as well as our invited speakers Antonio De Maio from the University of Naples Frederico II and Dangcj Aj_pi from Fcpgmr+U_rr Slgtcpqgrw. A welcome also extends to our industrial and kilitary speakers who will be presenting their Signal Processing Challenges and the presenters of scientific papers presenting their novel research through oral presentations and poster sessions. We look forward to some interesting debate and discussion throughout the conference and into the evening at the SSPD Wine Reception and Dinner held in Prince Philip Building, Royal College of Surgeons.

We would like to take this opportunity to thank the speakers, reviewers, session chairs and the technical committee for their contribution to this event.

We hope you enjoy our conference.

Mike Davies
Jonathon Chambers
Paul Thomas

Chairs, SSPD 2016

Technical sponsorship is provided by the IEEE Signal Processing Society and the IEEE Aerospace and Electronic Systems Society. Proceedings will be submitted to the Xplore Digital Library. The conference is organised by the University Defence Research Collaboration (UDRC) in Signal Processing, sponsored by the Defence Science and Technology Laboratory (Dstl) and the Engineering and Physical Sciences Research Council (EPSRC).

Thursday 22nd September 2016

8:30 Registration and Refreshments

9:00 Welcome and Opening
Mike Davies, University of Edinburgh / Jonathon Chambers, Newcastle University

9:10 Plenary Keynote: Sparse Sensing for Statistical Inference
Geert Leus, Delft University of Technology

Session 1: Tracking and Detection

10:10 1.0 - ÕÌÎÉŽÓÅÎÓÏÒ - ÕÌÎÉŽÔÁÒÇÅÔ 4ÒÁÃËÉÎÇ 4ÅÃÈÎÉÑÕÅ £ÏÒ 3ÐÁÃÅ 3ÉÔÕÁÔÉÏÎÁÌ ! × ÁÒÅÁÓÓ
DaniÅÌ #ÌÁÒË, (ÅÒÉÏŽ 7 ÁÔÔ 5 ÎÉÖÅÒÓÉÔÙ

10:40 1.1 An Adaptive Receiver Search Strategy for Electronic Support
Sabine Apfeld[1], Alexander Charlish[1], Wolfgang Koch[2], [1]Fraunhofer, [2]Fraunhofer/University of Bonn

11:05 Refreshments

11:30 1.2 New environmental dependent modeling with Gaussian particle filtering based implementation for ground vehicle tracking
Miao Yu[1], Yali Xue[1], Runxiao Ding[1], Hyondong Oh[1], Wen-Hua Chen[1], Jonathon Chambers[2], Loughborough University[1], Newcastle University[2]

11:55 1.3 Robust Detection of micro-UAS drones with L-band 3-D Holographic Radar
[1]Mohammed Jahangir, [1]Chris Baker, Aveillant Ltd[1]

12:20 1.4 Direction Finding Antenna Arrays with Improved Accuracy and Reduced Complexity and Size
[1]Houcem Gazzah, University of Sharjah[1]

12:45 Lunch

Session 2: Signal Processing Challenges – Industrial Perspective – Chair, Paul Thomas, Dstl

13:40 Industrial Speakers and Panel Discussion

Session 3: Poster Session

14:40 Posters and Refreshments available

Session 4: Radar and Lidar

16:10 4.0 Invited Speaker: Transmit Adaptivity in Radar
Antonio De Maio, University of Naples Federico II

16:40 4.1 Experimental Study on Full-Polarization Micro-Doppler of Space Precession Target in Microwave Anechoic Chamber
Jin Liu[1], Qihua Wu, Xiaofeng Ai[1], Feng Zhao[1], Jian'an Chen[1], [1]National University of Defense Technology

17:05 4.2 Fractional Fourier Transform Based Co-Radar Waveform: Experimental Validation
Domenico Gaglione[1], Carmine Clemente[1], Adriano Rosario Persico[1], Christos V. Ilioudis[1], Ian Proudler[2], John J Soraghan[1], [1]University of Strathclyde, [2]Loughborough University

17:30 Close and End of Day 1

19:30 Wine Reception and Meal (Prince Philip Building, Royal College of Surgeons)

Friday 23rd September 2016

8:45 Registration and Refreshments

9:15 Welcome to day 2
Mike Davies, University of Edinburgh / Jonathon Chambers, Newcastle University

9:25 Plenary Keynote: Taming the Torrent: Future Military Signal Processing and Information Fusion
Philip Perconti, US Army Research Laboratory

Session 4 cont.: Radar and Lidar

10:25 4.3 Discriminating Underwater LiDAR Target Signatures using Sparse Multi-spectral Depth Codes
Puneet S Chhabra[1], Aurora Maccarone[1], Aongus McCarthy[1], Andrew M Wallace[1], Gerald Buller[1],[1]Heriot-Watt University

10:50 4.4 Efficient Range Estimation and Material Quantification from Multispectral Lidar Waveforms
Yoann Altmann[1], Aurora Maccarone[1], Abderrahim Halimi[1], Aongus McCarthy[1], Gerald Buller[1], Steve McLaughlin[1], [1]Heriot-Watt University

11:15 Refreshments

Session 5: Signal Processing Challenges – Military User Perspective - Chair, Paul Thomas, Dstl

11:45 MOD Speakers and Panel Discussion

12:45 Lunch

Session 6: Synthetic Aperture Imaging

14:00 6.1 GMTI in circular SAR data using STAP
Emiliano Casalini[1], Daniel Henke[1], Erich H. Meier[1], [1]University of Zurich

14:25 6.2 Digital Elevation Model Aided SAR-based GMTI Processing in Urban Environments
Di Wu[1], Mehrdad Yaghoobi[1], Mike Davies[1], [1]University of Edinburgh

14:50 Refreshments

15:10 6.3 A Multi-Family GLRT for Detection in Polarimetric SAR Images
Luca Pallotta[1], Carmine Clemente[2], Antonio De Maio[1], Danilo Orlando[3], [1]University of Naples Federico II, [2]Strathclyde University, [3]Niccolò Cusano University

15:35 6.4 A Novel Motion Compensation Approach for SAS
Salvatore Caporale[1], Yvan Petillot[1], [1]Heriot-Watt University

16:00 Close

Poster Session

P01 **Spectral Library Clustering Using a Bayesian Information Criterion**
Jonathan Piper[1], John Duselis[2], [1]Dstl, [2]AFRL

P02 **Detection of manoeuvring low SNR objects in receiver arrays,**
Kimin Kim[1], Murat Uney[1], Bernard Mulgrew[1], [1]University of Edinburgh

P03 **A Modified Spectral Line Camera for Low Cost Anomaly Detection**
Oscar Somsen[1], [1]Netherlands Defense Agency

P04 **Bistatic Micro-Doppler Characteristics of Precessing Targets**
Xiaofeng Ai[1], Jin Liu, Feng Zhao[1], Jianhua Yang[1], Jian'an Chen[1], [1]National University of Defense Technology

P05 **High Dynamic Range Spectral Estimation for Incomplete Time Series**
Mike Newman[1], David Harvey[1], [1]Thales UK

P06 **Tracking small UAVs using a Bernoulli filter**
David Cormack[1], Daniel Clark[2], [1]Heriot-Watt University/Selex ES, [2]Heriot-Watt University

P07 **Robust Unmixing Algorithms for Hyperspectral Imagery**
Abderrahim Halimi[1], Yoann Altmann[1], Gerald Buller[1], Steve McLaughlin[1], William Oxford[2], Damien Clarke[2], Jonathan Piper[2], [1]Heriot-Watt University, [2]Dstl

P08 **Radar Filters Design in the Presence of Target Doppler Frequency and Interference Covariance Matrix Uncertainties**
Augusto Aubry[1], Antonio De Maio[2], Yongwei Huang[3], Marco Piezzo[4], [1]Universita degli studi di Napoli, [2]University of Naples Federico II, [3]The Hong Kong University of Science and Technology, [4]Elettronica S.p.A.

P09 **Experimental Analysis of Time Deviation on a Passive Localization System**
Hugo Seute[1], Ali Khenchaf[2], Jean-Christophe Cexus[2], Jean-François Grandin[3], Cyrille Enderli[3], [1]Thales Airborne Systems/ENSTA Bretagne, [2]ENSTA Bretagne, [3]Thales Airborne Systems

P10 **Beampattern and polarisation synthesis of 3D RF-seeker antenna arrays**
Luc Fourtinon[1], Alessio Balleri[2], Yves Quéré[3], Christian Person[4], Annaig Martin-Guennou[3], Eric Rius, Guillaume Lesueur[5], Thomas Merlet[5], [1]Cranfield University/Telecom-Bretagne, [2]Cranfield University, [3]Université de Brest, [4]Lab-STICC/MOM UMR CNRS, [5]Thales Air Systems

P11 **Adaptive M-estimation for Robust Cubature Kalman Filtering**
Changliang Zhang[1], Ruirui Zhi[1], Tiancheng Li[2], Juan Corchado[2], [1]Northwestern Polytechnical University, [2]University of Salamanca

P12 **Fractional Fourier Based Sparse channel estimation for multicarrier underwater acoustic communication system**
Yixin Chen[1], John J Soraghan[1], Carmine Clemente[1], Stephan Weiss[1], [1]University of Strathclyde

Poster Session

P13 **Multiple Spherical Arrays Design for Acoustic Source localization**
Xi Pan[1], Huayang Wang[1], Fangzhou Wang[1], Chengtian Song[1], [1]Beiijng Institute of Technology

P14 **Likelihood modelling of the Space Geodesy Facility laser ranging sensor for Bayesian filtering**
Christy Simpson[1], Andrew Hunter[1], Sergei Vorgul[1], Emmanuel D. Delande[1], Jose Franco[1], Daniel Clark[1], [1]Heriot-Watt University

P15 **Cramer-Rao Bounds for Distributed System Size Estimation Using Consensus Algorithms**
Sai Zhang[1], Cihan Tepedelenlioglu[1], Jongmin Lee[1], Henry Braun[1], Andreas Spanias[1], [1]Arizona State University

P16 **Joint Array and Spatial Sparsity Based Optimisation for DoA Estimation**
Mingyang Chen[1], Mark Barnard[1], Wenwu Wang[1], [1]University of Surrey

P17 **Scanning Emitter TMA by Two Fixed Observers using Time of Interception**
Zhang Yifei[1], Zhang Min[1], Fucheng Guo[1], [1]National University of Defense Technology

P18 **Enhanced-Range Intrusion Detection Using Pyroelectric Infrared Sensors**
Sami A Aldalahmeh[1], Amer Hamdan[1], Mounir Ghogho[2], Desmond McLernon[3], [1]Al-Zaytoonah University of Jordan, [2]University of Leeds/International University of Rabat, [3]University of Leeds

P19 **Knowledge-aided Adaptive Detection with Multipath Exploitation Radar**
Harun Hayvaci[1], Utku Kumbul[1], [1]TOBB University of Economics and Technology

Keynote Speakers

Prof. Geert Leus

Sparse Sensing for Statistical Inference:

Ubiquitous sensors generate prohibitively large data sets. Large volumes of such data are nowadays generated by a variety of applications such as imaging platforms and mobile devices, surveillance cameras, social networks, power networks, to list a few. In this era of data deluge, it is of paramount importance to gather only the data that is informative for a specific task in order to limit the required sensing cost, as well as the related costs of storing, processing, or communicating the data. The main goal of this talk is therefore to present topics that transform classical sensing methods, often based on Nyquist-rate sampling, to more structured low-cost sparse sensing mechanisms designed for specific inference tasks, such as estimation, filtering, and detection. More specifically, we present fundamental tools to achieve the lowest sensing cost with a guaranteed performance for the task at hand. Applications can be found in the areas of radar, multi-antenna communications, remote sensing, and medical imaging.

Biography

Geert Leus received the MSc and PhD degree in Applied Sciences from the Katholieke Universiteit Leuven, Belgium, in June 1996 and May 2000, respectively. Currently, Geert Leus is an "Antoni van Leeuwenhoek" Full Professor at the Faculty of Electrical Engineering, Mathematics and Computer Science of the Delft University of Technology, The Netherlands. His research interests are in the area of signal processing for communications. Geert Leus received a 2002 IEEE Signal Processing Society Young Author Best Paper Award and a 2005 IEEE Signal Processing Society Best Paper Award. He is a Fellow of the IEEE and a Fellow of EURASIP. Geert Leus was the Chair of the IEEE Signal Processing for Communications and Networking Technical Committee, and an Associate Editor for the IEEE Transactions on Signal Processing, the IEEE Transactions on Wireless Communications, the IEEE Signal Processing Letters, and the EURASIP Journal on Advances in Signal Processing. Currently, he is a Member-at-Large to the Board of Governors of the IEEE Signal Processing Society and a member of the IEEE Sensor Array and Multichannel Technical Committee. He finally serves as the Editor in Chief of the EURASIP Journal on Advances in Signal Processing.

Dr. Philip Perconti

Taming the Torrent: Future Military Signal Processing and Information Fusion:

Electronic devices, from unattended ground sensors to small radars, have become a ubiquitous part of Military operations. With the increased use of sensor systems comes an increased volume of data that must be processed, moved, assessed, and decided upon within the short time scales associated with battlefield operations. Onboard processing, information fusion, and other signal processing methods can be utilized to reduce the overall quantity of information flowing and to move toward giving the Soldier or decision-maker the best possible targeted information while limiting the resources required to generate the decision. An overview of sensor-technology and signal-processing ongoing in the US Army will be given.

Biography

Dr. Philip Perconti is a member of the Senior Executive Service and serves as the Acting Director of the U.S. Army Research Laboratory (ARL), the Army's premier laboratory for basic and applied research and analysis. ARL conducts research and analysis in weapons and materials, sensors and electron devices, computational and information sciences, human research and engineering, vehicle technology, and survivability and lethality analysis. ARL's Army Research Office executes the Army extramural basic research program in scientific and engineering disciplines. The Laboratory consists of approximately 2,000 civilian and military employees with an annual budget of over $1 billion. Prior to this, Dr. Perconti served as the Director of the Sensors & Electron Devices Directorate of the ARL. He was responsible for leading and transitioning the Army's primary basic and applied research programs in sensors, electronics, sensor information processing, and power and energy technologies. In addition, he led ARL's S&T campaign for Materials Research. His duties included operation of unique electronics and photonics materials fabrication and characterization facilities that enable world-class, Army-relevant, component research and development. He was also responsible for planning, executing and balancing mission and customer program needs to ensure science and technology dominance for the Army.

Invited Speakers

Dr. Antonio De Maio

Transmit Adaptivity in Radar:

Radar performance is strongly dependent on the transmit waveform and its parameters which must adapted depending on the surrounding environment, radar mission, goal, and task. Waveform adaptivity is a relatively new paradigm, involving a continuous variation of the transmitted signal, with the main purpose and aim of dynamically optimizing the radar performance to fulfill the more and more stressing radar performance requirements. In this talk some new trends in transmit signal optimization will be introduced and discussed. Specifically, the design of radar waveforms, sharing appealing features and ensuring spectral coexistence with other Radio Frequency (RF) systems, will be pursued according to a rigorous framework based on modern optimization theory.

Biography

Antonio De Maio was born in Sorrento, Italy, on June 20, 1974. He received the Dr.Eng. degree (with honors) and the Ph.D. degree in information engineering, both from the University of Naples Federico II, Naples, Italy, in 1998 and 2002, respectively. From October to December 2004, he was a Visiting Researcher with the U.S. Air Force Research Laboratory, Rome, NY. From November to December 2007, he was a Visiting Researcher with the Chinese University of Hong Kong, Hong Kong. Currently, he is a Professor with the University of Naples Federico II. His research interest lies in the field of statistical signal processing, with emphasis on radar detection and optimization theory applied to radar signal processing. Dr. De Maio is a Fellow member of IEEE and the recipient of the 2010 IEEE Fred Nathanson Memorial Award as the young (less than 40 years of age) AESS Radar Engineer 2010 whose performance is particularly noteworthy as evidenced by contributions to the radar art over a period of several years, with the following citation for “robust CFAR detection, knowledge-based radar signal processing, and waveform design and diversity”.

Bio:
Daniel Clark is an Associate Professor in Sensors and Systems at Heriot-Watt University, UK. His research interests are in the development of the theory and applications of multi-object estimation algorithms for sensor fusion problems. He has made a number of key contributions to the field of multiple-object filtering that span the development of novel algorithms and methodology for multi-object tracking to the deployment and demonstration for commercial applications.

He has collaborated closely with defence organisations internationally on a range of projects in multitarget tracking spanning theoretical algorithm development to practical deployment in collaboration with Dstl, BAE Systems, Finnmechanica, Thales, DCNS (France), SAGEM Defense (France), DST (Australia) and the USAF. His algorithms have been demonstrated in trials with BAE Systems for maritime trials, where they tracked ships in the Solent from live feed from radar and electro-optic sensors.

Multi-sensor Multi-target Tracking Techniques for Space Situational Awareness

Abstract: The UK and its international partners face a range of new challenges and priorities for defence and national security for space situational awareness (SSA). In particular, there is increasing concern about the hazards of space debris and potential harm for satellites and its impact on future space exploration activities. Space debris has largely been caused by waste products from human activity in recent years, and there are now several hundred thousand objects that have the potential to cause significant damage.

It is becoming increasingly important to be able to accurately model and track a large number of objects in order to avoid harm to expensive space-related infrastructure. Advanced surveillance capabilities are needed to be able to identify and monitor activities in earth's orbit. It is critically important to these surveillance activities to be able to detect, estimate, and track multiple potential threats across a variety of platforms with different sensing characteristics. Multiple-target tracking algorithms have been developed since the 1970s, yet these methods can suffer from systematic failure due to heuristics introduced for track management.

A radically different approach to multiple-target tracking has attracted a lot of attention in recent years, called Finite Set Statistics, considers the multi-sensor multi-target tracking problem in a unified way. Estimating target populations holistically enables operators to estimate the correct number of targets in challenging environments where there may be many false alarms and the targets are not always observed. This approach led to principled low computational cost solutions that can be deployed on real-time systems, known as multi-object filters.

This talk will describe the statistical methodology used to develop multi-object filters and show how it can be used to address a range of problems. The methods will be illustrated on a range of applications including space surveillance, maritime surveillance, autonomous robotics, and cell biology. The talk will highlight the unique challenges in multi-sensor fusion for space situational awareness and outline a strategy for addressing them.

Conference Committee

General Chairs

Mike Davies, University of Edinburgh
Jonathon Chambers, Loughborough University
Paul Thomas, Dstl

Publicity and Local Arrangements Chair

Janet Forbes, University of Edinburgh

Technical Programme Committee

Yvan Petillot - Heriot-Watt University
John Soraghan - University of Strathclyde
Bernard Mulgrew - University of Edinburgh
John Thompson - University of Edinburgh
Neil Robertson - Heriot-Watt University
James Hopgood - University of Edinburgh
Daniel Clark - Heriot-Watt University
Andrew Wallace - Heriot-Watt University
Mathini Sellathurai - Heriot-Watt University
Sangarapillai Lambothoran- Loughborough University
Ian Proudler - Loughborough University
Wen-Hua Chen - Loughborough University
Francisco Aparicio-Navarro - Loughborough University
Mahesh Banavar - Clarkson University
Mark Barnard - University of Surrey
Salvatore Caporale - University of Edinburgh
Rolf Baxter - Heriot-Watt University
Emmanuel Delande - Heriot-Watt University
Ioannis Kaloskampis - Cardiff University
James Nelson - University College London
Yan Pailhas - Heriot-Watt University
Keith Thompson - University of Strathclyde
Murat Uney - University of Edinburgh
Mehrdad Yaghoobi - University of Edinburgh
Miao Yu - Loughborough University
Cemre Zor - University of Surrey
Wenwu Wang - University of Surrey
Josef Kittler - University of Surrey
Philip Jackson - University of Surrey
Stephan Weiss - University of Strathclyde
Carmine Clemente - University of Strathclyde
John McWhirter - Cardiff University

Stephen McLaughlin - Heriot-Watt University
Ayre Nehorai - Washington University
Danilo Mandic - Imperial College London
Maria S. Greco - University of Pisa
Keith Brown - Heriot-Watt University
Rodrigo C. de Lamare - University of York
Andreas Spanias - Arizona State University
Randy Moses - Ohio State University
Vaughan Clarkson - University of Queensland
Brian Sadler - Army Research Laboratory
Chris Baker - Ohio State University/Aveillant
William Moran - University of Melbourne
Douglas Cochran - Arizona State University
Kin Leung - Imperial College London
Harry Schmitt - Physical Layer Systems, LLC
Neil Cade - Selex ES
Andy Stove - Stove Specialities
Neil Gordon - DSTO
Dave Nethercott - Dstl
Jordi Barr - Dstl
Brian Barber - Dstl
Gary Heald - Dstl
Steve Moore - Dstl
Angus Johnson - Thales
Richard Brind - Atlas Elektronik
Julian Deeks - Dstl
Moeness Amin - Villanova University
Yonggang Zhang - Harbin Engineering University
Malcolm McLeod - QinetiQ
Dean Thomas - Roke Manor
George Jacob - Dstl
Hugh Griffiths - University College London
Nick Goddard - Dstl
Yulia Hicks - Cardiff University
Alasdair Hunter - Dstl
Jeffrey Neasham - Newcastle University

Table of Contents

An Adaptive Receiver Search Strategy for Electronic Support

Sabine Apfeld, Alexander Charlish, Wolfgang Koch
Dept. Sensor Data and Information Fusion
Fraunhofer FKIE
Wachtberg, Germany
Email: {sabine.apfeld, alexander.charlish, wolfgang.koch}@fkie.fraunhofer.de

***Abstract*—In this paper, a search strategy for the detection of multifunctional radar emitters is proposed. The majority of today's literature regarding this topic models the intercept problem as that of the coincidence of two or more periodic window functions. Since this model is rather simplistic, in this paper the radars' illumination patterns are described by signal-to-noise ratio time series. To optimise the search dwells executed by an electronic support receiver, a constantly updated scan period estimate is calculated using the autocorrelation. The performance of the proposed algorithm is shown in comparison to several other approaches using a simulation framework.**

I. Introduction

Intercepting the radiations of potentially threatening emitters, which usually are radars, is a common task in the field of electronic support (ES). Radars of interest might be operating in a wide range of frequencies, spanning tens of gigahertz. An intercept receiver covering the complete frequency range at the same time with a high sensitivity would be expensive, large and heavy. To overcome this problem, the frequency range of interest is usually divided into smaller bands of the receiver's instantaneous bandwidth and scanned sequentially. A schedule which defines how long and when to dwell on which band constitutes a search strategy. Normally, the emitters to be intercepted use a directional antenna and scan their surveillance region. Thus, an intercept is only possible when the receiver is tuned to the frequency of the emitter and the emitter's main beam or a sidelobe is directed towards the receiver.

In the literature, this situation is commonly modelled using two window functions, which are periodically "on" and "off" (see e.g. [1]). One of the window functions describes the points in time when the emitter illuminates the receiver and the other one specifies the events of the (omni-directional) receiver being tuned to the frequency of the emitter. When both window functions are "on" at the same time, an intercept occurs.

Modelling the illuminations by a strictly periodic window function simplifies the situation significantly. However, this simplification is not representative of modern multifunction radars. Today's radars perform searching and tracking - and sometimes even other functions like communication and missile guidance - in an interleaved manner, breaking the periodicity of the scan pattern. Moreover, electronically steered phased array antennas are capable of instantaneously steering their beams and are not limited by mechanical parts which need to be rotated. Many authors (e.g. [2]–[8]) don't mention this fact or explicitly state that they don't consider phased array antennas (e.g. [9]). In [10], the authors argue that "due to their scanning function electronic beam steering antennas produce roughly periodic illuminations". Thus, they add jitter to the scan period, but still use a window function based model. In this paper, a complete antenna pattern model of an electronically steered phased array is used, allowing the sequence of illuminations to be described by a signal-to-noise ratio (SNR) time series. In addition, window functions usually only consider the main beam of the radar. In the presented approach, the radars can be intercepted and detected through the sidelobes as well.

Section II describes the developed algorithm in detail. The method used for evaluation and the results obtained are presented in Section III. Section IV gives the conclusion.

II. Developed Algorithm

In the presented algorithm, search and tracking dwells executed by the radars are considered. It is assumed that the receiver can differentiate between the two types of dwells, which is not an unrealistic assumption since typically different waveforms are used for different tasks.

At system startup, no information is available yet so the receiver begins scanning the frequency range of interest randomly. It uses a fixed dwell time and a fixed instantaneous bandwidth. SNR is calculated as given in Eq. 1. Here, G_t represents the emitter's antenna pattern. For the omni-directional receiver, G_r is assumed constant, independent from the angle of arrival (AoA).

$$SNR = \frac{\left(\sum_{p\in P} \frac{PK(p)\cdot PW(p)}{PRI(p)}\right) \cdot \lambda^2 \cdot G_t \cdot G_r}{(4\pi R)^2 \cdot k \cdot T \cdot B \cdot L_t \cdot L_r} \tag{1}$$

p : pulse received
P : set of pulses received
$PK(p)$: peak power of pulse p
$PW(p)$: pulse width of pulse p
$PRI(p)$: pulse repetition interval of pulse p

978-1-5090-0326-6/16/$31.00 ©2016 IEEE

λ : wavelength of the pulses received
G_t : transmit antenna gain in the direction of the receiver
G_r : receiver antenna gain
R : range between receiver and emitter
k : Boltzmann constant
T : noise temperature
B : receiver's instantaneous bandwidth
L_t, L_r : transmit and receive losses

This model of the SNR assumes noncoherent integration of pulses [11], however it doesn't take losses due to not performing matched filtering into account. Introducing these losses or even considering a different detector architecture would only result in a scaling of the SNR, which would not affect the developed algorithm.

Once the SNR on a band crosses the detection threshold T_D - a parameter of the receiver - the corresponding radio frequency (RF) is added to a list of active, tentative frequencies and the receiver stays tuned to that RF band for another d dwells. If the last one of these dwells results in the highest SNR, it listens for another dwell. It does so in order to explore the times of maximum SNR as a high SNR is desirable for accurate measurements of parameters like pulse repetition interval (PRI) or pulse width.

Bands in the list of tentative frequencies are visited more often in the further operation of the receiver in order to gain more knowledge about the illumination pattern. Algorithm 1 shows the procedure for selecting the next band. The probability for choosing each tentative frequency is scaled by y according to the number of frequencies in the list of tentative RFs until the scaled value reaches a maximum z. This is done to avoid dwelling on just very few frequencies with a very high probability. Scaling parameter y and maximum value z must lie between zero and one. This part constitutes the exploration phase of the strategy.

Algorithm 1 Select the next band in exploration phase.

Input: List of all RF bands (RFs), list of tentative RFs ($tentativeRFs$), scaling parameter y, max. value z
Output: Band for the next receiver dwell.

1: $r \leftarrow random \in (0, 1)$
2: **if** $r < \min(|tentativeRFs| \cdot y, z)$ **then**
3: **return** random band $\in RFs \setminus tentativeRFs$
4: **else**
5: **return** random band $\in tentativeRFs$
6: **end if**

If the receiver intercepts a search dwell and the SNR crosses the detection threshold, the autocorrelation of the intercepted SNR time series on that band is calculated. The autocorrelation is defined as the cross-correlation of a signal with itself. In the case at hand, the SNR time series is a signal discretised by the receiver dwells.

Thus, the autocorrelation is given by

$$(f \star f)(n) = \sum_{m=-\infty}^{\infty} f^*(m) f(m+n) \qquad n = 0, \pm 1, \pm 2, ... \tag{2}$$

where f^* is the complex conjugate of f with f being the intercepted SNR.

An estimate of the radar's scan period $\hat{p}$ is given by the position of the maximum of the autocorrelation, excluding the value at lag zero, multiplied by the receiver's dwell time t_{dwell}:

$$\hat{p} = \left| \underset{n \neq 0}{\operatorname{argmax}} \{(f \star f)(n)\} \right| \cdot t_{dwell} \tag{3}$$

If the standard deviation of the last j period estimates is smaller than a threshold T_{std}, the period is declared stable and dwells are scheduled for that frequency. Moreover, the band is removed from the list of tentative RFs because the exploration phase is finished. As an intercept is desired to happen when the SNR is maximal, future dwells are planned at the time of the last recorded global SNR maximum SNR_{max} plus integer multiples of the estimated period. Since the period can only be approximate due to interleaving with tracking dwells and uncertainties in estimation, the period is updated with each new detection of the corresponding emitter and dwells are rescheduled when a new global maximum in SNR is found. To account for a shift in period, only the last k SNR values are considered. Furthermore, several dwells are executed around the expected time of the next (local) SNR maximum. When a scheduled visit of the frequency band results in a SNR smaller than the threshold

$$T_{snr} = x \cdot SNR_{max} \tag{4}$$

with x set to be between zero and one, the number of dwells scheduled for the next visit is increased by i. After s misdetections, the period estimate is reset, the scheduled dwells are deleted and the band is again added to the list of tentative RFs, thus restarting the exploration phase.

When a tracking dwell crosses the detection threshold, a histogram of the differences in time of arrival (TOA) of the pulse bursts emitted by the radar on the corresponding frequency band is built. The maximum of that histogram is used as an estimate of one of the revisit times. Note that it is assumed that distinguishing the tracking dwells for different targets is not possible. Thus, several hypotheses for revisit times are kept. Each estimated revisit time generates a schedule for visiting the corresponding band. As for the search case, the RF is deleted from the list of tentative RFs and several dwells are executed around the scheduled time. However, as the targets move, the tracking dwells might quickly point into a direction where an intercept is not possible anymore. In addition, the revisit time estimates are rather rough, so scheduled dwells and the corresponding period estimate are directly deleted after the first misdetection. If after this deletion no revisit time estimate

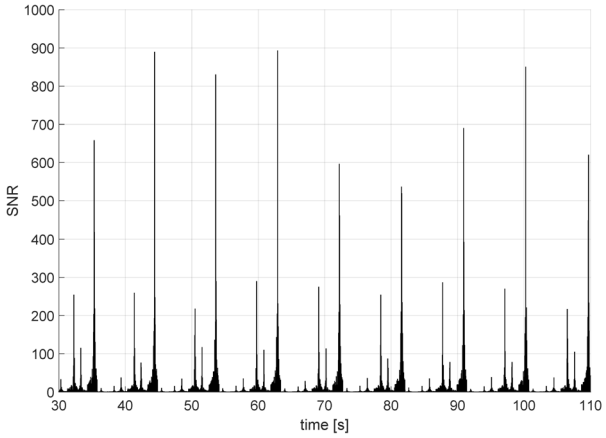

(a) Illuminations by the emitter.

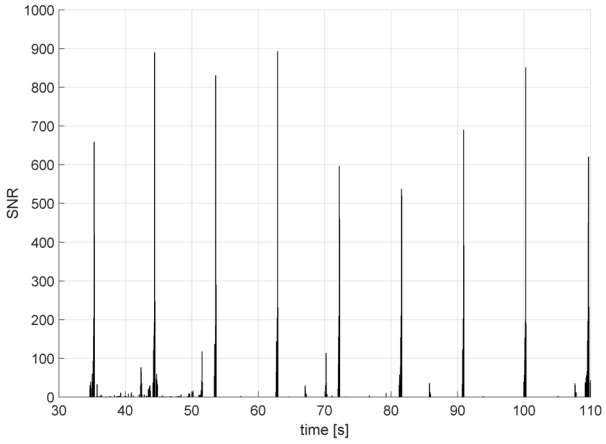

(b) Intercepted SNR at the receiver.

Fig. 1. Example of the illuminations generated by the emitter and the intercepted SNR time series at the receiver. The illumination pattern results from calculating the SNR at the receiver assuming that it's tuned the correct frequency the whole time.

exists anymore, the frequency is added again to the list of tentative RFs.

When there is no dwell scheduled, a random band is chosen with a higher probability for the frequencies in the list of tentative RFs (see Alg. 1).

Figure 1 shows an example of the illuminations generated by the emitter and the interceptions by the receiver. The SNR time series of Figure 1a depicts the illumination pattern that would result from the receiver being tuned to the frequency of the emitter for the whole time. In Figure 1b, the intercepted SNR at the receiver is shown. At (most of) the points in time where the SNR is zero, the receiver is tuned to a different frequency. From about 35 to 52 s simulated time many values are greater than zero, showing the exploration phase of the receiver in which it is tuned more often to the corresponding frequency. After the exploration phase is finished at about 52 seconds, it found a stable period estimate and starts scheduling for the local maxima of the SNR, as can be seen by the regularly spaced peaks. The dwells in between the SNR peaks

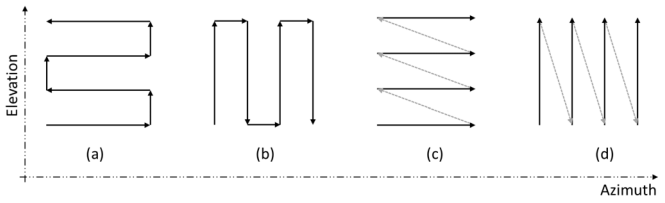

Fig. 2. Schematic representation of the scan patterns used. Grey arrows indicate a jump in beam position without dwelling.

are caused by the random search pattern used when there is no dwell scheduled. It also dwells on the known bands to be able to find a potentially undiscovered SNR maximum.

III. Evaluation & Results

In the following, the simulation framework used for evaluation as well as the results are presented.

A. Simulation Framework

Evaluation of the algorithm is performed using a simulation framework. An airborne - but for the sake of simplicity stationary - receiver tries to intercept and detect ground-based radars using phased array antennas. The stationary emitters are placed randomly in the scenario, but it is made sure that they illuminate the receiver at some point. The faces of the radars are fixed, tilted backwards a few degrees for a better surveillance of the flying targets. Those are placed randomly as well and are assigned a random moving direction and speed. Based on the target's speed, a revisit time is calculated which is used by the radars for scheduling tracking dwells. Without any targets, the emitters perform scanning of their surveillance region with one of four different patterns (see Fig. 2). When a target is in a radar's field of view, tracking dwells are inserted into the scan pattern, which is then delayed. Consequently, there is no strict periodicity in the illumination patterns anymore. Moreover, it means that more tracked targets cause an increase in aperiodicity.

Each radar uses a different operating mode for searching and tracking. These are randomly assigned and consist of different frequencies, PRIs and pulse widths. There is only one radar transmitting on each frequency at the same time. This choice was made to avoid implementing deinterleaving algorithms. Nevertheless, if assumed that the radars can be deinterleaved based on their signal characteristics, also multiple radars on the same frequency can be allowed.

During evaluation, the developed algorithm is compared to a slightly different version of itself and two other algorithms. The considered strategies are:

- Adaptive strategy: The algorithm proposed in this paper as described above.
- Adaptive, no tracking: A version of the developed algorithm without scheduling for tracking dwells, included to see the impact of estimating the track revisit times of the radars.

- Active RFs: Starts with a random search, then uses the list of active, tentative RFs and dwells on these with a higher probability, like in the exploration phase of the presented algorithm.
- Random: Just selects a random band for each dwell, but makes sure that each band is selected about the same number of times.

In each simulation, the number of targets is varied whereas the simulated time is always 5 min. Further constant parameters are the instantaneous bandwidth of 250 MHz and the dwell time of 50 ms for each receiver. Moreover, there are always 10 radars present and the scanned frequency band is 2-18 GHz. Each simulation consists of 30 runs. In each run, the scenario is created randomly but the different receiver search strategies are executed in the same scenario before creating a new one. Note that each radar illuminates the receiver at some point, but the SNR values of the illuminations don't necessarily cross the detection threshold. Thus, the results shown in the next section are to be seen as a comparison and not an absolute performance measure, since reaching a 100% detection rate might not be possible.

B. Results

In Figures 3-5 the results for the simulations are presented. Each figure shows the values for one of these criteria:

- Efficiency (%): Percentage of dwells on bands with an active emitter which resulted in a detection.
- Total number of detections over all of the simulation runs.
- Detected (%): Percentage of radars that was detected at least once.

As the results show, the two versions of the adaptive strategy always perform better in terms of efficiency and total number of detections. The percentage of radars detected at least once is best for the random strategy. This is due to the fact that the random strategy only explores the environment without exploiting the information it obtains. Thus, its efficiency as well as total number of detections are always much worse.

Exploiting the knowledge about active frequencies clearly outperforms the random strategy in terms of efficiency and number of detections. Estimating the radars' scan periods and scheduling according to the estimates increases the efficiency and the number of detections even more. However, scheduling for the tracking dwells doesn't seem to make a major difference in performance. As mentioned earlier, the revisit time estimates are rather rough and as the targets move, at some time the tracking dwells point in a direction where a detection is not possible anymore. Moreover, as opposed to the search pattern with several illuminations as the emitter sweeps past the receiver's position, the tracking dwells are only detectable for a short time instance which requires an accurate schedule. Thus, because of misdetections for scheduled tracking dwells, the algorithm directly deletes the corresponding estimates.

None of the criteria considered seems to depend on the number of targets present in the simulation environment. This might change when much more targets are present such that the radars are overloaded with tracking and only perform the required minimum of searching. An evaluation of this situation is planned for the future.

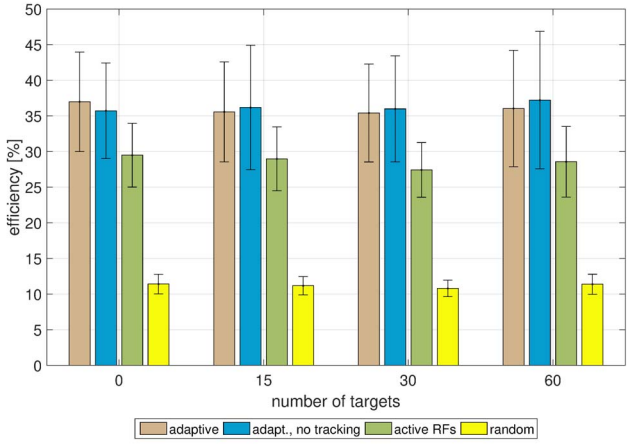

Fig. 3. Mean efficiency and standard deviation for the different search strategies and scenarios.

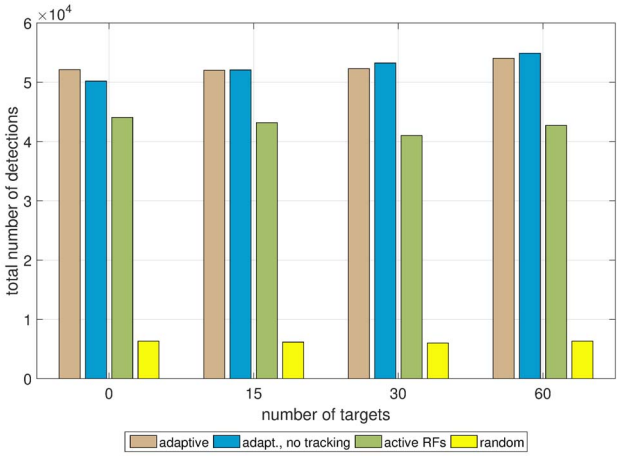

Fig. 4. Total number of detections for the different search strategies and scenarios.

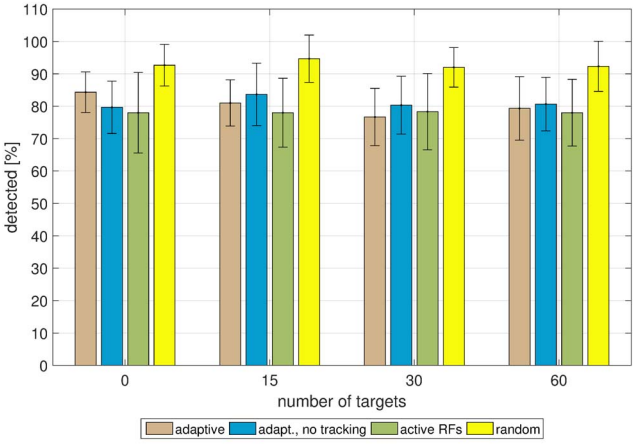

Fig. 5. Mean percentage of radars detected and standard deviation for the different search strategies and scenarios.

IV. Conclusion

An adaptive search strategy for the detection of multifunction radars has been proposed. The results obtained using simulations show that efficiency is improved significantly and more detections are achieved compared to non-adaptive algorithms. Also, modelling of the intercept/detection problem in electronic support using antenna patterns and not window functions was introduced. Using the intercepted SNR time series instead of a simple "on/off"-function allows for the detection of the radars' sidelobes. In addition, a more sophisticated use of the information collected is possible. This includes scheduling for the times of maximum SNR for an accurate measurement of the radars' waveform parameters and a more efficient use of the receiver's limited resources. The simulations demonstrate that the less complex version of the search strategy, which doesn't schedule for tracking dwells, provides an equally good performance as the complete algorithm. Thus, when regarding computational costs, the simpler version is a good approach.

References

[1] A. Self and B. Smith, "Intercept time and its prediction," *IEE Proceedings F Communications, Radar and Signal Processing*, vol. 132, no. 4, pp. 215–222, 1985.

[2] I. V. L. Clarkson, J. E. Perkins, and I. M. Y. Mareels, "Number / Theoretic Solutions to Intercept Time Problems," *IEEE Transactions on Information Theory*, vol. 42, no. 3, pp. 959–971, 1996.

[3] B. Dutertre, "Dynamic Scan Scheduling," *Proceedings of the 23rd IEEE Real-Time Systems Symposium*, pp. 327–336, 2002.

[4] E. El-Mahassni, S. Howard, and I. V. L. Clarkson, "A Markov-chain model for sensor scheduling in electronic support," *Conference Record of the Thirty-Eighth Asilomar Conference on Signals, Systems and Computers*, vol. 2, pp. 2183–2187, 2004.

[5] Y. Xun, M. Kokar, and K. Baclawski, "Using a Task-Specific QoS for Controlling Sensing Requests and Scheduling," *Proceedings of the Third IEEE International Symposium on Network Computing and Applications*, pp. 269–276, 2004.

[6] I. V. L. Clarkson, "Optimal Periodic Sensor Scheduling in Electronic Support," *Proceedings of the Defence Applications of Signal Processing*, 2005.

[7] ——, "Optimisation of Periodic Search Strategies for Electronic Support," *IEEE Transactions on Aerospace and Electronic Systems*, vol. 47, no. 3, pp. 1170–1784, 2011.

[8] C. Winsor and E. Hughes, "Optimisation and evaluation of receiver search strategies for electronic support," *IET Radar, Sonar & Navigation*, vol. 6, no. 4, pp. 233–240, 2012.

[9] Y. Xun, M. Kokar, and K. Baclawski, "Control Based Sensor Management for a Multiple Radar Monitoring Scenario," *Information Fusion*, vol. 5, no. 1, pp. 49–63, 2004.

[10] H. Glaude, C. Enderli, J.-F. Grandin, and O. Pietquin, "Learning of Scanning Strategies for Electronic Support using Predictive State Representations," *IEEE International Workshop on Machine Learning for Signal Processing*, pp. 1–6, 2015.

[11] R. Wiley, *ELINT: The Interception and Analysis of Radar Signals*. Artech House, 2006.

New environmental dependent modelling with Gaussian particle filtering based implementation for ground vehicle tracking

Miao Yu, Yali Xue, Runxiao Ding, Hyondong Oh and Wen-Hua Chen
Department of Aeronautical and Automotive Engineering,
Loughborough University, UK
{m.yu, y.xue, r.ding, h.oh, w.chen}@lboro.ac.uk

Jonathon Chambers
School of Electrical and Electronic Engineering,
Newcastle University, UK
jonathon.chambers@ncl.ac.uk.

***Abstract*—This paper proposes a new domain knowledge aided Gaussian particle filtering based approach for the ground vehicle tracking application. Firstly, a new form of modelling is proposed to reflect the influences of different types of environmental domain knowledge on the vehicle dynamic: i) a non-Markov jump model is applied with multiple models while transition probabilities between models are environmental dependent ii) for a particular model, both the constraints and potential forces obtained from the surrounding environment have been applied to refine the vehicle state distribution. Based on the proposed modelling approach, a Gaussian particle filtering based method is developed to implement the related Bayesian inference for the target state estimation. Simulation studies from multiple Monte Carlo simulations confirm the advantages of the proposed method over traditional ones, from both the modelling and implementation aspects.**

I. Introduction

Ground vehicle tracking is an important preliminary step in many applications such as surveillance, advanced driver assistance systems (ADAS) and autonomous vehicles. Many model based state estimation methods (i.e. Kalman or particle filtering based methods [1]), have been proposed for vehicle tracking. However, the majority of methods in [1] assume an open field environment in which the tracked vehicle(s) could move freely. This contradicts with the realistic scenario where the motion of the ground vehicle(s) is often affected by its operational environment. Information from the environment could be taken as domain knowledge and exploited in the development of tracking algorithms in order to enhance tracking quality.

Different approaches have been proposed to exploit domain knowledge for ground vehicle tracking. The most apparent domain knowledge is the road constraint information such as the constrained region imposed by a road map. Studies on road network-aided ground vehicle tracking have been reported in different works such as [2], [3] and [4]. In these works, different state estimation algorithms (such as the Gaussian (s) approximation filtering method in [2] and [4], and particle filtering method [3]) have been applied together with the road constraint information for the state estimation. Besides, the manoeuvre of a vehicle will also be affected by its surrounding environment. For example, a vehicle is likely to accelerate to overtake. To incorporate domain knowledge related to manoeuvre determination, [5] and [6] consider a non-Markov jump modelling system originally proposed in [7] for vehicle tracking. Multiple state models are applied to represent different possible vehicle movements. State-dependent model transition probabilities are then adopted to model vehicle manoeuvre type changes with respect to environmental conditions.

In our work, a new domain knowledge aided method is proposed for ground vehicle tracking. Compared with the aforementioned works, domain knowledge is exploited in a more comprehensive way; besides, a more efficient filtering algorithm is applied for the state estimation. Firstly, the non-Markov hybrid model framework in [7] is proposed to model multiple vehicle behaviours. For a particular dynamic model, both constraints and forces [8] are incorporated to refine the target state distribution. Based on the proposed model approach, a Gaussian particle filtering [9] based state dependent interactive multiple model Gaussian particle filtering (SD-IMMGPF) method is proposed. Compared with the traditional generic particle based filtering approach for the hybrid non-Markov jump model implementation as in [7], the measurement information is exploited for constructing an importance function to generate more effective particles.

The structure of this paper is listed as follows: The developed domain knowledge aided model is proposed in Section II. Bayesian inference and the proposed SD-IMMGPF approach are presented in Section III. Simulations in Section IV present the comparison results between the proposed method and others. Final conclusions and future works are presented in Section V.

II. Proposed environmental dependent model

In this section, we propose a new environmental dependent model approach for ground vehicle tracking, which exploits different environmental information in a comprehensive way for both the manoeuvre type determination and state dynamic/distribution refinement.

In a realistic scenario, a vehicle will move with different manoeuvre types, which can not be reflected by a single state model. In this way, multiple state models have been exploited for target tracking as in [10] and [11]. However,

978-1-5090-0326-6/16 /$31.00 ©2016 Crown

these approaches assume a Markov jump model, with transition probabilities between different state models being constant without considering any environmental information. However, the manoeuvre type of a certain target is actually environmentally related. For example, a vehicle will commonly overtake when it approaches another vehicle with a high speed and turn when it comes to a bend road segment. To this end, the non-Markov jump modelling framework as in [7] is adopted, for which the transition probabilities between different models are not constant but modeled in a state dependent way related to the target's surrounding environmental conditions.

A general dynamic model in the non-Markov jump modelling framework can be represented as:

$$\mathbf{x}_t = f(\mathbf{x}_{t-1}) + \mathbf{w}_t \tag{1}$$

where $\mathbf{x}_t$ represents the state vector, which usually includes the position and velocity for the vehicle tracking problem; $\mathbf{w}_t$ is generally known as the process noise term, which represents the model uncertainty; $f(\cdot)$ represents a dynamic function reflecting the desired target dynamics.

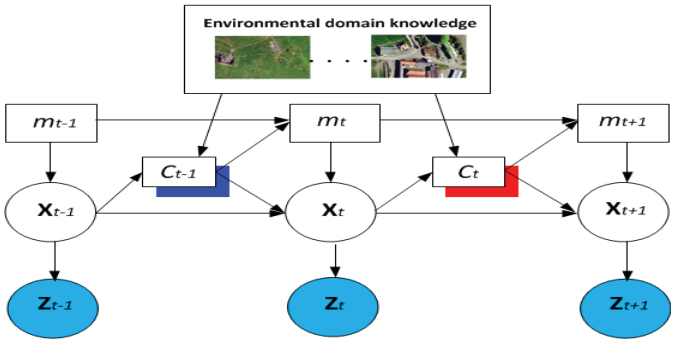

Fig. 1. The proposed modelling framework. Related parameters are defined as: $\mathbf{X}_t$: state vector, $\mathbf{Z}_t$: measurement vector, m_t: model index and C_t: surrounding environmental conditions of a target, which is dependent on the target state (i.e., position and velocity) and environmental domain knowledge (i.e., road map information, geographic data, moving obstacles information, etc.).

Currently most models (as in [12]) for target tracking do not consider any environmental information. So the predicted state distribution by (1) may contradict with the realistic environmental conditions (for example, the predicted position of a vehicle may be outside the road boundary). In this work, a new modelling framework is proposed as shown in Fig. 1. The non-Markov jump modelling framework is adopted. Furthermore, the target's surrounding environmental condition does not only determine the manoeuvre type but also refines a particular dynamic model and corresponding state distribution. The refinement of the state distribution is achieved by introducing *forces* and *constraints*.

A. Force based environmental effects modelling

In realistic scenarios, targets' movements are affected by the surrounding environment. For example, a vehicle keeps away from the road border to avoid collisions or it may be attracted by certain objects (such as the lane centreline).

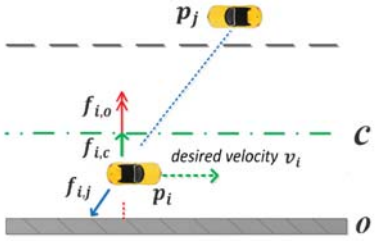

Fig. 2. The illustration of different forces for modelling environmental effects. $\mathbf{f}_{i,j}$ models the repulsive effect between vehicles i and j, $\mathbf{f}_{i,o}$ models the repulsive effect between the vehicle i and road boundary o and $\mathbf{f}_{i,c}$ models the effect that a vehicle tends to move along with the lane centreline c.

In [8], a force based method has been proposed to model such repulsive/attractive effects on pedestrians posed by their surrounding environment. This idea is exploited in this work for modelling the environmental influences on the vehicle dynamics. As in Fig. 2, different types of 'virtual forces' have been applied, which model the repulsive/attractive effects on a vehicle determined by its surrounding environmental conditions.

Same exponential force definition forms are applied to formulate the repulsive/attractive forces as in [8], with:

$$\begin{aligned} \mathbf{f}_{i,j}^{repulsive} &= a \cdot \exp(-b \cdot d)\mathbf{n}_{i,j} \\ \mathbf{f}_{i,j}^{attractive} &= a' \cdot (1 - \exp(-b' \cdot d))\mathbf{n}_{i,j}, \end{aligned} \tag{2}$$

where $\mathbf{f}_{i,j}^{repulsive}$ and $\mathbf{f}_{i,j}^{attractive}$ represent repulsive and attractive forces between objects i and j; a, b, a' and b' are constant parameter values; $\mathbf{n}_{i,j}$ ($\mathbf{n}_{j,i}$) represents the unit vector pointing from object i to j (j to i).

Forces from different objects are summed to a total one (denoted as $\mathbf{f}^e$) which represents the effect of the surrounding environmental conditions on the vehicle. In this way, an additional acceleration term $\mathbf{a}^e = \frac{\mathbf{f}^e}{m}$ is introduced and the original model of (1) is thus modified to reflect the influence of the environment on dynamic modelling. In general, the modified dynamic model can be represented as:

$$\mathbf{x}_t = f(\mathbf{x}_{t-1}) + I(\mathbf{a}^e) + \mathbf{w}_t \tag{3}$$

where the term $I(\mathbf{a}^e)$ is a function of $\mathbf{a}^e$, which is dependent on the particular dynamic model definition as in [12].

B. Constraint information

In reality, there are constraints existing in the realistic environment, which can be further applied to refine the state distribution. We denote the distribution determined by the force based model (3) as $p(\mathbf{x}_t)$, by incorporating the constraint information the distribution is truncated as:

$$p_C(\mathbf{x}_t) = \begin{cases} \frac{p(\mathbf{x}_t)}{\xi_t}, & \mathbf{x}_t \in C \\ 0, & otherwise \end{cases} \tag{4}$$

where $p_C(\mathbf{x}_t)$ represents the truncated distribution, C represents the constrained region and ξ_t is calculated as $\xi_t = \int_C p(\mathbf{x}_t) d\mathbf{x}_t$. The probability value which is out of the con-

straint region becomes zero. In this way, the uncertainty of the state distribution is further reduced.

III. State dependent interactive multiple model Gaussian particle filtering

Based on the new modelling approach as defined in the previous section and a proper measurement model, a state dependent interacting multiple model Gaussian particle filtering (SD-IMMGPF) algorithm is developed for the state estimation. Different from the generic SD-IMMPF method [7], the proposed algorithm applies Gaussian particle filtering for every mode-matched filter with an importance function constructed with both the state dynamics and measurement information, which generates more effective particles.

The proposed SD-IMMGPF algorithm is based on the exact Bayesian inference framework for a multiple model system, whose overall process is divided into four steps: mode mixing, state interaction, evolution and correction.

Mode mixing: The mode mixing is related to the evolution of the model probability between consecutive discrete time instances $t-1$ and t. Using the law of total probability, we have:

$$\begin{aligned} p(m_t = s|\mathbf{Z}_{t-1}) &= \sum_{r\in\mathcal{M}} p(m_t = s, m_{t-1} = r|\mathbf{Z}_{t-1}) \\ &= \sum_{r\in\mathcal{M}} p(m_t = s|m_{t-1} = r, \mathbf{Z}_{t-1}) p(m_{t-1} = r|\mathbf{Z}_{t-1}), \end{aligned} \tag{5}$$

where m_t represents the dynamic model index variable whose value m or r could be any one element in the set $\mathcal{M}$, which represents the model index ensemble. $\mathbf{Z}_{t-1}$ represents the measurements collection $\{\mathbf{z}_1, ..., \mathbf{z}_{t-1}\}$ during previous time instances. And $p(m_t = s|m_{t-1} = r, \mathbf{Z}_{t-1})$ can further be decomposed as:

$$\begin{aligned} &p(m_t = s|m_{t-1} = r, \mathbf{Z}_{t-1}) \\ &= \int \pi^E_{rs}(\mathbf{x}_{t-1}) \cdot p(\mathbf{x}_{t-1}|m_{t-1} = r, \mathbf{Z}_{t-1})\, \mathrm{d}\mathbf{x}_{t-1}. \end{aligned} \tag{6}$$

where $\pi^E_{rs}(\mathbf{x}_{t-1})$ represents the environmental information related state-dependent model transition probability between models r and s, which is problem-specific.

State interaction: State interaction generates the initial mode-conditioned density $p(\mathbf{x}_{t-1}|m_t = s, \mathbf{Z}_{t-1})$. According to the conditional probability relation and the law of total probability, one has:

$$p(\mathbf{x}_{t-1}|m_t = s, \mathbf{Z}_{t-1}) = \frac{\sum_{r\in\mathcal{M}} \pi^E_{rs}(\mathbf{x}_{t-1}) \cdot p(\mathbf{x}_{t-1}, m_{t-1} = r|\mathbf{Z}_{t-1})}{p(m_t = s|\mathbf{Z}_{t-1})}. \tag{7}$$

Domain knowledge aided state evolution: The state evolution step is to propagate the mode-conditioned state density from $t-1$ to t by the dynamic model. Given the initial density is provided in (7) and the s-th environmental information aided dynamic model, the mode-conditioned prior distribution $p(\mathbf{x}_t|m_t = s, \mathbf{Z}_{t-1})$ at t can be calculated as:

$$\begin{aligned} &p(\mathbf{x}_t|m_t = s, \mathbf{Z}_{t-1}) \\ &= \int p(\mathbf{x}_t|\mathbf{x}_{t-1}, m_t = s, \mathbf{Z}_{t-1}) p(\mathbf{x}_{t-1}|m_t = s, \mathbf{Z}_{t-1})\, \mathrm{d}\mathbf{x}_{t-1}. \end{aligned} \tag{8}$$

where $p(\mathbf{x}_t|\mathbf{x}_{t-1}, m_t = s, \mathbf{Z}_{t-1})$ is determined by the force aided dynamic model (3) and constraints (4).

Correction: Finally, the updated measurement is incorporated to correct the prior by following Bayes' rule:

$$\begin{aligned} p(\mathbf{x}_t, m_t = s|\mathbf{Z}_t) &\propto p(\mathbf{z}_t|\mathbf{x}_t, m_t = s) p(\mathbf{x}_t|m_t = s, \mathbf{Z}_{t-1}) \\ &\cdot p(m_t = s|\mathbf{Z}_{t-1}). \end{aligned} \tag{9}$$

The state estimation at time t can then be derived from the updated posterior distribution $p(\mathbf{x}_t, m_t = s|\mathbf{Z}_t)$.

A. SD-IMMGPF implementation

The SD-IMMGPF algorithm is then proposed to implement the above Bayesian inference. Initially, it starts at time $t-1$ with the set of weighted particles $\{\mathbf{x}^{r,k}_{t-1}, w^{r,k}_{t-1}; r \in \mathcal{M}, k \in \{1, \ldots, N\}\}$ to approximate the probability $p(\mathbf{x}_{t-1}, m_{t-1} = r|\mathbf{Z}_{t-1})$. Based on this, the Bayesian inference procedure is implemented as follows:

Mode mixing implementation: Prior mode probability in (5) is approximated with generated particles as:

$$p(m_t = s|\mathbf{Z}_{t-1}) \approx \sum_{r\in\mathcal{M}} \sum_{k=1}^{N} \pi^E_{rs}(\mathbf{x}^{r,k}_{k-1}) \cdot w^{r,k}_{t-1} \triangleq \Lambda^s_{t-1}, \tag{10}$$

where Λ^s_{t-1} is defined to facilitate the rest of the derivation.

State interaction implementation: The state interaction process can be implemented by inserting particles at $t-1$ with the different mode index r, into (7) such that

$$\begin{aligned} &p(\mathbf{x}_{t-1}|m_t = s, \mathbf{Z}_{t-1}) \approx \\ &\sum_{r\in\mathcal{M}} \sum_{k=1}^{N} \pi^E_{rs}(\mathbf{x}^{r,k}_{t-1}) w^{r,k}_{t-1} \delta(\mathbf{x}_{t-1} - \mathbf{x}^{r,k}_{t-1}) / \Lambda^s_{t-1}. \end{aligned} \tag{11}$$

Evolution and correction implementation:

For every mode a Gaussian particle filtering (GPF) [9] based approach is exploited. An importance function which is a Gaussian approximation of the mode-conditioned posterior distribution $p(\mathbf{x}_t|m_t = s, \mathbf{Z}_t)$ is constructed, from which effective particles are generated. Firstly, the mean μ^s_{t-1} and covariance Σ^s_{t-1} of a Gaussian distribution to approximate $p(\mathbf{x}_{t-1}|m_t = s, \mathbf{Z}_{t-1})$ are obtained as:

$$\begin{aligned} \mu^s_{t-1} &= \sum_{r\in\mathcal{M}} \sum_{k=1}^{N} \pi^E_{rs}(\mathbf{x}^{r,k}_{t-1}) w^{r,k}_{t-1} \mathbf{x}^{r,k}_{t-1} / \Lambda^s_{t-1} \\ \Sigma^s_{t-1} &= \sum_{r\in\mathcal{M}} \sum_{k=1}^{N} \pi^E_{rs}(\mathbf{x}^{r,k}_{t-1}) w^{r,k}_{t-1} (\mathbf{x}^{r,k}_{t-1} - \mu^s_{t-1}) \cdot (\mathbf{x}^{r,k}_{t-1} - \mu^s_{t-1})^T / \Lambda^s_{t-1} \end{aligned} \tag{12}$$

Based on the domain knowledge aided dynamic model and measurement model, the mean and covariance are then updated to obtain μ^s_t and Σ^s_t at time instance t, which determine a Gaussian distribution $N(\mathbf{x}_t|\mu^s_t, \Sigma^s_t)$ as an approximation of the distribution $p(\mathbf{x}_t|m_t = s, \mathbf{Z}_t)$. Different algorithms can be applied for the updating, in our work, the truncated

unscented Kalman filtering (t-UKF) scheme as in [13] is adopted, which exploits both the constraint information and unscented transformation to better deal with the non-linearities in both dynamic and measurement models.

A new set of particles $\{\mathbf{x}_t^{i,s}\}_{i=1,\ldots,N}$ is sampled from $N(\mathbf{x}_t|\mu_t^s, \Sigma_t^s)$. According to the concept of importance sampling in [1] and (9), the posterior distribution $p(\mathbf{x}_t, m_t = s|\mathbf{Z}_t)$ is approximated as:

$$p(\mathbf{x}_t, m_t = s|\mathbf{Z}_t) \approx \sum_i w_t^{i,s}\delta(\mathbf{x}_t - \mathbf{x}_t^{i,s}) \tag{13}$$

with particle weights $\{w_t^{i,s}\}_{i=1,\ldots,N}$ being estimated as:

$$w_t^{i,s} \propto \frac{p(\mathbf{z}_t|\mathbf{x}_t^{i,s}, m_t = s)N(\mathbf{x}_t^{i,s}|\mu_{t|t-1}^s, \Sigma_{t|t-1}^s)p(m_t = s|\mathbf{Z}_{t-1})}{N(\mathbf{x}_t^{i,s}|\mu_t^s, \Sigma_t^s)} \tag{14}$$

where $N(\mathbf{x}_t^s|\mu_{t|t-1}^s, \Sigma_{t|t-1}^s)$ is a Gaussian approximation of $p(\mathbf{x}_t|m_t = s, \mathbf{Z}_{t-1})$ and $p(\mathbf{z}_t|\mathbf{x}_t^s, m_t = s)$ is a measurement likelihood function determined by a particular measurement model. From the obtained particles and corresponding weights, both the state estimation and the s-th model probability can be estimated as:

$$\begin{aligned} \hat{\mathbf{x}}_t &= \sum_{s\in\mathcal{M}}\sum_{i=1}^{N} w_t^{i,s}\mathbf{x}_t^{i,s} \\ p(m_t = s) &= \sum_{i=1}^{N} w_t^{i,s} \end{aligned} \tag{15}$$

IV. Simulation Studies

The proposed method is tested in a simulated scenario as shown in Fig. 3, with two vehicles being simulated to move along two road segments in a total of 30s. The first vehicle is simulated to move with a constant velocity of 10 (m/s) along the straight road segment for 27.5 (s) after which a turning manoeuvre is performed with angular velocity 0.2 (rad/s) for 2.5 (s). The second vehicle firstly moves with a constant velocity of 12.5 (m/s) on the straight road segment for 8s before it begins to overtake the first vehicle. After 7 seconds, vehicle 2 overtakes vehicle 1 and moves again with 12.5 (m/s) for 7s along the straight segment. Then it begins to move along the bend road segment with an angular velocity of 0.2 (rad/s).

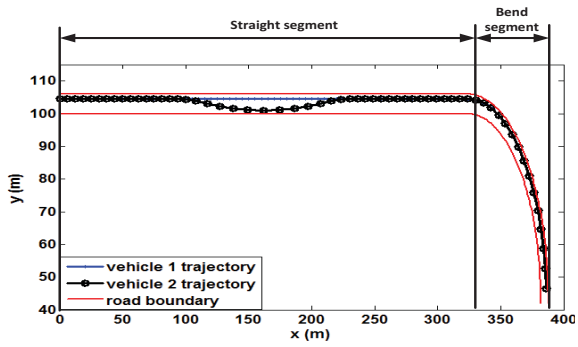

Fig. 3. Simulated vehicles trajectories.

Multiple dynamic models as in [12] are applied to model different manoeuvre types of vehicles, which include: a constant velocity (CV) model with a low process noise intensity level for modelling the CV manoeuvre, a CV model with a high process noise intensity level for modelling the overtaking manoeuvre and a constant turning (CT) model for modelling the turning manoeuvre. A sensor positioned at [200,30] (m) is applied to measure the range r_t and bearing angle θ_t of a particular vehicle with:

$$\mathbf{y}_t = \begin{bmatrix} r_t \\ \theta_t \end{bmatrix} = \begin{bmatrix} \sqrt{(x_s - x_t)^2 + (y_s - y_t)^2} \\ \arctan(\frac{y_s - y_t}{x_s - x_y}) \end{bmatrix} + \mathbf{n}_k \tag{16}$$

where $[x_t, y_t]$ represents a target's position at time instance t, $[x_s, y_s]$ represents the sensor position and $\mathbf{n}_t$ represents the measurement noise. In our work, we assume it as a Gaussian distribution with zero means and covariance $\begin{bmatrix} 5^2(m^2), & 0 \\ 0, & 0.02^2(rad)^2 \end{bmatrix}$. Currently, we assume that the sensor always receives the two vehicles' measurements without any measurement association ambiguities.

Based on the simulated scenario, dynamic and measurement models, the proposed method is applied for the vehicle tracking. The tracking results are compared with other methods from both *model* and *filtering algorithm*.

Model comparison: For the proposed modelling approach, the transition probabilities between different models are defined with respect to distances between a target and its surrounding objects (such as another vehicle and the bend road entry). The road region is applied as the constraints and forces are used to represented the repulsive effects of vehicle-to-vehicle and vehicle-to-boundary. These forces are defined in the form of (2) with the related parameters being selected empirically for the simulation study.

Comparisons are made between different modelling frameworks, including Markov jump (MJ) model, non-Markov jump (NMJ) model, non-Markov model with constraint information (CNMJ) and the proposed non-Markov modelling framework with both constraints and forces (FCNMJ). For a fair comparison, the same Gaussian particle filtering based approach is applied for every modelling method and the number of particles for every dynamic mode is chosen as $N = 300$. 100 Monte-Carlo simulations are performed. For every vehicle, the averaged position root-mean-square-errors (RMSEs) for every time instance is plotted in Fig. 4 corresponding to every modelling method. While the averaged RMSEs of the tracked trajectories compared with ground truth one are shown in Table I. From the results, we can see that the proposed modelling method exploiting the domain knowledge in the most comprehensive way, achieves the most accurate result for the trajectory tracking (as in Table I with the smallest averaged RMSEs for both vehicles) and lowest RMSEs during the majority of the time as shown in Fig. 4.

Filtering algorithms comparison: We compare different Bayesian inference implementation algorithms. The proposed modelling framework as in Section II is adopted, with the generic particle filtering based SD-IMMPF (N=3000 for one

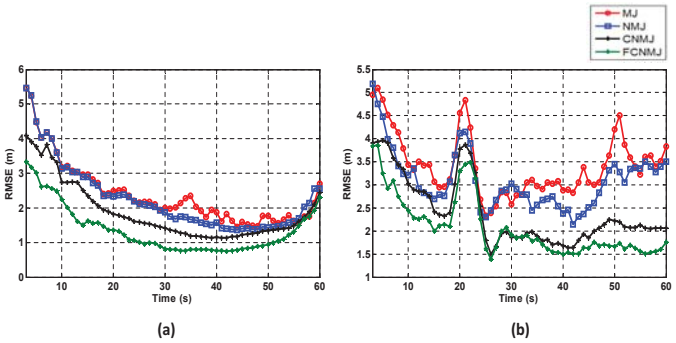

Fig. 4. Position RMSEs comparisons for vehicle 1 (a) and vehicle 2 (b) by different modelling approaches.

TABLE I
AVERAGED POSITION RMSES (M) COMPARISONS FOR DIFFERENT MODELLING APPROACHES

	MJ	NMJ	CNMJ	FCNMJ
Vehicle 1 RMSE (m)	2.52	2.43	2.17	1.51
Vehicle 2 RMSE (m)	3.45	3.25	2.42	2.10

dynamic model) and SD-IMMGPF approaches (N=300 for one dynamic model) implementation approaches being compared. The same state model is applied for these two approaches and the same 100 Monte-Carlo simulations have been performed for RMSEs analysis. From the comparison results as shown in Fig. 5 and Table II, we can see that the SD-IMMGPF approach achieves better performance, with smaller RMSEs being obtained (especially for vehicle 1 with around 45% of the RMSE reduction as implied in Table II) with a smaller number of particles and a low computational cost. The reason behind it is that the SD-IMMGPF approach exploits both the constraint and measurement information for more effective sampling.

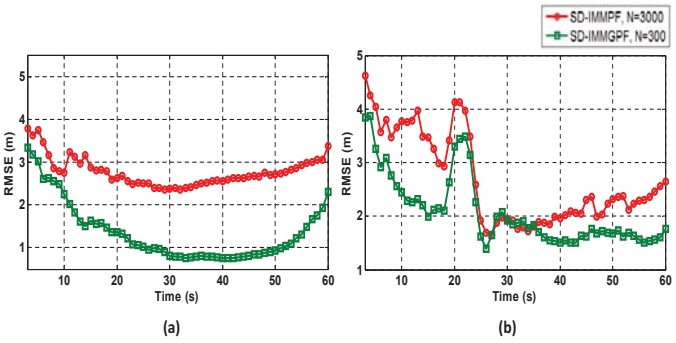

Fig. 5. Position RMSEs comparisons for vehicle 1 (a) and vehicle 2 (b) for different filtering algorithms

V. CONCLUSION

In this work, a new domain knowledge aided tracking method is proposed. A new environmental dependent model is developed. Multiple models are applied with the state dependent probabilities being used to model the realistic vehicle manoeuvre transitions. Both the constraint and force information are applied to refine the dynamic model and state distribution. Based on the modelling framework, a SD-IMMGPF approach is applied to implement the related Bayesian inference for the state estimation. Simulation studies show the advantages of the proposed method from both the modelling and implementation algorithm aspects. In the future, the proposed algorithm will be extended to a more complicated scenario with miss detections/false alarms and measurements association ambiguities.

TABLE II
AVERAGED POSITION RMSES (M) COMPARISONS FOR DIFFERENT FILTERING ALGORITHMS

	SD-IMMPF, N=3000	SD-IMMGPF, N=300
Vehicle 1 RMSE (m)	2.77	1.51
Vehicle 2 RMSE (m)	2.65	2.10
Computational time (s)	3.6	0.8

ACKNOWLEDGMENT

This work was supported by the UK Engineering and Physical Sciences Research Council (EPSRC) and the Ministry of Defence (MOD) University Defence Research Collaboration in Signal Processing under the grant number EP/K014307/1.

REFERENCES

[1] B. Ristic, S. Arulampalam, and N. Gordon, *Beyond the Kalman filter Particle filters for tracking applications*, Norwood, MA: Artech House, 2004.

[2] M. Ulmke and W. Koch, "Road-map assisted ground moving target tracking," *Aerospace and Electronic Systems, IEEE Transactions on*, vol. 42, no. 4, pp. 1264–1274, 2006.

[3] M. Yu, C. Liu, W. Chen, and J. Chambers, "A Bayesian framework with an auxiliary particle filter for GMTI-based ground vehicle tracking aided by domain knowledge," *In proceeding of SPIE 9091, Signal Processing, Sensor/Information Fusion, and Target Recognition XXIII*, vol. 9091, no. 1, pp. 1–14, 2014.

[4] H. Oh, H. Shin, S. Kim, A. Tsourdos, and B. White, "Airborne behaviour monitoring using Gaussian processes with map information," *IET Radar, Sonar and Navigation*, vol. 7, no. 4, pp. 393–400, 2013.

[5] T. Gindele, S. Brechtel, and R. Dillmann, "A probabilistic model for estimation driver behaviors and vehicle trajectory in traffic environment," in *13th International IEEE Annual Conference on Intelligent Transportation Systems, Madeira Island, Portugal*, 2010.

[6] G. Agamennoni, J. Nieto, and E. Nebot, "Estimation of multivehicle dynamics by considering contextual information," *IEEE Transactions on Robotics*, vol. 28, no. 4, pp. 855–870, 2012.

[7] H. Blom and E. Bloem, "Exact Bayesian and particle filtering of stochastic hybrid systems," *IEEE Transactions on Aerospace and Electronic Systems*, vol. 43, no. 1, pp. 55–70, 2007.

[8] D. Helbing, I. Farkas, and T. Viscek, "Simulating dynamic features of escape panic," *Nature*, vol. 407, pp. 487–490, 2000.

[9] J. Kotecha and P. Djuric, "Gaussian Particle Filtering," *IEEE Transactions on Signal Processing*, vol. 51, no. 10, pp. 2592–2601, 2003.

[10] E. Mazor, A. Averbuch, Y. Bar-Shalom, and J. Dayan, "Interacting Multiple Model Methods in Target Tracking: A Survey," *IEEE Transactions on Aerospace and Electronic Systems*, vol. 34, no. 1, pp. 103–123, 1998.

[11] Y. Boers and J. Driessen, "Interacting multiple model particle filter," *IEE Procceeding of Radar, Sonar and Navigation*, vol. 150, no. 5, pp. 344–349, 2003.

[12] X. Li and P. Jilkov, "Survey of maneuvering target tracking. part i: Dynamic models," *IEEE Trans. on Aerospace and Electronic Systems*, vol. 39, no. 4, pp. 1333–1364, 2003.

[13] O. Straka, J. Dunik, and M. Simandl, "Truncation nonlinear filters for state estimation with nonlinear inequality constraints," *Automatica*, vol. 48, no. 2, pp. 273–286, 2012.

Robust Detection of micro-UAS drones with L-band 3-D Holographic Radar™

Mohammed Jahangir and Chris Baker
Aveillant Limited
300 Science Park
Cambridge, UK
{mohammed.jahangir, chris.baker}@aveillant.com

***Abstract*—Unmanned Aerial Systems (UAS) are pilotless aircraft (drone) and are characterized by having very small radar cross-sections, relatively slow motion profiles and low operating altitudes compared with manned aircraft. As a direct consequence they are considerably more difficult to detect and track. This is exacerbated in traditional 2-D scanning radar which struggle to find a compromise between the conflicting needs to simultaneously have short re-visit times and high Doppler resolution. Here, we use Holographic Radar™ (HR) that employs a 2-D antenna array and appropriate signal processing to create a multibeam, 3-D, wide-area, staring surveillance sensor capable of achieving high detection sensitivity, whilst providing fine Doppler resolution with update rates of fractions of a second. The ability to continuously dwell on targets over the entire search volume enables HR to achieve a level of processing gain sufficient for detection of very low signature targets such as miniature UAS against a background of complex stationary and moving clutter. In this paper trials results are presented showing detection of a small hexacopter UAS using a 32 by 8 element L-Band receiver array. The necessary high detection sensitivity means that many other small moving targets are detected and tracked, birds being a principle source of clutter. To overcome this a further stage of processing is required to discriminate the UAS from other moving objects. Here, a machine learning decision tree classifier is used to reject non-drone targets resulting in near complete suppression of false tracks whilst maintaining a high probability of detection for the drone.**

Keywords—multi-beam, 3D, Doppler discrimination, air surveillance, UAS

I. INTRODUCTION

Conventional wide-area non-cooperative ground-to-air surveillance systems such as Primary Surveillance Radar (PSR) use a narrow beam scanning antenna to achieve all-round azimuth coverage. Scanning radars have to find a compromise between time on target and update rate. This can impede such systems from reliably detecting very weak signatures targets buried in strong non-stationary clutter. The central issue is that the sensor fails to collect sufficient information to distinguish targets of interest from interfering clutter. Holographic Radar™ (HR) [1] overcomes such short comings through achieving 100% time on target using a 2-D static multiple simultaneous receive beam antenna array. As the sensor is staring, the update rate can be very high (ultimately limited by the PRF) and as a direct consequence the radar is able to maintain very high detection and more importantly, discrimination performance even in the most challenging clutter environments.

In most air surveillance radar systems the processing algorithms are optimized for conventional aircrafts that have an RCS in the range of 1-100 m^2, have relatively smooth trajectories and operate at high altitudes thus making it easier to discriminate such targets from ground clutter and other surface targets. Micro-Unmanned Air Systems (Micro-UAS) also referred to as drones, have an RCS of up to 1000 smaller and tend to operate over shorter distances, slower speeds, lower altitudes and have more variable position, velocity and acceleration parameters, all acting collectively to make Micro-UAS targets much more difficult to detect.

The Aveillant HR technology [2, 3], has some crucial design elements that make it well suited to the detection of micro-UAS. A 2-D array provides vertical separation, the staring antenna enables longer coherent integration and thus very fine micro-Doppler resolution. This, in turn, provides for better detection and discrimination of slow moving objects against ground and non-stationary clutter. Initial experiments have been conducted with the HR to establish the potential for providing both a robust surveillance solution against micro-UASs as well as providing the key technology to enable their safe use for legitimate purposes [4]. Increased detection sensitivity against low observable targets extenuates the problem of false reports of moving targets such as birds, surface objects, clutter etc. The suppression of these confuser tracks are very crucial to ensuring that the surveillance sensor is able to provide reliable reporting of drone tracks alone. In this paper machine learning techniques are utilized to filter out the false targets. We report results achieved in discriminating micro-UAS from the huge numbers of false targets typical in detecting objects with such a low RCS.

The remainder of the paper is organized as follows. Section II provides an overview of the HR sensor and describes the HR prototype used to make real radar measurements. Section III reports on the detection performance that the HR is able to achieve for low observable targets compared to conventional air targets. Section IV describes the decision tree algorithm used for drone discrimination and the classification performance achieved with real drone trials data is reported in Section V. Finally, the overall conclusions are outlined in Section VI.

978-1-5090-0326-6/16/$31.00 ©2016 IEEE

II. Holographic Radar™ System Overview

There are three uniquely distinct elements to the HR architecture. The transmitter uses a broadbeam antenna to illuminate the whole of the desired search volume. It uses a static multi-element 2-D receiver array to also cover the whole of the illuminated search volume. The receiver array is digitized at each element level and processing allows to form multiple simultaneous receive beams. A 64-element version, using an 8x8 grid configuration for the receiver array, is pictured schematically in Fig. 1.

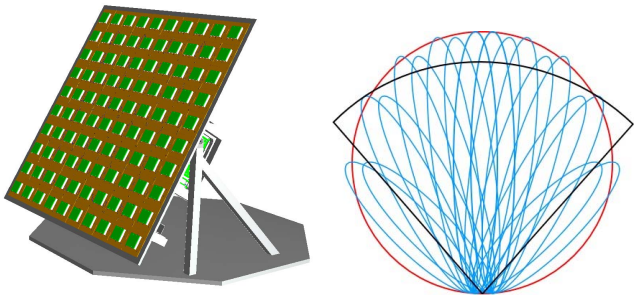

Fig. 1. *Example of the 64 element 2-D receiver array arranged in an 8x8 grid with an outer ring of dummy receivers.The plot on right shows a plan view of the nominal transmit and receiver beam patterns.*

With this fixed arrangements of beams, the sensor is able to continuously stare in all directions simultaneously thus enabling fine Doppler resolution via long and controllable dwell times. This fine Doppler resolution is utilized to exploit the target micro-Doppler signature characteristics over extended durations [5].

Naturally this results in a larger volume of data to be processed. The problem of processing such very large data volumes (~512 MB/s) in real-time is straight forward using current GPU processor technology. The ensuing high Doppler resolution in each range, azimuth and elevation cell is exploited to fine tune the post detection filtering rejecting potential false alarms such as those stationary objects that exhibit internal motions (e.g. trees, crops etc.) and preserves only detections from genuine air targets. The inherent 3-D nature of the receive array is also used to reject targets that are on or very close to the ground in a manner that can be tailored to a given scenario and application.

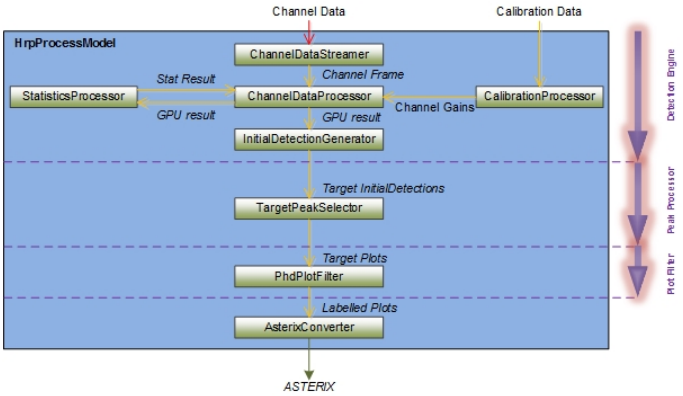

Fig. 2. *The Holographic Radar™ processing chain.*

The processing chain is split into three sub-stages as illustrated in Fig. 2. The first processing stage, the *Detection Engine,* processes the raw I/Q data from all the receiver channels to forms a 4-D data matrix comprising range, azimuth, elevation and pulse number. The temporal data is converted into frequency domain and thresholded to generate a list of candidate *initial detections* specifying range and Doppler.

The *peak processor* stage uses the *initial detections* as seeds to refine the search for detections within a receive beam. These detections are further filtered using characteristics such as amplitude, Doppler, etc., to distinguish genuine air target returns from others. The output detections are termed *target plots* and are passed to the final stage that performs tracking using a Probability Hypothesis Density (PHD) tracker [6]. The outputs are smoothed tracks that specify the track id, position and velocity for each reported target plot.

The HR variant used for the measurements reported here is the Theia 64A system, pictured in Fig. 3 and has a 32 by 8 receiver array. For the drone trials the system was configured to operate at short ranges and the processing was optimized for low observable targets. The sensor operating parameters for the drone trial configuration are summarised in Table 1.

Fig. 3. *Holographic Radar™ prototype with a 32x8 2-D recevier array.*

TABLE I. HR Operating Parameters Used for Drone Trials

Parameter	Value
Frequency	L band
Bandwidth	~2 MHz
Transmit power	~10 kW
Receiver channels	32 x 8
Azimuth coverage	90°
Elevation coverage	65°
Pulse Repetition Frequency (PRF)	~3.8 kHz
Update rate	~0.5seconds

III. Detection Performance

The standard configuration for the Theai 64A sensor optimizes detection of a $1m^2$ airborne target at a range of 20nmi. Performance was evaluated against a drone target and adjustments made to the processing configuration to optimize detection of such low observable targets.

As a reference a flight was conducted using a micro-light flying more-or-less radial trajectories. The GPS truth for one of these reference flights is plotted in Fig. 4. The figure also shows the radar location and its azimuth field of regard. Performance is evaluated using the tracker output which is plotted in Fig. 5 for the reference flight of the micro-light. The data shown is for a duration of approximately 2.5 minutes. The green markers are the micro-light track and any false targets are shown in blue. For the purpose of the analysis presented here, the range is clipped at 5km although the actual range extends much further. The Probability of Detection (PD) of the micro-light is measured to be 95% and the False Alarm Rate (FAR) is very close to 0%. The radar is actually detecting 100% of the time and the 5% drop in PD is due to the tracker declaration delay set, in this instance, to approximately 5 seconds.

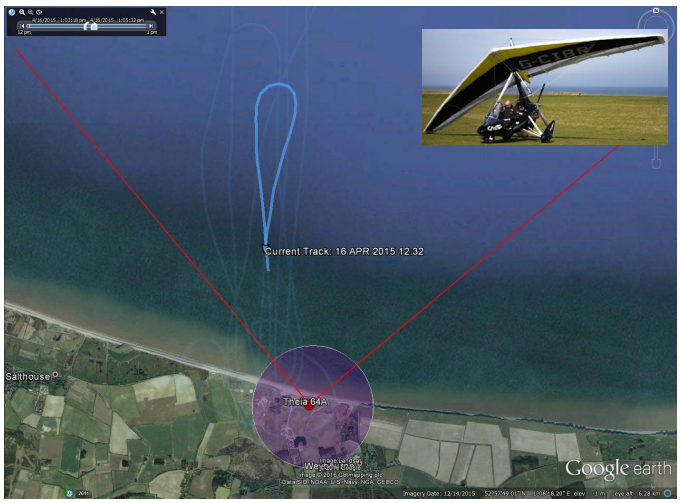

Fig. 4. *Micro-light (insert), GPS truth (blue line), HR location (red sphere), azimuth field of regard (red lines), blanking range (purple circle).*

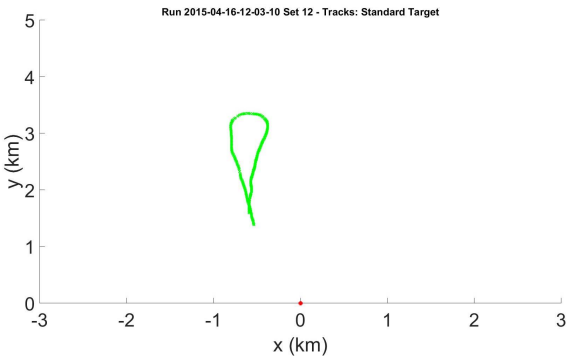

Fig. 5. *Radar tracker output showing the micro-light track in green. No false targets reported. Radar location marked in red.*

The micro-UAS test target selected is the remotely piloted hexacopter that weighs under 4kg and has diameter less than 0.6m. It has a maximum flight duration of a little less than 5 minutes and operates at altitude up to 500ft. The drone flights were launched from the coast and flown along more-or-less radial trajectories. An example of the GPS truth data, for one of the trials, is plotted in Fig. 6.

Fig. 6. *Hexacopter (insert), GPS truth (blue line), HR location (red sphere), azimuth field of regard (red lines), blanking range (purple circle).*

Using a standard form of configuration optimized for aircraft, the performance against the hexacopter, in the first instance, is very poor, with no tracks reported for the drone. There were some detections at the pre-tracker output but the PD is very low. Fig. 7 shows the detection output for a 2.5 minute duration of the test flight where the hexacopter was travelling inbound. This data will be referred to as set 3. The green markers are the drone detections and the missed detections are marked with the black circles. The blue markers are false plots. Thus at the pre-tracker stage, the false alarms remain low which translate into no false alarms at the tracker output. The pre-tracker PD however is only 33%. These intermittent detections then result in zero tracks after the tracker so the final PD for drone was 0%. This illustrates the need for a bespoke processing approach able to cope with the challenges presented by ultra-low RCS targets, flying low and slow trajectories.

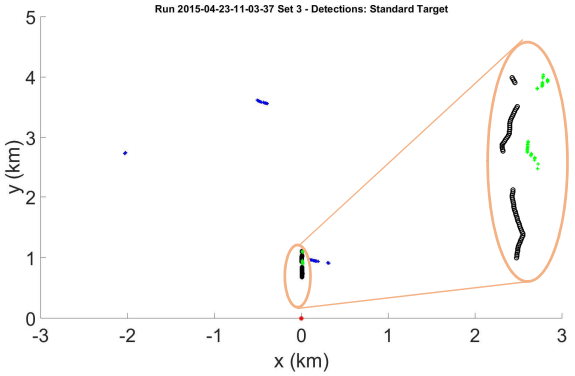

Fig. 7. *Radar detections (target plots) showing hexacopter detections (green), missed detections (black) and false targets (blue).*

The detection sensitivity can be enhanced for such low observable targets by reducing the amplitude threshold and permitting detections with lower Dopplers. With these changes the performance improves significantly for the hexacopter. Fig. 8 is the tracker output for the same data set 3 but this time with enhanced detection sensitivity. The reported PD for the hexacopter is 98%. There are however many more false tracks being reported which then inhibit the ability to identify the

correct track corresponding to the drone. These false tracks are caused due to low observable targets that are likely to compete with drones for example birds, surface targets, clutter etc. In this way it can be seen that to detect drones there needs to be sufficient sensitivity and that if there is, many other targets such as birds are also detected and a discrimination stage needs to be added to the overall processing chain. There are many ways that this can be implemented. Here we consider the use of a machine learning approach to filter the non-drone false tracks.

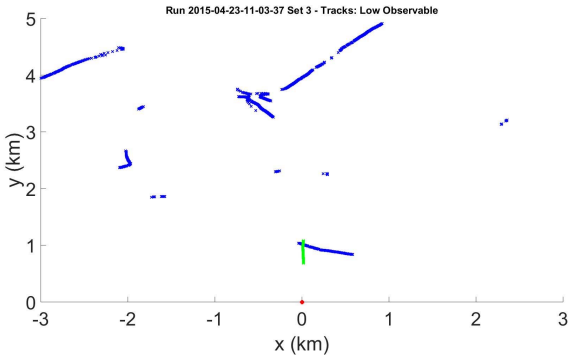

Fig. 8. *Radar tracker output optimised for low observable showing hexacopter tacks (green) and false target tracks (blue).*

IV. Decision TREE Based Classifier

The results obtained with the hexacopter demonstrate that HR is able to obtain high PD for micro-UAS. However, in the absence of any drone discrimination a high volume of false target tracks are also reported. A decision tree based machine learning algorithm [7] is now examined in terms of its ability to reject non-drone targets. It is a flow-chart like classifier in which each internal node represents a 'test' on a selected feature of the data, each branch represents the outcome of the test and each leaf node represents a class label i.e., drone or non-drone.

There are three stages to the implementation of a decision tree classifier; (1) selection of feature parameters, (2) learning and (3) predict. The feature parameters are based on the measurements generated at the detection stage. The detection outputs have a limited feature set comprising position, amplitude and Doppler. However, the feature set can be significantly expanded by using a pre-tracker to associate detections from multiple time steps into 'tracklets'. This enables the temporal derivative of each of the radar plot measurements to be added to the feature set. Examples are acceleration, Doppler rate, etc., all of which play a varying role in aiding discrimination.

The learning operation of the decision tree is performed off-line using recorded data. The training data is labelled as either drone using GPS truth data or non-drone for anything that is not associated with the drone truth data. The decision tree uses a greedy algorithm to establish the feature value that will provide the appropriate split of the training data so that the population purity of the subsequent child node is always increased. The population split is performed recursively until all the entries in the child node are either from the same class or when the population purity exceeds a pre-defined threshold. This is illustrated diagrammatically in Fig. 9. The final path from the root node to the leaf node defines the classification rule. The learning operation concludes with a decision tree model that specifies the feature sets and the classification rules that apply in discriminating drones from non-drone targets.

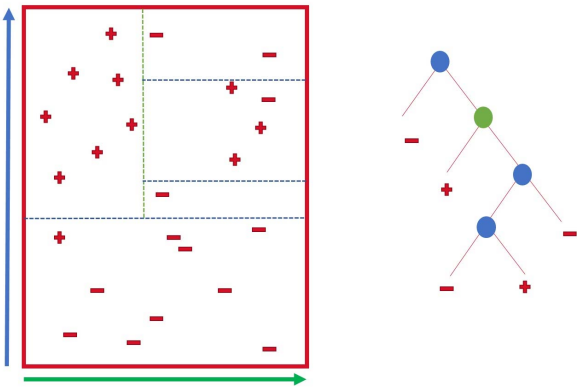

Fig. 9. *Decision tree schematics showing (left) population split and (right) node structure where blue node indicates majority population is class '-' and vice versa for a green node.*

The final prediction stage uses the decision tree to classify detections from each time step as either drone or non-drone. Only the former are passed to the tracker and the final output contains either true drone tracks or false positives that have been misclassified as drones.

V. Drone Classification Performance

The decision tree is trained on real data collected using the Theia 64A HR for a hexacopter. The training data excluded set 3 which is the data used to test the classifier. Altogether the training data was roughly 5 times larger compared to the test set. This, by no means, represents an optimal approach, nevertheless it provides a good illustration of achievable performance. Through a process of trial and error the following features have been found to be a good choice for the decision tree:

- Height: This is the height above the position of the radar. It is useful for separating ground targets from low altitude drones;
- Maximum height: This measures a moving average maximum height and helps again to eliminate targets that are at or close to surface;
- Track age: This measures the length of the current track as estimated by the pre-tracker, and is useful in rejecting short lived false tracks;
- Doppler: This measures instantaneous radial velocity;
- Acceleration: This measures the rate of change of the velocity vector and enables targets to be separated by turn rate;
- Jolt: This measures the rate of change of acceleration and enables targets to be separated according to the smoothness of their trajectory and number of turns made;

The classification performance achieved with the decision tree approach using data set 3 is summarized in the confusion matrix shown in Fig. 10. The 99% correct classification for non-

drone (class 1) means that the detection plots for data set 3 following classification are extremely clean (i.e., few false targets as can be seen in Fig. 11). It is interesting to note that the 18% missed classification of the drone is linked to the commencement of the track (as indicated by the black missed detections in Fig. 11). Within this early period of the track there is unlikely to be sufficient measurement history accumulated from the data to provide good estimates for features such as acceleration to enable robust discrimination. This highlights an important aspect of how classification function are to be executed and that the time to classification is an important criteria. A notion of classification declaration delay should be associated with the discriminator output. This will be synonymous with the declaration delay used in tracking algorithms to deal with track initiation.

Fig. 10. *Confusion matrix for drone (class=2) vs non-drone(class=1)*

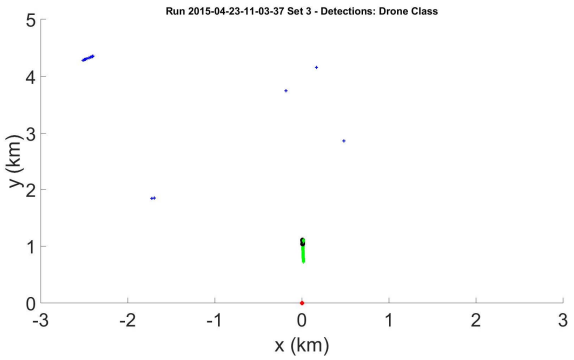

Fig. 11. *Radar detection (target plots) after drone discrimination showing hexacopter (green), missed detections (black) and non-drones (blue).*

The final tracker output obtained for set 3, after the detections have been filtered by the decision tree discriminator, is shown in Fig 12. There is just the one genuine track reported for the drone shown in green. The PD for the drone in this case is 88%. There is a single output generated for a non-drone false target (blue marker). Increasing the tracker declaration delay by just half a second from 5 seconds to 5.5 seconds removes all false targets from the final tracker output resulting in an overall FAR of 0%. Thus it is possible to achieve low false alarm rates for drones whilst managing to cope with the extremely high sensitivities needed to enable robust detection and discrimination of miniature UAS.

However, it should be kept in mind that these initial results, whilst encouraging, are based on limited data and need to be further evaluated using larger training and test data and against a wider range of drone target types.

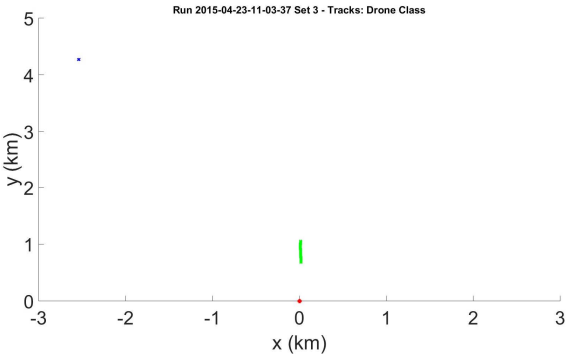

Fig. 12. *Radar tracks after drone discrimination showing hexacopter (green) and non-drones (blue).*

It is also important to understand how well training on one drone type will enable classification on different drone types and under different range of environmental conditions. It is equally important to understand how the classifier is able to distinguish between different non-drone classes of targets. Ultimately the drone discrimination effectiveness will be limited by the ability of the classifier to reject confuser targets.

The current version of the decision tree has been implemented into the real time processor and the HR system is able to perform the drone discrimination in live operations. Future work will extend the feature sets for the decision tree to include micro-Doppler signatures which will improve the class separability using aspect such as the propeller response from drones and the wing beat pattern from birds.

VI. Conclusions

Trials results have shown that HR offers good detection sensitivity against hexacopter micro-UAS. Furthermore, discrimination using 6 selected feature trained with a decision tree is able to remove almost all non-drone false targets. The training is performed off-line and the classification is carried out in real-time. The current version of the machine learning classifier is predominantly making use of features derived from the flight trajectory profile.

References

[1] Oswald, G. A. K., "Holographic surveillance radar," *Proc. SPIE 7308, Radar Sensor Technology XIII*, 73080D, US, 29 Apr.2009

[2] Quilter, T. & Jahangir M., "Performance of a 3D non-scanning array to detect targets in the presence of wind turbines," *ESAV' 14*, Italy, Sep. 2014

[3] Jahangir M., "Target centric wide-area 3-D surveillance using a non-scanning multibeam receiver array," *IEEE Radar 2015*, US, May 2015

[4] Jahangir M. & Quilter T., "The Practicality and Benefit of a 3-D Wide-Area Persistent Surveillance Micro-Doppler Radar," *IRS 2015*, Germany, Jun. 2015

[5] Clemente, C., Balleri, A., Woodbridge, K. and Soraghan, J. J., "Developments in target micro-Doppler signatures analysis: radar imaging, ultrasound and through-the-wall radar," *EURASIP Journal on Advances in Signal Processing*, **47**, Mar. 2013

[6] Wood, T. M., "Tracking in dense clutter with the phd filter," IMA Mathematics in Defence Conf., UK, Oct. 2009

[7] Loh W-Y., "Classification and regression trees," WIREs Data Mining Knowl Discov 1:14-23

DIRECTION FINDING ANTENNA ARRAYS WITH IMPROVED ACCURACY AND REDUCED COMPLEXITY AND SIZE

Houcem Gazzah

Dept. of Electrical and Computer Engineering, University of Sharjah, UAE, hgazzah@sharjah.ac.ae.

ABSTRACT

It has been recently demonstrated that optimal sensor placement can significantly improve target localization accuracy. This improvement is even more exacerbated when using arrays of directional sensors. However, the optimal array configuration is hard to obtain, typically requiring a high-complexity systematic search. In this paper, we propose a plausible modification of the optimization criterion that reduces the dimension of the search area while maintaining near-optimum performance.

Index Terms— Cramer Rao bounds, direction-of-arrival estimation, Cardioid sensors

1. INTRODUCTION

Signal snapshots are collected in order to estimate the Direction of Arrival (DOA) of a far-field narrow-band source. Not only the signal phase depends on the source DOA, but also the amplitude, should the sensors be directional. Estimation accuracy depends on the estimation algorithm, the array geometry and the source actual DOA. In the single source case, most popular algorithms are comparable as they (asymptotically) achieve the Cramer-Rao Bound (CRB) [1], a widely accepted performance measure of theoretical and practical importance [2]. For the sake of improving DOA estimation, a new approach has proved to be effective. In fact, proper sensor placement may improve performance significantly, as shown by many recent studies. There, antenna array geometries have been identified that exhibit lower CRB. This approach has been successfully applied to DOA estimation of deterministic [3], random [4, 5], far-field [6] and near-field sources [7].

Existing work has focused on arrays of omni-directional sensors, as frequently assumed in the DOA literature. A first attempt has been made in [8] to optimize the geometry of an array of directional sensors and, hence, address more realistic situations. Directional sensors translate into optimization problems that are analytically untractable even in the two-sensors case. Size is a critical design criterion for those systems, e.g. airborne and marine autonomous unmanned vehicles [9, 10], that can accommodate only a very small number of sensors.

In [8], it has been proved that: i) the two-sensor array with adapted-geometry is comparable in performance to larger-sized fixed-geometry arrays, and ii) the amount of improvement increases with the sensor directivity. In this regard, the practical limitation is the computational complexity of the optimization procedure, for instance, a 3D systematic search [8]. The present paper achieves a significant reduction of the computation burden, as the dimension of the search area is reduced from 3 to 2.

Such simplification is made possible thanks to a modification of the optimization criterion. Originally, the CRB is used as a scalar-valued cost function. As it may be DOA-dependent, focus has been brought onto the so-called isotropic arrays, for which the CRB is the same at all look directions. Unfortunately, it is not possible to design small-sized isotropic arrays, not even the popular Uniform Circular Arrays (UCA) [11]. In such case, a more suitable performance criterion is the expected CRB (ECRB), which depends on the DOA probabilistic distribution. Yet, CRB and ECRB have complex expressions if sensors are directional. To circumvent this difficulty, we adopt the (expected) Fisher information, i.e. the inverse of the CRB, as our design performance, one that leads to a closed-form expression of the array orientation. At the same time, performance is close to optimality, as confirmed through tests with arrays of cardioid sensors irradiated by a source at an arbitrarily distributed direction.

The paper is organized as follows. In Sec. 2, we introduce the observation model and recall previous results. In Sec. 3, an alternative criterion is proposed and the subsequent optimization algorithm is developed. The so-optimized array is calculated in Sec. 4 for a number of distributions, and its performance compared to that of the ECRB-optimized array. Finally, a conclusion is given in Sec. 5.

2. SIGNAL MODEL AND PREVIOUS RESULTS

A far-field source, characterized by DOA θ measured counter clockwise from the x-axis, is emitting a narrow-band signal $s(t)$ at wavelength λ in the direction of an array of two sensors. The first sensor is fixed at the origin O while the second sensor is placed at a distance $\rho\lambda$ from O, forming an angle ϕ with $[O, x)$ axis, ρ and ϕ are yet to be determined. The

978-1-5090-0326-6/16/$31.00 ©2016 IEEE

two identical sensors have a DOA-dependent response $g(\theta)$ so that orientations of the sensors are also to be determined.

We denote by ψ_1, ψ_2 and ϕ the respective orientations of the first sensor, the second sensor and the sensor array, as shown in Fig. 1. The geometrical optimization problem consists in determining the best choice of the triplet ϕ, ψ_1 and ψ_2, the remaining geometrical parameter ρ is assumed to be prefixed based on other antenna array design considerations, more likely in order to jugulate inter-sensors mutual coupling and array ambiguities.

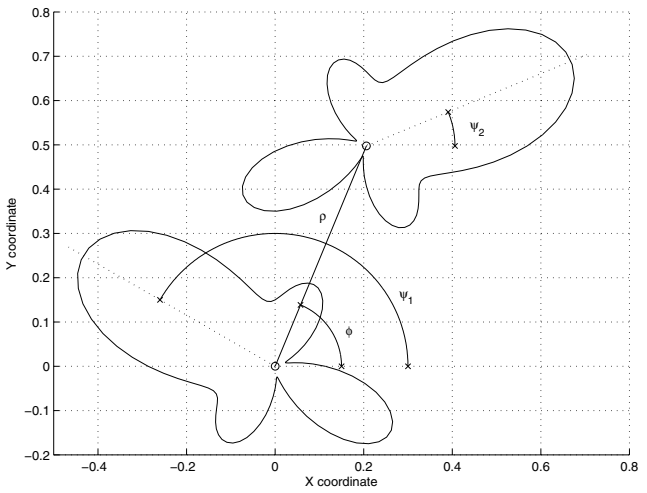

Fig. 1. Positions and orientations of the two directional sensors for an arbitrarily-shaped sensor response $g(\theta)$.

DOA estimation is attempted from received signal snapshots, collected at time moments $t_1, .., t_N$, all of the form

$$\mathbf{x}(t) = \begin{bmatrix} g(\theta-\psi_1) \\ g(\theta-\psi_2)\exp\left[j2\pi\rho\cos\left(\theta-\phi_m\right)\right] \end{bmatrix} s(t) + \begin{bmatrix} n_1(t) \\ n_2(t) \end{bmatrix} \tag{1}$$

where source signal $s(t)$ and noise snapshots $n_i(t)$ have respective power $\sigma_s^2 \hat{=} \mathrm{E}\left[|s(t)|^2\right]$ and $\sigma_n^2 \hat{=} \mathrm{E}\left[|n_i(t)|^2\right], i = 1, 2$. Under some regularity conditions [12], DOA localization ability, for a source in the direction θ, is described by

$$\mathrm{CRB}(\theta) = \frac{\sigma_n^2}{2N\sigma_s^2} F^{-1}(\theta), \tag{2}$$

where [8]

$$F(\theta) = \frac{\left[\frac{g'(\theta-\psi_1)}{g(\theta-\psi_1)} - \frac{g'(\theta-\psi_2)}{g(\theta-\psi_2)}\right]^2 + 4\pi^2\rho^2\sin^2\left(\theta-\phi\right)}{\frac{1}{g^2(\theta-\psi_1)} + \frac{1}{g^2(\theta-\psi_2)}}. \tag{3}$$

is known as the Fisher information. Notice that the above is unchanged if ϕ is replaced by $\phi+\pi$, or if (ψ_1, ψ_2) is replaced by (ψ_2, ψ_1). So, we will assume that ϕ is in $[0, \pi]$ and $\psi_2 \geq \psi_1$. When the source DOA is random, as assumed in this paper, the array DOA estimation performance is more conveniently assessed through the so-called $ECRB \hat{=} \mathrm{E}\left[CRB(\theta)\right]$. Minimization of $\mathrm{E}\left[1/F(\theta)\right]$ is possible by systematic search, thanks to the bounded nature of the investigated geometric parameters ϕ, ψ_1 and ψ_2, and may be affordable in a number of cases where the source DOA distribution remains unchanged for some time. Optimal array configurations based on this ECRB criterion have been reported in [8], along with their performance, and so for the most frequent cases of uniform and normal distributions. For more general cases (e.g. weighted sums of normal distributions), it is worth reducing the complexity of such a procedure. This objective is achieved in the next section, at the expense of optimality, but not dramatically so.

3. AN ALTERNATIVE OPTIMIZATION CRITERION

Instead of minimizing the ECRB, i.e. minimizing $\mathrm{E}\left[1/F(\theta)\right]$, we propose to maximize $\mathrm{E}\left[F(\theta)\right]$, following the intuition that the so-optimized array geometric configuration will achieve an ECRB close to the lowest possible ECRB. Hence, we will be opposing

$$(\Psi_1^\dagger, \Psi_2^\dagger, \Phi^\dagger) = \mathrm{argmin}\ \mathrm{E}\left[\frac{1}{F(\theta)}\right]$$

to

$$(\Psi_1, \Psi_2, \Phi) = \mathrm{argmax}\ \mathrm{E}\left[F(\theta)\right].$$

In order to preserve optimality, the geometric unknowns are determined by systematic search. While, for the former physically-relevant criterion, this search is over a 3D region [8], for the latter criterion dimensionality is reduced to 2D, as we will show promptly.

Complexity-wise, considering $\mathrm{E}\left[F(\theta)\right]$ allows for an easy derivation of the optimal value of ϕ. In fact, the adhoc criterion $\mathrm{E}\left[F(\theta)\right]$ is given by

$$I_0 - 2\pi^2\rho^2\left[\cos\left(2\phi\right) I_1 + \sin\left(2\phi\right) I_2\right] \tag{4}$$

where

$$I_0 = \mathrm{E}\left[\frac{\left[\frac{g'(\theta-\psi_1)}{g(\theta-\psi_1)} - \frac{g'(\theta-\psi_2)}{g(\theta-\psi_2)}\right]^2 + 2\pi^2\rho^2}{\frac{1}{g^2(\theta-\psi_1)} + \frac{1}{g^2(\theta-\psi_2)}}\right] \tag{5}$$

$$I_1 = \mathrm{E}\left[\frac{\cos\left(2\theta\right)}{\frac{1}{g^2(\theta-\psi_1)} + \frac{1}{g^2(\theta-\psi_2)}}\right] \tag{6}$$

$$I_2 = \mathrm{E}\left[\frac{\sin\left(2\theta\right)}{\frac{1}{g^2(\theta-\psi_1)} + \frac{1}{g^2(\theta-\psi_2)}}\right] \tag{7}$$

We can assume that, for arbitrarily distributed DOA, I_1 is non-zero with probability one. Hence, it becomes obvious that, at optimality, we have

$$\tan\left(2\phi\right) = \frac{I_2}{I_1}$$

so that $\phi = \frac{1}{2}\arctan\left(\frac{I_2}{I_1}\right)$ in $]-\pi/4, \pi/4[$, or $\phi = \frac{1}{2}\arctan\left(\frac{I_2}{I_1}\right) + \frac{\pi}{2}$ in $]\pi/4, 3\pi/4[$. We can also write that $\cos(2\phi) = \eta I_1/\sqrt{I_1^2 + I_2^2}$ and $\sin(2\phi) = \eta I_2/\sqrt{I_1^2 + I_2^2}$, for some sign parameter $\eta = \pm 1$, yet to be determined. This being replaced in (4), we realize that we have to maximize the following function of ψ_1 and ψ_2

$$\Gamma = I_0 - 2\eta\pi^2\rho^2\sqrt{I_1^2 + I_2^2}$$

In regard of the above, and assuming the probability density function (PDF) of θ is known, steps of the optimization algorithm are as follows

1. Set Γ to zero.
2. Determination of Ψ_1 and Ψ_2:
   (a) For ψ_1 spanning $0, \ldots, 2\pi$,
      i. For ψ_2 spanning $\psi_1, \ldots, 2\pi$,
         A. Evaluate I_0, I_1 and I_2 as shown in (5), (6) and (7), respectively.
         B. Calculate $\gamma = \max\{I_0 + 2\pi^2\rho^2\sqrt{I_1^2 + I_2^2}, I_0 - 2\pi^2\rho^2\sqrt{I_1^2 + I_2^2}\}$.
         C. If $\gamma > \Gamma$, then set $\Gamma = \gamma$, $\Psi_1 = \psi_1$ and $\Psi_2 = \psi_2$.
3. Determination of Φ:
   (a) Repeat step 2(a)iA with $\psi_1 = \Psi_1$ and $\psi_2 = \Psi_2$.
   (b) If $I_0 + 2\pi^2\rho^2\sqrt{I_1^2 + I_2^2} > I_0 - 2\pi^2\rho^2\sqrt{I_1^2 + I_2^2}$, then set $\eta = -1$. Otherwise, set $\eta = 1$.
   (c) If $\eta I_1 > 0$, then set $\Phi = \frac{1}{2}\arctan\left(\frac{I_2}{I_1}\right)$. Otherwise, set $\Phi = \frac{1}{2}\arctan\left(\frac{I_2}{I_1}\right) + \frac{\pi}{2}$.

4. VALIDATION

In order to compare the proposed adhoc criterion to the original ECRB-based criterion, we consider arrays of cardioid-type sensors, frequently used in acoustic systems [13]. They exhibit a directional response of the form:

$$g(\theta) = g_0[1 + \beta\cos(\theta)], \tag{8}$$

characterized by constant g_0 and, more importantly, by parameter β that controls the sensor directivity. We update (5)-(7) by introducing $I_k^\dagger \hat{=} I_k/g_0^2$, for $k = 1, 2$ and 3, obtained as

$$I_0^\dagger = \mathrm{E}\left\{ \frac{\beta^2\left[\frac{\sin(\theta-\psi_1)}{1+\beta\cos(\theta-\psi_1)} - \frac{\sin(\theta-\psi_2)}{1+\beta\cos(\theta-\psi_2)}\right]^2 + 2\pi^2\rho^2}{\frac{1}{[1+\beta\cos(\theta-\psi_1)]^2} + \frac{1}{[1+\beta\cos(\theta-\psi_2)]^2}} \right\} \tag{9}$$

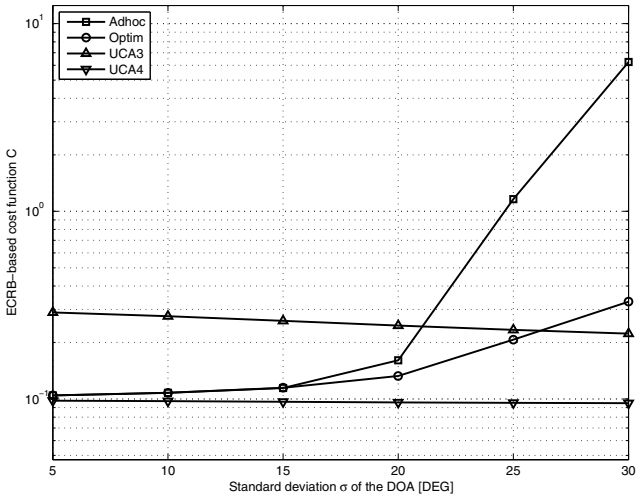

(a)

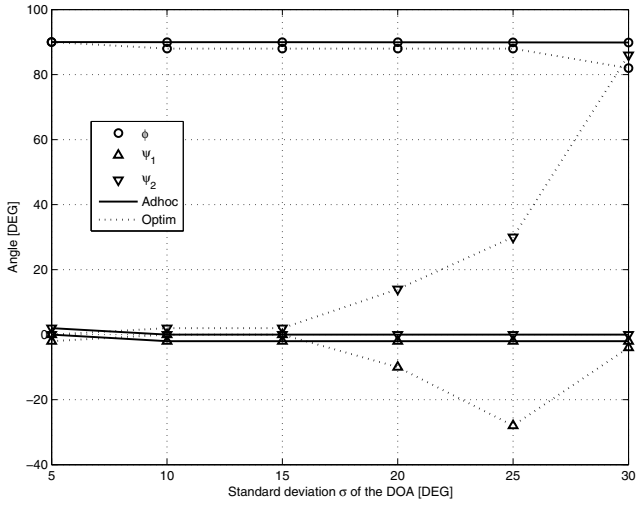

(b)

Fig. 2. Compared performance (a) and shape (b) of the two-sensor arrays for a zero-mean normally distributed source DOA with a standard deviation as shown along the horizontal axis. Sensors are such that $\beta = 0.4$.

$$I_1^\dagger = \mathrm{E}\left[\frac{\cos(2\theta)}{\frac{1}{[1+\beta\cos(\theta-\psi_1)]^2} + \frac{1}{[1+\beta\cos(\theta-\psi_2)]^2}}\right] \tag{10}$$

$$I_2^\dagger = \mathrm{E}\left[\frac{\sin(2\theta)}{\frac{1}{[1+\beta\cos(\theta-\psi_1)]^2} + \frac{1}{[1+\beta\cos(\theta-\psi_2)]^2}}\right] \tag{11}$$

Obviously, the optimization procedure remains unchanged if we replace I_1, I_2 and I_3 in (5), (6) and (7), by $I_1^\dagger$, $I_2^\dagger$ and $I_3^\dagger$, respectively. At the same time, the optimization proce-

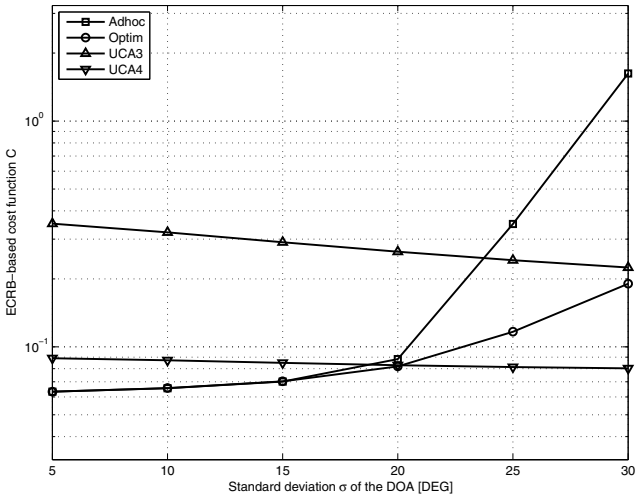

(a)

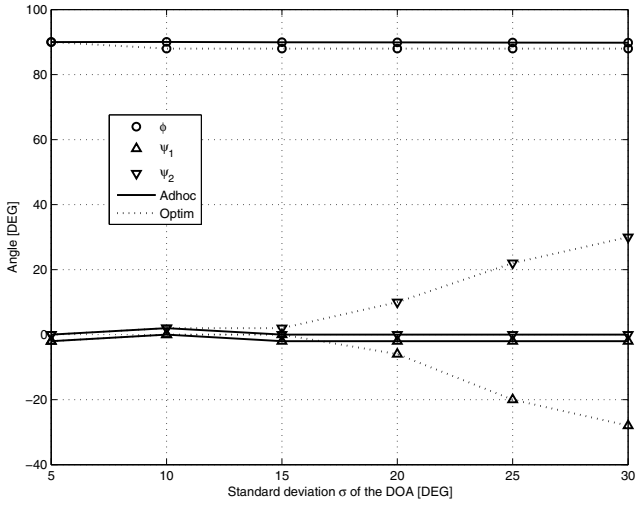

(b)

Fig. 3. Compared performance (a) and shape (b) of the two-sensor arrays for a zero-mean normally distributed source DOA with a standard deviation as shown along the horizontal axis. Sensors are such that $\beta = 0.8$.

dure (and the subsequent array geometries) become solely dependent on the directivity parameter β.

The near-optimum two-sensor array (optimized based on the adhoc criterion) is compared to the optimum two-sensor array (optimized based on the ECRB), and to the non-optimized fixed-geometry UCAs of 3 and 4 sensors. Sensors are spaced by half-a-wavelength in order to combat array ambiguities [14]. Orientations of the UCA sensors are fixed such that the main lobe is directed outwards [8, 15]. These direction finding arrays are compared based on the physically-relevant ECRB-based cost $C \doteq \frac{2g_0^2 N\sigma_s^2}{\sigma_n^2}\mathrm{ECRB}$. For the two-sensor array, we have

$$C = \int_{-\pi}^{\pi} \frac{\left\{\frac{1}{[1+\beta\cos(\theta-\psi_1)]^2} + \frac{1}{[1+\beta\cos(\theta-\psi_2)]^2}\right\} f(\theta)}{\beta^2\left[\frac{\sin(\theta-\psi_1)}{1+\beta\cos(\theta-\psi_1)} - \frac{\sin(\theta-\psi_2)}{1+\beta\cos(\theta-\psi_2)}\right]^2 + 4\pi^2\rho^2\sin^2(\theta-\phi)} d\theta.$$

Expressions of C for UCAs of different sizes can be found in [8].

The optimization problem depends on the DOA PDF. In Fig. 2 and Fig. 3, where β is successively equal to 0.4 and 0.8, we illustrate results for a zero-mean normally distributed DOA, as function of the distribution's standard deviation. We realize that the adhoc criterion performs closely to the optimum for low-to-moderate DOA uncertainty (expressed here by the standard deviation), as shown in Fig. 2(a) and Fig. 3(a). On the contrary, as illustrated in Fig. 2(b) and Fig. 3(b), the two competing arrays have different behaviors when uncertainty increases. On one hand, the adhoc criterion invariably points two sensors at the direction of the most probable DOA, regardless of how uncertain it is. On the other hand, the optimum criterion manages to take benefit from the uncertainty (i.e. from the prior) by pointing the two sensors away from the most probable DOA as this direction becomes less and less sure. On the positive side, the adhoc criterion always succeeds to deliver the optimum array direction ϕ. Also to be concluded from the comparison between Fig. 2 and Fig. 3, the adhoc criterion is closer to optimality when sensors are more directive.

In Fig. 4, we intend to evaluate the performance of the adhoc criterion in a more general scenario where the DOA PDF is given by

$$f(\theta) = \frac{\exp\left[-\frac{(\theta-\Omega)^2}{2\sigma^2}\right] + \exp\left[-\frac{(\theta+\Omega)^2}{2\sigma^2}\right]}{2\sigma\sqrt{2\pi}}.$$

We set $\sigma = 10$ [DEG] and let Ω span the range $[10, 90]$ [DEG], in order to check the potential of the adhoc criterion in arbitrary situations. It is clear from Fig. 4 that a worst case scenario happens when the two possible look directions are (close to be) orthogonal. Otherwise, near optimum performance can be achieved.

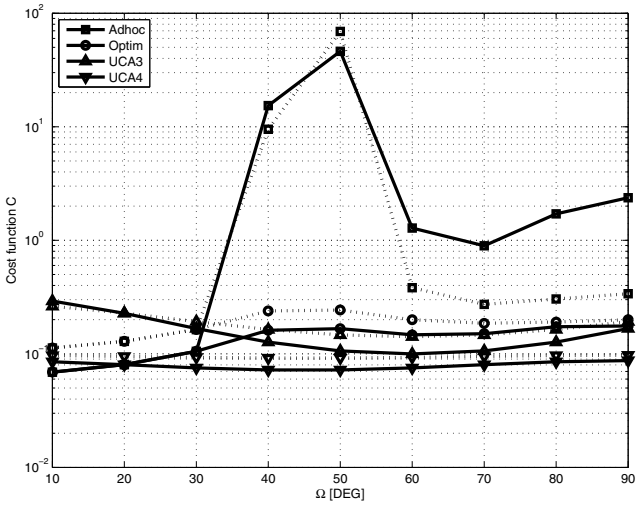

Fig. 4. Performance comparison for a source PDF characterized by two possible look directions $\pm\Omega$, with $\Omega = 10, 20, \ldots, 90$ [DEG]. Sensors are such that $\beta = 0.4$ (dotted line) and $\beta = 0.8$ (solid line).

5. CONCLUSION

In the context of DOA estimation using an array of two directional sensors, the Fisher information has a simpler analytical expression than the CRB and serves as the basis of a new design criterion to determine best locations and orientations of the sensors. The source DOA being randomly distributed, maximizing the average Fisher information is not, strictly speaking, equivalent to minimizing the averaged CRB. In practice, it is close to be the case. The moderate loss of optimality is compensated by a drastic simplification of the optimization procedure. A systematic search involves a 2D search region instead of the 3D region required by the CRB-based criterion.

6. REFERENCES

[1] H. Gazzah and J. P. Delmas, "Spectral efficiency of beamforming-based parameter estimation in the single source case," in *Proc. Statistical Signal Processing Workshop (SSP)*, 2011, pp. 153-156.

[2] F. Demmel, "Practical Aspects of Design and Application of Direction-Finding Systems," in *Classical and Modern Direction-of-Arrival Estimation*, T. E. Tuncer and B. Friedlander, Ed. Academic Press, 2009, pp. 53-92.

[3] H. Gazzah and K. Abed-Meraim, "Optimum Ambiguity-free directional and omni-directional planar antenna arrays for DOA estimation," *IEEE Trans. Signal Processing*, vol. 57, no. 10, pp. 3942-3253, Oct. 2009.

[4] Ü. Oktel and R. L. Moses, "A Bayesian approach to array geometry design," *IEEE Trans. Signal Process.*, vol. 53, no. 5, pp. 1919â1923, May 2005.

[5] H. Gazzah and J. P. Delmas, "Direction finding antenna arrays for the randomly located source," *IEEE Trans. Signal Process.*, vol. 60, no. 11, pp. 6063-6068, Nov. 2012.

[6] H. Gazzah and S. Marcos, "Cramer-Rao bounds for antenna array design," *IEEE Trans. Signal Process.*, vol. 54, no. 1, pp. 336-345, Jan. 2006.

[7] H. Gazzah and J. P. Delmas, "CRB based-design of linear antenna arrays for near-field source localization," *IEEE Trans. Antennas Propag.*, vol. 62, no. 4, pp. 1965-1974, April 2014.

[8] H. Gazzah, J. P. Delmas and Sérgio M. Jesus, "Direction finding arrays of directional sensors for randomly located sources," *IEEE Trans. Aerosp. Electron. Syst.*, accepted.

[9] D. Wang, P. F.J. Lermusiaux, P. J. Haley, D. Eickstedt, W. G. Leslie, H. Schmidt, "Acoustically focused adaptive sampling and on-board routing for marine rapid environmental assessment," *Elsevier Journal of Marine Systems*, 78 (2009), pp. S393âS407.

[10] H. Schmidt, J. G. Bellingham and J. W. Bales, "Mobile underwater arrays," U.S. Patents No. US Patent 5,894,450 (April 1999). https://encrypted.google.com/patents/US5894450.

[11] H. Gazzah and J. P. Delmas, "On isotropic circular arrays of anisotropic sensors," in *Proc. International Symposium on Signal Processing and Information Technology (ISSPIT)*, 2015, pp. 95-99.

[12] B. Porat and B. Friedlander, "Analysis of the asymptotic relative efficiency of the MUSIC algorithm," *IEEE Trans. Acoust., Speech, Signal Process.*, vol. 36, no. 4, pp. 532-544, Apr. 1988.

[13] D. D. Ellis, "Effect of cardiod and limaçon directional sensors on towed array reverbation response," *J. Canadian Acoust. Association*, vol. 34, no. 3, pp. 102-103, 2006.

[14] L. C. Godara and A. Cantoni, "Uniqueness and linear independence of steering vectors in array space," *J. Acoust. Soc. Amer.*, vol. 70, no. 2, pp. 467-475, Aug. 1981.

[15] B. R. Jackson, S. Rajan, B. Liao, and S. Wang, "Direction of arrival estimation using directive antennas in uniform circular arrays," *IEEE Trans. Antennas and Propag.*, vol. 63, no. 2, pp. 736-747, Feb. 2015.

Cognitive Radar Waveform Design for Spectral Compatibility

Augusto. Aubry, *Senior Member, IEEE*
Vincenzo. Carotenuto, *Member, IEEE*
Antonio De Maio, *Fellow, IEEE*
Università degli Studi di Napoli "Federico II"
DIETI, via Claudio 21 I-80125 Napoli, Italy
E-mail: {augusto.aubry, vincenzo.carotenuto, ademaio}@unina.it

Salvatore Iommelli, *Member, IEEE*
Ente di Formazione Professionale Maxwell
via G. A. Campano, 103/105, I-80145 Napoli, Italy
E-mail: s.iommelli@entemaxwell.it

***Abstract*— Radar performance is strongly dependent on the transmitted waveform and its parameters which must be adapted to the surrounding environment, radar mission, goal, and task. Waveform diversity is a relatively new paradigm involving a continuous variation and adaptation of the transmitted signal to dynamically optimize the radar performance and fulfill the more and more stressing requirements. In this context, cognitive radar waveform design in spectrally dense environments is a very challenging and topical problem. This paper deals with the synthesis of signals optimizing radar capabilities while satisfying spectral compatibility constraints. Specifically, the design of radar waveforms, sharing appealing features and ensuring spectral co-existence with other Radio Frequency (RF) systems, is introduced and discussed according to a rigorous framework.**

I. Introduction

The Radio Frequency (RF) electromagnetic (e.m.) spectrum is a limited natural resource necessary for an ever-growing number of services and systems. It is used in several applications, such as mobile communications, radio and television broadcasting, as well as remote sensing. Indeed, both high-quality/high-rate wireless services (4G and 5G) as well as accurate and reliable remote-sensing capabilities (Air Traffic Control (ATC), geophysical monitoring of Earth, defense and security applications) call for increased amounts of bandwidth [1], [2]. Besides, basic e.m. considerations, such as good foliage penetration [3], low path loss attenuation, reduced size of the devices push some systems to coexist in the same frequency band [4] (for instance VHF and UHF). As a result, the RF spectrum congestion problem has been attracting the interest of many scientists and engineers during the last few years and is currently becoming one among the hot topics in research field [5], [6].

A plethora of papers have addressed the problem of designing radar waveforms with a smart frequency allocation [7], so as to control the interference brought on overlayed wireless networks (communication and navigation systems), while enhancing radar performance requirements in terms of range-Doppler resolution, low range and Doppler sidelobes, detection, and tracking capabilities. In [8], a waveform design technique is introduced to confer some desired spectral nulls to the radar signal. The idea is to perturb a stepped frequency modulated pulse forcing an additional fast time polyphase code. The approach is extended in [9] to the case of continuous phase waveforms that place nulls at specific frequencies. An alternate projection algorithm for the construction of chirp-like constant-modulus signals with a single spectral null is proposed in [10], whereas in [11] its extension, addressing the production of multiple notches, is established. In [12], a fast coding technique based on alternate projections and successive fast Fourier transforms is developed to obtain sparse waveforms with a controlled Peak Sidelobe Level (PSL). In [13] and [14], sparse frequency constant modulus radar signals with a low Integrated Sidelobe Level (ISL) are built optimizing a suitable combination between the ISL metric and a penalty function accounting for the waveform frequency allocation. Finally, in [15], a spectrum-centric signal design is developed based on the minimization of the transmitted energy on a set of disjoint stop-band frequencies under a unimodularity constraint and AutoCorrelation Function (ACF) masking.

In this paper, cognitive procedures are proposed to devise radar waveforms that exhibits desirable spectral features (ensuring coexistence with overlayed wireless networks) and optimize radar detection performance. It is supposed that the radar system has the ability to predict the behaviour of surrounding licensed radiators, for instance using a Radio Environmental Map (REM), [16], containing geographical features, information on available wireless services as well as locations and activities of wireless transmitters. More in details, the described design techniques consider as figure of merit the Signal to Interference plus Noise Ratio (SINR) and optimize the transmitted radar waveform constraining the amount of interference energy on crowded/reserved frequency bands. Specifically, both global and local spectral compatibility requirements are considered at the design stage. To manage some relevant features of the radar probing signal, in addition to a requirement on the maximum radiated energy, a similarity-like constraint is enforced on the transmit sequence. By doing so, a control of some significant waveform characteristics, such as range-Doppler resolution, variations in the signal modulus, ISL, and PSL is provided. Hence, algorithms to devise optimized radar waveforms complying with the considered constraints are presented. Finally, some interesting case studies are reported highlighting the trade-off among the achievable

978-1-5090-0326-6/16/$31.00 ©2016 IEEE

SINR, spectral shape, and ACF features of the synthesized waveforms.

The remainder of the paper is organized as follows. In Section II, the model for the radar transmitted signal and the description of coexisting wireless systems are reported. In Section Section III, the constrained optimization problems for waveform design under either global or local spectral compatibility requirements are formulated and studied. In Section IV, the performance of the considered techniques is illustrated. Finally, Section V is devoted to conclusions and proposals for possible future research tracks.

II. System Model

Let $c(t)$ be the baseband equivalent of the transmitted radar pulse modeled as the superposition of N linearly modulated unitary energy sub-pulses. The code element associated with the i-th sub-pulse is denoted[1] by $c(i)$ whereas the vector $\boldsymbol{c} = [c(1), \ldots, c(N)]^T \in \mathbb{C}^N$ represents the fast-time radar code. The waveform at the receiver end is down-converted to baseband, undergoes a sub-pulse matched filtering operation, and then is sampled. As a result, the N-dimensional column vector $\boldsymbol{v} = [v(1), \ldots, v(N)]^T \in \mathbb{C}^N$ of the fast-time observations from the range-azimuth cell under test can be modeled as

$$\boldsymbol{v} = \alpha_T \boldsymbol{c} + \boldsymbol{n}, \tag{1}$$

with α_T a complex parameter accounting for channel propagation and backscattering effects from the target within the range-azimuth bin of interest and $\boldsymbol{n}$ the N-dimensional column vector containing the filtered disturbance signal samples, which is modeled as a complex, zero-mean, circularly symmetric Gaussian random vector with covariance matrix $\boldsymbol{M} = \mathbb{E}[\boldsymbol{n}\boldsymbol{n}^\dagger]$. As to the licensed radiators coexisting with the radar of interest, it is supposed that each of them is operating over a frequency band $\Omega_k = \left[f_1^k, f_2^k\right]$, $k = 1, \ldots, K$, where f_1^k and f_2^k denote the lower and upper normalized frequencies for the k-th system, respectively. To ensure spectral compatibility the radar has to properly shape its transmit waveform to manage the amount of interfering energy produced on the shared frequency bandwidths. Specifically, the energy radiated on the k-th band can be essentially evaluated as

$$\int_{f_1^k}^{f_2^k} S_c(f)\, df \quad = \quad \boldsymbol{c}^\dagger \boldsymbol{R}_I^k \boldsymbol{c}, \tag{2}$$

where $S_c(f) = \left|\sum_{n=1}^N \boldsymbol{c}(n) e^{-j2\pi f n}\right|^2$ is the Energy Spectral Density (ESD) of the fast-time code $\boldsymbol{c}$ and $\forall (m,l) \in \{1, \ldots, N\}^2$

$$\boldsymbol{R}_I^k(m,l) = \begin{cases} f_2^k - f_1^k & m = l \\ \dfrac{e^{j2\pi f_2^k (m-l)} - e^{j2\pi f_1^k (m-l)}}{j2\pi(m-l)} & m \neq l \end{cases}. \tag{3}$$

Thus, denoting by E_I^k, $k = 1, \ldots, K$, the acceptable level of disturbance on the k-th bandwidth, that is related to the quality of service required by the k-th telecommunication network, the interference energy produced on the shared frequency bandwidths can be controlled forcing the transmitted waveform to comply with one of the following conditions

- global design constraint

$$\sum_{k=1}^K w_k \boldsymbol{c}^\dagger \boldsymbol{R}_I^k \boldsymbol{c} \leq E_I\,; \tag{4}$$

- local design constraint

$$\boldsymbol{c}^\dagger \boldsymbol{R}_I^k \boldsymbol{c} \leq E_I^k, \quad k = 1, \ldots, K\,. \tag{5}$$

where $E_I = \sum_{k=1}^K w_k E_I^k$ and $w_k \geq 0$, $k = 1, \ldots, K$, specific weights. According to (4), a constraint on the global injected interference energy is forced [17]. In this case, different importance can be given to the coexisting wireless networks, for instance based on their distance from the radar and their tactical importance (i.e. navigation systems, military communications, public services, etc), appropriately choosing the coefficients. As to (5), a local control of the interference energy produced on each shared frequency bandwidth is pursued [18]. Remarkably, the REM represents the key instrument to gain the spectrum awareness required to force either the constraint (4) or (5).

III. Problem Formulation and Code Design

In this section, waveform design techniques that attempts to enhance the target detection probability while controlling both the amount of interfering energy produced in the licensed bands and some desirable features of the transmitted waveform is introduced. The figure of merit is the SINR defined as

$$\text{SINR} = |\alpha_T|^2 \boldsymbol{c}^\dagger \boldsymbol{R} \boldsymbol{c}\,, \tag{6}$$

To control some relevant features of the probing signal, other than an energy requirement ($\|\boldsymbol{c}\|^2 \leq 1$), a similarity-like constraint is enforced on the transmit sequence, i.e., $\|\boldsymbol{c} - \alpha_{c_0}\boldsymbol{c}_0\|^2 \leq \epsilon$, where the parameter $0 \leq \epsilon \leq 1$ rules the size of the trust hypervolume, $\boldsymbol{c}_0$ is a suitable reference code, and α_{c_0}, with $|\alpha_{c_0}|^2 \leq 1$, enables the modulation of the reference code energy.

The degree of freedom given by α_{c_0} allows to center the trust hypervolume along the reference code direction (i.e., in $\alpha_{c_0}\boldsymbol{c}_0$) according to the actual radar signal energy $\|\boldsymbol{c}\|^2$. As a result, a similarity between the sought radar code and the signature of the reference code is enforced. Interestingly, when $\|\boldsymbol{c}\|^2 = 1$ this constraint is equivalent to the conventional similarity. Notice that several reasons motivate its use [19]: an unconstrained optimization can lead to signals with significant

[1] We adopt the notation of using boldface for vectors $\boldsymbol{a}$ (lower case), and matrices $\boldsymbol{A}$ (upper case). The n-th element of $\boldsymbol{a}$ and the (m,l)-th entry of $\boldsymbol{A}$ are respectively denoted by $a(n)$ and $\boldsymbol{A}(m,n)$. The transpose and the conjugate transpose operators are denoted by the symbols $(\cdot)^T$ and $(\cdot)^\dagger$ respectively. $\mathbb{C}^N$ and $\mathbb{H}^N$ are respectively the sets of N-dimensional vectors of complex numbers and $N \times N$ Hermitian matrices. $\boldsymbol{A} \succeq \boldsymbol{0}$ means that $\boldsymbol{A}$ is a positive semidefinite matrix. $\boldsymbol{I}$ denotes the identity matrix. The Euclidean norm of the vector $\boldsymbol{x}$ is denoted by $\|\boldsymbol{x}\|$ whereas the modulus of the complex number x is denoted with $|x|$. The letter j represents the imaginary unit (i.e. $j = \sqrt{-1}$), while the letters i and k often serve as indexes. $\mathbb{E}[\cdot]$ denotes the statistical expectation.

modulus variations, poor range resolution, high peak sidelobe levels, and more generally with an undesired ambiguity function shape. These drawbacks can be partially circumvented forcing the solution to be similar to the signature of a known code $\boldsymbol{c}_0$ ($\|\boldsymbol{c}_0\|^2 = 1$), which shares some nice properties such as constant modulus and reasonable peak sidelobe level.

In line with the two different spectral compatibility requirements (4) and (5), the waveform design problem of interest can formulated as

$$\mathcal{P}_i \begin{cases} \max\limits_{\boldsymbol{c}\in\mathbb{C}^N, \alpha_{c_0}\in\mathbb{C}} & \boldsymbol{c}^\dagger \boldsymbol{R}\boldsymbol{c} \\ \text{s.t.} & \|\boldsymbol{c}\|^2 \le 1 \\ & \boldsymbol{c} \in \mathcal{H}_i \\ & \|\boldsymbol{c} - \alpha_{c_0}\boldsymbol{c}_0\|^2 \le \epsilon \\ & |\alpha_{c_0}|^2 \le 1 \end{cases}, \quad i = 1, 2, \tag{7}$$

where

$$\begin{aligned} \mathcal{H}_1 &= \left\{ \boldsymbol{c} \in \mathbb{C}^N : \sum_{k=1}^{K} w_k \boldsymbol{c}^\dagger \boldsymbol{R}_I^k \boldsymbol{c} \le E_I \right\} \\ \mathcal{H}_2 &= \left\{ \boldsymbol{c} \in \mathbb{C}^N : \boldsymbol{c}^\dagger \boldsymbol{R}_I^k \boldsymbol{c} \le E_I^k, k = 1, \ldots, K \right\}. \end{aligned} \tag{8}$$

A. Global Design Solution Technique

In this section Problem $\mathcal{P}_1$, which accounts for a global constraint about the spectral compatibility requirements, is studied. This design problem can be solved resorting to the analytical framework developed in [17], recasting it as a Quadratically Constrained Quadratic Programming (QCQP) problem which is, in general, difficult to solve [20], [21]. Hence, some hidden convexities can be exploited to compute the transmit signal maximizing the SINR with a polynomial complexity [17]. From a technical point of view $\mathcal{P}_1$ is equivalent to a SemiDefinite Programming (SDP) convex problem whose optimal solution $\boldsymbol{C}^\star$ allows the design of $\boldsymbol{c}^\star$ by means of a specific rank-one decomposition procedure [21]. Figure 1 summarizes the main steps involved in the optimal design.

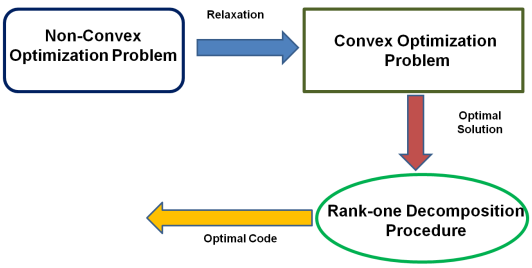

Fig. 1: Block scheme of the optimization procedure leading to the optimal transmit code for the global design.

B. Local Design Solution Technique

In this section Problem $\mathcal{P}_2$, accounting for local spectral compatibility constraints is considered. In [18], it is shown that $\mathcal{P}_2$ is a non-convex QCQP problem and, unlike $\mathcal{P}_1$ which is hidden convex, it belongs to the class of NP-hard problems [22] due to the presence of multiple spectral constraints. Hence, a procedure based on the SemiDefinite Relaxation (SDR) and randomization paradigm [22] is developed to synthesize in polynomial time solutions with quality guarantee. The main idea is to explore the one-dimension subspaces contained in the range span of the optimal solution to the SDP relaxation [18]. Figure 2 summarizes the main steps involved in the optimization algorithm.

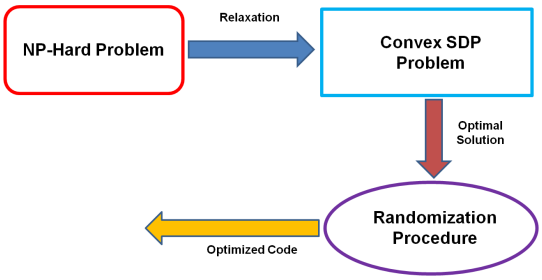

Fig. 2: Block scheme of the optimization procedure leading to the optimized transmit code ensuring local control on the radiated interfering energy.

IV. Performance Assessment

The performance of the proposed waveform design techniques are now shown in terms of achievable SINR value, spectral shape, autocorrelation features, and transmitted energy. Hereafter, a radar whose baseband equivalent transmitted signal has a two-sided bandwidth of 810 kHz (corresponding to a sampling frequency of $f_s = 810$ kHz) is considered. Additionally, the interference is composed of unlicensed narrowband continuous jammers, white interference, and licensed coexisting telecommunication networks spectrally overlaid to the radar of interest. The disturbance covariance matrix is modeled as

$$\boldsymbol{M} = \sigma_0 \boldsymbol{I} + \sum_{k=1}^{K} \frac{\sigma_{I,k}}{\Delta f_k} \boldsymbol{R}_I^k + \sum_{k=1}^{K_J} \sigma_{J,k} \boldsymbol{R}_{J,k}, \tag{9}$$

where $K = 7$ is the number of licensed radiators; $K_J = 2$ is the number of active and unlicensed narrowband jammers; $\Delta f_k = f_2^k - f_1^k$ is the bandwidth associated with the k-th licensed radiator, for $k = 1, \ldots, K$; $\sigma_{0_{\text{dB}}} = 0$ dB is the thermal noise level; $\sigma_{I,k}$ accounts for the energy of the k-th coexisting telecommunication network operating on the normalized frequency band $[f_1^k, f_2^k]$ ($\sigma_{I,k_{\text{dB}}} = 10$ dB, $k = 1, \ldots, K$); $\sigma_{J,k}$, $k = 1, \ldots, K_J$, accounts for the energy of the k-th active jammer ($\sigma_{J,1_{\text{dB}}} = 40$ dB, $\sigma_{J,2_{\text{dB}}} = 50$ dB); $\boldsymbol{R}_{J,k}$ is the normalized disturbance covariance matrix of the k-th active unlicensed jammer, defined as

$$\boldsymbol{R}_{J,k} = \boldsymbol{r}_{J,k} \boldsymbol{r}_{J,k}^\dagger, \; k = 1, \ldots, K_J,$$

with $r_{J,k}(n) = e^{j2\pi f_{J,k} n / f_s}$, where $f_{J,k}$ denotes the Doppler shift of the k-th jammer ($f_{J,1}/f_s = 0.7$, and $f_{J,2}/f_s = 0.75$).

As to the overlayed and foreseen telecommunication systems spectrally coexisting with the radar of interest we consider the following normalized baseband equivalent radar stop-

bands [23]

$$\begin{aligned}\Omega_1 &= [0.0000, 0.0617], \quad \Omega_2 = [0.0988, 0.2469],\\ \Omega_3 &= [0.2593, 0.2840], \quad \Omega_4 = [0.3086, 0.3827],\\ \Omega_5 &= [0.4074, 0.4938], \quad \Omega_6 = [0.5185, 0.5556],\\ \Omega_7 &= [0.9383, 1.0000].\end{aligned} \tag{10}$$

Additionally, we consider $E_{I\,\mathrm{dB}}^k = 10\log_{10}(E_I^k) = -20$ dB for $k \neq 3, 6$ and $E_{I\,\mathrm{dB}}^k = -30$ dB for the other frequency bands.

Concerning the reference code $\boldsymbol{c}_0$, we employ a unitary norm Linear Frequency Modulated (LFM) pulse with a duration of 200 μs and a chirp rate $K_s = (750\times10^3)/(200\times10^{-6})$ Hz/s which corresponds to $N = 162$ samples due to the considered sampling frequency. Finally, as to the global design we consider $E_I = \sum_{k=1}^{7} E_I^k$ and $R_I = \sum_{k=1}^{7} R_I^k$.

In Figure 3, the normalized (to $|\alpha_T|^2$) SINR and the transmitted energy versus ϵ for the waveforms synthesized according to the local design and the global design are shown. As expected, regardless of the design technique, the higher ϵ the better the detection performance. Besides, the two approaches provide similar SINR values and essentially achieve the same performance level for ϵ high enough.

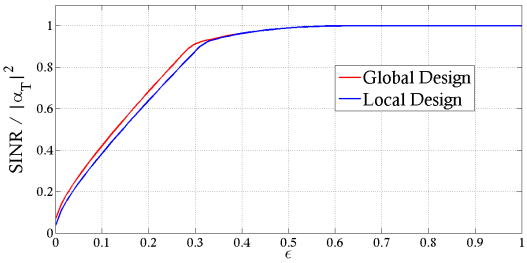

(a) Normalized SINR versus ϵ.

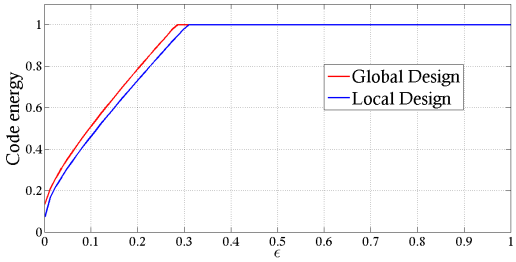

(b) Code energy versus ϵ.

Fig. 3: Comparison between global and local design in terms of normalized SINR and code energy.

In Figure 4, the ESD and the squared modulus of the normalized (to the peak value) ACF of the codes synthesized through both the design strategies, assuming $\epsilon = 0.31$, are reported. For comparison purposes the behaviour of the reference code $\boldsymbol{c}_0$ is displayed too. In Figure 4(a), the stop-bands where the licensed systems are located are shaded in light gray. The curves highlight the capability of the local design to perform a fine control of the amount of interference energy produced over the shared frequency bandwidths. In fact, unlike the global design that shares a flat ESD in the stop-bands, the code synthesized using the local design exhibits a spectral behaviour which closely follows the local spectral compatibility requirements. In fact, within the third and sixth stop-bands the ESD is lower than that in the others. Moreover, in Ω_4 and Ω_5 a higher ESD than in Ω_2 is observed. In a nutshell, the results clearly show the capability of the local design to grant the necessary quality of service to the overlayed radiators. Interestingly, the ACF obtained using the local and the global design share similar features as both satisfy the same similarity constraint.

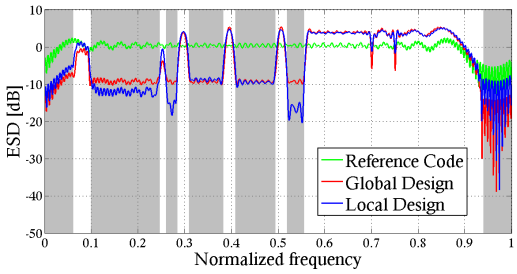

(a) ESD versus normalized frequency.

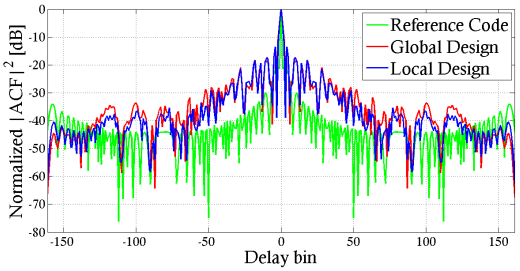

(b) Squared modulus of ACF versus delay bin.

Fig. 4: Comparison between global and local design in terms of ESD and ACF considering $\epsilon = 0.31$.

In Figure 5, the behaviour of the codes synthesized through $\mathcal{P}_2$ (in terms of ESD and normalized ACF) is reported for the three values of epsilon ($\epsilon = 0.001, 0.322, 0.584$). As expected, the code for $\epsilon = 0.001$ is almost aligned with $\boldsymbol{c}_0$. Moreover, it can be observed that increasing the similarity parameter ϵ smarter and smarter distributions of the useful energy are achieved. Indeed, an enhancement of the unlicensed jammer rejection as well as a possible reduction of the radar emission in correspondence of the shared frequencies is obtained. This is in agreement with the SINR trend of Figure 3(a). Finally, inspection of Figure 5(b) highlights that better SINR values and interference rejection are traded-off with worse and worse range resolutions and/or ISLs/PSLs.

V. Conclusions

This paper has considered the cognitive design of radar waveforms in a spectrally crowded environment where some frequency bands are shared among the radar and other telecommunication systems.

Either global and local spectral compatibility requirements have been considered at the design stage. Hence, polynomial

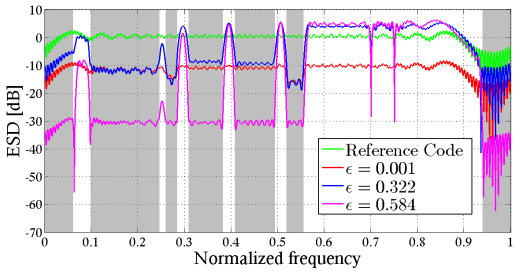

(a) ESD versus normalized frequency.

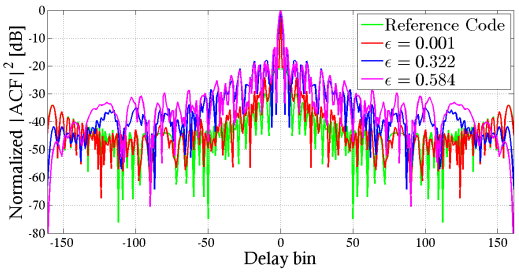

(b) Squared modulus of ACF versus delay bin.

Fig. 5: Local design results in terms of ESD and ACF.

computational complexity solution procedures have been described to synthesize optimized radar waveforms. The performance of the synthesized signals has been analyzed studying the tradeoff among the achievable SINR, spectral shape, ACF features, and radiated energy. Remarkably, the local constraint approach is able to ensure a precise control on the interference energy induced on each shared/reserved bandwidth at the price of a slight performance reduction.

Possible future research tracks might concern the development of robust frameworks to contrast transmitter impurities and the cognitive fully exploitation of the available multiple dimensions, i.e., spatial, temporal, and polarizations [24]–[26], to further improve system performance. Besides, it could be interesting to extend the local approach to account for unimodular waveforms (which is tantamount to introducing additional non-convex constraints) and signal-dependent interference (implying that the objective function is no longer quadratic) [27].

REFERENCES

[1] M. Wicks, "Spectrum crowding and cognitive radar," in *2nd International Workshop on Cognitive Information Processing (CIP)*, Elba Island, Italy, June 2010, pp. 452–457.

[2] L. S. Wang, J. P. McGeehan, C. Williams, and A. Doufexi, "Application of cooperative sensing in radar - communications coexistence," *IET Proceedings on Radar, Sonar and Navigation*, vol. 2, no. 6, pp. 856–868, July 2008.

[3] J. D. Taylor, *Ultra-Wideband Radar Technology*, CRC Press LLC, 2001.

[4] J. Salzman, D. Akamine, and R. Lefevre, "Optimal waveforms and processing for sparse frequency uwb operation," in *Proceedings of the 2001 IEEE Radar Conference*, Atlanta, USA, May 2001, pp. 105–110.

[5] H. Griffiths, "The challenge of spectrum engineering," in *European Radar Conference (EuRAD)*, Rome, Italy, October 2014, pp. 1–4.

[6] H. Griffiths, L. Cohen, S. Watts, E. Mokole, C. Baker, M. Wicks, and S. Blunt, "Radar spectrum engineering and management: Technical and regulatory issues," *Proceedings of the IEEE*, vol. 103, no. 1, pp. 85–102, January 2015.

[7] C. Nunn and L. R. Moyer, "Spectrally-compliant waveforms for wideband radar," *IEEE Aerospace and Electronics System Magazine*, vol. 27, no. 8, pp. 11–15, August 2012.

[8] K. Gerlach, "Thinned spectrum ultrawideband waveforms using stepped-frequency polyphase codes," *IEEE Transactions on Aerospace and Electronic Systems*, vol. 34, no. 4, pp. 1356–1361, October 1998.

[9] K. Gerlach, M. R. Frey, M. J. Steiner, and A. Shackelford, "Spectral nulling on transmit via nonlinear fm radar waveforms," *IEEE Transactions on Aerospace and Electronic Systems*, vol. 47, no. 2, pp. 1507–1515, April 2011.

[10] I. W. Selesnick, S. U. Pillai, and R. Zheng, "An iterative algorithm for the construction of notched chirp signals," in *IEEE International Radar Conference*, Washington DC, USA, May 2010, pp. 200–203.

[11] I. W. Selesnick and S. U. Pillai, "Chirp-like transmit waveforms with multiple frequency-notches," in *IEEE Radar Conference*, Kansas City, MO, USA, May 2011, pp. 1106–1110.

[12] R. Kassab, M. Lesturgie, and J. Fiorina, "Alternate projections technique for radar waveform design," in *International Radar Conference - Surveillance for a Safer World*, October 2009, pp. 1–4.

[13] H. He, P. Stoica, and J. Li, "Waveform design with stopband and correlation constraints for cognitive radar," in *2010 2nd International Workshop on Cognitive Information Processing (CIP)*, Elba Island, Italy, June 2010, pp. 344–349.

[14] G. Wang and Y. Lu, "Designing single/multiple sparse frequency waveforms with sidelobe constraint," *IET Proceedings on Radar, Sonar and Navigation*, vol. 5, no. 1, pp. 32–38, January 2011.

[15] L. Patton, C. A. Bryant, and B. Himed, "Radar-centric design of waveforms with disjoint spectral support," in *IEEE Radar Conference*, Atlanta, GE, USA, May 2012, pp. 1106–1110.

[16] Y. Zhao, J. Gaeddert, K. K. Bae, and J. H. Reed, "Radio environment map-enabled situation-aware cognitive radio learning algorithms," in *Software Defined Radio (SDR) Technical Conference*, Orlando (FL), USA, November 2006.

[17] A. Aubry, A. De Maio, M. Piezzo, and A. Farina, "Radar waveform design in a spectrally crowded environment via nonconvex quadratic optimization," *IEEE Trans. on Aerospace and Electronic Systems*, vol. 50, no. 2, pp. 1138–1152, April 2014.

[18] A. Aubry, V. Carotenuto, and A. De Maio, "Forcing multiple spectral compatibility constraints in radar waveforms," *IEEE Signal Processing Letters*, vol. 23, no. 4, pp. 483–487, April 2016.

[19] F. Gini, A. De Maio, and L. Patton, *Waveform Design and Diversity for Advanced Radar Systems*, The Institution of Engineering and Technology (IET), June 2011.

[20] A. Aubry, A. De Maio, Y. Huang, M. Piezzo, and A. Farina, "A new radar waveform design algorithm with improved feasibility for spectral coexistence," *IEEE Trans. on Aerospace and Electronic Systems*, vol. 51, no. 2, pp. 1029–1038, Apr. 2015.

[21] W. Ai, Y. Huang, and S. Zhang, "New results on hermitian matrix rank-one decomposition," in *Mathematical Programming*, vol. 128 of *Series A*, pp. 253–283. June 2011.

[22] S. He, Z.-Q. Luo, J. Nie, and S. Zhang, "Semidefinite relaxation bounds for indefinite homogeneous quadratic optimization," *SIAM Journal on Optimization*, vol. 19, no. 2, pp. 503–523, 2008.

[23] H. Leong and B. Sawe, "Channel availability for east coast high frequency surface wave radar systems," Technical Report DREO TR 2001-104, Defence Research Establishment, Ottawa (Ontario), November 2001.

[24] J. Li and P. Stoica, "Mimo radar with colocated antennas," *IEEE Signal Processing Magazine*, vol. 24, no. 5, pp. 106–114, Sep. 2007.

[25] A. Aubry, A. De Maio, and Y. Huang, "Mimo radar beampattern design via psl/isl optimization," *IEEE Trans. on Signal Processing*, vol. 64, no. 15, pp. 3955–3967, Aug. 2016.

[26] D. A. Garren, A. C. Odom, M. K. Osborn, J. S. Goldstein, S. U. Pillai, and J. R. Guerci, "Full-polarization matched-illumination for target detection and identification," *IEEE Trans. on Aerospace and Electronic Systems*, vol. 38, no. 3, pp. 824–837, Jul. 2002.

[27] A. Aubry, A. De Maio, M. Piezzo, M. N. Naghsh, M. Soltanalian, and P. Stoica, "Cognitive radar waveform design for spectral coexistence in signal-dependent interference," in *IEEE Radar Conference*, Cincinnati (OH), USA, May 2014, pp. 474–478.

Experimental Study on Full-Polarization Micro-Doppler of Space Precession Target in Microwave Anechoic Chamber

Liu Jin, Wu Qi-hua, Ai Xiao-Feng, Xiao Shun-Ping
State Key Laboratory of Complex Electromagnetic Environment Effects on Electronics and Information System
National University of Defense Technology
Changsha, Hunan, P.R China
liujin@nudt.edu.cn

***Abstract*—Based on the background of radar target detection and recognition of space precession targets, an experimental study on full-polarization micro-Doppler of those targets is introduced. The wide-band scattering properties of space precession targets are analyzed, and then the theoretical full-polarization micro-Doppler models are proposed. The scenario of the experiment is introduced, and the measured data are analyzed, and then the differences of full-polarization micro-Doppler of different scattering structures can be observed during precession.**

Keywords—Target Recognition; Precession; Microwave Anechoic Chamber; Micro-Doppler; Polarization; Wide Band

I. INTRODUCTION

Along with the improvement of radar measurement and modern signal processing, the description of target details, especially the precise description of the target's motion state and construction has become a research hotspot of radar detection.

Normally micro-motion is defined as the whole or parts of target's micro motion such as vibration, rotation and coning except translational motion[1][2]. Micro-motion is decided by the physical property such as the distribution feature of the target's mass and the dynamic characteristics, which can be regarded as the inherent motion forms. Micro-motion makes it possible to extract the target's features relating to physical property, which provides a novel path to non-cooperative target's detection and recognition[3][4].

Modern radar system is moving towards the ability of wide-band, full-polarization and coherent measurement, and provides an efficient tool for richer target information measurement. On the background of space precession target measurement, this paper aims to research the dynamical scattering properties of space precession targets by way of microwave anechoic chamber experiment. Based on the wide-band measurement experiment[5], the full-polarization micro-Doppler property of the space precession target is further analyzed, which supports the research of ballistic target recognition in midcourse for microwave radar.

II. WIDE-BAND SCATTERING PROPERTIES OF SPACE PRECESSION TARGETS

In high-frequency area, the total electromagnetic scattering can be seen as the composition of the electromagnetic scattering of some parts, and this special scattering point is defined as the equivalent scattering center[6]. For typical space precession target, the scattering mechanism of its nose cone is hyperboloid specular reflection, the equivalent scattering center slides with the change of the incidence direction[6]. And in some warhead designs the radius of the nose cone is small that the sliding can be ignored, in other words the equivalent scattering center can be seen to be fixed. The scattering mechanism of its torus is borderline diffraction[7], and its equivalent scattering center is the cross point of the incidence plane and the edge[6].

Considering the flat cone cylinder warhead, shown as Fig 1, when the radar line of sight $\mathbf{R}_{\text{los}}$ illuminates along the included angle with the cone axis β, a borderline scattering center will be formed at the joint part of the edge of the bottom and the cone-cylinder. The points B, C, D marked in figure 1 is the cross points of the incident plane and the edge of the two rings, and it is also the location of the borderline scattering center at the missile body, which can be strictly demonstrated using the method of equivalent currents[8]. Considering the shadowing effects, only one scattering center is formed at the edge of the bottom. Besides, when β is larger than the semi-cone angle, the scattering center at C will not exist. During the precession of the warhead, the target's symmetry axis will change, and then causing the change of the incident plane, therefore the scattering center will slide along the ring, not fixed.

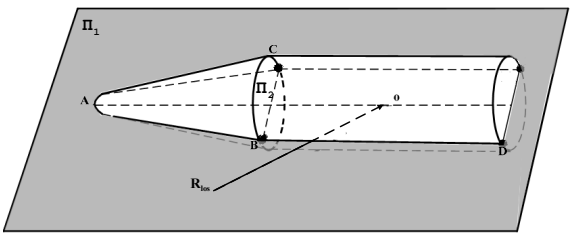

Fig 1. Equivalent scattering center of the precession target

In warhead designs, common structure of both the nose cone and rings is rotational symmetry. For this structure, the illuminated parts changes when the target circles around the symmetry axis, however the key factor determining the echo such as the surface shape and the medium doesn't change. Although the surface flow field of the electromagnetic wave affects the echo, its action time is short, usually several microseconds, therefore the scattering field can be regarded fixed. In this case, the scattering center of the warhead's main body will not change with the target spin, so the coning is the main influence of the precession.

This research is funded in part by National Science Foundation of China under contract 61101180 and 61401491.

978-1-5090-0326-6/16/$31.00 ©2016 IEEE

III. FULL-POLARIZATION MICRO-DOPPLER MODEL OF THE SPACE PRECESSION TARGET

As shown in Fig 2, precession is constituted by two parts, one is the spin circling the missile body's symmetry axis **Oz** with the angular velocity ω_r, and the other is the coning circling the precession axis **OZ** with the angular velocity ω_p. The included angle θ between **OZ** and **Oz** is the precession angle.

In Fig 2, R is the radar's position, O is the target's center of mass, **OX** is in the plane formed by **OZ** and **OR**, vertical to **OZ** and forming an acute angle with **OR**. **OY**, **OX** and **OZ** form a right-handed coordinate system, and call **OXYZ** the reference coordinate system. **Ox** is in the plane formed by **OZ** and **Oz**, vertical to **Oz** and forming an obtuse angle with **OZ**. **Oy**, **Ox** and **Oz** form a right-handed coordinate system, and call **Oxyz** the local coordinate system. At initial time, the included angle of the projection of **Oz** at **OXY** plane and **OX** is φ. The included angle β of **OR** and **OZ** is called the average aspect angle, and The included angle γ of **OR** and **Oz** is called the incident angle.

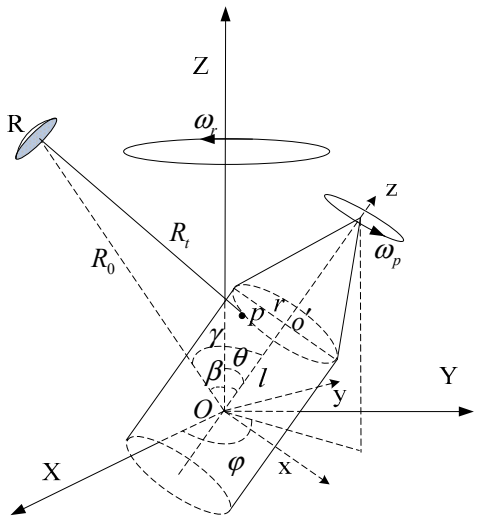

Fig 2. Precession model

Assume that there exists a scattering center p in the missile body, and R_t is the distance between radar R and the scattering center p. Radar transmits the pulse signal with the frequency f_0. The slow-time echo can be written as

$$\mathbf{s_r}(t)=\begin{bmatrix} s_{HHr}(t) & s_{HVr}(t) \\ s_{VHr}(t) & s_{VVr}(t) \end{bmatrix}=\mathbf{S}(t)\exp(j2\pi\frac{2f_0R_t}{c}) \quad (1)$$

Where $\mathbf{S}(t)=\begin{bmatrix} a_{HH}(t)\exp(j\phi_{HH}(t)) & a_{HV}(t)\exp(j\phi_{HV}(t)) \\ a_{VH}(t)\exp(j\phi_{VH}(t)) & a_{VV}(t)\exp(j\phi_{VV}(t)) \end{bmatrix}$ is the polarization scattering matrix at t.

According to the geometrical relationship, to an ideal scattering center which has fixed polarization scattering matrix and location at the missile body, assuming its coordinate in the local coordinate system is (x,y,z), its distance to the radar is

$$\begin{aligned} R_t &= R_0-\cos\beta(z\cos\theta+y\sin\theta)-x\sin\beta\cos(\omega_p t+\varphi) \\ &+y\sin\beta\cos\theta\sin(\omega_p t+\varphi)-z\sin\beta\sin\theta\sin(\omega_p t+\varphi) \end{aligned} \quad (2)$$

And the echo's Doppler frequency of a single polarization channel $ij(i=H,V;j=H,V)$ is

$$\begin{aligned} f_{dij} &= \frac{1}{2\pi}\frac{d\Phi(s_{ij}(t))}{dt}=\frac{2\omega_p f_0\sin\beta}{c}(x\sin(\omega_p t+\varphi) \\ &+y\cos\theta\cos(\omega_p t+\varphi)-z\sin\theta\cos(\omega_p t+\varphi)) \end{aligned} \quad (3)$$

To the scattering center of the nose cone, assume the coordinate of its top in the local coordinate system is $(0,0,z)$, and the distance to the radar is

$$R_t=R_0-z\cos\beta\cos\theta-z\sin\beta\sin\theta\sin(\omega_p t+\varphi)+\Delta R_t \quad (4)$$

Where ΔR_t is the slide distance.

And the echo's Doppler frequency of a single polarization channel $ij(i=H,V;j=H,V)$ is

$$\begin{aligned} f_{dij} &= \frac{1}{2\pi}\frac{d\Phi(s_{ij}(t))}{dt}=\frac{2\omega_p f_0\sin\beta}{c}(x\sin(\omega_p t+\varphi) \\ &+y\cos\theta\cos(\omega_p t+\varphi)-z\sin\theta\cos(\omega_p t+\varphi)) \end{aligned} \quad (5)$$

Where $\frac{1}{2\pi}\frac{d\phi_{ij}}{dt}$ is the Doppler frequency shift caused by the polarization scattering matrix phase change.

For the ring structure, assume the distance between its center and the center of mass is l, and the ring's radius is r, then the distance between the two equivalent scattering center and the radar can be expressed as

$$\begin{aligned} R_{1t} &= R_0-k\cos\alpha(\cos\theta\cos\beta+\sin\theta\sin\beta\cos(\omega_p t+\varphi)) \\ &-k\sin\alpha\sqrt{1-(\cos\theta\cos\beta+\sin\theta\sin\beta\cos(\omega_p t+\varphi))^2} \end{aligned} \quad (6)$$

$$\begin{aligned} R_{2t} &= R_0-k\cos\alpha(\cos\theta\cos\beta+\sin\theta\sin\beta\cos(\omega_p t+\varphi)) \\ &+k\sin\alpha\sqrt{1-(\cos\theta\cos\beta+\sin\theta\sin\beta\cos(\omega_p t+\varphi))^2} \end{aligned} \quad (7)$$

Where $k=\sqrt{l^2+r^2}$, $\alpha=\arctan(\frac{r}{l})$. The echo's Doppler frequency of a single polarization channel $ij(i=H,V;j=H,V)$ is

$$\begin{aligned} f_{1dij} &= \frac{1}{2\pi}\frac{d\Phi(s_{ij}(t))}{dt} \\ &=\frac{1}{2\pi}\frac{d\phi_{ij}}{dt}+\frac{2kf_0}{c}(\omega_p\cos\alpha\sin\beta\sin\theta\sin(\omega_p t+\varphi) \\ &-\frac{\omega_p\sin\alpha\sin\beta\sin\theta\sin(\omega_p t+\varphi)(\cos\beta\cos\theta+\sin\beta\sin\theta\cos(\omega_p t+\varphi))}{\sqrt{1-(\cos\theta\cos\beta+\sin\theta\sin\beta\cos(\omega_p t+\varphi))^2}}) \end{aligned} \quad (8)$$

$$f_{2dij} = \frac{1}{2\pi}\frac{d\Phi(s_{ij}(t))}{dt} = \frac{1}{2\pi}\frac{d\phi_{ij}}{dt} + \frac{2kf_0}{c}(\omega_p \cos\alpha \sin\beta \sin\theta \sin(\omega_p t + \varphi) + \frac{\omega_p \sin\alpha \sin\beta \sin\theta \sin(\omega_p t + \varphi)(\cos\beta\cos\theta + \sin\beta\sin\theta\cos(\omega_p t + \varphi))}{\sqrt{1-(\cos\theta\cos\beta + \sin\theta\sin\beta\cos(\omega_p t + \varphi))^2}}) \quad (9)$$

It is known by theoretical derivation:

1. The Doppler of the rotational symmetry precession target is determined by the precession angle, radar's average line-of-sight angle and the coning frequency.
2. The Doppler of the ideal scattering center's coning is sine function. And when non-ideal scattering exists, the coordinate in the local coordinate system will make the Doppler deviate the sine function.

Target's polarization characteristic changes with time, and the phase change of polarization scattering matrix affects Doppler frequency, and the amplitude change affects signal's intensity.

IV. Experimental Scene of Full-Polarization Micro-Doppler Measurement

According to the motion feature and structure of the warhead, researchers make the precession target model shown in Fig 3.

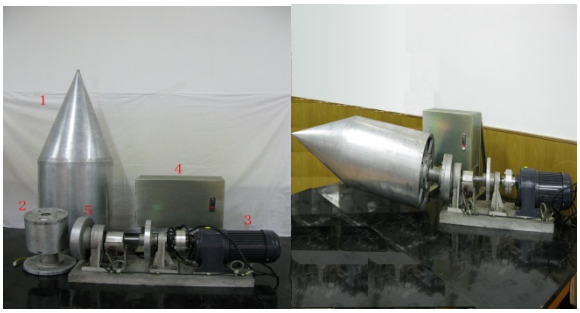

(a) individual components (b) combined model

Fig 3. The precession target model

Precession target is formed by five parts: warhead model, spin motor, coning motor, rotation coupling and control cabinet, which are marked as 1-5 in Fig3(a). By way of the combination of the target model, the change of the precession angle and the average line-of –sight angle and the change of the precession velocity, different motion states of different targets can be simulated.

The experiment is conducted in the compact microwave anechoic chamber, shown in Fig 4, the main facilities include network analyzer, transmit antenna, receive antenna, collimator reflector, antenna platform and target platform.

In microwave anechoic chamber measurements, network analyzer is used as transmit signal source and the echo processor. It works as a radar, being the key part of the system. network analyzer in this experiment is Agilent 8362B, its frequency range is 10MHz-20GHz[9], and the frequency range of the collimator reflector is 0.1GHz-40GHz, so this system can support the experiment from UHF band to Ku band.

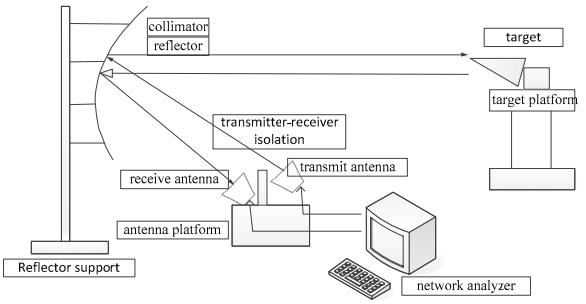

Fig 4. Microwave anechoic chamber measurement system of precession targets

The key of microwave anechoic chamber dynamic measurement is the expansion of network analyzer's dynamic data record function. In static measurements, network analyzer processes all the echoes at some specific posture averagely, and only makes one record. However in this experiment, the network analyzer is expected to simulate radar's detection, which requires continuously data record during target's motion. Dynamic data record can be realized by way of software development. according to the performance of Agilent 8362B, when the frequency range is 9GHz-10GHz and the interval is 5MHz, the data record frequency can reach 68Hz.

Connect the output of the network analyzer with the receive parts and the antenna of the band to be measured, and put the antennas on the focus of the collimator reflector, and isolate them by the transmitter-receiver isolation. Let the antenna's polarization be linear polarization, variable polarization measurement can be conducted by accurate antenna rotation facility.

V. Experiment Results Analysis

The experiment on full-polarization micro-Doppler of space precession target is conducted in the Microwave Lab of National University of Defense Technology. Fig 5 shows the experiment scene.

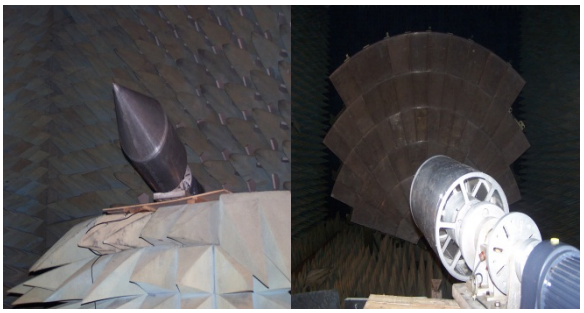

(a) Front and side view (b)Back view

Fig 5. Experiment scene of full-polarization micro-Doppler of space precession target

The scanning frequency range in this experiment is 9GHz-10GHz, the bandwidth is 1GHz and the interval is 5MHz. by IFFT transform to the data collected, HRRP can be get for target's current posture. Processing the HRRP by time-frequency analysis, micro-Doppler of different structures can be obtained during target's precession. The polarization scattering property is reflected in the time-frequency energy distribution shown in Fig 6. And Fig 7-10 gives out different structure's micro-Doppler of HH,HV,VH,VV polarization

channels, where (a) means the micro-Doppler of the nose cone,(b) means the micro-Doppler of the middle ring, (c) means the micro-Doppler of the bottom ring, the precession angle is 7.9, the average line-of-sight angle is 10.4° ,and the coning frequency is 0.26Hz.

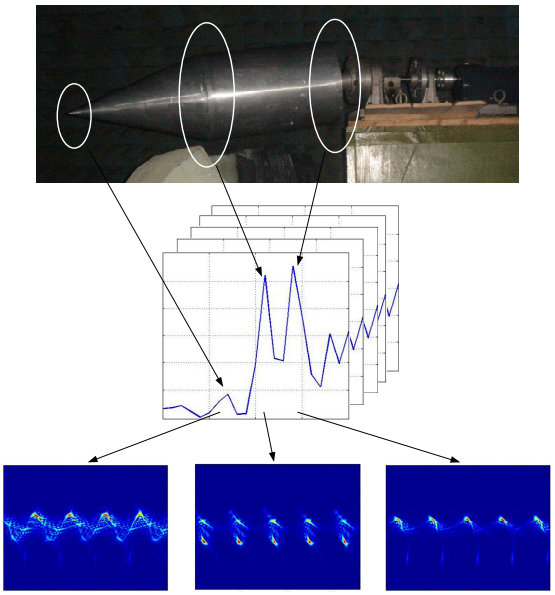

Fig 6. Measurement results analysis

Though observation, conclusions can be drawn as follows:

1. The warhead design is usually very simple due to the aerodynamics, so it has limited numbers of scattering centers. As shown in figure 6, HRRP is made up by three scattering centers, which is the nose cone, the middle ring and the bottom ring.

2. From Fig 7(a) and 10(a), for HH and VV polarization the micro-Doppler of the nose cone is sine. Figure 11 gives out the comparison of the measurement results and the theoretical micro-Doppler frequency according to formula (5) marked by the imaginary line for VV polarization. From Fig 8(a) and 8(b), for HV and VH polarization the echo of the nose cone is very weak, it's concluded that the echo energy of co-polarization is much larger than that of cross-polarization.

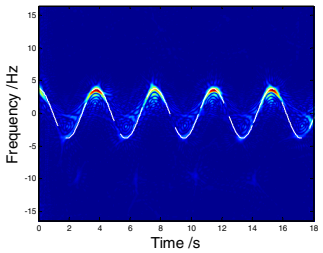

Fig 11.Comparison of the measurement results and the theoretical micro-Doppler frequency for the nose cone

3. From Fig7(b),8(b),9(b) and 10(b), the middle and bottom rings is the sliding scattering centers and the micro-Doppler deviates from sine function. Fig 12. gives out the comparison of the measurement results and the theoretical micro-Doppler frequency according to formula (8) and (9) which is marked by the imaginary line for VV polarization. Compare Fig 7(b) and 10(b) with Fig 8(b) and 9(b), the cross-polarization is one order of magnitude lower than the co-polarization. Besides, the micro-Doppler of the same structure for different polarizations differs slightly, which is caused by the polarization scattering matrix phase change in formula (1).

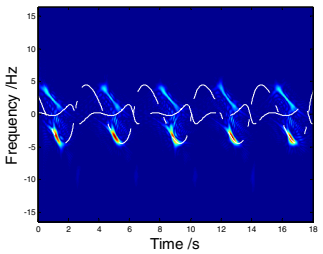

Fig 12. Comparison of the measurement results and the theoretical micro-Doppler frequency for the middle ring

4. From the comparison of Fig 7,8,9,10, the echo intensity of the nose cone is one order of magnitude lower than the ring structure. It shows that the scattering energy of ring structure is stronger than the nose cone. The scattering intensity of the nose cone is stable, while the scattering intensity of the ring structure is sensitive to the posture.

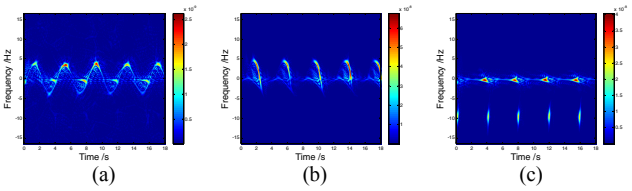

(a) (b) (c)

Fig 7. HH polarization

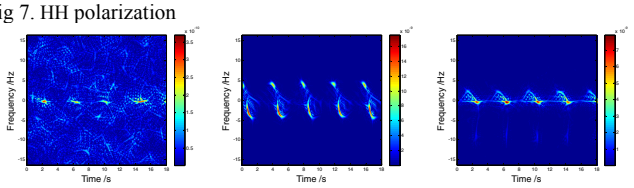

(a) (b) (c)

Fig 8 .HV polarization

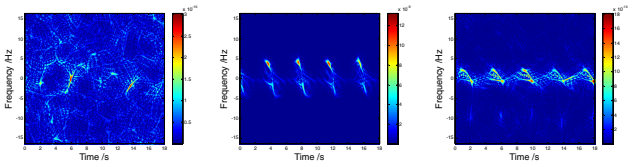

(a) (b) (c)

Fig 9. VH polarization

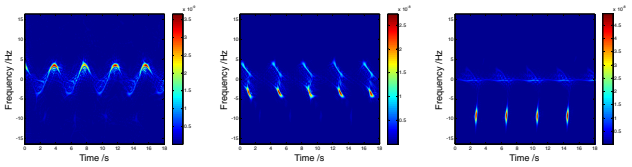

(a) (b) (c)

Fig 10. VV polarization

VI. Conclusion

In this paper the measurement system for precession target is built by precession target model design and expansion of microwave anechoic chamber dynamic measurement function. Based on this the full-polarization micro-Doppler characteristic of precession targets is studied. The experiment results are accordance with the theoretical results. Further we will take advantage of the microwave anechoic chamber measurement data to conduct the study on motion and structure feature extraction of precession targets based on spatial polarization.

References

[1] Zhuang Zhaowen, Liu Yongxiang, Li Xiang. The Achievements of Target Characteristic with Micro-Motion. ACTA ELECTRONICA SINICA.2007,vol.35(3),pp.520-525.

[2] V. C. Chen, F. Li, S. Ho, et al. Micro-doppler effect in radar: phenomenon, model and simulation study. IEEE Trans on Aerospace and Electronic Systems,2006, vol.42(1),pp. 2-21.

[3] Liu Yongxiang, Li Xiang ,Zhuang Zhaowen. Precession characteristic of space targets and applications in radar recognition. Progress in Natural Science.2004,vol.14(11),pp. 1329－1332.

[4] Wang Tao, Zhou Yin,Wang Xuesong, Xiao Shunping,Guo Guirong. Nutation Characteristic of Radar Targets and Nutation Frequency Estimation. Progress in Natural Science. 2006,vol.16(3),pp.344-350.

[5] Liu Jin, Wang Xuesong ,Ma Liang. Experimental Study on Dynamic Scattering Properties of Space Precession Target.acta aeronautica astronautica sinica. 2010,vol. 31(5),pp.1014-1023.

[6] Huang Peikang, Yin Hongcheng, Xu Xiaojian. Radar's Target characteristic. Beijing: Publishing House of Electronics Industry. 2005.

[7] Zhou Jianxiong. Reconstruction of 3D Scattering Center Model of Radar Targets in Optical Region. Changsha: National University of Defense Technology.2006.

[8] Ma Liang, Liu Jin, Wang Tao, Li Yongzhen, Wang Xuesong. Micro-Doppler Characteristic of Sliding Scattering Center for Rotational Symmetry. Science China: Information Science,2010,vol.40(1),pp.1-10.

[9] Agilent Technologies. E836B, E8363B, E8364B Agilent Technologies PNA Series Microwave Network Analyzers: Service Guide. 2008.

[10] N. Whitelonis, H. Ling Radar signature analysis using a joint time-frequency distribution based on compressed sensing. IEEE Trans on Antennas and Propagation, 2014,vol.62(2),pp.755-763.

Fractional Fourier Transform Based Co-Radar Waveform: Experimental Validation

Domenico Gaglione*, Carmine Clemente*, Adriano Rosario Persico*,
Christos V. Ilioudis*, Ian K. Proudler†, and John J. Soraghan*
*University of Strathclyde, CeSIP, EEE, 204, George Street, G1 1XW, Glasgow, UK
E-mail: domenico.gaglione, carmine.clemente, c.ilioudis, adriano.persico, j.soraghan@strath.ac.uk
† School of Electronic, Electrical and Systems Engineering, Loughborough University, Leicestershire, UK
E-mail: i.k.proudler@lboro.ac.uk

***Abstract*—A Fractional Fourier Transform (FrFT) based waveform design for joint radar-communication systems (Co-Radar) that embeds data into chirp sub-carriers with different time-frequency rates has been recently presented. Simulations demonstrated the possibility to reach data rates as high as 3.660 Mb/s while maintaining good radar performance compared to a Linear Frequency Modulated (LFM) pulse that occupies the same bandwidth. In this paper the experimental validation of the concept is presented. The system is considered in its basic configuration, with a mono-static radar that generates the waveforms and performs basic radar tasks, and a communication receiver in charge of the pulse demodulation. The entire network is implemented on a Software Defined Radio (SDR) device. The system is then used to acquire data and assess radar and communication capabilities.**

I. Introduction

The employment of joint radar-communication systems represents an innovative solution to the problem of continuously increasing demand on bandwidth [1] and the need to meet the low-SWaP (Size, Weight and Power consumption) requirements.

Applications that can benefit from the technology proposed in this paper include satellite and airborne Synthetic Aperture Radars (SARs) that need to share sensed data with a ground station rapidly [2]; nodes in a surveillance Multiple-Input Multiple-Output (MIMO) radar network that need to exchange information about targets; vehicles that need to interact in a intelligent transportation network [3]. All these applications may benefit from a joint-radar communication technology which shares bandwidth, power and hardware resources to perform radar and communication operations simultaneously.

A joint radar-communication system (Co-Radar) based on Fractional Fourier Transform (FrFT) waveform has been recently presented by the authors in [4]. The FrFT [5] was shown to be suitable for orthogonal waveforms generation for MIMO radar systems [6]–[9], and in this scenario it has been exploited to map complex modulated symbols into different chirp, or Linear Frequency Modulated (LFM), sub-carriers with different time-frequency rates. Simulations demonstrated the feasibility to reach data rate as high as 3.660 Mb/s, while maintaining good radar performance in terms of range resolution, Doppler resolution and Side Lobe Levels (SLLs) when compared with a LFM pulse that occupies the same bandwidth.

Different techniques of embedding data in the radar waveform have been previously proposed. In [10] and [11] information bits are sent by exploiting the orthogonality between up-chirp and down-chirp signals. Methods based on LFM pulses phase-modulated through Binary Phase Shift Keying (BPSK) and Minimum Shift Keying (MSK) symbols are presented in [12] and [13], respectively. Stepped-frequency [14] and Frequency Modulated Continuous Wave (FMCW) [15] based joint radar-communication systems have also been proposed, as well as Orthogonal Frequency Division Multiplexing (OFMD) based systems [16], [17]. However, none of these previous techniques is designed to achieve data rates up to 3.660 Mb/s at medium ranges.

In this paper the experimental validation of the FrFT based Co-Radar system [4] is reported. A basic configuration of the system is considered: a mono-static radar generates the FrFT waveforms, sends the pulses, listens to echoes and performs basic radar tasks, while a communication receiver demodulates the pulses.

The remainder of the paper has the following structure. Section II summarises the concept of the FrFT based Co-Radar waveform design framework presented in [4]. Section III describes its implementation on a Software Defined Radio (SDR) device, while the experimental setup and results are presented in Section IV. Finally, Section V concludes the paper.

II. FrFT Based Co-Radar System

In this section the FrFT based Co-Radar system [4] is presented. The FrFT [5] is a time-frequency representation of a signal and can be considered as a rotation by an arbitrary angle ϕ of the signal itself in the time-frequency plane, such that:

$$\phi = \frac{\pi}{2}\alpha \tag{1}$$

where α is called order of the transform. In the proposed system, FrFTs with different orders are used to map the modulated symbols into quasi-orthogonal chirp sub-carriers.

The block diagrams of the mono-static radar and the communication receiver in a simple FrFT based Co-Radar system scenario are shown in Figure 1 and described in the following.

A. Mono-Static Radar

The block diagram of the mono-static radar in the considered basic configuration of the FrFT based Co-Radar system is shown at the top of Figure 1. The serial-to-parallel (S/P) block is used to divide the long sequence of bits coming from

978-1-5090-0326-6/16/$31.00 ©2016 IEEE

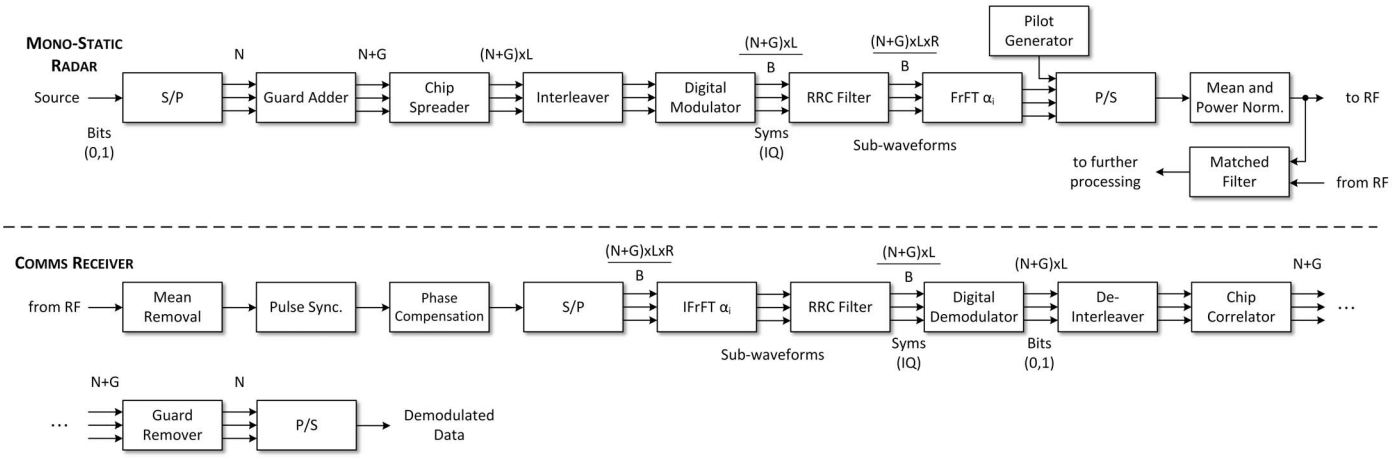

Figure 1. Block diagram of (top) the Mono-Static Radar and (bottom) the Communication Receiver of the FrFT based Co-Radar basic configuration [4].

the source into $C-1$ segments of N bits each, where C is the number of chirp sub-carriers composing the waveform. The 0-th order sub-carrier is not used to carry information bits. It accommodates a pilot waveform instead, used at the communication receiver for synchronisation and phase compensation. Since each pulse contains $N \times (C-1)$ information bits, the final bit rate is $N \times (C-1) \times \mathrm{PRF}$ b/s, where PRF stands for Pulse Repetition Frequency. In each segment, G guard bits are added at the end of the sequence in order to compensate for the group delay introduced by the Root Raised Cosine (RRC) filter. Then the sequence is spread by using a chip sequence; the chosen chip sequence is a L-long Barker code, which leads to a spread sequence of $(N+G) \times L$ bits. The interleaver is used to mitigate the Inter-Carrier Interference (ICI) that occurs in the middle of the sequence due to the overlap of the different chirp sub-carriers and that generates a burst of errors. It is applied only to the N bits of information and aims to spread the burst of errors across the entire spread sequence. The digital modulator maps a series of B bits into one of the $M = 2^B$ possible complex symbols belonging to the chosen modulation scheme (i.e. PSK), leading to a $(N+G) \times L/B$ long symbol sequence. The modulation scheme and the cardinality of its alphabet M can be adaptively chosen according to the conditions of the channel. The RRC filter is used to minimise the Inter-Symbol Interference (ISI) that may be caused by the channel. For efficiency, it is implemented as a multirate filter that up-samples the output by a factor R, leading to a final sequence of $(N+G) \times L \times R/B$ samples.

The $C-1$ sub-waveforms obtained after the RRC filter are then mapped to different chirp sub-carriers uniformly spaced in the time-frequency domain. Note that the FrFT is periodic in ϕ with period 2π, however rotations of ϕ and $\phi + \pi$ produce signals that overlap in the time-frequency plane. For this reason, only angles in the range $[0, \pi)$ are considered, that leads to $\alpha \in [0, 2)$. Thus, the uniformly spaced sub-carriers are obtained by choosing the i-th fractional order to be equal to $\alpha_i = i\bar{\alpha}, i = 1, \ldots, C-1$, where $\bar{\alpha} = \frac{2}{C}$. Finally, the parallel-to-serial (P/S) block combines the chirp modulated sub-waveforms and the pilot sub-waveform by adding them together. Specifically, the latter is a bi-phase coded signal run by a Coarse/Acquisition (C/A) code [18] given by:

$$p[n] = e^{j\pi\left(a[n]-\frac{1}{4}\right)} \tag{2}$$

where $a[n]$ is the selected C/A code properly up-sampled and truncated to match the length, in samples, of the Co-Radar waveform. Before sending the waveform to the Radio Frequency (RF) front-end, its mean is removed and the power is normalised such that all the transmitted pulses present the same power. While generating and transmitting the FrFT based pulses, the mono-static radar acquires the echoes and performs any needed radar task (i.e. matched filter with the transmitted pulse).

The spectrogram of a Co-Radar waveform with relatively few sub-carriers is shown in Figure 2 for clarity, although in practice many more sub-carriers would most likely be used. Each of them is the rotation by a specific angle, driven by the order of the FrFT, of a phase modulated signal (i.e. QPSK).

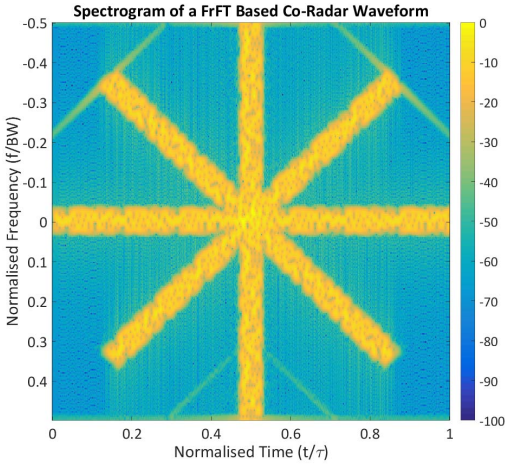

Figure 2. Spectrogram of a FrFT based Co-Radar waveform with 4 sub-carriers.

B. Communication Receiver

The communication receiver is shown at the bottom of Figure 1. All the operations are performed within a Pulse Repetition Interval (PRI). Before the pulse is synchronised and demodulated, the mean of the received signal is subtracted to remove the strong return from the background. The synchronisation is necessary since the pulse could fall anywhere within the PRI due to the transmitter-receiver distance, and the alignment with the pulse on a sample basis is needed to

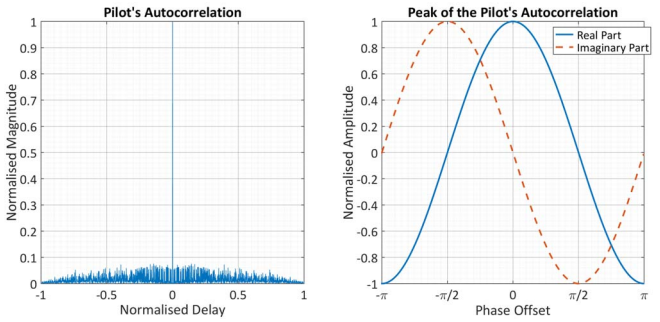

(a) (b)

Figure 3. Pilot waveform's (a) autocorrelation and (b) its peak's complex value on varying the phase offset.

perform the inverse FrFT. This is achieved by exploiting the good autocorrelation properties of the pilot waveform, shown in Figure 3(a).

The pilot waveform is also used to estimate the phase offset introduced by the channel. Figure 3(b) shows how the autocorrelation's complex-valued peak changes on varying the phase offset. In particular, when the offset is zero the real part of the peak reaches its maximum, while the imaginary part is zero. Hence, once the peak of the autocorrelation is detected by matched filtering the received signal with the pilot waveform, the phase offset can be estimated by evaluating the phase of the correlation peak. This phase estimation method is also robust with respect to the Doppler shift potentially present in the signal.

Once the synchronisation and the phase compensation are performed, the pulse can be demodulated. The S/P block splits and redirects the pulse, whose length is $(N+G) \times L \times R/B$ samples, to $C-1$ different IFrFT blocks that perform the inverse FrFT. Each sequence is then input of the RRC filter, which also down-samples the sub-waveform by a factor R. The digital demodulator translates the $(N+G) \times L/B$ long sequence of symbols in a sequence of $(N+G) \times L$ bits, according to the modulation employed. At this point, the de-interleaver performs the inverse operation of the interleaver.

The chip correlator block correlates the input spread sequence with the L-long Barker chip code used in transmission to extract $N+G$ bits, exploiting both the low correlation side lobes and the knowledge that the peaks of the correlation occur every L samples. Finally, the guard remover and the P/S blocks reconstruct the original stream by combining the N-long bit sequences coming from the $C-1$ different parallel branches.

III. FrFT Based Co-Radar on SDR

The FrFT based Co-Radar system is implemented by means of a SDR device, namely the National Instruments Universal Software Radio Peripheral (NI-USRP) 2943r. It has four in-phase and quadrature (IQ) channels, two receivers and two transmitters/receivers, and its working frequency ranges between 1.2 GHz and 6.6 GHz. It is provided with a fully programmable Xilinx Kintex-7 FPGA (Field-Programmable Gate Array) and can be connected to a host computer through a high-speed, low-latency PCI Express x4 ($\sim$800 MB/s). It is used with three wideband LB-2678-15 multi octave horn antennas produced by A-Info, two for the mono-static radar node and one for the communication receiver.

The USRP 2943r is programmed through NI software

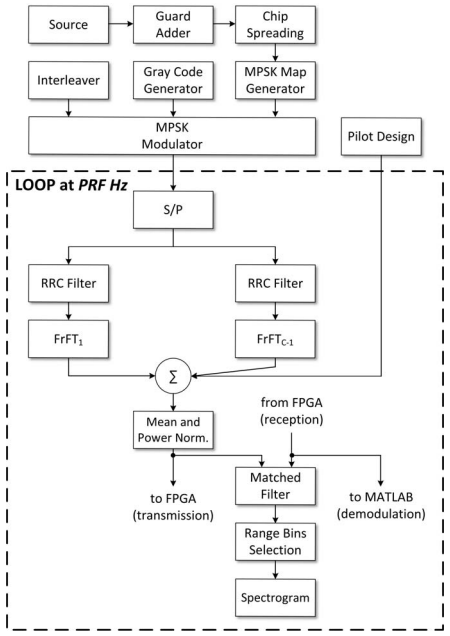

Figure 4. High-level block diagram of the FrFT based Co-Radar system's implementation in LabVIEW.

LabVIEW, and its high-level block diagram is shown in Figure 4. Within the loop that repeats every PRI, the FrFT based Co-Radar waveform is generated as described in the previous section and sent to the FPGA. The latter up-samples the signal in transmission to meet the 120 MHz data clock frequency of the device and interfaces with the RF front-end. Meanwhile, the received signal, down-sampled and coming from the FPGA, is sent both to a MATLAB session for the real-time pulse demodulation and to a matched filter with the transmitted pulse for further radar processing. Specifically, a real-time spectrogram is computed. This choice is driven by the limited power and bandwidth resources of the employed SDR device, which are not sufficient for more advanced radar operations. Outside the loop, the message to send is loaded and all the preliminary steps are performed.

IV. Experimental Setup and Results

The implemented FrFT based Co-Radar system is used in a controlled laboratory environment to acquire data and assess its communication and radar capability. The acquisition geometry is shown in Figure 5. The mono-static radar is placed at the bottom left, the communication receiver at the top right, while within the light blue area a person is walking towards and away from the radar to generate a Doppler signal.

The transmitted message is a 64×64 black and white

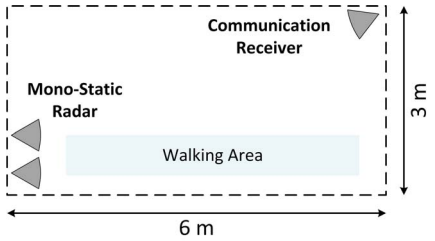

Figure 5. Acquisition geometry of the laboratory-based experimental campaign.

image with a bit depth 5. Carrier frequency is 3 GHz and the bandwidth is 1 MHz. The number of information bits per carrier, N, is 3, the length of the Barker code is $L = 7$ and Quadrature PSK (QPSK) is the employed modulation scheme, hence $B = 2$. The RRC filter is designed to span $S = 8$ symbols, with an up-sampling factor $R = 18$ and a roll-off factor $\beta = 0.4$. This leads to a guard of $G = 3$ bits. The total number of samples per waveform is 378, which means that the duration of the pulse is $\tau = 378\,\mu$s. The PRF is fixed to 83.33 Hz, giving a duty cycle of 3.15 %.

Different configurations are analysed by changing the number of sub-carriers, $C = 4, 6, 8, 10$, and modifying the transmitted power. The Signal-to-Noise Ratio (SNR) is estimated both at the mono-static radar and the communication receiver.

Communication performance is shown with solid lines in Figure 6, in terms of Bit Error Ratio (BER) averaged over 10 realisations vs SNR_{comms}. The dotted lines in Figure 6 show

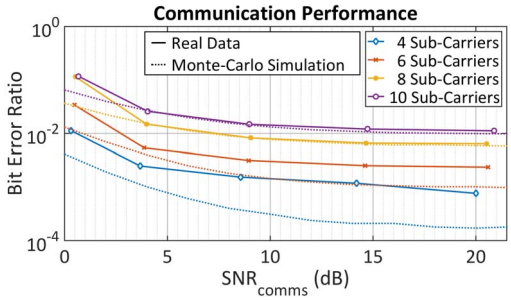

Figure 6. Communication performance on varying the SNR_{comms} and for different number of chirp sub-carriers.

the results obtained by running Monte-Carlo simulations with 10^5 iterations with the same parameters listed above, assuming the channel to be Rician with K-factor equal to 6 dB (indoor channel). They are used as comparison to validate the results on the acquired data. Note that no Forward Error Correction (FEC) method is used, since this is out of the scope of the present paper.

As expected, as the SNR_{comms} increases, the BER decreases. However, no significant further improvements are observed for SNR_{comms} greater than 15 dB, and this trend is confirmed by the results from the Monte-Carlo simulations, which clearly show plateaus. They are due to the overlap of the sub-carriers, which causes errors independently of the noise level. For the same reason, performance improves by reducing the number of sub-carriers.

The radar capabilities of the FrFT based Co-Radar are presented by showing spectrograms from the signals acquired during the laboratory-based experimental campaign. Figure 7 and Figure 8 show spectrograms when FrFT based Co-Radar pulses with $C = 4$ and $C = 8$ sub-carriers are used, respectively, and for two different values of SNR_{radar}. In all the cases the Doppler and micro-Doppler signature of the person walking towards and away from the radar is clearly visible.

V. Conclusion

The paper presented an experimental validation of the FrFT based Co-Radar system proposed in [4]. The system was successfully implemented on a SDR device and its performance demonstrated in a controlled laboratory environment. A basic configuration was considered with one mono-static radar and

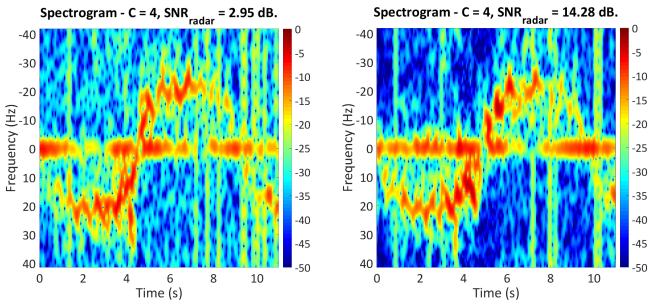

(a) (b)

Figure 7. Spectrograms obtained from FrFT based Co-Radar pulses with $C = 4$ and different SNR_{radar}. Window length 0.36 seconds, overlap 80 %. Person walking towards the radar approximately between 0-5 seconds and 10-11 seconds, and away from it between 5-10 seconds.

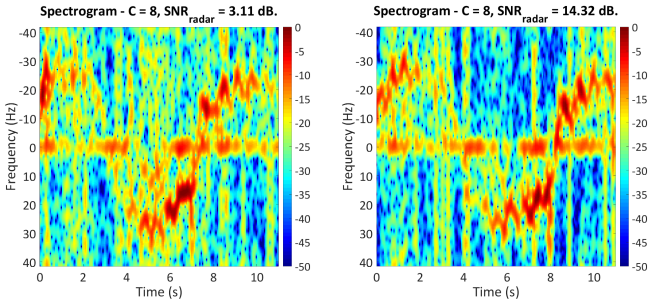

(a) (b)

Figure 8. Spectrograms obtained from FrFT based Co-Radar pulses with $C = 8$ and different SNR_{radar}. Window length 0.36 seconds, overlap 80 %. Person walking towards the radar approximately between 4-8 seconds, and away from it between 0-4 seconds and 8-11 seconds.

one communication receiver.

Communication performance was evaluated in terms of BER vs SNR_{comms} and resulted consistent with that obtained from Monte-Carlo simulations. It shows BER between 10^{-3} and 10^{-2} when no error detection and correction techniques are used. Due to the limited power and bandwidth resources of the employed SDR device, the radar capability of these novel waveforms is assessed by computing the spectrograms of the acquired signals. They clearly showed the main Doppler and micro-Doppler signature of a person walking towards and away from the radar. These preliminary results confirm the capability of the proposed novel waveforms of joint radar-communication operations.

Acknowledgment

This work was supported by the Engineering and Physical Sciences Research Council (EPSRC) Grant number EP/K014307/1 and the MOD University Defence Research Collaboration in Signal Processing.

References

[1] H. Griffiths, "The Challenge of Spectrum Engineering," in *2014 11th European Radar Conference (EuRAD)*, Oct 2014, pp. 1–4.

[2] S. Quan, W. Qian, J. Guq, and V. Zhang, "Radar-Communication Integration: An Overview," in *2014 IEEE 7th International Conference on Advanced Infocomm Technology (ICAIT)*, Nov 2014, pp. 98–103.

[3] D. Erricolo, H. Griffiths, L. Teng, M. C. Wicks, and L. L. Monte, "On the Spectrum Sharing Between Radar and Communication Systems," in *2014 International Conference on Electromagnetics in Advanced Applications (ICEAA)*, Aug 2014, pp. 890–893.

[4] D. Gaglione, C. Clemente, C. V. Ilioudis, A. R. Persico, I. Proudler, and J. J. Soraghan, "Fractional Fourier Based Waveform for a Joint Radar-Communication System," in *2016 IEEE Radar Conference (RadarConf)*, Philadelphia, USA, May 2016, pp. 811–816.

[5] H. M. Ozaktas, Z. Zalevsky, and M. A. Kutay, *The Fractional Fourier Transform with Applications in Optics and Signal Processing*. Wiley, Chichester, 2001.

[6] C. Clemente, I. Shorokhov, I. Proudler, and J. Soraghan, "Radar Waveform Libraries Using Fractional Fourier Transform," in *2014 IEEE Radar Conference*, May 2014, pp. 0855–0858.

[7] C. Clemente, C. Ilioudis, D. Gaglione, K. Thompson, S. Weiss, I. Proudler, and J. Soraghan, "Reuse of Fractional Waveform Libraries for MIMO Radar and Electronic Countermeasures," in *2014 6th International Symposium on Communications, Control and Signal Processing (ISCCSP)*, May 2014, pp. 505–508.

[8] C. Ilioudis, C. Clemente, I. Proudler, and J. Soraghan, "Constant Envelope Fractional Fourier Transform Based Waveform Libraries for MIMO Radar," in *2014 Sensor Signal Processing for Defence (SSPD)*, Sept 2014, pp. 1–5.

[9] C. Ilioudis, C. Clemente, I. Proudler, and J. Soraghan, "Performance Analysis of Fractional Waveform Libraries in MIMO Radar Scenario," in *2015 IEEE Radar Conference (RadarCon)*, May 2015, pp. 1119–1124.

[10] M. Roberton and E. Brown, "Integrated Radar and Communications Based on Chirped Spread-Spectrum Techniques," in *2003 IEEE MTT-S International Microwave Symposium Digest*, vol. 1, June 2003, pp. 611–614.

[11] G. N. Saddik, R. Singh, and E. Brown, "Ultra-Wideband Multifunctional Communications/Radar System," *IEEE Transactions on Microwave Theory and Techniques*, vol. 55, no. 7, pp. 1431–1437, July 2007.

[12] Z. Zhao and D. Jiang, "A Novel Integrated Radar and Communication Waveform Based on LFM Signal," in *2015 5th International Conference on Electronics Information and Emergency Communication (ICEIEC)*, May 2015, pp. 219–223.

[13] X. Chen, X. Wang, S. Xu, and J. Zhang, "A Novel Radar Waveform Compatible with Communication," in *2011 International Conference on Computational Problem-Solving (ICCP)*, Oct 2011, pp. 177–181.

[14] F. Hu, G. Cui, W. Ye, L. Kong, Y. Huang, and L. Yuan, "Integrated Radar and Communication System Based on Stepped Frequency Continuous Waveform," in *2015 IEEE Radar Conference (RadarCon)*, May 2015, pp. 1084–1087.

[15] W. Scheiblhofer, R. Feger, A. Haderer, and A. Stelzer, "Method to Embed a Data-Link on FMCW Chirps for Communication Between Cooperative 77-GHz Radar Stations, year = 2015, pages = 181-184, month = Sept,," in *Radar Conference (EuRAD), 2015 European*.

[16] C. Sturm and W. Wiesbeck, "Waveform Design and Signal Processing Aspects for Fusion of Wireless Communications and Radar Sensing," *Proceedings of the IEEE*, vol. 99, no. 7, pp. 1236–1259, July 2011.

[17] J. Zhao, K. Huo, and X. Li, "A Chaos-Based Phase-Coded OFDM Signal for Joint Radar-Communication Systems," in *2014 12th International Conference on Signal Processing (ICSP)*, Oct 2014, pp. 1997–2002.

[18] GPS ICD, "Global Positioning Systems Directorate System Engineering & Integration Interface Specification IS-GPS-200H," *Navstar GPS Space Segment/Navigation User Interfaces*, 2013.

Discriminating Underwater LiDAR Target Signatures using Sparse Multi-spectral Depth Codes

Puneet S Chhabra*, Aurora Maccarone, Aongus McCarthy, Andrew M Wallace and Gerald S Buller
School of Engineering and Physical Sciences, Heriot Watt University, Edinburgh, EH14 4AS

***Abstract*—The analysis and discrimination of underwater multi-spectral full-waveform LiDAR signatures acquired using a single-photon counting sensor is presented. We use a realistic scaled exemplar of a marine environment, with known and unknown targets, and show how we can both discriminate different materials and detect and locate mines. Each waveform is a temporal photon histogram whose inherent nature changes with the laser wavelength, target geometry and environment. Discriminatory dictionaries for target materials and mine types are learnt by making multi-spectral measurements. An accuracy of 97.8% and 98.7% was achieved for material and mine type discrimination, respectively.**

***Index Terms*—Photon counting, dictionary learning, multi-spectral, lidar, ATR, full-waveform, target discrimination**

I. Introduction

Terrestrial and aerial light detection and ranging (LiDAR) has enabled researchers to explore the third dimension, *depth*; this has advantages in remote sensing [1], bathymetric mapping [2], defence and security [3], and restoration and archaeology [4]. It is only recently that LiDAR systems have been built and tested for underwater applications. Commercial and academic focus [2] on bathymetric LiDAR has been on shallow waters and uses either monochromatic laser sources or a maximum of two wavelengths. This work is the first to report signal analysis and discrimination of underwater LiDAR data for mine counter-measures (MCM).

The multi-spectral depth imaging system [5] used in this study is based on the time-of-flight (ToF) approach using time-correlated single photon counting (TCSPC). Figure 1a illustrates a schematic of the experimental set-up. The TCSPC module (Hydraharp in Figure 2) time-stamps each photon event reflecting from a target and records it using a single-photon detector. The photon counts can then be time gated to form a histogram, a *full-waveform*, whose inherent nature depends on several factors, e.g., the laser wavelength, surface geometry and transmission medium. Figure 1b illustrates an *exemplar* used in this paper which has several targets embedded in a sand-cement-epoxy mixture, and was imaged in a tank filled with clear unfiltered tap water. Making such measurements is the first step to demonstrate how LiDAR could be used as an alternative to acoustic sensors for MCM purposes in very challenging environments.

*As a joint PhD candidate P. S. Chhabra is also with the University of Edinburgh. Correspondence: psc31@hw.ac.uk

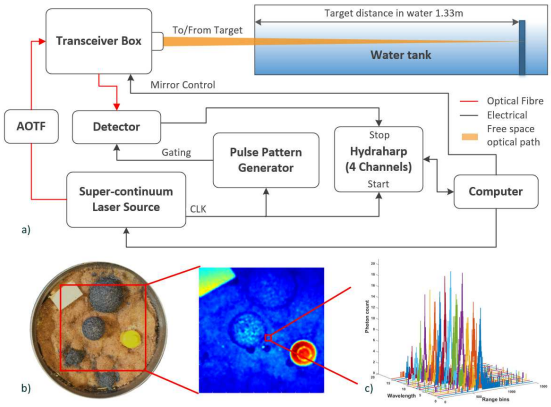

Fig. 1: a) A schematic of the experimental set-up; b) (left) an exemplar under investigation with different targets; (middle) Amplitude image, colour coded photon count, blue (low) to red (high) c) 16 full LiDAR waveforms at different wavelengths for a single pixel.

A. Contributions & Outline

The main contribution of this work is a novel approach to discriminate target signatures acquired by an underwater multi-spectral LiDAR system. This has been applied to identify both materials and specific targets for MCM.

In Section II we describe the basis of our approach, including firstly i) a "reflectance" aware spectral depth representation (SDR); and, secondly ii) a semi-supervised discriminatory objective function as an enhancement to the traditional sparse approximation scheme. In Section III we describe our implementation of the earlier theory, giving pseudocode descriptions of our software. The evaluation of the method on our own experimental data is given in Section IV. Finally, our conclusions are presented in Section V.

B. Experimental Setup

The experimental set-up is illustrated in Figure 1. Table I summarises the sensor equipment and acquisition parameters used. The exemplar was lowered underwater and kept at a distance of 1.33m from the SPC sensor. In order to limit the influence of any ambient illumination, the experiment was carried out in a dark room. The instrumental response was measured using a reference scatterer, a Spectralon panel, which was placed approximately at normal incidence to the beam. For

978-1-5090-0326-6/16/$31.00 ©2016 IEEE

TABLE I: Experiment Key Parameters

Parameter	Value
Environment	Clear unfiltered tap water
Laser System	NKT Photonics supercontinuum laser source and tunable filter fibre-coupled to the transceiver unit
Illuminating Wavelength	500nm - 725nm
Laser Beam Diameter	$\approx 300\mu m$
Laser Repetition Rate	19.5MHz
Acquisition Mode	Exemplar 1: 200 x 200 pixels Area: $5cm$ x $5cm$ Pixel acquisition time: 10ms
Histogram bin width	2ps
Histogram Length	4500 bins (after gating)
Avg. Optical Power	$\approx$ 300nW

each pixel a 4500 bin time-gated histogram is created with a depth resolution of $300\mu m$, which is referred to as, *Single Photon Counting* data in Figure 2. Such measurements are repeated for 16 wavelengths ranging between 500nm to 725nm, equally spaced by 15nm. The choice of the wavelengths hinges on a detailed, previous study [5].

II. The Proposed Approach - An Overview

The proposed approach summarised in Figure 2 has three main stages: i) spectral depth representation (SDR) (see Section II-A, where a representation based on the LiDAR equations and surface geometry is proposed; ii) signal approximation and discrimination (SAD) to create and learn spectral sparse codes of the representations produced in stage 1, Section III; and, iii) prediction where unseen target signatures are classified.

A. Stage 1 - Spectral Depth Representation

The following assumptions were made when processing raw multi-spectral SPC data: i) one peak per waveform was extracted at each wavelength; ii) SPC waveforms are aligned and normalised with respect to the Spectralon target, with 10% reflectance; iii) the laser beam width is less than surface differential. For a beam width of $300\,\mu m$, the smallest target diameter under-investigation was around $0.5\,cm$. Finally, iv) a fixed stand-off distance from the sensor is assumed and the sensor is stationary.

1) Spectral FW-LiDAR Features: In previous work for the analysis of urban and forest scenes using laser scanning, several classification and feature relevance algorithms [1], [6] have been proposed. However, these methods do not truly embed the full-waveform properties and the spectral reflectance of the observed objects. Our SDR representation captures such variations from the waveform and the point cloud data. For N acquired sets of waveforms at Λ wavelengths, $N \times \Lambda$ waveforms are processed and the echo properties are extracted, Eq. 2. The transmitted time signature of the super-continuum laser source is an exponential pulse and the degree of modulation on the backscattering beam depends on the surface geometry

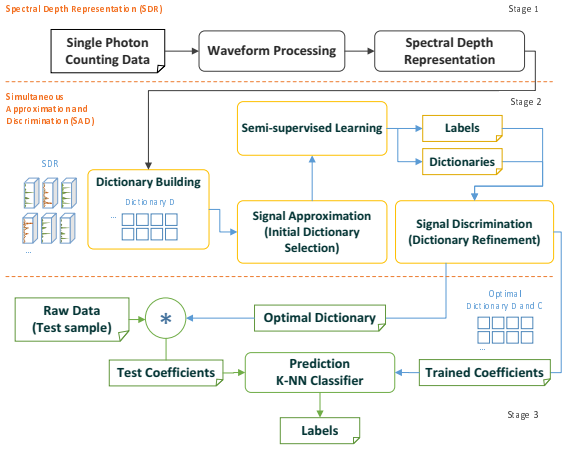

Fig. 2: The Proposed Approach.

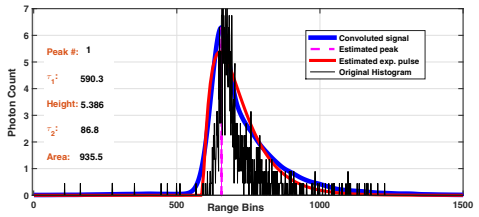

Fig. 3: An exponential pulse and a least-square fit to a returning target signature for a single wavelength.

and its spectral reflectance. Figure 3 illustrates one such return as a black curve. The pulse has the form

$$f(t) = k\left(e^{-t\mathcal{T}_1} - e^{-t\mathcal{T}_2}\right), \quad (t \geqslant 0),$$
$$\text{where, } k = \frac{\mathcal{T}_2 e^{(t_p - t_0)\mathcal{T}_1}}{(\mathcal{T}_2 - \mathcal{T}_1)}, \text{and} \quad t_p = \frac{\ln(\mathcal{T}_2/\mathcal{T}_1)}{(\mathcal{T}_2 - \mathcal{T}_1)} \tag{1}$$

The waveform processing module, stage 1 of Figure 2, finds the location within in each waveform where the average curvature, controlled by a specified region, is concave down, t_0. Once this location is identified, a least-square fit of a double exponential pulse provides the true position, the temporal parameters, $\mathcal{T}_1$, $\mathcal{T}_2$ and the area under the curve, A_λ. Figure 3 shows how an exponential pulse was fitted, the pink curve, to the incoming full-waveform, the black curve. The parameters $\mathcal{T}_1$ and $\mathcal{T}_2$, represent the fall and the rise of the exponential pulse respectively. These are computed at each wavelength.

2) Depth Representation (DR): The FW processing leads to a dense 3D point cloud. In order to capture local surface variations, a regional variance-covariance matrix was computed on the 3D point cloud. The radius, r, of the region shown in Figure 4 can be altered depending on the point cloud density. West et al. [6] show how Eigenvalues can be used to describe the local, spatial distribution of the 3D point cloud. They compute discrete moments within a neighbourhood that can describe the planarity, linearity, sphericity and anisotropy.

Table II illustrates how these properties are computed, provided the Eigenvalues $\mathcal{E}_1 > \mathcal{E}_2 > \mathcal{E}_3$. The Eigenvalues

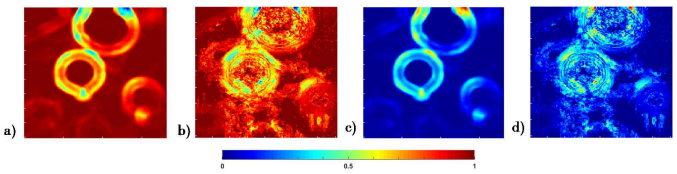

Fig. 4: Raster images of different geometric features computed for each 3D point, controlled using a local neighbourhood radius, r. (a) Anisotropy $A_{\mathcal{E}}$, b) Planarity $P_{\mathcal{E}}$, c) Sphericity $S_{\mathcal{E}}$ and d) Linearity $L_{\mathcal{E}}$ Table II.

TABLE II: Depth Representations using Eigenvalues

Linearity $L_{\mathcal{E}}$	$\frac{\varepsilon_1-\varepsilon_2}{\varepsilon_1}$	Sphericity $S_{\mathcal{E}}$	$\frac{\varepsilon_3}{\varepsilon_1}$
Planarity $P_{\mathcal{E}}$	$\frac{\varepsilon_2-\varepsilon_3}{\varepsilon_1}$	Anisotropy $A_{\mathcal{E}}$	$\frac{\varepsilon_1-\varepsilon_3}{\varepsilon_1}$

computed are invariant to 3D rotation [6] and view-point since they are computed locally. Four local 3D surface features, Anisotropy, $A_{\mathcal{E}}$, Planarity, $P_{\mathcal{E}}$, Sphericity, $S_{\mathcal{E}}$ and Linearity, $L_{\mathcal{E}}$ are computed within a neighbourhood, governed by radius r, of each 3D point. Finally, the depth D_z per pixel completes the SDR vector. A combined per-pixel representation was then fed into the stage 2 of the approach, the SAD. For each pixel, the SDR representation is a vector of 53 elements. For the experiments reported here, $\Lambda = 16$. Set one (elements 1 to 16) corresponds to the $\mathcal{T}_1$, set two (elements 17 to 32) corresponds to the $\mathcal{T}_2$, set three (elements 33 to 48) corresponds to A_λ. The remaining elements are the local geometric properties. So the final representation looks like

$$F_v = \Big[\{\mathcal{T}_{1,\lambda}\}_{\lambda=1}^{\Lambda}, \{\mathcal{T}_{2,\lambda}\}_{\lambda=1}^{\Lambda}, \{A_\lambda\}_{\lambda=1}^{\Lambda}, A_{\mathcal{E}}, P_{\mathcal{E}}, S_{\mathcal{E}}, L_{\mathcal{E}}, D_z\Big] \quad (2)$$

B. Stage 2 - Signal Approximation and Discrimination

Signal representation has a significant impact on the discriminatory nature of any classification system. Over the years, research in image characterisation has provided many compact and invariant representations e.g., image saliency, edge detections, bags-of-features (BoF) [7]. The BoF approach uses a vector quantisation (VQ) scheme in order to encode relationships between high-dimensional image patches belonging to the same class. In [7], VQ was applied to local regional histograms in order to generate cluster means. Cluster membership can be controlled in the higher-dimensional space and distance measures can be computed. The VQ scheme forces a cardinality constraint on cluster membership leading to a coarse representation of the input signal. This work proposes an alternative to the VQ scheme and not only relaxes the cardinality constraint but also improves the discriminatory capabilities. For completeness, first a short overview of the VQ method is presented in Section II-B1 followed by the proposed alternative formulation in Section II-B2.

1) Vector Quantisation: Let $\mathbf{W}$ be a set of SDR in a P-dimensional space, i.e., $\mathbf{W} = [w_1, ..., w_{\mathrm{N}}]^T \in \mathbb{R}^{\mathrm{N}\times\mathrm{P}}$. The VQ scheme applies a K-means clustering algorithm to solve the following problem

$$\arg\min_{\mathbf{Q},\mathbf{Z}} \sum_{n=1}^{N} ||w_n - q_n\mathbf{Z}||_2^2,\ Card\,(q_n) = 1, \quad |q_n| = 1, q_n \geqslant 0\,, \forall n, \quad (3)$$

where, $\mathbf{Z} = [z_1, ..., z_K]^T \in \mathbb{R}^{\mathrm{P}\times\mathrm{K}}$, are the K cluster centres, a *codebook* are unknown. $||.||_2^2$ and $|.|$ denotes the squared L_2 and L_1 norm, respectively. The cluster membership in Eq. (3) can be written as $\mathbf{Q} = [q_1, ..., q_N]^T$.

2) Discriminatory Sparse Codes: An alternative to a restrictive VQ approach is to relax the $Card\,(q_n)$ constraint to allow more than 1 non-zero element. In this work the traditional sparse approximation scheme was modified and a new discriminatory objective function was added. Suppose we have access to the best $\mathbf{Z}$, the new modified SAD problem can be written as

$$\arg\min_{\mathbf{Q},\mathbf{Z}} \left[\beta_2 \sum_{n=1}^{\mathrm{N}} ||w_n - q_n\mathbf{Z}||_2^2 + \beta_1 \sum_{n=1}^{\mathrm{N}} |q_n| + G\,(\mathbf{Q})\right], \quad \text{subject to}\, |q_n| \leqslant 1,\ \forall n = 1, 2, ..., N \quad (4)$$

In Eq. 4, the codebook $\mathbf{Z}$ is an *overcomplete* basis set, a *dictionary*, where $\mathrm{K} \gg \mathrm{P}$. The term $G\,(\mathbf{Q})$ is a discriminatory function that minimises inter-class and maximises intra-class variance. Detailed explanation of $G\,(\mathbf{Q})$ and step by step implementation of SAD is given in Section III. The penalising terms, β_1 and β_2 control the importance of the sparsity constraint and the reconstruction error, respectively.

The solution to (4) can be divided in to two steps: i) solve Eq. (4) with respect to $\mathbf{Q}$ and $\mathbf{Z}$. The dictionary, i.e, codebook, $\mathbf{Z}$ and coefficients $\mathbf{Q}$ are retained; ii) for a test signal, the coefficients are obtained by optimising Eq. (4) with respect to $\mathbf{Q}$ only. The individual functional blocks within each stage are explained in detail below along with their implementation details.

The discriminative nature of Eq. 4, $\mathrm{G}\,(\mathbf{Q})$ is expressed below. For a set of coefficients $\mathbf{Q} = [q_1, q_2, ..., q_{\mathrm{K}}]$, where $q_1, ..., q_k, ..., q_{\mathrm{K}}$ are the coefficients for the dictionary *atoms*, of which K_c samples are in class Ω_c, for $1 \leqslant c \leqslant \Omega$, the mean and variance for class Ω_c can be defined as:

$$\mu_c = \frac{1}{\mathrm{K}_c} \sum_{q\,\in\,\Omega_c} q\,; \quad \upsilon_c^2 = \frac{1}{\mathrm{K}_c} \sum_{z\,\in\Omega_c} ||z - \mu_c||_2^2 \quad (5)$$

The mean of all coefficient samples can be written as:

$$\mu = \tfrac{1}{\mathrm{K}} \textstyle\sum_{k=1}^{\mathrm{K}} q_k. \quad (6)$$

The *inter-class* scatter matrix, S_w and the *intra-class* scatter matrix, S_b can be defined as:

$$S_b = || \sum_{c=1}^{\Omega} \mathrm{K}_c\,(\mu_c - \mu)\ (\mu_c - \mu)^T\ ||_2^2\,; \quad S_w = \sum_{c=1}^{\Omega} \upsilon_c^2 \quad (7)$$

Finally, the Fisher discrimination function is defined as:

$$\mathrm{G}\left(\mathbf{Q}\right) = S_w^{-1} S_b, \tag{8}$$

Using Eq. (5) - (8), Eq. 4 can be solved using an orthogonal matching pursuit (OMP) algorithm [8]. The modified version, simultaneous approximation and discrimination (SAD) was presented in [3]. Algorithm 2 presents step by step details to solve Eq. 4.

III. Implementation Details - Pseudocode

In this section, the solution to Eq. (4) along with details of the discriminatory function $G(\mathbf{Q})$ is presented. First, the sparse codes for the SDR, from stage 1, are generated and a dictionary and their respective coefficients are learnt. Further, with the help of a semi-supervised clustering approach, these sparse codes are optimised for maximum discrimination. The pseudo-code to the approach in Figure 2 is presented in Algorithm 1.

A. Stage I - Lines 1 to 11

For a given set of input pixels, $\mathbf{W} \in \mathbb{R}^{\mathrm{N}}$, the aim is to create a representation that has a physical basis, LiDAR equations and target geometry. Lines 1 - 11 of Algorithm 1 generate a P-dimensional representation $\mathbf{F} \in \mathbb{R}^{(\mathrm{N}\times\Lambda)\times\mathrm{P}}$. In total, 40,000 waveforms were recorded for 16 different wavelengths. Lines 3 and 4 process each pixel for 16 different wavelengths. Lines 4 - 7 correct the intensity at each wavelength. For each pixel, line 7 aligns the 16 waveforms with respect to the system impulse, measurements made on a Spectralon target in advance and estimates the depth, point cloud matrix $\mathbf{P}$. Finally, line 10 compute the FW properties and geometric shape properties, as explained in Section II-A.

B. Stage II and III- Lines 12 to 21

Given a $\mathbf{F} \in \mathbb{R}^{(\mathrm{N}\times\Lambda)\times\mathrm{P}}$ matrix, the aim is to produce a set of sparse codes that are optimal and highly discriminatory, especially in identifying different materials. From a partially labelled set, U, line 13 selects a small sub-set, K, of representations, where $\mathrm{K} \gg \mathrm{P}$, and initialises them to $\mathbf{Z}$. Equation 4 is solved for $\mathbf{Q}$ and $\mathbf{Z}$ but without the optimisation add-on $G\left(\mathbf{Q}\right)$, Eq. 8. Solving Eq. 4 with the discriminatory function, $G\left(\mathbf{Q}\right)$ produces $\mathbf{Q}$ and $\mathbf{Z}$ that maximises the intra-class variance and minimises the inter-class variance. A semi-supervised approach can be adopted here, where labels are generated by clustering $\mathbf{Q}$ into three different clusters.

IV. Results and Analysis

The discriminatry performance of our approach is analysed using the exemplar of Figure 1a. Two sets of experiments were carried out: i) *Material Discrimination*: classify target signatures into three constituent materials, *sand*, *plastic* and *metal*, used to make the exemplar; ii) *Mine Discrimination*: classify different mine types, which not only differ in shape but also in material. Four different mines were used, *Plastic 1*, a cuboid shaped mine, *Plastic 2*, a spherical shaped mine, *Metal 1* and *Metal 2*, small and large spherical shaped metallic mines, respectively.

Input: SPC data $\mathbf{W} \in \mathbb{R}^{\mathrm{N}\times\Lambda}$, Partial labelled set, Ω
Output: Dictionary $\mathbf{Z}$, Coefficients $\mathbf{Q}$ and pixel labels
// **Stage I - SDR. See Section II-A**
1 **begin**
2 SDR matrix $\mathbf{F} \leftarrow [\,]$
3 **forall the** $n \in [1, \mathrm{N}]$ **do**
4 **forall the** $\lambda \in [1, \Lambda]$ **do**
5 CorrectIntensity$\left(w_{n,\lambda}, s_\lambda\right)$
6 **end**
7 $\mathbf{W}_{align} \leftarrow$ AlignWaveforms$\left(\{w_{n,\lambda}\}_{\lambda=1}^{\Lambda}\right)$
8 $\mathbf{P} \leftarrow$ EstimateDepth$(\mathbf{W}_{align})$
9 **end**
10 $\mathbf{F} \leftarrow$ SDR$\left(\mathbf{W}_{align}, \mathbf{P}\right)$ // Eq. 2
11 **end**
// **Stage II - SAD. See Section III-B**
12 **begin**
// Get ω random SDR's from set Ω
13 $\omega \in \mathrm{R}^{\mathrm{K}} \leftarrow$ Randperm$\left(\Omega\right)$, where $\mathrm{K} \gg \mathrm{P}$
$[\mathbf{Q}_{init}, \mathbf{Z}_{init}] \leftarrow$ Solve Eq. (4) without $G\left(\mathbf{Q}\right)$
14 $classIdx \leftarrow \mathrm{VQ}\left(\mathbf{Q}, \omega\right)$ // Eq. 3
// Dictionary selection. Algorithm 2
15 $[\mathbf{Q}, \mathbf{Z}, dictIdx] \leftarrow \mathrm{SAD}\left(\mathbf{F}, \mathbf{Z}_{init}, classIdx, param\right)$
// Reorder dictionary indices
16 $\mathbf{Z}_{opt} \leftarrow$ Reorder$\left(\mathbf{Z}, dictIdx\right)$
17 **end**
// **Stage III - Prediction**
18 **begin**
19 $labels \leftarrow$ Classify$\left(\mathbf{F}, \mathbf{Z}_{opt}, \mathbf{F}_{test}\right)$
20 **forall the** $i \in [1, \mathrm{N}]$ **do**
21 Distance$\left(\mathbf{Z}_{opt}, \mathbf{F}\right)$
22 **end**
23 $labels \leftarrow$ Sort$\left(\text{Distance}\left(\mathbf{Z}_{opt}, \mathbf{F}\right)\right)$
24 **return** $labels$
25 **end**

Algorithm 1: Pseudocode - Proposed Approach

Input: $\mathbf{F} = \{f_n\}_{n=1}^{N} \in \mathbb{R}^{\mathrm{N}\times\mathrm{P}}$, $\mathbf{Q} \in \mathbb{R}^{\mathrm{P}\times\mathrm{K}}$, β_1, β_2
Output: Dictionary, atom indices and coefficients
15.1 $\mathbf{R}_0 \leftarrow \mathbf{W}, dictIdx \leftarrow \phi$
15.2 **while** $\mathbf{R}_0 \rightarrow 0$ **do**
15.3 $t \leftarrow 0$ Select $z_k \in \mathbf{Z}$, such that

$$\min_{\mathbf{Q},\mathbf{Z}} \left[\beta_2 \sum_{n=1}^{\mathrm{N}} ||f_n - q_n\mathbf{Z}||^2 + \beta_1 \sum_{n=1}^{\mathrm{N}} |q_n|_1 + G\left(\mathbf{Q}\right) \right], \quad \text{subject to } |q_n| \leqslant 1,\ \forall n = 1, 2, ..., N$$

15.4 $dictIdx \leftarrow dictIdx \cup k$
// Projection and residual
15.5 $\mathbf{O}_t \leftarrow \mathbf{Q} * inv\left(\mathbf{Q}^T * \mathbf{Q}\right) * \mathbf{Q}^T$
15.6 $\mathbf{R}_t \leftarrow \mathbf{F} - \mathbf{O}_t\,\mathbf{F}$
15.7 $t \leftarrow t + 1$
15.8 **end**
15.9 **return** $\mathbf{Q}, \mathbf{Z}$, *dictIdx*

Algorithm 2: Pseudocode - SAD Module

TABLE III: Confusion Matrix - Material Discrimination

	Sand	**Plastic**	**Metal**
Sand	**0.9721**	0.0144	0.0133
Plastic	0.0151	**0.9823**	0.0024
Metal	0.0140	0.0035	**0.98239**

TABLE IV: Confusion Matrix - Mine Discrimination

	Plastic 1	**Plastic 2**	**Metal 1**	**Metal 2**	**Sand**
Plastic 1	**0.9755**	0	0.0020	0	0.0224
Plastic 2	0.0054	**0.9905**	0.0007	0.0020	0.0014
Metal 1	0.0014	0.0027	**0.9946**	0	0.0014
Metal 2	0.0014	0.0068	0	**0.9891**	0.0027
Sand	0.0102	0.0007	0	0.0007	**0.9884**

TABLE V: Effect of *Depth Representation* (DR) on accuracy

	Plastic 1	**Plastic 2**	**Metal 1**	**Metal 2**
Without DR(%)	92.65	95.65	97.62	98.10
With DR(%)	**97.55**	**99.05**	**99.46**	**98.91**

A. Experiment 1 - Material Discrimination

The confusion matrix for material discrimination is shown in Table III. A subset of 8520 target signatures, equally divided into three different materials was selected. A 10-fold cross-validation classification was then performed using the proposed approach resulting in a mean classification error rate of $\mathbf{0.021}\%$.

B. Experiment 2 - Mine Discrimination

The aim of this experiment was to seek answers for the following questions: i) can mines with structural variation but similar spectral signatures be classified correctly?, and, ii) what impact do the *Geometric* features, Section II-A2, have on classification? Table IV lists the confusion matrix for mine classification when geometric properties are included, using the full SDR representation, Eq. 2. A subset of 7350 target signatures, equally divided into five different classes was selected. The mean classification error rose by $\uparrow \mathbf{3.6}\%$ when geometry based DR was neglected. The effect on accuracy of classification for four different mines with and without DR is listed in Table V. Figure 5 illustrates the learnt coefficients, $\mathbf{Q}$, clustered into different mine types. The 3D point cloud, shown within, is segmented not only on the basis of their spectral content but also their geometric features. For illustration purposes, the clusters are plotted along three dimensions, area-under-curve, A_λ, sphericity, $S_\mathcal{E}$ and linearity, $L_\mathcal{E}$, respectively.

V. Conclusion

A novel spectral-depth representation is presented that is highly discriminatory in characterising different target signatures underwater. A custom-made realistically scaled exemplar with known and unknown targets has been investigated using a multi-spectral single photon counting LiDAR system. Multi-spectral measurements were made underwater on targets with

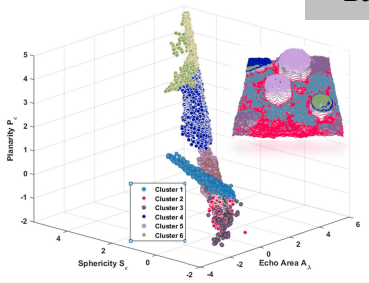

Fig. 5: Mine clusters using the spectral depth codes, $\mathbf{Q}$, on the spectral axis, echo area; and the depth axis, linearity and sphericity, respectively.

different shapes and materials, Section I-B. Using the proposed spectral depth representation sparse codes are optimised for maximum discrimination between different materials and mines, demonstrating accuracies of $\mathbf{97.8}\%$ and $\mathbf{98.7}\%$, respectively. Combining depth with spectral data, the approach is very effective at discriminating targets of different shapes, but with similar spectral response, or conversely of similar shape but having different spectra. When spectral features alone are considered, the discrimination error reported for Plastic 1 mine is 7.35%. But, when spectral and depth representation is considered, the error reduces to $\mathbf{2.45}\%$, Table V. This work has been the first to report the analysis and discrimination of multi-spectral underwater single photon counting LiDAR signals as an alternative to acoustic MCM.

Acknowledgment

This work was supported by the Engineering and Physical Sciences Research Council (EPSRC) under Grant EP/K014277/1 and the MOD University Defence Research Collaboration in Signal Processing.

References

[1] L. Guo, N. Chehata, C. Mallet, and S. Boukir, "Relevance of airborne lidar and multispectral image data for urban scene classification using random forests," *ISPRS Journal of Photogrammetry and Remote Sensing*, vol. 66, no. 1, pp. 56–66, 2011.

[2] A. G. Cottin, D. L. Forbes, and B. F. Long, "Shallow seabed mapping and classification using waveform analysis and bathymetry from shoals lidar data," *Canadian Journal of Remote Sensing*, vol. 35, no. 5, pp. 422–434, 2009.

[3] P. S. Chhabra, A. M. Wallace, and J. R. Hopgood, "Anomaly detection in clutter using spectrally enhanced ladar," in *SPIE Defense+ Security*, pp. 946508–946508, International Society for Optics and Photonics, 2015.

[4] J. C. Fernandez-Diaz, W. E. Carter, R. L. Shrestha, and C. L. Glennie, "Now you see it now you dont: Understanding airborne mapping lidar collection and data product generation for archaeological research in mesoamerica," *Remote Sensing*, vol. 6, no. 10, pp. 9951–10001, 2014.

[5] A. Maccarone, A. McCarthy, X. Ren, R. E. Warburton, A. M. Wallace, J. Moffat, Y. Petillot, and G. S. Buller, "Underwater depth imaging using time-correlated single-photon counting," *Optics Express*, vol. 23, no. 26, pp. 33911–33926, 2015.

[6] K. F. West, B. N. Webb, J. R. Lersch, S. Pothier, J. M. Triscari, and A. E. Iverson, "Context-driven automated target detection in 3d data," in *Defense and Security*, pp. 133–143, International Society for Optics and Photonics, 2004.

[7] G. Csurka, C. Dance, L. Fan, J. Willamowski, and C. Bray, "Visual categorization with bags of keypoints," in *Workshop on statistical learning in computer vision, ECCV*, vol. 1, pp. 1–2, Prague, 2004.

[8] J. A. Tropp, A. C. Gilbert, and M. J. Strauss, "Algorithms for simultaneous sparse approximation. part i: Greedy pursuit," *Signal Processing*, vol. 86, no. 3, pp. 572–588, 2006.

EFFICIENT RANGE ESTIMATION AND MATERIAL QUANTIFICATION FROM MULTISPECTRAL LIDAR WAVEFORMS

Y. Altmann, A. Maccarone, A. Halimi, A. McCarthy, G. S. Buller, S. McLaughlin†*

School of Engineering, Heriot-Watt University, Edinburgh, U.K.
Email: {Y.Altmann, am827, A.Halimi,A.McCarthy, G.S.Buller, S.McLaughlin}@hw.ac.uk

ABSTRACT

This paper describes a new Bayesian range estimation and spectral unmixing algorithm to analyse remote scenes sensed via multispectral Lidar measurements. To a first approximation, each Lidar waveform consists of the temporal signature of the observed target, which depends on the wavelength of the laser source considered and which is corrupted by Poisson noise. When the number of spectral bands considered is large enough, it becomes possible to identify and quantify the main materials in the scene, in addition to estimating classical Lidar-based range profiles. In this work, we adopt a Bayesian approach and the unknown model parameters are assigned prior distributions translating prior knowledge available (e.g., positivity, sparsity and/or smoothness). This prior model is then combined with the observation model (likelihood) to derive the joint posterior distribution of the unknown parameters which are inferred via maximum a posteriori estimation. Under mild assumptions often true in practice, we show that it is possible to find a global optimizer of the posterior by splitting the problem into two sequential steps estimating the unknown spectral quantities and the target ranges, respectively. The proposed methodology is illustrated via experiments conducted with real multispectral Lidar data aquired under controlled observation conditions.

***Index Terms*—** Multispectral Lidar, Depth imaging, Spectral unmixing, Poisson noise.

I. INTRODUCTION

Light detection and ranging (Lidar) systems are particularly useful to extract spatial features from three-dimensional (3D) scenes. Using single-photon techniques, it is possible to recover structural parameters of forest canopies such as vegetation height, leaf area indices and ground slopes. Spectral information about the scene is usually extracted using passive multispectral (MSI) and hyperspectral images (HSI). Such images are particularly useful to detect spectral variations caused for instance by changes in the canopy composition or by the presence of hidden vehicles or targets for defense applications.

Combining spatial and spectral information can be achieved by coupling Lidar data and multi/hyperspectral images [1], [2]. However, as in many multimodal data fusion problems, data synchronization issues in space (alignment, resolution) and time (dynamic scene, change of observation conditions, etc.) are still open issues. To tackle these problems, multispectral Lidar (MSL), which has recently received attention from the remote sensing community [3]–[5], presents as a promising alternative. Indeed, MSL systems have the ability to fully exploit the 3D distribution of objects, in particular for scenes including semi-transparent objects (e.g., vegetation or fences). In contrast to passive hyperspectral imaging systems which integrate the spectral response along the path of each optical ray, MSL systems measure the spectral response as a function of distance, e.g. depth into a forest canopy and can be used to detect and identify objects (e.g., buildings, vehicles, human activity) hidden for instance in vegetated areas.

In [5], [6], spectral unmixing techniques were developed to analyze 3D scenes composed of multi-layered objects, assuming that the spectral signatures of the materials composing the scenes were known and assuming linear mixing processes. In this paper we extend the method proposed in [5] to account for and identify possible deviations from the classical linear mixing model (LMM) used to estimate the amount/abundances of each endmember (assumed known) present in the scene. We assume that for each pixel, the photons emitted by the pulsed laser sources at different wavelength are reflected onto a single surface. This is typically the case for short to mid-range (up to dozens of metres) depth imaging where the divergence of the laser source(s) can be neglected.

Single-photon Lidar and thus MSL systems usually record, for each pixel/region of the scene, a histogram of time delays between emitted laser pulses and the detected photon arrivals. Due to the discrete nature of detected photons, Poisson noise models are more appropriate for single-photon MSL data than Gaussian noise models classically used when analysing HSIs. Due to the design of the proposed experiments (performed indoor here) and to simplify the estimation problem, we further assume that the ambient light and dark counts can be neglected. This assumption often holds for measurements by night or for mid-range imaging applications for which the laser power can be adjusted to reduce the acquisition time and thus the background counts. In this paper, we demonstrate the possibility of efficient 3D scene analysis by exploiting geometric and spectral information contained in MSL data (33 discrete wavelengths ranging from 500nm to 820nm), under favourable observation conditions. However, the proposed method can be extended to more difficult observation conditions, as discussed in the conclusions of the paper.

Adopting a classical Bayesian approach, appropriate prior distributions are chosen for the unknown parameters of the model and the joint posterior distribution of these parameters is then derived. Here we propose to estimate the unknown model parameters via maximum a posterior estimation. Unfortunately, the corresponding cost function to be optimized is often multimodal, which increases the risk of reaching a local as opposed to a global optimum. In this work, we show that under weak assumptions (often met in practice), it is possible to reach a global optimum using a two-step optimization scheme. More precisely, one can first estimate the mixing coefficients (abundances) involved in the spectral unmixing problem and then estimate the object ranges.

The remainder of the paper is organized as follows. Section II introduces the observation model associated with MSL returns for a single-layered object to be analyzed. Section III presents the Bayesian model associated with the spectral unmixing problem considered and the associated posterior distribution. Section IV describes the estimation strategy adopted to maximize the posterior of interest. Results of experiments conducted on real MSL data are shown and discussed in Section V and conclusions are reported in Section VI.

*Part of this work was supported by the EPSRC via grants EP/N003446/1, EP/K015338/1, EP/M01326X/1

†Part of this work was supported by the EPSRC via grant EP/J015180/1.

978-1-5090-0326-6/16/$31.00 ©2016 IEEE

II. PROBLEM FORMULATION

This section introduces the statistical observation model associated with MSL returns for a single-layered object which will be used in Section III for spectral unmixing of MSL data. We consider a 4-D array $\mathbf{Y}$ of Lidar waveforms and of dimension $N_{\text{row}} \times N_{\text{col}} \times L \times T$, where N_{row} and N_{col} stand for the number of rows and columns of the regular spatial sampling grid (in the transverse plane), L is the number of spectral bands or wavelengths used to reconstruct the scene and T is the number of temporal (corresponding to range) bins. Let $\mathbf{y}_{i,j,\ell} = [\mathbf{Y}]_{i,j,\ell,:} = [y_{i,j,\ell,1}, \ldots, y_{i,j,\ell,T}]^T$ be the Lidar waveform obtained in the pixel (i,j) (i.e., ith row and jth column) using the ℓth wavelength. The element $y_{i,j,\ell,t}$ is the photon count within the tth bin of the ℓth spectral band considered. Let $d_{i,j}$ be the position of an object surface at a given range from the sensor, whose spectral signature (observed at L wavelengths) is denoted as $\boldsymbol{\lambda}_{i,j} = [\lambda_{i,j,1}, \ldots, \lambda_{i,j,L}]^T$. According to [7], [8] and assuming that the ambient illumination and dark photon counts can be neglected, each photon count $y_{i,j,\ell,t}$ is assumed to be drawn from the following Poisson distribution

$$y_{i,j,\ell,t} | \lambda_{i,j,\ell}, t_{i,j} \sim \mathcal{P}\left(\lambda_{i,j,\ell} g_{0,\ell}(t - t_{i,j})\right) \tag{1}$$

where $g_{0,\ell}(\cdot)$ is the photon impulse response whose shape can differ between wavelength channels and $t_{i,j}$ is the characteristic time-of-flight of photons emitted by a pulsed laser source and reaching the detector after being reflected onto a target at range $d_{i,j}$ ($d_{i,j}$ and $t_{i,j}$ are linearly related in free-space propagation). Moreover, the impulse responses $\{g_{0,\ell}(\cdot)\}$ are assumed to be known and can usually be estimated during the imaging system calibration. We further assume that the spectral signatures of the scene surfaces can be decomposed as linear mixtures of R known spectral signatures $\mathbf{m}_r$ (also referred to as endmembers and gathered in the matrix $\mathbf{M} = [\mathbf{m}_1, \ldots, \mathbf{m}_R]$)

$$\boldsymbol{\lambda}_{i,j} = \mathbf{M}\boldsymbol{a}_{i,j}, \quad \forall i,j, \tag{2}$$

where $\boldsymbol{a}_{i,j} = [a_{i,j,1}, \ldots, a_{i,j,R}]^T$ contains the abundances of the R endmembers in the pixel (i,j). Note that due to physical considerations the unknown abundance vectors $\{\boldsymbol{a}_{i,j}\}_{i,j}$ are assumed to have positive entries. It is important to recall that in this work, we consider applications where the observed objects consist of a single visible surface per pixel. We do not consider cases where the photons can penetrate through objects (e.g., semi-transparent materials for which we would like to infer the internal composition) or be reflected onto multiple surfaces. This assumption allows the spectral unmixing problem to be reduced to a two spatial dimensions problem, which could be extended for distributed targets in future work. The problem addressed in this paper consists of jointly estimating the range of the targets (for all the image pixels) and solving the spectral unmixing problem (e.g., estimating the abundance vectors). The next section studies the proposed Bayesian model developed to solve the problem considered.

III. BAYESIAN MODEL

III-A. Likelihood

Assuming that the MSL waveforms $\mathbf{y}_{i,j} = \{y_{i,j,\ell,t}\}_{\ell,t}$ of a given pixel (i,j) result from the photons reflection onto a surface associated with the spectrum $\boldsymbol{\lambda}_{i,j}$, the likelihood associated with the pixel (i,j) can be expressed as $f(\mathbf{y}_{i,j}|\boldsymbol{\lambda}_{i,j}, t_{i,j}) = \prod_{\ell,t} f(y_{i,j,\ell,t}; \lambda_{i,j,\ell} g_{0,\ell}(t - t_{i,j}))$, when assuming that the detected photon counts, conditioned on their mean in all channels/spectral bands are independent. Considering that the noise realizations in the different pixels are independent, the joint likelihood can be expressed as

$$f(\mathbf{Y}|\boldsymbol{\Lambda}, \mathbf{T}) = \prod_{i,j} f(\mathbf{y}_{i,j}|\boldsymbol{\lambda}_{i,j}, t_{i,j}), \tag{3}$$

where $\boldsymbol{\Lambda} = \{\boldsymbol{\lambda}_{i,j}\}_{i,j}$ and $\mathbf{T}$ is a matrix gathering the target ranges.

III-B. Prior distributions

In this work, we do not account for the potential spatial correlations between the target distances in neighbouring pixels of the scene. Thus, each target position is considered as a discrete variable defined on $\mathbb{T} = \{t_{min}, \ldots, t_{max}\}$, such that $1 \leq t_{min} \leq t_{max} \leq T$ (in this paper we set $(t_{min}, t_{max}) = (501, T - 500)$ for $T = 4500$, see discussion in Section IV) and assign the target ranges independent uniform priors $p(t_{i,j} = t) = 1/T', \forall t \in \mathbb{T}$ where $T' = \text{card}(\mathbb{T})$. Note that more informative priors could be used, e.g., to capture potential spatial correlations affecting the range profiles, as in [8]. However, when the number of spectral bands L considered and the number of detected photon are significant, the depth estimation does not require informative regularization (as the L bands are used to estimate $t_{i,j}$). For this reason and for paper length constraints, we simply consider uniform priors here. Moreover, assuming prior independence between the ranges parameters $\{t_{i,j}\}_{i,j}$ yields

$$f(\mathbf{T}) = \prod_{i,j} p(t_{i,j}). \tag{4}$$

As often assumed when addressing spectral unmixing problem, we consider applications where the number of spectral components involved in the mixture of a given pixel is likely to be smaller than the number of endmembers R in the known matrix $\mathbf{M}$. This typically occurs when the surface hit by the laser source and visible by the detector is relatively small compared to the size of the scene objects. In such cases, it makes sense to consider prior models which promote sparse estimated abundances. Similarly, when the transverse spatial sampling of the scene (using either a raster scan on a regular grid or a detector array) is dense enough, the abundance maps often present spatial structures (e.g., smoothness) that can be incorporated within a prior model. In contrast to the model proposed in [5] and which did not consider spatially correlated abundances, in this work, we consider the following priors promoting sparse and piece-wise smooth abundance maps while ensuring the abundance positivity
$f(\mathbf{A}_r|\lambda_{1,r}, \lambda_{TV,r}) \propto$

$$\begin{cases} \exp\left[-\lambda_{1,r}||\mathbf{A}_r||_{1,1} - \lambda_{TV,r}\text{TV}\left(\mathbf{A}_r\right)\right] & \text{if } a_{i,j,r} \geq 0, \forall (i,j) \\ 0 & \text{else} \end{cases},$$

where $\mathbf{A}_r$ is an $N_{\text{row}} \times N_{\text{col}}$ matrix such that $[\mathbf{A}_r]_{i,j} = a_{i,j,r}$, $||\mathbf{A}_r||_{1,1} = \sum_{i,j} |a_{i,j,r}|$ and $\text{TV}(\cdot)$ denotes the total-variation (TV) regularization [9], [10]. The positive parameters $\lambda_{1,r}$ (resp. $\lambda_{TV,r}$) control the prior sparsity (resp. smoothness) of each abundance map $\mathbf{A}_r$. In this work, we set $\lambda_{1,r} = \lambda_1$ and $\lambda_{TV,r} = \lambda_{TV}, \forall r$ and these parameters are assumed to be fixed ($(\lambda_1, \lambda_{TV}) = (10, 100)$ in the results of Section V). Although the estimation of these hyperparameters is out of scope of this paper, note that they can be tuned via cross validation or adjusted via sequential optimization (see e.g., [11]).

Finally, assuming prior independence between the R abundance maps yields $f(\mathbf{A}|\lambda_1, \lambda_{TV}) = \prod_{r=1}^{R} f(\mathbf{A}_r|\lambda_1, \lambda_{TV})$.

III-C. Joint Posterior distribution

From the joint likelihood and prior model specified in Sections III-A and III-B, we can now derive the joint posterior distribution for $\mathbf{T}$ and $\mathbf{A} = \{\mathbf{A}_r\}_r$, given the observed waveforms $\mathbf{Y}$ and the value of the fixed hyperparameters $\boldsymbol{\Phi} = (\lambda_1, \lambda_{TV})$. Using Bayes' theorem, and assuming prior independence between $\mathbf{T}$, and $\{\mathbf{A}_r\}_r$, the joint posterior distribution associated with the proposed Bayesian model is given by

$$f(\mathbf{T}, \mathbf{A}|\mathbf{Y}, \boldsymbol{\Phi}) \propto f(\mathbf{Y}|\mathbf{T}, \mathbf{A}) f(\mathbf{A}|\boldsymbol{\Phi}) f(\mathbf{T}) \tag{5}$$

IV. ESTIMATION STRATEGY

The posterior distribution (5) models our complete knowledge about the unknowns given the observed data and the prior information available. In a similar manner to [5], we exploit this posterior to perform joint depth estimation and spectral unmixing of the MSL data. However, while a minimum mean squared error (MMSE) estimator was used in [5], here we consider the following joint maximum a posteriori (MAP) estimator

$$(\widehat{\mathbf{T}}, \widehat{\mathbf{A}}) = \underset{\mathbf{T},\mathbf{A}}{\operatorname{argmax}} f(\mathbf{T}, \mathbf{A}|\mathbf{Y}, \mathbf{\Phi}), \tag{6}$$

which can also be obtained by minimizing the negative log-posterior $-\log\left(f(\mathbf{T}, \mathbf{A}|\mathbf{Y}, \mathbf{\Phi})\right)$. Although is can be shown that $f(\mathbf{Y}|\mathbf{T}, \mathbf{A})$ is log-concave with respect to (w.r.t.) $\mathbf{A}$, computing the estimator in (6) is generally challenging, mainly because $f(\mathbf{Y}|\mathbf{T}, \mathbf{A})$ can be multimodal w.r.t. $\mathbf{T}$. In [5] a simulation method was used to handle the possibly multimodal likelihood (3) based on the full 4D data cube. As will be shown below, here the joint depth estimation and spectral unmixing problem is solved with a reduced computational cost using efficient optimization methods (under mild conditions discussed below). Indeed, we show that the estimator in (6) can be obtained by first computing $\widehat{\mathbf{A}}$ and then $\widehat{\mathbf{T}}$.

From (1) it can be seen that

$$\tilde{y}_{i,j,\ell}|\lambda_{i,j,\ell}, t_{i,j} \sim \mathcal{P}\left(\lambda_{i,j,\ell}\tilde{g}_{i,j,\ell}\right), \tag{7}$$

where $\tilde{y}_{i,j,\ell} = \sum_{t=1}^{T} y_{i,j,\ell,t}$ and $\tilde{g}_{i,j,\ell} = \sum_{t=1}^{T} g_{0,\ell}(t - t_{i,j})$. That is, the integrated waveform (summed over the time bins) for each pixel and wavelength follows a Poisson distribution whose mean only depends on spectral parameters $\lambda_{i,j,\ell} = \mathbf{m}_{\ell,:}\boldsymbol{a}_{i,j}$ scaled by $\tilde{g}_{i,j,\ell}$ which contains only information about the range of the target. The additional assumption considered in this work concerns the values of $\tilde{g}_{i,j,\ell}$. More precisely, we assume that $\tilde{g}_{i,j,\ell}$ is constant for all possible values of $t_{i,j} \in \mathbb{T}$. This occurs in practice when $\mathbb{T}$ is far from the boundaries of $(1, T)$ compared to the spread of the impulse responses $g_{0,\ell}(\cdot)$. In our experiments, the supports of the instrumental responses are shorter than 500 time bins and we ensured the histograms of time-of-flights were long enough not to clip any target peak. This motivates our choice of (t_{min}, t_{max}) in Section III-B. Under this additional assumption, we have

$$\begin{aligned}\log\left(\textstyle\prod_t f(y_{i,j,\ell,t}|\lambda_{i,j,\ell}, t_{i,j})\right) &= \log\left(f(\tilde{y}_{i,j,\ell}|\lambda_{i,j,\ell}, t_{i,j})\right) + c_{i,j,\ell} \\ &= \log\left(f(\tilde{y}_{i,j,\ell}|\lambda_{i,j,\ell})\right) + c_{i,j,\ell},\end{aligned} \tag{8}$$

where $c_{i,j,\ell}$ is a constant which does not depend on $\lambda_{i,j,\ell}$. Note that $c_{i,j,\ell}$ depends on $t_{i,j}$ though and should be noted $c_{i,j,\ell}(t_{i,j})$. However, we do not explicit this dependency and use $c_{i,j,\ell}$ to lighten the notations. Combining (5),(6) and (8) yields

$$\begin{aligned}(\widehat{\mathbf{T}}, \widehat{\mathbf{A}}) &= \underset{\mathbf{T},\mathbf{A}}{\operatorname{argmin}} -\log(f(\mathbf{A})) - \log(f(\mathbf{T})) \\ &- \sum_{i,j,\ell} \log\left(f(\tilde{y}_{i,j,\ell}|\lambda_{i,j,\ell})\right) + c_{i,j,\ell},\end{aligned} \tag{9}$$

where we notice that the optimization w.r.t. $\mathbf{A}$ does not depend on the value of $\mathbf{T}$. Thus, we can first estimate $\widehat{\mathbf{A}}$ (it reduces to estimating the marginal MAP estimator of $f(\mathbf{A}|\mathbf{Y}, \mathbf{\Phi})$ and then compute $\widehat{\mathbf{T}}$ which also maximizes the conditional $f(\mathbf{T}|\mathbf{Y}, \widehat{\mathbf{A}}, \mathbf{\Phi})$. In addition to splitting to estimation of $\mathbf{A}$ and $\mathbf{T}$ into two simple sequential steps, one of the main advantages of the proposed approach (over the method considered in [5]) is its low computational complexity while providing a global optimum of (5). Indeed, the estimation of $\mathbf{A}$ is achieved using only a reduced number of summarizing features (i.e., $\{\tilde{y}_{i,j,\ell}\}$) from the original data. The next paragraph details how to sequentially compute $\widehat{\mathbf{A}}$ and $\widehat{\mathbf{T}}$.

IV-A. Estimating $\widehat{\mathbf{A}}$

Eq. (7) can be rewritten in matrix form as

$$\widetilde{\mathbf{Y}} \sim \mathcal{P}\left(\widetilde{\mathbf{M}}\widetilde{\mathbf{A}}\right) \tag{10}$$

where $\widetilde{\mathbf{Y}}$ is an $L \times N_{\text{row}}N_{\text{col}}$ matrix gathering the elements $\tilde{y}_{i,j,\ell}$, $\widetilde{\mathbf{M}}$ corresponds to the endmember matrix whose columns have been scaled by $\tilde{g}_{i,j,\ell}$, $\widetilde{\mathbf{A}}$ and is the $R \times N_{\text{row}}N_{\text{col}}$ reshaped abundance matrix. Consequently, computing $\widehat{\mathbf{A}}$ reduces to unmixing the integrated waveforms $\widetilde{\mathbf{Y}}$ under Poisson noise assumption, using the prior model/regularization described in Section III-B and estimating $\widetilde{\mathbf{A}}$ via MAP estimation. The corresponding minimization problem

$$\min_{\mathbf{A} \succeq \mathbf{0}} C(\mathbf{A}) + \lambda_1 \sum_r ||\mathbf{A}_r||_{1,1} - \lambda_{TV} \sum_r \text{TV}\left(\mathbf{A}_r\right) \tag{11}$$

is can be solved using any state-of-the art convex optimization algorithm since $C(\mathbf{A}) = -\log(f(\widetilde{\mathbf{Y}}|\widetilde{\mathbf{M}}\widetilde{\mathbf{A}}))$ is proper, lower semicontinuous and convex [12] (in practice $\mathbf{M}$ has positive entries and is full-rank). Here we used an instance of alternating direction method of multipliers (ADMM) similar to PIDAL-TV [12] but other alternative algorithms could have been used (e.g., SPIRAL [13]). Comparison of algorithms for solving (11) is out of scope of this paper and the interested reader is invited to consult [10], [12] for details about the ADMM implementation using TV and ℓ_1 regularization. It is interesting to recall here that although solving (9) requires the whole observation matrix $\mathbf{Y}$, estimating $\mathbf{A}$ only requires the integrated waveforms, which drastically reduces the computational complexity of the problem.

IV-B. Estimating $\widehat{\mathbf{T}}$

As discussed above, $\widehat{\mathbf{T}}$ can be obtained by maximizing $f(\mathbf{T}|\mathbf{Y}, \widehat{\mathbf{A}}, \mathbf{\Phi})$. Moreover, it can be seen for (5) that

$$f(\mathbf{T}|\mathbf{Y}, \widehat{\mathbf{A}}, \mathbf{\Phi}) = \prod_{i,j} f(t_{i,j}|\mathbf{y}_{i,j}, \mathbf{M}\hat{\boldsymbol{a}}_{i,j}) \tag{12}$$

with $f(t_{i,j}|\mathbf{y}_{i,j}, \mathbf{M}\hat{\boldsymbol{a}}_{i,j}) \propto f(\mathbf{y}_{i,j}|t_{i,j}, \mathbf{M}\hat{\boldsymbol{a}}_{i,j})/T'$. Consequently, the elements of $\widehat{\mathbf{T}}$ can be estimated independently (and in a parallel manner). Since $t_{i,j}$ is assumed to be discrete and can only take value in finite set $\mathbb{T}$, the estimation of $\widehat{\mathbf{T}}$ is straightforward. Note that since we compute the values of $f(t_{i,j}|\mathbf{y}_{i,j}, \mathbf{M}\hat{\boldsymbol{a}}_{i,j})$ for all possible values of $t_{i,j} \in \mathbb{T}$, we can derive measures of uncertainty about the ranges (see Section V).

V. SIMULATION RESULTS

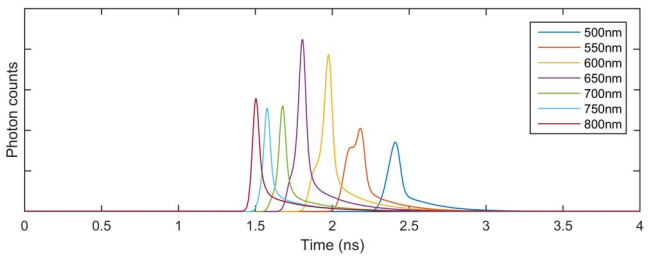

Fig. 1. Examples of instrumental impulse responses measured with an acquisition of 100s at different wavelengths $(500, 550, 600, 650, 700, 750$ and 800nm)

V-A. Experiment description

We assess the performance of the proposed method to analyse the depth and spectral profiles of a 5×5 cm scene (see Fig. 2 (a)) composed of 8 objects made of polymer clay and mounted on real tree leaves and fixed onto a dark-grey backboard at a distance of 1.8m from a time-of-flight scanning sensor, based on time-correlated single photon counting (TCSPC). The transceiver system and data acquisition hardware used for this work is broadly similar to that described in [14]–[18], which was previously developed at Heriot-Watt University. The measurements have been performed indoor, in the dark to limit the influence of ambient illumination. The scene has been scanned using a regular spatial grid of 190×190 pixels and $L = 33$ regularly spaced wavelengths ranging from 500nm to 820nm. The histograms consist of $T = 3000$ bins of 2ps, which represents a depth resolution of 300μm per bin. The power of the supercontinuum laser source has been adjusted from preliminary runs and the per-pixel acquisition time is 10ms for each wavelength.

The instrumental impulse responses $g_{0,\ell}(\cdot)$ (partly depicted in Fig. 1) were estimated from preliminary experiments by analysing the distribution of photons reflected onto a Lambertian scatterer placed at a known distance over a long period of time (100s here). Fig. 1 illustrates the fact that the response of imaging system can change in amplitude and shape, depending on the wavelength considered due to the wavelength-dependent characteristics of its different elements (e.g., supercontinuum laser source, detector, lenses). Notice also the delays between the different peaks mainly due to the different (and wavelength-dependent) path lengths of the light in the imaging system. These delays can be compensated for as part of the calibration and do not have a significant influence on the imaging performance.

If a single wavelength was to be used to estimate the depth profile, the variations of the peak shape could make the choice of the most relevant wavelength difficult as the depth estimation accuracy mainly depends on the amplitude (reflectivity estimation) and width (depth estimation) of the peak. Of course, the depth estimation performance also depends on the spectral signatures of the objects of the scene (e.g., some objects can have a low reflectivity at a given wavelength and are thus hardly detectable). By considering several wavelengths to estimate the depth profile, we can expect a more robust depth estimation (each object needs to be visible at at least one wavelength) as we benefit from potential redundancy between the different spectral bands.

V-B. Unmixing results

Fig. 3 shows the spectral signatures of the $R = 9$ endmembers manually extracted from the the data (based on the known position of the different objects) and Fig. 4 depicts the corresponding estimated abundance maps. Although the leaves and most clay objects present close shades of green in Fig. 2 (a), Fig. 3 shows that the leaf spectra are significantly different from the green clay spectra which have similar shapes (and thus makes the unmixing problem particularly difficult). Nevertheless, the estimated abundances are generally in good agreement with the RBG image as it is possible to identify the regions where the different materials are present.

V-C. Depth estimation

Fig. 2 (b) shows the depth/range image estimated using the proposed method (i.e., after having estimated the abundance maps) which is in very good agreement with the structure of the scene in Fig. 2 (a) (the reference range being set to the range of the backboard). In particular, it is possible to detect subtle depth variations (e.g., central veins of the leaves, depth gap between the leaves and the board). To evaluate the quality of the depth estimation, we compute for each pixel the posterior probability $f(t_{i,j} = \hat{t}_{i,j}|\mathbf{y}_{i,j}, \mathbf{M}\hat{\boldsymbol{a}}_{i,j})$ in (12). The corresponding probability map in Fig. 2 (c) illustrates the high concentration of

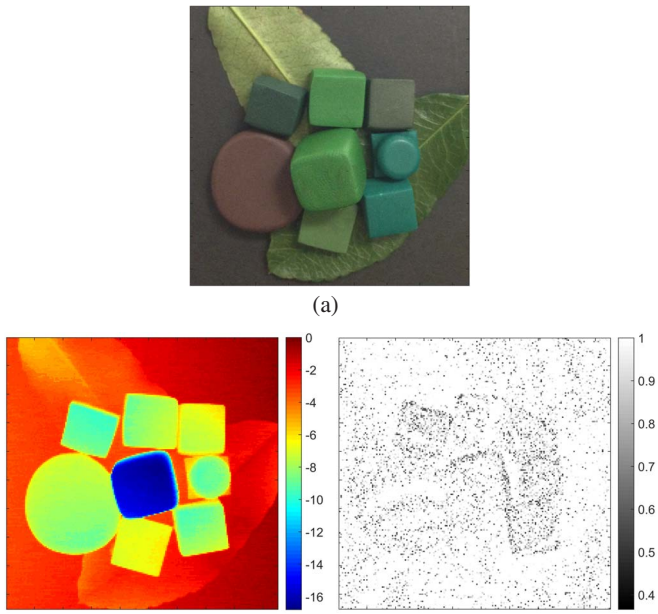

Fig. 2. (a): Standard RGB image of the scene composed of different coloured clays and leaves fixed on a dark-grey backboard. (b) Estimated depth/range image in millimetre (the reference range corresponds to the backboard range). (c) Posterior probabilities of actual ranges to be within the 0.3mm interval around $\hat{d}_{i,j} = (3/2).10^8\hat{t}_{i,j}$.

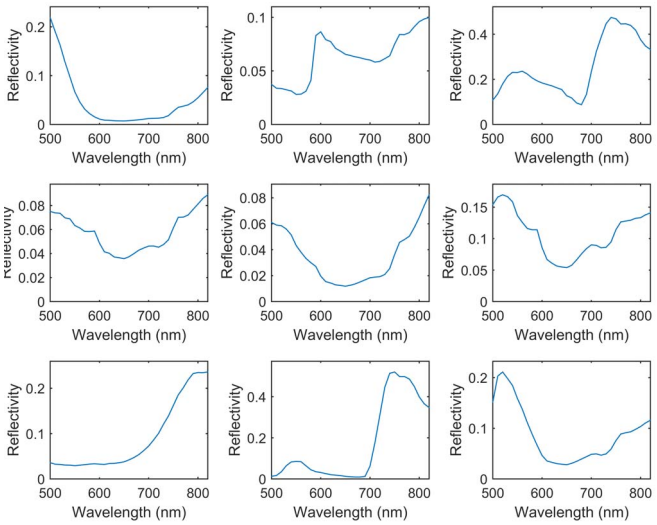

Fig. 3. Spectral signatures of the $R = 9$ endmembers used to analyse the MSL data (corresponding abundance maps depicted in Fig. 4).

$f(t_{i,j}|\mathbf{y}_{i,j}, \mathbf{M}\hat{\boldsymbol{a}}_{i,j})$ around $\hat{t}_{i,j}$ which translates an accurate depth estimation. Indeed, $f(t_{i,j} = \hat{t}_{i,j}|\mathbf{y}_{i,j}, \mathbf{M}\hat{\boldsymbol{a}}_{i,j})$ is higher than 95% in most pixels, the lower probabilities being associated with regions where the surface orientations yields lower photon counts and thus higher uncertainties about the object ranges. Note however that $f(t_{i,j} \in (\hat{t}_{i,j} - 1, \hat{t}_{i,j} + 1)|\mathbf{y}_{i,j}, \mathbf{M}\hat{\boldsymbol{a}}_{i,j})$ is higher than 99% for more than 99% of the pixels, leading to confidence intervals at 99% smaller than 0.9mm for almost all estimated ranges.

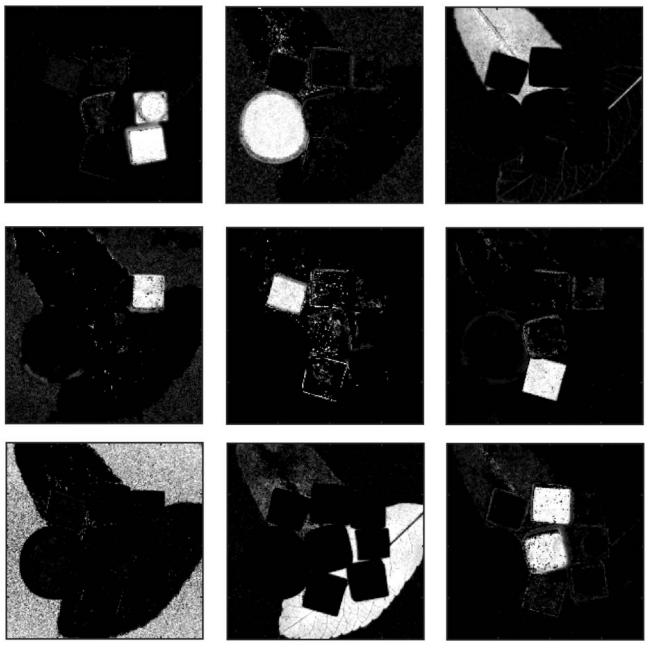

Fig. 4. Estimated abundance maps (all images have the same dynamic, i.e., between 0 and 1).

VI. CONCLUSION

We have proposed a new Bayesian model and a fast joint depth estimation and spectral unmixing algorithm for 3D scene analysis from MSL data. Assuming the ambient illumination can be neglected, the spectra of the scene surfaces visible by the imaging system were decomposed into linear mixtures of known endmembers, potentially corrupted by sparse deviations/anomalies. Adopting a Bayesian approach, prior distributions were assigned to the unknown model parameters; in particular sparsity and smoothness promoting priors were used to encode the spatial organization of the abundance maps. Including ambient illumination and dark count levels in the observation model (as in [8], [18]–[20]) is the obvious next step from a more general application of the proposed method. This can be done easily by including additional background terms in (1). Note that the proposed method can still be applied if the background levels are known (or estimated beforehand) by modifying the cost function in (9) (the resulting cost function remains convex with respect to $\mathbf{A}$). In future work, and especially for remote sensing applications, it will be crucial to account for the presence of distributed (multi-layered) targets and anomalies (e.g., objects present in isolated pixels and/or presenting spectral signatures which differ from the main objects of the scene), which would yield multiple returns in the MSL data. This could potentially allow the estimation of real 3D abundance profiles.

VII. REFERENCES

[1] M. Dalponte, L. Bruzzone, and D. Gianelle, "Fusion of hyperspectral and lidar remote sensing data for classification of complex forest areas," *IEEE Trans. Geosci. and Remote Sensing*, vol. 46, no. 5, pp. 1416–1427, May 2008.

[2] S. J. Buckley, T. H. Kurz, J. A. Howell, and D. Schneider, "Terrestrial lidar and hyperspectral data fusion products for geological outcrop analysis," *Computers & Geosciences*, vol. 54, no. 0, pp. 249–258, 2013.

[3] A. M. Wallace, C. J. Nichol, and I. H. Woodhouse, "Recovery of forest canopy parameters by inversion of multispectral lidar data," *Remote Sensing*, vol. 4, no. 2, pp. 509–531, 2012.

[4] T. Hakala, J. Suomalainen, S. Kaasalainen, and Y. Chen, "Full waveform hyper-spectral lidar for terrestrial laser scanning," *Opt. Express*, vol. 20, no. 7, pp. 7119–7127, Mar 2012.

[5] Y. Altmann, A. Wallace, and S. McLaughlin, "Spectral unmixing of multispectral lidar signals," *IEEE Trans. Signal Process.*, vol. 63, no. 20, pp. 5525–5534, Oct. 2015.

[6] A. M. Wallace, A. McCarthy, C. Nichol, X. Ren, S. Morak, D. Martinez-Ramirez, I. Woodhouse, and G. S. Buller, "Design and evaluation of multispectral lidar for the recovery of arboreal parameters," *IEEE Trans. Geoscience and Remote Sensing*, vol. 52, no. 8, pp. 4942–4954, Aug 2014.

[7] S. Hernandez-Marin, A. M. Wallace, and G. J. Gibson, "Bayesian analysis of lidar signals with multiple returns," *IEEE Trans. Patt. Anal. Mach. Intell.*, vol. 29, no. 12, pp. 2170–2180, Dec 2007.

[8] Y. Altmann, X. Ren, A. McCarthy, G. S. Buller, and S. McLaughlin, "Lidar waveform based analysis of depth images constructed using sparse single-photon data," *IEEE Trans. Image Processing*, vol. 25, no. 5, pp. 1935–1946, 2016.

[9] A. Chambolle, "An algorithm for total variation minimization and applications," *J. of Mathematical Imaging and Vision*, vol. 20, no. 1-2, pp. 89–97, 2004.

[10] M. D. Iordache, J. M. Bioucas-Dias, and A. Plaza, "Total variation spatial regularization for sparse hyperspectral unmixing," *IEEE Trans. Geosci. and Remote Sensing*, vol. 50, no. 11, pp. 4484–4502, Nov. 2012.

[11] M. Pereyra, J. M. Bioucas-Dias, and M. A. T. Figueiredo, "Maximum-a-posteriori estimation with unknown regularisation parameters," in *Signal Processing Conference (EUSIPCO), 2015 23rd European*, Aug. 2015, pp. 230–234.

[12] M. Figueiredo and J. Bioucas-Dias, "Restoration of poissonian images using alternating direction optimization," *IEEE Trans. Image Processing*, vol. 19, no. 12, pp. 3133–3145, 2010.

[13] Z. T. Harmany, R. F. Marcia, and R. M. Willett, "This is spiral-tap: Sparse poisson intensity reconstruction algorithms - theory and practice," *IEEE Transactions on Image Processing*, vol. 21, no. 3, pp. 1084–1096, March 2012.

[14] A. McCarthy, R. J. Collins, N. J. Krichel, V. Fernández, A. M. Wallace, and G. S. Buller, "Long-range time-of-flight scanning sensor based on high-speed time-correlated single-photon counting," *Appl. Opt.*, vol. 48, no. 32, pp. 6241–6251, Nov. 2009.

[15] N. J. Krichel, A. McCarthy, and G. S. Buller, "Resolving range ambiguity in a photon counting depth imager operating at kilometer distances," *Opt. Express*, vol. 18, no. 9, pp. 9192–9206, April 2010.

[16] A. M. Wallace, J. Ye, N. J. Krichel, A. McCarthy, R. J. Collins, and G. S. Buller, "Full waveform analysis for long-range 3d imaging laser radar," *EURASIP Journal on Advances in Signal Processing*, vol. 2010, no. 1, p. 896708, 2010.

[17] A. McCarthy, X. Ren, A. D. Frera, N. R. Gemmell, N. J. Krichel, C. Scarcella, A. Ruggeri, A. Tosi, and G. S. Buller, "Kilometer-range depth imaging at 1550 nm wavelength using an InGaAs/InP single-photon avalanche diode detector," *Opt. Express*, vol. 21, no. 19, pp. 22 098–22 113, Sept. 2013.

[18] Y. Altmann, X. Ren, A. McCarthy, G. S. Buller, and S. McLaughlin, "Target detection for depth imaging using sparse single-photon data," in *Proc. IEEE Int. Conf. Acoust., Speech, and Signal Processing (ICASSP)*, Shanghai, China, 2016.

[19] A. Kirmani, D. Venkatraman, D. Shin, A. Colao, F. N. C. Wong, J. H. Shapiro, and V. K. Goyal, "First-photon imaging," *Science*, vol. 343, no. 6166, pp. 58–61, 2014.

[20] D. Shin, A. Kirmani, V. Goyal, and J. Shapiro, "Computational 3d and reflectivity imaging with high photon efficiency," in *Proc. IEEE Int. Conf. Image Processing (ICIP)*, Oct. 2014, pp. 46–50.

GMTI in circular SAR data using STAP

Emiliano Casalini
Remote Sensing Laboratories
University of Zurich
e-mail: emiliano.casalini@geo.uzh.ch

Daniel Henke
Remote Sensing Laboratories
University of Zurich
e-mail: daniel.henke@geo.uzh.ch

Erich Meier
Remote Sensing Laboratories
University of Zurich
e-mail: erich.meier@geo.uzh.ch

***Abstract*—This paper presents method and results of a Ground Moving Target Indication (GMTI) experiment using multi-channel Synthetic Aperture Radar (M-SAR) data collected by the four channel F-SAR system. The proposed approach is based on sub-aperture processing, Space-Time Adaptive Processing (STAP), constant false alarm rate (CFAR) thresholding and geocoding. The results are validated and compared with results of the same data set from a previous approach based on a combination of single-channel (SC) and Along-Track Interferometry (ATI) detections. It is shown that the STAP-based technique guarantees better performances when detecting moving targets with a small Radar Cross Section (RCS).**

I. Introduction

Nowadays, SAR-GMTI is becoming increasingly important since acquiring knowledge about moving objects and simultaneously imaging the area of interest has considerable advantages for both civil and non-civil applications. Monitoring and counting vehicles on highways or detecting non-cooperative moving targets on ground may demand different performances but they do ask for a common core processing. In the past decades several solutions have been proposed in order to design a SAR system with GMTI capabilites. A simple taxonomy is based upon the number of receiving channels. Therefore, we may divide these systems into two groups: single-channel systems and multi-channel systems. The first ones are SAR systems with a single receiving antenna connected to a single receiver. They were initially proposed since generating multi-channel data was not feasible in terms of processing burden, hardware complexity and costs. Viceversa, most recent state-of-the-art methods for SAR-GMTI such as ATI [1], Displaced Phase Center Array (DPCA) [2] and STAP [3-4] rely on multi-channel data.

DPCA and STAP-based techniques make use of multiple receiving channels to suppress the signal back-scattered by stationary targets (clutter), thus making the detection of small slow moving targets easier. More specifically, STAP processes the pulses collected by M antenna elements at N pulse repetition intervals (PRI). These space-time samples are then combined in such a way that the output signal-to-interference-pluse-noise-ratio (SINR) is maximized. Such a processing defines a 2-D filter which increases detection rates with respect to any 1-D space or time filter. Unfortunately, the main drawback of STAP is its computational burden which is a function of the N spatial degrees-of-freedom and M temporal degrees-of-freedom (DOFs). Sub-optimal STAP configurations were then designed in order to limit the overall number of spatial and temporal DOFs and make STAP suitable for real life applications [3-4]. While SAR-STAP was mainly applied to linear flight patterns [5], less attention was placed on the advantages of circular SAR data. The circular acquisition geometry used in this paper yields an extended illumination time which leads to longer moving object detection times. Furthermore, a more detailed analysis of STAP detection capabilities under a changing illumination geometry becomes feasible given a circular flight pattern. This allows the validation of STAP detection capability with respect to the aforementioned criteria. Additionally, a comparison with SC/ATI combined detections was conducted demonstrating that STAP can contribute to a better detection capability especially for small RCS objects. Initial results show an increase from 30% using SC/ATI to 80% with STAP.

In Section II-A we briefly introduce the test site, then we describe the F-SAR sensor and list its specifications. In Sections II-(B-E) each single stage of the processing chain is described in detail. Section II-F outlines the validation method while section III analyses and evaluates the achieved results. Finally, in Section IV we summarize the overall results and suggest potential future investigations.

II. Method

A method for GMTI using circular M-SAR real data is introduced and described. The main steps of the processing chain are as follows: *(1)* a pre-processing block implementing sub-aperture processing, track linearization and array calibration, *(2)* a sub-optimal STAP processing known as Adjacent Bin Post Doppler STAP (ABPD-STAP) [6], *(3)* a CFAR thresholding to detect moving targets and *(4)* geocoding. The aforementioned processing chain is capable of achieving ground moving target detections in spite of a circular flight path and attitude perturbations.

A. Test site and sensor

The study area for the SAR-GMTI experiment was a highway intersection close to the municipality of Oensingen, located in the canton of Solothurn, Switzerland (see Fig. 1).

The SAR sensor utilized in the experiment is the F-SAR sensor designed by DLR [7]. The system comprises one transmitting antenna and four equally spaced receiving antennas with an inter-element spacing of 20 cm. Elevation and azimuth angle are respectively 30.3 and 7.3 degrees.

The transmitted signal is a down-chirp signal centered around

978-1-5090-0326-6/16/$31.00 ©2016 IEEE

Fig. 1. Geocoded SAR image of the test site Oensingen.

a 9.6 GHz carrier frequency with bandwidth equals to 100 MHz and the theoretical range resolution is approximately 1.5 m. The slow time signal was sampled with a Pulse Repetition Frequency (PRF) of approximately 2016 Hz. The whole batch of data comprises more than 300 k pulses (ca. 149 s) collected on a circular acquisition geometry. The flight path has an approximate diameter of 3.5 km, a mean altitude above ground of 2.7 km, and an average platform velocity of 76 m/s.

B. Data pre-processing

The data were firstly divided into a large number of highly *overlapping apertures with reduced bandwidth* (OAwrB) with a step size of 200 pulses (ca. 0.1 s) between subsequent OAwrB. Each of the OAwrB was defined by extracting a coherence processing interval (CPI) of 700 pulses (circa 0.34 s) from the whole data set. This aperture is small enough to guarantee a valid post-Doppler STAP filtering and limits target range migration within few range-Doppler cells. The following step consists of track linearization and forward velocity compensation: this was only possible since a very precise global positioning system (GPS) was installed on-board the airborne platform. The OAwrB were then processed to achieve range compression and a Fast Fourier Transform (FFT) was performed along the slow-time axis to map the received signal into the range-Doppler domain. Fig. 2 shows the range-Doppler map of Channel #1 for a given OAwrB. Even though range-Doppler maps are not always straightforward interpretable, some of the underlying structures are clearly visible. This is due to the meter range resolution and to the CPI duration which is long enough to compress the signal along the Doppler axis. In fact, we can recognize the highway intersection, some agricultural fields and few buildings characterized by dominant scatterers. The presence

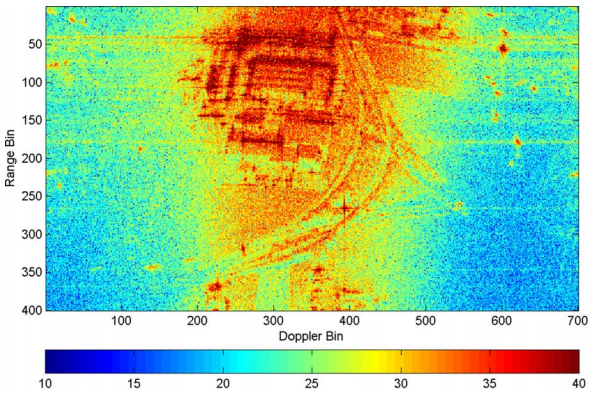

Fig. 2. Range-Doppler map before STAP: Channel #1, OAwrB #106.

of grassland and urban area suggests that the background clutter is very likely to be heterogeneous and this will have to be accounted for when performing moving targets detection. Finally, the last step of the pre-processing stage is the array calibration, which is crucial when using techniques that exploit amplitude and phase differences of the signals collected by an array. The main goal is to remove any antenna pattern imbalances between the array elements so that their transfer functions are as similar as possible. The technique that was implemented is the *adaptive 2-D calibration* proposed by Ender [8]: this approach is useful when no information about the antenna patterns is available.

C. STAP processing

In order to remove or at least mitigate the impact of background clutter the ABPD-STAP technique has been applied to each Fourier-transformed OAwrB. Post-Doppler approaches imply a theoretical decoupling of the samples at adjacent Doppler bins allowing an independent and separate clutter suppression for each one of them. Nonetheless, even if the Fourier-transformed signals are less correlated than the time-domain ones, some correlation persists. For this reason the so called *order 2 extended factored processing* [6] was adopted. That is, two adjacent correlation values (one for each side) were included giving a total of three Doppler bins. The interference-pluse-noise covariance matrix is then estimated as follows:

$$\boldsymbol{R}(k,w) = \frac{1}{K}\sum_{k=1}^{K} \boldsymbol{Z}(k,\boldsymbol{w}) * \boldsymbol{Z}^{'}(k,\boldsymbol{w}) \qquad (1)$$

$$\boldsymbol{w} = [(w-1)\ w\ (w+1)]$$

being $'$ the conjugate transpose operator, while k and w identify respectively the range bin and the Doppler bin. Given the spatially dependent nature of clutter, the K bins were selected by means of a sliding window strategy [9] and a fixed number of neighbouring range-gates were discarded in order to avoid target self-nulling. The STAP filter weights are defined by

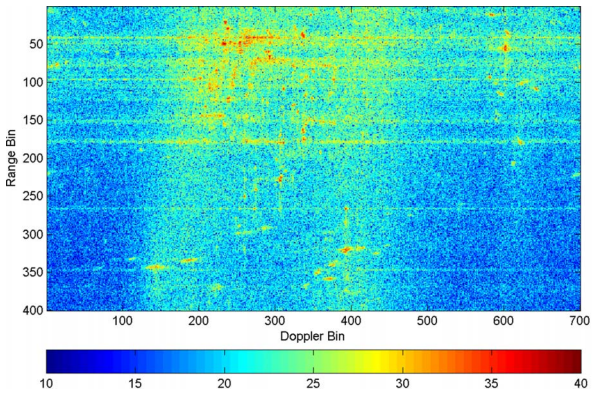

Fig. 3. Range-Doppler map after STAP: OAwrB #106.

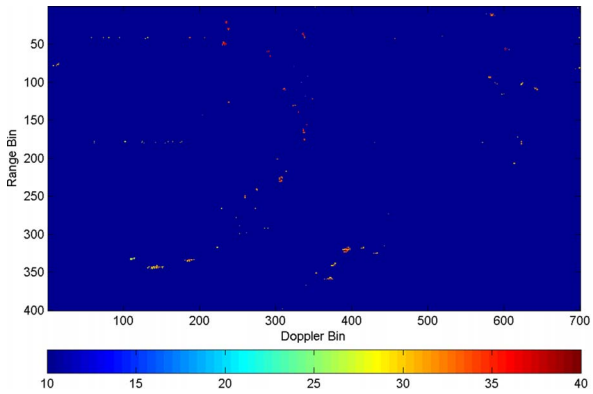

Fig. 4. Range-Doppler map after STAP and MT detection: OAwrB #106.

$$\boldsymbol{h}(k,w) = \boldsymbol{R}^{-1}(k,w) * \boldsymbol{v}(w) \tag{2}$$

where $\boldsymbol{v}$ is the steering vector which maximizes the signal centered around Doppler bin w. Finally, STAP filtering is implemented as

$$\tilde{\boldsymbol{Z}}(k,w) = \boldsymbol{h}^{'}(k,w) * \boldsymbol{Z}(k,\boldsymbol{w}) \tag{3}$$

yielding the results shown in Fig. 3.

D. Moving targets detection

The decision whether a moving target is present in the range-Doppler map is made by a 3-step detection scheme [10]. The final detection mask is defined by computing the *logical AND* of three different binary masks. The first one aims at removing false alarms lying outside the antenna main beam: a threshold is defined as function of the noise level and its variance. Range-Doppler cells containing values falling below this threshold are very likely not containing any useful signal. The second binary mask is designed in order to remove clutter residues [11]. In fact, as one can see by comparing Fig. 2 with Fig. 3, the proposed ABPD-STAP technique is not capable of completely removing the background clutter. Dominant scatterers are likely to survive the STAP filtering, especially when the SAR scene is heterogeneous. The third binary mask is the result of a CFAR thresholding. From Eq. (3) we can easily derive the so called Maximum-Likely Quotient (MLQ) statistic which reflects the highly variant back-ground reflectivity of the SAR scene. The *scaled F-distribution* proposed in [12] proved to be the one providing the best fit. The very last step consists of removing single cell potential detections from the *AND* mask, that is detections occupying only one range-Doppler cell were suppressed.

The results of this detection scheme are shown in Fig. 4 where one can recognize the candidates for moving targets.

E. Geocoding

The masked range-Doppler map (as shown in Fig. 4) is the input for the geocoding step. Moving target candidates are back-projected directly to a three-dimensional reconstruction grid as we are interested in mapping them into a geocoded reference system. This is possible since the linearized aircraft position is known and a very accurate digital elevation model (DEM) was available. In order to accomplish it, *Time Domain Back-Projection* (TDBP) [13] was used. Note that here we have range-Doppler STAP-filtered signals while usual inputs for the TDBP are the base-band range-compressed signals. An Inverse FFT (IFFT) was then performed along the Doppler axis to transform the filtered signals back into the time-domain. The TDBP calculates the geocoded image as follows:

$$OAwrB_{FLT} =$$

$$= \left[\sum_{t=1}^{N} s_{FLT}\left(\frac{R}{c}, t\right) e^{i2\pi f_c \tau}\right] e^{-i2k_c R(x_0,y_0,z_0)} \tag{4}$$

$$R = \sqrt{(X(t)-x_0)^2 + (Y(t)-y_0)^2 + (Z(t)-z_0)^2}$$

where t and τ correspond respectively to slow-time and fast-time. $(X(t), Y(t), Z(t))$ is the sensor position in global Cartesian coordinates along the slow-time, k_c is the frequency wavenumber at carrier frequency f_c and c is the speed of light. s_{FLT} is the base-band range-compressed STAP-filtered signal at slow time t.

F. Validation method

In order to validate the overall processing chain, the outputs of the STAP approach are compared with the ones of a SC/ATI based approach [14] where the same data set was processed. In addition, ground-truth measurements are available from *(a)* a camcorder equipped with a GPS clock overlooking the test site and *(b)* speed camera pictures and times of each single car or truck passing during the over-flight. With this information, we could not only validate the accuracy of the STAP moving target detections, but also outline a brief comparison between the STAP-based approach and the SC/ATI combined approach based on five test objects.

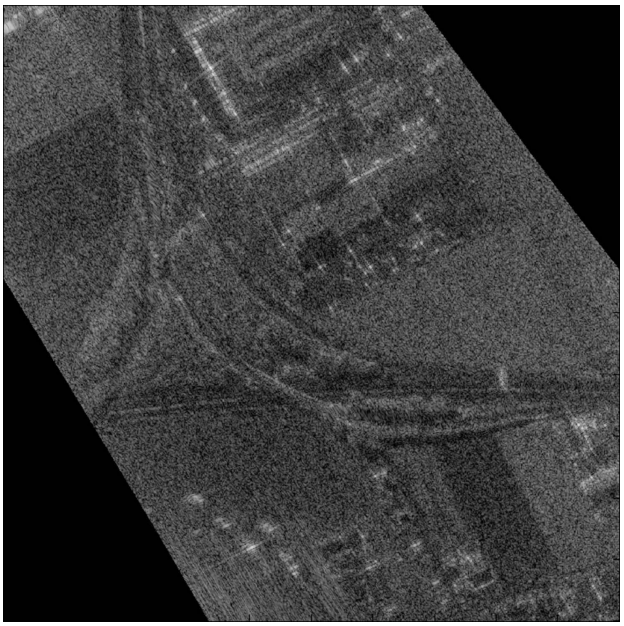

Fig. 5. Geocoded SAR image: Channel #1, OAwrB #106.

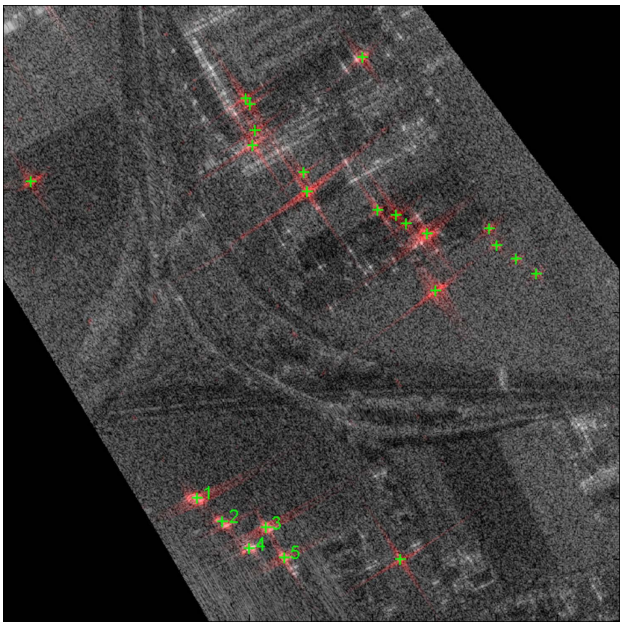

Fig. 6. STAP-derived detections on top of the SAR image: OAwrB #106. (Green crosses) Moving target detections. (Red) Moving targets' responses.

III. Results

To define a fair comparison between different approaches, the CFAR thresholding of Section II-B was defined in such a way that the number of STAP potential detections could match the ones from the other approaches (SC & ATI). That is, the FA ratio of the three methods were similar. The set of five moving target detections was analyzed over 100 consecutive OAwrB (circa 10 s). Fig. 5 shows the geocoded SAR image; Fig. 6 shows the STAP-derived detections overlaid on top of it. The five test moving targets are marked by the numbers 1-5 and can be found in the bottom-left of Fig. 6.

TABLE I
Detecion results

	SC	**ATI**	**SC ∩ ATI**	**STAP**
MT #1	95	66	98	100
MT #2	42	53	93	90
MT #3	41	57	87	94
MT #4	46	66	93	95
MT #5	3	29	29	81

The results are summarized in Table I. The overall performances of the STAP approach proved to be better than SC and ATI if those are taken singularly. The reason behind this gap is simple. The SC approach works fine as long as the target is outside the antenna main beam but fails when target with small RCS are within the main beam. Viceversa, ATI works better in the center of the antenna beam but its detection performances are affected by clutter: in fact, the phase of a moving target hidden in strong clutter is mainly driven by the clutter itself (see [14]). However, when combining these two approaches together the detection rate rise substantially. STAP still shows an overall better detection rate but the gap is considerably smaller. More specifically, large moving targets with big RCS (see Table I, MT #1) are reliably detectable by both approaches. On the contrary, moving targets with a smaller RCS (see Table I, MT #5) represent a more challenging task for SC/ATI combined approach (only 30% detection rate) while STAP still guarantees a robust detection rate of 80%. As for the STAP missed detections of MT #2-5, they were mainly caused by the sliding-window secondary data selection for the estimation of the covariance matrix. In fact, for few apertures the test moving targets were at the same Doppler and very close in range to a line of dominant scatterers. The presence of strong fixed targets in the secondary data led to the moving target in the cell under test being nulled when applying the STAP filter. However, based on these five test objects and using circular SAR data, we can conclude that STAP is relatively unaffected by the illumination geometry.

IV. Conclusions

We have introduced a method based on OAwrB and STAP processing to identify ground moving targets in circular SAR data. The proposed algorithm was evaluated by comparing it with the SC/ATI detections of the same data set. The achieved results are promising as the algorithm proved to be capable of detecting moving targets with reliable detection rates. This approach could potentially be an option for detecting and tracking non-cooperative moving targets in a non-civil scenario irrespective of the acquisition geometry. However, the algorithm should be modified to be capable of managing dense vehicle and man-made target environments. This would guarantee enhanced performances that are more suitable for

such applications. Further investigations shall include a more detailed comparison between SC, ATI and STAP in order to assess whether STAP is the best technique for any environment and any configuration. If that is not the case, following steps shall focus on merging different approaches in order to increase the overall detection rate at a fixed FA ratio.

ACKNOWLEDGMENT

The authors would like to thank the SAR Technology Department at the German Aerospace Center DLR for their cooperation and for providing the raw data for the experiments. This work was conducted at the Remote Sensing Laboratories, Department of Geography, University of Zurich, Zurich, Switzerland.

REFERENCES

[1] E. Chapin and C. W. Chen, "Airborne along-track interferometry for GMTI," *IEEE Aerospace and Electronic Systems Magazine*, vol. 24, no. 5, pp. 13-18, May 2009.

[2] C. H. Gierull and I. C. Sikaneta, "Raw data based two-aperture SAR ground moving target indication," in *Geoscience and Remote Sensing Symposium, 2003 IEEE International*, vol. 2, pp. 1032-1034, Jul. 2003.

[3] R. Klemm, *Principles of Space-Time Adaptive Processing*, London, U.K.: IEE, 2002.

[4] J. H. G. Ender, "Space-time processing for multichannel synthetic aperture radar," *Electronics & Communication Engineering Journal*, vol. 11, no. 1, pp. 29-38, Feb. 1999.

[5] D. Cerutti-Maori, J. Klare, A. R. Brenner, and J. H. G. Ender, "Wide-area traffic monitoring with the SAR/GMTI system PAMIR," *IEEE Transactions on Geoscience and Remote Sensing*, vol. 46, no. 10, pp. 3019-3030, Oct. 2008.

[6] R. DiPietro, "Extended factored space-time processing for airborne radar systems," in *Signals, Systems and Computers, 1992. 1992 Conference Record of The Twenty-Sixth Asilomar Conference on*, vol. 1, pp. 425-430, Oct. 1992.

[7] A. Reigber *et al.*, "System status and calibration of the F-SAR airborne SAR instrument," in *Geoscience and Remote Sensing Symposium, 2011 IEEE International*, pp. 1520-1523, Jul. 2011.

[8] J. H. G. Ender, "The Airborne Experimental Multi-Channel SAR System AER-II", in *Synthetic Aperture Radar, 1996. EUSAR. European Conference on*, pp. 49-52. Mar. 1996.

[9] G. K. Borsari and A. O. Steinhardt, "Cost-efficient training strategies for space-time adaptive processing algorithms," in *Signals, Systems and Computers, 1995. 1995 Conference Record of the Twenty-Ninth Asilomar Conference on*, vol. 1, pp. 650-654, Oct. 1995.

[10] D. Cerutti-Maori, W. Burger, J. H. G. Ender, and A. R. Brenner, "Experimental results of ground moving target detection achieved with the multi-channel SAR/MTI system PAMIR," in *European Radar Conference, 2005. EURAD 2005*, pp. 45-48, Oct. 2005.

[11] W. Burger, "Dealing with target nulling and clutter inhomogeneities in STAP," in *Synthetic Aperture Radar, 2012. EUSAR. 9th European Conference on*, pp. 380-383, Apr. 2012.

[12] D. Cerutti-Maori, C. H. Gierull, and J. H. G. Ender, "Experimental verification of SAR-GMTI improvement through antenna switching," *IEEE Transactions on Geoscience and Remote Sensing*, vol. 48, no. 4, pp. 2066-2075, Apr. 2010.

[13] O. Frey, C. Magnard, M. Ruegg, and E. Meier, "Focusing of airborne synthetic aperture radar data from highly nonlinear flight tracks," *IEEE Transactions on Geoscience and Remote Sensing*, vol. 47, no. 6, pp. 1844-1858, Jun. 2009.

[14] D. Henke, E. Mendez Dominguez, D. Small, M. E. Schaepman, and E. Meier, "Moving Target Tracking in Single- and Multichannel SAR," *IEEE Transactions on Geoscience and Remote Sensing*, vol. 53, no. 6, pp. 3146-3159, Jan. 2015.

Digital Elevation Model Aided SAR-based GMTI Processing in Urban Environments

Di Wu, Mehrdad Yaghoobi and Mike Davies
School of Engineering
University of Edinburgh
UK, EH9 3JL
Email: {D.Wu, m.yaghoobi-vaighan, mike.davies}@ed.ac.uk

***Abstract*—This paper presents a work for imaging the moving targets and estimating their velocities with better accuracies using the Digital Elevation Map (DEM) in urban environments under multi-channel Synthetic Aperture Radar (SAR) scenarios. Given the received phase histories pre-processed by channel balancing techniques, we employ Ground Moving Target Indicator (GMTI) methods to detect the moving targets, and apply the DEM to assist imaging the observed scene and estimating the states of the targets. Specifically the DEM can be leveraged to calibrate the positions of the moving targets and give further constraints on the estimations of velocities. The described work is demonstrated through the AFRL Gotcha challenge data. We present the positions of the relocated targets along with their velocity estimations as the experimental results.**

***Index Terms*—SAR, GMTI, digital elevation map**

I. Introduction

SAR was originally developed as a flexible sensing technique to produce high resolution images of the observed scene for surveillance purposes. In particular, SAR-based GMTI aims to indicate the moving targets within SAR images and estimate the moving target parameters including their physical positions and velocities. The developments on GMTI techniques in the last decade significantly captured the attention from the SAR community due to its capabilities in promoting situational awareness. In practice, SAR imaging assumes that the observed scene contains only static targets. Therefore, moving targets will introduce blurrings and displacements to the SAR images, and they need to be relocated and refocused using GMTI techniques.

Within the multi-channel SAR framework, widely used GMTI techniques include Displaced Phase Center Antenna (DPCA), Along Track Interferometry (ATI) and Space-time Adaptive Processing (STAP) [1][2][3]. DPCA and ATI are subtractive methods which suppress the clutter and reveal the moving targets with magnitudes and interference phases respectively. STAP can be taken as the extended version of DPCA and it is well known to be computationally expensive. Take the ATI as an example, radial velocities of the moving targets can be estimated and the moving targets can then be relocated accordingly. However, in particular scenarios where the monitored region has significant variations on elevations, the localisations of the targets will be distorted and inconsistencies will show up if we compare the relocated targets to the ground truth target path.

In this paper, we discuss how the DEM can be utilised to enhance the relocations of the moving targets and improve the estimations of targets' states. The remainder of the paper is organized as follows. Section two describes the signal modeling of a standard multi-channel SAR system with a specific terrain map. In section three, the DEM aided SAR/GMTI processings are presented. We first introduce the SAR basics and GMTI approaches. Then we focus on incorporating the DEM into the moving target imaging and the target states estimations. In section four, we demonstrate the performance of the proposed methods using the real airborne SAR data. Conclusions are presented in section five.

II. Signal Modeling

In Fig. 1 we depict a standard multi-channel SAR system in the spotlight mode with a number of moving targets in the observed scene. A terrain map is associated with the monitored region. The phase centres of antennas are equally spaced with a distance d along the flight path of the platform. Let the azimuth time (slow time) of the transmitted pulses be τ_n where $n = \{1, 2, ..., N\}$ is the pulse number; $\mathbf{r}(\tau_n)$ be the instantaneous spatial position of one target at τ_n; $r_i^{(t)}(\tau_n)$ and $r_i^{(o)}(\tau_n)$ denote the distance from the target to the $i-$th antenna and the distance from the scene origin to the corresponding antenna position respectively. Within a short sub-aperture, we can assume that the platform velocity is a constant v_p.

For the target at $\mathbf{r}(\tau_n)$, the discrete received phase histories from the $i-$th channel after the de-chirping process (the movement of the platform is compensated with reference to the scene origin) can be formulated as:

$$Y_i(f_k, \tau_n) = A_i \sigma(\mathbf{r}(\tau_n)) \exp\left(-\frac{j4\pi f_k u_i(\tau_n)}{c}\right) \qquad (1)$$

where $\{f_k | k = 1, 2, ..., K\}$ denotes the range frequencies; A_i represents a nominal factor which accounts for the beam pattern and energy loss for the $i-$th channel; $\sigma(\mathbf{r}(\tau_n))$ is the complex reflectivity of the target at $\mathbf{r}(\tau_n)$; c is the speed of light and $u_i(\tau_n)$ is the differential range $r_i^{(t)}(\tau_n) - r_i^{(o)}(\tau_n)$. Given that we have multiple targets in the observed scene, the received data can be assembled by accumulating the received signals from all the targets. Thus, the received data can be further reformulated in the matrix-vector form as

978-1-5090-0326-6/16/$31.00 ©2016 IEEE

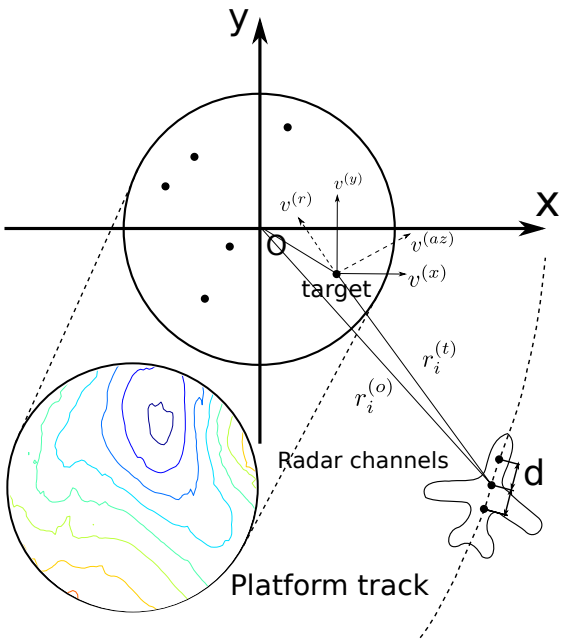

Fig. 1. The geometry of a multi-channel SAR system with moving targets in the monitored scene which is associated with a terrain map.

$\mathbf{Y}_i = \Phi_F(\mathbf{X})$, where Φ_F is the forward projection operator to map the image domain to the data domain and $\mathbf{X} \in \mathbb{C}^{M\times L}$ denotes the collection of the target reflectivities.

III. Digital Elevation Model Aided SAR/GMTI

Based on the described multi-channel SAR system we focus on the DEM aided SAR/GMTI processings in this section. How the terrain information can help locate the moving targets and estimate their states will be discussed in details.

A. SAR Pre-processing

Given that the phase histories have been range compressed and range-migration corrected, it has been reported that for two channels the signals in Doppler and range-frequency domain can be approximated with the equations [4]:

$$\begin{aligned} Y_1(\omega,\Omega) &\cong c(\omega)h_1(\Omega)D_1(q(\omega)) \\ Y_2(\omega,\Omega) &\cong c(\omega)h_2(\Omega)D_2(q(\omega))exp(-j\frac{d}{2v_p}\omega) \end{aligned} \tag{2}$$

where $c(\omega)$ is the nominal factor to denote the complex Doppler dependencies, $h_i(\Omega)$ is the transfer function with the range frequency Ω for the $i-$th channel, D_i is the antenna pattern for the $i-$th channel, and $q(\omega)$ is the directional cosine history over the Doppler frequency ω.

From (2) it is shown that the phase histories can be balanced with two functions in azimuth and range directions respectively, i.e. $H_{az}(\omega)$ and $H_{rg}(\Omega)$ in (3), to retrieve the same responses for stationary targets between different channels.

$$\begin{aligned} H_{az}(\omega) &= \frac{D_1(q(\omega))}{D_2(q(\omega))exp(-j\frac{d}{2v_p}\omega)} \\ H_{rg}(\Omega) &= \frac{h_1(\Omega)}{h_2(\Omega)} \end{aligned} \tag{3}$$

This process is especially crucial for subtractive GMTI methods such as DPCA and ATI which reveal moving targets in SAR images through the differences between channels. Specifically the phase history for the second channel can be balanced via $\widetilde{\mathbf{Y}}_2(\omega,\Omega) = \mathbf{Y}_2(\omega,\Omega)H_{az}(\omega)H_{rg}(\Omega)$. An adaptive 2D channel balancing technique was proposed to update $H_{az}(\omega)$ and $H_{rg}(\Omega)$ with iterations [4]. We will employ this approach to pre-process the SAR data in the remainder of the paper.

In practice, we tend to employ more azimuth samples to better mitigate the imperfect balances along the range direction. However, $H_{az}(\omega)$ have strong degradations in amplitudes among azimuth frequencies, and this will induce less calibration accuracies for the azimuth samples in high frequencies. The simple solution is to estimate $H_{az}(\omega)$ and $H_{rg}(\Omega)$ with a number of azimuth samples and preserve only the low frequencies in $H_{az}(\omega)$.

B. SAR Imaging and GMTI

The SAR imaging process can be interpreted as approximating the pseudo inverse of the forward projection operator Φ_F^0. Let the discrete grid on which the SAR image is formed be $\mathbb{G}_{ml} = (x_m, y_l, 0)$ and the range files $\Delta\mathbf{R}_{mln} = \|\mathbf{r}(\tau_n) - \mathbb{G}_{ml}\| - \|\mathbf{r}(\tau_n)\|$, where $m = \{1,2,...,M\}$, and $l = \{1,2,...,L\}$. The well known matched filter and back projection techniques realise the image formation via $\mathbf{X} = \Phi_B^0(\mathbf{Y}_i)$ in which the backward projection operator Φ_B^0 is the Hermitian transpose of Φ_F^0:

$$X(m,l) = \sum_{k=1}^{K}\sum_{n=1}^{N} Y_i(f_k,\tau_n)\exp\left(\frac{j4\pi f_k \Delta\mathbf{R}_{mln}}{c}\right) \tag{4}$$

Based on the imaging mechanism, multiple targets detection algorithms are valid to mark the ground moving targets in the formed images. In particular, DPCA is implementing the subtractions among the formed SAR images between different channels, ATI is realised by multiplying the formed image from a channel with the conjugate of the complex image from another channel, a compressed sensing based method is exploiting the sparsities pixel-wise in the image domain [5], and a sparse regularised minimisation model is generalising the moving targets and background separation problem as an optimisation framework [6].

In general, these GMTI techniques are all capable of detecting displaced targets in SAR images and estimating their radial velocities. For the rest of the paper, we employ a fast back projection approach [7] to do efficient high-resolution SAR imaging, and the sparsity based optimisation method we previously developed to realise the targets detection and radial velocities estimations [6].

C. Moving Targets Relocations with DEM

Since we can indicate the moving targets in SAR images based on the aforementioned approaches, here we aim to integrate the GMTI outputs and DEM into the SAR imaging algorithm (4). Given the velocity vector $\mathbf{V}_t = (v_t^{(x)}, v_t^{(y)}, v_t^{(z)})$ for a moving target and the subdata $\mathbf{Y}_t$ which corresponds with this target, the image formation of this specific target with DEM can be written as:

$$X_t(m,l) = \sum_{k=1}^{K}\sum_{n=1}^{N} Y_t(f_k,\tau_n)\times \exp\left(\frac{j4\pi f_k(\|\mathbf{r}(\tau_n) - \mathbb{G}'_{ml} - \mathbf{V}_t\tau_n\| - \mathbf{R}_0(\tau_n))}{c}\right) \tag{5}$$

where $\mathbb{G}'_{ml} = (x_m, y_l, z(m,l))$ is the physical grid with the elevation information, the enriched range files $\Delta\mathbf{R}'_{mln} = \|\mathbf{r}(\tau_n) - \mathbb{G}'_{ml} - \mathbf{V}_t\tau_n\| - \mathbf{R}_0(\tau_n)$ contain the DEM and target states, and $\mathbf{R}_0(\tau_n) = \|\mathbf{r}(\tau_n) - \mathbf{r}_{ref}\|$ denotes the distance files with azimuth time between the platform and a reference point $\mathbf{r}_{ref}$. Here the reference point $\mathbf{r}_{ref}$ is the scene center which can incorporate the DEM, and it can be pre-computed as a constant vector.

To be specific, the fast SAR imaging technique [7] operates by splitting the raw data into blocks and calculate the pixel reflectivities in parallel within each data block. The imaging implementation for each block still follows the basic back projection format. Therefore, it is straightforward to utilise the DEM and velocity information in the fast image formation by manipulating the differential range $\Delta\mathbf{R}'_{mln}$ in (5), i.e. incorporating the DEM into $\mathbb{G}'_{ml}$ and $\mathbf{r}_{ref}$, and setting $\Delta\mathbf{R}'_{mln} = \|\mathbf{r}'(\tau_n) - \mathbb{G}'_{ml}\| - \mathbf{R}_0(\tau_n)$ where $\mathbf{r}'(\tau_n) = \mathbf{r}(\tau_n) - \mathbf{V}_t\tau_n$, to achieve moving targets imaging with better relocations. Therefore, the computations remain consistent with (4) in the imaging process and the fast SAR imaging technique [7] still holds.

In a number of scenarios we only have the estimated radial velocities or our emphasis is on the target relocations, the differential range can be approximated via:

$$\begin{aligned}\Delta\mathbf{R}'_{mln} &\cong \|\mathbf{r}(\tau_n) - \mathbb{G}'_{ml}\| + v_t^{(rad)}\tau_n - \mathbf{R}_0(\tau_n) \\ &= \|\mathbf{r}(\tau_n) - \mathbb{G}'_{ml}\| - \mathbf{R}'_0(\tau_n)\end{aligned} \tag{6}$$

where $v_t^{(rad)}$ describes the radial velocity with which the target moves away from the antenna, and the distance files $\mathbf{R}_0(\tau_n)$ can be flexibly replaced with $\mathbf{R}'_0(\tau_n)$ to enforce the radial velocity constraint in moving targets relocations.

D. Moving Target States Estimation

There has been a number of investigations in estimating moving target states/velocities. For example, it is well known that the radial velocities of moving targets correspond to the phase differences between SAR images from different channels in ATI [8][9], and the azimuth velocities can be estimated through bank of filters[10]. It was suggested in [11] that the azimuth velocities of moving targets can be charactered with a Fractional Fourier transform in the time-frequency domain. In [12] it was reported that the estimated velocities can be selected by best focusing the targets to give sharp image patterns and also maintaining the data fidelity.

Here the utilisation of DEM can give us a direct estimation on the $v_t^{(z)}$ in $\mathbf{V}_t$ by differentiating the elevations, which provides us a further constraint on the velocity estimations. It can also be used as an auxiliary criterion to help calibrate the velocities estimated by other methods. Especially when the targets are moving on roads in urban environments, the geometrical information of the road can be used in combination with the DEM to estimate the target states in three directions $(v_t^{(x)}, v_t^{(y)}, v_t^{(z)})$.

IV. EXPERIMENTAL RESULTS

In this section we demonstrate the exploitation of DEM in AFRL GOTCHA data set [13] and compare our estimations to the ground truth data. An X-band SAR system with three Radar channels operates in an urban environment and collects 71 seconds raw data (PRF is 2.17 kHz and the transmitted chip is centred at 9.6 GHz). The original data $\mathbf{Y}_1$, $\mathbf{Y}_2$ and $\mathbf{Y}_3$ were intentionally range-gated from 5400 range samples to 384 range samples for memory considerations. We replace the missing range samples with zeroes and rebuild the complete phase histories $\mathbf{Y}_i \in \mathbb{C}^{5400\times 200}$ where $i = \{1,2,3\}$. Then with the 2D channel balancing technique presented in [4], we keep calibrating the raw phase histories with 8000 azimuth samples and only preserve the 800 calibrated samples in the low frequencies till all data has been processed.

A. DEM Setup

Note that the DEM is absent in the original dataset, we need to extract proper DEM data for the experiments. A coarse DEM on a regular 80×60 grid with latitude and longtitude ranges of 0.0240 and 0.0250 respectively was obtained from the United States Geological Survery (USGS) seamless dataset. The coarse DEM coverage was initially chosen to be larger than the observed scene of our SAR system for further processing.

Since the monitored region does not match the retrieved DEM pair $(\mathbb{G}_{coarse}, \mathbf{E}_{coarse})$ at this stage where $\mathbb{G}_{coarse}$ denotes a grid on the xy-plane (similar to $\mathbb{G}_{ml}$) and $\mathbf{E}_{coarse}$ are the corresponding elevation values, we have to find a reference point $(\mathbb{X}_{ref}, E_{ref})$ so that the elevation map $(\mathbb{G}_{ml}, \mathbf{E}_{ml})$ can be estimated by shifting the $(\mathbb{G}_{coarse}, \mathbf{E}_{coarse})$ based on this point $(\mathbb{X}_{ref}, E_{ref})$, and then interpolating on the imaging grid $\mathbb{G}_{ml}$.

Given that we have the ground truth GPS information of one moving target $(\mathbb{X}_t, \mathbf{E}_t)$, where $\mathbb{X}_t$ contains its xy positioning information and $\mathbf{E}_t$ are the corresponding z coordinates, and they form a path on the terrain surface, the reference point $(\mathbb{X}_{ref}, E_{ref})$ can be estimated by best matching the path to the DEM:

$$\min_{\mathbb{X}_{ref}, E_{ref}} \frac{1}{2}\|\mathbf{E}_t - \Gamma(\mathbb{G}_{coarse} - \mathbb{X}_{ref}, \mathbf{E}_{coarse} - E_{ref}, \mathbb{X}_t)\|_2^2 \tag{7}$$

where $\Gamma(\mathbb{X}_{raw}, \mathbf{Z}_{raw}, \mathbb{X}_{new})$ is the operator to interpolate the surface $(\mathbb{X}_{raw}, \mathbf{Z}_{raw})$ at the query points $\mathbb{X}_{new}$, and return the estimated elevation values.

The interpolated DEM shifted with the reference point is shown in Fig. 2. As shown in the DEM, the monitored region has significant elevation variations.

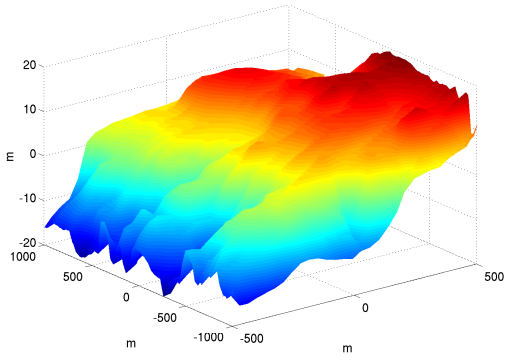

Fig. 2. The estimated DEM which is associated with the imaging grid.

B. Moving Targets Relocations

Given the estimated DEM and pre-processed phase histories, here we focus on the processing of the GOTCHA data from azimuth number 144001 to 146000 and compare the relocations to the ground truth GPS of one moving target. The data is divided into five sub-apertures and each sub-aperture contains 400 azimuth samples.

We first employ the GMTI technique described in [6] and estimate the radial velocities of the moving targets for the five sub-apertures. Here other GMTI techniques which are able to give estimations on radial velocities can also be used. As we have estimated the velocity map for the whole image, the estimated velocities can vary from pixel to pixel and the accuracies of relocations are very sensitive to the estimated radial velocities. Instead of giving a single estimation on the radial velocity, we consider a small 30×30 window around the target for which we have the ground truth, and introduce an estimation bar to give a range for the estimated radial velocity. We denote the minimum/mean/maximum radial velocities in the estimation bar for the $i-$th sub-aperture as $v_i^{(rad,min)}$, $v_i^{(rad,mean)}$ and $v_i^{(rad,max)}$ respectively. In this way we allow certain estimation tolerances for the target radial velocities. These radial velocities can then be used in (5) and (6) to give moving targets relocations. As we now have a range for the estimated radial velocities, this will induce different relocated positions and build up a window to indicate its possible locations. The filled region in Fig. 3 stands for the boundary of all possible target positions.

We extract the five relocated positions of the moving target in five sub-apertures based on the radial velocity estimation bar, and compare the relocated target path to the ground truth GPS. The results can be found in Fig. 3.

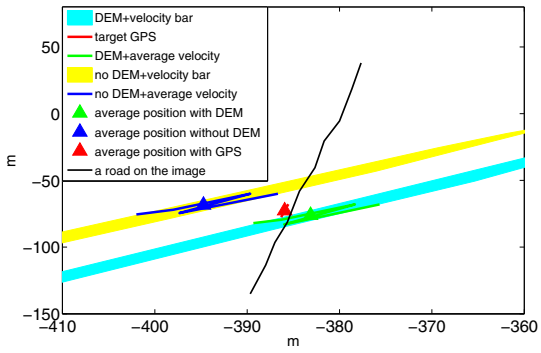

Fig. 3. Comparisons between the ground truth path of the moving target and the relocations (with and without the DEM). The black line indicates the road in the SAR image.

As shown in Fig. 3, the relocated path of the target with DEM (green line) is significantly closer to the ground truth (red line) and the road (black line) than the relocated path without DEM (blue line). As the five sub-apertures correspond to only 1 second during the flight, the ground truth target path is approximately linear. We can therefore compare the average relocated locations of five sub-apertures, i.e. the ones marked with ▲ (green and blue) in Fig. 3, to the ground truth (red triangle). The average relocated positions with and without DEM are deviated from the ground truth for 4.4 m and 9.8 m respectively. The improvement is about the same level as the elevation map.

C. Moving Targets Parameters Estimation

The DEM can be further exploited in the estimation of moving targets velocities. Since the target is likely to move slowly in the z direction, $v_t^{(z)}$ can be estimated by differentiating the positions of the moving target. It gives us an additional constraint on the velocities to help estimate the full state of the target. Particularly in the urban environment, the moving target is likely to move on the roads. The direction of the road gives us another restriction on the velocity estimations. Furthermore, the velocity estimations can be calibrated by allowing errors in radial velocity estimations, i.e. relocating the moving target to the intersection of the road and its possible locations (the filled region in Fig. 3). Calibrated relocated positions of the target give us calibrated radial velocity estimations and therefore promote the accuracy of the estimated radial velocity.

Here we first calibrate the radial velocity estimations. The estimated radial velocity of the target $v_t^{(rad)}$ is adjusted to relocate the moving target to the road (black line). Based on the road direction in the formed image, we can approximately leverage this equation $v_t^{(y)} = 14.1 \times v_t^{(x)}$. Then its velocity in z direction $v_t^{(z)}$ can be estimated by differentiating its relocated positions. The accuracy on estimating $v_t^{(z)}$ is thus limited by the accuracy of the DEM. Specifically, with the normalised vector in radial direction $\mathbf{n}^{(rad)}$ which goes from the target to the platform, the $(v_t^{(x)}, v_t^{(y)}, v_t^{(z)})$ and $v_t^{(rad)}$ follow this

TABLE I
COMPARISONS BETWEEN THE GROUND TRUTH AND ESTIMATIONS

sub-aperture number	1	2	3	4	5
estimated $v_t^{(x)}$ (m/s)	0.88	0.9	0.94	0.95	1.0
ground truth $v_t^{(x)}$ (m/s)	0.99	1.03	1.07	1.1	1.14
estimated $v_t^{(y)}$ (m/s)	12.4	12.72	13.2	13.4	14.1
ground truth $v_t^{(y)}$ (m/s)	12.9	13.1	13.3	13.5	13.7
estimated $v_t^{(z)}$ (m/s)	0.1	0.12	0.2	0.17	0.38
ground truth $v_t^{(z)}$ (m/s)	0.32	0.28	0.25	0.21	0.2

restriction:

$$v_t^{(rad)} = v_t^{(x)}\langle \mathbf{u}_x, \mathbf{n}^{(rad)} \rangle + v_t^{(y)}\langle \mathbf{u}_y, \mathbf{n}^{(rad)} \rangle + v_t^{(z)}\langle \mathbf{u}_z, \mathbf{n}^{(rad)} \rangle \tag{8}$$

where $\mathbf{u}_x$, $\mathbf{u}_y$ and $\mathbf{u}_z$ are the unit vectors in x, y and z directions respectively, $\langle \cdot, \cdot \rangle$ is the dot product operator.

Based on (8), we can estimate the target velocities $(v_t^{(x)}, v_t^{(y)}, v_t^{(z)})$. We compare our estimations to the ground truth and show the results in Table I. It can be seen that the estimations on the target velocities match the ground truth with high accuracies. In practice, the geometrical information and DEM can be used as the auxiliary restrictions on other velocity estimation approaches to give SAR/GMTI applications better robustness.

V. CONCLUSION

This paper presents a work for relocating moving targets and estimating targets' states with DEM in SAR/GMTI scenarios. Specifically by modeling the DEM in the SAR imaging and moving targets relocation scheme, the positioning of the moving targets can be further improved. Also the DEM can give us rough estimations on the z direction velocities, and it can be combined with geometrical information especially in urban environments to give further criteria to calibrate velocity estimations. The experimental results based on the GOTCHA GMTI dataset illustrate the effectiveness of the presented processings.

ACKNOWLEDGMENT

This work was supported by the Engineering and Physical Sciences Research Council (EPSRC) grants [EP/K014277/1]; and the University Defence Research Collaboration (UDRC) in Signal Processing.

REFERENCES

[1] S. Chiu and C. Livingstone, "A comparison of displaced phase centre antenna and along-track interferometry techniques for RADARSAT-2 ground moving target indication," *Canadian Journal of Remote Sensing*, vol. 31, no. 1, pp. 37–51, 2005.

[2] I. Sikaneta and C. Gierull, "Ground moving target detection for along-track interferometric SAR data," in *Aerospace Conference, 2004. Proceedings. 2004 IEEE*, vol. 4, March 2004, pp. 2227–2235 Vol.4.

[3] J. Ward, "Space-time adaptive processing for airborne radar," in *Space-Time Adaptive Processing (Ref. No. 1998/241), IEE Colloquium on*, Apr 1998, pp. 2/1–2/6.

[4] C. Gierull, "Digital channel balancing of along-track interferometric SAR data," in *Technical Memorandum DRDC Ottawa TM 2003-024*. Defence R&D, Ottawa, Canada, March 2003.

[5] L. Prunte, "GMTI from multichannel SAR images using compressed sensing," in *Synthetic Aperture Radar, 2012. EUSAR. 9th European Conference on*, April 2012, pp. 199–202.

[6] D. Wu, M. Yaghoobi, and M. Davies, "A new approach to moving targets and background separation in multi-channel SAR," in *2016 IEEE Radar Conference*, 2016.

[7] S. Kelly and M. Davies, "A fast decimation-in-image back-projection algorithm for SAR," in *Radar Conference, 2014 IEEE*, May 2014, pp. 1046–1051.

[8] R. M. Goldstein and H. Zebker, "Interferometric radar measurement of ocean surface currents," 1987.

[9] A. Budillon, V. Pascazio, and G. Schirinzi, "Amplitude/phase approach for target velocity estimation in AT-InSAR systems," in *2008 IEEE Radar Conference*, May 2008, pp. 1–5.

[10] G. Palubinskas, F. Meyer, H. Runge, P. Reinartz, R. Scheiber, and R. Bamler, "Estimation of along-track velocity of road vehicles in sar data," in *Remote Sensing*. International Society for Optics and Photonics, 2005, pp. 59 820T–59 820T.

[11] S. Chiu, "Application of fractional fourier transform to moving target indication via along-track interferometry," *EURASIP Journal on Advances in Signal Processing*, vol. 2005, no. 20, pp. 1–11, 2005.

[12] D. Wu, M. Yaghoobi, and M. Davies, "Sparsity based ground moving target imaging via multi-channel SAR," in *Sensor Signal Processing for Defence (SSPD), 2015*, Sept 2015, pp. 1–5.

[13] S. M. Scarborough, C. H. Casteel, Jr., L. Gorham, M. J. Minardi, U. K. Majumder, M. G. Judge, E. Zelnio, M. Bryant, H. Nichols, and D. Page, "A challenge problem for SAR-based GMTI in urban environments," *Proc. SPIE*, vol. 7337, pp. 73 370G–73 370G–10, 2009.

A Multi-Family GLRT for Detection in Polarimetric SAR Images

L. Pallotta, *Member, IEEE*, C. Clemente, *Member, IEEE*, A. De Maio, *Fellow, IEEE*, and D. Orlando, *Senior Member, IEEE*

***Abstract*— This paper deals with detection from multi-polarization SAR images. The problem is cast in terms of a composite hypothesis test aimed at discriminating between the Polarimetric Covariance Matrix (PCM) equality (absence of target in the tested region) and the situation where the region under test exhibits a PCM with at least an ordered eigenvalue smaller than that of a reference covariance. This last setup reflects the physical condition where the back scattering associated with the target leads to a signal, in some eigen-directions, weaker than the one gathered from a reference area where it is a-priori known the absence of targets. A Multi-family Generalized Likelihood Ratio Test (MGLRT) approach is pursued to come up with an adaptive detector ensuring the Constant False Alarm Rate (CFAR) property. At the analysis stage, the behaviour of the new architecture is investigated in comparison with a benchmark (but non-implementable) and some other adaptive sub-optimum detectors available in open literature. The study, conducted in the presence of both simulated and real data, confirms the practical effectiveness of the new approach.**

***Index Terms*— CFAR, Covariance Matrix Equality, MGLRT.**

I. Introduction

Polarimetric SAR images provide enhanced information on the imaged scene that can be exploited for improved target detection, recognition and scene classification [1]. Following the imaging stage, target detection can be applied and improved performance are achievable exploiting the multi-polarimetric nature of the data. Detectors exploiting the polarimetric information have been developed for specific applications including change [2], [3], [4], oil spill [5], [6] and ship detection [7].
In this paper, the problem of target detection is formulated in terms of a binary hypothesis test aimed at discriminating between the presence and the absence of variations in the Polarimetric Covariance Matrix (PCM) of the radar returns. The presence of targets such as oil spills and ship wakes modifies the backscattering of sea surface. The idea is to compare the region under test, which possibly contains targets, to a reference area where only echoes from the sea are present. Without loss of generality, in this paper we will focus on the specific case of oil spills, where it is reasonable to assume that the PCM of data containing oil slicks share eigenvalues smaller than or equal to the PCM of the sea returns. The decision problem is solved applying the GLRT and the devised architecture is referred to as Positive Definite Difference GLRT (PDD-GLRT). At the design stage, it is assumed that the rank difference between the two covariance matrices is known. However, this assumption might not be met in practical scenarios, since such a-priori information is not available at the receiver. In order to circumvent this drawback, the previous results are extended to come up with a decision rule capable of properly estimating the rank difference. This goal is achieved exploiting the Multi-family GLRT (MGLRT) [8] and the devised decision rule is referred to as Multi-family PDD-GLRT (M-PDD-GLRT). Finally, numerical examples are provided to prove the effectiveness of the proposed approach also in comparison with existing strategies for oil spills detection.

The remainder of this paper is organized as follows. Section II is devoted to the problem formulation. The derivations of the PDD-GLRT and its multi-family modification are reported in Section III. Section IV analyzes the performance in terms of detection probability on simulated and real data. Some concluding remarks and future research tracks are given in Section V.

Notation

Vectors and matrices are denoted by boldface lower-case and upper-case letters, respectively. Symbols $\det(\cdot)$ and $\mathrm{tr}\,(\cdot)$ denote the determinant and the trace of a square matrix, respectively. Symbol $\mathbb{H}^N$ is used to represent the set of $N \times N$ hermitian matrices, while $\boldsymbol{I}$ and $\mathbf{0}$ represent the identity matrix and the null vector or matrix, respectively, both of proper dimensions. The curled inequality symbol $\succeq$ is used to denote generalized matrix inequality: for any $\boldsymbol{A} \in \mathbb{H}^N$, $\boldsymbol{A} \succeq \mathbf{0}$ means that $\boldsymbol{A}$ is a positive semi-definite matrix. Symbols $(\cdot)^T$ and $(\cdot)^\dagger$ stand for transpose and conjugate transpose, respectively. Finally, the acronym iid means independent and identically distributed while the symbol $E[\cdot]$ denotes statistical expectation.

II. Problem Formulation

A multi-polarization SAR sensor, for each pixel of the image under test, measures $N = 3$ complex returns, which are collected from three different polarimetric channels (namely HH, HV, and VV). The N returns associated with the same

Luca Pallotta is with CNIT, viale G.P. Usberti, n. 181/A - 43124 Parma, c/o udr Università "Federico II", via Claudio 21, I-80125 Napoli, Italy. E-mail: luca.pallotta@unina.it

Carmine Clemente is with University of Strathclyde, Centre for Excellence in Signal and Image Processing, EEE, 204, George Street, G1 1XW, Glasgow, UK. E-mail: carmine.clemente@strath.ac.uk

A. De Maio is with the Dipartimento di Ingegneria Elettrica e delle Tecnologie dell'Informazione, Università degli Studi di Napoli "Federico II", via Claudio 21, I-80125 Napoli, Italy. E-mail: ademaio@unina.it

D. Orlando is with the Engineering Faculty of Università degli Studi "Niccolò Cusano", via Don Carlo Gnocchi 3, 00166 Roma, Italy. E-mail: danilo.orlando@unicusano.it

978-1-5090-0326-6/16/$31.00 ©2016 IEEE

pixel are organized in the specific order HH, HV, and VV to form the vector $\boldsymbol{X}(l_1, l_2)$, $l_1 = 1, \ldots, L_1$ and $l_2 = 1, \ldots, L_2$ (L_1 and L_2 represent the vertical and horizontal size of the image, respectively). Therefore, the sensor provides a 3-D data stack $\boldsymbol{X}$ of size $L_1 \times L_2 \times N$ which is referred to as datacube, whose pictorial representation is given in Fig. 1.

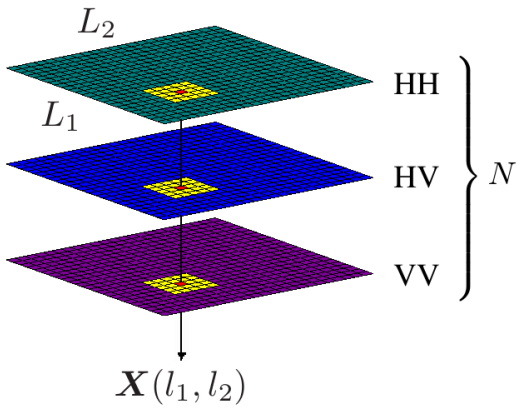

Fig. 1. A pictorial representation of the construction of the datacube for polarimetric images.

Starting from the datacube $\boldsymbol{X}$ of the scene illuminated by the radar, for each pixel under test, we extract a rectangular neighborhood $\mathcal{A}$ of size $K = W_1 \times W_2 \geq N$. We denote by $\boldsymbol{Z} = [\boldsymbol{z}_1 \ \ldots \ \boldsymbol{z}_K] \in \mathbb{C}^{N \times K}$ the matrix whose columns are the vectors of the polarimetric returns from the pixels of $\boldsymbol{X}$ which fall in the region $\mathcal{A}$. The matrix $\boldsymbol{Z}$ is modeled as a random matrix, whose columns are assumed iid random vectors drawn from a complex circular zero-mean Gaussian distribution with positive definite covariance matrix $\boldsymbol{R}$.

Our goal is to identify those regions of $\boldsymbol{X}$ that exhibit variations of the covariance matrix $\boldsymbol{R}$ with respect to a preassigned reference region. Specifically, the presence of specific objects in the observed scene yields signal echoes with spectral properties different from those associated with the background [5], [6]. For instance, consider an oil spill on the sea surface, whose reflectivity coefficient reduces the intensity of the backscattering signal. Thus, if we denote by $\boldsymbol{R}_{\mathcal{A}_1}$ and $\boldsymbol{R}_{\mathcal{A}_2}$ the PCMs of a region $\mathcal{A}_1$ containing sea returns and of a region $\mathcal{A}_2$ associated with a target, respectively, physical argumentations on backscattering lead to the condition $\boldsymbol{R}_{\mathcal{A}_1} - \boldsymbol{R}_{\mathcal{A}_2} \succeq \boldsymbol{0}$.

Based on the aforementioned observations, the detection problem addressed in this work can be written in terms of the following hypothesis test

$$\begin{cases} H_0 : \begin{cases} \boldsymbol{z}_k \sim C\mathcal{N}(\boldsymbol{0}, \boldsymbol{R}) & k = 1, \ldots, K \\ \boldsymbol{y}_m \sim C\mathcal{N}(\boldsymbol{0}, \boldsymbol{R}) & m = 1, \ldots, M \end{cases} \\ H_1 : \begin{cases} \boldsymbol{z}_k \sim C\mathcal{N}(\boldsymbol{0}, \boldsymbol{R}_1) & k = 1, \ldots, K \\ \boldsymbol{y}_m \sim C\mathcal{N}(\boldsymbol{0}, \boldsymbol{R}_1 + \boldsymbol{R}_2) & m = 1, \ldots, M \end{cases} \end{cases} \tag{1}$$

where

- $\boldsymbol{z}_k$, $k = 1, \ldots, K$, and $\boldsymbol{y}_m$, $m = 1, \ldots, M$, are statistically independent random vectors[1].
- matrices $\boldsymbol{R}$ and $\boldsymbol{R}_1$ are full-rank, namely $\text{Rank}(\boldsymbol{R}) = \text{Rank}(\boldsymbol{R}_1) = N$;
- the rank of $\boldsymbol{R}_2$, say p, is assumed known and within the interval $(0, \ N]$.

Moreover, we assume that $K \geq N$ and $M \geq N$ to ensure that the PCMs

$$\boldsymbol{G} = \sum_{k=1}^{K} \boldsymbol{z}_k \boldsymbol{z}_k^{\dagger} \quad \text{and} \quad \boldsymbol{H} = \sum_{m=1}^{M} \boldsymbol{y}_m \boldsymbol{y}_m^{\dagger} \tag{2}$$

are full-rank with probability 1.

III. Detector Design

In this section, an adaptive decision rule is devised resorting to the GLRT design criterion. To this end, let us define $\boldsymbol{Z}_K = [\boldsymbol{z}_1 \ \ldots \ \boldsymbol{z}_K]$ and $\boldsymbol{Y}_M = [\boldsymbol{y}_1 \ \ldots \ \boldsymbol{y}_M]$, then the likelihood functions of $\boldsymbol{Z}_K$ and $\boldsymbol{Y}_M$ under H_0 and H_1 are given by

$$f(\boldsymbol{Z}_K, \boldsymbol{Y}_M; \boldsymbol{R}, H_0) = \left[\frac{1}{\pi^N \det(\boldsymbol{R})}\right]^{K+M} \exp\left\{-\text{tr}\left[\boldsymbol{R}^{-1}(\boldsymbol{G} + \boldsymbol{H})\right]\right\} \tag{3}$$

and

$$f(\boldsymbol{Z}_K, \boldsymbol{Y}_M; \boldsymbol{R}_1, \boldsymbol{R}_2, H_1) = \left[\frac{1}{\pi^N}\right]^{K+M} \frac{\exp\left\{-\text{tr}\left[\boldsymbol{R}_1^{-1}\boldsymbol{G}\right] - \text{tr}\left[(\boldsymbol{R}_1 + \boldsymbol{R}_2)^{-1}\boldsymbol{H}\right]\right\}}{[\det(\boldsymbol{R}_1)]^K [\det(\boldsymbol{R}_1 + \boldsymbol{R}_2)]^M}, \tag{4}$$

respectively. Now, observe that the GLRT for the problem at hand is

$$\frac{\max_{\boldsymbol{R}_1} \max_{\boldsymbol{R}_2} f(\boldsymbol{Z}_K, \boldsymbol{Y}_M; \boldsymbol{R}_1, \boldsymbol{R}_2, H_1)}{\max_{\boldsymbol{R}} f(\boldsymbol{Z}_K, \boldsymbol{Y}_M; \boldsymbol{R}, H_0)} \underset{H_0}{\overset{H_1}{\gtrless}} \eta. \tag{5}$$

Under the above assumptions, it is possible to show that the generalized likelihood ratio (5) is statistically equivalent[2] to

$$\Lambda_p(\boldsymbol{Z}_K, \boldsymbol{Y}_M) \underset{H_0}{\overset{H_1}{\gtrless}} \eta, \tag{6}$$

where

$$\Lambda_p(\boldsymbol{Z}_K, \boldsymbol{Y}_M) = \begin{cases} 1, & \text{if } p^* < p, \\ \displaystyle\prod_{i=1}^{p^*} \frac{(1 + \delta_i)^{K+M}}{\delta_i^M}, & \text{otherwise}, \end{cases} \tag{7}$$

δ_i, $i = 1, \ldots, p^*$, are p^* eigenvalues of $\boldsymbol{G}^{-1}\boldsymbol{H}$ with p^* being the minimum between the number of eigenvalues of $\boldsymbol{G}^{-1}\boldsymbol{H}$ greater than M/K and p.

The above architecture will be referred to in the following as PDD-GLRT. In the next subsection, we apply the Exponential Embedded Family (EEF) framework [8], [9] to devise an architecture based upon the PDD-GLRT that does not use any a priori information on the rank of $\boldsymbol{R}_2$.

[1]For the sake of simplicity, in the following, we neglect the possible low correlation level between adjacent pixels.

[2]The proof is omitted for the sake of brevity.

A. Multi-Family PDD-GLRT

In the present subsection, we introduce a variant to the PDD-GLRT which does not need the above a-priori information. Specifically, the binary hypotheses considered before become multiple nested instances each tied up to a rank value of $\boldsymbol{R}_2$, that is denoted by $r(i) = i$, $i = 1, \ldots, N$. In this scenario, the classical GLRT cannot be used and, hence, we resort to the MGLRT [8] [9] that allows the PDD-GLRT to be utilized also in the case where the rank is not known. Specifically, the MGLRT can be written in terms of the EEF computed for a given model order[3] i, $i = 1, \ldots, N$, [9] namely

$$\max_{i \in \{1,\ldots,N\}} \text{EEF}(i) \underset{H_0}{\overset{H_1}{\gtrless}} \eta, \tag{8}$$

where

$$\begin{aligned} \text{EEF}(i) = \Bigg(& \zeta_{G_i}(\boldsymbol{Z}_K, \boldsymbol{Y}_M) \\ & -r(i) \left[\log \left(\frac{\zeta_{G_i}(\boldsymbol{Z}_K, \boldsymbol{Y}_M)}{r(i)} \right) + 1 \right] \Bigg) \times \\ & \text{u} \left(\frac{\zeta_{G_i}(\boldsymbol{Z}_K, \boldsymbol{Y}_M)}{r(i)} - 1 \right), \quad i = 1, \ldots, N. \end{aligned} \tag{9}$$

In the last equation, $\zeta_{G_i}(\boldsymbol{Z}_K, \boldsymbol{Y}_M)$ is two times the logarithm of the PDD-GLRT decision statistic with $p = i$, namely

$$\zeta_{G_i}(\boldsymbol{Z}_K, \boldsymbol{Y}_M) = 2 \log \Lambda_i(\boldsymbol{Z}_K, \boldsymbol{Y}_M), \tag{10}$$

whereas $\text{u}(\cdot)$ is the Heaviside step function. Thus, when there are multiple nested alternative hypotheses, the MGLRT first computes the PDD-GLRT for each hypothesis, $\zeta_{G_i}(\cdot)$ say, applies the transformation (9) to construct the EEF(i), and chooses the hypothesis attaining the maximum. For the sake of completeness, we provide below the explicit expression of $\zeta_{G_i}(\boldsymbol{Z}_K, \boldsymbol{Y}_M)$, which contains the constants which have been incorporated into the threshold of the PDD-GLRT, i.e.,

$$\begin{aligned} \zeta_{G_i}(\boldsymbol{Z}_K, \boldsymbol{Y}_M) = & -2(K+M) r(i) \log(K+M) \\ & + 2Kr(i) \log(K) + 2Mr(i) \log(M) \\ & - 2M \sum_{n=1}^{r(i)} \log \delta_i + 2(K+M) \sum_{n=1}^{r(i)} \log(1+\delta_i). \end{aligned} \tag{11}$$

IV. Performance Analyses

In this section, we investigate the performances of the proposed detectors in terms of Probability of Detection (P_D). For comparison purposes, we also plot the performance curves of other approaches available in the open literature. More precisely, we consider the GLRT devised in [3], [4], [6], whose expression is

$$\Lambda_{\text{GLRT}} = \frac{[\det(\boldsymbol{G} + \boldsymbol{H})]^{(K+M)}}{[\det(\boldsymbol{G})]^K [\det(\boldsymbol{H})]^M} \underset{H_0}{\overset{H_1}{\gtrless}} \eta, \tag{12}$$

[3]The model order is represented by the rank of $\boldsymbol{R}_2$.

the Maximum Likelihood Detector (MLD) proposed in [6] given by

$$\Lambda_{\text{MLD}} = \frac{\det(\boldsymbol{H})}{\det(\boldsymbol{G})} \underset{H_0}{\overset{H_1}{\gtrless}} \eta, \tag{13}$$

and the Single Likelihood Detector (SLD) proposed in [6] whose decision statistic is

$$\Lambda_{\text{SLD}} = \text{tr}\left(\boldsymbol{G}^{-1}\boldsymbol{H}\right). \tag{14}$$

In order to better analyze the behavior of all these detectors, the comparisons also include the clairvoyant counterparts, namely the Likelihood Ratio Test (LRT) and the clairvoyant SLD (C-SLD). More precisely, the former is statistically equivalent to

$$\begin{aligned} \Lambda_{\text{LRT}} = \text{tr}\,[& \boldsymbol{R}^{-1}(\boldsymbol{G}+\boldsymbol{H}) \\ & - \boldsymbol{R}_1^{-1}\boldsymbol{G} - (\boldsymbol{R}_1+\boldsymbol{R}_2)^{-1}\boldsymbol{H}] \underset{H_0}{\overset{H_1}{\gtrless}} \eta, \end{aligned} \tag{15}$$

while the latter has the following expression

$$\Lambda_{\text{C-SLD}} = \text{tr}\left(\boldsymbol{R}_1^{-1}\boldsymbol{H}\right). \tag{16}$$

The analysis is conducted on both simulated and real SAR data. In the latter case, we prove the effectiveness of the newly proposed detectors in terms of the capability to detect oil spills over the sea surface.

A. Detection Capability on Simulated Data

This subsection is devoted to the performance analysis using computer simulated data for a preassigned value of Probability of False Alarm (P_{FA}). Specifically, the numerical examples are obtained by means of standard Monte Carlo counting techniques. The detection thresholds and the P_D values are evaluated resorting to $100/P_{FA}$ and 10^3 independent trials, respectively. The nominal P_{FA} is set to 10^{-4}. As to the vector size, it is chosen equal to 3 to account for the fact that SAR sensors collect data using three different polarizations, whereas as to the parameter p the value $p = 2$ is considered.

The simulated data, $\boldsymbol{z}_k$, $k = 1, \ldots, K$, and $\boldsymbol{y}_m$, $m = 1, \ldots, M$, are modeled as N-dimensional zero-mean complex circular Gaussian vectors with covariance matrices $\boldsymbol{R}_1 = \boldsymbol{I}$ and $\boldsymbol{R}_1 + \boldsymbol{R}_2$, respectively. Matrix $\boldsymbol{R}_2$ is rank deficient and is defined as $\boldsymbol{R}_2 = |\alpha|^2 \boldsymbol{p}_1 \boldsymbol{p}_1^\dagger + |\beta|^2 \boldsymbol{p}_2 \boldsymbol{p}_2^\dagger$, where the N-dimensional steering vectors, $\boldsymbol{p}_1$ and $\boldsymbol{p}_2$, have been chosen as

$$\begin{aligned} \boldsymbol{p}_1 &= [1, 0, \ldots, 0]^T, \\ \boldsymbol{p}_2 &= [0, 1, 0, \ldots, 0]^T, \end{aligned} \tag{17}$$

and $|\alpha|^2 = |\beta|^2$, so as $\boldsymbol{R}_2$ is a rank-2 matrix.

The SNR is defined as

$$\text{SNR} = |\alpha|^2 \boldsymbol{p}_1^\dagger \boldsymbol{R}_1^{-1} \boldsymbol{p}_1 + |\beta|^2 \boldsymbol{p}_2^\dagger \boldsymbol{R}_1^{-1} \boldsymbol{p}_2 = 2|\alpha|^2. \tag{18}$$

In Fig. 2, we plot P_D versus SNR assuming $K = M = 9$. It turns out that the PDD-GLRT and the MLD perform better than all the other adaptive architectures. In addition, the M-PDD-GLRT exhibits some losses with respect to the PDD-

GLRT even though both detectors outperform the GLRT and the SLD with a gain of about 1 dB at $P_D = 0.9$. As last remark, note that the PDD-GLRT suffers a detection loss of about 5 dB with respect to the LRT (or the C-SLD).

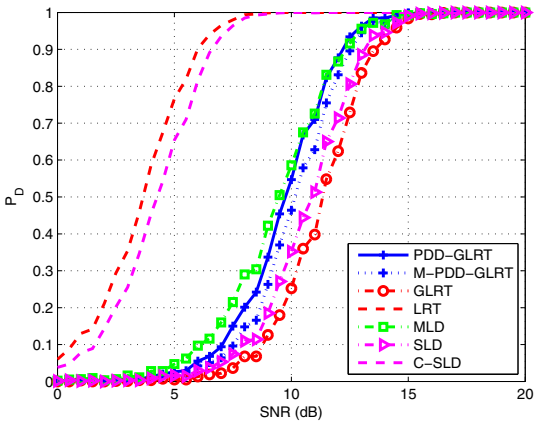

Fig. 2. P_D versus SNR for PDD-GLRT (+-marked blue solid curve), M-PDD-GLRT (+-marked blue dotted curve), GLRT (○-marked red dot-dashed curve), LRT (red dashed curve), MLD (□-marked green dot-dashed curve), SLD (▷-marked magenta dot-dashed curve), C-SLD (magenta dashed curve), for a nominal $P_{FA} = 10^{-4}$. The other simulation parameters are $K = 9$, $M = 9$, $N = 3$, and $p = 2$.

In Fig. 3, we focus on a smaller number of test data, i.e., $M = 4$, leaving the same value of K as in Fig. 2. From the figure, it can be observed that there is a general worsening in the receivers' performance. The figure highlights also that the PDD-GLRT and the M-PDD-GLRT achieve the best performances with the former performing better than the latter. Finally, the GLRT is the worst with a loss higher than 3 dB if compared to the PDD-GLRT and its multi-family version.

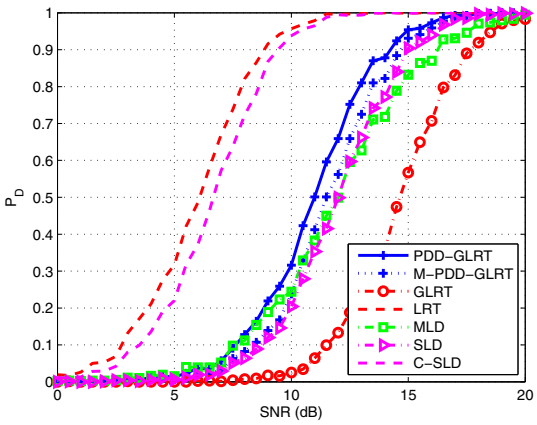

Fig. 3. P_D versus SNR for PDD-GLRT (+-marked blue solid curve), M-PDD-GLRT (+-marked blue dotted curve), GLRT (○-marked red dot-dashed curve), LRT (red dashed curve), MLD (□-marked green dot-dashed curve), SLD (▷-marked magenta dot-dashed curve), C-SLD (magenta dashed curve), for a nominal $P_{FA} = 10^{-4}$. The other simulation parameters are $K = 9$, $M = 4$, $N = 3$, and $p = 2$.

Summarizing, the PDD-GLRT seems a reasonable choice since it exhibits a more robust behavior than the counterparts being the one less sensitive to parameters variations and giving in all the analyzed situations acceptable performances. In other words, the PDD-GLRT represents a kind of "all seasons" architecture.

B. Test on Real Radar Data

As final part of the performance analysis, in this subsection, we evaluate the effectiveness of the new detectors on real SAR data. More precisely, we use a data set obtained from the *GOMoil_07601_10052_101_100622_L090_CX_02* SAR image which is composed of sea data containing an oil spill on it. The image has been acquired on 22nd of June 2010, during the British Petroleum oil spill incident in the Gulf of Mexico (known also as the Deepwater Horizon Oil Spill). This image contains a scene acquired with a sensor exploiting all the polarizations and the corresponding polarimetric overlay is reported in Fig. 4.

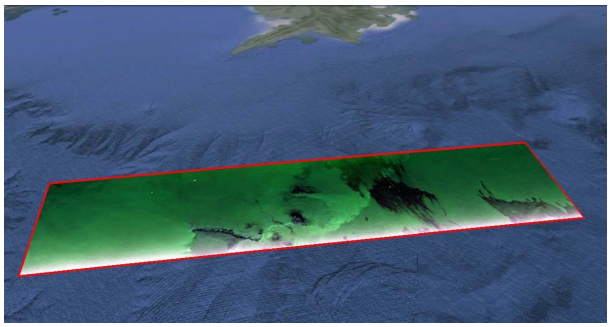

Fig. 4. Three polarization color overlay of the SAR image GO-Moil_07601_10052_101_100622_L090_CX_02.

The data set is a sub-image of 3000×2000 pixels, whose span (i.e., $|HH|^2 + |VV|^2 + 2|HV|^2$) [1] expressed in dB values is also displayed in Fig. 5.

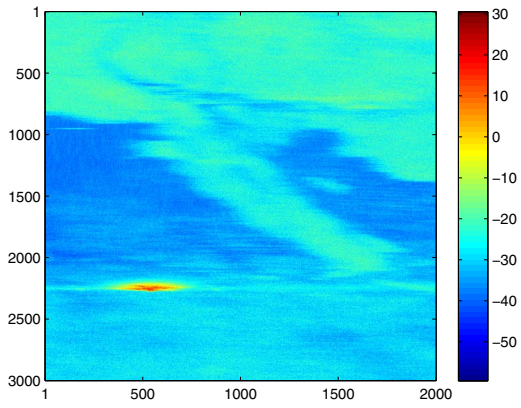

Fig. 5. Real L-band data SAR image GO-Moil_07601_10052_101_100622_L090_CX_02. Span (in dB) of the reference image of size 3000×2000 pixels.

Fig. 6 shows the detection results applying detector (8) over the described SAR image, where the test is performed assuming the following parameter setting (notice that $N = 3$

since we have three polarization images). A sea data pixel is chosen as reference to compute the sample covariance $\boldsymbol{H}$ from a 3×3 (i.e., $M = 9$) window centered in that pixel. Then, a window of size 3×3 (i.e., $K = 9$) is slided over the SAR image to test all the pixels and to compute the sample matrix $\boldsymbol{G}$. Finally, the threshold is chosen to ensure a nominal P_{FA} of 10^{-3}, extracting a cluster of only sea data composed of 10^5 pixels and choosing the 100-th value in the decreasing ordered statistics. The results is a detection map where the white pixels are those associated to oil spills detections, while the black pixels are representative of the sea data (no-detections). The results show that the multi-family PDD is able to ensure reliable detection of oil spills over sea. An important notice is that the number of looks, in a real environment, has to be chosen to manage the trade off between the accuracy of covariance estimation and the amount of heterogeneity.

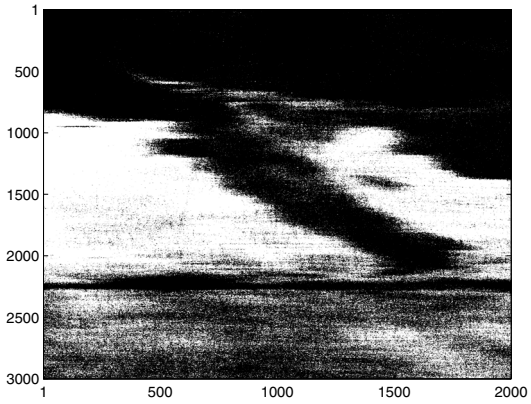

Fig. 6. Real L-band data SAR GO-Moil_07601_10052_101_100622_L090_CX_02 detection map for the M-PDD-GLRT with $K = 9$, $M = 9$, and $N = 3$. The detection map has been obtained with a nominal $P_{FA} = 10^{-3}$. White pixels are the detections.

V. Conclusions

Multi-polarization SAR detection has been considered in this paper to test the equality of two polarimetric sample covariance matrices constructed from a reference area (where it is known the absence of targets) and a test region (where it is necessary to establish the spot presence), respectively. The alternative hypothesis is represented by the instance where the PCM within the reference area exhibits at least an ordered eigenvalue greater than the corresponding one extracted from the PCM of the area under test. First of all, assuming the exact knowledge about the number of different eigenvalues between the reference and tested PCMs, the PDD-GLRT is devised. Then, to come up with a fully adaptive detector without any a priori assumption about the aforementioned number, the M-PDD-GLRT is introduced.

At the analysis stage, the oil spill detection case has been analysed and examples have been provided to prove the effectiveness of the proposed approach also in comparison with existing strategies. To this end, both simulated and real multi-polarization SAR data have been used. Possible future research track might concern the extension of the approach to the case of a joint multi-frequency and multi-polarization processing as well as to consider the presence of a non-Gaussian backscattering due to sea.

Acknowledgment

The authors would like to acknowledge NASA/JPL for providing the SAR data. The work of C. Clemente was sponsored by the Engineering and Physical Sciences Research Council (EPSRC) Grant number EP/K014307/1 and the MOD University Defence Research Collaboration in Signal Processing.

References

[1] J. S. Lee and E. Pottier, *Polarimetric Radar Imaging: From Basics to Applications*, CRC Press, 2009.

[2] V. Carotenuto, A. De Maio, C. Clemente, and J. J. Soraghan, "Invariant Rules for Multipolarization SAR Change Detection," *IEEE Transactions on Geoscience and Remote Sensing*, vol. 53, no. 6, pp. 3294–3311, June 2015.

[3] L. M. Novak, "Change Detection for Multi-polarization, Multi-pass SAR," in *SPIE Conference on Algorithms for Synthetic Aperture Radar Imagery XII*, Orlando, FL, March 2005, pp. 234–246.

[4] K. Conradsen, A. A. Nielsen, J. Schou, and H. Skriver, "A Test Statistic in the Complex Wishart Distribution and its Application to Change Detection in Polarimetric SAR Data," *IEEE Transactions on Geoscience and Remote Sensing*, vol. 41, no. 1, pp. 4–19, 2003.

[5] P. Lombardo and C.J. Oliver, "Optimum Detection and Segmentation of Oil-Slicks using Polarimetric SAR Data," *IEE Proceedings Radar, Sonar and Navigation*, vol. 147, no. 6, pp. 309–321, December 2000.

[6] P. Lombardo, D. I. Conte, and A. Morelli, "Comparison of Optimised Processors for the Detection and Segmentation of Oil Slicks with Polarimetric SAR Images," in *IEEE International Geoscience and Remote Sensing Symposium (IGARSS)*, 2000, vol. 7, pp. 2963–2965.

[7] A. Marino and I. Hajnsek, "Statistical Tests for a Ship Detector Based on the Polarimetric Notch Filter," *IEEE Transactions on Geoscience and Remote Sensing*, vol. 53, no. 8, pp. 4578–4595, Aug 2015.

[8] S. M. Kay, "The Multifamily Likelihood Ratio Test for Multiple Signal Model Detection," *IEEE Signal Processing Letters*, vol. 12, no. 5, pp. 369–371, 2005.

[9] S. M. Kay, "Exponentially Embedded Families-New Approaches to Model Order Estimation," *IEEE Transactions on Aerospace and Electronic Systems*, vol. 41, no. 1, pp. 333–345, 2005.

A Novel Motion Compensation Approach for SAS

Salvatore Caporale and Yvan Petillot

Institute of Sensors, Signals and Systems, Heriot-Watt University, Edinburgh, Scoltland, UK
Email: s.caporale@hw.ac.uk

***Abstract*—Synthetic aperture systems rely on accurate knowledge of Transmitter (Tx) and Receiver (Rx) positions at each ping. In Synthetic Aperture Sonar (SAS), due to the nature of propagation and navigation in water, they have to be estimated by either physical sensors or raw data or a combination of these and employed to compensate motion errors. Hence, motion compensation is a major issue in SAS. In this paper we propose a new image domain based motion compensation approach which is intended to loosen the restrictions imposed by previously proposed approach such as Displaced Phase Center Approximation (DPCA) and the dependency on an accurate Inertial Navigation System (INS). The real bistatic observation model is replaced by a virtual bistatic model which allows for taking into account rotations between Txs and Rxs. The ping to ping displacements are then obtained by minimizing an error function between the projections on vector space intersections.**

I. Introduction

Synthetic Aperture Sonar (SAS) systems share with Synthetic Aperture Radar (SAR) many practical and theoretical aspects, as they were originally introduced by moving the synthetic aperture paradigm from radar to sonar. Therefore, most image formation algorithms which have been conceived for SAR have been also considered in SAS literature [1]. Despite the overlapping concepts such as range migration and range invariant resolution, underwater SAS systems are operated in a much more challenging environment than SAR as (i) the navigation in water is affected by non-negligible errors and cannot always rely on an external accurate positioning system; (ii) motion errors are comparable to the wavelength hence their effect on image formation algorithm is remarkably destructive; (iii) due to relatively small sound velocity in water with respect to the range of interest, the desired along track resolution cannot be achieved by means of a vehicle provided with a single Transmitter (Tx) and Receiver (Rx) and moving a reasonable along track speed [2], [3].

For the above mentioned reasons, SAS systems are usually equipped with an accurate Inertial Navigation System (INS) to recover the real navigated trajectory. Moreover, each ping consists of a single Tx and an array of Rxs, allowing for a higher along track sampling rate, hence a higher along track speed [4]. However, from ping to ping a certain degree of redundancy is imposed to perform data based motion estimation known as Displaced Phase Center Approximation (DPCA) which is coupled with the inertial navigation for a more accurate motion compensation [5], [6]. From a high-level system design point of view, DPCA is used to obtain a finer differential ping to ping displacement estimation while the INS is needed to guarantee the cumulative error between pings does not affect the intrinsic range migration compensation of synthetic aperture image formation. A typical SAS system and the way it operates are illustrated in Fig. 1

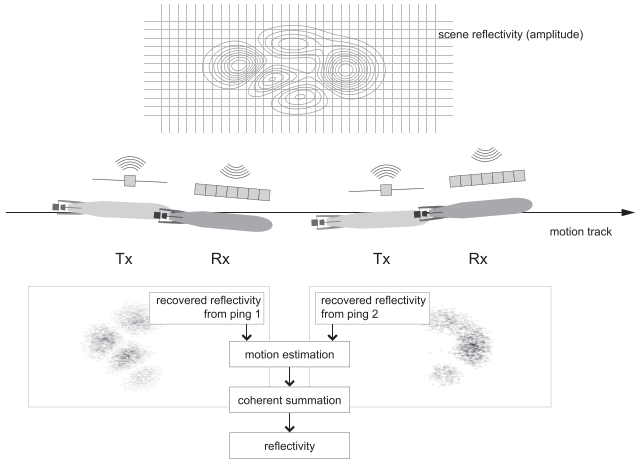

Fig. 1. Schematic representation of a SAS system and processing. Each array is collecting an observation, then the motion errors with respect to the prescribed trajectory are estimated, finally the observations are merged together coherently.

The present work attempts to tackle the problem of motion compensation in SAS from a more general algebraic point of view. The goals include (i) dealing with non straight trajectory, such as circular, or partially unknown ones, (ii) reducing the hardware cost by relying on less accurate INS and (iii) analysing theoretical limits in performing unsupervised motion compensation.The proposed approach is based on the following idea. Given two observations acquired by means of a single Tx and array of Rxs at two different relatively close locations, the projection on the intersection subspace between them can be recovered by either one of the two observations. Hence, when the displacement is not known, the comparison between the projections on the intersection subspace as a function of the hypothetical displacement can be set as an error function. The paper shows that this function is locally convex and its minimum point identifies the displacement. The computational burden to perform this operation is remarkable, but it allows for a much smaller redundancy, less restrictions and less prior information than other techniques such as DPCA.

978-1-5090-0326-6/16/$31.00 ©2016 Crown

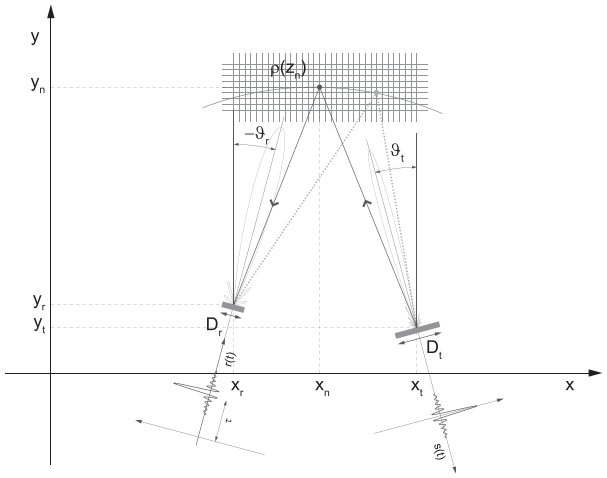

Fig. 2. The adopted single Tx and Rx bistatic two-dimensional acoustic model. The figure also shows two different propagation paths corresponding to two reflectors sharing the same round trip time, thus lying on the ellipsis having the Tx and the Rx as foci.

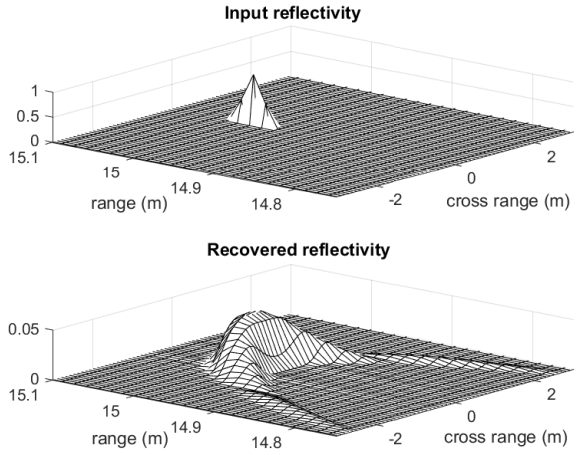

Fig. 3. An ideal impulse-wise reflectivity (top) and the reflectivity which can be recovered by means of a single Tx and Rx monostatic observation. The impulse energy migrates at different range along a circular trajectory centred on the Tx/Rx position.

The paper is organized as follows. Section II reviews the acoustic model and SAS, Sections III illustrates the proposed motion compensation procedure and some conclusions are drawn in Section IV.

II. Acoustic and SAS Model

In this Section we first review the observation model for a single Tx and Rx acoustic system when a generic signal is given as input, then we show how this can be employed to retrieve the scene reflectivity when multiple observations are combined together. A simplified two-dimensional model is considered and all the sensors are assumed to be still. Finally, SAS is described as a collection of such single Tx and Rx systems.

A. Acoustic Model

Given a Tx at position $z_t = (x_t, y_t)$ of length D_t and orientation ϑ_t and a hydrophone at position $z_r = (x_r, y_r)$ of length D_r and orientation ϑ_r, the system response to an input complex passband function $s(t)$ with respect to a scene whose complex reflectivity is expressed by $\rho(z)$, with $z = (x, y)$ can be obtained by:

$$r(t) = \int_z \rho(z)\, \alpha(z_t, z_r, z, \vartheta_t, \vartheta_r)\, s(t - \tau(z_t, z_r, z))\, \mathrm{d}z \quad (1)$$

where τ is the delay corresponding to the propagation from z_t to z and from z to z_r, α is an attenuation factor taking into account (i) the attenuation due to the propagation distance from z_t to z and from z to z_r and (ii) the transmission and reception radiation patterns. With regard to the attenuation, we consider the exploding sources model where the $\alpha^2 \propto \delta(z_t, z) + \delta(z_r, z) \propto \tau(z_t, z_r, z)$ rather than $\alpha^2 \propto \delta(z_t, z)\delta(z_r, z)$, where δ is the distance operator. The model (3) is represented in Fig. 2.

When $s(t)$ is a narrowband impulse modulated at frequency f_0, the above model can be used for observing $\rho(z)$. A suitable sampling grid $z_n = (x_n, y_n)$ matching the available bandwidth is introduced so that the reflectivity is represented as the input vector $\rho(z_n)$. By setting $G(z_n)$ as the Green's function of the system

$$G(z_n) = \alpha(z_t, z_r, z_n, \vartheta_t, \vartheta_r) e^{-j2\pi f_0 \tau(z_t, z_r, z_n)}, \quad (2)$$

the following output time-sampled signal $\phi(t_m)$ can be obtained as

$$\phi(t_m) = A(t_m, z_n)\, G(z_n) \rho(z_n) \quad (3)$$

where the matrix $A(t_n, z_n)$ performs the discrete-space integration of equation (1), which is basically done by an interpolation kernel and a summation. From a numerical point of view, $A(t_m, z_n)$ is usually defined by its transpose one, since defining an interpolation along the intrinsic one dimensional time axis t_m is easier than doing it over the fictitious space axis z_n. We consider a Non-Uniform Fast Fourier Transform (NUFFT) based time interpolation [7], having an approximately linear complexity and high accuracy.

The integral in (1) and its space discrete equivalent in (3) clearly perform a dimensionality reduction from the two-dimensional space z_n to the one dimensional space t_m. In fact, all points lying on the ellipsis having z_t and z_r as foci are intrinsically ambiguous with respect to the Tx Rx pair. This is also represented in Fig. 2 where we highlighted a propagation path (dotted line) having the same delay as the one relative to the generic point z_n. As a consequence, inverting (3) recovers the reflectivity $\rho(z)$ affected by defocusing along ellipsis, as illustrated in Fig. 3. Due to the radiation patterns, this defocusing increases with range.

B. SAS model

The working principle of a synthetic aperture consists in performing multiple observations at prescribed transmission and reception locations along a (usually straight) path, called along track or cross range. By doing so, a longer aperture is emulated and a narrower beam is obtained in the direction orthogonal to the track, called range. The emulation is performed by signal processing and allows for getting a constant resolution along range.

Given a set of Txs and Rxs $z_{l,t}$ and $z_{l,r}$, $l \in \mathbb{Z}$, the observation model of SAS can be written as the column vector of $\phi_l(t_m) = A_l(t_m, z_n)\, G_l(z_n)\, \rho(z_n)$. In case each observation is a monostatic system, i.e. $z_{l,t} = z_{l,r} = z_l$, and z_l are uniformly spaced along the cross range direction by $D/4$, with $D = \max(D_t, D_r)$, then $\rho(z_n)$ can be approximately recovered with a cross range resolution equal to $D/2$ by the transpose observation operator, also know as backprojection

$$\rho(z_n) \approx \sum_{l\in\mathbb{Z}} G_l^*(z_n) A_l^\dagger(z_n, t_m) \phi_l(t_m) \tag{4}$$

which has been conveniently rewritten as a sum of backprojections of each single Tx and Rx system. As for getting a cross range resolution equal to $D/2$ a sampling on the along track by $L/2$ has been considered, the oversampling ratio is equal to 2. Many variations of this setup have been considered in the literature in order to decrease the oversampling ratio and employ different reconstruction techniques.

Practical SAS systems are realized by means of an Autonomous Underwater Vehicle (AUV). Hence, the speed v of the vehicle has to be set according to the wanted along track sampling and the desired maximum range. As an instance, in case of an AUV equipped with a single Tx and Rx, $v \leq D/4\max(\tau(z_{l,t}, z_{l,r}, z_n)) = Dc/8R$, where R is the maximum range. For $R = 150\,\mathrm{m}$ and $D = 5\,\mathrm{cm}$, we get $v = 6.25\,\mathrm{cm/sec}$. A more reasonable speed is obtained by providing AUV with an array of N equispaced Rxs at distance $L = D/2$ and a single Tx. By doing so, a single transmitted ping allows for N observations, thus gaining a N factor on the speed. Such a SAS system is a collection of bistatic single Tx and Rx systems. If the range of interest is sufficiently large with respect to the wavelength, it can be approximately modelled as a collection of monostatic systems such that $\bar{z}_l = \mu(z_{l,t}, z_{l,r})$, where μ is the midpoint operator. This model is referred to as Phase Center Approximation (PCA).

III. Motion Estimation

The proposed technique can be summarized by two main steps, (i) Tx to Rx motion estimation for each ping and (ii) ping to ping motion estimation. Both these procedures require the estimation of three differential parameters, that is the horizontal and vertical displacements and the relative rotation. The ping to ping estimation estimation is possible thanks to the fact that pings are partially overlapped, whereas there is no evidence that Tx to Rx motion can be inferred. Employing PCA would allow for neglecting the Tx to Rx estimation, but this would affect the behaviour of the ping to ping estimation. Hence, we first introduce an approximate model called Effective Phase Center Approximation (EPCA) which allows to reduce the Tx to Rx estimation to relative rotation only, then we present an heuristic procedure to estimate it and finally we incorporate this a ping to ping displacement estimation based on projections on intersection subspaces.

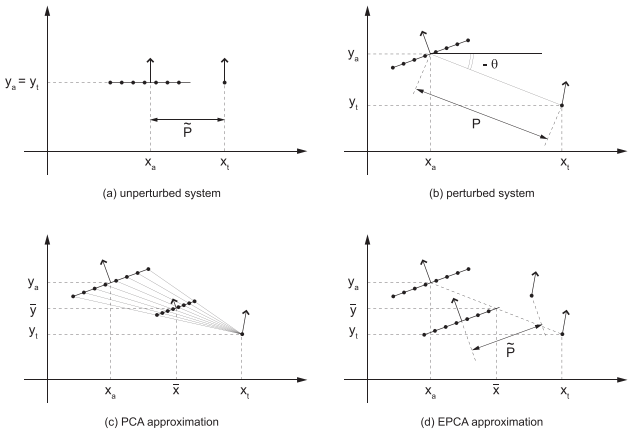

Fig. 4. Illustration of the PCA and the proposed EPCA allowing to take into account of the Tx orientation. The system in (d), with regard to the position of the Tx with respect to the receiving array, is equal to the one in (a) and lies along the same line as the PCA system in (c). Also, the PCA of the system in (d) is the system in (c).

A. Effective Phase Center Approximation

Given that the receiving array is composed by N Rxs at distance $D_r = D_t/2$, we can represent the whole bistatic system by specifying the array midpoint and orientation and the Tx position and orientation:

$$\begin{aligned}\sigma_r &= (x_a, y_a, \vartheta_r) = ((x_{1,r} + x_{N,r})/2, (y_{1,r} + y_{N,r})/2, \vartheta_r)\\ \sigma_t &= (x_t, y_t, \vartheta_t) = (x_a + P\cos\theta, y_a + P\sin\theta, \vartheta_t)\end{aligned}$$

where P is the distance between $(\tilde{x}_a, \tilde{y}_a)$ and $(\tilde{x}_t, \tilde{y}_t)$ and $\theta = \mathrm{atan}((y_a - y_t)/(x_a - x_t))$ is the slope of the line passing by them. The position of the Tx takes into account the physical position of the Tx with respect to the array midpoint and the motion of the vehicle between the transmission and the reception. The PCA model is a system composed by N Rxs at distance $D_r/2$ and specified by the midpoint between (x_a, y_a) and (x_t, y_t) and the orientation of the array:

$$\bar{\sigma} = (\bar{x}, \bar{y}, \vartheta_r) = (((x_a + x_t)/2, (y_a + y_t)/2, \vartheta_r).$$

The PCA model, being obtained as an average, can be looked at as a non bijective operation, meaning that many different bistatic model having the same PCA can be identified. Among these, we aim to find a new model $\tilde{\sigma}_r$, $\tilde{\sigma}_t$, which will be referred to as EPCA, such that the distance between the Tx

and the Rx midpoint is equal to a prescribed distance $\tilde{P}$ and the line passing by them is aligned with the array. We get:

$$\tilde{\sigma}_r = (\tilde{x}_a, \tilde{y}_a, \vartheta_r) = (\bar{x} - \tilde{P}/2 \cos\vartheta_r, \bar{y} - \tilde{P}/2 \sin\vartheta_r, \vartheta_r)$$
$$\tilde{\sigma}_t = (\tilde{x}_t, \tilde{y}_t, \vartheta_t) = (\bar{x} + \tilde{P}/2 \cos\vartheta_r, \bar{y} + \tilde{P}/2 \sin\vartheta_r, \vartheta_t).$$

By doing so, the bistatic situation will be simply identified by $\tilde{\sigma}_r$, the distance $\tilde{P}$ and the differential rotation $\gamma = \vartheta_t - \vartheta_r$. In fact, it holds:

$$\tilde{\sigma}_t = (\tilde{x}_a + \tilde{P}\cos\vartheta_r, \tilde{y}_r + \tilde{P}\sin\vartheta_r, \vartheta_r + \gamma).$$

The distances P and $\tilde{P}$ can be thought of as the distance between (x_a, y_a) and (x_t, y_t) with and without motion errors respectively. If motion errors are relatively small with respect to the PCA, i.e. $P \approx \tilde{P}$, the validity of PCA also implies the validity of EPCA. The illustrated concepts and approximations are represented in Fig. 4.

B. Tx to Rx Rotation Estimation

When the observation from a single ping is considered, the absolute position and rotation are arbitrary. Hence, it is sensible to set $\tilde{\sigma}_r = (0, 0, 0)$ and $\tilde{\sigma}_t = (\tilde{P}, 0, \gamma)$, where γ is unknown and its estimation will be indicated as $\gamma + \beta$. Let us introduce the reconstructed images by the backprojection and pseudoinverse as a function of the angle estimation error β:

$$\tilde{\rho}_\beta(z_n) = \tilde{T}^{\dagger}_{\gamma+\beta}(z_n, \cdot)\, T_\gamma(\cdot, z_m)\, \rho(z_m)$$
$$\breve{\rho}_\beta(z_n) = \tilde{T}^{-1}_{\gamma+\beta}(z_n, \cdot)\, T_\gamma(\cdot, z_m)\, \rho(z_m)$$

where T_γ is the column matrix of the real observation matrixes $A_{l,\gamma} G_{l,\gamma}$, $l = 1, \ldots, N$, while $\tilde{T}_{\gamma+\beta}$ is the EPCA operator with respect to the estimated angle $\gamma + \beta$. $\tilde{\rho}_\beta(z_n)$ does not exhibit remarkable variations as β varies, whereas $\breve{\rho}_\beta(z_n)$ is strongly affected. In more detail, when $\beta \approx 0$, the distribution of the energy on the reconstructed image tends to be uniform on the observed visible scene, i.e. the pseudoinverse operation compensates for the radiation patterns. When the estimated orientation is not matched, the pseudoinverse operation enhances parts of the visible scene in a way which does not fit the backprojection. A heuristic procedure for estimating β consists in setting a suitable error function

$$\varepsilon(\beta) = f(\breve{\rho}_\beta(z_n), \tilde{\rho}_\beta(z_n)) \tag{5}$$

and find its minimum. The chosen error function has crucial importance. An exhaustive analysis of the estimation accuracy is out of the scope of this paper. Fig. 5 shows an example obtained in simulation. The setup is the same as the one described in Section II, hence $N = 32$, the midrange is 37.5 m with a range interval of 2 m, $\tilde{P} = 10\,\text{cm}$, $\gamma = 0.025\,\text{rad}$, $x_t - \tilde{x}_t = y_t - \tilde{y}_t = 1.25\,\text{cm}$ and $x_r - \tilde{x}_r = y_r - \tilde{y}_r = -1.25\,\text{cm}$. An estimation accuracy of about $5^{-3}\,\text{rad} \simeq 1/4\,\text{degree}$ has been obtained by considering a simple L^2-norm of the difference between $\breve{\rho}_\beta(z_n)$ and $\tilde{\rho}_\beta(z_n)$ on a signal consisting of sand ripples with an additional phantom object in the center of the scene. Furthermore, the considered error function results to be convex in the interval of interest. The accuracy increases up to $1^{-3}\,\text{rad} \simeq 1/20\,\text{degree}$ in case a scene with a random

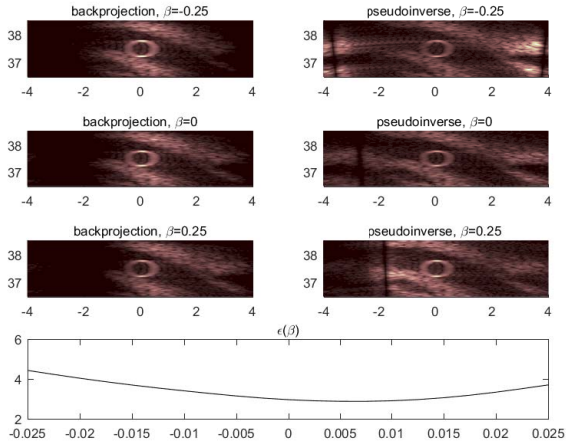

Fig. 5. Estimation of the relative orientation between transmission and reception: the pseudoinverse image (right) is compared to the backprojected one (left) at various hypothetical angle $\beta + \gamma$ (top to bottom). The error function (bottom) features a minimum close to the actual relative rotation.

reflectivity $\rho(z_n)$ is considered, as the reflectivity randomness guarantees a uniform energy distribution making the L^2-norm work better. A norm weighted by local energy could be used to increase the accuracy on generic non uniform reflectivity.

C. Ping to Ping Displacement Estimation

Let us first introduce some notations. We set

$$\breve{\rho}^{(p)}(z_n) = (\tilde{T}^{(p)})^{-1}(z_n, \cdot)\, T_\gamma(\cdot, z_m)\, \rho(z_m)$$

representing the recovered reflectivity at ping p, and the orthogonal projector on the subspace identified by the EPCA of ping p

$$Q^{(p)} = (\tilde{T}^{(p)})^{-1} \tilde{T}^{(p)}.$$

According to EPCA, two consecutive pings p and q are completely represented by $\tilde{\sigma}_r^{(p)}$ and $\tilde{\sigma}_r^{(q)}$ and the transmitters relative rotations $\gamma^{(p)}$ and $\gamma^{(q)}$, which are assumed to be already estimated. The ping q can be specified with respect to ping p by

$$\tilde{\sigma}_r^{(q)} = (\tilde{x}_a^{(p)} + U\cos\vartheta_r^{(p)} + \mu, \tilde{y}_a^{(p)} + U\sin\vartheta_r^{(p)} + \nu, \vartheta_r + \xi)$$

where $U = L(N - K)$ is the distance between $(\tilde{x}_a^{(p)}, \tilde{y}_a^{(p)})$ $(\tilde{x}_a^{(q)}, \tilde{y}_a^{(q)})$ in absence of motion errors and K is the number of superimposed array elements like in DPCA.

In order to estimate the μ, ν and ξ, we propose to consider the projection on the intersection of subspaces identified by orthogonal projectors $Q^{(p)}$ and $Q^{(q)}$:

$$\psi = \lim_{i\to\infty} (Q^{(q)}Q^{(p)})^i \rho = \lim_{i\to\infty} (Q^{(p)}Q^{(q)})^i \rho$$

which can be approximated from either $\breve{\rho}^{(p)}$ or $\breve{\rho}^{(q)}$:

$$\psi^{(p)} \simeq \lim_{i\to\infty} (Q^{(p)}Q^{(q)})^i \breve{\rho}^{(p)}$$
$$\psi^{(q)} \simeq \lim_{i\to\infty} (Q^{(q)}Q^{(p)})^i \breve{\rho}^{(q)}.$$

Since the displacement between p and q is unknown, we define following shift and rotate operator

$$Q^{(q)} = S_{\tilde{\mu},\tilde{\nu},\tilde{\xi}}[Q^{(p)}]$$

by which we can compute the projections on the intersection space as a function of the hypothetical displacement $\tilde{\mu}$, $\tilde{\nu}$, $\tilde{\xi}$:

$$\psi^{(p)}_{\tilde{\mu},\tilde{\nu},\tilde{\xi}} = \lim_{i\to\infty} (Q^{(p)} S_{\tilde{\mu},\tilde{\nu},\tilde{\xi}}[Q^{(p)}])^i \breve{\rho}^{(p)}$$
$$\psi^{(q)}_{\tilde{\mu},\tilde{\nu},\tilde{\xi}} = \lim_{i\to\infty} (S_{\tilde{\mu},\tilde{\nu},\tilde{\xi}}[Q^{(p)}] Q^{(p)})^i \breve{\rho}^{(q)}$$

In general, for non-null $\breve{\rho}^{(p)}$ and $\breve{\rho}^{(q)}$ we have

$$\psi^{(p)}_{\tilde{\mu},\tilde{\nu},\tilde{\xi}} = \psi^{(q)}_{\tilde{\mu},\tilde{\nu},\tilde{\xi}} \quad \Leftrightarrow \quad (\mu,\nu,\xi) = (\tilde{\mu},\tilde{\nu},\tilde{\xi}).$$

In practice they will not be equal because of approximation errors. However, $\psi^{(p)}_{\tilde{\mu},\tilde{\nu},\tilde{\xi}}$ and $\psi^{(q)}_{\tilde{\mu},\tilde{\nu},\tilde{\xi}}$ can be employed for building an error function. It has been experimentally observed that an error function such as the L^2-norm of the projection absolute value difference, i.e.

$$\zeta(\tilde{\mu},\tilde{\nu},\tilde{\xi}) = \left\| \left|\psi^{(p)}_{\tilde{\mu},\tilde{\nu},\tilde{\xi}}\right| - \left|\psi^{(q)}_{\tilde{\mu},\tilde{\nu},\tilde{\xi}}\right| \right\|_2 \tag{6}$$

is convex in the interval of interest of $(\tilde{\mu},\tilde{\nu},\tilde{\xi})$ but does not feature a minimum in the neighbourhood (μ,ν,ξ) with sufficient accuracy. Conversely, the L^2-norm of the projections difference (without discarding the phase information), i.e.

$$\eta(\tilde{\mu},\tilde{\nu},\tilde{\xi}) = \left\| \psi^{(p)}_{\tilde{\mu},\tilde{\nu},\tilde{\xi}} - \psi^{(q)}_{\tilde{\mu},\tilde{\nu},\tilde{\xi}} \right\|_2 \tag{7}$$

allows for an estimation of the minimum point with a much higher accuracy, but its behaviour is not convex in the optimization space. Hence, by means of an optimization switching from objective function ζ to objective function η when the latter is locally convex, the relative displacement can be accurately identified.

The results of a simulation are shown in Fig. 6. The number of overlapping array elements is $K = 2$ and the number of elements is $N = 32$. This situation could not be tackled by other techniques in literature, which need a larger K. For the sake of illustration, we plotted the function ζ and η along one-dimensional subspaces. The intervals have been chosen in order to highlight that η is more accurate but exhibits some oscillations and local minima. The accuracy which can obtained, being a small fraction of the wavelength, is compliant to SAS requirements.

The computational burden of this proposed approach is large because of the iterations involved in the orthogonal projectors, in the intersection subspace calculations and in the optimization. A multiresolution approach could be developed to reduce the computational cost when the optimization is still far from the minimum point. Moreover, it could be performed just on specific subsampled grid of the whole scene, such as at specific range on small range interval. Finally, it can work with a much smaller ratio K/N with respect to existing techniques and it does not rely on the navigation to ensure that the redundant array elements from p to q are correctly superimposed.

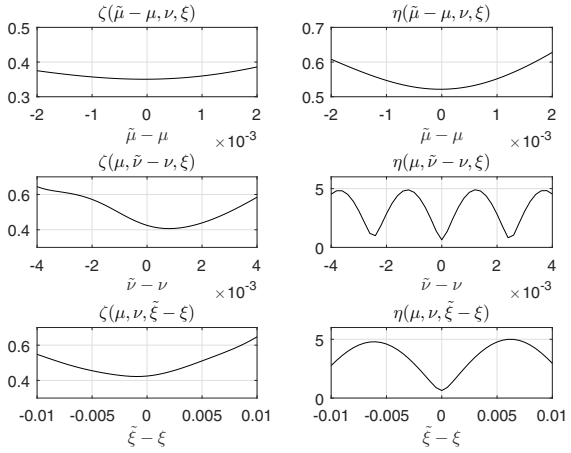

Fig. 6. Error functions estimating the ping to ping displacement in terms of horizontal vertical and rotation from top to bottom. A function discarding the phase information is employed for a preliminary estimation (left), then a function including phase is employed for a finer search (right).

IV. Conclusion

A novel motion compensation technique for SAS not relying on fine navigation prior information has been introduced. The proposed approach is based on the comparison between the projections on intersection subspace of different observations. The model requires also an estimation of the relative rotation between the transmission and the reception, which has been performed by means of an heuristic procedure.

V. Acknowledgements

This work was supported by the Engineering and Physical Sciences Research Council (EPSRC) Grant number EP/J015180/1 and the MOD University Defence Research Collaboration in Signal Processing.

References

[1] C. Cafforio, C. Prati, and F. Rocca, "Sar data focusing using seismic migration techniques," *IEEE Transactions on Aerospace and Electronic Systems*, vol. 27, no. 2, pp. 194–207, Mar 1991.

[2] D. Billon and M. A. Pinto, "Some general considerations for synthetic aperture sonar design," in *OCEANS '95. MTS/IEEE. Challenges of Our Changing Global Environment. Conference Proceedings.*, vol. 3, Oct 1995, pp. 1665–1670 vol.3.

[3] M. P. Hayes and P. T. Gough, "Synthetic aperture sonar: A review of current status," *IEEE Journal of Oceanic Engineering*, vol. 34, no. 3, pp. 207–224, July 2009.

[4] A. Bellettini and M. Pinto, "Design and experimental results of a 300-khz synthetic aperture sonar optimized for shallow-water operations," *IEEE Journal of Oceanic Engineering*, vol. 34, no. 3, pp. 285–293, July 2009.

[5] A. Bellettini and M. A. Pinto, "Theoretical accuracy of synthetic aperture sonar micronavigation using a displaced phase-center antenna," *IEEE Journal of Oceanic Engineering*, vol. 27, no. 4, pp. 780–789, Oct 2002.

[6] H. J. Callow, M. P. Hayes, and P. T. Gough, "Motion-compensation improvement for widebeam, multiple-receiver sas systems," *IEEE Journal of Oceanic Engineering*, vol. 34, no. 3, pp. 262–268, July 2009.

[7] J. A. Fessler and B. P. Sutton, "Nonuniform fast fourier transforms using min-max interpolation," *IEEE Transactions on Signal Processing*, vol. 51, no. 2, pp. 560–574, Feb 2003.

Spectral Library Clustering Using a Bayesian Information Criterion

Jonathan Piper and John Duselis
Dstl Porton Down, United Kingdom

***Abstract*—Unsupervised classification of spectral libraries provides groups of spectra which may be of use in material detection or identification processes for hyperspectral imagery. It can also be used to discover associations between materials' spectra that can help analysts to interpret spectral data. We use the assumption of a Gaussian Mixture Model, combined with a Bayesian Information Criterion (BIC) for determination of the number of mixture components, to model a spectral library and assign its members to clusters. This process provides a natural method to include spectra within multiple classes where this is appropriate. The process is demonstrated for a library of mineral spectra. Results are compared with the minerals' geological classifications and with the results of other published clustering processes.**

I. Introduction

Hyperspectral imaging is an increasingly important remote sensing technique, used in a range of applications such as mineral exploration, precision agriculture and environmental monitoring. In many of these applications, the sensor is used to identify particular substances of interest (for example, minerals or plant species) by comparison of remote obeservations with known spectra stored in a library. [1]

In this paper we apply established techniques for unsupervised clustering to data held in a spectral library, for the purpose of discovering informative relationships between those spectra. The groups of spectra formed in this way may be useful for a range of applications. For example, using the Adaptive Coherence/Cosine Estimator algorithm [2] with a multi-dimensional target subspace, defined by spectra from a cluster, creates a detector for a class of related materials rather than a single specific spectrum. This could be used to detect substances whose exact composition is variable, or objects whose spectral reflectance varies due to effects such as weathering or contamination. As another example, in Multiple Endmember Spectral Mixture Analysis [3], it is possible to reduce the computational effort required for identifying appropriate mixture models by grouping endmembers into clusters with similar characteristics. [4]

It is possible to define clusters of spectra manually, or produce clusters from user-defined starting points using a supervised classification method. However, these approaches have several disadvantages: they would usually require a trained analyst with detailed knowledge of the subject matter (for example, a geologist in the context of mineral mapping); it may be hard to determine the true origin of a spectrum if the accompanying metadata is poor; and it may be intractable to use manual processes for a very large library. Therefore an unsupervised clustering process may be preferred. A significant additional benefit is that an unsupervised process could be used to discover previously unknown relationships between library members.

In order to fully describe the relationships between spectra, it may be appropriate to place spectra in more than one group. For example, chemical compounds may display spectral features corresponding to more than one ion, bond, or functional group. Objects may consist of mechanical mixtures of different compounds, each contributing different spectral features. An example is shown in Figure 1, which shows spectra for the minerals illite and montmorillonite as well as for a mixture of the two. In this case it would be appropriate to place the mixed spectra in both the illite and montmorillonite groups. Our technique differs from previous work on clustering of spectral libraries in that it allows for this kind of multiple membership (unlike [5]) whilst also attempting to determine a number of clusters that most appropriately fits the data (unlike [6]).

The paper begins with background information on spectral libraries, clustering techniques and the Bayesian Information Criterion. The subsequent section describes the results of applying the proposed technique to a library of mineral spectra, and a comparison of those results with the geological classification of those minerals.

II. Background

A. Spectral library clustering - prior work

There have been several previous attempts to apply unsupervised clustering to spectral libraries. The authors of [5], [7] build a classifier by obtaining clusters from random subsets of the libraries in order to train and test. They use the Calinski-Harabasz criterion for determing the number of clusters via k-means, which tries to maximize the inter-cluster variance while minimizing the intra-cluster variance.

The authors of [6] use k-means clustering of spectra in combination with a unique compound distance measurement. The clustering results are then used in a process for identifying materials in spectral imagery. They do not determine the optimal number of clusters. Rather, they assume that grouping spectra into a smaller number of larger clusters reveals the large-scale structure in the dataset, whereas smaller, more-numerous clusters reveal the detailed, small-scale structure.

The authors of [8] have the specific goal of estimating the organic matter content of soil using reflectance spectra, and find that by using different models for different clusters

978-1-5090-0326-6/16/$31.00 ©2016 Crown

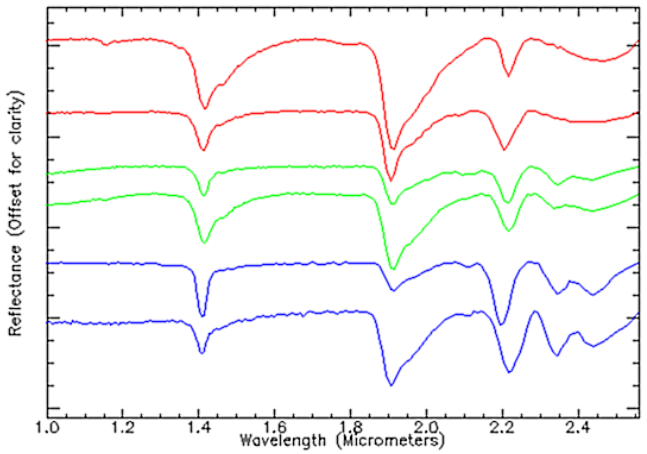

Fig. 1. Short-wave infrared reflectance spectra of montmorillonite (red), illite (blue) and a mixture of the two (green), plotted with continuum removal. Note the feature at approx. 2.35μm, common to illite and mixture spectra.

of spectra their estimates can be improved. Their clustering process determines an optimum number of clusters using three distinct measures for clustering quality ("fuzzy performance index","modified partition entropy" and "clustering independence index") but they do not use the BIC.

B. Unsupervised learning to determine the correct model

A full explanation of unsupervised learning is beyond the scope of this article, but a brief summary of the methods used in our approach is provided below. A comprehensive treatment of the subject can be found in [9].

1) Spectral Libraries: The spectra used for comparison with those obtained from an image are stored within spectral libraries. Such a library usually provides a single reflectance spectrum for each of the many materials it contains. Each spectrum is a vector whose elements indicate the proportion of light reflected from a surface at a particular wavelength. The range and number of spectra within a library depends on its intended purpose, but a comprehensive library for use in remote sensing may contain tens of thousands of signatures.

Formally, let h be a modelled spectrum (an "observation") of dimensionality p. A library consists of n observations across the same dimensionality comprising a data matrix H of dimensions $p \times n$:

$$H = [h_1, \ldots, h_n] \tag{1}$$

2) PCA: The dimensionality of spectral vectors can be large, and may exceed the number of observations available. Dimensionality reduction is achieved by Principal Component Analysis (PCA). The original data matrix, H of $n \times p$ dimensions will be reduced to include only the components necessary to account for a specified proportion of the variance. Specifically, let X be a matrix of size $n \times l$ with $1 < l < p$ that uses the first l principal components to transform:

$$H_L = HX \tag{2}$$

3) Clustering Technique: Our technique uses a Gaussian Mixture Model which allows formalization that is conducive to unsupervised learning [10] [11]. This assumes that the observations come from a multivariate probability distribution with mutliple components, each of which has a Gaussian distribution (we use the terms "cluster" and "component" interchangeably). Briefly, and taking directly from [12] while customizing some notation, a GMM λ is:

$$P(H_L(j)|\lambda) = \sum_{i=1}^{M} w_i g(H_L(j)|\mu_i, \Sigma_i) \tag{3}$$

$$\lambda = \{\omega_i, \mu_i, \Sigma_i\}, i = 1, \ldots, k \tag{4}$$

Here $H_L(j)$ is an observation from the library (j=1, $\ldots$, n). $g(H_L(j)|\mu_i, \Sigma_i)$, $i = 1, \ldots, k$, are the component Gaussian densities with mean μ_i and covariance matrix Σ_i. Each component is weighted by a factor w_i. The Σ_i can be constrained in a number of ways to improve estimation of the covariance parameters with the limited data available. We use four different approaches. In three the parameters are estimated individually for each component: "spherical", in which covariances are zero and all variances equal; "diagonal", in which covariances are zero but variances can be unequal; and "full", in which variances and covariances can take any value. We also employ the "tied" covariance matrix type: a full covariance matrix that is the same for each component.

GMMs were determined using Expectation Maximization methods in the normal way. Using the resulting models, the likelihood of observations belonging to particular components can be estimated. Each observation can be assigned to the single cluster for which the probability is highest, or it can be assigned to any cluster for which the probability passes a defined threshold. [9] In the following, the former case is referred to as "single-membership", the latter as "multiple membership."

It is important to consider whether a multivariate Gaussian distribution is an appropriate model for a cluster of spectra in a library. The Gaussian model underpinned the analysis of hyperspectral target detectors for many years, although it is known that real data usually deviate from it. [2] There is evidence that multivariate t-distributions provide a better model for hyperspectral image data. [13] However, [2] suggests that a Gaussian random vector is sufficient to account for the "intrinsic spectral variability" of a material, and that the use of more generalized elliptically contoured distributions is necessary specifically to account for "environmental effects associated with the illuminated pixel area". This implies that the Gaussian model may be appropriate when considering library, as opposed to image, data. Regardless of these considerations, the multivariate Gaussian is a simple and well-understood model that provides for correlation between different wavebands of a spectrum, which is why it was chosen for use in this work.

4) Bayesian Information Criterion: The number of components, k, is one of the inputs to the GMM process, but since we are employing unsupervised learning we have no

TABLE I
NUMBER OF GROUND-TRUTH CLASSES AT EACH LEVEL OF THE HIERARCHY

Type	Group	Mineral
17	117	214

prior knowledge of the correct k. A number of measures have been proposed to quantify how well a particular GMM fits the data. These include the Akaike Information Criterion, Bayesian Information Criterion and Calinski-Hrabasz (review [14] for a survey). These measures are employed by clustering for a range of values of k, and then choosing the model whose score indicates the best fit. We used the Bayesian Information Criterion (BIC) for reasons described by the authors of [15] and evaluated it for $k = 2, \ldots, m$, with m being large. Formalizing:

For a particular model λ_j, its BIC can be shown to be

$$BIC_j = -2 \cdot ln(M_j) + k \cdot ln(n) \tag{5}$$

Where M_j is the maximized likelihood function for that model, k is the model dimensionality, and n is the sample size (number of observations). Choosing the optimal model is satisfying the argument:

$$\lambda = min(BIC_1, ..., BIC_m) \tag{6}$$

In the case of models whose BICs show insignificant differences, such as model j implying $BIC_j - BIC_{min} < 2$, as determined by parameters in [16], the lower dimensionality model was chosen.

III. EXPERIMENTATION

A. Data and Environment

The process was tested using mineral spectra from the U.S. Geological Survey Digital Spectral Library, splib06a. [17] These data were chosen because the accompanying metadata includes labels that can be used as truth data to assess the classifier. Additionally, some of the same data were used in [5], allowing for comparison of results. Some spectra were excluded due to incomplete coverage of the required waveband or a lack of metadata. The resulting dataset included 455 spectra covering the 0.4-2.5μm spectral range with 420 wavebands. The metadata include a "mineral type", a "group" and a mineral name, together forming a hierarchy of labels. As an illustration, consider Figure 1 in which the minerals shown all belong to the Phyllosilicate group, but each have different mineral types. Table I indicates the number of labels present at each tier of the hiearchy. The "mineral type" and "group" tiers correspond approximately to the "sub-class" and "group" of [5].

In their raw form the data are not suitable for use with the BIC because the observation space is of a similar size to the feature space. Therefore dimensionality reduction was implemented using PCA. [18]

All tests were run on a Windows 8 platform, with Intel® Xeon® E7-4890 CPU at 2.8GHz and 15GB of RAM. The process was implemented using Python(x,y) 2.7 and modelling was accomplished using the *scikit-learn* module. [19] Parameters passed to the routine included the spectral data; the proportion of the variance to retain after dimensionality reduction, set at 0.99, yielding 9 principal components; and a range of cluster numbers to consider, $k = [2, 75]$. The exemplar data presented took 143 seconds to execute.

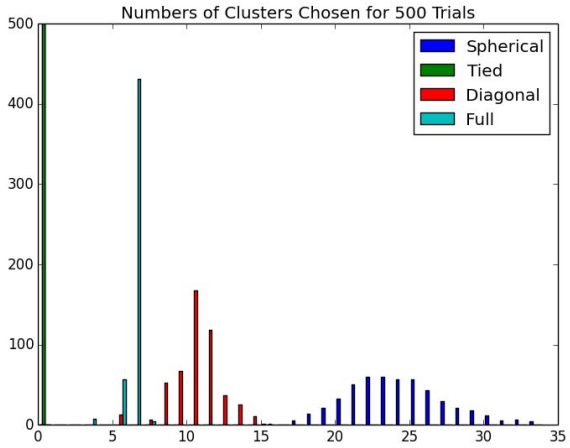

Fig. 2. Histogram of cluster numbers determined through BIC for 500 different initializations of the clustering process (c.f. Table I)

B. Results and Discussion

First we consider whether the process has produced the correct number of clusters. Although we begin from the assumption that our data form clusters described by the truth classes, we have no prior expectation regarding which level of the truth class hierarchy will show the clearest delineation between classes, and therefore which set of truth classes we would expect our results to match with. Figure 2 shows the numbers of clusters generated for each of the different covariance parametrisations, for 500 initializations of the clustering process. It is apparent that the numbers are substantially different from those for the "Group" and "Mineral" tiers of the truth clusters (Table I), but that the numbers are somewhat comparable between the "Type"' tier and the "Spherical" and "Diagonal" covariance forms. This could be considered to indicate that the most "natural" clusters for the data occur at this scale; however, further analysis is required to determine if this is actually the case. Note that since the "Tied" covariance form only produced a single cluster, it is generally excluded from further analysis.

There are various possible methods for assessing the accuracy of a clustering process. For the sake of comparison, we present some results from the methods adopted in [5]. Two main performance measures were used in that case: a "Purity Index" (PI) which depends on the extent to which a cluster's members belong to only a single ground-truth cluster, and a method based on confusion matrices.

The PI is a number between 0 and 1 which describes the purity of a cluster (1 being perfectly pure). The average PI across all clusters has been evaluated for our various different input

TABLE II
AVERAGE PURITY INDEX FOR ALL CLUSTERS PRODUCED FOR A SPECIFIC SET OF INPUT PARAMETERS

Covariance type and multiple membership	Type	Group	Mineral
Spherical, single	0.53	0.44	0.33
Diagonal, single	0.57	0.53	0.42
Full, single	0.38	0.42	0.47
Spherical, multiple	0.41	0.46	0.31
Diagonal, multiple	0.57	0.48	0.44
Full, multiple	0.33	0.34	0.47

parameters, and the results are shown in Table II. It can be seen that single-membership generally results in higher purity than allowing multiple membership, which is unsurprising. It can also be seen that where the number of clusters is larger, the purity is higher. This too is unsurprising, since when the observations are forced into too small a number of clusters, it is expected that the clusters would become more diverse and therefore less pure. The values here are somewhat lower than those presented in [5], which generally fall in the range 0.6-1.0. This can be explained by noting that in [5] the number of observations is quite large compared with the number of clusters; indeed, in the example presented, the majority of clusters contain only one observation. Therefore, it is to be expected that this purity measure would be much higher. Where each observation is its own cluster the purity measure would be perfect; however, under these circumstances, the clustering results lose all power to demonstrate relationships between the observations.

The other analysis method employed in [5] uses confusion matrices to assess the accuracy of assigning spectra from a test set to the clusters generated by their algorithm using a measure called silhouette width. Its results therefore depend not just on the quality of the clusters, but also on the effectiveness of this assignment process. Since we have not specified a process by which our clusters will be exploited, this is not an appropriate test for us to perform.

An alternative method to quantify the accuracy of clustering uses the so-called Jaccard Index (JI) [20]:

$$JI = \frac{TPs}{TPs + FPs + FNs} \tag{7}$$

In the above, *TPs* (true positives) is the number of observations that have been correctly assigned to a cluster; *FPs* (false positives) is the number of observations assigned to a cluster that should not have been; and *FNs* (false negatives) is the number of observations that were not assigned to the cluster, but should have been.

The JI can be used to assess the overall quality of the clustering produced by our process using a similar approach to that used in [5]: a cluster is labelled with the name of the truth cluster to which it most closely corresponds, based on JI. It is then possible to identify numbers of true positives, false positives and false negatives for each cluster. These can be added individually (so that, for example, the total number of true positives is the sum of true positives for each individual cluster) and used with (7) to compute a JI for the entire clustering. Results for this are presented in Table III. These values fall in the range 0…1, with 1 indicating a perfect result.

TABLE III
OVERALL JACCARD INDEX OF CLUSTERING RESULTS

Covariance type and multiple membership	Type	Group	Mineral
Spherical, single	0.12	0.21	0.22
Diagonal, single	0.21	0.28	0.22
Full, single	0.25	0.25	0.19
Spherical, multiple	0.10	0.15	0.16
Diagonal, multiple	0.15	0.18	0.14
Full, multiple	0.20	0.18	0.13

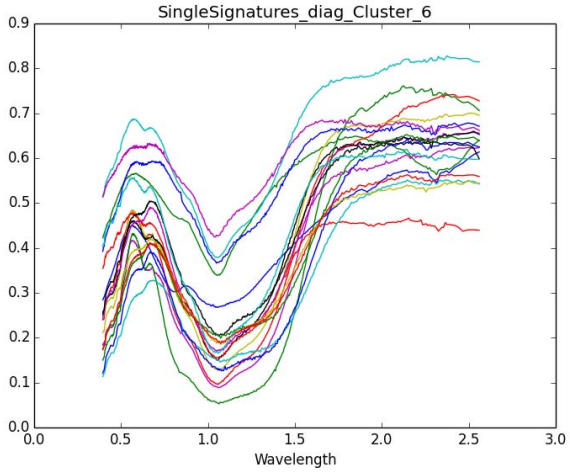

Fig. 3. Example cluster, obtained assuming diagonal covariance matrix and single cluster membership. This cluster achieves a JI of 0.85 compared with the "Olivine" group.

It can be seen that all scores are substantially less than 1. This can partly be attributed to the fact that in most cases the number of classes generated by our algorithm is substantially less than the number of truth classes (compare table I and Figure 2). Thus, many of our clusters include members from outside the most similar truth class; they include a large number of false positives.

Some good scores are achieved for individual clusters, an example of which is included as Figure 3. Such cases tend to be associated with very pure clusters that match a relatively small truth cluster.

Some other trends can be noted. Clusters with multiple membership tend to have lower scores. Analysis of tables of JI for a particular clustering suggest that several factors contribute: some clusters that score highly in the single-membership case show a significant reduction in score for the multiple membership case, presumably because of reduced purity and therefore an increased number of false positives. According to the overall JI the diagonal covariance parametrisation produces the best results, and the spherical parametrisation the worst. This is somewhat surprising, since

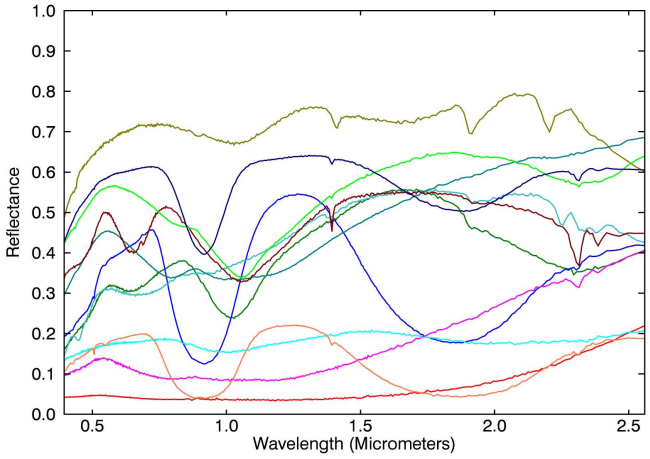

Fig. 4. Subset of spectra from the Pyroxene Group, demonstrating spectral diversity.

the spherical version usually produces numbers of clusters closer to the numbers of truth clusters, which might have been assumed to improve the quality of the result.

The average JI is best for the middle ("Group") tier of the truth cluster hierarchy. This could be an indication of the scale at which our data cluster most naturally, but there may be other explanations. Low scores for the lower ("Mineral") tier could be associated with high numbers of false positives. At this level the number of truth classes greatly exceeds the number generated by the algorithm, so few classes will be a pure representation of a truth class. Low scores for the upper ("Type") tier may be due to a dearth of pure ground-truth clusters, which tend to be associated with high-scoring individual clusters. The Group tier may represent a happy medium between these two effects. It should also be noted, though, that for individual clustering results there is little consistency between the best-scoring set of truth clusters.

Finally, consideration should be given to the appropriateness of the truth clusters. Figure 4 shows a subset of the members of one such cluster, the Pyroxene Group. It can be seen that these spectra exhibit considerable diversity, even though they have been categorised as being related in mineralogical terms. It is questionable whether it is reasonable to expect an unsupervised (or even a supervised) classification algorithm to associate these spectra together given the range of features that they exhibit.

IV. Future Work

In future various improvements to the clustering process should be tested: other criteria for determining the optimal cluster number should be considered (in addition to BIC); different distance measures should be tested for the clustering process; and more consideration should be given to setting the probability threshold used when assigning spectra to multiple clusters.

Of equal importance to developing the clustering algorithm is developing methods for testing it. More work on analysing clustering quality is needed, as is a set of truth classes known to accurately reflect relationships between spectra.

V. Acknowledgements

The authors would like to thank Professor Jim Davis of Ohio State University for his guidance in this investigation.

References

[1] M. T. Eismann, "Hyperspectral remote sensing." SPIE Bellingham, 2012.

[2] D. Manolakis, D. Marden, and G. A. Shaw, "Hyperspectral image processing for automatic target detection applications," *Lincoln Laboratory Journal*, vol. 14, no. 1, pp. 79–116, 2003.

[3] D. A. Roberts, M. Gardner, R. Church, S. Ustin, G. Scheer, and R. Green, "Mapping chaparral in the santa monica mountains using multiple endmember spectral mixture models," *Remote Sensing of Environment*, vol. 65, no. 3, pp. 267–279, 1998.

[4] W. J. Okin, G. S. Okin, D. A. Roberts, and B. Murray, "Multiple endmember spectral mixture analysis: Endmember choice in an arid shrubland," in *JPL Airborne Earth Science Workshop*, vol. 8, 1999, pp. 99–17.

[5] G. A. Marzo, T. L. Roush, and R. C. Hogan, "Automated classification of visible and infrared spectra using cluster analysis," *Journal of Geophysical Research: Planets*, vol. 114, no. E8, 2009.

[6] E. M. Bassett and L. S. Kalman, "Material taxonomy for object identification in hydice imagery," pp. 268–279, 1996.

[7] G. A. Marzo, T. L. Roush, A. Blanco, S. Fonti, and V. Orofino, "Cluster analysis of planetary remote sensing spectral data," *Journal of Geophysical Research: Planets*, vol. 111, no. E3, 2006.

[8] Z. Shi, Q. Wang, J. Peng, W. Ji, H. Liu, X. Li, and R. A. Viscarra Rossel, "Development of a national vnir soil-spectral library for soil classification and prediction of organic matter concentrations," *Science China Earth Sciences*, vol. 57, no. 7, pp. 1671–1680, 2014.

[9] R. Duda, P. Hart, and D. Stork, *Pattern Classification, 2nd Ed.* John Wiley and Sons, Inc, 2001.

[10] C. Fraley and A. E. Raftery, "How many clusters? which clustering method? answers via model-based cluster analysis." *Comput. J.*, vol. 41, no. 8, pp. 578–588, 1998.

[11] M. A. T. Figueiredo and A. K. Jain, "Unsupervised learning of finite mixture models," *IEEE Trans. on Pattern Analysis and Machine Intelligence*, vol. 24, no. 3, pp. 381 – 396, March 2002.

[12] D. A. Reynolds, "Gaussian mixture models," in *Encyclopedia of Biometrics*, S. Z. Li and A. K. Jain, Eds. Springer US, 2009, pp. 659–663.

[13] D. Manolakis and D. Marden, "Non gaussian models for hyperspectral algorithm design and assessment," in *Geoscience and Remote Sensing Symposium, 2002. IGARSS '02. 2002 IEEE International*, vol. 3, June 2002, pp. 1664–1666 vol.3.

[14] M. Halkidi, Y. Batistakis, and M. Vazirgiannis, "On clustering validation techniques," *Journal of Intelligent Information Systems*, vol. 17, pp. 107–145, 2001.

[15] A. A. Neath and J. E. Cavanaugh, "The bayesian information criterion: background, derivation, and applications," *Wiley Interdisciplinary Reviews: Computational Statistics*, vol. 4, no. 2, pp. 199–203, 2012.

[16] R. Kass and A. Raftery, "Bayes factors," *Journal of the American Statistical Association*, pp. 773–795, 1995. [Online]. Available: http://www.stat.washington.edu/people/raftery/Research/PDF/kass1995.pdf

[17] R. Clark and et al, "Usgs digital spectral library splib06a: U.s. geological survey, digital data series 231," 2007. [Online]. Available: http://speclab.cr.usgs.gov/spectral.lib06

[18] G. Schwarz, "Estimating the dimension of a model," *Ann. Statist.*, vol. 6, no. 2, pp. 461–464, 03 1978.

[19] F. Pedregosa, G. Varoquaux, A. Gramfort, V. Michel, B. Thirion, O. Grisel, M. Blondel, P. Prettenhofer, R. Weiss, V. Dubourg, J. Vanderplas, A. Passos, D. Cournapeau, M. Brucher, M. Perrot, and E. Duchesnay, "Scikit-learn: Machine learning in Python," *Journal of Machine Learning Research*, vol. 12, pp. 2825–2830, 2011.

[20] P. Jaccard, "The distribution of the flora in the alpine zone.1," *New Phytologist*, vol. 11, no. 2, pp. 37–50, 1912. [Online]. Available: http://dx.doi.org/10.1111/j.1469-8137.1912.tb05611.x

Detection of manoeuvring low SNR objects in receiver arrays

Kimin Kim, Murat Üney and Bernard Mulgrew
Institute for Digital Communications, School of Engineering,
The University of Edinburgh, EH9 3JL, Edinburgh, UK
Emails:{K.Kim, M.Uney, B.Mulgrew}@ed.ac.uk

***Abstract*—In this work, we are interested in detecting manoeuvring objects in high noise background using an active sensor with a uniform linear array (ULA) receiver and propose a joint pulse integration and trajectory estimation algorithm. This algorithm allows us to detect low SNR objects by integrating multiple pulse returns while taking into account the possibility of object manoeuvres. In the proposed algorithm, the detection is performed by a Neyman-Pearson test, i.e., a likelihood ratio test. The likelihood function used in this test accommodates the radar ambiguity function evaluated in accordance with object related parameters such as location, velocity and reflection coefficient. The trajectory estimation is performed by Bayesian recursive filtering based on the state model of the location and velocity parameters. The reflection coefficient is estimated by a maximum likelihood (ML) estimator. These estimates are used in pulse integration, leading to coherent integration during a coherent processing interval (CPI) and non-coherent integration across consecutive CPIs. We also compare the proposed algorithm with conventional techniques.**

I. Introduction

Detection of manoeuvring objects in a relatively high noise background is a challenging task and a highly desired capability in wide area surveillance applications. In these applications, active sensor systems, for example radar systems, are often used. Detection in active sensing involves transmitting modulated pulse trains towards the surveillance region, and, testing the hypothesis that the received signal contains reflected versions of the transmitted waveforms against the noise only signal hypothesis. The received signal varies with object related parameters such as range (equivalently, time of flight), velocity (equivalently, doppler shift) and effective reflection coefficient. The data for testing object existence consists of samples obtained after correlating (or, matched filtering) this signal with expected waveforms corresponding to selected values of these parameters [1, Chp.1]. Equivalently, the range-bearing and doppler space is uniformly separated into bins.

For low SNR objects, the reflected pulse energy is on a level very similar to the noise background. This makes detection difficult because a single measurement set (i.e., the data set for a single emitted pulse) is likely to fail in providing sufficient evidence of object existence. For this reason, multiple measurements (i.e., data sets for multiple pulse returns) need to be considered by summing up the reflected pulse energy across them, which is often referred to as pulse integration. In principle, prolonging the integration time increases the chances that a low SNR object can be detected. Conventional pulse integration such as coherent integration and non-coherent integration (see, e.g, [1, Chp.6]), however, perform integration for the same bins without taking into account the possibility of object movements across them. This leads to failure in collecting all the evidence contained in the received signals over time when the object is manoeuvring. An alternative is to use matched filters that are tuned to various trajectories [2], however, the number of filters required easily becomes excessive with increasing integration time.

It is possible to perform long time integration, on the other hand, by estimating the object trajectory and selecting data samples for pulse integration accordingly. This corresponds to adaptive synthesis of matched filters tuned to trajectories, in a sense. Trajectory estimation based on the data used for pulse integration is often referred to as track-before-detect (see, for example [3], [4]). These algorithms often use the modulus of the complex data sampled with pulse-width period and assume that the statistics of the reflection coefficient is known. It is desirable to estimate this quantity, however, this requires more samples than one can collect at this sampling rate within a coherent processing interval (CPI) [5]. Moreover, in [6], it is argued that taking the phase of the complex reflection coefficient into account improves the detection performance. An algorithm which uses both the modulus and the phase of the data, i.e., the complex data, collected with a sampling rate much higher than the aforementioned rate is proposed in [7]. This scheme performs long time integration by simultaneously estimating the reflection coefficient and range of the reflector position along a bearing line.

In this work, we consider a uniform linear array (ULA) receiver and propose a joint pulse integration and trajectory estimation algorithm, which uses complex data sampled with pulse-width period. The data captures spatio-temporal information and is stacked as a cube of range, bearing and doppler bins. The reflection coefficient within a CPI is estimated using a maximum likelihood approach. This quantity is used in the likelihood for trajectory estimation as well as pulse integration. The ULA structure allows us to estimate the reflection coefficient with favourable accuracy using the limited amount of data available in a CPI. As a result, coherent processing takes place within a CPI followed by non-coherent integration across consecutive CPIs. This approach results in an integrated value close to the best achievable using true trajectory.

978-1-5090-0326-6/16/$31.00 ©2016 IEEE

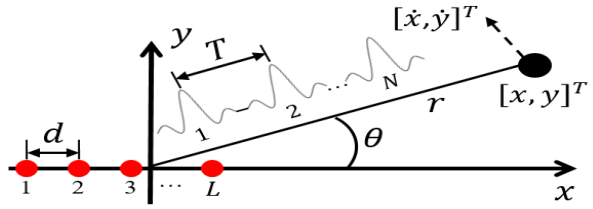

Fig. 1. Illustration of the problem scenario with a ULA (red dots) centered at the origin of the Cartesian plane and a low SNR object at $[x, y]^T$ with velocity $[\dot{x}, \dot{y}]^T$.

Section II of this article gives details of the scenario considered and the problem definition. In Section III, we introduce the proposed algorithm which involves trajectory estimation, and, derive the maximum likelihood estimator for the reflection coefficient that is required for tracking. In Section IV, we demonstrate the proposed algorithm in an example scenario and conclude in Section V.

II. Problem Statement

We consider a transmitter that emits N pulses followed by silent periods towards a surveillance region. These pulses are reflected back by objects in this region. We assume that the reflectors remain coherent in this time interval, also known as a coherent processing interval (CPI). A ULA receiver co-located with the transmitter receives the reflected versions of the transmitted waveforms with additive noise. This receiver consists of L elements spaced with d distance. The reflections are characterised by the reflector kinematic state $X = [x, y, \dot{x}, \dot{y}]^T$, where $[x, y]^T$ is the location in 2D Cartesian coordinates, $[\dot{x}, \dot{y}]^T$ is velocity, and $(.)^T$ denotes transpose. This scenario is illustrated in Fig. 1.

A. Signal model

For a reflector with kinematic parameters X, the corresponding signal is characterised by a spatial steering vector $s_s(\theta)$ and a temporal vector $s_t(r, \omega_d)$, where (θ, r) is the polar coordinates of the point $[x, y]^T$ in Cartesian coordinates, i.e.,

$$\theta = \tan^{-1}\left(\frac{y}{x}\right), \; r = \sqrt{x^2 + y^2}.$$

ω_d is the doppler angular frequency given by

$$\omega_d = \frac{4\pi}{\lambda_c}\left(\dot{x}\cos(\theta) + \dot{y}\sin(\theta)\right),$$

where λ_c is the carrier wavelength.

The spatial steering vector is specified by the geometry of the ULA

$$s_s(\theta) = [1, \exp\left(-j\omega_c \frac{d}{c}\sin(\theta)\right), \ldots, \exp\left(-j\omega_c (L-1)\frac{d}{c}\sin(\theta)\right)]^T, \quad (1)$$

where d is the internal element spacing, L is the number of elements in the array, $\omega_c = 2\pi f_c$ is the carrier angular frequency, and c is the speed of light.

The temporal vector $s_t(r, \omega_d)$ is given by

$$s_t(r, \omega_d) = [\exp\left(-j\omega_c \frac{2r}{c}\right), \exp\left(-j\omega_c \frac{2r}{c}\right)\exp(j\omega_d T), \ldots, \exp\left(-j\omega_c \frac{2r}{c}\right)\exp\left(j\omega_d (N-1)T\right)]^T, \quad (2)$$

where T is pulse repetition interval (PRI), i.e., the time period between the N pulses. In the forward signal model for the ULA, the spatial and temporal vectors are combined as

$$s(\theta, r, \omega_d) = s_s(\theta) \otimes s_t(r, \omega_d), \quad (3)$$

where $\otimes$ denotes the Kronecker product operator.

The reflections in the received signal of the ULA are searched by matched filtering, which computes the correlation of the transmitted waveform with the received signal. The filter output is sampled in fast time which uniformly divides the range space into range bins of width Δr. Doppler space is also discretised with $\Delta\omega_d$ steps as well as the bearing space which is sampled with steps $\Delta\theta$. As a result, the data vector in a CPI under the hypothesis that a reflector exists in the $i = [i_1, i_2, i_3]$th bearing-range-doppler bin with an unknown reflection coefficient A is found as

$$Z(i) = A s(i_1\Delta\theta, i_2\Delta r, i_3\Delta\omega_d) + n, \quad (4)$$

where $s(.)$ is given by (3), $n \sim \mathcal{CN}(.; \mathbf{0}, \sigma^2\mathbf{I})$ is additive white complex Gaussian noise vector, and A is an unknown complex constant. The data vector $Z_k(i)$ at the k^{th} CPI is hence

$$Z_k(i) = \begin{cases} A_k s_k(i_1\Delta\theta, i_2\Delta r, i_3\Delta\omega_d) \\ \quad + n_k(i_1, i_2, i_3) & , H_1 \text{ holds}, \\ n_k(i_1, i_2, i_3) & , H_0 \text{ holds}, \end{cases} \quad (5)$$

where H_1 is the hypothesis that a reflector exists in the i^{th} bin, H_0 is the null hypothesis, and, $k = 1, \ldots, K$ indexes integration over K CPIs.

B. Problem definition

Our goal is to decide on the existence of an object moving along a trajectory $X_{1:K}$. We use the Neyman-Pearson test [8, Chp.3] which is a likelihood ratio test, for this purpose. The input to the test is the set of complex measurement vectors $\{Z_k(i_k)\}_{k=1:K}$, where $i_k = [i_{k,1}, i_{k,2}, i_{k,3}]$ corresponds to the bearing-range-doppler bin associated with $(\theta_k, r_k, \omega_{d_k})$ of X_k.

The likelihood ratio test for an object with the trajectory $X_{1:K}$ is then given by

$$L(Z_{1:K}(i_{1:K})|X_{1:K}, A_{1:K}) \underset{H_0}{\overset{H_1}{\gtrless}} \mathcal{T}_K \quad (6)$$

where the ratio L of the likelihood for the object existence hypothesis and the likelihood for the noise only signal hypothesis factorises over time as

$$L(Z_{1:K}(i_{1:K})|X_{1:K}, A_{1:K}) = \prod_{k=1}^{K} L_k(Z_k(i_k)|X_k, A_k) = \prod_{k=1}^{K} \frac{l(Z_k(i_k)|X_k, A_k, H_1)}{l(Z_k(i_k)|H_0)}, \quad (7)$$

where L_k denoting the likelihood ratio at the k^{th} CPI. The numerator and denominator in (7) –considering (5)– are found as

$$l(Z_k(i_k)|X_k, A_k, H_1) = \left(\frac{1}{\pi\det(\sigma^2\mathbf{I})}\right)\exp\left(\frac{-|Z_k(i_k) - A_k s_k(\theta_k, r_k, \omega_{d_k})|^2}{\sigma^2\mathbf{I}}\right), \quad (8)$$

$$l(Z_k(i_k)|H_0) = \left(\frac{1}{\pi \det(\sigma^2\mathbf{I})}\right) \exp\left(\frac{-|Z_k(i_k)|^2}{\sigma^2\mathbf{I}}\right), \quad (9)$$

where $\sigma^2\mathbf{I}$ is the noise covariance. An explicit expression for the instantaneous likelihood ratio in (7) is obtained after substituting from (8) and (9) as follows,

$$L_k(Z_k(i_k)|X_k, A_k) = \exp\left(\frac{-|Z_k(i_k) - A_k s_k(\theta_k, r_k, \omega_{d_k})|^2 + |Z_k(i_k)|^2}{\sigma^2\mathbf{I}}\right). \quad (10)$$

The problem we consider is simultaneous estimation of $X_{1:K}$ and evaluation of the likelihood ratio test in (6) by evaluating (7)–(10) for $k = 1, \ldots, K$. Note that, this also involves estimation of the reflection coefficient $A_{1:K}$ and specification of the test threshold $\mathcal{T}_K$, as well. Estimation of all of these parameters, specification of a constant false alarm rate (CFAR) threshold and evaluation of the test are detailed in Section III.

III. Joint pulse integration and trajectory estimation

A. Trajectory estimation using coherent returns

Let us consider object trajectory (i.e., the kinematic parameters) estimation using coherent returns. For estimating the kinematic parameters $X_{1:K}$, we use a Markov state space model and perform Bayesian recursive filtering given by the following prediction and update recursions:

$$\begin{aligned} p(X_k|Z_{1:k-1}) &= \int p(X_k|X_{k-1}) p(X_{k-1}|Z_{1:k-1}) dX_{k-1} \quad (11)\\ p(X_k|Z_{1:k}) &\propto p(Z_k|X_k, A_k) p(X_k|Z_{1:k-1}), \end{aligned}$$

where $p(X_k|Z_{1:k})$ is the posterior probability density function of the object state, $p(Z_k|X_k, A_k)$ is the measurement likelihood, and, $p(X_k|X_{k-1})$ is the Markov transition density of the object state X_k.

The measurement likelihood is given by

$$\begin{aligned} p(Z_k|X_k, A_k) &= l(Z_k(i_k)|X_k, A_k) \prod\nolimits_{j \neq i_k} l(Z_k(j)|H_0) \\ &\propto L_k(Z_k(i_k)|X_k, A_k), \quad (12) \end{aligned}$$

where the second line follows after dividing both parts of the first equality by the product of the noise-only hypothesis likelihood for all range-bearing-doppler bins. Therefore, we use the following update for filtering

$$p(X_k|Z_{1:k}) \propto L_k(Z_k(i_k)|X_k, A_k) p(X_k|Z_{1:k-1}). \quad (13)$$

The object dynamic model is selected as a random acceleration model, i.e.,

$$X_k = F X_{k-1} + b_{k-1}, \quad F \triangleq \begin{bmatrix} 1 & 0 & \Delta & 0 \\ 0 & 1 & 0 & \Delta \\ 0 & 0 & 1 & 0 \\ 0 & 0 & 0 & 1 \end{bmatrix} \quad (14)$$

where b_{k-1} is process noise (modelling manoeuvres), which is zero-mean Gaussian with a known covariance $\mathbf{\Sigma}$, and Δ is the time interval at each sate between two consecutive CPIs. Hence, $p(X_k|X_{k-1}) = \mathcal{N}(X_k; FX_{k-1}, \mathbf{\Sigma})$.

We use a sequential Monte Carlo (SMC) realisation of Bayesian recursive filtering known as the particle filter [9]. Particle filters propagate weighted samples of probability densities in order to represent them. In particular, we use the bootstrap filtering approach: Given a set of particles $\{X_{k-1}^{(j)}, \zeta_{k-1}^{(j)}\}_{j=1}^{M}$ representing the posterior in (13) at time $k-1$, we obtain particles for the prediction density in (11) by sampling from the Markov transition, and obtain M particles $\{X_k^{(j)}, \zeta_{k-1}^{(j)}\}_{j=1}^{M}$ with $X_k^{(j)} \sim p(.|X_{k-1}^{(j)})$.

Then, the posterior at k is represented by $X_k^{(j)}$s with weights updated using the likelihood ratio given in (10), i.e.,

$$\begin{aligned} \zeta_k^{(j)} &= \frac{\tilde{\zeta}_k^{(j)}}{\sum_{i=1}^{M} \tilde{\zeta}_k^{i}}, \quad (15)\\ \tilde{\zeta}_k^{i} &\propto \zeta_{k-1}^{(j)} L_k(Z_k(i_k^{(j)})|X_k^{(j)}, A_k^{(j)}). \end{aligned}$$

Given the posterior weighted particles, the estimated state at the k^{th} CPI based on the measurements $Z_{1:k}$ is given by

$$\hat{X}_k \triangleq \sum_{j=1}^{M} \zeta_k^{(j)} X_k^{(j)}. \quad (16)$$

We check the weighted particles for degeneracy after normalising the weights (see, e.g., [9]). The degeneracy test N_{eff} is conducted by

$$N_{eff} = \frac{1}{\sum_{i=1}^{M} {\zeta_k^{(j)}}^2} < \mathcal{B}, \quad (17)$$

where $\mathcal{B}$ is the minimum number of effective particles allowed. We perform re-sampling (with replacement) whenever the condition in (17) is met.

B. Maximum likelihood estimator for the reflection coefficient

Let us consider the estimation of $A_k^{(j)}$ for evaluating the likelihood of the object existence hypothesis. Given the object state $X_k^{(j)}$, we use a maximum likelihood (ML) estimation approach by solving

$$\hat{A}_k^{(j)} = \arg\max_{A_k^{(j)}} \log l(Z_k(i_k^{(j)})|X_k^{(j)}, A_k^{(j)}, H_1), \quad (18)$$

where the likelihood above is given by (8) and $\hat{A}_k^{(j)}$ denotes the ML estimation of $A_k^{(j)}$.

For the sake of simplicity in notation, we denote the $i_k^{(j)}$th data vector $Z_k(i_k^{(j)})$ by Z_k in this section. After taking the natural logarithm of (8), we obtain

$$\begin{aligned} &\log l(Z_k|X_k^{(j)}, A_k^{(j)}, H_1) = \\ &- Z_k^H (\sigma^2\mathbf{I})^{-1} Z_k + 2\Re\left({A_k^{(j)}}^* \mathrm{s}_k(\theta_k^{(j)}, r_k^{(j)}, \omega_{d_k}^{(j)})^H (\sigma^2\mathbf{I})^{-1} Z_k\right) \\ &- |A_k^{(j)}|^2 \mathrm{s}_k(\theta_k^{(j)}, r_k^{(j)}, \omega_{d_k}^{(j)})^H (\sigma^2\mathbf{I})^{-1} \mathrm{s}_k(\theta_k^{(j)}, r_k^{(j)}, \omega_{d_k}^{(j)}). \quad (19) \end{aligned}$$

where $(.)^*$ denotes complex conjugation, $(.)^H$ is the Hermitian transpose, and, $\Re(.)$ takes the real part of its complex argument. The partial derivative of (19) with respect to $A_k^{(j)}$ is given by

$$\frac{\partial \log l(Z_k|X_k^{(j)}, A_k^{(j)}, H_1)}{\partial A_k^{(j)}} = 2\mathrm{s}_k(\theta_k^{(j)}, r_k^{(j)}, \omega_{d_k}^{(j)})^H(\sigma^2\mathbf{I})^{-1}Z_k$$
$$- 2A_k^{(j)}\mathrm{s}_k(\theta_k^{(j)}, r_k^{(j)}, \omega_{d_k}^{(j)})^H(\sigma^2\mathbf{I})^{-1}\mathrm{s}_k(\theta_k^{(j)}, r_k^{(j)}, \omega_{d_k}^{(j)}). \quad (20)$$

The ML solution in (18) is found by setting (20) to zero, i.e.,

$$\frac{\partial \log l(Z_k|X_k^{(j)}, A_k^{(j)}, H_1)}{\partial A_k^{(j)}} = 0$$

which is satisfied at

$$\hat{A}_k^{(j)} = \frac{s_k(\theta_k^{(j)}, r_k^{(j)}, \omega_{d_k}^{(j)})^H(\sigma^2\mathbf{I})^{-1}Z_k}{s_k(\theta_k^{(j)}, r_k^{(j)}, \omega_{d_k}^{(j)})^H(\sigma^2\mathbf{I})^{-1}s_k(\theta_k^{(j)}, r_k^{(j)}, \omega_{d_k}^{(j)})}, \quad (21)$$

where $s_k(\theta_k^{(j)}, r_k^{(j)}, \omega_{d_k}^{(j)}) \in \mathbb{C}^{LN\times 1}$ is the noise free spatio-temporal vector found by evaluating (3) at $X_k^{(j)}$, $\sigma^2\mathbf{I} \in \mathbb{R}^{LN\times LN}$ is the noise covariance, $Z_k \in \mathbb{C}^{LN\times 1}$ corresponds to the measurements in the k^{th} CPI from the bearing-range-doppler bin of $X_k^{(j)}$ (i.e., $i_k^{(j)}$), and $\hat{A}_k^{(j)} \in \mathbb{C}^{1\times 1}$ is the estimated reflection coefficient.

Next, we substitute the ML estimate given in (21) together with $X_k^{(j)}$ in (8) and (15) so as to update the weights of the particles. Here, the term in the numerator of (21) provides coherent integration of $L \times N$ measurement samples.

C. Long time integration for detection

Now let us consider long time integration in order to decide on the object existence. The integration described above can integrate reflection coefficient from $k = 1$ to K and also take into account the estimated object state $\hat{X}_{1:K}$. We substitute the estimate of the kinematic parameters $\hat{X}_k$ found by using the SMC recursions and (16) in (21). This results with the ML estimate of the reflection coefficient $\hat{A}_k$ at $\hat{X}_k$, i.e.,

$$\hat{A}_k = \frac{s_k(\hat{\theta}_k, \hat{r}_k, \hat{\omega}_{d_k})^H(\sigma^2\mathbf{I})^{-1}Z_k}{s_k(\hat{\theta}_k, \hat{r}_k, \hat{\omega}_{d_k})^H(\sigma^2\mathbf{I})^{-1}s_k(\hat{\theta}_k, \hat{r}_k, \hat{\omega}_{d_k})}. \quad (22)$$

After obtaining $\hat{X}_k$ and $\hat{A}_k$ for $k = 1, \ldots, K$, we substitute these values in (the natural logarithm of) (10) and the likelihood ratio test in (6). The detection test is performed by

$$\log L(Z_{1:K}|\hat{X}_{1:K}, \hat{A}_{1:K}) \underset{H_0}{\overset{H_1}{\gtrless}} \log \mathcal{T}_k \quad (23)$$

Doing so provides coherent integration of $L \times N$ samples within a CPI, and, non-coherent integration across CPIs by taking into account $\hat{X}_{1:k}$. Here, $\log \mathcal{T}_k$ is a CFAR threshold for the log-likelihood ratio at the k^{th} step.

D. Constant false alarm rate threshold

The CFAR detection threshold $\mathcal{T}_k$ can be calculated as a function of the selected probability of false alarm P_{fa}. First, the likelihood of the noise only signal hypothesis in (9) is considered, which can be written as

$$p(Z_k|H_0) = \frac{1}{\pi k\sigma^2}\exp\left(-\frac{|Z_k|^2}{k\sigma^2}\right), \quad (24)$$

where Z_k is the k^{th} measurement. Second, the P_{fa} of a threshold test is given by the integration of $p(Z_k|H_0)$ when Z_k is over a threshold $\mathcal{T}_k$. In other words,

$$P_{fa} = \int_{\mathcal{T}_k}^{+\infty} p(Z_k|H_0)dZ_k = \frac{1}{\pi\sigma\sqrt{k}}\int_{\frac{\mathcal{T}_k}{\sqrt{k\sigma^2}}}^{+\infty}\exp\left(-|t|^2\right)dt$$
$$= \frac{1}{2\sigma\sqrt{\pi k}}\mathrm{erfc}\left(\frac{\mathcal{T}_k}{\sqrt{k\sigma^2}}\right), \quad (25)$$

where $\mathrm{erfc}(.)$ is the complementary error function (see, e.g., [1, Chp.6]). The detection threshold $\mathcal{T}_k$ at the k^{th} step of integration is calculated by

$$\mathcal{T}_k = \sqrt{k\sigma^2}\mathrm{erfc}\left(2\sigma\sqrt{\pi k}P_{fa}\right)^{-1}, \quad (26)$$

where $\mathrm{erfc}(.)^{-1}$ is the inverse complimentary error function. Given a false alarm rate, we now have an expression for the threshold value of the likelihood ratio test in (23).

IV. Example

In this section, we demonstrate the proposed detection approach through an example. We consider a scenario in which a single pulsed radar transmitter emits $N = 20$ linear frequency modulated (i.e., chirp) waveforms during a CPI. A single object with initial sate $X_0 = [1000\mathrm{m}, 1000\mathrm{m}, 60\mathrm{m/s}, 10\mathrm{m/s}]^T$ moves along an unknown trajectory across consecutive CPIs in accordance with the manoeuvring object dynamic model using (14). A co-located ULA receiver receives reflected versions of the transmitted pulses with the signal model in (5). Table I shows the parameters of the transmitted pulses used in this scenario. Based on these parameters, the bearing resolution can be found as $\Delta\theta = 5.1^\circ$ using $\Delta\theta = 2\sin^{-1}\left(\frac{0.891}{L}\right)$ (see, e.g., [10]) and the range resolution is found using the formula $\Delta r = c/2B$ as 150m. This is illustrated in Fig. 2, where the blue and red dashed lines indicate the bearing resolution and the range resolution boundaries, respectively. Furthermore, the velocity resolution ΔV given by $\frac{\lambda_c}{2NT}$ is found as 7.5m/s (or, equivalently the doppler resolution is $\Delta\omega = 4\pi f_c\frac{\Delta V}{c}T$ which evaluates as $0.314\mathrm{deg/s}$).

We apply the proposed algorithm for testing object existence on range-bearing and velocity bins with $M = 600$ particles initially selected as a 30×20 element uniform grid within the

TABLE I
TRANSMITTED SIGNAL PARAMETERS

Parameter	Value
Carrier frequency f_c	10GHz
Bandwidth B	1MHz
Pulse repetition interval T	100us
Coherent processing interval (CPI) Δ	0.1s
Number of pulses during a CPI N	20
Number of elements on ULA L	20

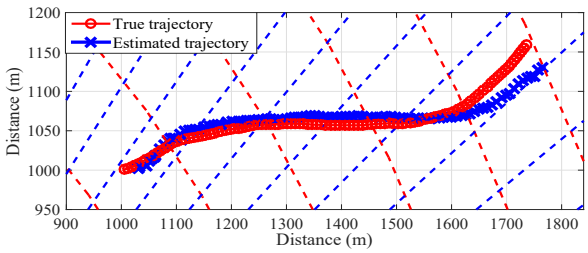

Fig. 2. Example scenario: A -2dB object follows a trajectory (red line) across range-bearing bins (separated by dashed lines). The proposed algorithm simultaneously estimates the trajectory (blue line) and performs a likelihood ratio test for detection.

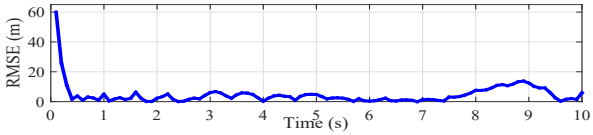

Fig. 3. RMSE of the trajectory estimate obtained by using the proposed algorithm in a typical experiment with a -2dB SNR manoeuvring object.

bin under test. We also use the proposed algorithm for long time integration spanning 10s with a CPI interval of 0.1s. The reflection coefficient is generated from a complex Gaussian density leading to an expected SNR of -2dB.

In this example, when the bin under test contains an object, the particles converge to the underlying state, the integrated value rises above the CFAR threshold, and the algorithm detects the object. When there is no object, the particles lead to a low likelihood value for object existence. A typical estimated trajectory is given in Fig. 2 (blue crossed line). The estimated trajectory is reasonably close to the true trajectory (red line). The root mean square error (RMSE) of this estimate is given in Fig. 3, which indicates a reasonably low value after only a few steps (equivalently, CPIs).

Now, let us consider pulse integration and detection using the proposed method. We generate 100 measurement sets for the scenario described (Fig. 2) and compare the long time-integration value obtained using the proposed algorithm with the best integration achievable if the true trajectory of the object was known. Fig. 4 illustrates the average long-time integration value (solid blue line) with ± 1 standard deviation bounds (dash dotted lines). The average integrated energy reaches a value of 56.5 at $t = 10$s which is very close to the best achievable result using the true object trajectory (dashed red line). Next, we consider the CFAR threshold (solid magenta line) calculated using (26) for $P_{fa} = 10^{-8}$. It is seen that in all simulations, the proposed algorithm yields an integration value that exceeds the CFAR threshold and reports object detection. Conventional integration methods, i.e., coherent (black line) and non-coherent (green line) integration fail to exceed the CFAR threshold and detect the object, in all experiments.

Next, we consider probability of the detection P_d as a function of time. We calculate this probability for the proposed algorithm empirically and depict in Fig. 5 in comparison with integration using the true object trajectory. The P_d for the proposed approach (solid blue line) increases over time, as

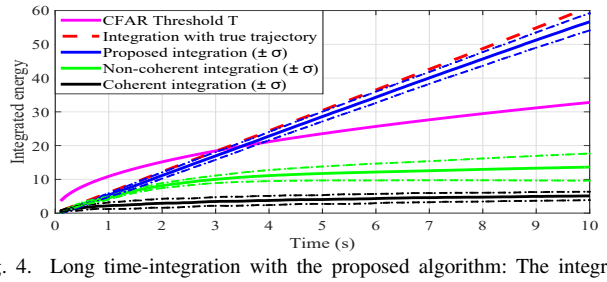

Fig. 4. Long time-integration with the proposed algorithm: The integrated value (solid blue line) versus time (dash-dotted lines indicate ± 1 standard deviation σ bounds), the best achievable integration using the true trajectory (dashed red line) and the CFAR threshold (solid magenta line). Conventional non-coherent (green line) and coherent (black line) integration fail to exceed the detection threshold. The results are averaged over 100 MC simulations.

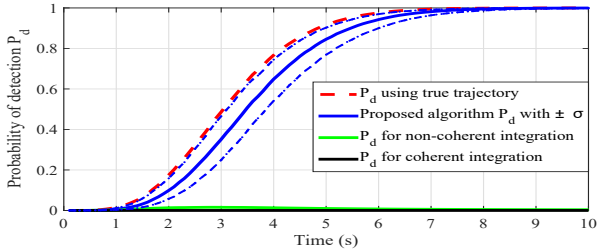

Fig. 5. Probability of detection (P_d) versus time in 100 MC simulations: The proposed long time integration algorithm (solid blue line and $\pm\sigma$ bounds rendered with blue dashed-lines), the best achievable P_d with integration using the complete knowledge of the true trajectory (red dashed line), non-coherent integration (green), and coherent integration (black).

more returns from the object is integrated. Note that the rate of increase is very similar to the P_d using true trajectory (red dashed line). It exceeds 0.5 after $t = 3.5$s and reaches almost 1 by $t = 7$s. Conventional non-coherent and coherent integrations yield zero P_d, in this scenario.

V. Conclusion

In this work, we proposed a joint pulse integration and trajectory estimation algorithm for detecting low SNR manoeuvring targets. This algorithm allows us to estimate the reflected pulse energy for each possible state and then add them using coherent integration during a CPI. We also use non-coherent integration across consecutive CPIs. This integration approach results in an integrated value close to the best achievable if we had full knowledge of the true trajectory. Future work includes further experimentation for the characterisation of the algorithm under different SNR working conditions.

Acknowledgement

This work was supported by the Engineering and Physical Sciences Research Council (EPSRC) grants EP/J015180/1 and EP/K014277/1, and the MOD University Defence Research Collaboration (UDRC) in Signal processing.

References

[1] M. Richards, *Fundamentals of Radar Signal Processing*, ser. Professional Engineering. Mcgraw-hill, 2005.

[2] X. Chen, J. Guan, N. Liu, and Y. He, "Maneuvering target detection via radon-fractional fourier transform-based long-time coherent integration," *IEEE Trans. Sig. Proc.*, vol. 62, no. 4, pp. 939–953, Feb 2014.

[3] Y. Boers and J. Driessen, "Multitarget particle filter track before detect application," *IEE Proceedings on Radar, Sonar and Navigation*, vol. 151, no. 6, pp. 351–357, Dec 2004.

[4] E. Grossi, M. Lops, and L. Venturino, "A novel dynamic programming algorithm for track-before-detect in radar systems," *IEEE Trans. Sig. Proc.*, vol. 61, no. 10, pp. 2608–2619, May 2013.

[5] M. Uney, B. Mulgrew, and D. Clark, "Maximum likelihood signal parameter estimation via track before detect," in *Sensor Signal Processing for Defence (SSPD), 2015*, Sept 2015, pp. 1–5.

[6] S. Davey, M. Rutten, and B. Cheung, "Using phase to improve track-before-detect," *IEEE Transactions on Aerospace and Electronic Systems*, vol. 48, no. 1, pp. 832–849, Jan 2012.

[7] O. Rabaste, C. Riche, and A. Lepoutre, "Long-time coherent integration for low snr target via particle filter in track-before-detect," in *15th Int. Conf. Information Fusion (FUSION)*, July 2012, pp. 127–134.

[8] S. Kay, *Fundamentals of Statistical Signal Processing: Detection theory*, ser. Prentice Hall Signal Processing Series. Prentice-Hall PTR, 1998.

[9] M. Arulampalam, S. Maskell, N. Gordon, and T. Clapp, "A tutorial on particle filters for online nonlinear/non-gaussian bayesian tracking," *IEEE Trans. Sig. Proc.*, vol. 50, no. 2, pp. 174–188, Feb 2002.

[10] H. L. Van Trees, *Optimum Array Processing*. John Wiley & Sons, Inc., 2002, ch. 2, Arrays and Spatial Filters, pp. 17–89.

A Modified Spectral Line Camera for Low Cost Anomaly Detection

Oscar JG Somsen. Netherlands Defense Academy. Den Helder

***Abstract*— Spectral cameras are a valuable tool for anomaly detection because the spectral information provides more opportunities than a monochrome or color camera to distinguish targets from the background. We are currently working on the adaptation of a spectral line camera for outdoor use and for anomaly detection. This requires consideration of spectral calibration, lighting variation and adaptation of detection algorithms. When effective, this may provide a low coast alternative for full spectral detection.**

Keywords—Spectral imaging, Anomaly detection

I. INTRODUCTION

Anomaly detection is an essential aspect of situational awareness and military actions. To prepare timely action it is important to leave sufficient time for classification and identification so anomaly detection should take place as early as possible when the anomaly is at a large distance and difficult to distinguish from the background. Spectral cameras are valuable for anomaly detection and often used for this purpose [1-6]. While a monochrome detector provides one value for each pixel in the image (intensity) and a color camera provides two additional values (to characterize color) a multi-spectral camera provides more than three values, typically with the help of color filters while a so called hyperspectral camera provides a large number of values for each pixel. The latter is achieved by separating the wavelengths with a prism or grating and detecting the intensity at each wavelength separately.

The additional information provided by a spectral camera is helpful for detection. Two objects with the same color may still be distinguished by considering the spectrum so that a spectral camera may not only be useful for detection but also for classification an identification. Also, the near-infrared can be included in a single camera. Furthermore, when an object is (much) smaller than the pixel size so that its signal is mixed with that of the background, the spectral information may help to detect it [1]. This makes the spectral camera especially suitable for anomaly detection. A range of algorithms is available to distinguish anomalies from the background [2-4] and research is also done for economic algorithms for example for unmanned vehicles [5,6]. Algorithms may depend on atmospheric disturbance or background [1] or on the type of application that the detector is used for [6].

Unfortunately, spectral cameras are costly, largely because two spatial and one spectral dimension have to be separated. A low cost alternative is formed by the line camera which images only a single line from the scenery. Spectral line cameras are typically used for industrial assembly line applications. However, they may be adapted for outdoor detection. A full spectral image may be obtained by scanning the camera across the scenery but a line camera may also be used to monitor specific line shaped areas such as the horizon where indeed many distant anomalies a situated.

In a previous publication we took the first steps in assembling the spectral line camera [7]. At present we extend this by improving techniques for wavelength calibration, focusing and adaptation to lighting conditions so that application under non standardized outdoor conditions becomes possible. With enhanced acquisition and analysis our final aim is to enhance capabilities of distinguishing objects from the background to eventually outperform a comparable color camera.

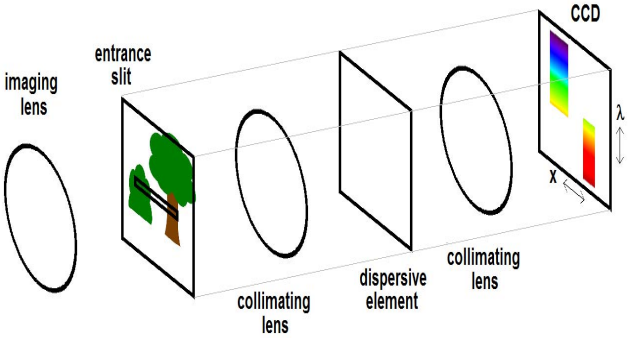

Figure 1: Schematic of a spectral imaging setup. Scenery is imaged to the entrance slit, spectrally separated and recorded by a CCD

II. METHODS

The operation of a spectral line camera is illustrated in figure 1. First part is the imaging lens which images the scenery onto the entrance slit of the so called spectral imager. The slit selects a line from the image. The imager itself is typically a tube with optics that images the entrance slit to the exit plane while simultaneously using a dispersive element such as a prism or grating to separate the wavelengths in the direction perpendicular to the line. The exit plane is a little beyond the end of the tube so that it can be projected onto the CCD-chip of a camera to record the image. The columns within the image correspond to the location on the imaged line while the rows within that column correspond to the wavelength that is being detected.

For our project we use the SpectroCam V10 spectral imagers supplied by SpectraPartners (400-1000 nm) combined with the WATEX 902h2 supreme camera (sensitivity 400 nm (50%) – 1000 nm (5%)). This low light monochrome camera was selected because only the intensity of each part of the spectral image should be detected. The camera can be attached to the spectral imager so that the spectral image is projected directly onto the CCD. For now we use a separate lens to image the scenery unto the entrance slit of the imager. A separate camera is attached to the assembly so that we can monitor which part of the scenery is being imaged. For the moment we are using a

978-1-5090-0326-6/16/$31.00 ©2016 IEEE

basic webcam for this purpose. The images of both cameras are captured and transferred to a PC for processing (currently with MATLAB).

Focusing the spectral camera is non-trivial because it images a small part of the scenery and the image is not easily recognizable. For indoor imaging a white board is placed a few meters away from the camera. A large dark sheet is placed in the center so that the dark and light part are visible in the spectral image. The imaging lens is positioned to increase sharpness. Next a dark vertical strip is moved horizontally until it becomes visible in the image. A vertical line is drawn that marks one side of the image. The same is done from the other side. Finally the strip is moved vertically on one side of the image until it becomes visible. A mark is drawn on the outside to indicate the height of the acquired line image. This is repeated on the other side (which should give almost the same height). These four lines indicate which part of scenery is imaged. Objects can be placed there for study and to further improve focusing.

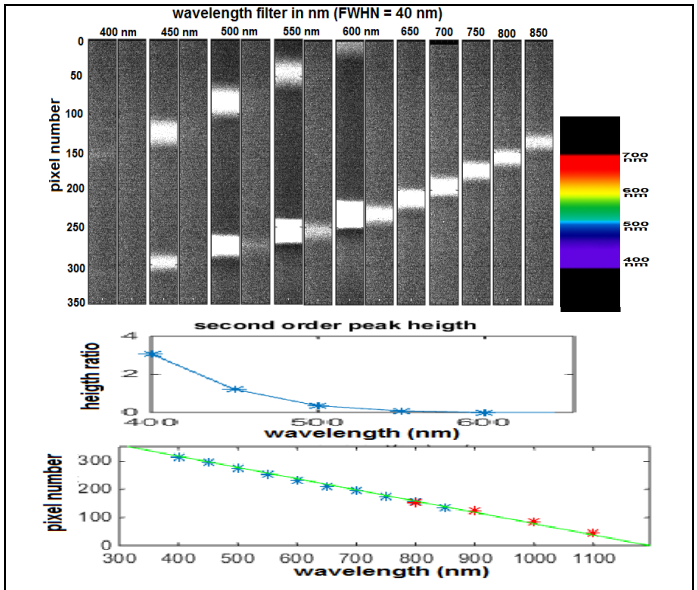

Figure 2: Spectral Calibration. Top: Series of images taken through narrow band interference filters (40 nm FWHM). For 400-600 nm a second series was taken at higher intensity. Visible spectrum shown for comparison. Bottom: Ratio of second and first order peak height and pixel number vs wavelength (blue) or double wavelength (second order: red)

III. RESULTS

Figure 1 shows our results for spectral calibration. A set of interference filters is placed one by one in front of the spectral imager and the image is recorded. No imaging lens is needed for this as long as the correct amount of light falls into the camera. As can be seen the images show a horizontal band at the specific wavelength. An picture of the visible spectrum is included for comparison. These images were also used for spectral focusing of the setup. The distance between imager and camera is modified to decrease recorded bandwidth. When the width is minimal the setup is spectrally in focus. Below 600 nm the intensity of the bands strongly decreased. Therefore we recorded a second set of images a higher light intensity for better analysis. Below 600 nm also a second band appears in the image. This is of second order passband of the dispersive grid and appears at double the actual wavelength and also with double the width. E.g. signal of 500 nm also appears at the location of 1000 nm. From this we can see that the imager may record signals from 300 nm up to 1200 nm (better than specified) provided that the camera is sufficiently sensitive at these wavelengths.

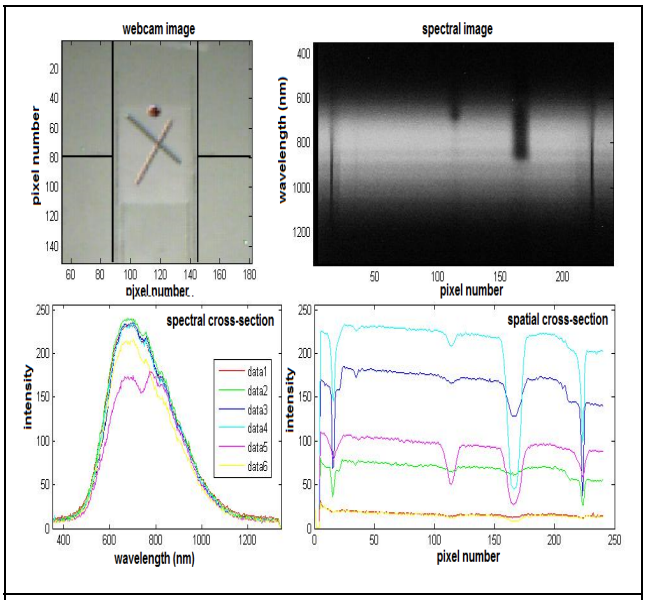

Figure 3: Spectral image. Top: webcam image (left) with slanted green and red line and T-shaped makers indicating the area that is acquired and (right) the actual spectral image plotted in gray scale (white is high intensity). Bottom: cross-sections at various regions in the image (left) and at wavelengths (right)

In the right window of figure 2 we quantified the spectral results. It shows a graph of the pixel number of the center of the recorded band vs the wavelength of the filter. This was obtained by fitting the spectra by hand with Gaussian bands. Also the results of the second order bands are included (at double the wavelength of the filter). The width of these bands was also double. The results follow a straight line although differences around 10 nm do appear. A linear fit is used for calibration of wavelength. This was checked during a further experiments by regularly placing filters in front of the camera. Based on that a small quadratic correction in the order of 10 nm was later included to improve the calibration [not shown]. The spectra of the interference filters can also be used to remove the second order contributions from recorded spectra. By comparing the heights of the spectra with two band we can determine the second order contribution that light between 400 and 500 nm produces in the 800-1000 nm region. This ratio is shown as a function of wavelength. Above 500 nm the contribution is small but below 450 nm is its more than 100%. Thus the second order contribution can be estimated for any recorded spectrum and subtracted.

A typical spectral image result is shown in figure 3. The target in this case is formed by a slanted green and red line printed on a white paper sheet. The top left image is recorded with the webcam. The two T-shaped markers have been added

to indicate the line area that is acquired by the spectral camera. Two black lines were also drawn on the background. These lines also appear in the spectral image on the left and right side. Of the two slanted lines in the webcam image only a narrow cross-section appears in the spectral image. The red line is dark in the blue part of the spectrum. The green line appears dark throughout the visible. The bottom panels in figure 3 show various spatial cross-sections (horizontal) taken from long to short wavelengths. The narrow lines can be used for spatial focusing: The distance between imaging lens and imager is modified until to reduce their width in the image. When the width is minimal the setup is spatially focused. The cross-section results indicate that at some wavelengths most of the light is absorbed but other areas also appear dark where only a small part of light is absorbed.

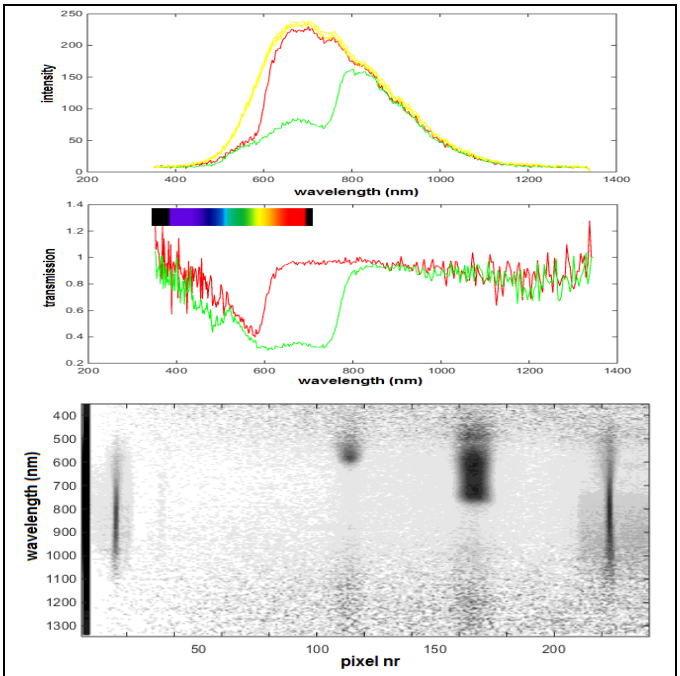

Figure 4: Spectral analysis of the image in figure 3. Top: spectra of the red and green band and three (white) background bands and transmission (band / background intensity) of red and green band. Right: transmission image (see text)

For a quantitative assessment we consider the spectra of the various 'objects' in the image of figure 3. For this we extracted the spectrum of the red- and green band (columns: 112-116 and 162-173 respectively) from the image and three white background spectra in between the two bands and on both sides. The resulting spectra are shown in figure 4. The three white spectra are very similar indicating a homogeneous background. The intensity is highest in the visible region (400-700 nm, although the blue side (400-500 nm) is quite weak) and the near infrared. This intensity spectrum is a combination of the spectrum of the light source, reflection by the background, transmission of the imager and sensitivity of the camera. The red band has lower intensity in the 500-600 nm region (blue-green). The green band has low intensity in all regions except the near infrared (> 800 nm) but mainly absorbs above 600 nm (red) which makes it indeed a dark green color.

The color is characterized not so much by the intensity at each wavelength but more the differences with the background. This is also how the human eye distinguished color. For this reason we also show the transmission spectra which are obtained by dividing the intensity of a band by the (averaged) spectrum of the white background. Also we can prepare a transmission image by dividing the spectral image in figure 3 by the background spectrum. This is shown at the bottom of figure 4 and does indeed provide more information than the original spectral image, especially in the low intensity regions (< 500 nm and > 1100 nm).

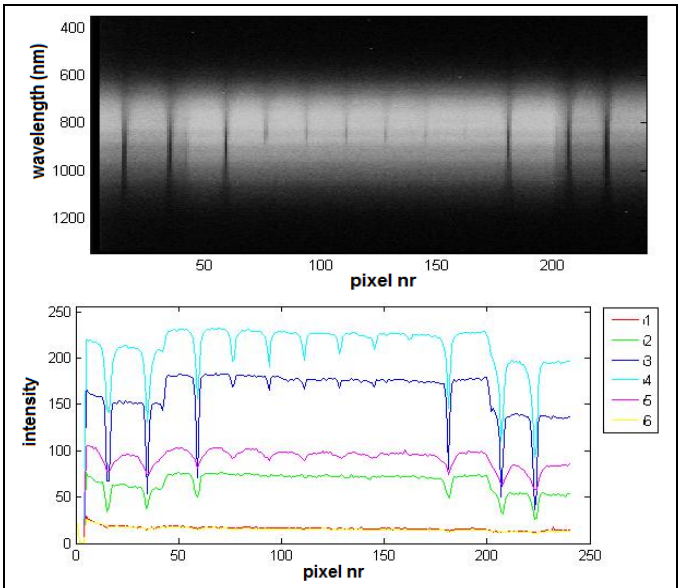

Figure 5: Resolution test. Left: Spectral image of a target with six green lines 0.1-0.8 mm in the center. Left: Spatial cross-sections from long to short wavelength.

Since we propose to use the camera mainly for resolution enhancement (to enable detection of small distant anomalies) we did a test of resolution performance. For this purpose we used six printed green lines on white paper varying in width from 0.1 to 0.8 mm placed at a distance of 5 m from the camera. This recording was also done inside with lighting condition adjusted for optimal results. While our camera is equipped with automatic exposure time adjustment, this does not work satisfactory because a camera intended for public use typically accepts saturation in part of the image while we need linear response throughout. Thus light intensity should be reduced until the entire image is unsaturated.

The resulting spectral image is shown in figure 5. The paper has two black lines on either side and four more black lines were drawn on the surrounding white board. These six black lines are clearly visible and dark at all wavelengths. The green lines are also clearly distinguished although the narrowest line has low contrast. Thus the obtained resolution is better than $0.1 \times 10^{-3}/5 = 2 \times 10^{-5}$ rad = 0.02 mrad and we should be able to further improve this. The distance between the outermost green lines was 95 mm, thus a pixel corresponds approximately to 1 mm so that all lines are of sub-pixel size.

Figure 5 also shows cross sections at various wavelengths (from long to short). In the widest line the absorption can be strong. At some wavelengths 50% of the light is absorbed. The

lines in the spectral image cannot become narrower since they are already of sub-pixel size. Instead, we can see in the cross-sections that the contrast decreases. In the narrowest line the intensity dip is no more than a few percent. Nevertheless it can still be distinguished even with the naked eye.

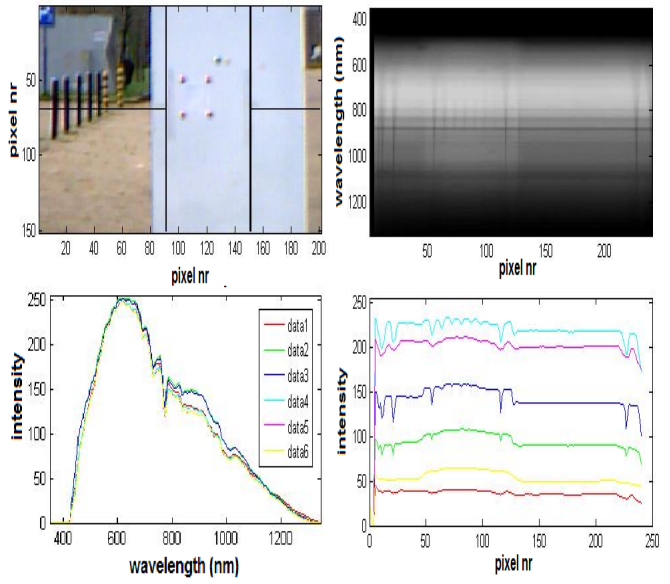

Figure 6: Outside resolution experiment. Resolution target (see figure 5) placed outside at 10 m from the camera. Panels as in figure 3 (webcam image, spectral image, spectral- and spatial cross-sections.

So far we have only considered cases that were done in the laboratory with carefully adjusted lighting conditions. However, we have equipped the imager with an adjustable iris so that it can also be used under variable lighting conditions. As a final test, we took the camera outside and placed the aforementioned resolution target at 10 m distance. The results are shown in figure 6. The focusing was unfortunately affected by moving the camera as can be seen by some blurring of the spectral image. Also we found that the camera still picks up stray light even though we already included shielding between imaging lens and imager. This becomes dominant when the iris diameter is strongly reduced and further stray light shielding will have to be introduced.

Nevertheless spectral image and the spatial cross-sections illustrate that the camera still manages to detect at least 5 of the six green lines in the resolution target. Also, the spectral cross-sections are interesting. Compared to inside lighting it extends considerably further, both to the short- and long wavelength regions indicating that the camera can indeed be applied for study at this wide range of wavelengths. The distance of 10 m may appear short compared to the intended purpose of detecting anomalies near the horizon. However an extension to larger distances and infinity should not be a major problem.

IV. Discussion

In this paper we investigated the possibility of adapting a spectral line camera for outdoor anomaly detection. We considered wavelength calibrating and characterize second order contributions. Next we considered acquisition of a target with colored lines. The background spectra are non-constant but drop off towards the blue and (infra)red end of the spectrum. While this appears natural to the eye we obtain a better detection by calculating the ratio of each spectrum to that of the background and presenting this on gray scale. The spectra of the target lines agreed with the colors while more characteristics can be obtained from the infrared region.

We characterized spatial resolution that can be obtained so far and found that we could easily distinguish an 0.1 mm target line at a distance of 5 m (0.02 mrad resolution). These target lines were significantly smaller than the pixel size. A further test could be to distinguish more than one target line (with different color) within a pixel. As a final test we also performed a resolution test outside to evaluate performance at higher light conditions. While the camera still suffers from stray light which needs to be remedied it still was able to achieve the same high resolution.

At present our camera still requires technical development, as described above, to fully use its potential. The achievements cannot yet be compared to those published for 2D spectral cameras [2, 5, 6]. As anomalies we have only been able to characterize lines against a homogeneous background. Although we were able to acquire and analyze outdoor images we have not yet been able to do this with natural scenery. A typical scene that we wish to explore is the detections of vessels near the horizon at sea or on flat land. However, with the required improvements the spectral line camera will become be suitable for the desired anomaly detection purpose and may provide an economic alternative for 2D specatral imagers.

References

[1] D Manolakis, D Marden & GA. Shaw. 2003. Hyperspectral Image Processing for Automatic Target Detection Applications. Lincoln Laboratory Journal 14(1).

[2] MT Eismann, AD Stocker & NM Nasrabadi. 2009. Automated hyperspectral cueing for civilian search and rescue. Proceedings of the IEEE 97(6): 1031-1055.

[3] CI Chang & M Hsueh. 2006. Characterization of anomaly detection in hyperspectral imagery. Sensor Review 26(2): 137-146.

[4] TE Smetek & KW Bauer. 2008. A comparison of multivariate outlier detection methods for finding hyperspectral anomalies. Military Operations Research 13(4): 19-43.

[5] Y Tarabalka, TV Haavardsholm, I Kasen, T Skauli. 2009. Real-time anomaly detection in hyperspectral images using multivariate normal mixture models and GPU processing. Journal of Real-Time Image Processing 4(3): 287-300.

[6] T Marshall & LN Perkins. 2015. Color outlier detection for search and rescue. Technical Report No. ECE-2015-01. Department of Electrical and Computer Engineering. Boston University

[7] OJG Somsen. 2016. Outdoor Anomaly Detection with a Spectroscopic Line Detector. Proceedings International Conference on Electronics, Information and Communication Engineering (ICEICE 2015): 1551-1555

Bistatic Micro-Doppler Characteristics of Precession Targets

Ai Xiaofeng[1,2], Zeng Yonghu[1], Zhao Feng[2], Liu Jin[2], Chen Jianan[2]
State Key Laboratory of Complex Electromagnetic Environment Effects on Electronics and Information System, Luoyang 471003,China
School of Electronic Science and Engineering, National University of Defense Technology Changsha 410073, China
Email: anxifu2001@163.com

***Abstract*—Micro-motion is one of the most important features for radar target recognition. Firstly, the bistatic micro-Doppler models corresponding to the bistatic scattering centers of the precession targets are derived. Then, The dynamic simulation method of the bistatic echo of the precession target is presented using the bistatic scattering coefficients obtained via electromagnetic calculations, and the bistatic scattering coefficients of the blunt-nosed biconical model are calculated using the multilevel fast multipole method. Finally, the theoretic analysis is verified by comparing the time-frequency distribution of the bistatic echo sequences with the theoretical bistatic micro-Doppler. This research is helpful for utilizing the bistatic micro-Doppler for feature extraction and recognition of spatial micro-motion targets.**

Keywords—bistatic radar; micro-motion; micro-Doppler; time-frequency analysis

I. INTRODUCTION

Micro-motion is one of the most important features for radar target recognition. V.C. Chen studied the radar target micro-motion and micro-Doppler phenomenon, and played an important role in the micro-Doppler effect analysis and micro-motion feature extraction [1]. Spatial targets maintain stability by rapid spinning and a precession occurs if the spinning is disturbed by an external interference. Ma Liang established the monostatic micro-Doppler mathematical model of precession warhead target based on sliding-type scattering center and verified it by dynamic measurement experiment in anechoic chamber, which described the micro-Doppler characteristic of the precession target more accurately [2].

In recent years, bistatic micro-Doppler characteristics analysis, feature extraction and recognition of micro-motion targets have gained worldwide attention. Ref.[3] analyzes the difference and connection between the bistatic and monostatic micro-Doppler briefly. The literature [4] discusses bistatic micro-Doppler of vibration target and expanded the study scope of micro-Doppler. Ref.[5] utilizes the mono-/bi-static micro-Doppler simultaneously for estimating the real radius of spinning target based on T/R-R bistatic radar configuration. In the literature [6], the bistatic micro-Doppler of the multistatic observation of the human target is obtained by the netted radar experimental system, which fully proves that the multistatic observation is beneficial to improve the performance of target recognition.

The monostatic micro-Doppler characteristic analysis and feature extraction of spatial micro-motional targets have been studied comprehensively [1], while bistatic micro-Doppler characteristic analysis is not enough, especially experimental data is little. In this sense, the bistatic micro-Doppler of spatial targets with precession micro-motion is studied and their characteristics are analyzed through dynamic simulation with the electromagnetic calculation data.

The remainder of this paper is organized as follows: Section 2 introduces the bistatic micro-Doppler model of the precession cone-shaped target, which is based on the bistatic sliding scattering center. Section 3 simulates the bistatic echo of precession target with electromagnetic calculation data and the time-frequency distribution validates the proposed model. Section 4 concludes this paper.

II. BISTATIC MICRO-DOPPLER MODEL OF PRECESSION TARGET

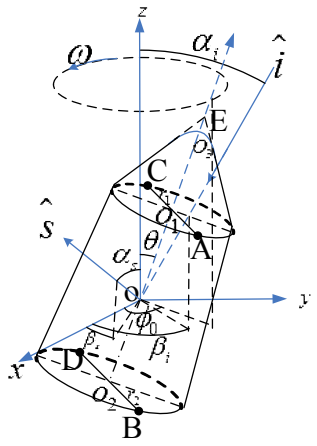

Fig. 1. Precession blunt-nosed biconical model

A blunt-nosed biconical model is shown in Fig.1. O is centroid and O_3 is the vertex. The cone radius above is r_1 and

This work is supported in part by the National Natural Science Foundation of China (No. 61401491, 61490692-2).

978-1-5090-0326-6/16/$31.00 ©2016 IEEE

the second cone radius is r_2. $|OO_3|$ is the distance between the centroid and vertex, $|OO_1|$ is the distance between the centroid and the center of first cone bottom and $|OO_2|$ is the distance between the centroid and the center of second cone bottom. The precession angle frequency is ω and the precession angle is defined as θ. *z*-axis is along the precession axis, and x-axis, y-axis and z-axis meet the right-hand law. The azimuth and pitching angles of incident vector $\hat{\mathbf{i}}$ are defined as β_i and α_i, and the scattering direction $\hat{\mathbf{s}}$ as β_s and α_s.

According to the geometrical diffraction theory [7], five bistatic scattering centers of the blunt-nosed biconical model are located at the intersection of the vertex, cone-cylinder edge and bottom edge and the plane that is constructed by the symmetry axis and the bisector of the bistatic angle, and they are labeled as A,B,C,D,E. These bistatic scattering centers changes with the target moving and bistatic geometric configuration. Especially, for the fixed bistatic radar, these bistatic scattering centers will slide on the edge continuously with the target precession. This motion is no longer a simple sinusoidal law and the bistatic micro-Doppler model is derived as follows.

Assuming the angle between the projection of the symmetry axis and the x-axis in the xoy plane is ϕ_0 at $t=0$, and then the angle θ_i between the incident vector and the symmetry axis can be expressed as

$$\cos\theta_i = \cos\theta\cos\alpha_i + \sin\theta\sin\alpha_i\cos(\omega t+\phi_0) \tag{1}$$

The angle θ_s between the scattering vector and the symmetry axis can be expressed as

$$\cos\theta_s = \cos\theta\cos\alpha_s + \sin\theta\sin\alpha_s\cos(\omega t+\phi_0-\beta_s) \tag{2}$$

The bistatic angle ψ satisfies

$$\cos(\psi) = \sin\alpha_i\sin\alpha_s\cos(\beta_i-\beta_s)+\cos\alpha_i\cos\alpha_s \tag{3}$$

According to the spatial geometry, the azimuth angle of the LOS of the receiver in the local ordinates [8], can be approximated by the following expression

$$\cos\varphi_s \approx \frac{\cos\psi-\cos\theta_i\cos\theta_s}{\sin\theta_i\sin\theta_s} \tag{4}$$

The bistatic scattering coefficients are decided by the angles (θ_i, θ_s, φ_s).

The bisector vector of the biststic angle can be expressed as

$$\overline{\mathbf{os}} = \frac{[\sin\alpha_i\cos\beta_i+\sin\alpha_s\cos\beta_s \quad \sin\alpha_i\sin\beta_i+\sin\alpha_s\sin\beta_s \quad \cos\alpha_i+\cos\alpha_s]}{\sqrt{2[1+\cos\alpha_i\cos\alpha_s+\sin\alpha_i\sin\alpha_s\cos(\beta_i-\beta_s)]}} \tag{5}$$

Let the angle between $\overline{\mathbf{os}}$ and z-axis is α, and the angle between the projection of $\overline{\mathbf{os}}$ in the xoy plane and the x-axis is ϕ_1, then

$$\begin{cases} \overline{\mathbf{os}} = [\sin\alpha\cos\phi_1 \quad \sin\alpha\sin\phi_1 \quad \cos\alpha]^T \\ \sin\alpha_i\cos\beta_i+\sin\alpha_s\cos\beta_s = 2\cos(\psi/2)\sin\alpha\cos\phi_1 \\ \sin\alpha_i\sin\beta_i+\sin\alpha_s\sin\beta_s = 2\cos(\psi/2)\sin\alpha\sin\phi_1 \\ \cos\alpha_i+\cos\alpha_s = 2\cos(\psi/2)\cos\alpha \end{cases} \tag{6}$$

According to the bistatic range and differential, the bistatic micro-Doppler of the scattering center E can be expressed as follows.

$$\begin{aligned} f_E(t) = |OO_3|\frac{f_0}{c}\omega\sin\theta[&-(\sin\alpha_i\cos\beta_i+\sin\alpha_s\cos\beta_s)\sin(\omega t+\phi_0) \\ &+(\sin\alpha_i\sin\beta_i+\sin\alpha_s\sin\beta_s)\cos(\omega t+\phi_0)] \end{aligned} \tag{7}$$

where f_0 is the carrier frequency and *c* is the light speed.

And the bistatic micro-Doppler model of the scattering centers A and C can be expressed as

$$\begin{aligned} f_{A,C}(t) = \frac{f_0}{c}\omega\sin\theta[&|OO_1|(\sin\alpha_i\cos\beta_i+\sin\alpha_s\cos\beta_s)\sin(\omega t+\phi_0) \\ &-|OO_1|(\sin\alpha_i\sin\beta_i+\sin\alpha_s\sin\beta_s)\cos(\omega t+\phi_0) \\ &-k(\cos\alpha_i+\cos\alpha_s)(\sin\alpha_i\cos\beta_i+\sin\alpha_s\cos\beta_s)\cos\theta\sin(\omega t+\phi_0) \\ &+k(\sin\alpha_i\sin\beta_i+\sin\alpha_s\sin\beta_s)(\cos\alpha_i+\cos\alpha_s)\cos\theta\cos(\omega t+\phi_0) \\ &+0.5k(\sin\alpha_i\sin\beta_i+\sin\alpha_s\sin\beta_s)^2\sin\theta\sin 2(\omega t+\phi_0) \\ &-0.5k(\sin\alpha_i\cos\beta_i+\sin\alpha_s\cos\beta_s)^2\sin\theta\sin 2(\omega t+\phi_0) \\ &+k(\sin\alpha_i\sin\beta_i+\sin\alpha_s\sin\beta_s)(\sin\alpha_i\cos\beta_i+\sin\alpha_s\cos\beta_s) \\ &\sin\theta\cos 2(\omega t+\phi_0)] \end{aligned} \tag{8}$$

where

$$k = \pm\frac{r_1}{2\cos(\psi/2)\sqrt{1-[\sin\alpha\sin\theta\cos(\omega t+\phi_0-\phi_1)+\cos\alpha\cos\theta]^2}}.$$

By substituting (6) into (7)(8), the bistatic micro-Doppler can be expressed as

$$f_E(t) = -2|OO_3|\frac{f_0}{c}\omega\cos\frac{\psi}{2}\sin\alpha\sin\theta\sin(\omega t+\phi_0-\phi_1) \tag{9}$$

$$\begin{aligned} f_{A,C}(t) = -2\frac{f_0}{c}\omega\cos\frac{\psi}{2}\sin\theta\sin\alpha\sin(\omega t+\phi_0-\phi_1) \\ \left(-|OO_1|\pm r_1\Delta(t)/\sqrt{1-\Delta^2(t)}\right) \end{aligned} \tag{10}$$

where $\Delta(t) = \sin\alpha\sin\theta\cos(\omega t+\phi_0-\phi_1)+\cos\alpha\cos\theta$.

Similarly, the bistatic micro-Doppler model of the scattering centers B and D can be expressed as

$$f_{B,D}(t)=\frac{2f_0}{c}\omega\cos\frac{\psi}{2}\sin\alpha\sin\theta\cos\left(\omega t+\phi_0-\phi_1\right)\left(-\left|OO_2\right|\mp r_2\Delta(t)\Big/\sqrt{1-\Delta^2(t)}\right) \tag{11}$$

According to the bistatic micro-Doppler expression of each scattering center, it can be found that the bistatic micro-Doppler is more complex compared with the monostatic case, which is induced by the incident vector and scattering vector. The bistatic micro-Doppler of the scattering center on the cone vertex is a sinusoidal, while the others are no longer sinusoidals. The bistatic micro-Dopplers are consistent with the monostatic micro-Dopplers observed on the bisector of bistatic angle [2], while the amplitude ratio is $\cos(\psi/2)$. Less parameter appears in the bistatic micro-Doppler model in (9)(10)(11) via simplification, and it should be beneficial to feature extraction.

III. DYNAMIC SIMULATION AND ANALYSIS

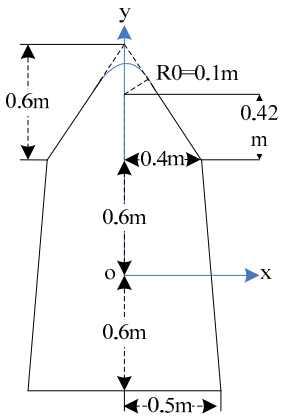

Fig. 2. blunt-nosed biconical model

A conductive blunt-nosed biconical model is constructed using FEKO software to verify the previously described analysis using the parameters shown in Fig.2. And the electromagnetic calculation parameters are listed in Table 1. A three-dimensional complex matrix $\mathbf{D}_{M\times N\times L}$ (M is the number in the incident direction, N and L represent the numbers in the scattering direction) is obtained with the multilevel fast multipole method. Here, M=901, N=901, L=901.

TABLE I. ELECTROMAGNETIC CALCULATION PARAMETERS

Parameter	Unit	Value
Frequency	GHz	8
Incident elevation	deg	0~180
Scattering elevation	deg	0~180
Scattering azimuth	deg	0~180
Angle interval	deg	0.2

The simulation parameters are as follows: $\theta=10°$, $\phi_0=\pi/2$ and $\omega=\pi$ rad/sec. The pulse repetition frequency is 400 Hz, and the observation time is 2 second. In the simulation scene, these angles (θ_i, θ_s and φ_s) change with the target's procession and are calculated via (1)(2)(4)in series. Then, the bistatic scattering coefficients that correspond to (θ_i, θ_s and φ_s) are extracted from the data matrix. Taking the classic short time Fourier transform (STFT) on them, the time-frequency distribution can be obtained as shown in Fig.3. And the dynamic simulation flow chart is described as follows.

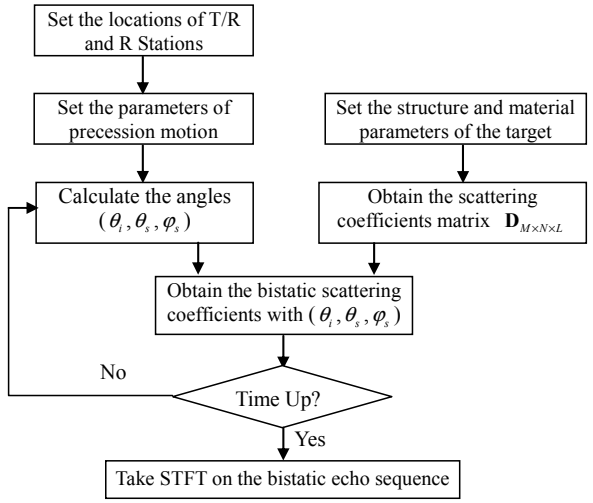

Fig. 3. Figure 1 Flow chart of the dynamic simulation

Fig.4 shows the time-frequency distribution with different parameters, and the dashed lines represent bistatic micro-Doppler calculated via (9)(10)(11). The traces of the peak values in the time-frequency images are consistent with the theoretical curves, which validates the bistatic micro-Doppler model. It also can be found that the bistatic scattering centers can be observed only on condition that both the incident and scattering fields can cover them. Bistatic scattering centers A, B and E can be observed in Fig.(a), while only scattering center A and B can be seen in Fig.4(b). Twice scintillation effects appear in Fig.4 (c) and (d) due to specular scattering. With the same incident direction, the bistatic micro-Doppler observed in different scattering directions are quite different, as shown in Fig.4 (a)(b)(c) and Fig.4 (d)(e)(f). Anyway, the simulation results show that the bistatic micro-Doppler usually can not completely reflect all the target scattering center, but the target feature can also be extracted with a priori information. What's more, more comprehensive information can be obtained by multistatic observations, and multiple-aspect fusion can get more conducive to the characteristics of target recognition.

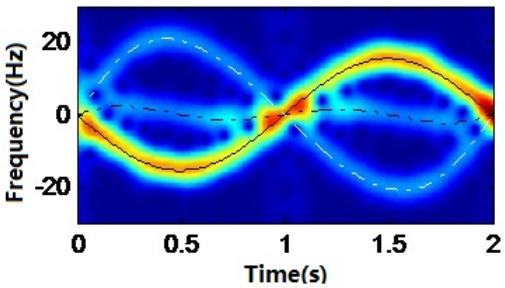

(a) $(\alpha_i,\beta_i,\alpha_s,\beta_s)=(45^\circ,0^\circ,20^\circ,0^\circ)$

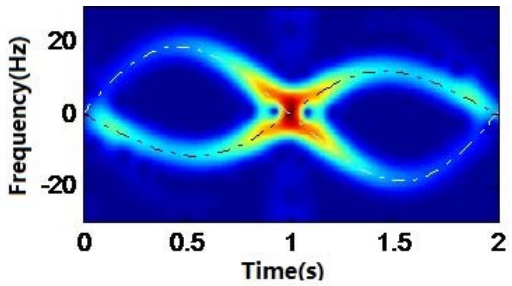

(b) $(\alpha_i, \beta_i, \alpha_s, \beta_s) = (45^\circ, 0^\circ, 100^\circ, 0^\circ)$

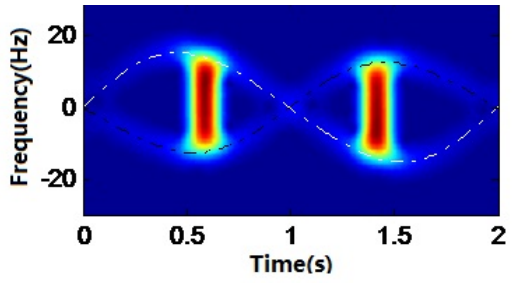

(c) $(\alpha_i, \beta_i, \alpha_s, \beta_s) = (45^\circ, 0^\circ, 120^\circ, 0^\circ)$

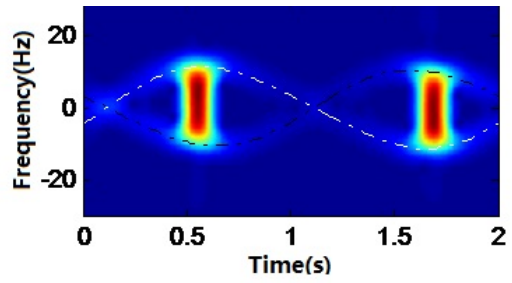

(d) $(\alpha_i, \beta_i, \alpha_s, \beta_s) = (135^\circ, 0^\circ, 40^\circ, 45^\circ)$

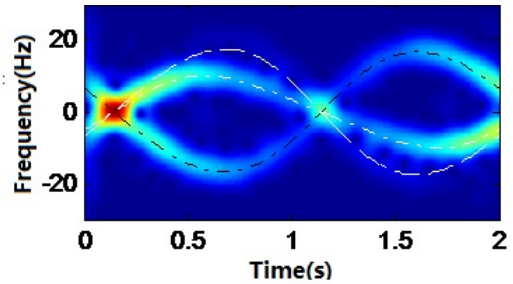

(e) $(\alpha_i, \beta_i, \alpha_s, \beta_s) = (135^\circ, 0^\circ, 80^\circ, 45^\circ)$

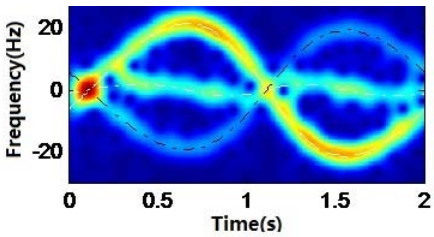

(f) $(\alpha_i, \beta_i, \alpha_s, \beta_s) = (135^\circ, 0^\circ, 140^\circ, 45^\circ)$

Fig. 4. Time-frequency distribution of precession blunt-nosed biconical model

IV. Conclusions

This paper deduced the bistatic micro-Doppler mode of precession target, which is validated by dynamic simulation via the bistatic scattering coefficients calculated by FEKO software. Although the bistatic micro-Doppler model can be simplified as the monostatic case, the complexity of bistatic geometry configurations leads to large differences in observed target characteristics, which bring new challenges in utilizing the bistatic micro-Doppler for feature extraction and recognition. Only part of the scattering centers can be observed with one observation aspect from the dynamic simulation, whereas the entirety of all scattering centers can be observed by multi-aspect observation. Future studies will consider a method for simultaneous extraction of the target size and precession angle via multiple receivers.

Acknowledgment

Ai Xiaofeng thanks Doctor Zou Xiaohai for electromagnetic calculation.

References

[1] V.C. Chen. The Micro-Doppler Effect in Radar. Norwood, MA: Artech House, 2011.

[2] MA Liang, LIU Jin and WANG Tao, et al, "Micro-Doppler characteristics of sliding-type scattering center on rotationally symmetric target," Science China: Information Sciences, vol. 54, pp. 1957-1967, September 2011.

[3] Chen V C, Rosiers des A and Lipps R. "Bistatic ISAR range-doppler image and resolution analysis," IEEE Radar Conference 2009, Rome, Italy, pp.1-5, May. 4-8, 2009.

[4] Zhu Ren-fei, Zhang Qun, Zhu Xiao-peng, et al. "Micro-Doppler analysis of vibrating target in Bistatic Radar," 2nd Asian-Pacific Conference on Synthetic Aperture Radar, Xi'an,China, pp.981-984, 2009.

[5] Ai Xiao-feng, Zou Xiao-hai, Yang Jian-hua, et al. "Feature extraction of rotating target based on bistatic micro-Doppler analysis," IEEE CIE Radar Conference 2011, Chengdu, China, pp.609-612, Oct. 24-27, 2011.

[6] Smith G E, Woodbridge K, Baker C J, et al. "Multistatic micro-Doppler radar signatures of personnel targets," IET signal processing, vol. 4, pp. 224-233, March,2010.

[7] Ai Xiaofeng, Zou Xiaohai, Li Yongzhen, et al. "Bistatic scattering centres of cone-shaped targets and target length estimation," Science China: Information Sciences, vol. 55, pp. 2888-2898, December 2012.

[8] Xiaofeng Ai, Xiaohai Zou, Jin Liu, et al. "Bistatic high range resolution profiles of precessing cone-shaped targets," IET Radar Sonar & Navigation, vol 7, pp.615-622, July, 2013.

High Dynamic Range Spectral Estimation for Incomplete Time Series

Mike Newman and David Harvey
Thales UK, Research & Technology
Reading, UK, RG2 0SB
Email: mike.newman@uk.thalesgroup.com

***Abstract*—Estimating complex spectra is a widespread operation in signal processing and in some applications a high dynamic range, which requires low sidelobe levels, is essential. For data with uniform sample spacing, weightings are commonly applied to Fourier transforms to suppress sidelobes, increasing dynamic range at the cost of some loss of spectral resolution. However, if a significant proportion of the samples lack data, conventional weightings suffer from high sidelobe levels. While a wide range of linear and non-linear techniques has been proposed to tackle this problem, they are not suitable in applications, such as Synthetic Aperture Radar (SAR), which require a high dynamic range. We propose criteria that allow optimal weights to be computed for any pattern of sample times. The resulting weighted Fourier transform has advantages of inexpensive computation, easily understood characteristics arising from its linearity, a position-independent impulse response and importantly the transform is phase preserving. Potential applications include wideband radar, where spectral gaps are needed for coexistence with other systems; multifunction radar, where imaging is interrupted by other tasks; and bistatic radar, where the spectrum of a transmitter of opportunity may be incomplete. In the context of SAR, high dynamic range, phase preserving spectral estimation supports post-processing such as interferometry and coherent change detection.**

I. Introduction

We consider the problem of estimating a high dynamic range, complex spectrum from an incomplete set of equally-spaced samples. The signals of interest are sums of complex sinusoids of unknown frequency: it is important that the spectral sidelobes of the strongest signals do not mask the weaker signals. Spectral estimation has a number of signal processing applications, but we were motivated in particular by Synthetic Aperture Radar (SAR) imaging, where dynamic ranges in excess of 60 dB are desirable. In radar applications, missing samples may represent times at which the radar did not operate or frequencies where no useful signal was received. In this paper, we will generally discuss transforming "time series" to the "frequency domain", but obviously the physical meaning of the domains has no mathematical significance.

One simple estimation technique (the "unweighted transform") replaces missing samples with zeros, then Fourier transforms. However, when more than a small number of samples are missing the resulting spectra are severely degraded by sidelobes. [1] considered interpolation to estimate the missing samples and [2] apodisation of the result to reduce sidelobes. However, such techniques are more effective at improving image appearance than in accurately reconstructing the regions degraded by sidelobes.

Compressive sensing techniques appear to address this problem and have been investigated (e.g. [3]). Non-parametric techniques, derived from adaptive beamforming have also been applied [4]. These techniques can improve the appearance of images, but they are non-linear: they may improve reconstruction accuracy for strong signals, but their treatment of small signals is difficult to analyse and they will have limited dynamic range.

For complete time series, optimal weightings for Fourier transforms have been studied extensively [5], but the techniques typically used in their design do not seem to have obvious generalisations to the missing sample case. It is natural to consider *ad hoc* generalisations of these weightings, for example applying a standard weighting across the entire data set or across each continuous section (Fig. 1). Such approaches typically split the mainlobe or give high sidelobe levels and generally perform poorly compared with either the unweighted transform or using only the longest section of continuous data.

Standard weightings have linear phase as a result of their symmetry, and with simple linear phase correction become "phase preserving". In the typical case where missing samples are distributed asymmetrically, phase preservation requires special consideration.

With incomplete time series, "Maximum Energy Windowing" selects weighting to maximise the energy in the mainlobe response: [6] investigated this but concluded that it was not effective for general patterns of missing samples. We follow a similar idea, but recognise that unconstrained optimisation can give weightings that suffer from problems such as very high noise-gain, mainlobe-splitting and uncontrolled phase variations. We propose constraints that allow effective weights to be found as the solution of a tractable optimisation problem. In the remainder of this paper we explain the choice of objective function and constraints, present results for some example sampling patterns, and describe potential applications of the techniques and the extensions that these would require.

II. Analysis

A. Data model

Consider a complex-valued signal $s(t)$ sampled at a monotonically increasing sequence of times t_j $(1 \leq j \leq N)$. We

978-1-5090-0326-6/16/$31.00 ©2016 IEEE

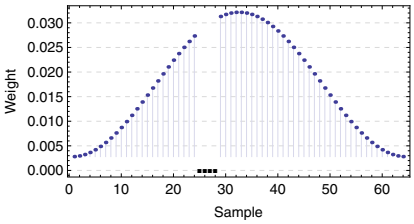

(a) Hamming weighting

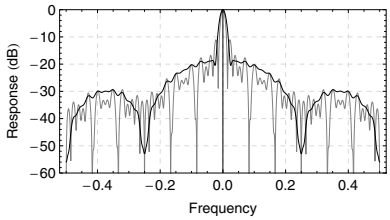

(b) Hamming response - note the high level of sidelobes

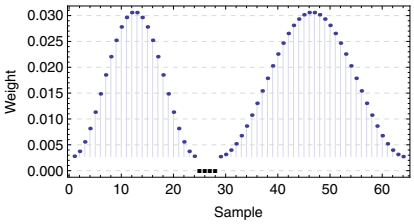

(c) Split Hamming weighting

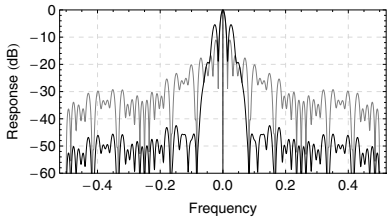

(d) Split Hamming response - note the split mainlobe

Fig. 1. Example of *ad hoc* weightings and transform response with 4 missing samples. Weighted and unweighted responses shown in black and grey respectively.

assume only that the input signal is band-limited, that is, its spectrum is zero beyond a known, finite limit.

B. Band-pass filters

We propose a spectral estimator implemented as a bank of band-pass filters. The centre frequencies of these filters could be chosen arbitrarily, but in general practice they will be equally spaced. Each band-pass filter is implemented by mixing the signal down to zero-frequency then applying the same low-pass filter. This implementation is effectively a weighted Discrete Fourier Transform (DFT). For suitable sets of sample times, this can be efficiently implemented with a Fast Fourier Transform (FFT). The output for the filter centred at frequency F is

$$\sum_{j=1}^{N} w_j s(t_j) e^{-2\pi i F(t_j - T)} \tag{1}$$

where T is the centre time, chosen to control the filter's phase as explained in II-E, and w_j are the filter weights. To simplify presentation, summation limits (always 1 to N) are omitted in the remainder of this paper.

C. Sidelobe suppression

For the filter centred at F, the response to a complex sinusoid of frequency f, phase ϕ is

$$S_F(f) = \sum_j w_j e^{2\pi i (f-F)(t_j - T) + i\phi}. \tag{2}$$

The power of the response, assuming w_i real, is given by

$$|S_F(f)|^2 = \sum_{j,k} w_j w_k e^{2\pi i (f-F)(t_j - t_k)}. \tag{3}$$

We define a pass-band ($|f-F| < \Delta f$) and a stop-band ($\Delta f < |f - F| < \Delta F$). To optimise the selectivity of the filter, we make the pass-band narrow and select the weights to minimise the stop-band power. As the signal is bandlimited, we can assume that any unwanted signals lie in the stop-band and have a uniform density over it.

Defining a real-symmetric square matrix $\mathbf{A}$ with elements

$$A_{jk} = 2\Delta F \operatorname{sinc} 2\Delta F(t_j - t_k) - 2\Delta f \operatorname{sinc} 2\Delta f(t_j - t_k) \tag{4}$$

and using $\mathbf{w}$ to represent the vector of weights, the stop-band power can be written as

$$\int_{-\Delta F}^{\Delta F} |S_F(f)|^2 \,\mathrm{d}f - \int_{-\Delta f}^{\Delta f} |S_F(f)|^2 \,\mathrm{d}f = \mathbf{w}^T \mathbf{A} \mathbf{w}. \tag{5}$$

To avoid the trivial minimum $\mathbf{w} = 0$, we constrain the coefficients to give constant gain for $f = F$

$$S_F(F) = \sum_j w_j = 1 \tag{6}$$

which can conveniently be written as $\mathbf{w}^T \mathbf{1} = 1$ where $\mathbf{1}$ is a vector of ones. The constrained optimisation problem is then

$$\text{minimise} \quad \mathbf{w}^T \mathbf{A} \mathbf{w} \quad \text{subject to} \quad \mathbf{w}^T \mathbf{1} = 1, \tag{7}$$

which is solved by $\mathbf{w} \propto \mathbf{A}^{-1}\mathbf{1}$.

D. Noise gain

In general, the weights that solve (7) are likely to have both positive and negative values. For a weight vector $\mathbf{w}$, the noise gain for a white noise input is given by $\mathbf{w}^T\mathbf{w}$, the sum of the squares of the weights. When $\mathbf{A}$ is poorly conditioned (some of its eigenvalues are small) $\mathbf{w}$ is likely to have interspersed positive and negative weights with large magnitude, giving a high noise gain.

The noise gain can be controlled by adding a constraint of the form

$$\mathbf{w}^T \mathbf{w} \leq G^2. \tag{8}$$

This new optimisation problem can be written in terms of Lagrange multipliers λ and μ as

$$\text{minimise} \quad \mathbf{w}^T\mathbf{A}\mathbf{w} + \lambda(\mathbf{w}^T\mathbf{1} - 1) + \mu(\mathbf{w}^T\mathbf{w} - G^2). \quad (9)$$

This has solution

$$\mathbf{w} \propto (\mathbf{A} + \mu\mathbf{I})^{-1}\mathbf{1} \quad (10)$$

where μ is chosen to ensure that constraint (8) is satisfied. This change regularises the optimisation problem, making poor conditioning of $\mathbf{A}$ tolerable.

E. Phase preservation

Consider an input sinusoid of frequency f and phase 0. Ideally the response

$$S_F(f) = \sum_j w_j e^{2\pi i(f-F)(t_j-T)} \quad (11)$$

should have the same phase. The phase is given by

$$\phi_F(f) = \operatorname{Im} \log S_F(f) \quad (12)$$

which ideally would be zero, independent of F. Except in the case with symmetric sampling, this is not possible, but we can constrain the choice of weights to limit the phase variation.

Consider the derivatives of $S_F(f)$ and $\phi_F(f)$ at $f = F$. Writing $\sigma_m = \sum_j w_j t_j^m$, we have

$$\begin{aligned} S_F(F) &= \sigma_0 \\ S'_F(F) &= (2\pi i)\left(\sigma_1 - \sigma_0 T\right) \\ S''_F(F) &= (2\pi i)^2\left(\sigma_2 + \sigma_0 T^2 - 2\sigma_1 T\right) \\ S'''_F(F) &= (2\pi i)^3\left(\sigma_3 - \sigma_0 T^3 + 3\sigma_1 T^2 - 3\sigma_2 T\right) \end{aligned} \quad (13)$$

$$\begin{aligned} \phi_F(F) &= 0 \\ \phi'_F(F) &= 2\pi\left(\tfrac{\sigma_1}{\sigma_0} - T\right) \\ \phi''_F(F) &= 0 \\ \phi'''_F(F) &= (2\pi)^3\left(-\tfrac{2\sigma_1^3}{\sigma_0^3} + \tfrac{3\sigma_2\sigma_1}{\sigma_0^2} - \tfrac{\sigma_3}{\sigma_0}\right). \end{aligned} \quad (14)$$

The first phase derivative $\phi'_F(F)$ can be zeroed by using a constraint $T = \frac{\sigma_1}{\sigma_0}$. In addition we apply a constraint on the third derivative

$$\left|-\tfrac{2\sigma_1^3}{\sigma_0^3} + \tfrac{3\sigma_2\sigma_1}{\sigma_0^2} - \tfrac{\sigma_3}{\sigma_0}\right| \le \Delta. \quad (15)$$

In this expression, the σ terms are all dependent on the weights, complicating the optimisation. However, this constraint can be simplified using the other equality constraints already mentioned and introducing a further constraint and a variable K, proportional to the curvature of the peak,

$$\sigma_0 = 1, \quad \sigma_1 = T, \quad \sigma_2 = K + T^2 \quad (16)$$

allowing the constraint (15) to be written as

$$\left|3KT + T^3 - \sigma_3\right| \le \Delta. \quad (17)$$

There are two obvious ways in which we might select values for T and K: either by finding the values that minimise the objective function or by treating them as parameters that we use to tune the resulting response. No problems have been observed in taking T to minimise the objective function. However, since K controls the curvature of the peak of the response, we have found that it is valuable to adjust it in conjunction with the pass-band limit Δf to trade resolution for sidelobe level; selecting K to minimise the objective function tends to give narrow peaks with high first sidelobes.

F. Optimisation problem

Collecting the constraints together, the problem becomes

$$\begin{aligned} \text{minimise} \quad & \mathbf{w}^T\mathbf{A}\mathbf{w} \quad \text{with respect to } \mathbf{w}, T \\ \text{subject to} \quad & \textstyle\sum_j w_j^2 \le G^2 \\ & \textstyle\sum_j w_j = 1 \\ & \textstyle\sum_j w_j t_j = T \\ & \textstyle\sum_j w_j t_j^2 = K + T^2 \\ & \left|3KT + T^3 - \textstyle\sum_j w_j t_j^3\right| \le \Delta. \end{aligned} \quad (18)$$

We will now outline a method of solution with $\Delta = 0$. Write $\mathbf{B} = \mathbf{A} + \mu\mathbf{I}$, define a matrix $\mathbf{T}_{jm} = t_j^m$, put the 4 constraints linear in $\mathbf{w}$ in vector form as $\mathbf{w}^T\mathbf{T} = \mathbf{f}(T)$ and introduce a length 4 vector of Lagrange multipliers $\mathbf{\Lambda}$. The augmented objective function is

$$\frac{1}{2}\mathbf{w}^T\mathbf{B}\mathbf{w} + (\mathbf{w}^T\mathbf{T} - \mathbf{f}(T))\mathbf{\Lambda} \quad (19)$$

Differentiating (19) with respect to $\mathbf{w}$ and zeroing gives

$$\mathbf{B}\mathbf{w} + \mathbf{T}\mathbf{\Lambda} = 0 \quad \text{and hence} \quad \mathbf{w} = -\mathbf{B}^{-1}\mathbf{T}\mathbf{\Lambda} \quad (20)$$

Differentiating (19) with respect to T and zeroing gives $\mathbf{f}'(T)\mathbf{\Lambda} = 0$ while substituting for $\mathbf{w}$ in the constraint gives

$$\mathbf{\Lambda}^T\mathbf{T}^T\mathbf{B}^{-1}\mathbf{T} = \mathbf{f}(T). \quad (21)$$

These can be solved to obtain T and $\mathbf{\Lambda}$, and hence $\mathbf{w}$. The solution process is iterated with different values μ as needed to satisfy the noise-gain constraint, $\mathbf{w}^T\mathbf{w} \le G^2$. As the constraints are cubic in T there can be up to 3 real solutions: obviously the one corresponding to the global minimum is selected. It is interesting to note that in the symmetrically-sampled case there will be a local minimum with symmetric weights but there may also be a pair of mirror-image weightings. The symmetric weighting may not be the global minimum.

III. Results

A. Parameter choice

A number of parameters of the optimisation remain to be specified: Δf and ΔF defining the lower and upper limits of the filter stop-band, and G, K and Δ constraining the noise gain, the peak width and the cubic phase respectively. We will not attempt rigorous analysis of these, but make a number of observations. The lower stop-band limit Δf has a natural size given approximately by the resolution of the unweighted response or some multiple of it: varying it while controlling the peak curvature with K can be effective at trading resolution for

TABLE I
PARAMETERS FOR EXAMPLES

	N	ΔF	Δf	K	G (dB)	Δ
Full	64	0.50	0.025	0.174	1.2	0.0
Composites	46	0.45	0.031	0.120	2.9	0.0
Notched	60	0.50	0.031	0.060	3.0	0.0
Banded	56	0.50	0.042	0.050	3.5	0.0
Extended	224	0.50	0.013	0.080	2.9	0.0

sidelobe level. The upper stop-band limit ΔF needs to be wide enough to pass the signals of interest and so it cannot be seen as a free parameter to be varied to optimise the performance: nevertheless it is interesting to note that reducing its value can significantly improve the response. The noise gain G allows a trade off between noise amplification and sidelobe level, with modest increases in noise amplification sometimes giving significant decreases in sidelobe level. We have not fully explored the benefits in relaxing the phase constraint Δ.

B. Examples

To illustrate an initial exploration, we show (Fig. 2) a number of artificial examples with missing samples and parameters chosen to show the potential of the technique. We have not attempted a detailed optimisation of the parameters or tried to systematically quantify performance. We use the unweighted transform as a performance reference (we are not aware of any alternative that performs better) and consider the following examples:

1) *Full*: with 64 equally-spaced samples
2) *Composites*: as *Full*, omitting prime-numbered samples
3) *Notched*: as *Full*, omitting samples 25-28
4) *Banded*: as *Full*, omitting samples 17-20, 49-50, 57-58
5) *Extended*: as *Banded*, stretched four times (256 samples omitting samples 65-80, 193-200, 225-232).

The first four examples, using a small number of sample points, illustrate both resolution and sidelobe level in a single graph. The last demonstrates that sidelobes can be controlled with larger data sets. The parameters for each example are given in Table I. The noise gain specified is measured relative to that of the unweighted transform.

IV. APPLICATIONS AND EXTENSIONS

We have described estimation of the spectrum of a time series, using a weighted Fourier transform. Clearly, a similar analysis applies to the inverse operation, estimation of a time series from a set of frequency samples. The technique might be used in radar systems which have missing frequencies due to interference, jamming or regulatory requirements that limit use of the frequency band. The missing frequencies might be specified in advance or identified automatically during operation. A multifunction radar might interleave operations, for example imaging and tracking, giving a time series with missing samples. Some bistatic radars rely on transmitters of opportunity, including communication transmitters, which can have spectra with nulls.

We have applied the technique in SAR image formation using airborne radar data with simulated frequency notches, showing that this allows the formation of high dynamic range images, free of unexpected artefacts. Further, as the techniques are linear and phase preserving, we have demonstrated that the resultant images are suitable for further processing, in particular, Coherent Change Detection (CCD). CCD is particularly useful for the detection of tracks on soft surfaces. These soft surfaces generally act as weak, distributed radar reflectors; high dynamic range images are therefore essential.

In SAR applications, it is common to use Taylor or similar weightings [7] which control sidelobes in two regions, near and far, with higher sidelobes allowed in the near region. The techniques described here could be extended to achieve this, by constraining the power in the near region and minimising the power in the far region. For SAR applications with time-varying interference, it would be useful to estimate two-dimensional spectra with arbitrary patterns of missing samples. In principle, the techniques described here have a natural extension to higher dimensions, but the number of samples involved will increase.

With a large number of samples N, the cost of constructing the matrix $\mathbf{A}$ and solving the related linear systems is at least $O(N^2)$. This cost can be reduced by constructing the matrix in a suitably factorised form.

In some applications the signal has a natural sampling, for example, estimating a range profile using a stepped frequency radar. In other cases, it is natural to think of the signal as a continuous function, sampled above the Nyquist rate: details of precise sample time should not matter. However, this is not directly matched to the missing sample model described in this paper and it would be useful to establish a rigorous connection between them.

V. CONCLUSION

We have demonstrated a practical scheme that, for arbitrary sampling patterns, selects optimal weights for FFT spectral estimation. For many sampling patterns it is possible to trade resolution for sidelobe level, giving useful combinations of resolution and dynamic range allowing suitable weightings to be determined for many signal processing applications.

The promising results obtained suggest it would be valuable to extend this work in the following ways:

1) Understand how the parameters affects performance and how their choice can be optimised and automated.
2) Make a formal connection between the technique and continuous signal theory, to apply it more effectively in cases that are not an exact fit to the current data model.
3) Reduce the computational complexity with N samples from $O(N^2)$, supporting its use with real-time identification of missing samples.

ACKNOWLEDGMENT

Application of the techniques described here to SAR imaging was studied as part of a study funded by Centre for Defence Enterprise (CDE24983).

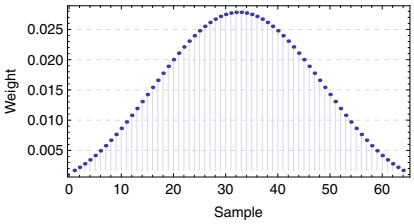

(a) *Full*: weighting

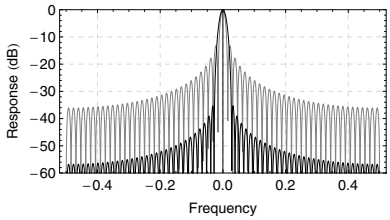

(b) *Full*: response

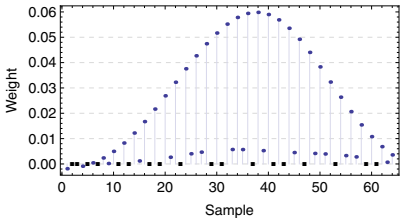

(c) *Composites*: weighting

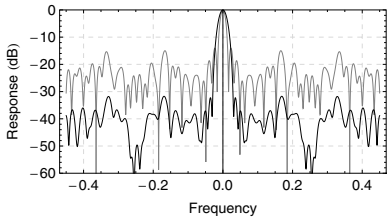

(d) *Composites*: response

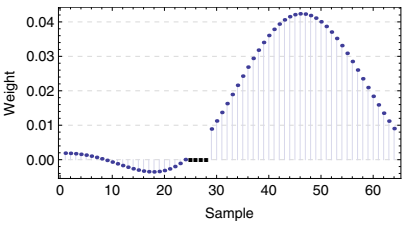

(e) *Notched*: weighting

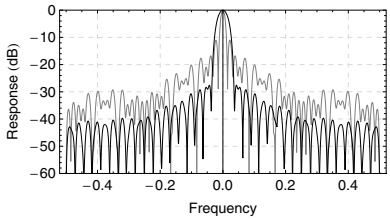

(f) *Notched*: response

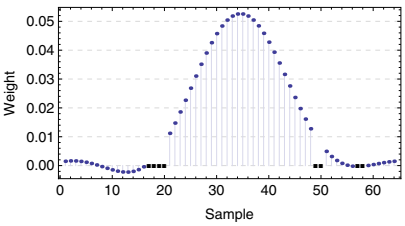

(g) *Banded*: weighting

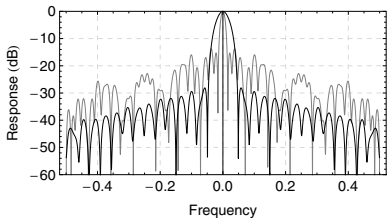

(h) *Banded*: response

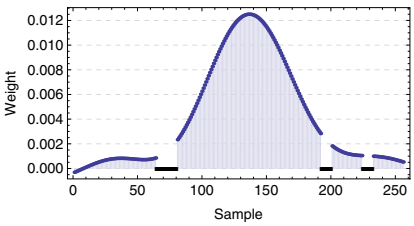

(i) *Extended*: weighting

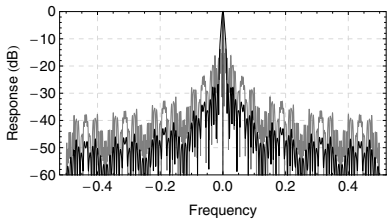

(j) *Extended*: response

Fig. 2. Weighting (missing samples marked on x-axis) and response (weighted and unweighted shown in black and grey respectively)

REFERENCES

[1] R. Tough, K. Ward, P. Shepherd, and H. Barn, "The Enhancement of Interrupted SAR Imagery," in *2006 Electromagnetic Remote Sensing Defence Technology Centre Conference*, 2006.

[2] R. Tough, K. Ward, and P. Shepherd, "Interrupted SAR operation and classification performance," in *2007 Electromagnetic Remote Sensing Defence Technology Centre Conference*, 2007.

[3] S. I. Kelly, G. Rilling, M. Davies, and B. Mulgrew, "Iterative image formation using fast (Re/Back)-projection for spotlight-mode SAR," in *2011 IEEE RadarCon (RADAR)*. IEEE, May 2011, pp. 835–840.

[4] D. Vu, L. Xu, M. Xue, and J. Li, "Nonparametric Missing Sample Spectral Analysis and Its Applications to Interrupted SAR," *IEEE Journal of Selected Topics in Signal Processing*, vol. 6, no. 1, pp. 1–14, Feb. 2012.

[5] F. J. Harris, "On the use of windows for harmonic analysis with the discrete Fourier transform," *Proceedings of the IEEE*, vol. 66, no. 1, pp. 51–83, Jan. 1978.

[6] F. M. Dickey, L. A. Romero, and A. W. Doerry, "SAR Window Functions: A Review and Analysis of the Notched Spectrum Problem," Sandia National Labs., Albuquerque, NM (US); Sandia National Labs., Livermore, CA (US), Tech. Rep., 2002.

[7] W. G. Carrara, R. M. Majewski, and R. S. Goodman, *Spotlight Synthetic Aperture Radar: Signal Processing Algorithms*. Boston: Artech House, Jul. 1995.

Tracking small UAVs using a Bernoulli filter

David R. Cormack
School of Engineering and Physical Sciences
Heriot-Watt University
Edinburgh
EH14 4AS, UK
drc9@hw.ac.uk

Daniel E. Clark
School of Engineering and Physical Sciences
Heriot-Watt University
Edinburgh
EH14 4AS, UK
D.E.Clark@hw.ac.uk

***Abstract*—The necessity for maintaining surveillance in airborne environments is ever growing. Criminals and terrorists are finding new and elaborate means of attack, and small UAVs such as quadcopters and hexacopters could be a possible threat. Their small size and agile movement will make them difficult to detect. This work aims to determine whether or not these small UAVs can be detected at short range using radar, and if so, track them over time using a suitable filter such as a Bernoulli filter.**

***Index Terms*—Bernoulli, filter, radar, UAV, quadcopter, hexacopter, tracking**

I. Introduction

Over the last five to ten years, there have been many new developments in the field of small UAVs, namely quadcopters and hexacopters [1]. Many of these units are readily available to hobbyists and amateur pilots from many electronics stores on the high street [2], [3]. With their small size and agile movement, these small UAVs could pose a major threat to defence and security [4]. A number of high-profile news stories have highlighted this potential threat, such as the spying on French landmarks, the inciting of a riot at a football match in Serbia, and the UAV that crashed into seating at the US Open tennis in New York in 2015 [5]–[7]. The major issue surrounding these small UAVs is their detectability using a reliable sensor. All of these threats could have been avoided, had the small UAVs been detected and tracked at an early stage, and countermeasures set in motion.

Radar tracking works best with a low density of targets, and each target moves with a predictable dynamical model. A number of environmental factors can have an effect on the accuracy of tracking, such as the weather conditions and the terrain that surrounds the target. These tracking methods may encounter various problems when either a very large number of detections are gained, or a limited number from a small target for example. These small targets may be difficult to distinguish from the clutter around them.

This paper will introduce one method of detecting and tracking a small UAV over time, using a radar developed by Leonardo, and a Bernoulli Gaussian Sum filter [8]. Section II will give a background to the small UAVs in question, including how detectable they should be to radar. Section III will discuss the test that was set up in order to gain real data sets for use in the tracking algorithm. Section IV introduces the Bernoulli filter and it's implementation, with the results shown in Section V.

II. Small UAVs/Quadcopters

The defence sector currently have an interest in detecting these small UAVs, and developing safe countermeasures to bring them down if they pose a threat [9]. As the UAVs are almost invisible to the naked eye at distances further than 300 metres, a suitable sensor such as radar will be required to detect them at further ranges. Their detectability is based on the theory of Radar Cross Section [10]. If all of the radar energy focused on the target was reflected evenly in all directions, the RCS would be equal to the target's cross-sectional area with respect to the radar. In this application however, some of the energy will be absorbed by the UAV's structure, and the reflected energy will not distribute evenly in all directions. The value of RCS will vary for a target, depending on factors such as the material it is made from, and its orientation with respect to the radar. The structure of a target can also amplify radar returns in particular detections if a signal bounces multiple times within the structure before being deflected away. Right angles are particularly good at doing this.

As an initial assessment of how detectable this type of UAV is, a widely-available quadcopter was placed inside a large anechoic chamber at Leonardo in Edinburgh, UK. The quadcopter that was used is the DJI Phantom II [11]. It is widely available in many electronics stores. The output RCS plot for this UAV is shown in Fig. 1. The structure of the quadcopter can be seen, with strong reflections coming from the front of the object as expected. In order to build up this RCS plot, the quadcopter was placed on top of a polystyrene plinth and rotated through 360° in increments of 0.25°. At each increment, a burst of RF energy is directed towards the UAV and the strength of the returned signal is measured. This intensity in dB is then plotted, with hotter colours indicating stronger returns. The testing was performed across a frequency range between 6 GHz and 18 GHz to give coverage in both the X-band and Ku-band. The RCS varying with the target's orientation to the radar, and the RCS varying with the transmission frequency can be seen in Fig. 2 and Fig. 3 respectively.

978-1-5090-0326-6/16/$31.00 ©2016 IEEE

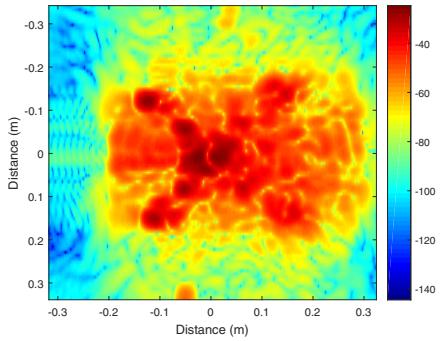

Fig. 1. RCS plot for DJI Phantom II Quadcopter. The RCS at each point on the plot has been frequency-averaged between 6 GHz and 18 GHz to give the result. The colour scale is given in dBsm. [12].

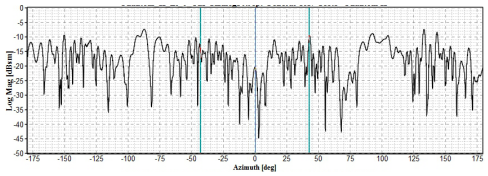

Fig. 2. RCS varying with target orientation. The green vertical lines show -45° and +45°. Again the resultant RCS has been frequency-averaged between 6 GHz and 18 GHz. [12].

It was found that the peak RCS value gained during this test was -24.6dBsm. Using this value in a form of the radar range equation,

$$\sqrt[4]{\frac{P_t \tau G^2 \sigma \lambda^2}{4\pi^3 k T_s L(SNR)}} \tag{1}$$

where P_t is the peak transmit power in Watts, τ is the pulse duration, G is the radar's gain, σ is the RCS of the target, λ is the radar's operating wavelength, k is the Boltzmann constant, T_s is the system noise temperature and L is the overall system loss in decibels, it is possible to determine the maximum range that the UAV should be detectable at. This was calculated to be approximately 1.2 kilometres using a specification of a variant of the PicoSAR radar which is designed and manufactured by Leonardo. More information about this radar will be given in Section III.

III. Trial Setup

In order to test the theory, a ground trial was set up to see if these small UAVs would be detectable using AEXAR, an experimental variant of the Leonardo PicoSAR radar [13]. It has

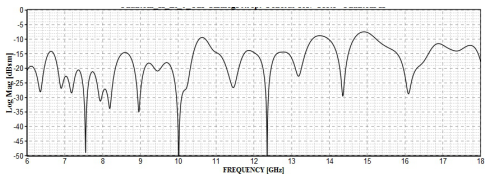

Fig. 3. RCS varying with radar transmission frequency. The turntable is kept static at 0° and the transmission frequency is varied to give the result. [12].

Fig. 4. DJI Inspire I Quadcopter [14].

Fig. 5. DJI S900 Hexacopter [15].

a larger array antenna than the standard radar, and transmits more power, making it more likely to detect smaller targets, especially at shorter ranges. The quadcopter and hexacopter used as a part of this trial are not the same as the one used in the anechoic chamber experiment, so the RCS result and the maximum range calculation can only be inferred as an estimate. The UAVs used can be seen in Figures 4 and 5. The data collected during this trial has then been used to develop the tracking method described later in Section IV.

The trial was performed on the 20th of August 2015, at East Fortune Airfield in East Lothian, GB. The radar was located inside the back of a van, which was positioned at the West end of the runway. The UAVs and their pilot were located 1 kilometre away at the other end of the runway. The radar was kept in its fixed position mode with a scan pattern between -6° and +6°. In order to gain a reading for the background noise and clutter in the surveillance region, a null test was performed. The UAVs were initially flown in a linear motion towards and away from the radar, in order to gain a maximum Doppler shift and to detect the target outside of the main beam clutter region. After completing these tests, the UAVs were flown in a much more random pattern inside the surveillance region, including circular paths and tight agile turns. A number of different radar waveforms were used, including changes to the Pulse Repetition Frequency and Chirp Bandwidth of the transmitted signal.

IV. Bernoulli Filtering

The Bernoulli filter, also known as a joint target-detection and tracking (JoTT) filter [16], can be seen to be the optimal Bayes filter for a single dynamic target that can randomly appear and disappear from the surveillance region in question. The key to this type of filtering is the inclusion of the existence binary random variable. The Bernoulli Random Finite Set formulation is different to that of traditional approaches, in that the state is treated as its own set, rather than a vector.

Further work has been carried out in the area of Bernoulli filtering, such as the use of data from multiple sensors to gain a more accurate track on a single target [17] and the development of a multi-Bernoulli filter to track multiple targets at the same time [18].

The model used in this simulation is that of the detector output measurements for point targets [8]. It is assumed that at each time step, the target in question will generate one single detection and all other detections at that time will be assumed to be false alarms. The number of false alarms will be assumed to be modelled by the Poisson distribution.

A. Filter Equations

1) Prediction: With the inclusion of the probability of existence variable, it must also be predicted and updated at each time step. The prediction equation can be shown to be,

$$q_{k|k-1} = p_b(1 - q_{k-1|k-1}) + p_s q_{k-1|k-1} \tag{2}$$

where p_b is the probability of target birth, and p_s is the probability of target survival. This equation effectively states that a predicted target could come from a new birth, such as a target entering the surveillance region, or from a target surviving from the previous time step. When implementing this kind of filter, it will be assumed that there will be a linear Gaussian transition, likelihood and birth model, with both the probability of detection and the probability of survival being constant. The birth model $b_{k|k-1}(x)$ is expressed as a single Gaussian of the form

$$w_{b,k}\mathcal{N}(x; m_{b,k}, Q_{b,k}) \tag{3}$$

where, $w_{b,k}$ represents the birth weights, $m_{b,k}$ represents the birth mean positions and $Q_{b,k}$ represents the birth position covariance. The prediction equations will follow those of a basic Kalman filter. The predicted spatial PDF can also be expressed as a Gaussian sum of the form,

$$s_{k|k-1}(x) = \sum_{i=1}^{N_{k|k-1}} w_{k|k-1}^{(i)}\mathcal{N}(x; m_{k|k-1}^{(i)}, P_{k|k-1}^{(i)}) \tag{4}$$

where $w_{k|k-1}^{(i)}$ are the predicted weights, $m_{k|k-1}^{(i)}$ are the predicted means and $P_{k|k-1}^{(i)}$ are the predicted covariances. The sum of the weights must be equal to 1.

2) Update: The update equations for this type of Bernoulli filter make use of those found in the update stage of a basic Kalman filter. The equation used for updating the probability of existence is,

$$q_{k|k} = \frac{1 - \Delta_k}{1 - q_{k|k-1}\Delta_k} q_{k|k-1} \tag{5}$$

where,

$$\Delta_k = p_D\left[1 - \sum_{z\in Z_k}\sum_{i=1}^{N_{k-1}} \frac{w_{k-1}^{(i)} q_k^{(i)}(z)}{\lambda_c c(z)}\right] \tag{6}$$

$c(z)$ is the density of the Poisson clutter process and λ_c is the clutter rate.

The update equation for the spatial PDF is,

$$s_{k|k}(x) = \frac{(1 - p_D)}{1 - \Delta_k} s_{k|k-1}(x) + \frac{p_D}{1 - \Delta_k} \times \sum_{z\in Z_k}\sum_{i=1}^{N_{k|k-1}} \frac{w_{k|k-1}^{(i)} q_k^{(i)}(z)}{\lambda_c c(z)} \mathcal{N}(x; m_{k|k}^{(i)}, P_{k|k}^{(i)}) \tag{7}$$

where,

$$q_k^{(i)}(z) = \mathcal{N}(z; \eta_{k|k-1}^{(i)}, S_{k|k-1}^{(i)}),$$

$$\eta_{k|k-1}^{(i)} = J m_{k|k-1}^{(i)},$$

$$S_{k|k-1}^{(i)} = J P_{k|k-1}^{(i)} J^T + R_k,$$

$$m_{k|k}^{(i)} = m_{k|k-1}^{(i)} + K_k^{(i)}(z - \eta_{k|k-1}^{(i)}),$$

$$P_{k|k}^{(i)} = P_{k|k-1}^{(i)} + K_k^{(i)} J P_{k|k-1}^{(i)},$$

$$K_k^{(i)} = P_{k|k-1}^{(i)} J^T [S_{k|k-1}^{(i)}]^{-1},$$

and J is a Jacobian matrix.

B. Practical Implementation

The probability of detection p_D was set to 0.99 and the probability of target birth p_b to 0.1. A large number of false alarms were being generated by trees swaying in the wind, and from vehicles moving around at the sides of the runway. The clutter rate λ_c has been set at 5 per scan. Due to the radar's position being stationary during the course of the trial, conventional methods of reducing the angular uncertainty such as were not available. The radar was operating at its higher bandwidth and digitiser rate, meaning that more samples were being taken in range, and therefore reducing the uncertainty in this dimension. Both of these uncertainties have been built into the model.

After the model has been declared and set up, the radar measurements are read in. For each detection gained, such as the one highlighted in Fig. 6, the radar will generate a target report that contains relevant information such as the target's position with respect to the radar. Data from each of these reports can be read in as a measurement z, which is stored in Z_k, where k is the time step. As the radar platform is kept stationary, it will be assumed that it is located at $(0, 0, 0)$ in the XYZ Cartesian space. Each measurement z will have the form,

$$[r, \dot{r}, \phi, \theta]'$$

where r is the range, $\dot{r}$ is the range rate, ϕ is the azimuthal angle and θ is the elevation angle. The state vector X will contain 6 elements and be defined as,

$$[x, \dot{x}, y, \dot{y}, z, \dot{z}]'$$

where x, y, z are the positions and $\dot{x}, \dot{y}, \dot{z}$ are the velocities with respect to each axis. One Gaussian birth term will be used at each time-step and will have a large initial covariance in order to deal with the high number of false alarms. In this scenario, no measurements are initially available at the first

time-step, so the initial probability of existence will be set at a value of 0.98.

The update stage has been built with the inclusion of the Extended Kalman filter equations to account for any non-linearities. Standard elimination and pruning schemes have been included to reduce the number of Gaussian components. The merging function uses the Hellinger distance [19] to determine whether Gaussians are located close enough to each other.

Algorithm 1 Prediction stage

given $\{w_{k-1}^{(i)}, m_{k-1}^{(i)}, P_{k-1}^{(i)}\}_{i=1}^{N_{k-1}}$

$q_{k-1|k-1} = q_{k|k-1}$

$q_{k|k-1} = p_b(1 - q_{k-1|k-1}) + (1 - p_D)q_{k-1|k-1}$

procedure PREDICTION FOR BIRTH TARGETS

$i = 0$

for $j = 1, \ldots, N_{\gamma,k}$ **do**

$i = i + 1$

$w_{k|k-1}^{(i)} = \frac{w_{\gamma,k}^{(j)} p_b (1 - q_{k-1|k-1})}{q_{k|k-1}}$

$m_{k|k-1}^{(i)} = m_{\gamma,k}^{(j)}$

$P_{k|k-1}^{(i)} = P_{\gamma,k}^{(j)}$

end for

end procedure

procedure PREDICTION FOR EXISTING TARGETS

for $j = 1, \ldots, N_{k-1}$ **do**

$i = i + 1$

$w_{k|k-1}^{(i)} = \frac{(1-p_D) q_{k-1|k-1}}{q_{k|k-1}} w_{k-1}^{(j)}$

$m_{k|k-1}^{(i)} = F_{k-1} m_{k-1}^{(j)}$

$P_{k|k-1}^{(i)} = F_{k-1} P_{k-1}^{(j)} F_{k-1}^T + Q_{k-1}$

end for

$N_{k|k-1} = i$

end procedure

V. RESULTS

As can be seen in Fig. 6, the small UAV is successfully detected by the radar. It appears as the bright flash to the right of the main beam clutter region. In Fig. 7 and Fig. 8, the + symbols represent the detections that have been recorded by the radar, and the o symbols represent the estimates that have been given out from the filter. It can be seen in Fig. 8 that the Bernoulli filter provides very accurate track on the target in the Y-axis. This variation in Y-coordinate correlates with the flight path taken by the pilot on the day, directly towards and away from the radar. The discontinuity that appears at approximately time step 80 is due to the UAV decelerating quickly to a hover. The filter coasts its estimates for a number of time steps and then detects the UAV again successfully. In both Fig. 7 and Fig. 8, there are a number of detections that do not lie on the target track. These are generated due to clutter such as trees swaying in the wind, and also targets that are not of interest, such as farm vehicles working in a nearby field.

Algorithm 2 Update stage

procedure UPDATE

for $j = 1, \ldots, N_{k|k-1}$ **do**

$m_k^{(j)} = m_{k|k-1}^{(j)}$

$P_k^{(j)} = P_{k|k-1}^{(j)}$

end for

for $z \in Z_k$ **do**

for $j = 1, \ldots, N_{k|k-1}$ **do**

$K_k^{(j)} = P_{k|k-1}^{(j)} J^T (S_{k|k-1}^{(j)})^{-1}$

$m_k^{(\ell N_{k|k-1}+j)} = m_{k|k-1}^{(j)} + K_k^{(j)} (z - \eta_{k|k-1}^{(j)})$

$P_k^{(\ell N_{k|k-1}+j)} = P_{k|k-1}^{(j)} - K_k^{(j)} J (P_{k|k-1}^{(j)})^T$

$\hat{w}_k^{(j)} = w_{k|k-1}^{(j)} \mathcal{N}(z; \eta_{k|k-1}^{(j)}, S_{k|k-1}^{(j)})$

end for

end for

if $Z_k = \emptyset$ **then**

$\Delta_k = p_D$

$q_{k|k} = \frac{1-\Delta_k}{1-q_{k|k-1}\Delta_k} q_{k|k-1}$

for $j = 1, \ldots, N_{k|k-1}$ **do**

$w_k^{(j)} = \frac{(1-p_D)}{1-\Delta_k} w_{k|k-1}^{(j)}$

end for

else

$\Delta_k = p_D (1 - \sum_{i=1}^{N_{k|k-1}} \hat{w}_k)$

$q_{k|k} = \frac{1-\Delta_k}{1-q_{k|k-1}\Delta_k} q_{k|k-1}$

$n = N_{k|k-1}$

for $j = 1, \ldots, N_{k|k-1}$ **do**

$w_k^{(j)} = \frac{(1-p_D)}{1-\Delta_k} w_{k|k-1}^{(j)}$

end for

for $z \in Z_k$ **do**

for $j = 1, \ldots, N_{k|k-1}$ **do**

$n = n + 1$

$w_k^{(n)} = \frac{p_D}{1-\Delta_k} \hat{w}_k^{(\ell N_{k|k-1}+j)}$

end for

end for

end if

$N_k = \ell N_{k|k-1} + N_{k|k-1}$

end procedure

output $\{w_k^{(i)}, m_k^{(i)}, P_k^{(i)}\}_{i=1}^{N_k}$

VI. CONCLUSIONS

The Bernoulli Gaussian Sum filter has successfully given sensible estimates of the UAVs position and tracked it over time. The filter has dealt with the false alarms that are present at close range.

VII. ACKNOWLEDGMENTS

The authors thank Dr. David Greig, Dr. Anthony Swain and Andrew Glass in the Systems Engineering department at Leonardo, Edinburgh for their time and contribution to this project. This includes the funding to carry out the radar trial in the field, the use of the AEXAR radar, and the radar data used to develop the Bernoulli filter.

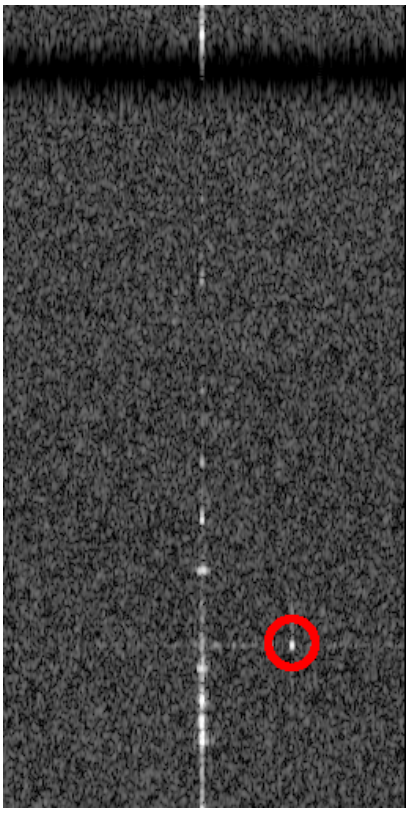

Fig. 6. Detection highlighted on range/Doppler map [12].

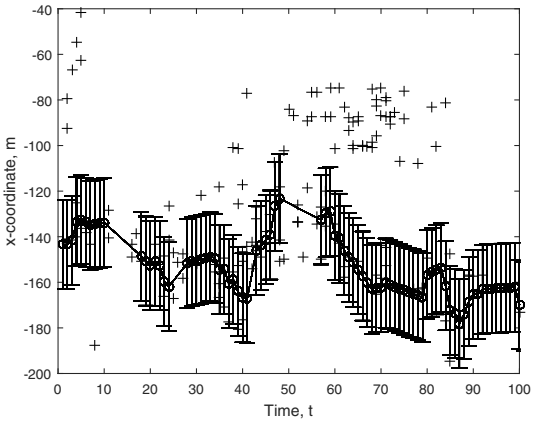

Fig. 7. X coordinates of detections and estimates plotted over time. [12].

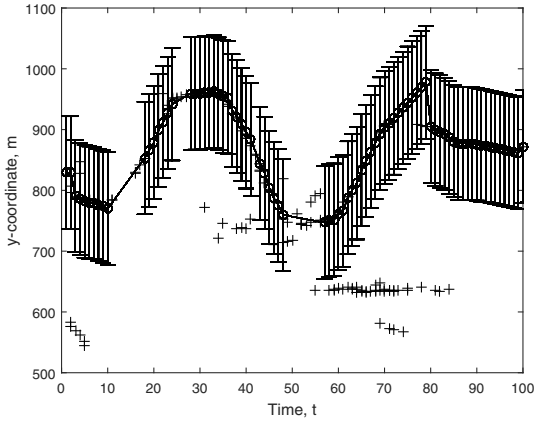

Fig. 8. Y coordinates of detections and estimates plotted over time. [12].

REFERENCES

[1] DroneBuff, "What's the best quadcopter?" November 2015. [Online]. Available: http://dronebuff.com/whats-best-quadcopter/

[2] Maplin, "Radio Controlled Drones — Maplin," March 2016. [Online]. Available: http://www.maplin.co.uk/c/gadgets-toys-and-hobbies/radio-controlled/radio-controlled-drones

[3] Menkind, "Drones, Quadcopters and Quadrotor — Menkind," March 2016. [Online]. Available: http://www.menkind.co.uk/remote-control/drones-quadcopters

[4] BBC, "Warning over drones use by terrorists," January 2016. [Online]. Available: http://www.bbc.co.uk/news/technology-35280402

[5] D. Mail, "New terror alert for France after 'at least' five drones are spotted flying above paris landmarks including Eiffel Tower and the US Embassy," February 2015. [Online]. Available: http://www.dailymail.co.uk/news/article-2966482/New-terror-alert-France-five-drones-spotted-flying-Paris-landmarks-including-Eiffel-Tower-embassy.html

[6] BBC, "Serbia v Albania: Drones, flags and violence in abandoned match," October 2014. [Online]. Available: http://www.bbc.co.uk/sport/football/29624259

[7] ——, "US Open: New York teacher arrested after drone crashes into stands," September 2015. [Online]. Available: http://www.bbc.co.uk/news/world-us-canada-34155773

[8] B. Ristic, B. Vo, B. Vo, and A. Farina, "A Tutorial on Bernoulli filters: Theory, Implementations and Applications," *IEEE Transactions on Signal Processing*, vol. 61, pp. 3406–3430, 2013.

[9] Finmeccanica, "Finmeccanica - Selex ES launches Falcon Shield Counter-UAV system," September 2015. [Online]. Available: http://www.finmeccanica.co.uk/-/falcon-shield-launch

[10] RadarTutorialEU, "Radar Basics - Radar Cross Section," March 2016. [Online]. Available: http://www.radartutorial.eu/01.basics/Radar%20Cross%20Section.en.html

[11] DJI, "Phantom 2 - The Spirit of Flight — DJI," February 2016. [Online]. Available: http://www.dji.com/product/phantom-2

[12] D. R. Cormack, "Tracking of Difficult Targets in a Challenging Environment," Master's thesis, School of Engineering and Physical Sciences, Heriot-Watt University, 2015.

[13] Finmeccanica, "PicoSAR - Detail," March 2016. [Online]. Available: http://www.finmeccanica.com/en/-/picosar-1

[14] D. Wiki, "Inspire 1 - DJI Wiki," August 2015. [Online]. Available: http://wiki.dji.com/en/index.php/Inspire-1

[15] DJI, "Spreading Wings S900 - Highly portable, powerful aerial system for the demanding filmmaker — DJI," August 2015. [Online]. Available: https://www.dji.com/product/spreading-wings-s900

[16] R. P. Mahler, "Statistical Multisource-Multitarget Information Fusion," 2007.

[17] B. Vo, C. See, N. Ma, and W. Ng, "Multi-Sensor Joint Detection and Tracking with the Bernoulli filter," *IEEE Transactions on Aerospace and Electronic Systems*, vol. 48, pp. 1385–1402, 2012.

[18] B. Vo, B. Vo, R. Hoseinnezhad, and R. Mahler, "Robust Multi-Bernoulli Filtering," *IEEE Journal of Selected Topics in Signal Processing*, vol. 7, pp. 399–409, 2013.

[19] S. Nagappa, D. Clark, and R. Mahler, "Incorporating Track Uncertainty into the OSPA Metric," in *2011 Proceedings of the 14th International Conference on Information Fusion (FUSION)*, 2011.

ROBUST UNMIXING ALGORITHMS FOR HYPERSPECTRAL IMAGERY

Abderrahim Halimi[(1)], *Yoann Altmann*[(1)], *Gerald S. Buller*[(1)], *Steve McLaughlin*[(1)],
William Oxford[(2)], Damien Clarke[(2)], and Jonathan Piper[(2)]

[(1)] School of Engineering and Physical Sciences, Heriot-Watt University, Edinburgh U.K.
[(2)] Defence Science and Technology Laboratory, Porton Down, Salisbury, Wiltshire U.K.

ABSTRACT

The linear mixture model (LMM) assumes a hyperspectral pixel spectrum to be a linear combination of endmember spectra corrupted by additive noise. This model is widely used for spectral unmixing mainly because of its simplicity. However, the LMM can be inappropriate in presence of nonlinear effects, endmember variability or outliers. This paper presents a comparison between recent robust hyperspectral unmixing algorithms. The mixture models are first introduced followed by the description of their associated unmixing algorithms. The algorithms are then analyzed when considering a real image acquired over the region of Porton Down in England. The results discuss the behavior of each algorithm to unmix these data and compare their ability to detect the natural or man-made outliers in the scene. The obtained results highlight the potential of the studied mixture models to overcome the current limitations of the LMM.

Index Terms— Hyperspectral imagery, robust unmixing, Bayesian estimation, optimization, MCMC, anomaly detection and analysis

I. INTRODUCTION

Spectral unmixing (SU) of hyperspectral images (HSI) has been the subject of intensive interest over the last two decades. It consists of distinguishing the materials (endmembers) and quantifying their proportions (abundances) in each pixel of an observed image. The linear mixture model (LMM) is the widely used model for SU mainly because of its simplicity. However, this model can be inappropriate for some hyperspectral scenarios, namely in the presence of a nonlinearity (NL) such as multiple scattering [1], [2], endmember variability (EV) [3]–[5], or outliers (rarely represented materials, faulty detector,...). These effects emphasize the need for robust HS unmixing strategies able to deal with these mismodelling effects [6]–[8].

This paper compares three recent mixture models accounting for the presence of residual components (RC) or outliers. The three models assume that the observed pixels result from a convex combination of the endmembers of the scene, corrupted by an additive term modeling deviations from the classical LMM. This residual term has different characteristics depending on the studied phenomenon. For instance, [6] considers a spatially-sparse positive RC suitable for the capture of nonlinearity effects, [7] proposes a spatial-spectral correlated support (i.e., the set of spatial/spectral locations where anomalies occur) for the RC and [8] presents a spatial-spectral smooth RC to better approximate endmember variability and/or nonlinearity. The properties of these models will be further discussed in Section II.

Estimating the abundances and the RC associated with these mixture models is an ill-posed problem that requires the introduction of prior knowledge regarding these parameters. From a Bayesian perspective, this goal can be achieved by assigning them appropriate prior distributions. From an optimization perspective, the prior knowledge can be seen as additional regularization terms. The two approaches (i.e., Bayesian and optimization formulations) will be further discussed in the paper when describing the three models. Indeed, the authors of [6] consider a coordinate descent algorithm (CDA) to minimize a regularized similarity measure. Two distance measures have been considered corresponding to the squared Euclidean distance (SED), and the Kullback-Leibler divergence (KLD). The regularization terms include the positivity of the RC and the spatial sparsity of the energies of the RC by considering an ℓ_{21} mixed norm. This norm is known as a collaborative regularization since it uses the information of the residuals in all the spectral bands to promote spatial group-sparsity. The authors of [7] adopt a Bayesian approach and define an anomaly prior model to capture the spatial/spectral structure of the potential RC. They then use a Markov chain Monte-Carlo (MCMC) method to approximate appropriate Bayesian estimators (i.e., minimum mean squares estimator (MMSE) and maximum a posteriori (MAP) estimator) [9]. The Bayesian model considers a Gaussian likelihood (related to the noise statistics) while assuming band-dependent noise variance. The model also enforces a spatial-spectral correlation on the RC support by considering a 3D Markov random fields model [5], [10]. In [8], the authors adopt a Bayesian approach while they approximate the MAP estimator by maximizing the resulting posterior distribution using a CDA. As in [7], [11], [12], the Bayesian model considers centered Gaussian noise with band-dependent variance. This model enforces a spectral smoothness on the RC by considering Gaussian process [13] and spatial correlation between the RC energies by using a gamma Markov random fields prior [14], [15]. The studied models and estimation algorithms are analyzed using a hyperspectral image acquired over Porton Down in England. The results obtained are very promising and show the potential of the studied mixture models to overcome the limitations of the LMM.

The paper is structured as follows. Section II introduces the considered mixture models to deal with the RC. The optimization formulation, the hierarchical Bayesian models and the estimation algorithms associated with each model are described in Section III. Section IV shows results obtained using a real hyperspectral image. Conclusions and future work are finally reported in Section V.

II. MIXTURE MODELS

The robust formulations considered are based on a residual component analysis model [16] that is expressed as the sum of a linear model and a residual term. The general observation model for the $(L \times 1)$ pixel spectrum $\boldsymbol{y}_n$ is given by

$$\begin{aligned} \boldsymbol{y}_n &= \sum_{r=1}^{R} a_{r,n}\boldsymbol{m}_r + \boldsymbol{\phi}_n + \boldsymbol{e}_n \\ &= \boldsymbol{M}\boldsymbol{a}_n + \boldsymbol{\phi}_n + \boldsymbol{e}_n, \end{aligned} \quad (1)$$

This work was supported by the EPSRC Grants EP/J015180/1, EP/N003446/1, and EP/K015338/1

978-1-5090-0326-6/16/$31.00 ©2016 IEEE

where $\boldsymbol{a}_n = (a_{1,n}, \cdots, a_{R,n})^T$ is the $(R \times 1)$ vector of abundances associated with the nth pixel, R is the number of endmembers, $\boldsymbol{e}_n$ is an additive noise, L is the number of spectral bands, $\boldsymbol{M} = (\boldsymbol{m}_1, \cdots, \boldsymbol{m}_R)$ is the endmember matrix that is assumed known (either picked out from a spectral library if available, or extracted using an endmember extraction algorithm) and $\boldsymbol{\phi}_n$ is a residual term that might have different characteristics depending on the studied effect. Due to physical constraints, the abundance vector $\boldsymbol{a}_n$ satisfies the following positivity and sum-to-one (PSTO) constraints

$$a_{r,n} \geq 0, \forall r \in \{1, \ldots, R\} \quad \text{and} \quad \sum_{r=1}^{R} a_{r,n} = 1. \tag{2}$$

Eq. (1) shows a general model that can be adapted to account for different robust mixture models. In this paper, we consider three variants: (i) the robust nonnegative matrix factorization (RNMF) proposed in [6], (ii) the robust Bayesian linear unmixing (RBLU) proposed in [7], and (iii) the residual component analysis with mismodelling effects (RCA-ME) proposed in [8]. Table I presents the main outlier and noise prior statistical properties assumed by each method and the next sections describe in more details their properties.

Table I. Characteristics of the robust models. "Spar." stands for sparsity, "pos." for positivity, "val." for values and "correl." for correlation.

	Residuals			Statistics
	Pos.	Spatial	Spectral	
RNMF	✓	Spar. energies	None	-SED -KLD
RBLU	X	Correl. and spar. support	Correl. support	$\mathcal{N}(\boldsymbol{0}, \boldsymbol{\Sigma})$
ME	X	Correl. energies	Correl. val.	$\mathcal{N}(\boldsymbol{0}, \boldsymbol{\Sigma})$

II-A. RNMF

The RNMF model is given by [6]

$$\boldsymbol{y}_n^{\text{RNMF}} = \sum_{r=1}^{R} a_{r,n} \boldsymbol{m}_r + \boldsymbol{r}_n \tag{3}$$

where $\boldsymbol{r}_n, \forall n$ denote positive residuals that are due to the presence of nonlinear effects such as the bilinear models of [17]–[19] and the polynomial model of [20]. Therefore, this positivity assumption is physically well-motivated for multi-layered models (e.g., scenes where significant multiple reflections can occur). In addition, the RNMF model assumes that the nonlinear spectra are spatially sparse, i.e., the majority of the pixels follows the LMM while only some pixels include an additional residual term. Note, however, that the RNMF does not assume any spectral structure for the residuals. The RNMF estimates the parameter of interest using two measures of similarity between the observed spectrum $\boldsymbol{y}_{\ell,n}$ and the spectrum $\boldsymbol{y}_{\ell,n}^{\text{RNMF}}$. The first one is the SED, given by $\sum_{\ell,n} \left(\boldsymbol{y}_{\ell,n} - \boldsymbol{y}_{\ell,n}^{\text{RNMF}}\right)^2$, and the second one is the KLD, given by $\sum_{\ell,n} \left(\boldsymbol{y}_{\ell,n}^{\text{RNMF}} \log \frac{\boldsymbol{y}_{\ell,n}^{\text{RNMF}}}{\boldsymbol{y}_{\ell,n}} \right. \left. - \boldsymbol{y}_{\ell,n}^{\text{RNMF}} + \boldsymbol{y}_{\ell,n} \right)$. Finally, RNMF is an unsupervised algorithm that estimates both the endmembers, the abundances and the residuals. However, for comparison purposes, this paper considers the supervised case (known endmember matrix $\boldsymbol{M}$) and only estimates the remaining parameters. This can be easily implemented by skipping the endmember update step of the iterative estimation process (see [6] for details on the algorithm implementation).

II-B. RBLU

The RBLU model follows (1) while considering additive centered Gaussian noise with a diagonal covariance matrix $\boldsymbol{\Sigma} = \text{diag}\left(\boldsymbol{\sigma}^2\right)$ as follows $\boldsymbol{e}_n \sim \mathcal{N}(\boldsymbol{0}, \boldsymbol{\Sigma})$, where $\boldsymbol{\sigma}^2 = \left(\sigma_1^2, \cdots, \sigma_L^2\right)^T$ is an $(L \times 1)$ vector containing the noise variances. In addition, the outliers $\boldsymbol{\phi}_n = \boldsymbol{z}_n \odot \boldsymbol{x}_n, \forall n$ are represented by a term-wise product $\odot$ between the support variable $\boldsymbol{z}_n$ (which is an $L \times 1$ vector of 0s and 1s) and the vector of values $\boldsymbol{x}_n$. Note that the outliers are assumed to share a correlated support $\boldsymbol{Z} = [\boldsymbol{z}_1, \cdots, \boldsymbol{z}_N]$, i.e., the spatial and spectral neighbors of a corrupted pixel (with outliers in a given spectral band) are more likely to contain corruption. The outlier structure is modeled via a 3D Ising model and generalizes the model studied in [21] which assumed the support sets of outliers to have a fixed structure. However, the values of these corruptions contained in $\boldsymbol{X} = [\boldsymbol{x}_1, \cdots, \boldsymbol{x}_N]$ are independent which enables flexibility in this model to capture different physical phenomena such as local spectral and/or spatial variations (e.g., intrinsic material spectral variability, illumination changes, scarcely represented endmembers,...). Note also that RBLU enforces spectral and spatial sparsity among the corrupted pixels. Finally, and as previously described, this paper considers the supervised case and RBLU will be used to estimate the parameters of interest while considering a known endmember matrix $\boldsymbol{M}$.

II-C. RCA-ME

In a similar fashion to RBLU, the RCA-ME model considers additive centered Gaussian noise with a diagonal covariance matrix $\boldsymbol{\Sigma} = \text{diag}\left(\boldsymbol{\sigma}^2\right)$. To represent different physical phenomena such as nonlinearity and/or endmember variability, the outliers $\boldsymbol{\phi}_n = \boldsymbol{d}_n, \forall n$ are assumed to present some spectral smoothness. Indeed, for bilinear and polynomial based nonlinearity models, the outliers result from a (nonlinear) combination of endmembers that are generally smooth (when the endmembers themselves are smooth). In addition, it has been shown in [8] that endmember variability can also be approximated by assuming spectrally smooth residuals. Note that RCA-ME also assumes the energies of the outliers to be spatially correlated. Note finally that RCA-ME accounts for spatial illumination variability by relaxing the abundance sum-to-one constraint, however, for a comparison purpose, this paper assumes the absence of this variability and maintains the abundance sum-to-one constraint.

III. UNMIXING ALGORITHMS

This section presents the optimization formulation, the hierarchical Bayesian models and the estimation algorithms associated with each model.

III-A. Optimization problem for RNMF

Considering a known endmember matrix $\boldsymbol{M}$, the RNMF estimates the unknown parameters by solving the following problem

$$\min_{\boldsymbol{A},\boldsymbol{R}} \mathcal{C}_{\text{RNMF}}(\boldsymbol{A}, \boldsymbol{R}) = D(\boldsymbol{Y}|\boldsymbol{M}\boldsymbol{A} + \boldsymbol{R}) + \lambda ||\boldsymbol{R}||_{2,1} \tag{4}$$

s.t. the positivity of $\boldsymbol{A}$ and $\boldsymbol{R}$ and to the sum-to-one constraint on $\boldsymbol{A}$, where $\boldsymbol{A} = [\boldsymbol{a}_1, \cdots, \boldsymbol{a}_N]$, $\boldsymbol{R} = [\boldsymbol{r}_1, \cdots, \boldsymbol{r}_N]$, $D(x|y)$ is the distance measure between x and y and $||\boldsymbol{R}||_{2,1} = \sum_{n=1}^{N} \sqrt{\boldsymbol{r}_n^\top \boldsymbol{r}_n}$ is a mixed norm that imposes spatial sparsity on the energies of $\boldsymbol{R}$. This problem is solved using a coordinate descent algorithm (CDA) that sequentially updates the two matrices $\boldsymbol{R}$ and $\boldsymbol{A}$. More precisely, while fixing $\boldsymbol{A}$, RNMF updates $\boldsymbol{R}$ using a majorization-minimization algorithm. Then, fixing $\boldsymbol{R}$, RNMF updates $\boldsymbol{A}$ using a non-negative gradient descent algorithm. The resulting iterative algorithm was found experimentally to decrease the value of the objective function at each iteration [6].

III-B. Bayesian model for RBLU

Using Bayes rule, the noise statistics (likelihood) and the prior knowledge about the parameter of interest $\boldsymbol{\Theta}_1 = \left(\boldsymbol{A}, \boldsymbol{\Sigma}, \boldsymbol{X}, \boldsymbol{Z}, s^2, \boldsymbol{\beta}\right)$ lead to the following posterior distribution

$$f\left(\boldsymbol{\Theta}_1|\boldsymbol{Y}\right) \propto f(\boldsymbol{Y}|\boldsymbol{\Theta}_1) f\left(\boldsymbol{A}\right) f\left(\boldsymbol{\Sigma}\right) f\left(\boldsymbol{X}|s^2\right) f\left(\boldsymbol{Z}|\boldsymbol{\beta}\right) f\left(s^2\right) f\left(\boldsymbol{\beta}\right), \tag{5}$$

where s^2 and $\boldsymbol{\beta}$ are two hyperparameters related to the value of the outliers, and to the correlation of the outlier supports, respectively. RBLU uses a stochastic optimization mechanism to adjust the parameters $\boldsymbol{\beta}$ of the Markov random field associated with the support $\boldsymbol{Z}$. The remaining parameters are sampled according to the target posterior distribution (5) using an MCMC algorithm. The generated samples are then used to approximate the minimum mean square estimator (MMSE) or the maximum a-posteriori (MAP) estimator of the parameters. The obtained algorithm benefits from the good convergence properties of the MCMC approach [9] while it suffers from a high computational cost.

III-C. Bayesian model for RCA-ME

Similarly to RBLU, the CDA-ME adopts a Bayesian approach leading to the following posterior

$$f\left(\boldsymbol{\Theta}_2|\boldsymbol{Y}\right) \propto f(\boldsymbol{Y}|\boldsymbol{\Theta}_2) f\left(\boldsymbol{A}\right) f\left(\boldsymbol{\Sigma}\right) f\left(\boldsymbol{D}|\boldsymbol{\epsilon}\right) f\left(\boldsymbol{\epsilon}, \boldsymbol{w}\right), \tag{6}$$

where $\boldsymbol{\Theta}_2 = (\boldsymbol{A}, \boldsymbol{\Sigma}, \boldsymbol{D}, \boldsymbol{\epsilon}, \boldsymbol{w})$, $\boldsymbol{\epsilon}$ and $\boldsymbol{w}$ are two hyperparameters introducing the spatial correlation of the outlier energies (see [8] for more details). CDA-ME approximates the MAP estimator of $\boldsymbol{\Theta}$ by sequentially updating the different parameters. In each step, the posterior distribution is maximized w.r.t. one parameter, the other being fixed. Thus, the algorithm iteratively updates each parameter by maximizing its conditional distribution either by an analytical solution (as for $\boldsymbol{\epsilon}$, $\boldsymbol{w}$, $\boldsymbol{D}$, $\boldsymbol{\Sigma}$) or by using the fast SUNSAL algorithm [22] (as for $\boldsymbol{A}$). According to proposition 2.7.1 in [23], the limit points of the sequence generated by CDA are stationary points of (6), since the maximum of that function w.r.t. $\boldsymbol{\Theta}$ along each coordinate is unique.

IV. RESULTS

This section evaluates the performance of the robust algorithms described above when applied to a real hyperspectral data set. All simulations have been implemented using MATLAB R2015a on a computer with Intel(R) Core(TM) i7-4790 CPU@3.60GHz and 32GB RAM.

IV-A. Data description

The real image used in this section was acquired in July 2014 by Defence Science and Technology Laboratory (DSTL) over Porton Down (U.K.). The dataset contains $L = 140$ spectral bands recorded from the visible to near infrared (415 to 990 nm) with a spatial resolution of about 0.2 metres. The unmixing algorithms have been applied to a scene of size 400×200 pixels which is composed of $R = 5$ components: grass, tree, soil 1, road, and soil 2, and other man-made outliers as shown in Fig. 1 (see green and white spots). This image is interesting since it potentially includes nonlinearity effect between the tree and soil, endmember variability for the grass area and man-made sparse outliers, which makes it suitable for the assessment of the algorithms presented in this paper. The endmember associated with the $R = 5$ components have been manually selected by choosing the purest pixels in each component's region.

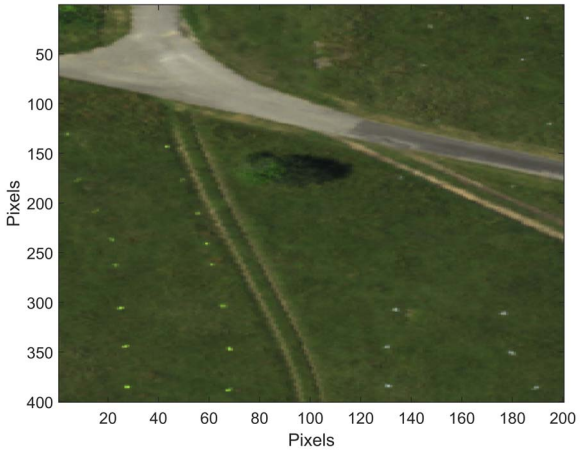

Fig. 1. An example of the hyperspectral image data used in the analysis

IV-B. Comparison between the algorithms

The abundances of the real image have been estimated by the robust algorithms and the LMM based SUNSAL algorithm [22]. After using SED and KLD similarity measures for the RNMF and $\lambda \in [0.01\lambda_0, \lambda_0, 2\lambda_0]$, where λ_0 is the suggested value in [6], we found that the best reconstruction error, given by $\text{RE} = \sqrt{\frac{1}{NL}\sum_{n=1}^{N} \|\hat{\boldsymbol{y}}_n - \boldsymbol{y}_n\|^2}$), is obtained when considering the KLD measure and $\lambda = 0.01\lambda_0$. The following RNMF results are related to this parameter configuration. Fig. 2 shows the obtained abundance maps where a white (black) pixel indicates a large (small) proportion of the corresponding materials. Overall, the obtained abundances are in good agreement except RMNF that show slightly different tree and grass abundances (which can be explained by the high similarity between the tree and grass spectra). Note that some of the man-made outliers are detected as a soil abundances (see far right-hand side plots of Fig. 2).

Table II shows the obtained RE and spectral angle mapper, $\text{SAM} = \frac{1}{N}\sum_{n=1}^{N} \arccos\left(\frac{\hat{\boldsymbol{y}}_n^T \boldsymbol{y}_n}{\|\boldsymbol{y}_n\| \, \|\hat{\boldsymbol{y}}_n\|}\right)$, between the observed and reconstructed spectra with the considered algorithms. This table shows that the robust algorithms provide smaller RE and SAM than the LMM based SUNSAL algorithm. However, this is achieved at a price of a higher computational cost especially for the MCMC-based RBLU algorithm. An interesting property of the robust algorithms is their ability to show outlier energy maps as presented in Fig. 3 (left). The nonlinearity effect present between the tree-soil is detected by all the algorithms. In contrast to RBLU and CDA-ME, RNMF does not detect the shadow as an outlier since it generally reduces the reflectance and can be seen as a negative outlier, which is ignored in RNMF because of the outlier positivity constraint. The three algorithms succeeded in capturing the endmember variability effect affecting the grass with CDA-ME detecting the larger region. It is also of interest to note that the algorithms detect the man-made sparse outliers. Considering the RE maps in Fig. 3 (right), it is clear that the RE of RNMF is higher in shadowed regions while RBLU and CDA-ME present low RE.

Fig. 4 shows some randomly selected outlier spectra obtained with the three robust algorithms. These spectra show a similar global shape while they highlight the properties of each algorithm. Indeed, it can be seen that the RNMF algorithm focuses on the nonlinearity effect (i.e., positive outliers) while it avoids negative spectra that are mainly related to shadowing and endmember

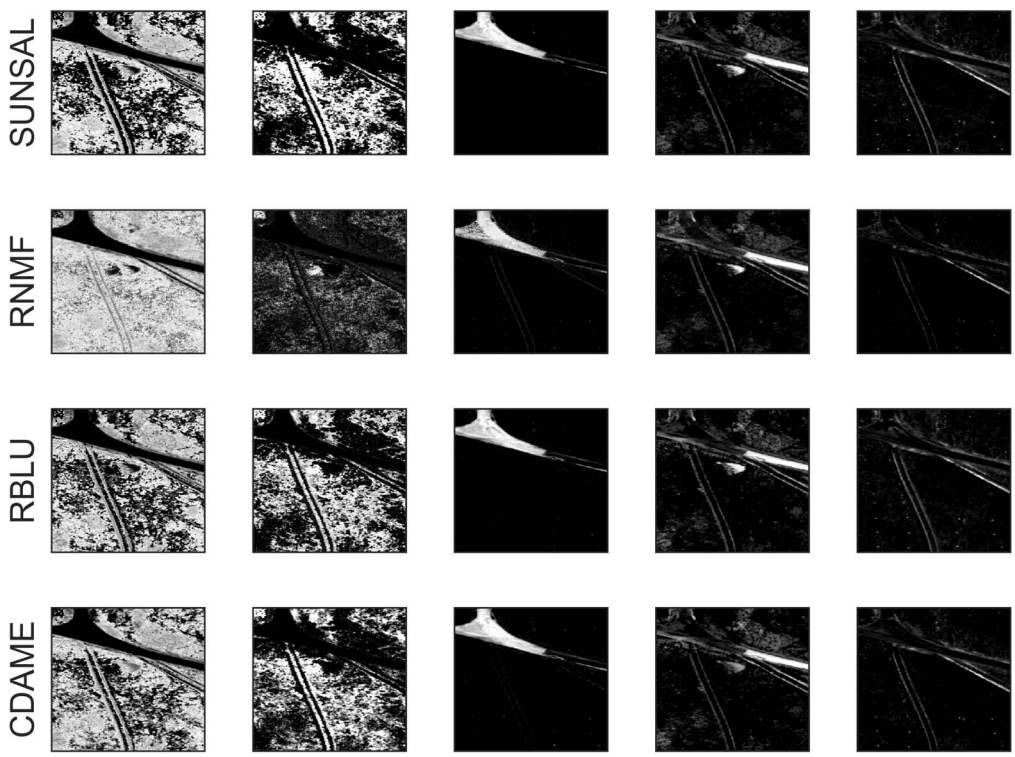

Fig. 2. Estimated abundance maps with different algorithms (all images have the same dynamic, i.e., between 0 and 1). From left to right: grass, tree, soil 1, road, and soil 2.

variability effects. Moreover, it is interesting to note that RBLU allows the absence of outliers (null spectra) which is an advantage of imposing sparsity on the support of the outliers instead of their values. Note finally that Fig. 4 also highlights the smooth spectral property of CDA-ME.

Finally, Table III summarizes the pros and cons of each model. A few comments should be made regarding the noise robustness and the endmember columns. Both RBLU and CDA-ME consider Gaussian noise with band dependent variances, thus, they are robust to the spectral variation of the noise. SUNSAL and RNMF (with SED) consider independent and identically distributed Gaussian noise which is less robust to the spectral variation of the noise. However, RNMF considers a general formulation that allows the use of the KLD measure, which makes it suitable to process images corrupted by non Gaussian noise. Note finally that both RNMF and RBLU can estimate the endmembers, while SUNSAL and CDA-ME assume a known endmember matrix $\boldsymbol{M}$. This property has been reported in table III for completeness, but the reader should be aware that the endmembers have been assumed known in this paper.

Table II. Unmixing performance on a real images (400×200 pixels).

	RE ($\times 10^{-3}$)	SAM ($\times 10^{-2}$)	Time (min)
SUNSAL	9.32	3.34	0.03
RNMF	7.17	2.05	23.92
RBLU	4.28	2.32	1440
CDA-ME	3.87	2.21	6.98

Table III. Comparison of the robust algorithms. (+++) best results, (-) fair results.

	Effects	Time	RE	Noise	Endm.
SUNSAL	LMM	+++	-	-	-
RNMF	LMM + NL	+	+	++	+
RBLU	LMM + NL EV + Shadow	-	++	++	+
CDAME	LMM + NL EV + Shadow	++	+++	++	-

V. CONCLUSIONS

This paper presented a comparison between three robust mixture models and their associated unmixing algorithms. The three mixture models are expressed as the sum of a linear model and a residual term. The latter depended on the model considered and showed different characteristics as reported in Table I. In contrast to RBLU and CDA-ME that considered Gaussian statistics, RNMF adopted a general formulation that allowed the use of two similarity measures.

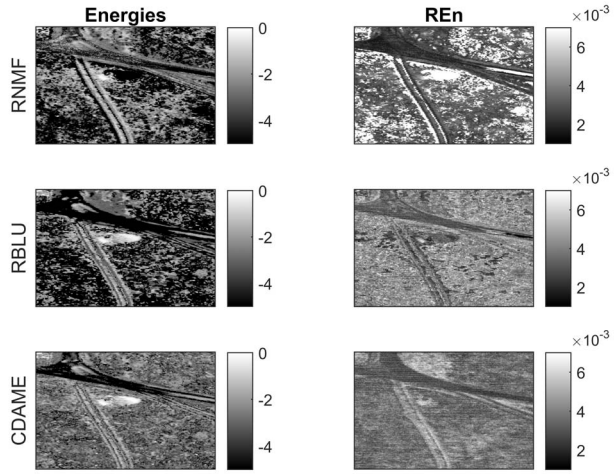

Fig. 3. (Left) square root of the energies of the residuals obtained with $||\hat{\boldsymbol{\phi}}_n||$. (Right) reconstruction error between the reconstructed pixel $\hat{\boldsymbol{y}}_n$ and the observed spectra $\boldsymbol{y}_n$ obtained with $\text{RE}_n = \frac{1}{\sqrt{L}}||\hat{\boldsymbol{y}}_n - \boldsymbol{y}_n||$.

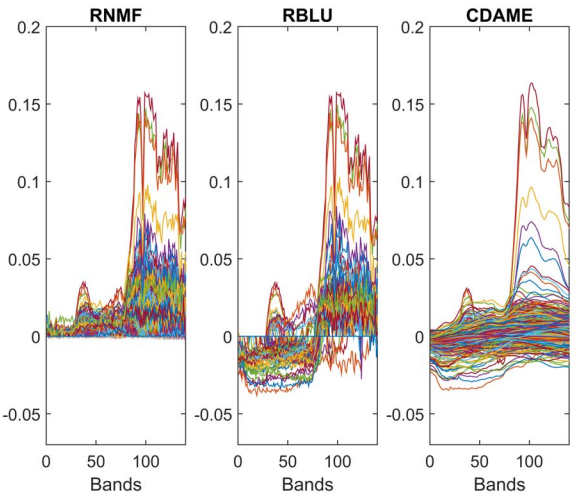

Fig. 4. Example of outlier spectra for (left) RNMF, (middle) RBLU and (right) CDAME.

Both RNMF and CDA-ME used a CDA to minimize their cost functions, while RBLU considered a Markov chain Monte-Carlo to approximate the Bayesian estimators. A comparison between these strategies was achieved by analyzing of a real image containing different effects (such as nonlinearity, endmember variability, outliers and shadow). The results obtained highlighted the benefit of the robust models with respect to the classical linear model. The pros and cons of each model were summarized in Table III, to provide the reader with a useful tool to choose the suitable model/algorithm for his case. Future work includes the use of these models to detect the presence of outliers using hypothesis tests [24]. Considering an efficient optimization algorithm to maximize the RBLU posterior distribution is also an interesting issue which deserves to be investigated.

VI. REFERENCES

[1] R. Heylen, M. Parente, and P. Gader, "A review of nonlinear hyperspectral unmixing methods," *IEEE J. Sel. Topics Appl. Earth Observat. Remote Sens.*, vol. 7, no. 6, pp. 1844–1868, June 2014.

[2] N. Dobigeon, J.-Y. Tourneret, C. Richard, J. Bermudez, S. McLaughlin, and A. Hero, "Nonlinear unmixing of hyperspectral images: Models and algorithms," *IEEE Signal Process. Mag.*, vol. 31, no. 1, pp. 82–94, Jan 2014.

[3] B. Somers, G. P. Asner, L. Tits, and P. Coppin, "Endmember variability in spectral mixture analysis: A review," *Remote Sensing of Environment*, vol. 115, no. 7, pp. 1603 – 1616, 2011.

[4] A. Zare and K. Ho, "Endmember variability in hyperspectral analysis: Addressing spectral variability during spectral unmixing," *IEEE Signal Process. Mag.*, vol. 31, no. 1, pp. 95–104, Jan 2014.

[5] A. Halimi, N. Dobigeon, and J.-Y. Tourneret, "Unsupervised unmixing of hyperspectral images accounting for endmember variability," *IEEE Trans. Image Process.*, vol. 24, no. 12, pp. 4904–4917, 2015.

[6] C. Févotte and N. Dobigeon, "Nonlinear hyperspectral unmixing with robust nonnegative matrix factorization," *IEEE Trans. Image Process.*, pp. 4810–4819, Dec. 2015.

[7] Y. Altmann, S. McLaughlin, and A. Hero, "Robust linear spectral unmixing using anomaly detection," *IEEE Trans. Computational Imaging*, pp. 74–85, June 2015.

[8] A. Halimi, P. Honeine, and J. M. Bioucas-Dias, "Hyperspectral unmixing in presence of endmember variability, nonlinearity or mismodelling effects," in *ArXiv e-prints*, Nov. 2015.

[9] C. P. Robert and G. Casella, *Monte Carlo Statistical Methods*. New York: Springer-Verlag, 1999.

[10] O. Eches, N. Dobigeon, and J.-Y. Tourneret, "Enhancing hyperspectral image unmixing with spatial correlations," *IEEE Trans. Geosci. Remote Sens.*, vol. 49, no. 11, Nov 2011.

[11] Y. Altmann, N. Dobigeon, S. McLaughlin, and J.-Y. Tourneret, "Unsupervised post-nonlinear unmixing of hyperspectral images using a Hamiltonian Monte Carlo algorithm," *IEEE Trans. Image Process.*, vol. 23, no. 6, pp. 2663–2675, June 2014.

[12] Y. Altmann, M. Pereyra, and S. McLaughlin, "Bayesian nonlinear hyperspectral unmixing with spatial residual component analysis," *IEEE Trans. Image Process.*, vol. 1, no. 3, pp. 174–185, Sept. 2015.

[13] C. E. Rasmussen and C. K. I. Williams, *Gaussian Processes for Machine Learning*. London, England: The MIT Press, 2006.

[14] O. Dikmen and A. Cemgil, "Gamma markov random fields for audio source modeling," *IEEE Trans. Audio, Speech, Language Process.*, vol. 18, no. 3, pp. 589–601, March 2010.

[15] A. Halimi, G. S. Buller, S. McLaughlin, and P. Honeine, "Bayesian filtering of smooth signals: Application to altimetry," in *ArXiv e-prints*, Feb. 2016.

[16] A. A. Kalaitzis and N. D. Lawrence, "Residual components analysis," in *Proc. ICML*, 2012, pp. 1–3.

[17] W. Fan, B. Hu, J. Miller, and M. Li, "Comparative study between a new nonlinear model and common linear model for analysing laboratory simulated-forest hyperspectral data," *International Journal of Remote Sensing*, vol. 30, no. 11, pp. 2951–2962, June 2009.

[18] J. M. Bioucas-Dias and J. M. P. Nascimento, "Nonlinear mixture model for hyperspectral unmixing," in *Proc. SPIE Image and Signal Processing for Remote Sensing XV*, L. Bruzzone, C. Notarnicola, and F. Posa, Eds., vol. 7477, no. 1. SPIE, 2009, p. 74770I.

[19] A. Halimi, Y. Altmann, N. Dobigeon, and J.-Y. Tourneret, "Nonlinear unmixing of hyperspectral images using a generalized bilinear model," *IEEE Trans. Geosci. Remote Sens.*, vol. 49, no. 11, pp. 4153–4162, 2011.

[20] Y. Altmann, A. Halimi, N. Dobigeon, and J.-Y. Tourneret, "Supervised nonlinear spectral unmixing using a postnonlinear mixing model for hyperspectral imagery," *IEEE Trans. Image Process.*, vol. 21, no. 6, pp. 3017–3025, June 2012.

[21] G. E. Newstadt, A. O. Hero, and J. Simmons, "Robust spectral unmixing for anomaly detection," in *Proc. IEEE-SP Workshop Stat. and Signal Processing*, June 2014, pp. 109–112.

[22] J. Bioucas-Dias and M. Figueiredo, "Alternating direction algorithms for constrained sparse regression: Application to hyperspectral unmixing," in *Proc. IEEE GRSS Workshop on Hyperspectral Image and SIgnal Processing: Evolution in Remote Sensing (WHISPERS)*, June 2010, pp. 1–4.

[23] D. P. Bertsekas, *Nonlinear programming*. Belmont, Massachusetts: Athena Scientific, 1995.

[24] Y. Altmann, N. Dobigeon, and J. Y. Tourneret, "Nonlinearity detection in hyperspectral images using a polynomial post-nonlinear mixing model," *IEEE Trans. Image Process.*, vol. 22, no. 4, pp. 1267–1276, April 2013.

Radar Filters Design in the Presence of Target Doppler Frequency and Interference Covariance Matrix Uncertainties

Augusto Aubry and Antonio De Maio
Università degli Studi di Napoli "Federico II"
Dipartimento di Ingegneria Elettrica e delle Tecnologie dell'Informazione
Via Claudio 21, I-80125 Naples, Italy
Email: augusto.aubry@unina.it
ademaio@unina.it

Yongwei Huang
School of Information Engineering
Guangdong University of Technology
University Town, Panyu
Guangzhou 510006, China
Email: ywhuang@gdut.edu.cn

Marco Piezzo
Elettronica S.p.A.
Via Tiburtina Valeria
km 13.7, I-00131 Rome, Italy
Email: marco.piezzo@elt.it

***Abstract*—This paper considers the design of robust filters for radar pulse-Doppler processing when the interference is a wide sense stationary random process. The Signal-to-Interference-plus-Noise Ratio (SINR) at the filter output is considered as the figure of merit to optimize under a multitude of requirements accounting for Doppler filter sidelobes as well as uncertainties both in the received useful signal component and interference covariance matrix. The design is analytically formulated as a constrained optimization problem whose solvability is thoroughly studied. Specifically, a polynomial time solution technique to get the optimal filter is proposed exploiting the representation of non-negative trigonometric polynomials via linear matrix inequalities, the spectral factorization theorem, and the duality theory. Last but not least, a detailed analysis of the optimum filter performance is provided showing the trade-offs involved in the design and the gain achievable over some already known counterparts.**

I. Introduction & Problem Formulation

Doppler processing represents the key tool to increase the Signal-to-Clutter-power-Ratio (SCR) in coherent radar systems, when the antenna and waveform parameters are set [1]. Because of the different Doppler signatures associated with targets, clutter, and noise, it is possible to mitigate the interference competing with the useful signal and detect targets embedded in heavy clutter. Additionally, Doppler techniques can also provide measurements of the target radial velocity which is useful for threat assessment, target recognition, and track initialization. Hence, it is not surprising that the design of optimized Doppler processors has been a hot research activity within the radar community since 60's. In fact, many studies have been directed toward the synthesis of advanced and highly performing non-adaptive/adaptive filters fulfilling the more and more stressing radar performance requirements [2], [3], [4], [5]. In a coherent pulsed radar, the N-dimensional vector $\boldsymbol{z} = [z_1, z_2, \ldots, z_N]^T \in \mathbb{C}^N$ of the slow-time observations, from the range-azimuth-elevation cell under test, can be modelled as [1]

$$\boldsymbol{z} = \alpha \boldsymbol{s}(\nu) + \boldsymbol{n},$$

where

- $\boldsymbol{s}(\nu) = [s_1, \ldots, s_N]^T \in \mathbb{C}^N$ denotes the target steering vector, with $s_i = \exp(j2\pi(i-1)\nu)$, $\nu = f_d T$ the target normalized Doppler frequency, f_d the target Doppler frequency, and T the Pulse Repetition Interval (PRI);
- $\alpha \in \mathbb{C}$ accounts for the terms involved into the radar range equation;
- $\boldsymbol{n} = [n_1, n_2, \ldots, n_N]^T \in \mathbb{C}^N$, modeled as a complex, zero mean, circularly symmetric random vector with covariance matrix $\boldsymbol{R}_0 = \mathbb{E}[\boldsymbol{n}\boldsymbol{n}^\dagger] \succ \boldsymbol{0}$, is the vector of the disturbance samples[1].

In a Doppler processor the data vector $\boldsymbol{z}$ undergoes a specific linear transformation [1, Chap. 14, 17], leading to the statistic $\sum_{n=1}^{N} w_n^* z_n = \boldsymbol{w}^\dagger \boldsymbol{z}$, where $\boldsymbol{w} = [w_1, \ldots, w_N]^T \in \mathbb{C}^N$ represents the Doppler filter. A widely used figure of merit

[1]**Notation.** We adopt the notation of using boldface for vectors $\boldsymbol{a}$ (lower case), and matrices $\boldsymbol{A}$ (upper case). The transpose and the conjugate transpose operators are denoted by the symbols $(\cdot)^T$ and $(\cdot)^\dagger$ respectively. $\boldsymbol{I}$ and $\boldsymbol{0}$ denote respectively the identity matrix and the zero matrix (their size is determined from the context); $\boldsymbol{e}_n$ is the column vector with the n-th column of $\boldsymbol{I}$. $\mathbb{R}^N$, $\mathbb{C}^N$, and $\mathbb{H}^N$ are respectively the sets of N-dimensional vectors of real numbers, complex numbers, and $N \times N$ Hermitian matrices. For any $\boldsymbol{A} \in \mathbb{H}^N$, $\boldsymbol{A} \succeq \boldsymbol{0}$ means that $\boldsymbol{A}$ is a positive semidefinite matrix ($\boldsymbol{A} \succ \boldsymbol{0}$ for positive definiteness). **diag** $(\cdot)$ is the column vector containing the principal diagonal of the matrix argument, whereas $\lambda_{max}(\cdot)$ and $\lambda_{min}(\cdot)$ denote, respectively, the maximum and the minimum eigenvalue. For $\boldsymbol{x} \in \mathbb{C}^N$, the matrix **Diag**$(\boldsymbol{x})$ is the $N \times N$ diagonal matrix, whose i-th diagonal element is x_i, for $i = 1, \ldots, N$, whereas the symbol $\|\boldsymbol{x}\|$ denotes its Euclidian norm. $\odot$ represents the Hadamard product. The spectral norm, Frobenius norm, and the trace of $\boldsymbol{X}$ are indicated respectively with $\|\boldsymbol{X}\|_2$, $\|\boldsymbol{X}\|_F$, and tr $(\boldsymbol{X})$. The imaginary unit is only represented by the letter j (i serves as index). For any complex number x, we use $\Re(x)$ and $\Im(x)$ to denote respectively the real and the imaginary parts of x; also, $|x|$ and x^* represent the modulus and the conjugate of x. $\mathbb{E}[\cdot]$ denotes statistical expectation. For any optimization Problem $\mathcal{P}$, $v(\mathcal{P})$ represents its optimal value.

978-1-5090-0326-6/16/$31.00 ©2016 IEEE

to assess the performance of a Doppler filter $\boldsymbol{w}$ is the Signal-to-Interference-plus-Noise Ratio (SINR), given by

$$\text{SINR}(\nu, \boldsymbol{R}_0) = |\alpha|^2 |\boldsymbol{w}^\dagger \boldsymbol{s}(\nu)|^2 / \boldsymbol{w}^\dagger \boldsymbol{R}_0 \boldsymbol{w},$$

where $|\alpha|^2|\boldsymbol{w}^\dagger \boldsymbol{s}(\nu)|^2$ and $\boldsymbol{w}^\dagger \boldsymbol{R}_0 \boldsymbol{w}$ represent the useful and the interference energy at the output of the filter, respectively.

For known Doppler and interference covariance matrix, the receiver maximizing the SINR is the Capon filter [6] $\bar{\boldsymbol{w}}^\star = {\boldsymbol{R}_0}^{-1} \boldsymbol{s}(\nu)$. Nevertheless, in practical scenarios both $\boldsymbol{R}_0$ and ν are unknown and a possible way to cope with this uncertainty is the use of a set of $K \geq N$ training data vectors $\boldsymbol{z}(i) \in \mathbb{C}^N$, $i = 1, \ldots, K$, free of useful signal component and sharing the same spectral characteristics of $\boldsymbol{n}$ (homogeneous environment). Hence, the sample covariance matrix $\hat{\boldsymbol{R}} = \frac{1}{K} \sum_{i=1}^{K} \boldsymbol{z}(i) \boldsymbol{z}(i)^\dagger$ is used in place of $\boldsymbol{R}_0$ leading to the so called Sample Matrix Inversion (SMI) filter [7] $\bar{\boldsymbol{w}}^\star_{\text{SMI}} = \hat{\boldsymbol{R}}^{-1} \boldsymbol{s}(\bar{\nu})$, where $\bar{\nu}$ is a nominal Doppler value usually chosen as the mean value of the target Doppler uncertainty interval. However, the SMI algorithm experiences severe SINR losses [4], when mismatches affect either the steering vector $\boldsymbol{s}(\bar{\nu})$ or the disturbance covariance matrix, for instance due to the presence of interfering targets or clutter discretes in the sample covariance matrix or a large Doppler uncertainty set. Several advanced filtering techniques have been proposed during the years, to deal with these non-idealities. Some interesting and technically sound procedures can be found in[3], [4], [5], [8], [9], [10], [11], and [12].

In this paper, to mitigate the deleterious effects of knowledge inaccuracies about the actual target Doppler frequency and disturbance covariance matrix, we focus on the synthesis of a filter optimizing the worst-case (over Doppler and disturbance covariance matrix mismatches) system performance in terms of achievable SINR. In addition, to prevent interference from outliers, i.e., targets belonging to the same range cell of the target of interest but with different Doppler frequencies, we force a constraint on the receive filter to control its Doppler response within the sidelobe region.

Specifically, assuming $\boldsymbol{w} \neq \boldsymbol{0}$, we deal with the following max-min optimization problem

$$\mathcal{P}_1 \begin{cases} \max\limits_{\boldsymbol{w}} \quad \min\limits_{\boldsymbol{R}, \boldsymbol{s}} \quad \dfrac{|\boldsymbol{w}^\dagger \boldsymbol{s}|^2}{\boldsymbol{w}^\dagger \boldsymbol{R} \boldsymbol{w}} \\ \qquad\quad \text{s.t.} \quad \boldsymbol{R} \in \Omega \\ \qquad\qquad\quad \boldsymbol{s} \in \mathcal{S} \\ \qquad\qquad\quad \boldsymbol{w} \in \mathcal{H} \end{cases} \tag{1}$$

where

1) Ω is a convex compact subset of positive definite Toeplitz matrices, accounting for the uncertainty over the disturbance covariance matrix.
2) $\mathcal{S} = \left\{ \boldsymbol{s} \in \mathbb{C}^N : \boldsymbol{s} = [1, e^{j2\pi\nu}, \ldots, e^{j2\pi(N-1)}]^T, \ \nu \in [\nu_1, \nu_2] \right\}$ is the set of potential steering vectors $\boldsymbol{s}$, accounting for the uncertainty on the parameter ν which lies within $\Theta_1 = [\nu_1, \nu_2]$.
3) $\mathcal{H} = \left\{ \boldsymbol{w} \in \mathbb{C}^N : \max\limits_{\nu \in \Theta_2} |\boldsymbol{w}^\dagger \boldsymbol{s}(\nu)|^2 \leq \zeta \min\limits_{\nu \in \Theta_1} |\boldsymbol{w}^\dagger \boldsymbol{s}(\nu)|^2 \right\}$ is the set of receive filters $\boldsymbol{w}$ whose output level in the sidelobe regions $\Theta_2 = [\nu_3, \nu_4]$, is lower than or equal to ζ times the minimum level in Θ_1 (with $\Theta_1 \cap \Theta_2 = \emptyset$).

The remainder part of the work is organized as follows. Section II focuses on the solution of the formulated optimization problem. In Section III, the performance of the new procedure is assessed considering some illustrative examples. Finally, in Section IV, conclusions are drawn.

II. Robust Doppler Filter Design

In this section, an algorithm to find in polynomial time an optimal solution to the considered robust design problem is developed. A first step toward this goal is provided by the following equivalent[2] representation of Problem $\mathcal{P}_1$

$$\mathcal{P}_2 \begin{cases} \max\limits_{\boldsymbol{w}} \quad \min\limits_{\boldsymbol{R}} \quad \dfrac{1}{\boldsymbol{w}^\dagger \boldsymbol{R} \boldsymbol{w}} \\ \qquad\quad \text{s.t.} \quad \boldsymbol{R} \in \Omega\,, \\ \qquad\qquad\quad |\boldsymbol{w}^\dagger \boldsymbol{s}|^2 \geq 1, \quad \forall \boldsymbol{s} \in \mathcal{S}\,, \\ \qquad\qquad\quad \max\limits_{\nu \in \Theta_2} |\boldsymbol{w}^\dagger \boldsymbol{s}(\nu)|^2 \leq \zeta\,. \end{cases} \tag{2}$$

Problem $\mathcal{P}_2$ is still a non-convex optimization problem, since its feasible set $|\boldsymbol{w}^\dagger \boldsymbol{s}|^2 \geq 1$, $\forall \boldsymbol{s} \in \mathcal{S}$, is a non-convex set. Nevertheless, exploiting the special structure of $\mathcal{P}_2$, it can be shown that the following Proposition 2.1 holds true (whose proof is given in [14])

Proposition 2.1: Let us define Problem $\mathcal{P}_3$

$$\mathcal{P}_3 \begin{cases} \min\limits_{\boldsymbol{c}} \quad \max\limits_{\boldsymbol{R}} \quad 2\Re\left\{\boldsymbol{c}^\dagger \boldsymbol{r}\right\} - c_0 r_0 \\ \qquad\quad \textit{s.t.} \quad c_0 + 2\Re\left\{\sum_{k=1}^{N-1} c_k e^{-j2\pi\nu k}\right\} \geq 0, \\ \qquad\qquad\qquad\quad \forall\, \nu \in [0,1] \\ \qquad\qquad\quad c_0 + 2\Re\left\{\sum_{k=1}^{N-1} c_k e^{-j2\pi\nu k}\right\} \geq 1, \\ \qquad\qquad\qquad\quad \forall\, \nu \in [\nu_1, \nu_2] \\ \qquad\qquad\quad c_0 + 2\Re\left\{\sum_{k=1}^{N-1} c_k e^{-j2\pi\nu k}\right\} \leq \zeta, \\ \qquad\qquad\qquad\quad \forall\, \nu \in [\nu_3, \nu_4] \\ \qquad\qquad\quad \boldsymbol{R} \in \Omega\,, \end{cases} \tag{3}$$

where $\boldsymbol{c} \in \mathbb{C}^N$ *and* $\boldsymbol{r} = [r_0, r_1, \ldots, r_{N-1}]^T \in \mathbb{C}^N$ *is the first column of the matrix* $\boldsymbol{R}$*. Then,* $v(\mathcal{P}_2) = v(\mathcal{P}_3)$*; additionally, given an optimal solution* $\boldsymbol{c}^\star$ *to* $\mathcal{P}_3$*, an optimal solution* $\boldsymbol{w}^\star$ *to* $\mathcal{P}_2$ *is the only vector satisfying*

$$|H(z)|^2 = c_0^\star + 2\Re\left\{\sum_{k=1}^{N-1} c_k^\star z^{-k}\right\} \quad \forall\, z \in \mathbb{C} : |z| = 1\,, \tag{4}$$

[2]Two optimization Problems $\mathcal{P}_{i_1}$ and $\mathcal{P}_{i_2}$ are claimed equivalent if they share the same optimal value and, given a solution to one problem, it is possible to obtain a solution to the other, and vice versa. Furthermore, By "solvable", we mean that the problem is feasible and bounded (below or above, respectively for minimization and maximization problems), and the optimal value is attained, see [13, p. 15].

with $H(z) = \sum_{k=0}^{N-1} w_{k+1}^{\star} z^{-k}$*, such that all the roots of* $H(z)$ *lie within the unit circle* $|z| \leq 1$*. Furthermore, given* $\boldsymbol{w}^{\star}$*, an optimal solution* $\boldsymbol{c}^{\star}$ *to* $\mathcal{P}_3$ *complies with* $c_k^{\star} = \sum_{l=k}^{N-1} w_{l+1}^{\star} (w_{l+1-k}^{\star})^*$, $k = 0, 1, \ldots, N-1$.

An efficient procedure that can be used to find a vector satisfying (4) is reported in [15]. Notice that Problem $\mathcal{P}_3$ is a convex optimization problem; however its feasible set is defined through an infinite number of linear inequalities significantly complicating the search for an optimal solution. In order to circumvent this drawback, let us introduce the following quantities:

1) $\boldsymbol{f}_m = [1, e^{-jm\frac{2\pi}{2N-1}}, \ldots, e^{-j(2N-2)m\frac{2\pi}{2N-1}}]^T$, $m = 0, \ldots, 2N-2$;
2) $\boldsymbol{e}_1 = [1, 0, \ldots, 0]^T \in \mathbb{R}^N$;
3) $\boldsymbol{d} = [d_0, d_1, \ldots, d_{2N-2}]^T$, $d_k = \cos[2\pi k/(2N-1) - (\pi(\nu_1 + \nu_2))] - \cos[\pi(\nu_2 - \nu_1)]$;
4) $\widehat{\boldsymbol{d}} = [\widehat{d}_0, \widehat{d}_1, \ldots, \widehat{d}_{2N-2}]^T$, $\widehat{d}_k = \cos[2\pi k/(2N-1) - (\pi(\nu_3 + \nu_4))] - \cos[\pi(\nu_4 - \nu_3)]$.

Then, exploiting the SemiDefinite Program (SDP) representation of the trigonometric polynomials [15], Proposition 2.2 holds true (see [14])

Proposition 2.2: Problem $\mathcal{P}_3$ *is equivalent to the convex optimization Problem* $\mathcal{P}_4$

$$\mathcal{P}_4 \begin{cases} \min\limits_{\boldsymbol{c}, \boldsymbol{X}, \{\boldsymbol{X}_i\}_{i=1}^4} & \max\limits_{\boldsymbol{R}} \; 2\Re\left\{\boldsymbol{c}^{\dagger}\boldsymbol{r}\right\} - c_0 r_0 \\ \textit{s.t.} & \boldsymbol{c} = \hat{\boldsymbol{F}}^{\dagger}\mathbf{diag}\left(\hat{\boldsymbol{F}}\boldsymbol{X}\hat{\boldsymbol{F}}^{\dagger}\right), \\ & \boldsymbol{c} - \boldsymbol{e}_1 = \hat{\boldsymbol{F}}^{\dagger}\mathbf{diag}\left(\hat{\boldsymbol{F}}\boldsymbol{X}_1\hat{\boldsymbol{F}}^{\dagger}\right) + \\ & \qquad + \hat{\boldsymbol{F}}^{\dagger}\left(\boldsymbol{d} \odot \mathbf{diag}\left(\hat{\boldsymbol{F}}_1\boldsymbol{X}_2\hat{\boldsymbol{F}}_1^{\dagger}\right)\right), \\ & \zeta\boldsymbol{e}_1 - \boldsymbol{c} = \hat{\boldsymbol{F}}^{\dagger}\mathbf{diag}\left(\hat{\boldsymbol{F}}\boldsymbol{X}_3\hat{\boldsymbol{F}}^{\dagger}\right) + \\ & \qquad + \hat{\boldsymbol{F}}^{\dagger}\left(\widehat{\boldsymbol{d}} \odot \mathbf{diag}\left(\hat{\boldsymbol{F}}_1\boldsymbol{X}_4\hat{\boldsymbol{F}}_1^{\dagger}\right)\right), \\ & \boldsymbol{R} \in \Omega, \\ & \boldsymbol{X} \succeq \mathbf{0}, \boldsymbol{X}_i \succeq \mathbf{0},\, i = 1, \ldots, 4, \end{cases} \tag{5}$$

where $\hat{\boldsymbol{F}} = [\boldsymbol{f}_0, \boldsymbol{f}_1, \ldots, \boldsymbol{f}_{N-1}] \in \mathbb{C}^{(2N-1)\times N}$*, and* $\hat{\boldsymbol{F}}_1 = [\boldsymbol{f}_0, \boldsymbol{f}_1, \ldots, \boldsymbol{f}_{N-2}] \in \mathbb{C}^{(2N-1)\times(N-1)}$.

Summarizing, an optimal solution $\boldsymbol{w}^{\star}$ to $\mathcal{P}_1$, can be obtained in polynomial time through **Algorithm 1**.

Algorithm 1 :Robust Receive Filter Design

Require: Θ_1, Θ_2, ζ, Ω, N.
Ensure: An optimal solution $\boldsymbol{w}^{\star}$ to $\mathcal{P}_1$.
1: Solve the convex Problem $\mathcal{P}_4$ finding an optimal solution $\boldsymbol{c}^{\star}$.
2: Exploit $\boldsymbol{c}^{\star}$ to find $\bar{\boldsymbol{w}}$ satisfying (4).
3: output $\boldsymbol{w}^{\star} = \bar{\boldsymbol{w}}$.

As to the uncertainty set on the interference covariance matrix, some suitable constraints have been proposed in [16], which can be represented as

$$\Omega_1 = \left\{\boldsymbol{R} : \boldsymbol{R} = \sigma_n^2\boldsymbol{I} + \boldsymbol{M}, \lambda_{max}(\boldsymbol{R})/\lambda_{min}(\boldsymbol{R}) \leq K_{max}, \boldsymbol{M} \succeq \mathbf{0}, \sigma_n^2 \geq \sigma^2\right\},$$

where $\boldsymbol{M}$ accounts for colored interference and clutter, whereas σ_n^2 refers to the power of the white disturbance term. The parameters $\sigma^2 > 0$ and $K_{max} > 1$ represent respectively a lower bound on the white disturbance power and an upper bound on the condition number. Additional meaningful requirements that can be accounted for at the design stage to characterize $\boldsymbol{R}$ are

$$\Omega_2 = \left\{\boldsymbol{R} : \|\boldsymbol{R} - \hat{\boldsymbol{R}}_0\|_F^2 \leq \epsilon^2, \int_{I_B} \mathbb{E}[|\boldsymbol{n}^{\dagger}\boldsymbol{s}(\nu)|^2]d\nu \leq E_B, \bar{P} - \epsilon_P \leq \mathrm{tr}\,(\boldsymbol{R}) \leq \bar{P} + \epsilon_P\right\},$$

where $\hat{\boldsymbol{R}}_0$ is a Toeplitz estimate of the actual covariance matrix, [17], ϵ accounts for the size of the trust region, and $E_B > 0$ rules the interference energy over the spectral interval $I_B = \{\nu : \nu \in [\nu_d - \epsilon_\nu/2, \nu_d + \epsilon_\nu/2]\}$ (ν_d is the central frequency, whereas ϵ_ν defines the width of I_B). Finally, $\bar{P} > 0$ is the expected disturbance energy and $\epsilon_P > 0$ controls the size of the associate trust interval. Thus, accounting for the stationarity of the disturbance vector $\boldsymbol{n}$, a suitable model for Ω is

$$\left\{\boldsymbol{R} : \boldsymbol{R} \in \overline{\Omega}, \boldsymbol{R} \text{ is a positive semi-definite Toeplitz matrix}\right\}, \tag{6}$$

with $\overline{\Omega} = \Omega_1 \cap \Omega_2$. Before concluding this section it is worth pointing out that Ω in (6) can be expressed in terms of Linear Matrix Inequalities (LMIs). As a results, under some mild technical conditions, $\mathcal{P}_4$ boils down to an SDP problem.

III. Performance Analysis

In this section the performance analysis of the proposed class of Doppler filters is developed with reference to a radar transmitting a coherent burst of $N = 32$ pulses. $K = N$ homogeneous training data vectors $\boldsymbol{z}(1), \ldots, \boldsymbol{z}(K) \in \mathbb{C}^N$, modelled as independent and identically distributed (i.i.d.) complex normal random vectors with zero-mean and covariance matrix $\boldsymbol{R}_0$, are available at the receive side. Hence, denoting by $\hat{\boldsymbol{R}}$ the resulting sample covariance matrix, the design parameters involved in (6) are set as: $K_{\max} = \lambda_{\max}(\hat{\boldsymbol{R}})/\lambda_{\min}(\hat{\boldsymbol{R}})$, $\sigma^2 = 1$, $\epsilon = \sqrt{0.025\,\mathrm{tr}\,(\boldsymbol{C})}$, with $\boldsymbol{C} = (1/N)\,\mathrm{tr}\,(\hat{\boldsymbol{R}}^{\dagger} \otimes \hat{\boldsymbol{R}})$ [17], and $\epsilon_P = 0.15 \times \bar{P}$, with $\bar{P} = \max(\sigma^2 N, \mathrm{tr}\,(\hat{\boldsymbol{R}}))$. Furthermore, $I_B = \Theta_1$ and $E_B = 1.1 \times E_{B0}$, where

$$E_{B0} = \int_{I_B} \left(\boldsymbol{s}(\nu)^{\dagger}\hat{\boldsymbol{R}}\boldsymbol{s}(\nu)\right) d\nu.$$

Besides, $\hat{\boldsymbol{R}}_0$ is computed projecting $\hat{\boldsymbol{R}}$ over the closed convex set (6) excluding the similarity constraint in Ω_2. Finally, unless otherwise stated, $\zeta = -32$ dB is forced in the sidelobe constraint.

A bimodal clutter model is considered to describe the presence of statistically independent ground and sea clutters

in addition to the white noise; specifically [18],

$$\begin{aligned}\boldsymbol{R}_0(n,m) &= \mathrm{CNR}_S \rho_S^{(n-m)^2} e^{j2\pi(n-m)f_S} + \\ &\quad \mathrm{CNR}_G \rho_G^{|n-m|} + \sigma_n^2 \delta_{n-m},\end{aligned}$$

$(m,n) = \{0,\ldots,N-1\}^2$, where $\sigma^2_{n,\mathrm{dB}} = 2$ dB is the white noise power level, $\mathrm{CNR}_{S,\mathrm{dB}} = 10$ dB and $\mathrm{CNR}_{G,\mathrm{dB}} = 25$ dB denote the power for the sea and the ground clutter, respectively; $\rho_S = 0.8$ and $\rho_G = 0.95$ are the one-lag correlation coefficients for the sea and the ground clutter, respectively; $f_S = 0.2$ is the normalized Doppler frequency of the sea clutter, whereas δ_k is the Kronecker delta function.

For comparison purposes, the performance of some counterparts available in the open literature are also reported; precisely

- $\boldsymbol{w}_1^\star$: the Capon filter [6] with ν the equal to the mean Doppler value, say $\bar{\nu}$;
- $\boldsymbol{w}_2^\star$: the SMI filter [7];
- $\boldsymbol{w}_3^\star$: the filter devised according to [2], assuming as nominal direction $\boldsymbol{a} = \boldsymbol{s}(\bar{\nu})$ and evaluating the size of the trust region, say ϵ_3, through the procedure illustrated in [4]: 1) draw out L steering vectors $\boldsymbol{s}(\nu_l)$ with $\nu_l \in \Theta_1$, $l = 1,\ldots,L$ ($L = 100$ equally-spaced frequency values); 2) set $\epsilon_3 = \min\left(\max_l \{\|\boldsymbol{s}(\nu_l) - \boldsymbol{a}\|\}, \sqrt{N} - 10^{-1}\right)$;
- $\boldsymbol{w}_4^\star$: the filter obtained via the algorithm in [4], considering the covariance matrix uncertainty set $\mathcal{U} \equiv \Omega$ and evaluating the parameters $\boldsymbol{P}$ and $\tilde{\boldsymbol{s}}$ characterizing the ellipsoidal uncertainty region, through the following procedure, [4]: 1) repeat steps 1 involved in synthesis of filter $\boldsymbol{w}_3^\star$; 2) define the ellipsoid center as $\tilde{\boldsymbol{s}} = (1/L)\sum_{l=1}^{L} \boldsymbol{s}(\nu_l)$; 3) let $\bar{\boldsymbol{s}}_l = \boldsymbol{s}(\nu_l) - \tilde{\boldsymbol{s}}$, $l = 1,\ldots,L$ and compute $\bar{\boldsymbol{P}} = (1/L)\sum_{l=1}^{L} \bar{\boldsymbol{s}}_l \bar{\boldsymbol{s}}_l{}^\dagger$; 3) evaluate $\alpha_P = \max_l \left\{\bar{\boldsymbol{s}}_l{}^\dagger \bar{\boldsymbol{P}}^{-1} \bar{\boldsymbol{s}}_l\right\}$ and set $\boldsymbol{P} = \bar{\boldsymbol{P}}/\alpha_P$;
- $\boldsymbol{w}_5^\star$: the filter devised through the algorithm in [3], selecting the design parameters via the following procedure, [4]: 1) repeat steps 1 and 2 involved in the design of $\boldsymbol{w}_4^\star$; 2) set as nominal direction either $\boldsymbol{a}^1 = \boldsymbol{s}(\bar{\nu})$ or $\boldsymbol{a}^2 = \tilde{\boldsymbol{s}}$ and evaluate the corresponding uncertainty size as $\epsilon_5^i = \max_l \left\{\|\boldsymbol{s}(\nu_l) - \boldsymbol{a}^i\|\right\}$, $i = 1,2$; 3) select the filter parameters $(\boldsymbol{a}, \epsilon_5)$ as the pair $(\boldsymbol{a}^i, \epsilon_5^i)$, $i = 1,2$, that provides the best average performance.

Finally, the Doppler filter devised through the proposed procedure is referred to as $\boldsymbol{w}_6^\star$.

The performance assessment of the aforementioned Doppler filters is studied in terms of average SINR value (over $\mathrm{MC} = 100$ i.i.d. realizations of K secondary data sets) achieved in correspondence of the Doppler frequency $\nu \in [0,1[$, i.e., $\widehat{\mathrm{SINR}}(\nu) = (1/\mathrm{MC})\sum_{m=1}^{\mathrm{MC}} |\boldsymbol{w}^{m\dagger}\boldsymbol{s}(\nu)|^2 / \boldsymbol{w}^{m\dagger}\boldsymbol{R}\boldsymbol{w}^m$, where $\boldsymbol{w}^m$ represents the Doppler filter devised according to a specific design strategy for the m-th set of secondary data $m = 1,\ldots,MC$.

In **Figure 1**, we illustrate the performance of the Doppler filters $\boldsymbol{w}_i^\star$, $i = 1,\ldots,6$, when $\Theta_1 = [\bar{\nu} - 2/N, \bar{\nu} + 2/N]$ and $\Theta_2 = [0, \bar{\nu} - 3.5/N] \bigcup [\bar{\nu} + 3.5/N, 1]$ with $\bar{\nu} = 10/N$. Specifically, **Figure 1a** reports $\widehat{\mathrm{SINR}}(\nu)$ whereas **Figure 1b** displays the normalized (to the maximum value) average Energy Transfer Function (ETF) versus ν of some Doppler filters, i.e., the square modulus of their frequency response. The sets Θ_1 and Θ_2 are shaded in light green and red, respectively.

As expected, $\boldsymbol{w}_1^\star$ achieves the highest SINR value in correspondence of $\bar{\nu}$ due to the exact knowledge of both $\boldsymbol{R}_0$ and the target Doppler frequency. Nevertheless, the Capon filter is not able to provide reasonable SINR values in the other Doppler frequencies of interest. Besides, its adaptive version $\boldsymbol{w}_2^\star$ experiences a significant SINR loss also in correspondence of the nominal target frequency $\bar{\nu}$, further highlighting the importance of robust filtering design strategies. In this respect, inspection of **Figure 1a** reveals that $\boldsymbol{w}_6^\star$ exhibits a worst average SINR (within the Doppler uncertainty set Θ_1) higher than the counterparts, with gains of about 1.64 dB, 4.73 dB, and 42 dB over $\boldsymbol{w}_4^\star$, $\boldsymbol{w}_5^\star$, $\boldsymbol{w}_3^\star$, respectively. These gains stem from the description accuracy of the uncertainty sets granted by the proposed class of filters and confirm the effectiveness of the devised framework. Otherwise stated, the ellipsoidal model may not be able to faithfully reproduce $\mathcal{S}$ leading to some SINR losses. Furthermore, the filters $\boldsymbol{w}_i^\star$, $i = 1,2,3,4,5$, share a poor behaviour in correspondence of the sidelobe region Θ_2 reflecting the fact their design strategy does not account for any sidelobe constraint. This is indeed shown by **Figure 1b**, where the reported ETF curves highlight that, unlike $\boldsymbol{w}_6^\star$, $\boldsymbol{w}_4^\star$ (that is the major competitor to $\boldsymbol{w}_6^\star$ in terms of achieved worst SINR value) exhibits very high sidelobes. As a consequence, unlike $\boldsymbol{w}_6^\star$, the presence of outliers may seriously impair the performance of $\boldsymbol{w}_4^\star$.

IV. Conclusions

Constrained design of radar Doppler filters has been considered assuming the output SINR as performance measure. To account for possible mismatches between the design and the operative conditions some specific uncertainty sets have been associated with both the target Doppler frequency and the interference covariance matrix. Besides, a constraint on the filter sidelobe response has been enforced to control the amount of interference energy produced by targets lying in the same range cell as the target of interest.

The results have highlighted that the new class of filters may ensure enhanced worst-case performance (in terms of achieved SINR value) over some already available counterparts. As a consequence, the devised algorithm represents a viable means to mitigate the deleterious effects of modelling mismatches while keeping satisfactory SINR values.

References

[1] M. A. Richards, J. A. Scheer, and W. A. Holm, *Principles of Modern Radar: Basic Principles.* Raleigh, NC: Scitech Publishing, 2010.

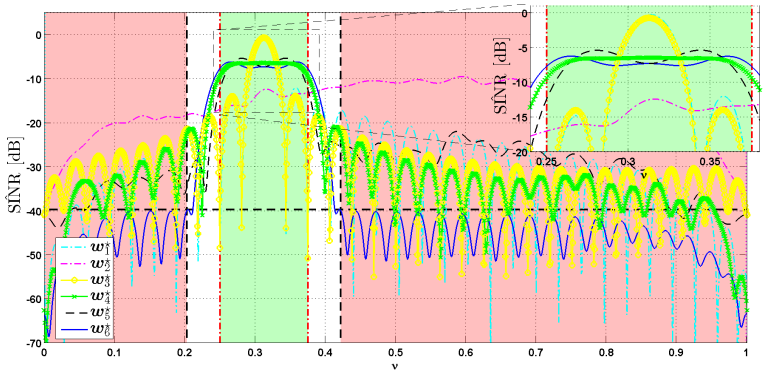

Figure 1a: $\widehat{\text{SINR}}$ vs ν for $\boldsymbol{w}_i^\star$, $i = 1, \ldots, 6$. $\zeta = -32$ dB, $\Theta_1 = [\bar{\nu} - 2/N, \bar{\nu} + 2/N]$, $\Theta_2 = [0, \bar{\nu} - 3.5/N] \bigcup [\bar{\nu} + 3.5/N, 1]$, and $\bar{\nu} = 10/N$.

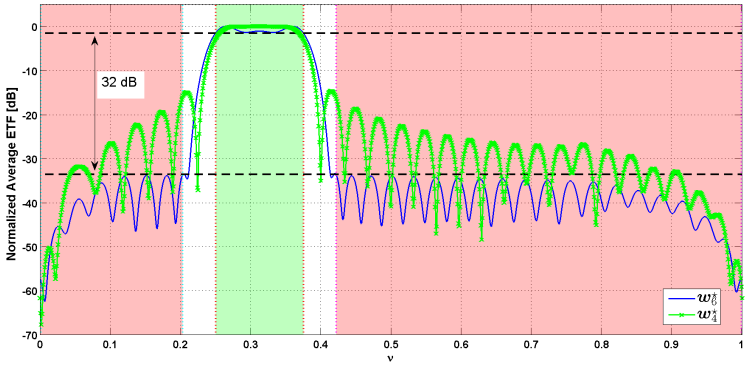

Figure 1b: Normalized average ETF vs ν for $\boldsymbol{w}_4^\star$ and $\boldsymbol{w}_6^\star$. $\zeta = -32$ dB, $\Theta_1 = [\bar{\nu} - 2/N, \bar{\nu} + 2/N]$, $\Theta_2 = [0, \bar{\nu} - 3.5/N] \bigcup [\bar{\nu} + 3.5/N, 1]$, and $\bar{\nu} = 10/N$.

[2] S. A. Vorobyov, A. B. Gershman, and Z. Q. Luo, "Robust Adaptive Beamforming using Worst-Case Performance Optimization: A Solution to the Signal Mismatch Problem", *IEEE Trans. on Sign. Proc.*, Vol. 51, No. 2, pp. 313 - 324, February 2003.

[3] J. Li, P. Stoica, and Z. Wang, "Doubly Constrained Robust Capon Beamforming", *IEEE Trans. on Sign. Proc.*, Vol. 52, No. 9, pp. 2407 - 2423, July 2004.

[4] S. J. Kim, A. Magnani, A. Mutapcic, S. Boyd, and Z. Q. Luo, "Robust Beamforming via Worst-Case SINR Maximization", *IEEE Trans. on Sign. Proc.*, Vol. 56, No. 6, pp. 1539 - 1547, April 2008.

[5] A. De Maio, Y. Huang, M. Piezzo, S. Zhang, and A. Farina, "Design of Radar Receive Filters Optimized According to L_p-Norm Based Criteria", *IEEE Trans. on Sign. Proc.*, Vol. 59, No. 8, pp. 4023 - 4029, August 2011.

[6] J. Capon, "High-Resolution Frequency Wavenumber Spectrum Analysis",*Proceedings of the IEEE*, Vol. 57, No. 8, pp. 1408 - 1418, August 1969.

[7] I. S. Reed, J. D. Mallett, and L. E. Brennan, "Rapid Convergence Rate in Adaptive Arrays", *IEEE Trans. on Aerosp. and Elect. Syst.*, Vol. AES-10, No. 6, pp. 853 - 863, November 1974.

[8] R. G. Lorenz and S. P. Boyd, "Robust Minimum Variance Beamforming", *IEEE Trans. on Sign. Proc.*, Vol. 53, No. 5, pp. 1684 - 1696, May 2005.

[9] Z. L. Yu, W. Ser, M. H. Er, Z. Gu, and Y. Li, "Robust Adaptive Beamformers Based on Worst-Case Optimization and Constraints on Magnitude Response", *IEEE Trans. on Sign. Proc.*, Vol. 57, No. 7, pp. 2615 - 2628, July 2009.

[10] A. Khabbazibasmenj, S. A. Vorobyov, and A. Hassanien, "Robust Adaptive Beamforming Based on Steering Vector Estimation With as Little as Possible Prior Information", *IEEE Trans. on Sign. Proc.*, Vol. 60, No. 6, pp. 2974 - 2987, June 2012.

[11] S. Shahbazpanahi, A. B. Gershman, Z.-Q. Luo, and K. M. Wong, "Robust adaptive beamforming for general-rank signal models," *IEEE Trans. on Sign. Proc.*, Vol. 51, No. 9, pp. 2257 - 2269, September 2003.

[12] A. Aubry, V. Carotenuto, and A. D. Maio, "New Results on Generalized Fractional Programming Problems With Toeplitz Quadratics," *IEEE Sign. Proc. Lett.*, Vol. 23, No. 6, pp. 848 - 852, June 2016.

[13] A. Ben-Tal and A. Nemirovski, *Lectures on Modern Convex Optimization*, http://www.isye.gatech.edu/faculty-staff/profile.php?entry=an63.

[14] A. Aubry, A. De Maio, Y. Huang, and M. Piezzo, "Robust Design of Radar Doppler Filters", in press on *IEEE Trans. on Sign. Proc.*, 2016.

[15] T. Roh and L. Vandenberghe, "Discrete transforms, semidefinite programming, and sum-of-squares representations of nonnegative polynomials", *SIAM J. Optim.*, Vol. 16, No. 4, pp. 939 - 964, 2006.

[16] A. Aubry, A. De Maio, L. Pallotta, and A. Farina, "Maximum Likelihood Estimation of a Structured Covariance Matrix with a Condition Number Constraint," *IEEE Trans. on Sign. Proc.*, Vol. 60, No. 6, pp. 3004 - 3021, June 2012.

[17] H. Li, P. Stoica, and J. Li, "Computationally Efficient Maximum Likelihood Estimation of Structured Covariance Matrix", *IEEE Trans. on Sign. Proc.*, Vol. 40, No. 5, pp. 1314 - 1323, May 1999.

[18] A. Farina, F. Gini, V. Greco, and P. H. Y. Lee, "Improvement Factor for Real Sea-Clutter Doppler Frequency Spectra", *IET Proc. on Radar Sonar Navig.*, Vol. 143, No. 5, pp. 341 - 344, October 1996.

Experimental Analysis of Time Deviation on a Passive Localization System

Hugo Seuté, Cyrille Enderli,
Jean-François Grandin
Thales Airborne Systems
2 Avenue Gay Lussac, 78990 Elancourt, FRANCE
email: {hugo.seute, cyrille-jean.enderli,
jean-francois.grandin}@fr.thalesgroup.com

Ali Khenchaf, Jean-Christophe Cexus
Lab-STICC, UMR CNRS 6285, ENSTA Bretagne
2 Rue François Verny, 29806 Brest, FRANCE
email: {ali.khenchaf, jean-christophe.cexus}
@ensta-bretagne.fr

***Abstract*—In Electronic Warfare, and more specifically in the domain of passive localization, accurate time synchronization between platforms is decisive, especially on systems relying on TDOA (Time Difference Of Arrival) measurements. This paper investigates this issue by presenting an analysis in terms of synchronization performance of an experimental passive localization system based on off-the-shelf components. This system is detailed, as well as the methodology used to carry out the acquisition of real data. This experiment has been realized with two different kinds of clock. The results obtained in the two cases are compared through the analysis of their Allan time deviation. The choice of this metric is explained and its properties are discussed in the scope of an airborne bi-platform passive localization context. Conclusions are drawn regarding the overall performance of the system.**

Keywords—synchronization; time deviation; TDOA; passive localization; USRP (Universal Software Radio Peripheral)

I. INTRODUCTION

Historically, most passive localization systems based on electromagnetic radiation have been developed in the context of Electronic Warfare (EW), and were denoted as ESM (Electronic Support Measures). Various military applications have emerged, where ESM devices are mounted on board different kinds of platforms: airborne [1], naval [2] or even spatial [3].

Passive localization systems use the properties of a signal received at different positions and/or dates in order to compute an estimate of the position of the radiating source. These systems differ from communication systems in that the source does not cooperate with the receiver, thus the waveform is unknown *a priori* and cannot be used to calculate an estimate of the position of the source.

Traditionally, these systems have relied on AOA (Angle Of Arrival) measurements to triangulate the position of the source, but this technique needs time to give an accurate position estimate. This is why other types of measurements have been introduced. Many modern techniques used in passive localization now rely on time based (or frequency based) measurements on different platforms. For example, multilateration techniques are based on the calculation of Time / Frequency Difference Of Arrival (T/FDOA) [1]-[3], [4]-[5], and scan-based localization techniques use the dates of interception of the main lobe of a rotating emitter [6]. Since the measurements depend on the time on two or more remote platforms, several clocks are needed. All clocks have imperfections which make them drift, yet a single time base must be maintained all along the measurement time, hence the need to synchronize the two devices [5].

Synchronization can be done in practice by exchanging a signal in different configurations: one-way, two-ways, common view [7]. It is also possible to dispense with a sync signal if beacons of known positions can be seen by the receivers [8].

This article focuses on a system designed for TDOA localization in a short-base airborne ESM context. This is a challenging scenario for a synchronized system because the measured time differences are small (100 – 1.000 ns) thus the synchronization error must be kept well under these values in order to have good precision [5]. In the scope of this article we will try to determine what performance in sync error we can expect in real-life situations via implementation and analysis of a full synchronization system, comprised of hardware (clocks, digital receivers) and software (delay estimation algorithm) processing.

The paper is organized as follows: Section 2 presents some theoretical background on clock impairments and how to characterize sync error; Section 3 describes the methodology and the experimental process of the measurements which were carried out; In Section 4 the results for two different types of embedded clocks are shown and analyzed from an operational point of view; finally, global conclusions and perspectives are presented in Section 5.

II. TIMEKEEPING ISSUES

A clock can be modeled as a device producing a sine wave output of the form [9]:

$$V(t) = \big(V_0 + \epsilon(t)\big)\sin\big(2\pi f_0 t + \phi(t)\big). \quad (1)$$

where V_0 is nominal peak output voltage, $\epsilon(t)$ amplitude noise, f_0 nominal frequency and $\phi(t)$ phase fluctuation (noise). In the case of time and frequency analysis, we can

978-1-5090-0326-6/16/$31.00 ©2016 IEEE

usually ignore the $\epsilon(t)$ term. From there we can identify two parameters of interest [9]:

- Time fluctuation:

$$x(t) = \phi(t)/2\pi f_0. \quad (2)$$

- Fractional frequency, derived from the latter:

$$y(t) = dx(t)/dt. \quad (3)$$

Due to the non-stationary nature of $\phi(t)$, these quantities cannot be analyzed through traditional statistics, the standard variance estimator will not converge as the number of samples increases [10]. In order to have a way to evaluate the amount of fluctuation of fractional frequency $y(t)$, the Allan variance $\sigma_y^2(\tau)$ was introduced [9][11]. It measures the variance of the difference of two values of y spaced by a time τ. Other versions of the Allan variance were developed, like the modified Allan variance, whose estimates converge more quickly and are capable to distinguish between more types of noise [9][12]. The expression of its estimate in terms of time data is:

$$Mod\ \sigma_y^2(\tau) = \frac{1}{2m^2\tau^2(N-3m+1)} \times$$

$$\sum_{j=1}^{N-3m+1} \left[\sum_{i=j}^{j+m-1}(x_{i+2m} - 2x_{i+m} + x_i)\right]^2. \quad (4)$$

where τ is the time horizon on which the variance is calculated, x_k the k^{th} sample of a dataset containing N values of $x(t)$ sampled every T_s, and $m = \tau/T_s$ the number of samples of $x(t)$ contained in the time horizon τ (m must be an integer such as $m \geq 1$).

The time Allan variance is based on the modified (frequency) Allan variance and characterizes the time error of a clock [13]. It can be expressed as:

$$\sigma_x^2(\tau) = (\tau^2/3) \cdot Mod\ \sigma_y^2(\tau). \quad (5)$$

All the considerations stated above refer to the characterization of a single clock. But in practice it is not possible to measure the absolute fluctuations of a clock ($x(t)$ and $y(t)$) without having another clock to use as a time reference for t. Therefore $x(t)$ and $y(t)$ do not represent the absolute fluctuation of a single clock but the fluctuations of a clock relative to another reference clock. $x(t) = 0$ s means that at a date t the two clocks are perfectly aligned with each other.

$\sigma_x(\tau)$ can be interpreted as the standard deviation of the time error between the clocks considering an integration time of τ. For example, considering that the time error is a white phase noise (such as in the simulation illustrated on Figure 1a), we have $\sigma_x(\tau) \propto 1/\sqrt{\tau}$ [13] (as shown on Figure 1b). It means that the lowest standard deviation of the error is attained when $\tau \to \infty$, so the synchronization process must apply a correction offset corresponding to the mean of as many values of $x(t)$ as possible.

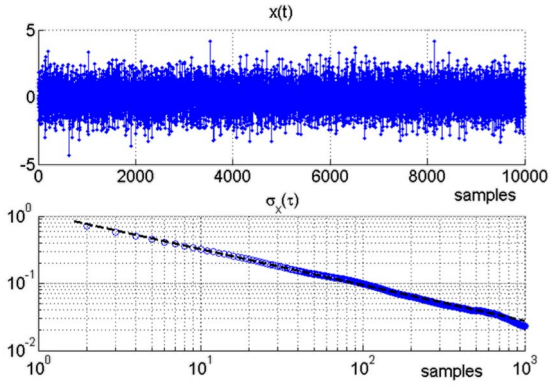

Fig. 1. Representation of time error as a function of time (Fig. 1a, *top*) and time deviation as a function of integration time (Fig. 1b, *bottom*) of a simulated white phase noise process.

On the contrary, if the time error can be modeled by a white frequency noise (like the simulation in Figure 2a), we have $\sigma_x(\tau) \propto \sqrt{\tau}$ [13] (see Figure 2b). In this situation, the lowest standard deviation is achieved when $\tau \to 0$ i.e. $T_s \to 0$. In this case, the best synchronization strategy is to sample $x(t)$ at the highest frequency and use the vector of time errors to correct the time base, without any averaging.

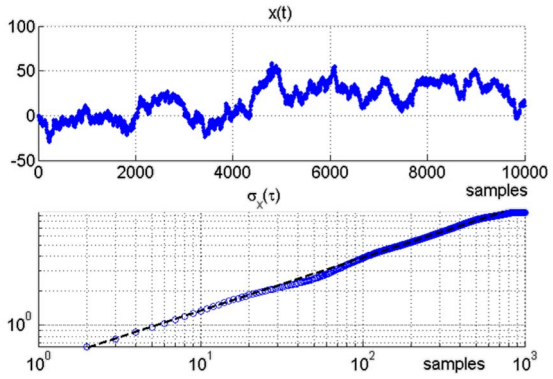

Fig. 2. Representation of time error as a function of time (Fig. 2a, *top*) and time deviation (Fig. 2b, *bottom*) of a simulated white frequency noise process.

In the case of a complex noise model composed of the sum of different noise types (for example in Figure 3, white phase noise and white frequency noise), the function $\sigma_x(\tau)$ may reach a minimum τ_0. Again, an example is given in Figure 3. There, a good way to have a synchronized time base may be to compute the mean of $x(t)$ (which is sampled every T_{s0} with $T_{s0} \leq \tau_0$) on a sliding window of width τ_0 and use the series of these means as a correction.

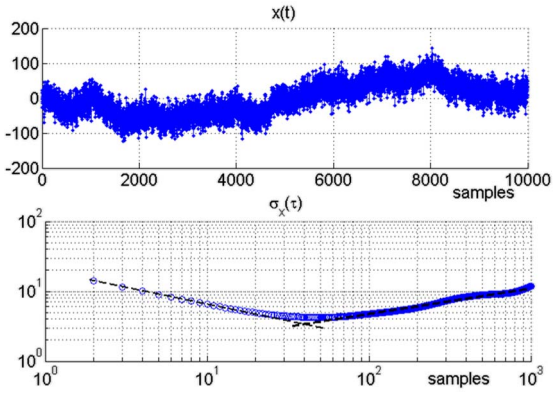

Fig. 3. Representation of time error as a function of time (Fig. 3a, *top*) and time deviation as a function of integration time (Fig. 3b, *bottom*) of a simulated noise process composed of both white phase noise and white frequency noise.

Now we will try to apply the same type of analysis and identify the noise type of real time error data that could have been obtained in an actual ESM system.

III. Methodology and Measurements

In this section will be described the experimental protocol used to acquire time fluctuation data on a passive bi-platform localization system. What we want to evaluate here is not just the performance (in terms of time error) of the clocks of the receivers, but the overall performance of a whole passive system, composed of two remote receivers, including their internal hardware and software processing, their clock and their synchronization protocol.

The receivers used for this experimental study are two Software Defined Radio (SDR) platforms based on a USRP B210 (receiver #1) and a B200 (receiver #2) card, linked to a laptop computer to record the data. This setup was chosen because it allows quick development and experimentation tasks on radiofrequencies from 70 MHz to 6 GHz, it is quite cheap and is available off-the-shelf. Experimental studies on TDOA have already been carried out on USRP devices such as [14] but they did not analyze thoroughly synchronization error.

Here, in order to have an accurate way to measure time error between two receivers, a synchronization system has been developed (Figure 4), based on the emission of a periodic sync signal. The emitter of this signal is actually collocated with receiver #1, inside the B210 card.

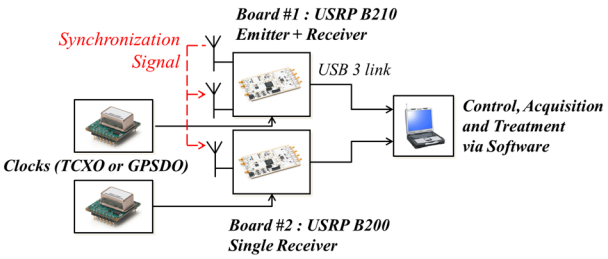

Fig. 4. Diagram of the experimental set-up.

The sync signal is used for two things:

- When it is detected (via a simple threshold detector on the signal's band), the receivers start recording a fixed number of samples into a timestamped file. This avoids to record permanently and to have a huge amount of data to process in the following steps.
- The complex envelopes of the sync signals recorded by the two receivers are processed to accurately obtain the time difference between them

This delay estimation process is described in [15] and [16]. It is done in four steps, as illustrated on Figure 5: First the complex envelopes are cross-correlated, next the points around the main peak of the cross-correlation function are selected, these points are then interpolated by a parabola, and finally the apex of the parabola is computed, which corresponds to the final estimate of the delay between the two signals. In our experiment, the two receivers are situated right next to each other so the difference of path of the sync signal between the two platforms can be neglected. Thus the value at the output of the delay estimation chain directly corresponds to an estimate $\hat{x}(t)$ of $x(t)$ the time error between each receiver.

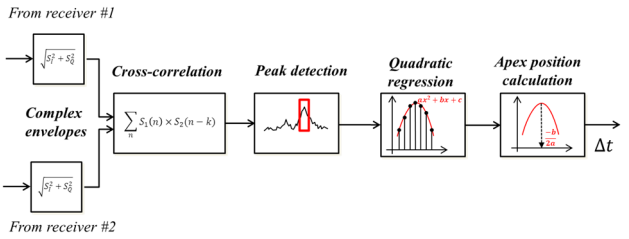

Fig. 5. Diagram of the delay estimation process

Due to these different purposes, there are different requirements on this signal:

- When cross-correlation is computed from the envelope of the signals contained in the two files, the cross-correlation peak must be unambiguous: there must be a single peak which occurs inside an interval of possible delays. Indeed, if the sync signal is periodic with a short period – shorter than the maximum time offset expected between the two records – there will be several cross-correlation peaks that could correspond to a consistent delay estimation.
- This cross-correlation peak needs to be narrow to improve the accuracy of delay estimation. In [15] is stated that the standard deviation of the time offset estimation is proportional to $1/\beta$, where β is the "root mean square radian frequency" of the cross-correlated signals, defined by

$$\beta = 2\pi \left[\frac{\int_{-\infty}^{\infty} f^2 W_s(f) df}{\int_{-\infty}^{\infty} W_s(f) df} \right]^{1/2} \quad (6)$$

where $W_s(f)$ is the signal power density spectrum. Hence the synchronization signal needs to have high frequency components to provide accurate delay estimation.

A signal complying with these requirements has been chosen arbitrarily (represented on Figure 6). It is composed of a carrier modulated in amplitude by a low and a high frequency signal (satisfying respectively the first and second requirement).

$$s(t) = \sin(2\pi f_1 t)\sin(2\pi f_2 t)e^{j2\pi f_{LO} t}. \quad (7)$$

where f_1 and f_2 are the frequencies of the modulated signals and f_{LO} is the carrier frequency.

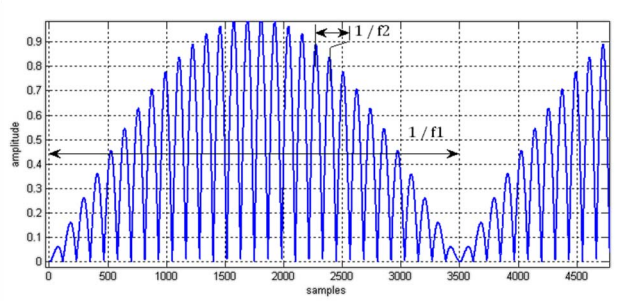

Fig. 6. A representation of the envelope of the sync signal with $f_1 =$ 1 kHz and $f_2 = 30$ kHz, sampled every $T = 143$ ns

The settings used during the measurements are grouped on Table 1.

TABLE I. VALUES OF THE PARAMETERS OF INTEREST

P.	Value	Description
T_s	10 s	Sync signal period of emission
T	143 ns	Sampling period
D_r	200 ms	Duration of the record of the sync signal
f_1	1 kHz	Frequency of the first modulation of the sync signal
f_2	3 MHz	Frequency of the second modulation of the sync signal
f_{LO}	5 GHz	Nominal frequency of the local oscillators on the receivers and emitter

Now that we have a system capable of giving time fluctuations measurements between two receivers, the next step is to produce these data in conditions that are consistent with operational contexts.

IV. MESUREMENT ANALYSIS

Two experiments have been carried out, each featuring a different type of clock (A or B). The same clock type is mounted on both receivers on an experiment. Clocks type A are TCXO (Temperature Compensated crystal Oscillator) and clocks type B are GPSDO (GPS Disciplined Oscillator), which are clocks actually based on the same TCXO but joined to an internal control loop using the 1-PPS (Pulse Per Second) signal from a GPS receiver as a reference.

Figure 7 represents two series of time fluctuation measurements $\hat{x}(t)$ between the two platforms, with the reception system fitted either with clocks type A or clocks type B. Figure 8 shows the Allan time deviation computed from the latter measurements using (4) and (5). The acquisition time for these experiments was 4 hours. The Allan deviation plot is limited to 1 hour (3600 s), because values of $\sigma_{\hat{x}}(\tau)$ for τ close to acquisition time may not be relevant (less samples are averaged, the confidence interval is too large). In other applications, longer acquisition time is often used to analyze the long term behavior of a clock, but in our context of airborne ESM, it appears unlikely that the platforms remains in flight and unable to synchronize for more than an hour.

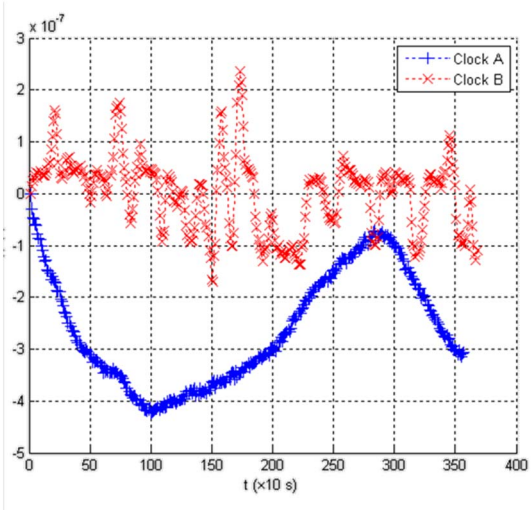

Fig. 7. Measured time error $\hat{x}(t)$ between platforms, for the two experiments

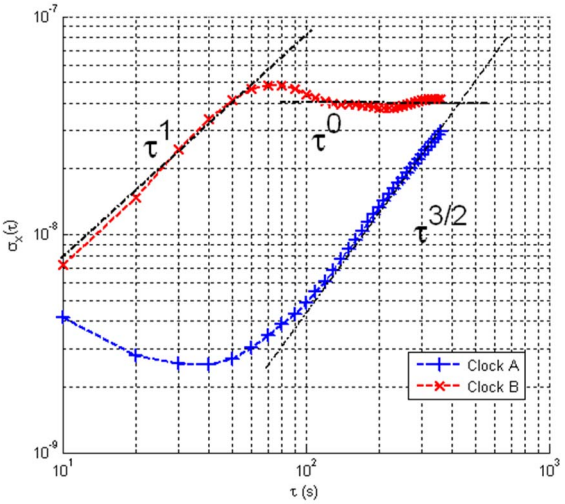

Fig. 8. Experimental Allan time deviation $\sigma_{\hat{x}}(\tau)$ between platforms

What we can see from the time deviation plot (Fig. 8) is that the free running clocks (type A) have good short term stability but when it is left unsynchronized for a long time, time deviation $\sigma_{\hat{x}}(\tau)$ increases proportionally to $\tau^{3/2}$, which is characteristic of a random walk frequency modulation noise [13]. Type A clocks reach a minimum time deviation of 2.5 ns. This minimum is reached when $\hat{x}(t)$ is averaged during a period $\tau_0 = 40$ s.

Clocks type B have a worse short term stability, probably because of an internal control loop which may introduce some high frequency noise in the system. Time deviation increases proportionally to τ, which is representative of a flicker frequency modulation noise [13]. But then it becomes constant (i.e. $x(t)$ is affected by flicker phase modulation noise) after 60 seconds, showing a time deviation of $\sigma_{\hat{x}}(\tau > 60\text{ s}) \approx 40$ ns, which is coherent with time accuracy for a GPS signal [17].

If we extrapolate the results, we see that the minimum time deviation is achieved by using clock A when $\tau < 350$ s and clock B when $\tau > 350$ s. So if the synchronization

period T_s is high (or even infinite: no sync signal exchanged), a GPSDO appears to be the best choice. Typically, this case can happen if the datalink providing synchronization capabilities to the receivers is restricted or unavailable (for stealth purposes or because of jamming). On the contrary, if a short period synchronization signal is available, a standard TCXO seems to be a better option. This is the most common case, where the platforms are not flying inside a hostile zone.

For a TDOA system, the overall standard deviation of the TDOA measurement error is given by:

$$\sigma_{TDOA} = \sqrt{\sigma_{\hat{x}}(\tau)^2 + \sigma_i^2}. \quad (8)$$

where σ_i^2 is the variance of the instrumental error, considered constant over time and independent from synchronization error. In the system we have studied, the time deviation analysis has given a lower bound on the TDOA error: $\sigma_{TDOA} \geq 2.5$ ns. This analysis also helped to determine some conditions to attain this lower bound: in our case a TCXO must be used and a correction offset must be calculated by averaging time fluctuations for 40 s around the dates of the TDOA measurements.

V. Conclusion

The objective of this paper was to point out that the tools developed in frequency analysis (and more particularly the Allan Time Deviation) are very useful to characterize the performances of distributed passive localization systems. These tools help understand the operational impact of technological decisions such as the choices concerning the type of oscillator or the synchronization period of the datalink. In order to attain this objective, a simple but realistic bi-platform system has been set up and time error data has been generated using two different sets of clock. Time deviation has been computed from these data, and from the time deviation plot different operational conclusions have been drawn.

In this paper we only focused on time error noise, but the same principles could be extended to characterize complicated noise processes from other kinds of sensors, such as Inertial Measurements Units (IMU).

References

[1] Arena, L.; Orlando, D., "Passive location developments in Elettronica SpA: System applications," in *Digital Communications - Enhanced Surveillance of Aircraft and Vehicles (TIWDC/ESAV), 2014 Tyrrhenian International Workshop on*, pp.130-134, 15-16 Sept. 2014.

[2] D. Wooller, "System considerations for naval ESM," in *Communications, Radar and Signal Processing, IEE Proceedings F*, vol. 132, no. 4, pp. 212-214, July 1985.

[3] Yang Zheng Bin, Wang Lei, Chen Pei Qun and Lu An Nan, "Passive satellite localization using TDOA/FDOA/AOA measurements," *Conference Anthology, IEEE*, China, 2013, pp. 1-5.

[4] Musicki, D.; Koch, W., "Geolocation using TDOA and FDOA measurements," in *Information Fusion, 2008 11th International Conference on*, pp.1-8, June 30 - July 3 2008.

[5] Seute, H.; Grandin, J.-F.; Enderli, C.; Khenchaf, A.; Cexus, J.-C., "Why synchronization is a key issue in modern Electronic Support Measures," in *Radar Symposium (IRS), 2015 16th International*, pp.794-799, 24-26 June 2015.

[6] Hmam, H., "Scan-based emitter passive localization," in *Aerospace and Electronic Systems, IEEE Transactions on* , vol.43, no.1, pp.36-54, January 2007.

[7] Cheng, L.; Hailes, S.; Wilson, A., "Towards Precise Synchronisation in Wireless Sensor Networks," in *Embedded and Ubiquitous Computing (EUC), 2010 IEEE/IFIP 8th International Conference on*, pp.208-215, 11-13 Dec. 2010.

[8] Pelant, M.; Stejskal, V., "Multilateration system time synchronization via over-determination of TDOA measurements," in *Digital Communications - Enhanced Surveillance of Aircraft and Vehicles (TIWDC/ESAV), 2011 Tyrrhenian International Workshop on*, pp.179-183, 12-14 Sept. 2011.

[9] IEEE Standard Definitions of Physical Quantities for Fundamental Frequency and Time Metrology--Random Instabilities - Redline," in *IEEE Std 1139-2008 (Revision of IEEE Std 1139-1999) - Redline*, pp.1-51, Feb. 27 2009.

[10] Allan, D.W., "Should the classical variance be used as a basic measure in standards metrology?," in *Instrumentation and Measurement, IEEE Transactions on* , vol.IM-36, no.2, pp.646-654, June 1987.

[11] Allan, D.W., "Statistics of atomic frequency standards," in *Proceedings of the IEEE* , vol.54, no.2, pp.221-230, Feb. 1966.

[12] Allan, D.W.; Barnes, J.A., "A Modified "Allan Variance" with Increased Oscillator Characterization Ability," in *Thirty Fifth Annual Frequency Control Symposium. 1981*, pp.470-475, 27-29 May 1981.

[13] Allan, D.W.; Weiss, M.A.; Jespersen, James L., "A frequency-domain view of time-domain characterization of clocks and time and frequency distribution systems," in *Frequency Control, 1991, Proceedings of the 45th Annual Symposium on*, pp.667-678, 29-31 May 1991.

[14] Seong Han Cho; Sang Rae Yeo; Heon Ho Choi; Chansik Park; Sang Jeong Lee, "A design of synchronization method for TDOA-based positioning system," in *Control, Automation and Systems (ICCAS), 2012 12th International Conference on*, pp.1373-1375, 17-21 Oct. 2012.

[15] Stein, S., "Algorithms for ambiguity function processing," in *Acoustics, Speech and Signal Processing, IEEE Transactions on* , vol.29, no.3, pp.588-599, Jun 1981.

[16] Seute, H.; Grandin, J.-F.; Enderli, C.; Khenchaf, A.; Cexus, J.-C., " Experimental Measurement of Time Difference Of Arrival," in *Radar Symposium (IRS), 2016 17th International*, in press.

[17] GPSDO Datasheet, Ettus Research, May 2014.

Beampattern and polarisation synthesis of 3D RF-seeker antenna arrays

Luc Fourtinon[1,3], Alessio Balleri[1], Yves Quéré[2], Christian Person[3], Annaig Martin-Guennou[2], Eric Rius[2], Guillaume Lesueur[4], Thomas Merlet[4]

[1]Centre for Electronic Warfare, Cranfield University, Shrivenham, SN6 8LA, UK

[2]Université de Brest, CNRS, UMR 3192 Lab-STICC, 6 avenue le Gorgeu, CS 93837, 29238 Brest Cedex, France

[3]Telecom-Bretagne, Technopole Brest-Iroise, CS 83818, 29238, Brest Cedex, France

[4]Thales Optronique S.A.S, 2 Avenue Gay Lussac, 78996 Élancourt, France

***Abstract*—Existing missile radar seekers use a mechanical rotating antenna to steer the radiating beam in the direction of the target. Recent research is investigating the possibility to replace the mechanical RF seeker with a novel 3D conformal antenna, embedded below the radome, that can steer the beam electronically. 3D conformal antenna arrays may offer many advantages, such as a higher gain and an extended coverage, and new degrees of freedom which derive from the resulting higher flexibility in the choice of the 3D shape. Despite this, they also present new technical challenges, related to the robustness of the beampattern characteristics as a function of the steering angle, that must be addressed.**

The overall objective of our research is to design, prototype and assess the performance of novel 3D conformal antenna arrays for RF seekers. In order to do this, a first study has been carried out to generate and display the polarisation pattern of any 3D antenna arrays. In this paper, we present an electromagnetic antenna tool that has been developed to carry out an analysis of beamforming and polarisation for any shape of 3D antennas. The program imports the pattern of an individual element of the array and generates the global radiation pattern by coherently summing the contribution of each element. One feature of the tool is the calculation of the polarisation pattern induced by the conformation which provides a complete description of the time varying electric field of the array.

List of symbols

Symbol	Meaning
E_x, E_y, E_z	Components of the electric field
E_{xrot}, E_{yrot}, E_{zrot}	Components of the rotated electric field
E_n	Electric field of the n-th antenna element
E_{total}	Electric field of the whole array
k	Wave number
$\mathbf{r}$	Position vector of the n-th element
$\mathbf{u}_n$	Vector direction of a unity sphere
E_θ	Elevation component of the field
E_φ	Azimuth component of the field
χ	Ellipticity
ρ	E_θ/E_φ
θ, φ	Steering directions in the 3D space

I. Introduction

Existing RF seeker antennas are flat and steer the beam with a rotational mechanism. This technology of antenna has many drawbacks: it is slow, bulky and fragile, it offers a limited coverage, and cannot provide tracks of multiple targets simultaneously. To counteract these drawbacks, a 3D conformal electronically steerable antenna is proposed. The 3D shape offers a wider elevation coverage and the electronic control results in a faster moving beam that can potentially allow multi-target tracking. The mechanical system removal may also reduce the RF seeker weight and costs and increase the system robustness against the vibrations produced by the high-speed missile (up to Mach 4). Recent technological advances, such as 3D printing and new selective metallisation technology, have ensured that the production of 3D antennas is now feasible at a relatively low cost. A sketch of a 3D antenna is shown in Fig. 1.

It is well known that for a flat array with aligned and identical elements, the global radiation pattern and polarisation show the same properties of that of a single element. However, when the elements are conformed over a 3D shape, single element contributions interfere with one another and this results in a different and a complex co-pol and cross-pol pattern. Because of this, further studies are required to find suitable 3D solutions. In the existing literature, a lot of work has been carried out to optimise the radiation pattern of a given array exploiting various existing optimisation methods [1], [2], [3]. In [4], the authors presented a fast iterative method to optimise the co-polarisation and cross-polarisation patterns of an antenna array consisting of dipoles conformed over a truncated cone shape. They showed that the use of a simple radiating element results in a significant limitation in the control of the radiating beam. In [5], the authors optimised the excitation in order to achieve sidelobes and cross-polarisation levels 30dB below the co-pol main beam. They carried out their analysis using a sphere covered with dual-polarised patch elements. In [6], the author optimised the excitation of the elements to reach a desired radiation pattern of a difference channel. The spherical representation and the 3rd Ludwigs definition [7] were used in [1] - [6] to minimise the cross-

978-1-5090-0326-6/16/$31.00 ©2016 IEEE

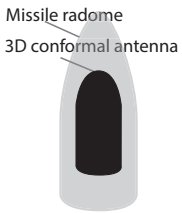

Fig. 1: Antenna below the radome

polarisation pattern of a 3D array. Other works, such as [8], have analysed the polarisation by characterising the magnitude of the ratio between the co-pol and cross-pol components. Most of previous studies have investigated the polarisation properties by analysing the co-pol and cross-pol patterns. However, there is little work in the literature attempting to fully describe the polarisation for 3D antennas in all directions and very little results, if any, showing how the vector that identifies the electric field rotates as a function of time.

The overall objective of our research is to design, prototype and assess the performance of novel 3D conformal antenna arrays for RF seekers. In this paper, we present a Matlab tool that has been developed to compute the radiation pattern of any 3D arrays. The array can be built with any type of element and the 3D pattern is obtained by first importing the radiation pattern of each element from a finite element software and then by coherently adding all the single contributions. The software allows the study of the pattern of any antenna shape and displays the resulting polarisation pattern either by plotting the polarisation ellipse or by displaying the magnitude and directivity of co-pol and cross-pol components.

In section II, the description of the Matlab program is given. In section III, an example with two orthogonal elements is presented to illustrate the complexity and the impact of the conformation on the polarisation. Finally a half-sphere antenna polarisation is investigated as a potential shape for RF-seeker.

II. The Matlab tool program

In order to progressively go towards the design and optimisation of a complex RF-seeker antenna, a Matlab program has been developed to study the pattern of any 3D antenna array. A scheme of the program framework is given in Fig. 2. The developed software allows the user to import the radiation pattern of any element once computed with a simulation software (e.g. HFSS). This allows the study of arrays consisting of complex elements for which an analytical expression of the pattern is unknown. The main shape of the array is selected and implemented by indicating the location of the phase centres of each element and then the elements are rotated in 3D around their phase centres to produce a specific antenna design. The array beampattern is calculated by applying a suitable phase difference to each element and then by superimposing each contribution to compute the global array pattern. This tool allows the testing of complex shapes with high flexibility.

1) Radiation pattern rotation: The rotation of an antenna element is carried out in two steps. Firstly, the vectors of

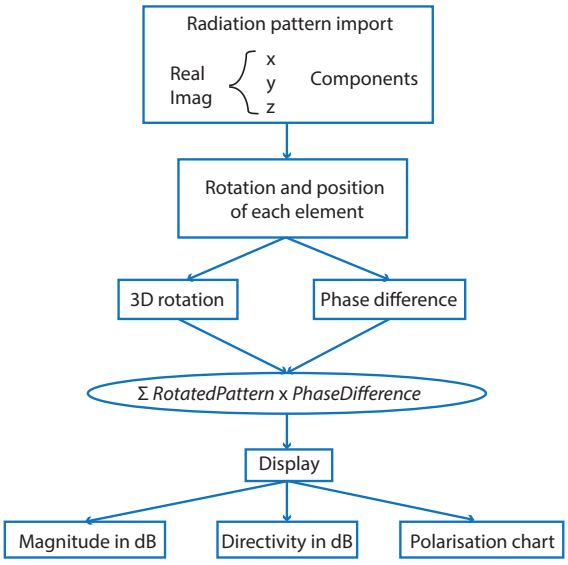

Fig. 2: Scheme of the Matlab tool

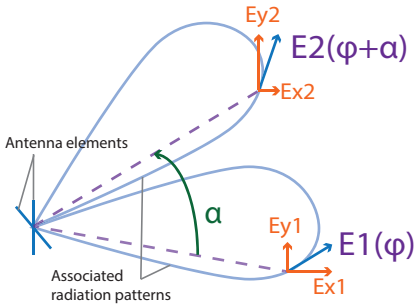

Fig. 3: Scheme of the rotation

the radiation pattern are rotated and secondly their location is changed. This two step rotation is illustrated in Fig. 3. We assume a vector E_1 tangent to an element antenna radiation pattern. This element antenna is rotated by an angle α, it also rotates the radiation pattern and the vector becomes E_2. Hence, once rotated, the components (E_{x1}, E_{y1}) of the original vector E_1 become (E_{x2}, E_{y2}). Secondly, the position of the vector is changed, in this example, it is rotated from the angle φ to the angle $\varphi + \alpha$.

Mathematically, the first step is achieved by multiplying the 3 components of the field, E_x, E_y, E_z, by a rotation matrix M to obtain the new components: E_{xrot}, E_{yrot}, E_{zrot}.

$$\begin{bmatrix} E_{xrot} \\ E_{yrot} \\ E_{zrot} \end{bmatrix} = M \begin{bmatrix} E_x \\ E_y \\ E_z \end{bmatrix} \tag{1}$$

The second step consists in moving the location of the vectors from the direction (θ_i, φ_i) to the direction (θ_j, φ_j).

2) The coherent sum: Once the rotation is applied and the new expression of the electric field is known for the n-th element $\mathbf{E}_n(\theta_n, \varphi_n)$, the coherent sum is carried out as:

$$\mathbf{E}_{total}(\theta, \varphi) = \sum_n \mathbf{E}_n(\theta_{nj}, \varphi_{nj}) \cdot e^{-jk\mathbf{r}\cdot\mathbf{u}_n} \tag{2}$$

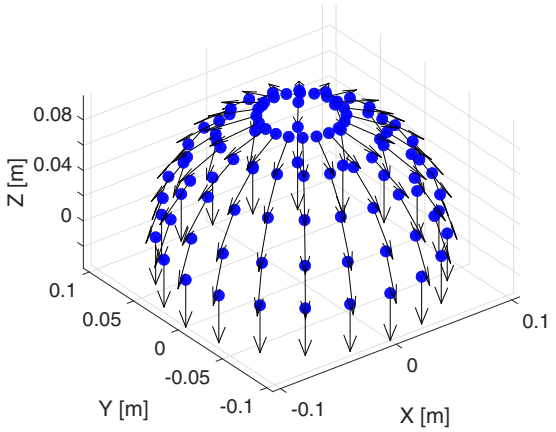

Fig. 4: Positions (blue sphere) and orientations (black arrows) of the half-sphere antenna elements

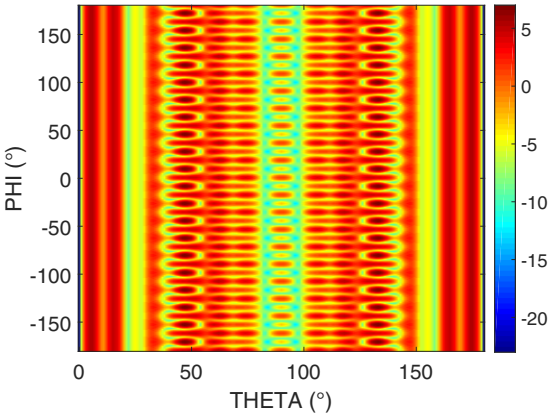

Fig. 5: Half-sphere radiation pattern

where $e^{-jk\mathbf{r}\cdot\mathbf{u}_n}$ is the phase shift and k is the wave number. The phase term in equation 2 can also be seen as a 3D array factor. The calculation of the phase in all the directions is carried out by a scalar product of the position vector $\mathbf{r}$ with all the vector direction $\mathbf{u}_n$ of the unity sphere. Then sum of all the elements with their respective phase is carried out to obtain and lead to the total radiation pattern: $\mathbf{E}_{total}(\theta, \varphi)$.

Finally the result can be displayed according to user choice, in amplitude, directivity or polarisation. The following section will expand this latter option.

3) Example of a 3D array: An example of the output of the Matlab tool is given for a half-sphere shape covered with 100 Hertzian dipoles. The array consists of 5 rings of 20 elements each, and these are arranged so that the spacing between elements increases as the angle θ increases. There is no element at $\theta = 0°$. The topology and the radiation pattern are shown in Fig. 4 and Fig. 5.

Results show that the resulting pattern is periodical with repeating sidelobes and nulls. The number of repetition is 20 and this, as expected, matches the number of elements in each ring. The pattern shows a low gain at $\theta = 0°$ due to the fact that each element has an opposite phase with respect to the z-symmetric axis of the array.

The simulation results of the software can be displayed as the magnitude or directivity of the radiation pattern. When the array polarisation state is sought, the main axis of the polarisation ellipse is given thanks to the polarisation chart which is introduced in Section III.

III. The Polarisation Chart

One of the key features of the developed tool is the polarisation chart. The analysis of the polarisation is a fundamental point for future studies of the radar seeker performance. The effects of target depolarisation can only be investigated if the emitted antenna polarisation is perfectly known. Hence, it is an imperative to have a complete description of all the components of the electromagnetic field in all directions. Our tool provides the polarisation state of the emitted signal and

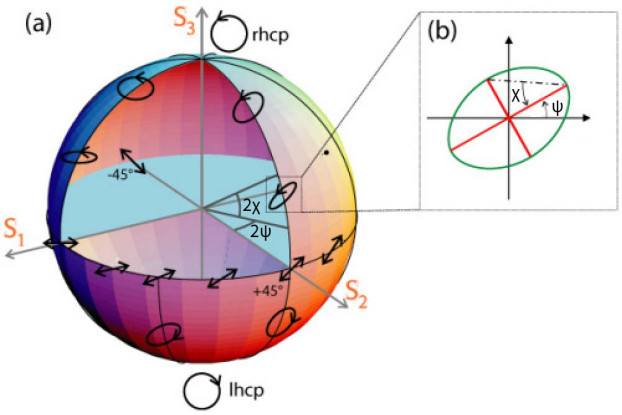

Fig. 6: (a) The Poincare sphere and the elliptic states ; (b) The ellipse parameters

the time-trace of the electric field vector. A first convenient representation gathers the amplitude and elliptical trajectory of the electric vector by multiplying the θ and φ components of the field, E_θ and E_ϕ, by a phase varied from $\varphi_{var} = 0°$ to $360°$.

$$E = \begin{bmatrix} 0 \\ E_\theta e^{j\varphi_{var}} \\ E_\phi e^{j\varphi_{var}} \end{bmatrix}$$

Another representation uses the Stokes parameters which identify a point on the Poincaré sphere [9]. Each point of a sphere represents a unique state of the polarisation as shown in Fig. 6 and hence provides a figure of merit of the ellipticity of the electric field trajectory. The expression of the ellipticity in the Poincare sphere is given by the expression:

$$\chi = \frac{1}{2}\arcsin\left(\frac{Imag(\rho)}{1+\mid \rho^2 \mid}\right) \tag{3}$$

where $\rho = \frac{E_\theta}{E_\phi}$.

A. Example of 2 orthogonal Hertzian dipoles

In order to show how polarisation can change for effect of a 3D conformation we present a simple example with Hertzian

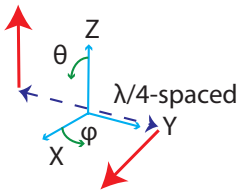

Fig. 7: Scheme of the two orthogonal Hertzian dipoles

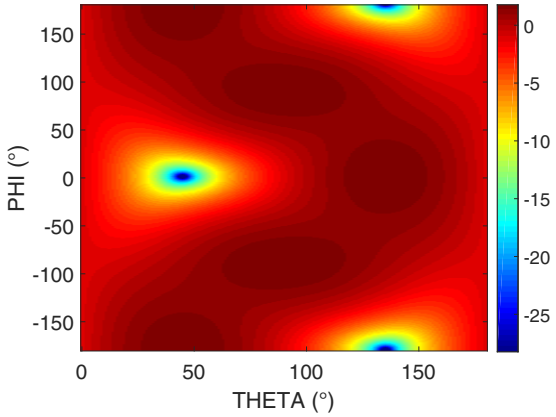

Fig. 8: Radiation pattern in directivity (dB) of the two orthogonal elements

dipoles. For this element, the Poynting vector points in all directions and in a typical spherical coordinate system, the electric field is fully described by the θ component. The dipole radiates a pure linear polarisation in all directions.

Let us consider the case of two orthogonal $\frac{\lambda}{4}$-spaced Hertzian dipoles arranged as shown in Fig. 7. This configuration was chosen as it is arguably between the simplest possible options in the 3D space, but as the same time, it highlights how much complex the polarisation pattern can be for 3D and conformal antennas. It is also simple enough to allow an experimental verification of the theoretical results. We assume that the dipoles are ideal and that there is no cross coupling between elements.

The result of the constructive and destructive interferences is shown in Fig. 8 with a plot of the directivity of the electric field. Results show that a null and a maximum occur at $(\theta = 45°, \varphi = 0°)$ and $(\theta = 135°, \varphi = 0°)$. However, the gain itself does not provide any insight about the polarisation state of the emitted field.

There are at least three directions in the space for which the results of the polarisation can be easily predicted.

- P1: In the z-direction, we have a null from the vertical element and a maximum value from the horizontal one along the θ-component, hence, we should have a linear polarisation.
- P2: In the x-direction, the reasoning is reversed, we have a maximum from the vertical element and a null from the horizontal one, hence, the polarisation is again linear.
- P3: In the y-direction, we have a maximum radiated by each antenna and a phase of $90°$ between each component due to the $\frac{\lambda}{4}$-distance between each element, consequently we should have a circular polarisation.

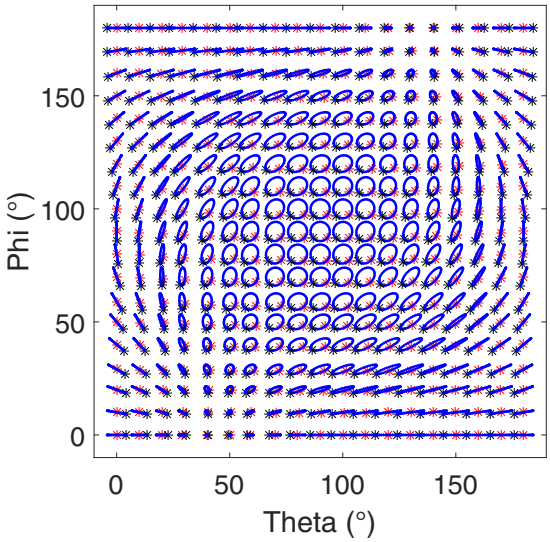

Fig. 9: Polarisation chart of the two orthogonal elements

The results of the simulation for the polarisation chart are shown in Fig. 9. The references of the θ and φ angles are given in Fig. 7. The ellipticity of the field varies from linear to circular as expected passing through many different elliptic states. The field rotation directions are also indicated by the black and red dots. From black to red dots, the phase is increasing from $0°$ to $90°$. Hence the array radiates right handed circular polarisation.

We compare the simulation results with the three previous predictions:

- P1: In the z-direction or ($\theta = 0°$,$\varphi = X$) the value of the ellipticity is $\chi = 0°$, which means linear, this is correct.
- P2: In the x-direction or ($\theta = 90°$,$\varphi = 0°$) the value of the ellipticity is $\chi = 0°$,which means linear, this is also correct.
- P3: In the y-direction or ($\theta = 90°$,$\varphi = 90°$) the ellipticity is $\chi = 45°$, which means circular, this is correct again.

If a linear polarisation is desired in all directions, and the simulations show a very low amplitude where the field tends to be circular, this may not be a problem. That is why cumulating both information on the ellipticity and amplitude is necessary. However, results stay qualitative and this is why ellipticity calculated with the Stokes parameters can be used as a figure of merit. Results are shown in Fig. 10 for all directions of the unit sphere. The values of the ellipticity diagram are between $0°$ and $45°$ after calculating the absolute value of the χ parameter. If the polarisation is linear the value is $\chi = 0°$ and if it is circular we have $\chi = 45°$. Otherwise the field is elliptic. The values of the ellipticity are confirmed in the prediction directions.

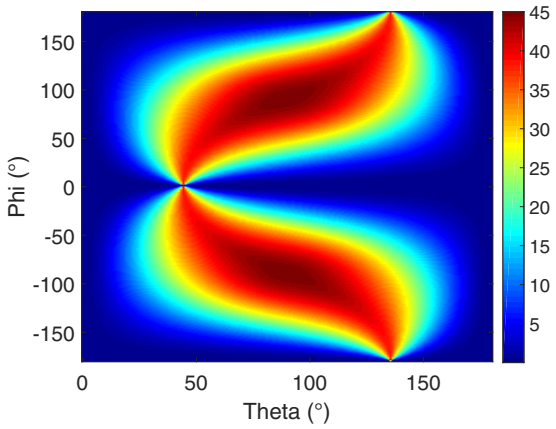

Fig. 10: Ellipticity of the two orthogonal elements

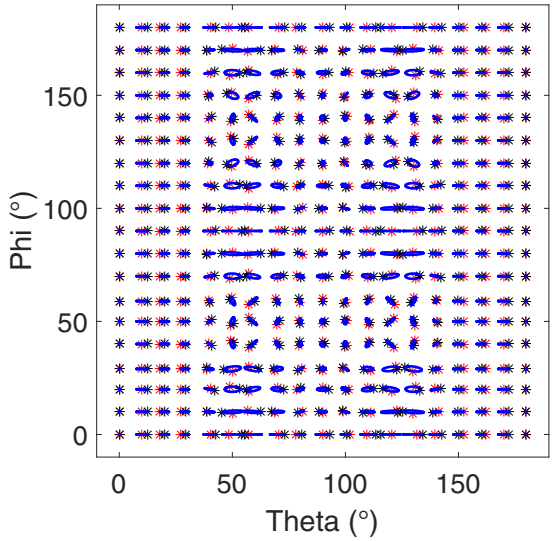

Fig. 11: Polarisation chart of the half-sphere array

B. *Polarisation ellipticity of a half-sphere*

For completeness, the result of the polarisation analysis are presented for the example of the half-sphere. The polarisation chart and ellipticity are shown in Fig. 11 and 12. As expected the antenna radiates both linear and circular polarisation. Results also show that the polarisation is mostly linear and in the directions where circular polarisation is radiated, the radius of the ellipse is large meaning that the energy radiated is high. Thus it may be desirable to change the element orientation to avoid this effect. These results were somehow predictable. The polarisation of one dipole is contained in the θ component but after the rotation of the element a part of the field goes into the φ-component by projection. Because of this we can expect circular polarisation in some directions for the total radiated field.

IV. Conclusion and Future work

In this paper, we present a Matlab tool that has been developed to compute the radiation pattern of any 3D arrays. A simple example with two dipole elements has been presented where the emitted polarisation could be verified. A half-sphere with 100 elements has also been studied to show the efficiency of the tool. The Matlab tool can display the polarisation state of the emitted field. This is an important effect induced by the conformation and which requires further research. Future work will look at controlling the polarisation deviation as a function of the element orientation, the effect of non-linear array and the effect of the polarisation deviation on the radar performance.

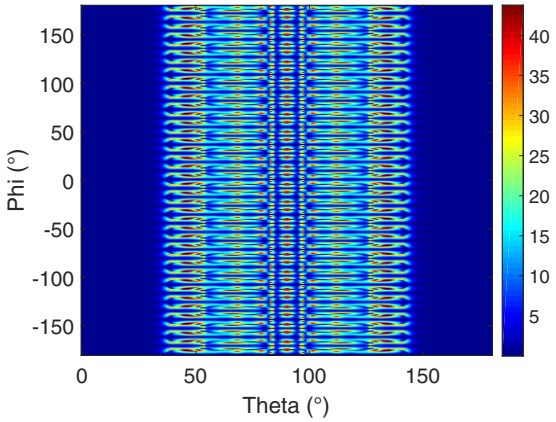

Fig. 12: Ellipticity of the half-sphere array

Acknowledgment

We thank La Direction Générale de l'Armement (DGA) for the financial support towards the PhD of Luc Fourtinon.

References

[1] B. H. Wang, Y. Guo, Y. L. Wang, and Y. Z. Lin, "Frequency-invariant pattern synthesis of conformal array antenna with low cross-polarisation," *IET Microwaves, Antennas Propagation*, vol. 2, no. 5, pp. 442–450, August 2008.

[2] D. W. Boeringer and D. H. Werner, "Efficiency-constrained particle swarm optimization of a modified bernstein polynomial for conformal array excitation amplitude synthesis," *IEEE Transactions on Antennas and Propagation*, vol. 53, no. 8, pp. 2662–2673, Aug 2005.

[3] M. Dinnichert, "Full polarimetric pattern synthesis for an active conformal array," in *Phased Array Systems and Technology, 2000. Proceedings. 2000 IEEE International Conference on*, 2000, pp. 415–419.

[4] M. Comisso and R. Vescovo, "Fast co-polar and cross-polar 3d pattern synthesis with dynamic range ratio reduction for conformal antenna arrays," *IEEE Transactions on Antennas and Propagation*, vol. 61, no. 2, pp. 614–626, Feb 2013.

[5] C. Dohmen, J. W. Odendaal, and J. Joubert, "Synthesis of conformal arrays with optimized polarization," *IEEE Transactions on Antennas and Propagation*, vol. 55, no. 10, pp. 2922–2925, Oct 2007.

[6] L. I. Vaskelainen, "Iterative least-squares synthesis methods for conformal array antennas with optimized polarization and frequency properties," *IEEE Transactions on Antennas and Propagation*, vol. 45, no. 7, pp. 1179–1185, Jul 1997.

[7] A. Ludwig, "The definition of cross polarization," *IEEE Transactions on Antennas and Propagation*, vol. 21, no. 1, pp. 116–119, Jan 1973.

[8] K. F. Lee, K. M. Luk, and P. Y. Tam, "Crosspolarisation characteristics of circular patch antennas," *Electronics Letters*, vol. 28, no. 6, pp. 587–589, March 1992.

[9] K. Naishadham, "Introduction to radar polarimetry," in *Principles of Modern Radar, Vol. II Advanced Techniques*, J. A. S. William L. Melvin, Ed. SciTech Bublishing, 2013, ch. 13, pp. 589–629.

Adaptive M-estimation for Robust Cubature Kalman Filtering

Changliang Zhang, Ruirui Zhi
School of Mechanical Engineering
Northwestern Polytechnical University
Xi'an, China
{zhangchangliang, zhirr}@mail.nwpu.edu.cn

Tiancheng Li, Juan M. Corchado
School of Sciences
University of Salamanca
Salamanca, Spain
{t.c.li, corchado}@usal.es

***Abstract*—As a l_1/l_2 norms-based estimation method, Huber's M-estimation has provided an efficient method to deal with measurement outliers for robust filtering, which has been applied to the cubature Kalman filter (CKF), namely Huber's M-estimation based robust CKF (HCKF) and its square-root version (HSCKF). To further handle abnormal measurement noise, an adaptive method is proposed in this paper to adjust the measurement noise covariance used in the Huber's M-estimation approach based on the difference between actual and theoretical innovation covariance, leading to adaptive HCKF (AHCKF) and adaptive HSCKF (AHCKF). Simulation results on a typical target tracking model have demonstrated their advantages over existing approaches in terms of estimate accuracy, outlier-robustness and reliability.**

***Keywords*—Robust estimation; M-estimation; point estimator; Kalman filter; target tracking**

I. INTRODUCTION

Dynamic state estimation has been a long-standing research topic concerned with the sequential process of estimating the state evolving over time that is periodically observed by sensors. The optimal recursive estimator in the Bayesian sense requires the complete posterior density of the state to be determined as a function of time. For a limited class of linear and Gaussian models, the Bayesian estimator is the exact Kalman filter which is a linear minimum mean square error (LMMSE) estimator for Gaussian linear system [1]. But, for a general nonlinear filtering problem, there is no analytic closed-form solution but one has to seek some forms of approximation.

A common solution to approximate the arbitrary posterior density is sampling, which can be either random or deterministic. In the former case, the particle filter has gained the most popularity but it suffers from the intensive computation and has its own problems [2]. On the other hand, deterministic sampling, though most limited to the Gaussian uncertainty family, can be computationally much faster and has inspired a variety of different implementations such as the unscented Kalman filter (UKF), central difference Kalman filter (CDKF), divided difference filter (DDF), Gauss-Hemet filtering (GHF) and cubature Kalman filter (CKF) and square-root CKF (SCKF) [3], which differ from each other in the way to "deterministically" construct the samples to calculate the statistics of the Gaussian distribution after nonlinear transformation; see the surveys e.g. [4-5]. In particular, the CKF/SCKF is suitable for high-dimensional systems and enjoys better numerical stability, computational efficiency and accuracy [3].

These Kalman-type filters are essentially point estimators which assume that both the process and measurement noises are known in priori. This is however unrealistic but instead they are often missing and have to be learned from either training data or online data; the latter is related to the robust filtering design and is the concern of this paper. For this, a maximum likelihood estimator was proposed to estimate the system noise based on the state residual (which is the estimate discrepancy between before and after the measurement update) in [6]. It was proposed to use the previous sensor data sequences to estimate the current noise covariance [7]. Furthermore, Busse [8] and Lee [9] proposed "sliding window" methods to account for more history information, gaining better results. However, these methods are ineffective to outliers (i.e. the measurement noise has a large singular value that is significantly abnormal). To overcome this, a noise statistic estimator was developed [10] to accommodate modeling uncertainties for robustness based on the principle of maximum a posterior (MAP). On the other hand, an adaptive method was proposed to switch between standard, adaptive and robust KF through measuring the innovation, to deal with clutter in both processes and measurements [11]. The modulation regimen used therein is a single element attached on the corresponding matrix, unlike Huber's M (maximum-likelihood-type)-estimation. Another robust and adaptive KF was proposed in [12], in which at any epoch, an initial state estimator is firstly calculated using only the current measurement through Huber's M-estimation for robustness, which is used to improve the prior estimate of the noise covariance. The procedure can not only resist the influence of outlying kinematic model errors, but also control the effects of measurement outliers.

The M-estimation that was proposed by Huber [13] based on generalized maximum likelihood estimation (MLE) can handle clutter in both processes and measurements. It was proposed to be applied in the KF for robust filtering [14], and then extended to other point estimators, such as, robust DDF [15], robust UKF [16-18] and robust CKF [19-21]. These robust M-estimation methods however cannot adjust the noise covariance adaptively when it does not match with the truth. The problem will become more severe in the case of significant outliers. To overcome this deficiency, in this paper, we propose an adaptive M-estimation strategy which aims to automatically adjust the measurement noise covariance, gaining adaptivity in addition to the robustness gained by Huber's M-estimation. The M-estimation realized in our approach will modify the prior estimate of the covariance, different to [18]. Our algorithms, owning enhanced adaptivity and robustness, are realized with both CKF and SCKF, referred to as adaptive M-estimation based CKF (AHCKF) and SCKF (AHSCKF), respectively.

The work is partly funded by Marie Skłodowska-Curie Individual Fellowships (Grant no. 709267)

978-1-5090-0326-6/16/$31.00 ©2016 IEEE

The reminder of the paper is organized as follows. Huber's M estimation is briefly given in Section II. Our improvement is given in Section III. Simulation evaluation is given in terms of estimation accuracy, filtering stability, and robustness in Section IV. We conclude in Section V.

II. HUBER'S M-ESTIMATION

We start with the following discrete-time state-space model

$$\begin{aligned} x_k &= f(x_{k-1}) + w_k \\ y_k &= h(x_k) + v_k \end{aligned} \tag{1}$$

where k is the time, $x_k \in \mathbb{R}^n$ is the state, $y_k \in \mathbb{R}^{n_y}$ is the measurement, $f(\cdot)$ and $h(\cdot)$ are the state transition and measurement functions, w_k and v_k are the zero-mean Gaussian process noise and zero-mean Gaussian measurement noise with covariance matrixes Q and R respectively, i.e.

$$\begin{aligned} E(w_k) = 0, \;\; E(w_k w_j^T) = Q\delta_{kj} \\ E(v_k) = 0, \;\; E(v_k v_j^T) = R\delta_{kj} \end{aligned} \tag{2}$$

where δ_{kj} is Kronecker-delta function.

We would omit the detail of the CKF and SCKF due to the page limitation and review Huber's M-estimation [13-18] in brief. For Gaussian noises, the M-estimation can make the upper bound of progressive estimated variance to a minimum, and its robustness is better than l_2-norm estimation while keeping the estimated efficiency of l_1-norm estimation. Considering the state model given by (1), assume the state x is subject to a Gaussian distribution with mean μ and covariance Σ. The M-estimation of state x is given by minimizing the following cost function

$$J(x) = \rho\left(\Sigma^{-1/2}(x-\mu)\right) \tag{3}$$

where $\rho(\cdot)$ is an appropriate positive symmetric function. This is different from MLE that minimizes $(x-\mu)^T\Sigma^{-1}(x-\mu)$.

More specifically, on the predicted state $\hat{x}_{k|k-1}$ we have

$$x_k = \hat{x}_{k|k-1} + \delta x_k \tag{4}$$

where δx_k is state prediction error with covariance $P_{k|k-1}$.

Given the measurement matrix H_k

$$H_k = \left(P_{k|k-1}^{-1} P_{xy,k|k-1}\right)^T \tag{5}$$

where $P_{xy,k|k-1}$ is the state-measurement cross-covariance calculated using cubature samples [3], the measurement function can be reformulated in matrix as (a linear regression model)

$$\begin{bmatrix} y_k - h(x_{k|k-1}) + H_k \hat{x}_{k|k-1} \\ \hat{x}_{k|k-1} \end{bmatrix} = \begin{bmatrix} H_k \\ I \end{bmatrix} x_k + \begin{bmatrix} \eta_k \\ -\delta x_k \end{bmatrix} \tag{6}$$

Definite the quantities

$$D_k = \begin{bmatrix} R_k & O_{n_y \times n} \\ O & P_{k|k-1} \end{bmatrix} \tag{7}$$

$$z_k = D_k^{-1/2} \begin{bmatrix} y_k - h(\hat{x}_{k|k-1}) + H_k \hat{x}_{k|k-1} \\ \hat{x}_{k|k-1} \end{bmatrix} \tag{8}$$

$$M_k = D_k^{-1/2} \begin{bmatrix} H_k \\ I \end{bmatrix} \tag{9}$$

$$\chi_k = D_k^{-1/2} \begin{bmatrix} \eta_k \\ -\delta x_k \end{bmatrix} \tag{10}$$

Then the linear regression problem can be written as

$$z_k = M_k x_k + \chi_k \tag{11}$$

Huber's M-estimation minimizes the cost function

$$J(x_k) = \sum_{i=1}^{n_y+n} \rho(u_i) \tag{12}$$

where u_i refers to the ith component of the residual vector $u = M_k x_k - z_k$, and the function $\rho(\cdot)$ is known as the "score function", which can be defined as [19, 22, 24],

$$\rho(u_i) = \begin{cases} \dfrac{1}{2}u_i^2, & |u_i| \le c \\ c|u_i| - \dfrac{1}{2}c^2, & |u_i| > c \end{cases} \tag{13}$$

where c is a tuning threshold parameter.

Setting the partial derivative of (12) as zero gives

$$\sum_{i=1}^{n_y+n} \frac{\partial \rho(u_i)}{\partial u_i} \cdot \frac{\partial u_i}{\partial x_{k,l}} = 0 \quad l = 1, 2, ..., n \tag{14}$$

where, $x_{k,l}$ is the ith component of state vector. Denoting

$$w_i = \frac{\partial \rho(u_i)}{u_i \partial u_i}, \;\; i = 1, 2, ..., n_y + n \tag{15}$$

We have

$$w_i = \begin{cases} 1, & |u_i| \le c \\ \dfrac{c}{|u_i|}, & |u_i| > c \end{cases} \tag{16}$$

Eq. (14) can be rewritten as

$$\sum_{i=1}^{n_y+n} w_i u_i m_{i,l} = 0, \quad l = 1, 2, ..., n \tag{17}$$

which in the matrix form is

$$M_k^T W u = 0 \tag{18}$$

where $m_{i,l}$ refers to the element of M_k at ith row and lth column, $W = diag[w_1 \;\; w_2 \;\; ... \;\; w_{n_y+n}]$.

An iterative solution to (17/18) could be given [14-18] as

$$\hat{x}_k^{(j+1)} = (M_k^T W^{(j)} M_k)^{-1} M_k^T W^{(j)} z_k \tag{19}$$

where the superscript *j* refers to the iteration index. Finally, the state estimate error covariance matrix is computed from

$$P_{k|k} = (M_k^T W M_k)^{-1} \tag{20}$$

Usually, the number of iterations is only one. And the initial value could be $(M_k^T M_k)^{-1} M_k^T z_k$.

III. ADAPTIVE M-ESTIMATION BASED CKF/SCKF

Any model-specific filters have their actual performance dominated by the veracity/quality of the model [23] (including parameters). If something occur "unexpectedly", e.g. (estimated) noise covariance differs significantly from the truth, the filter will deteriorate or even fail. For this, to render the M-estimation immunized to abnormal measurements, we propose to online compare the innovation covariance between the theoretical expectation and the truth for abnormal detection.

Given that the received measurements are normal (namely, consistent with the truth), the true innovation covariance Σ_k equals to the calculated one $P_{yy,k|k-1}$, i.e.

$$\Sigma_k = P_{yy,k|k-1} = P_{y,k|k-1} + R_k \tag{21}$$

where $P_{y,k|k-1}$ is the auto-covariance, and is calculated using the $2n$ samples of updated state $\boldsymbol{X}_{i,k|k-1}$ (see e.g., [3]) as

$$P_{y,k|k-1} = \frac{1}{2n}\sum_{i=1}^{2n} \boldsymbol{Y}_{i,k|k-1} \boldsymbol{Y}_{i,k|k-1}^T - \hat{y}_{k|k-1}\hat{y}_{k|k-1}^T \tag{22}$$

where $\boldsymbol{Y}_{i,k|k-1} = h(\boldsymbol{X}_{i,k|k-1}), \hat{y}_{k|k-1} = \sum_{i=1}^{2n} \boldsymbol{Y}_{i,k|k-1}$.

One sliding window strategy to compute Σ_k is based on the former *m* innovation estimator.

$$e_k = y_k - \hat{y}_{k|k-1} \tag{23}$$

$$\Sigma_k = \frac{1}{m}\sum_{j=0}^{m} e_{k-j} e_{k-j}^T \tag{24}$$

The simplest way is to use the current innovation vector only (namely $m = 1$ in (24)) for computing Σ_k, i.e.

$$\Sigma_k = e_k e_k^T \tag{25}$$

If an abnormal measurement occurs, Eq. (21) will no longer hold except adding a time variant scalar factor a_k $(a_k \geq 1)$ [14] i.e.

$$\Sigma_k = P_{y,k|k-1} + a_k R_k \tag{26}$$

or equivalently,

$$\begin{aligned} tr(\Sigma_k) &= tr(P_{y,k|k-1} + a_k R_k) \\ &= tr(P_{y,k|k-1}) + a_k tr(R_k) \end{aligned} \tag{27}$$

where $tr(\cdot)$ denotes the trace of the related matrix.

From (27), we have

$$a_k = \frac{tr(\Sigma_k) - tr(P_{y,k|k-1})}{tr(R_k)} \tag{28}$$

The adaptive factor a_k is close to 1 when and only when the measurement is normal. Therefore, it provides a measure to detect the measurement abnormality and once abnormal measurements occur, a larger factor a_k shall be (calculated and) used for adjusting. The process can be described as follows.

Given $y_k \sim N(\hat{y}_{k|k-1}, P_{yy,k|k-1})$, $e_k \sim N(0, P_{yy,k|k-1})$ we have

$$\bar{e}_k = V_k^T (y_k - \hat{y}_{k|k-1}) = V_k^T e_k \tag{29}$$

$$\Lambda_k = V_k^T P_{yy,k|k-1} V_k \tag{30}$$

where the column vector of V_k is standardized feature vector, satisfying $V_k^T = V_k^{-1}$ and $P_{yy,k|k-1} = V_k \Lambda_k V_k^T$, and so we have

$$\bar{e}_k \sim N(0, \Lambda_k) \tag{31}$$

which can be used for normality test as (31) only holds for the normal measurement [24], which treats e_k as a whole unit without distinguishing its dimensions. In contrast, we propose to treat each dimension separately for finer (more sensitive) test. This is possible because Λ_k is a diagonal matrix for which the elements of vector $\bar{e}_k$ are independent with each other.

$$\bar{e}_{i,k} \sim N(0, \Lambda_{i,k}), \quad i = 1, 2, ..., n_y \tag{32}$$

where $\Lambda_{i,k}$ denotes the *i*th diagonal element of Λ_k.

Therefore, in the proposed normality test approach, different confidence coefficients/thresholds N_{i,a_i} are used in different dimensions. The measurement data is identified to be abnormal when and only at least one dimension does not meet the normality test. The adaptive factor a_k is then given as follows

$$a_k = \begin{cases} \dfrac{tr(\Sigma_k) - tr(P_{y,k|k-1})}{tr(R_k)}, & \text{any } i\text{: } |\bar{e}_{i,k}| > N_{i,\alpha_i} \\ 1, & \text{otherwise} \end{cases} \tag{33}$$

We can see that $P\{|\bar{e}_{i,k}| > N_{i,\alpha_i}\} = 1 - \alpha_i, 0 < 1 - \alpha_i < 1$, a smaller test threshold N_{i,α_i} implies more sensitive detection, which is suitable to be used in significant abnormal cases. As a rule of thumb, we recommend $N_{i,\alpha_i} \in [\Lambda_{i,k}, 5\Lambda_{i,k}]$, in which $N_{i,\alpha_i} = 3\Lambda_{i,k}$ corresponds to a confidence coefficient 99.74%.

In summary, the gained adaptive factor α_k will be used to replace the measurement noise covariance R by $\alpha_k R$, in the HCKF or HSCKF. This will enable the filter to detect abnormal measurement and to apply adjusting by α_k when abnormal is detected. This leads to the so-called adaptive HCKF (AHCKF) and adaptive HSCKF (AHCKF) respectively.

IV. SIMULATION

To verify the effectiveness of the proposed adaptive M-estimation method in both AHCKF and AHSCKF, we use the target tracking model as given in [3] with the same parameters. The true target is initialized with $N(x_0, P_{0|0})$, where $x_0 = [1000\text{m}, 300\text{ms}^{-1}\ 1000\text{m}\ 0\text{ms}^{-1}\ -3°\text{s}^{-1}]$, $P_{0|0} = \text{diag}[100\text{m}^2\ 10\text{m}^2\text{s}^{-2} 100\text{m}^2\ 10\text{m}^2\text{s}^{-2}\ 100\text{mrad}^2\text{s}^{-2}]$.

The target state transition model is given as

$$x_k = \begin{bmatrix} 1 & \frac{\sin \Omega T}{\Omega} & 0 & -\frac{1-\cos \Omega T}{\Omega} & 0 \\ 0 & \cos \Omega T & 0 & -\sin \Omega T & 0 \\ 0 & \frac{1-\cos \Omega T}{\Omega} & 1 & \frac{\sin \Omega T}{\Omega} & 0 \\ 0 & \sin \Omega T & 0 & \cos \Omega T & 0 \\ 0 & 0 & 0 & 0 & 1 \end{bmatrix} x_{k-1} + v_k \tag{34}$$

where $T = 1\text{s}$ is the sampling time; $\Omega = -3°s^{-1}$ is the turn rate, $v_k \sim N(0, Q)$, $Q = \text{diag}[0.1M \;\; 0.1M \;\; 1.75 \times 10^{-4}T]$ with

$$M = \begin{bmatrix} T^3/3 & T^2/2 \\ T^2/2 & T \end{bmatrix}$$

The observation is a range and bearing vector given by

$$\begin{bmatrix} r_k \\ \theta_k \end{bmatrix} = \begin{bmatrix} \sqrt{\xi_k^2 + \eta_k^2} \\ \tan^{-1}(\eta_k / \xi_k) \end{bmatrix} + w_k \tag{35}$$

where $w_k \sim N(\cdot; 0, R_k)$, with $R_k = \text{diag}([\sigma_r^2, \sigma_\theta^2]^T)$, $\sigma_r = 10\text{m}$, $\sigma_\theta = \sqrt{10}\text{mrads}^{-1}$.

The measurement data generated by the normal measurement model are denoted as '*data0*' namely the healthy data. On the other hand, the following five groups of morbid conditions are also simulated based on *data0* to generate different types of morbid measurement data.

data1 & *data1'*: three deviations $[75\text{ m} \;\; 0.2\text{ rad}]^T$, $[7.5\text{ m} \;\; 0.02\text{ rad}]^T$ are respectively added to the measurement noise w_k when $20 < k < 60$ and $mod(k, 8) = 0$, where $mod(a, b)$ gives the remainder of a/b.

Data2: for $mod(k, 8) = 0$, set $y_k = [0\text{ m} \;\; 0\text{ rad}]^T$, i.e. the measurements are missing when $mod(k, 8) = 0$.

Data3: set the measurement noise w_k as a mixed Gaussian noise, e.g. $p_{w_k} = (1-\alpha)N(0, R_1) + \alpha N(0, R_2)$, where α is the percentage, in our simulation we set $\alpha = 0.8$, $R_1 = \begin{bmatrix} 100\text{ m}^2 & 15\text{ m mrad} \\ 15\text{ m mrad} & 10\text{ mrad}^2 \end{bmatrix}$, $R_2 = \begin{bmatrix} 10000\text{ m}^2 & 10\text{ m mrad} \\ 10\text{ m mrad} & 100\text{ mrad}^2 \end{bmatrix}$.

First, we choose different $N_\alpha \in [\Lambda_\alpha, 5\Lambda_\alpha]$ and compare the average RMSE of position (over 50 Monte Carlo runs; each for $20 < k < 60$) produced by AHCKF when using '*data1*' and '*data1'* ' respectively. Then in a single run, we choose the maximum (minimum) suggestion of N_α, i.e. $N_\alpha = 5\Lambda_\alpha (N_\alpha = \Lambda_\alpha)$ using '*data1'* '('*data1*'). The results are plotted in Fig.1.

As shown in the upper subfigure in Fig. 1, for '*data1'* ' that has smaller abnormal mutations, larger test thresholds e.g., $N_\alpha = 4 \sim 5\Lambda_\alpha$ result in higher estimation accuracy while for "*data1*" that has significant abnormal mutations, lower $N_\alpha = 1 \sim 2\Lambda_\alpha$ result in higher estimation accuracy. This indicates that, the more significant the abnormal mutation is, the larger the test threshold N_α should be. Further on, as shown in the middle subfigure of Fig. 1, due to the significant abnormal mutations in measurements, smaller a_k (green) tends to gain higher accuracy. In the bottom subfigure, a_k is much larger than 1 only in the case that the abnormal mutation is significant, otherwise a_k almost equals to 1 indicating that the filter does not benefit much from the adaptive M-estimation in this case.

In the next, four groups of measurement data including '*data0*', '*data1*', '*data2*', '*data3*', are independently used with the standard CKF, the HCKF, the NRCKF in [16] and proposed AHCKF and the AHSCKF. Their separate RMSEs of position, velocity and turn rate given in Figure 2-5 respectively. From the results, we can have the following findings.

(I). On '*data0*' that are normal healthy measurement data, the performances of all CKFs are almost the same, indicating that robust filtering design is not necessary in this case while it will not cause side effects.

(II). From Fig. 3 to Fig. 5, with the emergence of abnormal measurements, CKF performs badly in all cases due to the lack of robustness, while AHCKF and AHSCKF have gained the best accuracy among all. These are consistent with our theoretical expectation. More specifically, in Fig. 3, the estimation errors given by HCKF and AHCKF have "peaks" (indicating very worse accuracy) when abnormal measurements occur. In these cases, HCKF does not work well, because the score function rescales the measurement covariance weakly. In contrast, AHCKF benefits much from the use of the adaptive factor a_k to adapt according to abnormal noises.

(III). In the case of mixture Gaussian measurement noises (see Fig.5), the standard CKF has good results for $0 \le k \le 60$. But, it loses tracking at last. This also exposes the weakness of KF-type point estimators and the necessity for robustness design. In contrast, HCKF and AHCKF perform batter. Here, since the measurement errors are small, the superiority of AHCKF is not as significant as compared to HCKF as so shown in Figs. 3~4, although it still outperforms HCKF and NRCKF.

(IV). In all cases, AHSCKF slightly outperforms AHCKF, demonstrating better quality.

V. CONCLUSION

An adaptive M-estimation method has been proposed to adjust the measurement noise covariance for robust recursive estimation to accommodate abnormal measurement noise. It has been implemented in two versions of robust CKFs: HCKF and HSCKF, resulting in the adaptive HCKF and adaptive HSCKF respectively. Simulations on a typical target tracking model demonstrate the effectiveness of the proposed method.

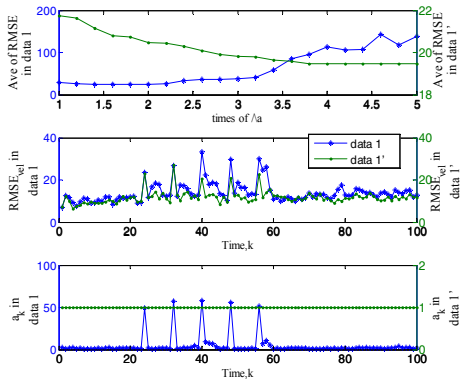

Fig. 1 Top: Average RMSE of position during $20 < k < 60$ for different $N_\alpha (1\Lambda_\alpha \sim 5\Lambda_\alpha)$; Middle and bottom: RMSE of position and a_k when threshold N_α equals to $5\Lambda_\alpha$ in '*data 1'* ' and to Λ_α in '*data 1*'.

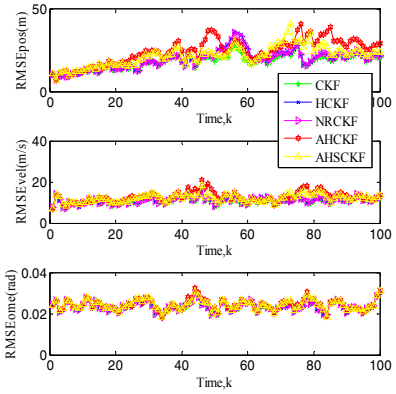

Fig. 2 RMSE of position, velocity and turn rate when using '*data0*'

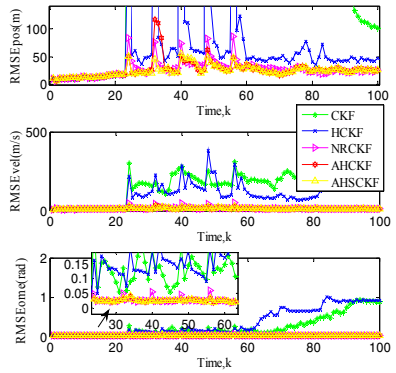

Fig. 3 RMSE of position, velocity and turn rate when using '*data1*'

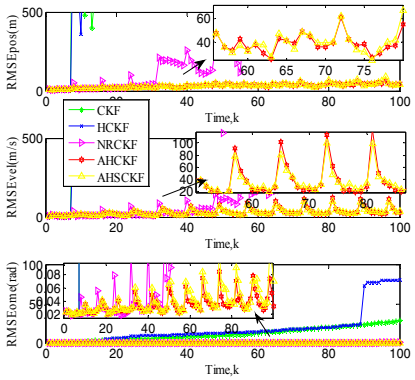

Fig. 4 RMSE of position, velocity and turn rate when using '*data2*'

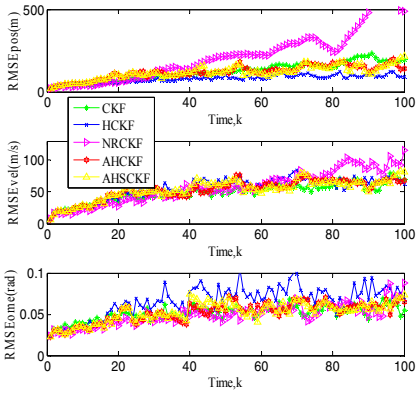

Fig. 5 RMSE of position, velocity and turn rate when using '*data3*'

It is necessary to note that, both the (Huber's) M-estimation and the proposed adaptive M-estimation methods are based on the assumption that the models are correct, which however is limited in practice and shall be removed in a completely robust system.

REFERENCES

[1] R.E. Kalman, "A new approach to linear filtering and prediction problems," Journal of basic Engineering, vol. 82, pp.35-45, 1960.

[2] T. Li, S. Sun, T.P. Sattar, and J.M. Corchado, "Fight sample degeneracy and impoverishment in particle filters: A review of intelligent approaches," Exp. Sys. W. App., vol. 41, pp. 3944-3954, June 2014.

[3] I. Arasaratnam, and S. Haykin, "Cubature kalman filters," IEEE Transactions on Automatic Control, vol. 54, pp. 1254-1269, June 2009.

[4] Y. Wu, D. Hu, M. Wu, and X. Hu, "A numerical-integration perspective on Gaussian filters," IEEE Tran. Signal Proc., vol. 54, pp. 2910-2921, August 2006.

[5] P. Stano, Z. Lendek, J. Braaksma, R. Babuška, C. De Keizer, and A. J. Den Dekker, "Parametric Bayesian Filters for Nonlinear Stochastic Dynamical Systems: A Survey," IEEE Transactions on Cybernetics, vol. 43, pp. 1607-1624, December 2013.

[6] P.S. Maybeck, Stochastic Models, Estimation, and Control, Academic press, 1972.

[7] X.J. Tang, J.L. Wei, and K. Chen, "Square-root adaptive cubature Kalman filter with application to spacecraft attitude estimation," 15th International Conference on Information Fusion, pp. 1406-1412, 2012.

[8] F.D. Busse, J.P. How, and J. Simpson, "Demonstration of adaptive extended Kalman filter for low earth orbit formation estimation using CDGPS," Journal of the Institute of Navigation, vol. 50, pp. 79-93, 2003.

[9] D.J. Lee, and K.T. Alfriend. "Adaptive sigma point filtering for state and parameter estimation," AIAA/AAS ASCE. Rhode Island, vol. 2, pp. 897-916, 2004.

[10] L.Q. Zhao, J.L. Wang, T. Yu, H. Jian, and T.J. Liu, "Design of adaptive robust square-root cubature Kalman filter with noise statistic estimator," Applied Mathematics and Computation, vol. 256, pp.352-367, 2015.

[11] G.B. Chang, "Kalman filter with both adaptivity and robustness," Journal of Process Control, vol. 24, pp. 81-87, March 2014.

[12] Y. Yang, H. He, and G. Xu, "Adaptively robust filtering for kinematic geodetic positioning," Journal of Geodesy, vol. 75, pp.109-116, 2001.

[13] P.J. Huber, "Robust estimation of a location parameter," The Annals of Mathematical Statistics, vol. 35, pp.73-101, 1964.

[14] K.R. Koch, and Y. Yang, "Robust Kalman filter for rank deficient observation models," Journal of Geodesy, vol. 72, pp.436-441, 1998.

[15] C.D. Karlgaard, H. Schaub, "Huber-based divided difference filtering," Journal of Guidance, Control, and Dynamics, vol. 30, pp. 885-891, 2007.

[16] X. Wang, N. Cui, and J. Guo, "Huber-based unscented filtering and its application to vision-based relative navigation," IET Radar, Sonar & Navigation, vol. 4, pp.134-141, February 2010.

[17] L. Chang, B. Hu, G. Chang, and A. Li, "Huber-based novel robust unscented Kalman filter," IET Science, Measurement & Technology, vol. 6, pp.502-509, November 2012.

[18] L.B. Chang, B.Q. Hu, G.B. Chang, and A. Li, "Multiple outliers suppression derivative-free filter based on unscented transformation," J. Guidance, Control, and Dynamics, vol.35, pp.1902-1907, 2012.

[19] Y. Huang, L.H. Wu, and F. Sun. Robust Cubature Kalman filter based on Huber M estimator. Control and Decision, vol. 29, no.3, p. 572-576, 2014.

[20] K. Li, B. Hu, L. B. Chang, Y. Li, Robust square-root cubature Kalman filter based on Huber's M-estimation methodology, Proceedings of the Institution of Mechanical Engineers, Part G: Journal of Aerospace Engineering June, vol. 229 no. 7 1236-1245, 2015.

[21] H. Wu, S.X. Chen, B.F. Yang, and K. Chen, Robust cubature Kalman filter target tracking algorithm based on generalized M-estiamtion, Acta Phys. Sin. vol. 64, no. 21 (2015) 218401, 1-8.

[22] W. Li, D.R. Gong, M.H. Liu, J.A. Chen, and D.P. Duan, "Adaptive robust Kalman filter for relative navigation using global position system," IET Radar, Sonar & Navigation, vol.7 pp. 471-479, 2013.

[23] T. Li, J.M. Corchado, J. Bajo, S. Sun, and J.F. De Paz, "Effectiveness of Bayesian Filters: An Information Fusion Perspective," Information Sciences, vol. 329, pp. 670-689, February 2016.

[24] C. Hajiye, H.E. Soken. A novel adaptive unscented Kalman filter for pico satellite attitude estimation[C] //PHYSCON 2011, September 5-8, 2011, León, Spain. 2011: 1-7.

Fractional Fourier Transform Based Co-Radar Waveform: Experimental Validation

Domenico Gaglione*, Carmine Clemente*, Adriano Rosario Persico*,
Christos V. Ilioudis*, Ian K. Proudler†, and John J. Soraghan*
*University of Strathclyde, CeSIP, EEE, 204, George Street, G1 1XW, Glasgow, UK
E-mail: domenico.gaglione, carmine.clemente, c.ilioudis, adriano.persico, j.soraghan@strath.ac.uk
† School of Electronic, Electrical and Systems Engineering, Loughborough University, Leicestershire, UK
E-mail: i.k.proudler@lboro.ac.uk

***Abstract*—A Fractional Fourier Transform (FrFT) based waveform design for joint radar-communication systems (Co-Radar) that embeds data into chirp sub-carriers with different time-frequency rates has been recently presented. Simulations demonstrated the possibility to reach data rates as high as 3.660 Mb/s while maintaining good radar performance compared to a Linear Frequency Modulated (LFM) pulse that occupies the same bandwidth. In this paper the experimental validation of the concept is presented. The system is considered in its basic configuration, with a mono-static radar that generates the waveforms and performs basic radar tasks, and a communication receiver in charge of the pulse demodulation. The entire network is implemented on a Software Defined Radio (SDR) device. The system is then used to acquire data and assess radar and communication capabilities.**

I. Introduction

The employment of joint radar-communication systems represents an innovative solution to the problem of continuously increasing demand on bandwidth [1] and the need to meet the low-SWaP (Size, Weight and Power consumption) requirements.

Applications that can benefit from the technology proposed in this paper include satellite and airborne Synthetic Aperture Radars (SARs) that need to share sensed data with a ground station rapidly [2]; nodes in a surveillance Multiple-Input Multiple-Output (MIMO) radar network that need to exchange information about targets; vehicles that need to interact in a intelligent transportation network [3]. All these applications may benefit from a joint-radar communication technology which shares bandwidth, power and hardware resources to perform radar and communication operations simultaneously.

A joint radar-communication system (Co-Radar) based on Fractional Fourier Transform (FrFT) waveform has been recently presented by the authors in [4]. The FrFT [5] was shown to be suitable for orthogonal waveforms generation for MIMO radar systems [6]–[9], and in this scenario it has been exploited to map complex modulated symbols into different chirp, or Linear Frequency Modulated (LFM), sub-carriers with different time-frequency rates. Simulations demonstrated the feasibility to reach data rate as high as 3.660 Mb/s, while maintaining good radar performance in terms of range resolution, Doppler resolution and Side Lobe Levels (SLLs) when compared with a LFM pulse that occupies the same bandwidth.

Different techniques of embedding data in the radar waveform have been previously proposed. In [10] and [11] information bits are sent by exploiting the orthogonality between up-chirp and down-chirp signals. Methods based on LFM pulses phase-modulated through Binary Phase Shift Keying (BPSK) and Minimum Shift Keying (MSK) symbols are presented in [12] and [13], respectively. Stepped-frequency [14] and Frequency Modulated Continuous Wave (FMCW) [15] based joint radar-communication systems have also been proposed, as well as Orthogonal Frequency Division Multiplexing (OFMD) based systems [16], [17]. However, none of these previous techniques is designed to achieve data rates up to 3.660 Mb/s at medium ranges.

In this paper the experimental validation of the FrFT based Co-Radar system [4] is reported. A basic configuration of the system is considered: a mono-static radar generates the FrFT waveforms, sends the pulses, listens to echoes and performs basic radar tasks, while a communication receiver demodulates the pulses.

The remainder of the paper has the following structure. Section II summarises the concept of the FrFT based Co-Radar waveform design framework presented in [4]. Section III describes its implementation on a Software Defined Radio (SDR) device, while the experimental setup and results are presented in Section IV. Finally, Section V concludes the paper.

II. FrFT Based Co-Radar System

In this section the FrFT based Co-Radar system [4] is presented. The FrFT [5] is a time-frequency representation of a signal and can be considered as a rotation by an arbitrary angle ϕ of the signal itself in the time-frequency plane, such that:

$$\phi = \frac{\pi}{2}\alpha \tag{1}$$

where α is called order of the transform. In the proposed system, FrFTs with different orders are used to map the modulated symbols into quasi-orthogonal chirp sub-carriers.

The block diagrams of the mono-static radar and the communication receiver in a simple FrFT based Co-Radar system scenario are shown in Figure 1 and described in the following.

A. Mono-Static Radar

The block diagram of the mono-static radar in the considered basic configuration of the FrFT based Co-Radar system is shown at the top of Figure 1. The serial-to-parallel (S/P) block is used to divide the long sequence of bits coming from

978-1-5090-0326-6/16 /$31.00 ©2016 IEEE

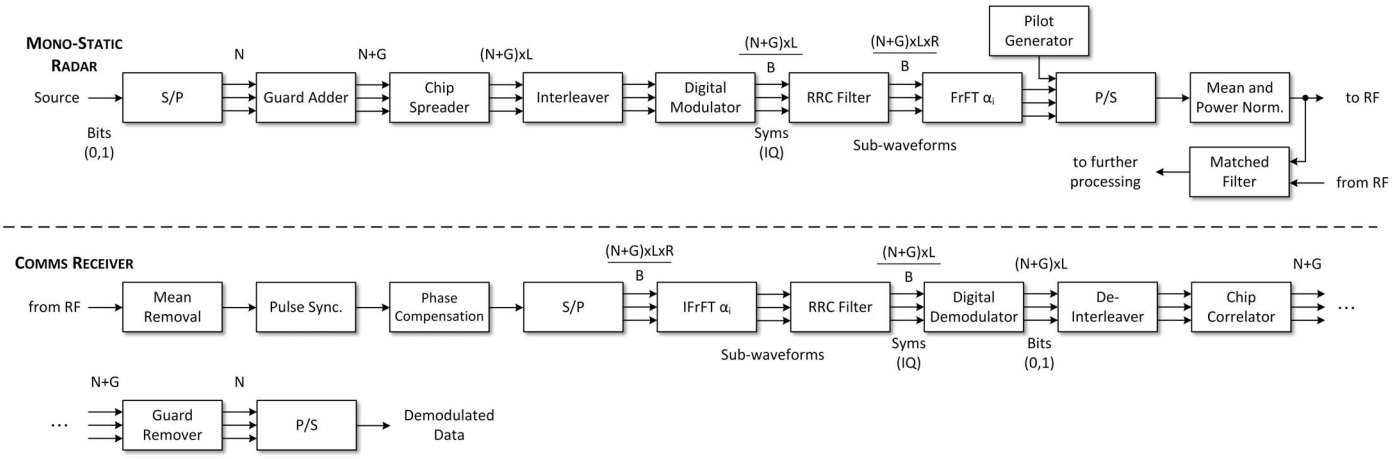

Figure 1. Block diagram of (top) the Mono-Static Radar and (bottom) the Communication Receiver of the FrFT based Co-Radar basic configuration [4].

the source into $C-1$ segments of N bits each, where C is the number of chirp sub-carriers composing the waveform. The 0-th order sub-carrier is not used to carry information bits. It accommodates a pilot waveform instead, used at the communication receiver for synchronisation and phase compensation. Since each pulse contains $N \times (C-1)$ information bits, the final bit rate is $N \times (C-1) \times \mathrm{PRF}$ b/s, where PRF stands for Pulse Repetition Frequency. In each segment, G guard bits are added at the end of the sequence in order to compensate for the group delay introduced by the Root Raised Cosine (RRC) filter. Then the sequence is spread by using a chip sequence; the chosen chip sequence is a L-long Barker code, which leads to a spread sequence of $(N+G) \times L$ bits. The interleaver is used to mitigate the Inter-Carrier Interference (ICI) that occurs in the middle of the sequence due to the overlap of the different chirp sub-carriers and that generates a burst of errors. It is applied only to the N bits of information and aims to spread the burst of errors across the entire spread sequence. The digital modulator maps a series of B bits into one of the $M = 2^B$ possible complex symbols belonging to the chosen modulation scheme (i.e. PSK), leading to a $(N+G) \times L/B$ long symbol sequence. The modulation scheme and the cardinality of its alphabet M can be adaptively chosen according to the conditions of the channel. The RRC filter is used to minimise the Inter-Symbol Interference (ISI) that may be caused by the channel. For efficiency, it is implemented as a multirate filter that up-samples the output by a factor R, leading to a final sequence of $(N+G) \times L \times R/B$ samples.

The $C-1$ sub-waveforms obtained after the RRC filter are then mapped to different chirp sub-carriers uniformly spaced in the time-frequency domain. Note that the FrFT is periodic in ϕ with period 2π, however rotations of ϕ and $\phi + \pi$ produce signals that overlap in the time-frequency plane. For this reason, only angles in the range $[0, \pi)$ are considered, that leads to $\alpha \in [0, 2)$. Thus, the uniformly spaced sub-carriers are obtained by choosing the i-th fractional order to be equal to $\alpha_i = i\bar{\alpha}, i = 1, \ldots, C-1$, where $\bar{\alpha} = \frac{2}{C}$. Finally, the parallel-to-serial (P/S) block combines the chirp modulated sub-waveforms and the pilot sub-waveform by adding them together. Specifically, the latter is a bi-phase coded signal run by a Coarse/Acquisition (C/A) code [18] given by:

$$p[n] = e^{j\pi\left(a[n]-\frac{1}{4}\right)} \tag{2}$$

where $a[n]$ is the selected C/A code properly up-sampled and truncated to match the length, in samples, of the Co-Radar waveform. Before sending the waveform to the Radio Frequency (RF) front-end, its mean is removed and the power is normalised such that all the transmitted pulses present the same power. While generating and transmitting the FrFT based pulses, the mono-static radar acquires the echoes and performs any needed radar task (i.e. matched filter with the transmitted pulse).

The spectrogram of a Co-Radar waveform with relatively few sub-carriers is shown in Figure 2 for clarity, although in practice many more sub-carriers would most likely be used. Each of them is the rotation by a specific angle, driven by the order of the FrFT, of a phase modulated signal (i.e. QPSK).

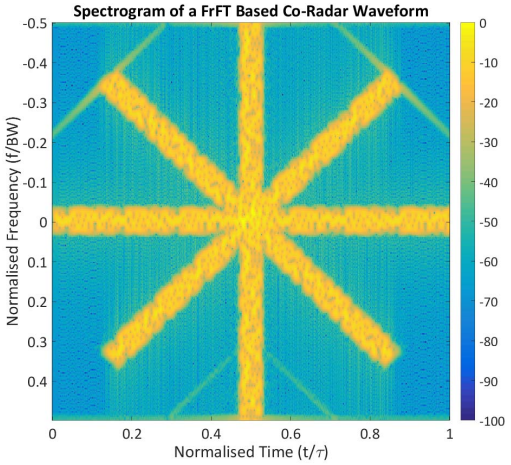

Figure 2. Spectrogram of a FrFT based Co-Radar waveform with 4 sub-carriers.

B. Communication Receiver

The communication receiver is shown at the bottom of Figure 1. All the operations are performed within a Pulse Repetition Interval (PRI). Before the pulse is synchronised and demodulated, the mean of the received signal is subtracted to remove the strong return from the background. The synchronisation is necessary since the pulse could fall anywhere within the PRI due to the transmitter-receiver distance, and the alignment with the pulse on a sample basis is needed to

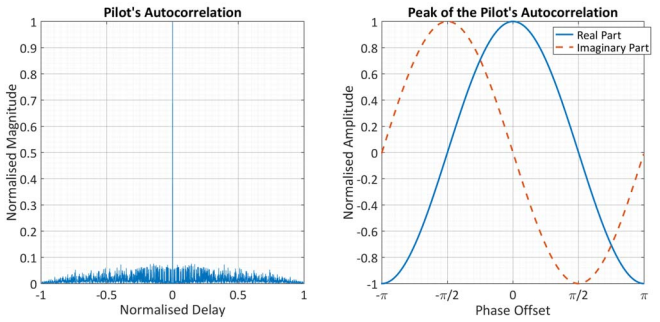

(a) (b)

Figure 3. Pilot waveform's (a) autocorrelation and (b) its peak's complex value on varying the phase offset.

perform the inverse FrFT. This is achieved by exploiting the good autocorrelation properties of the pilot waveform, shown in Figure 3(a).

The pilot waveform is also used to estimate the phase offset introduced by the channel. Figure 3(b) shows how the autocorrelation's complex-valued peak changes on varying the phase offset. In particular, when the offset is zero the real part of the peak reaches its maximum, while the imaginary part is zero. Hence, once the peak of the autocorrelation is detected by matched filtering the received signal with the pilot waveform, the phase offset can be estimated by evaluating the phase of the correlation peak. This phase estimation method is also robust with respect to the Doppler shift potentially present in the signal.

Once the synchronisation and the phase compensation are performed, the pulse can be demodulated. The S/P block splits and redirects the pulse, whose length is $(N+G) \times L \times R/B$ samples, to $C-1$ different IFrFT blocks that perform the inverse FrFT. Each sequence is then input of the RRC filter, which also down-samples the sub-waveform by a factor R. The digital demodulator translates the $(N+G) \times L/B$ long sequence of symbols in a sequence of $(N+G) \times L$ bits, according to the modulation employed. At this point, the de-interleaver performs the inverse operation of the interleaver.

The chip correlator block correlates the input spread sequence with the L-long Barker chip code used in transmission to extract $N+G$ bits, exploiting both the low correlation side lobes and the knowledge that the peaks of the correlation occur every L samples. Finally, the guard remover and the P/S blocks reconstruct the original stream by combining the N-long bit sequences coming from the $C-1$ different parallel branches.

III. FrFT Based Co-Radar on SDR

The FrFT based Co-Radar system is implemented by means of a SDR device, namely the National Instruments Universal Software Radio Peripheral (NI-USRP) 2943r. It has four in-phase and quadrature (IQ) channels, two receivers and two transmitters/receivers, and its working frequency ranges between 1.2 GHz and 6.6 GHz. It is provided with a fully programmable Xilinx Kintex-7 FPGA (Field-Programmable Gate Array) and can be connected to a host computer through a high-speed, low-latency PCI Express x4 (∼800 MB/s). It is used with three wideband LB-2678-15 multi octave horn antennas produced by A-Info, two for the mono-static radar node and one for the communication receiver.

The USRP 2943r is programmed through NI software

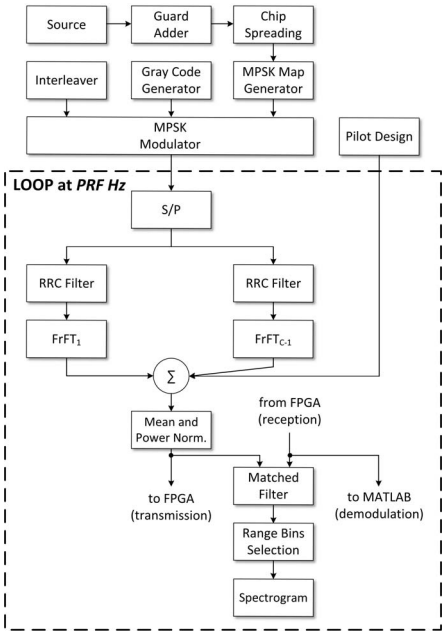

Figure 4. High-level block diagram of the FrFT based Co-Radar system's implementation in LabVIEW.

LabVIEW, and its high-level block diagram is shown in Figure 4. Within the loop that repeats every PRI, the FrFT based Co-Radar waveform is generated as described in the previous section and sent to the FPGA. The latter up-samples the signal in transmission to meet the 120 MHz data clock frequency of the device and interfaces with the RF front-end. Meanwhile, the received signal, down-sampled and coming from the FPGA, is sent both to a MATLAB session for the real-time pulse demodulation and to a matched filter with the transmitted pulse for further radar processing. Specifically, a real-time spectrogram is computed. This choice is driven by the limited power and bandwidth resources of the employed SDR device, which are not sufficient for more advanced radar operations. Outside the loop, the message to send is loaded and all the preliminary steps are performed.

IV. Experimental Setup and Results

The implemented FrFT based Co-Radar system is used in a controlled laboratory environment to acquire data and assess its communication and radar capability. The acquisition geometry is shown in Figure 5. The mono-static radar is placed at the bottom left, the communication receiver at the top right, while within the light blue area a person is walking towards and away from the radar to generate a Doppler signal.

The transmitted message is a 64×64 black and white

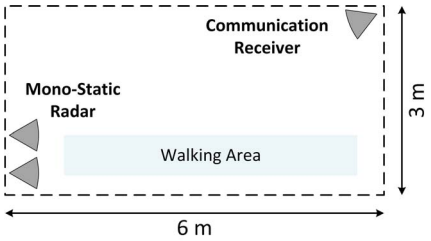

Figure 5. Acquisition geometry of the laboratory-based experimental campaign.

image with a bit depth 5. Carrier frequency is 3 GHz and the bandwidth is 1 MHz. The number of information bits per carrier, N, is 3, the length of the Barker code is $L = 7$ and Quadrature PSK (QPSK) is the employed modulation scheme, hence $B = 2$. The RRC filter is designed to span $S = 8$ symbols, with an up-sampling factor $R = 18$ and a roll-off factor $\beta = 0.4$. This leads to a guard of $G = 3$ bits. The total number of samples per waveform is 378, which means that the duration of the pulse is $\tau = 378\,\mu$s. The PRF is fixed to 83.33 Hz, giving a duty cycle of 3.15 %.

Different configurations are analysed by changing the number of sub-carriers, $C = 4, 6, 8, 10$, and modifying the transmitted power. The Signal-to-Noise Ratio (SNR) is estimated both at the mono-static radar and the communication receiver.

Communication performance is shown with solid lines in Figure 6, in terms of Bit Error Ratio (BER) averaged over 10 realisations vs SNR_{comms}. The dotted lines in Figure 6 show

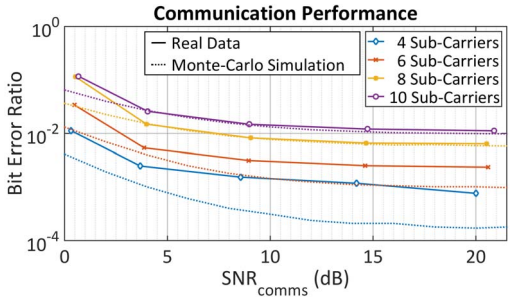

Figure 6. Communication performance on varying the SNR_{comms} and for different number of chirp sub-carriers.

the results obtained by running Monte-Carlo simulations with 10^5 iterations with the same parameters listed above, assuming the channel to be Rician with K-factor equal to 6 dB (indoor channel). They are used as comparison to validate the results on the acquired data. Note that no Forward Error Correction (FEC) method is used, since this is out of the scope of the present paper.

As expected, as the SNR_{comms} increases, the BER decreases. However, no significant further improvements are observed for SNR_{comms} greater than 15 dB, and this trend is confirmed by the results from the Monte-Carlo simulations, which clearly show plateaus. They are due to the overlap of the sub-carriers, which causes errors independently of the noise level. For the same reason, performance improves by reducing the number of sub-carriers.

The radar capabilities of the FrFT based Co-Radar are presented by showing spectrograms from the signals acquired during the laboratory-based experimental campaign. Figure 7 and Figure 8 show spectrograms when FrFT based Co-Radar pulses with $C = 4$ and $C = 8$ sub-carriers are used, respectively, and for two different values of SNR_{radar}. In all the cases the Doppler and micro-Doppler signature of the person walking towards and away from the radar is clearly visible.

V. Conclusion

The paper presented an experimental validation of the FrFT based Co-Radar system proposed in [4]. The system was successfully implemented on a SDR device and its performance demonstrated in a controlled laboratory environment. A basic configuration was considered with one mono-static radar and

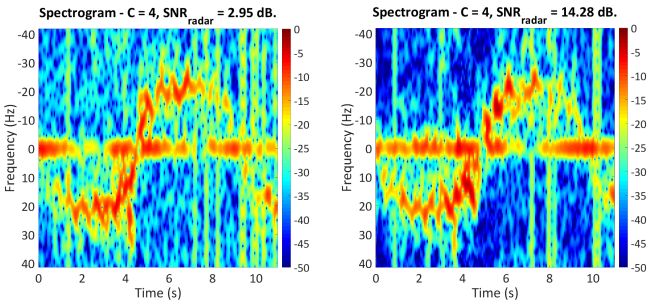

(a) (b)

Figure 7. Spectrograms obtained from FrFT based Co-Radar pulses with $C = 4$ and different SNR_{radar}. Window length 0.36 seconds, overlap 80 %. Person walking towards the radar approximately between 0-5 seconds and 10-11 seconds, and away from it between 5-10 seconds.

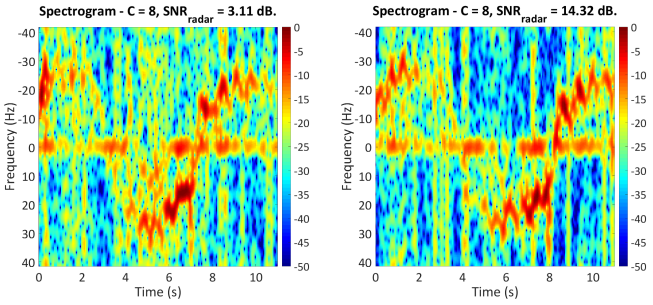

(a) (b)

Figure 8. Spectrograms obtained from FrFT based Co-Radar pulses with $C = 8$ and different SNR_{radar}. Window length 0.36 seconds, overlap 80 %. Person walking towards the radar approximately between 4-8 seconds, and away from it between 0-4 seconds and 8-11 seconds.

one communication receiver.

Communication performance was evaluated in terms of BER vs SNR_{comms} and resulted consistent with that obtained from Monte-Carlo simulations. It shows BER between 10^{-3} and 10^{-2} when no error detection and correction techniques are used. Due to the limited power and bandwidth resources of the employed SDR device, the radar capability of these novel waveforms is assessed by computing the spectrograms of the acquired signals. They clearly showed the main Doppler and micro-Doppler signature of a person walking towards and away from the radar. These preliminary results confirm the capability of the proposed novel waveforms of joint radar-communication operations.

Acknowledgment

This work was supported by the Engineering and Physical Sciences Research Council (EPSRC) Grant number EP/K014307/1 and the MOD University Defence Research Collaboration in Signal Processing.

References

[1] H. Griffiths, "The Challenge of Spectrum Engineering," in *2014 11th European Radar Conference (EuRAD)*, Oct 2014, pp. 1–4.

[2] S. Quan, W. Qian, J. Guq, and V. Zhang, "Radar-Communication Integration: An Overview," in *2014 IEEE 7th International Conference on Advanced Infocomm Technology (ICAIT)*, Nov 2014, pp. 98–103.

[3] D. Erricolo, H. Griffiths, L. Teng, M. C. Wicks, and L. L. Monte, "On the Spectrum Sharing Between Radar and Communication Systems," in *2014 International Conference on Electromagnetics in Advanced Applications (ICEAA)*, Aug 2014, pp. 890–893.

[4] D. Gaglione, C. Clemente, C. V. Ilioudis, A. R. Persico, I. Proudler, and J. J. Soraghan, "Fractional Fourier Based Waveform for a Joint Radar-Communication System," in *2016 IEEE Radar Conference (RadarConf)*, Philadelphia, USA, May 2016, pp. 811–816.

[5] H. M. Ozaktas, Z. Zalevsky, and M. A. Kutay, *The Fractional Fourier Transform with Applications in Optics and Signal Processing*. Wiley, Chichester, 2001.

[6] C. Clemente, I. Shorokhov, I. Proudler, and J. Soraghan, "Radar Waveform Libraries Using Fractional Fourier Transform," in *2014 IEEE Radar Conference*, May 2014, pp. 0855–0858.

[7] C. Clemente, C. Ilioudis, D. Gaglione, K. Thompson, S. Weiss, I. Proudler, and J. Soraghan, "Reuse of Fractional Waveform Libraries for MIMO Radar and Electronic Countermeasures," in *2014 6th International Symposium on Communications, Control and Signal Processing (ISCCSP)*, May 2014, pp. 505–508.

[8] C. Ilioudis, C. Clemente, I. Proudler, and J. Soraghan, "Constant Envelope Fractional Fourier Transform Based Waveform Libraries for MIMO Radar," in *2014 Sensor Signal Processing for Defence (SSPD)*, Sept 2014, pp. 1–5.

[9] C. Ilioudis, C. Clemente, I. Proudler, and J. Soraghan, "Performance Analysis of Fractional Waveform Libraries in MIMO Radar Scenario," in *2015 IEEE Radar Conference (RadarCon)*, May 2015, pp. 1119–1124.

[10] M. Roberton and E. Brown, "Integrated Radar and Communications Based on Chirped Spread-Spectrum Techniques," in *2003 IEEE MTT-S International Microwave Symposium Digest*, vol. 1, June 2003, pp. 611–614.

[11] G. N. Saddik, R. Singh, and E. Brown, "Ultra-Wideband Multifunctional Communications/Radar System," *IEEE Transactions on Microwave Theory and Techniques*, vol. 55, no. 7, pp. 1431–1437, July 2007.

[12] Z. Zhao and D. Jiang, "A Novel Integrated Radar and Communication Waveform Based on LFM Signal," in *2015 5th International Conference on Electronics Information and Emergency Communication (ICEIEC)*, May 2015, pp. 219–223.

[13] X. Chen, X. Wang, S. Xu, and J. Zhang, "A Novel Radar Waveform Compatible with Communication," in *2011 International Conference on Computational Problem-Solving (ICCP)*, Oct 2011, pp. 177–181.

[14] F. Hu, G. Cui, W. Ye, L. Kong, Y. Huang, and L. Yuan, "Integrated Radar and Communication System Based on Stepped Frequency Continuous Waveform," in *2015 IEEE Radar Conference (RadarCon)*, May 2015, pp. 1084–1087.

[15] W. Scheiblhofer, R. Feger, A. Haderer, and A. Stelzer, "Method to Embed a Data-Link on FMCW Chirps for Communication Between Cooperative 77-GHz Radar Stations, year = 2015, pages = 181-184, month = Sept,," in *Radar Conference (EuRAD), 2015 European*.

[16] C. Sturm and W. Wiesbeck, "Waveform Design and Signal Processing Aspects for Fusion of Wireless Communications and Radar Sensing," *Proceedings of the IEEE*, vol. 99, no. 7, pp. 1236–1259, July 2011.

[17] J. Zhao, K. Huo, and X. Li, "A Chaos-Based Phase-Coded OFDM Signal for Joint Radar-Communication Systems," in *2014 12th International Conference on Signal Processing (ICSP)*, Oct 2014, pp. 1997–2002.

[18] GPS ICD, "Global Positioning Systems Directorate System Engineering & Integration Interface Specification IS-GPS-200H," *Navstar GPS Space Segment/Navigation User Interfaces*, 2013.

Multiple Spherical Arrays Design for Acoustic Source localization

Xi Pan, Huayang Wang, Fangzhou Wang and Chengtian Song
School of Mechatronical Engineering
Beijing Institute of Technology
Beijing, China
Email: { panxi,wanghuayang, grace1380, songct }@bit.edu.cn

***Abstract*— This paper considers the design and analysis of distributed multiple spherical arrays for acoustic source localization. The proposed multiple spherical array structures are based on the spherical harmonic multiple signal classification (MUSIC) algorithm for multiple acoustic sources localization. The new structures consist of several identical spheres with uniform placement of microphones on each sphere. In this paper, the influence of the size and the distributions of the multiple spheres have been evaluated by using the direction of arrival (DOA) estimation method for multiple sources in order to obtain some rules about the spherical array design.**

Keywords*— DOA estimation; acoustic detection; spherical harmonic analysis; MUSIC; multiple spherical arrays

I. INTRODUCTION

For the passive acoustic source localization, the time delay of arrival (TDOA) is one of the usual methods, which can deal with the single source at the given time [1]. The subspace techniques, multiple signal classification (MUSIC) and estimation of signal parameters via rotational invariance technique (ESPRIT), are widely used in the direction of arrival (DOA). These algorithms can solve the problem of multiple source localization [2-3].

The MUSIC based on the spherical harmonic analysis has been proposed to obtain better performance [4]. In [5], instead of using the sampling signal directly from the arrays, the sound field is decomposed into spherical harmonic components and then the harmonic components are used in the MUSIC algorithm to calculate the correlation matrix. Teutsch and Kellermann [3, 6] proposed the "eigenbeams" (EBs)-ESPRIT localization method for multiple wideband acoustic sources and the "eigenbeams" are actually the spherical harmonic. In [7], the spherical harmonic based MUSIC algorithm (SH-MUSIC) is proposed in which the spherical harmonic transformation is operated before the MUSIC algorithm to perform the estimation.

For the spherical harmonic analysis, the microphones are usually arranged regularly in a single array structure, such as the circular array or the spherical array [8-10]. In this paper, the multiple sphere arrays (MSA) are presented in which a set of spheres are dispersedly placed following some rules while the microphones on each sphere are distributed regularly. MSA arrays can not only reduce the number of microphones on each sphere, which is restricted by the volume of single sphere, but can also obtain higher estimation accuracy and efficiency. The authors have modeled the multiple spherical arrays and have discussed the influence of sphere size and the distributions of multiple spheres on the direction of arrival (DOA) estimation. These elements have been evaluated by using the improved spherical harmonic MUSIC algorithm and some results about the multiple spherical array design have been obtained.

II. SPHERICAL HARMONIC MUSIC ALGORITHM

In this paper, the following assumptions are made: (a) All applied waves are plane waves. (b) The azimuth angle θ and ϑ are both measured counterclockwise from x axis. (c) The pitch angle ϕ and φ are both measured down from z axis.

Supposing that S narrowband plane waves with unit magnitude impinge on a sphere from directions (θ_s, ϕ_s), so the incident field $P_l(\mathrm{r}, \vartheta, \varphi)$ at the observe points on the sphere surface can be expressed as [11]:

$$\begin{aligned} P_l(\mathrm{r}, \vartheta, \varphi) &= \sum_{s=1}^{S} w_s e^{i\mathbf{k}_s \cdot \mathbf{r}} \\ &= \sum_{n=0}^{\infty} \sum_{m=-n}^{m=n} 4\pi (i)^n \times \left[\sum_{s=1}^{S} w_s j_n(\mathrm{kr}) Y_{nm}(\vartheta, \varphi) \mathrm{Y}_{nm}^{*}(\theta_s, \phi_s) \right] \end{aligned} \tag{1}$$

where w_s and $\mathbf{k}_\mathbf{s}$ are the weight and the direction vector of the s^{th} source, $|\mathbf{k}_\mathbf{s}| = k_1, \cdots, k_s, \cdots, k_S$ and k_s is the wavenumber of s^{th} source, $\mathbf{r}$ is a vector describing the location of the observe point and $j_n(\mathrm{kr})$ is the spherical Bessel function. '$*$'denotes the complex conjugation and Y_{nm} is the spherical harmonic of order n and degree m

$$Y_{nm}(\vartheta, \varphi) = \sqrt{\frac{2n+1}{4\pi} \frac{(n-|m|)!}{(n+|m|)!}} P_{n|m|}(\cos\vartheta) e^{jm\varphi} \tag{2}$$

where $P_{n|\mathrm{m}|}$ is the associated Legendre function. Spherical harmonic describes an orthonormal decomposition of sound field pressure. In practical application, the number of terms in (1) cannot be infinite, thus, it can be replaced with N which is mainly determined by the size of the sphere [12].

According to [4], considering S sources with directions (θ_s, ϕ_s) (s =1, 2, ..., S) and a sphere with $M = T \times H$ uniformly

978-1-5090-0326-6/16/$31.00 ©2016 IEEE

distributed microphones, a spherical harmonic decomposition coefficient a_{nm} is defined as:

$$\bar{a}_{nm} = \sum_{s=1}^{S} \sum_{t=1}^{T \times H} w_s e^{i\mathbf{k}_s \cdot \mathbf{r}} Y_{nm}^*(\vartheta_t, \varphi_t) \sin\vartheta_t \Delta\vartheta\Delta\varphi \tag{3}$$

where $\Delta\vartheta = \pi / T, \Delta\varphi = 2\pi / H$.

Suppose M observe points with directions (ϑ_t, φ_t) (t =1, 2, ..., M) on the sphere, the decomposition coefficient can be expressed in matrix form:

$$P_{nm} = \left[\bar{a}_{00}, \bar{a}_{1-1}, \bar{a}_{10}, \bar{a}_{11}, ..., \bar{a}_{NN} \right]^T \tag{4}$$

where P_{nm} is a $(N+1)^2 \times 1$ matrix, it can be decomposed into several multiplicative matrix forms:

$$P_{nm} = B \times C \times W \tag{5}$$

$$B = \begin{bmatrix} Y_{00}^*(\vartheta_1, \varphi_1) & Y_{00}^*(\vartheta_2, \varphi_2) & \cdots & Y_{00}^*(\vartheta_M, \varphi_M) \\ Y_{1-1}^*(\vartheta_1, \varphi_1) & Y_{1-1}^*(\vartheta_2, \varphi_2) & \cdots & Y_{1-1}^*(\vartheta_M, \varphi_M) \\ Y_{10}^*(\vartheta_1, \varphi_1) & Y_{10}^*(\vartheta_2, \varphi_2) & \cdots & Y_{10}^*(\vartheta_M, \varphi_M) \\ Y_{11}^*(\vartheta_1, \varphi_1) & Y_{11}^*(\vartheta_2, \varphi_2) & \cdots & Y_{11}^*(\vartheta_M, \varphi_M) \\ \vdots & \vdots & \ddots & \vdots \\ Y_{NN}^*(\vartheta_1, \varphi_1) & Y_{NN}^*(\vartheta_2, \varphi_2) & \cdots & Y_{NN}^*(\vartheta_M, \varphi_M) \end{bmatrix} \times \Delta\vartheta\Delta\varphi \tag{6}$$

$$C = \begin{bmatrix} e^{i\mathbf{k}_1 \cdot \mathbf{r}_1} \sin\vartheta_1 & e^{i\mathbf{k}_2 \cdot \mathbf{r}_1} \sin\vartheta_1 & \cdots & e^{i\mathbf{k}_s \cdot \mathbf{r}_1} \sin\vartheta_1 \\ e^{i\mathbf{k}_1 \cdot \mathbf{r}_2} \sin\vartheta_2 & e^{i\mathbf{k}_2 \cdot \mathbf{r}_2} \sin\vartheta_2 & \cdots & e^{i\mathbf{k}_s \cdot \mathbf{r}_2} \sin\vartheta_2 \\ \vdots & \vdots & \ddots & \vdots \\ e^{i\mathbf{k}_1 \cdot \mathbf{r}_M} \sin\vartheta_M & e^{i\mathbf{k}_2 \cdot \mathbf{r}_M} \sin\vartheta_M & \cdots & e^{i\mathbf{k}_s \cdot \mathbf{r}_M} \sin\vartheta_M \end{bmatrix} \tag{7}$$

$$W = [w_1 \quad w_2 \quad \cdots w_S]^T \tag{8}$$

where B is $(N+1)^2 \times M$ matrix, C is $M \times S$ matrix and W is $S \times 1$ matrix of received signal array. Assume $A=B \times C$, then (5) can be simplified to

$$P_{nm} = A \times W \tag{9}$$

where A is a $(N+1)^2 \times S$ steering matrix. Now P_{nm} can be used to perform the DOA estimation using the MUSIC algorithm through the following processes. First, the correlation matrix can be obtained:

$$R_{nm} = E\left\{ P_{nm} P_{nm}^H \right\} \tag{10}$$

In practical application, suppose there are K samples, so R_{nm} can be estimated as:

$$\bar{R}_{nm} = \frac{1}{K} \sum_{k=1}^{K} P_{nm}(k) P_{nm}^H(k) \tag{11}$$

Taking eigenvalue decomposition of $\bar{R}_{nm}$:

$$eigen(\bar{R}_{nm}) = \left[E_a, E_n \right] \tag{12}$$

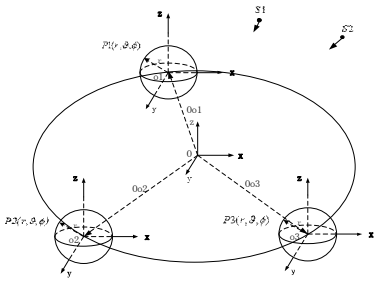

Fig.1. Geometry of three spherical arrays.

where E_a and E_n are the signal and noise subspaces, respectively. Then the spectrum equation respect to the direction of the source can be obtained:

$$spectrum(\theta, \phi) = \frac{1}{a^T \left[E_n E_n^* \right] a} \tag{13}$$

where a is the steering vector which is a column of A for any direction. By scanning (θ, ϕ), the peaks of the spectrum will be in conformity to the signals' directions.

III. MULTIPLE SPHERICAL ARRAYS

In this section, the spherical harmonic MUSIC algorithm with single spherical arrays is extended to multiple spherical arrays. The coordinate mapping method is used to map the independent coordinate system of each sphere to the global coordinate system. The spherical harmonic coefficients matrix is obtained by the spherical harmonic decomposition of the signals received by each sphere and then the MUSIC algorithm is used to scan the wave direction.

Assuming that there are L irregularly placed spheres of radius r, each with identical uniform distribution of microphones, while their self-coordinates are located as a circle of radius R on a plane as shown in Fig.1. Assuming $M = T \times H$ microphones on each sphere, (3) and (1) can be rewritten in the following forms, respectively [5]:

$$\bar{a}_{nm}^{(l)} = \sum_{t=1}^{M} P_{(l)}(\vartheta_t, \varphi_t) Y_{nm}^{(l)*}(\vartheta_t, \varphi_t) \sin\vartheta_t \Delta\vartheta\Delta\varphi \tag{14}$$

$$P_{(l)}(\vartheta_t, \varphi_t) = \sum_{s=1}^{S} w_s e^{ik(\mathbf{r}_{ol} + \mathbf{r}_t) \cdot \bar{\mathbf{y}}_s} \tag{15}$$

where $P_{(l)}(\vartheta_t, \varphi_t)$ is the measured pressure on the l^{th} sphere at point (ϑ_t, φ_t) , $k = 2\pi f / c$ with frequency f and c is the speed of sound, and $\bar{\mathbf{y}}_s$ is the direction vector respect to the s^{th} source. $\mathbf{r}_{ol}$ is the direction vector from the origin of the coordinate to the center of the l^{th} sphere while $\mathbf{r}_t$ is the direction vector from the center of the l^{th} sphere to the t^{th} microphone on the sphere $(|\mathbf{r}_{ol}| = R, \ |\mathbf{r}_t| = r)$. By substituting (15) into (14), following is obtained :

$$\bar{a}_{nm}^{(l)} = \sum_{s=1}^{S} \sum_{t=1}^{M} w_s e^{ik(\mathbf{r}_{ol} + \mathbf{r}_t) \cdot \bar{\mathbf{y}}_s} Y_{nm}^{(l)*}(\vartheta_t, \varphi_t) \sin\vartheta_t \Delta\vartheta\Delta\varphi \tag{16}$$

Also it can be expressed as:

$$P_{nm}^{L} = \left[\bar{a}_{nm}^{(1)} \quad \bar{a}_{nm}^{(2)} \quad \cdots \quad \bar{a}_{nm}^{(l)} \quad \cdots \quad \bar{a}_{nm}^{(L)} \right]^{T} = \left[B \times C^{(1)}, \cdots, B \times C^{(l)}, \cdots, B \times C^{(L)} \right]^{T} \times W \tag{17}$$

where P_{nm}^{L} is the decomposition coefficient for multiple spherical array, B and W has the same structure as single spherical array, and $C^{(l)}$ is an $M \times S$ matrix given by

$$C^{(l)} = \begin{bmatrix} e^{jk(\mathbf{r}_{ol}+\mathbf{r}_1)\cdot\bar{\mathbf{y}}_1} \sin\vartheta_1 & e^{jk(\mathbf{r}_{ol}+\mathbf{r}_1)\cdot\bar{\mathbf{y}}_2} \sin\vartheta_1 & \cdots & e^{jk(\mathbf{r}_{ol}+\mathbf{r}_1)\cdot\bar{\mathbf{y}}_S} \sin\vartheta_1 \\ e^{jk(\mathbf{r}_{ol}+\mathbf{r}_2)\cdot\bar{\mathbf{y}}_1} \sin\vartheta_2 & e^{jk(\mathbf{r}_{ol}+\mathbf{r}_2)\cdot\bar{\mathbf{y}}_2} \sin\vartheta_2 & \cdots & e^{jk(\mathbf{r}_{ol}+\mathbf{r}_2)\cdot\bar{\mathbf{y}}_S} \sin\vartheta_2 \\ \vdots & \vdots & \ddots & \vdots \\ e^{jk(\mathbf{r}_{ol}+\mathbf{r}_M)\cdot\bar{\mathbf{y}}_1} \sin\vartheta_M & e^{jk(\mathbf{r}_{ol}+\mathbf{r}_M)\cdot\bar{\mathbf{y}}_2} \sin\vartheta_M & \cdots & e^{jk(\mathbf{r}_{ol}+\mathbf{r}_M)\cdot\bar{\mathbf{y}}_S} \sin\vartheta_M \end{bmatrix} \tag{18}$$

Using matrix A^{L} to substitute the $(N+1)^2 \times M$ matrix in (17):

$$A^{L} = \left[B \times C^{(1)}, \cdots, B \times C^{(l)}, \cdots, B \times C^{(L)} \right]^{T} \tag{19}$$

where A^{L} is steering matrix of multiple spherical array, (17) can be simplified as:

$$P_{nm}^{L} = A^{L} \times W \tag{20}$$

Then, according to (10)-(13), the direction of the sources can be found using the multiple spherical arrays.

IV. Multiple Spherical Arrays Design and Simulation

In this section, a set of multiple spherical arrays is formulated, the main factor, such as the size of each sphere and the distributions of the multiple spheres, are analyzed by estimating the DOA using the spherical harmonic MUSIC algorithm and the design rules are shown in the last. For all the following simulations, five sound sources were used, which directions are $(90°,120°)$, $(120°,60°)$, $(180°,150°)$, $(240°,60°)$ and $(270°,120°)$, respectively, and their frequency range are from 0.8 kHz to 1 kHz. The comparison of performance is given in terms of root mean square error (RMSE) (averaged over the sources).

A. single sphere arrays with different radius

In this subsection, four types of single sphere arrays with different radius are designed to indicate the influence of the sphere size on DOA estimation, and the microphones on each single sphere array are distributed in $M=T\times H=5\times 6$ as shown in Fig.2 (a).

The spherical harmonic decomposition order N, that is $N=\sqrt{M}-1$, is set to $N=4$ and the response curve of 4 order Bessel function is drawn, as shown in Fig.2 (b). In order to improve the estimation accuracy, it is assumed that $kr<6$ to keep the response away from zero point, which appears on the response curve when the value of kr is 7.59. The maximum frequency value $f_H = 1KHz$ is brought into $kr<6$ $(k=2\pi f/c)$, and $r<0.3m$ is obtained. The radius of these single sphere arrays are set as 0.2m, 0.3m, 0.4m and 0.5m.

When the signal to noise ratios (SNR) of the five sound sources are 0 dB, the estimation results for all of these four structures are shown in Fig.4. The figures show that the DOA estimation accuracy is getting better with increase in r, while r is less than 0.3m, but when r is more than 0.3m, the accuracy have started to degrade, which is due to the influence of the zeroes of the Bessel's function.

Assuming that the SNR of the five sources range are from -10dB to 30dB simultaneously. For different SNR, simulations are operated of 200 times in order to get azimuth angle RMSE and estimation probability. As Fig.3 (a) shows, when the SNR increases, the RMSE degrades, and when r=0.3m the RMSE of azimuth angle is lower than that of the other radius at the same SNR, which also proves the above conclusion.

B. multiple spherical arrays with same and different radius

According to the previous analysis, when the sound source frequency band is certain, there are limits to the size of the sphere and when the radius of the sphere is determined, the DOA estimation accuracy can be affected by the frequency of the sound signal, that is to say the signal frequency f and the sphere radius r are inversely related.

In this subsection, the advantages of multiple spherical array with same radius against different radius are discussed, as shown in Fig.5 (a) and (b). Three spheres with same and different radius are placed as a circle of $1m$ radius, and thirty microphones are distributed on each sphere with same arrangement as the single spherical array. In Fig.5 (a), the radii of all three spheres are 0.3m and the three spheres in Fig.5 (b) have radius 0.1m, 0.3m, and 0.5m.

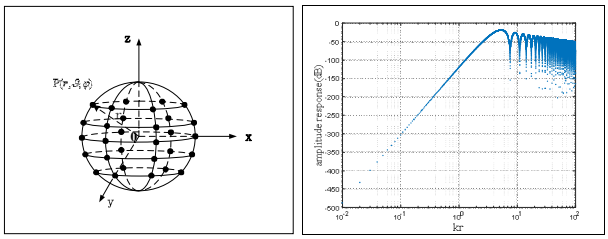

(a) (b)

Fig.2 (a) The microphones distribution on a single sphere array in $T\times H$: where T depicts the latitude numbers on the sphere while H indicates the number of microphones on each latitude. (b) 4th order Bessel function response curve

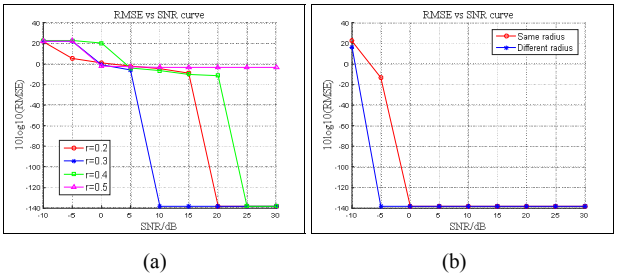

(a) (b)

Fig.3. Azimuth angle RMSE under different SNR (a) single sphere arrays with different radius (b) multiple spherical arrays with same and different radius

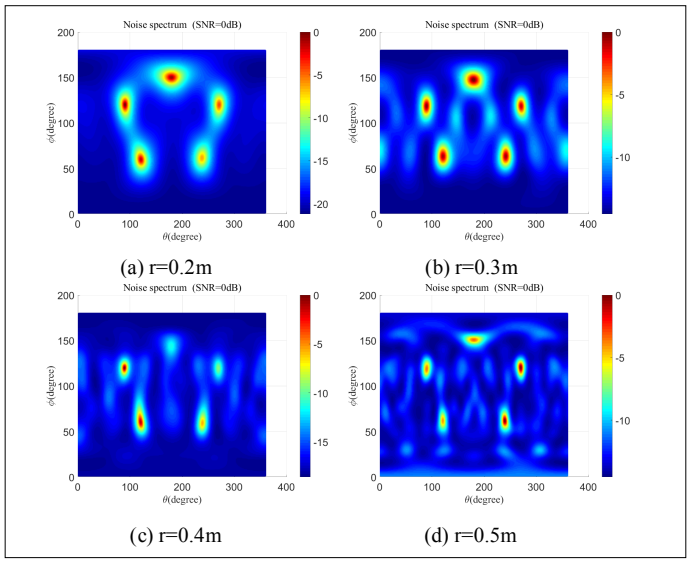

Fig.4. DOA estimation results of single sphere arrays with different radius.

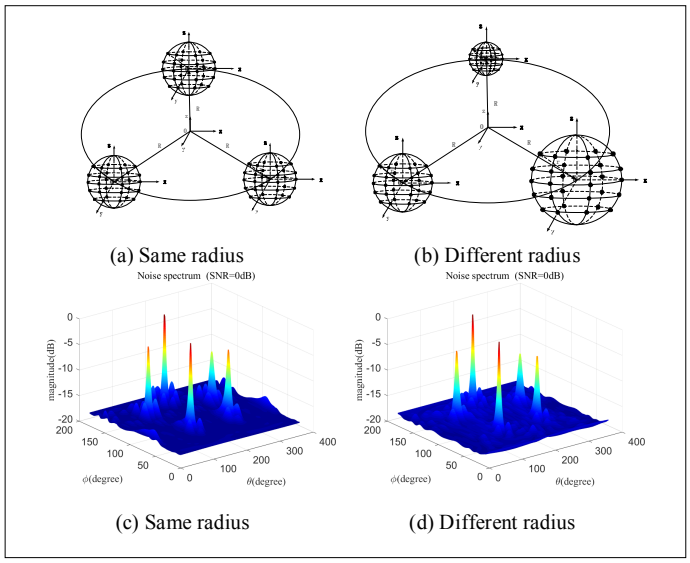

Fig.5. Multiple spherical array structures with same and different radius and their DOA estimation results

The DOA estimation results with SNR=0 are shown in Fig.5 (c) and (d), respectively. The spectrum using the structure with different radius is clearer and the side lobe is less as compared to the structure with same radius. The azimuth angle RMSE vs SNR curve is show in Fig.3 (b), which indicate that different radius has lower RMSE than that of the same radius at low SNR, leading to better estimation performance in noisy environment.

C. multiple spherical arrays with different distribution

In DOA estimation, the sampling microphones with a single spherical distribution are more effective than that of planar or linear distribution [11]. In this subsection, four types of array structures with different distributions are designed as shown in Fig.6. Each of the multiple spherical arrays is composed of five spheres of radius 0.2m and on each sphere, thirty microphones are distributed in same arrangement as a single spherical array. In linear and cross distributions, the interval between each sphere is 0.5m; in circular distribution, five spheres are placed as a circle of radius 0.5m on a given plane; and in spherical distribution, five spheres are placed on a sphere of radius 0.5m, where two spheres are distributed on the spherical poles and three spheres are uniformly placed in the equatorial plane of the big sphere.

Fig.7 illustrates the estimation performance with SNR=0dB. The estimation accuracy with linear distribution is the worst and the cross and circular distributions are similar. The spectrum peak with spherical distribution is sharper than that of the other three types of distributions.

The azimuth angle and pitch angle RMSE under different SNR are show in Fig.8 (a) and (b) respectively. The RMSE of azimuth angle with linear distribution is the worst in four arrays, and the other three types of distributions is similar. But the RMSE of pitch angle with spherical distribution is significantly better than the other three types of distributions.

In the case of two plane waves from directions (θ_1,ϕ) and (θ_2,ϕ), the angle resolution is calculated by (21) and (22):

$$Q_{peak}=[Q(\theta_1,\phi)+Q(\theta_2,\phi)]/2 \tag{21}$$

$$Q(\Delta\theta)=Q_{peak}-Q(\theta_m,\phi) \tag{22}$$

where $Q(\theta,\phi)=$ spectrum(θ,ϕ), $\theta_m=(\theta_1+\theta_2)/2$, $\Delta\theta=|\theta_1-\theta_2|$, Making ϕ=90°, increase the $\Delta\theta$ to get the angle resolution of azimuth angle which is show in Fig.8 (c). Then making $\theta=180°$, increase the $\Delta\phi$ in the same way to get

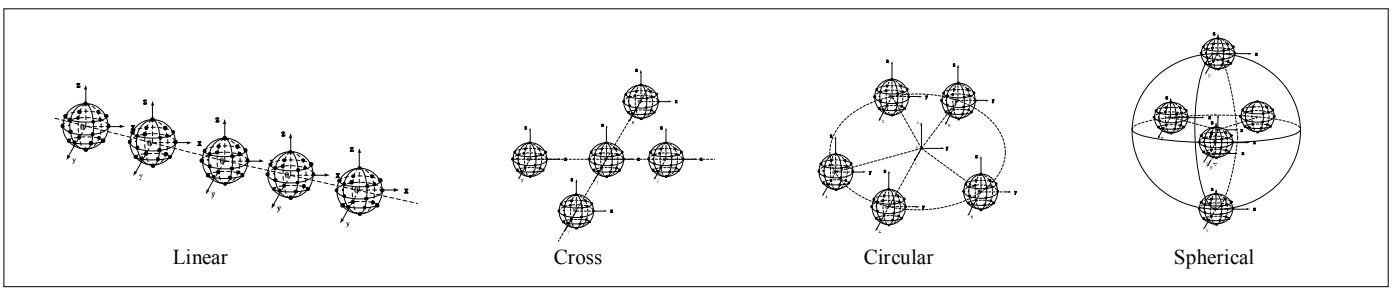

Fig.6. Spherical structure arrays with linear, cross, circular and spherical distributions

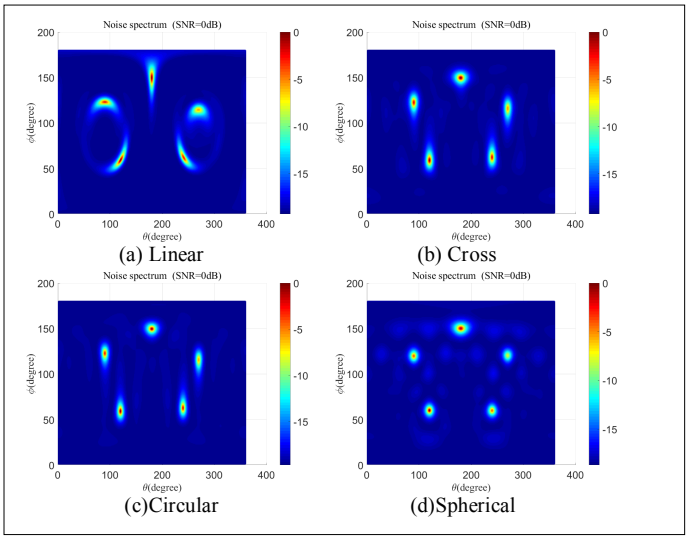

Fig.7. The results of DOA estimation of multiple spherical arrays with different distribution

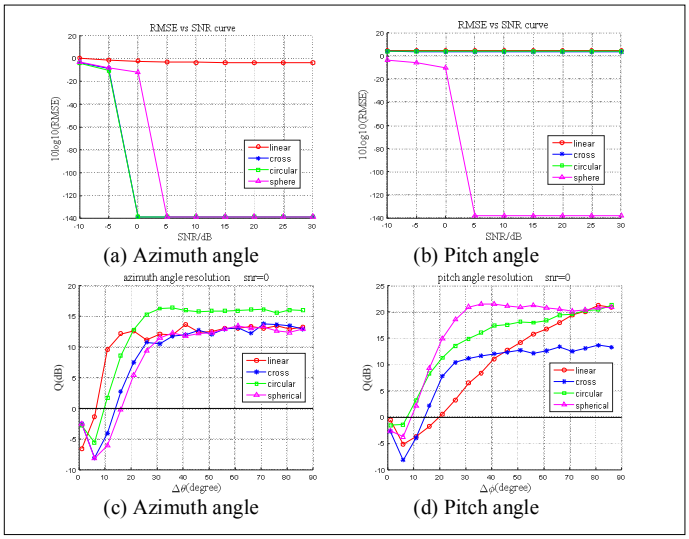

Fig.8. (a) Azimuth angle RMSE of four arrays under different SNR (b) Pitch angle RMSE of four arrays under different SNR (c) Azimuth angle resolution of four arrays (d) Pitch angle resolution of four arrays

the angle resolution of pitch angle that is show in Fig.8 (d). The azimuth angle resolution of linear and circular distribution are better than that of the other two, but it should be noted that the pitch angle resolution of spherical array is clearly superior than all others.

D. Design rules of multiple spherical array

According to the above mentioned simulations, the design rules for multiple spherical array structure are: (a) for open spherical structure, the radius of the spherical structure should be in a certain range due to the influence of the zeroes of the Bessel's function. (b) By placing the spherical structures with different radius in MAS arrays, the estimation accuracy can be improved and the frequency bandwidth of sound sources can be increased. (c) For the distribution of the multiple spheres in MSA arrays, the better spatial symmetry of the array structure will result in improved estimation accuracy.

V. Conclusion

In this paper, several types of multiple spherical array structures with different sizes and distributions of spheres have been developed for the DOA estimation of multiple sources based on the spherical harmonic MUSIC algorithm. The simulation results have demonstrated that the multiple arrays can more accurately deal with multiple sources by using a multiple spherical array structure with more spherical structures, good spatial symmetry and proper radius. Possible future work will include the application of this structure and algorithm to rigid aperture.

Acknowledgment

This research is partly sponsored by National Natural Science Foundation of China (no.61401027).

Reference

[1] J. Benesty, “Adaptive eigenvalue decomposition algorithm for passive acoustic source localization,” Journal Acoustical Society of America, vol. 107, pp. 384–391,2000.

[2] H. Wang and M. Kaveh, “Coherent signal-subspace processing for the detection and estimation of angle of arrival of multiple wideband sources,” IEEE Transactions on Acoustics, Speech, and Signal Processing, vol. 33, pp. 823–831, 1985.

[3] H. Teutsch and W. Kellermann, “Eb-esprit: 2d localization of multiple wideband acoustic sources using eigenbeams,” in ICASSP, 2005, pp. 89–92.

[4] F. Z. Wang and X. Pan, “Acoustic Sources Localization in 3D Using Multiple Spherical Arrays,” J Electr Eng Technol. 2016, pp.709-718, unpublished.

[5] F. Z. Wang, X. Pan, X. Chen and P. Gong,“ Localization of 3D acoustic sources based on multiple spherical apertures,” in 2014 International Symposium on Communications and Information Technologies (ISCIT), pp.138-142, 2014

[6] H. Teutsch and W. Kellermann, “Acoustic source detection and localization based on wavefield decomposition using circular microphone arrays,” Journal of the Acoustical Society of America, vol. 120, pp. 2724-2736, Nov. 2006.

[7] X. Li, S. F. Yan, X. C. Ma, and C. H. Hou, “Spherical harmonics music versus conventional music,” Applied Acoustic, vol. 72, pp. 646-652, 2011.

[8] A. Gupta and T.D. Abhayapala, “Three-dimensional sound field reproduction using multiple circular loud-speaker arrays,” IEEE Transactions on Audio Speech and Language Processing, vol. 19, pp. 1149–1159, 5 2011.

[9] P.K.T. Wu, N. Epain, and C.T. Jin, “A dereverberation algorithm for spherical microphone arrays using compressed sensing techniques,” in ICASSP IEEE International Conference on Acoustic Speech and Signal Processing, Kyoto, Japan, Mar. 2012, pp. 4053-4056.

[10] X. Mestre and M. A. Lagunas, “Modified subspace algorithms for doa estimation with large arrays,” IEEE Transactions on Signal Processing, vol. 56, pp. 598-614, Feb. 2008.

[11] D.B. Ward and T.D. Abhayapala, “Theory and design of high order sound field microphones using spherical microphone array,” in ICASSP, 2 2002, pp. 1781–1784.

[12] T.D. Abhayapala T.S. Pollock and R.A. Kennedy, “Characterization of 3d spatial wireless channels,” in IEEE 58th Vehicular Technology Conference, 4 2003, p-p. 123–127.

Likelihood modelling of the Space Geodesy Facility laser ranging sensor for Bayesian filtering

C. Simpson, A. Hunter, S. Vorgul, E. Delande, J. Franco, D. Clark
School of Engineering & Physical Sciences, Heriot-Watt University, Edinburgh, UK
{ccs30, alh31, sv112, E.D.Delande, jf139, D.E.Clark}@hw.ac.uk

J. Rodriguez Perez
NERC-BGS Space Geodesy Facility, Herstmonceux, UK
josrod@nerc.ac.uk

***Abstract*—This work analyzes the data output of laser ranging data collected from the Space Geodesy Facility (Herstmonceux, UK), and proposes a bespoke likelihood function for its processing in the context of Bayesian filtering. It is then illustrated in a single-target Bayesian filter, performing successfully on simulated and real data, under a variety of noise profiles encountered in typical outputs of the sensor.**

I. Introduction

Maintaining an up-to-date catalogue of the near-Earth orbiting objects, including space debris and man-made satellites, has been identified as a key objective of the Space Situational Awareness (SSA) activity, a topic of growing interest, and a challenge whose difficulty is increasing with the growing number of objects populating the near-Earth space [1]. The detection and tracking of orbiting objects is supported by a range of specific ground-based sensing stations for SSA activities, forming an heterogeneous network (radars, telescope, cameras, etc.) from which noisy measurements of different nature are collected by the individual stations. Fusing the information collected from various space sensing assets through a detection and tracking algorithm is an open challenge, that requires some automation in the pre-processing of each data type produced by individual sensors into a coherent probabilistic description of the tracked objects. Casting Satellite Laser Ranging (SLR) data in a Bayesian framework is a necessary step towards this goal.

As part of a coordinated SSA initiative integrating UK and international assets to maintain a common catalogue of orbiting objects, it is important to have accurate probabilistic models of the sensors that integrate it. This type of analysis has been previously carried out for range-only radars [3], Doppler radars [2], and optical sensors [4], [5]. A strategy for using these models in a multi-target tracking scenario has been discussed in [2].

In this paper the output of the range-only laser sensor at the Herstmonceux Space Geodesy Facility (SGF) is analysed in order to design a sensor model for filtering purposes. The sensor model is then exploited for the design of a single-target Bayesian filter, for which implementations based on a Kalman [6] and a particle filter [7] are explored.

This paper is structured as follows. Section II provides a bried description of the Herstmonceux Space Geodesy Facility, and the specifics of the output data. Section III discusses the modelling of the target tracking algorithm, including the bespoke sensor model for the Herstmonceux Space Geodesy Facility, and the design of the resulting single-target Bayesian filter. The tracking algorithm is then tested on simulated and real data in Section IV.

II. The Space Geodesy Facility

The Space Geodesy Facility in Herstmonceux (East Sussex, UK) [8] is a multi-technique geodetic observatory operating an SLR station, an absolute gravimeter and several Global Navigation Satellite System (GNSS) receivers. Along with forty other similar sites around the world, the SGF in Herstmonceux forms part of the International Laser Ranging Service (ILRS) [9]. The SLR technique, used primarily for geodetic purposes, measures the time of flight of short laser pulses as they travel between the observing stations and orbiting satellites equipped with retroreflectors [10], [11]. Satellites routinely tracked by the ILRS network include low Earth orbiters with scientific payloads (e.g. Grace, Jason-3, Swarm), passive geodetic targets (e.g. LAGEOS, LARES), and various GNSS constellations (e.g. GLONASS, BeiDou, GPS). Capable of providing measurements with sub-centimetre accuracy and precision, SLR is one of the four space geodetic techniques contributing to the realisation of the International Terrestrial Reference Frame [12]. Beyond geodetic applications, SLR can also be employed to track uncooperative space debris objects (i.e. no retroreflectors present) [13], [14].

An Nd:Van pulsed laser (1 KHz repetition rate, 10 ps FWHM pulse width, 1.1 mJ/pulse) at the frequency-doubled wavelength of 532 nm is employed at the SGF laser station. The receiver telescope is a 0.5 m Cassegrain reflector equipped with a Single Photon Avalanche Diode (SPAD) detector. The timing measurements are provided by a home built event timer of 1 ps resolution and 5 ps precision. A strictly single-photon tracking policy is followed at SGF for all satellite targets, whereby the energy levels of the returned pulses are controlled and limited to ensure that, on average, only a single photon is contained in each reflected pulse. This ensures that the

978-1-5090-0326-6/16/$31.00 ©2016 IEEE

laser retroreflector arrays carried onboard the satellite targets are sampled in their entirety, with no preferential detections obtained from points closer to the ground station. In order to limit the negative impact of background and dark noise events, the detector is gated shortly earlier (typically 100 ns) than the predicted range to the satellite. This is necessary due to the high sensitivity of the sensor and the present background radiation. The distribution of returns, excluding actual satellite reflections, are adequately described with a negative exponential distribution, as the detection events follow Poisson statistics. The specific characteristics of the distribution of detected pulses from the satellite targets depend on the shape and orientation of the laser retroreflector arrays.

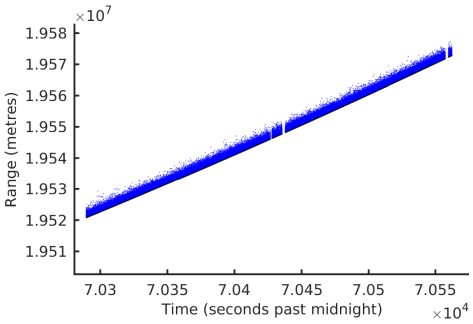

a) Batch 746

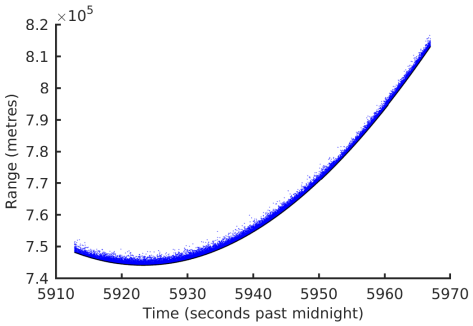

b) Batch 540

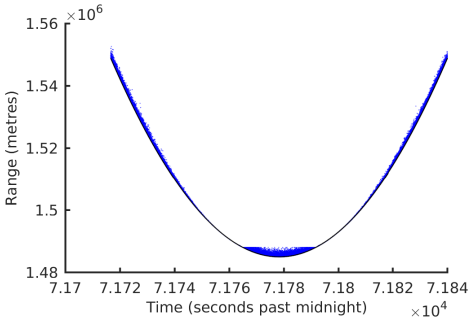

c) Batch 737

Fig. 1: SLR output data. The ground truth is depicted with a black line, the data points are in blue.

Three datasets collected from the SGF laser, named 746, 540, 737 for different satellite passes, were exploited in the context of this paper and are depicted in Fig. 1. These datasets are illustrative of the obtained data. The identities of the observed satellites is known, and the ground truth, shown in Fig. 1 and in subsequent figures, is obtained from an available catalogue. These figures illustrate the typical features of the raw ranging data collected at SGF, though they all present a very noticeable skewness in the data distribution around the ground truth, as explained above and highlighted in the data residuals depicted in Fig. 2. Note in particular the uneven distribution in batch 737 , whose atypical shape in the lower range values is due to a temporal problem in the receiver hardware[1].

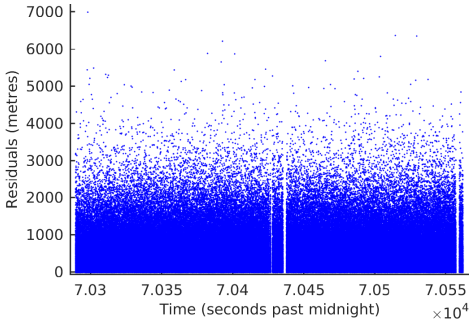

a) Batch 746

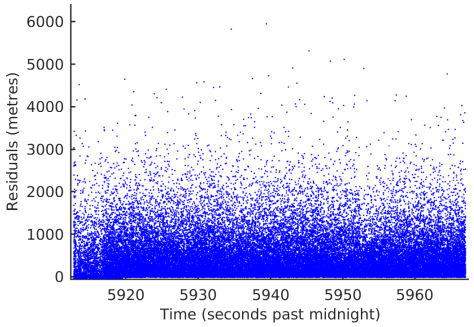

b) Batch 540

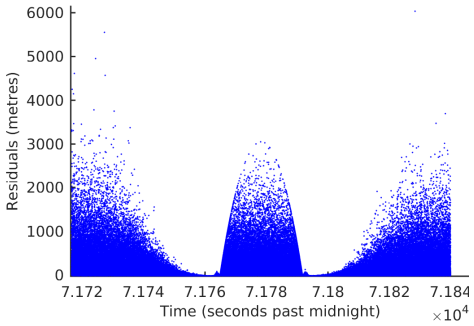

c) Batch 737

Fig. 2: SLR residual data. The data points are in blue.

III. Tracking Algorithm

This section presents the target tracking algorithm proposed in this paper, constructed with the Bayesian estimation framework and designed specifically to process data laser ranging sensors as exploited in the Herstmonceux Space Geodesy Facility.

A. Bayesian estimation: generalities

The state of the target, describing its range r and radial velocity $\dot{r}$ with respect to the sensor, is denoted by the

[1]This is caused by laser overlap, which happens when a pulse is fired at the same time a detector is gated. The pulse backscatters off the atmosphere and triggers the detector. This run was recorded when the overlap avoidance routine was disabled.

vector $x = [r, \dot{r}]' \in \mathcal{X}$, belonging to some target state space $\mathcal{X} \subset \mathbb{R}^2$ covering the admissible values for the target state. In the context of Bayesian filtering, the information on the target state maintained by the operator includes some measure of *uncertainty* associated to the filtered estimate, and is represented by some probability distribution p on the state space $\mathcal{X}$. The time is indexed with some integer k, marking the epochs of data collection.

During the *prediction step* the *predicted distribution* $p_{k|k-1}$, representing the information on the target state at time k prior to the collection of the current observation z_k, is propagated from the output p_{k-1} of the previous time step through the operator's knowledge about the target's dynamic behaviour. During the *updated step* the predicted distribution is corrected to the *posterior distribution* p_k, through the collected observation z_k and the operator's knowledge about the sensor's characteristics (measurement noise, probability of detection, false alarm rate, etc.).

B. Target modelling

Since the target state only depicts the range and radial velocity of the object while passing over the sensor, the target trajectory throughout the observation window is relatively simple and the target motion at time step k is constructed with a simple constant velocity model [15], i.e.

$$x_k = \begin{bmatrix} 1 & \Delta_k \\ 0 & 1 \end{bmatrix} x_{k-1} + n_k, \tag{1}$$

where Δ_k denotes the duration (in unit time) since the last time step $k-1$, $n_k \sim \mathcal{N}(\mathbf{0}, Q_k)$ denotes the process noise, drawn from a Gaussian distribution with zero mean and covariance matrix

$$Q_k = \sigma_k^2 \begin{bmatrix} \frac{\Delta_k^3}{3} & \frac{\Delta_k^2}{2} \\ \frac{\Delta_k^2}{2} & \Delta_k \end{bmatrix}, \tag{2}$$

where the standard deviation σ_k is a model parameter.

C. Sensor modelling

Since the sensor provides data on range only, an observation collected is described by a scalar $z \in \mathcal{Z}$, belonging to some observation space $\mathcal{Z} \subset \mathbb{R}$ covering the admissible values for the observation state.

The peculiar data distribution of the sensor (see Section II) led to the design of a bespoke sensor model for the processing of the Herstmonceux SGF data. Since there is a photon return for every pulse, and the time index of the Bayesian flow coincides with the epochs of data collection (see Section III-A), there is one and only one measurement collected per time step. Due to the reasons discussed in section II, the data distribution has an inverse exponential shape, resulting in the data being skewed in favour of lower ranges (see Fig. 2).

However, little is known about the frequency at which the pulse misses the object of interest, or about the distribution of the background returns and dark noise. For the purpose of filtering, therefore, all the data shall be treated as observations stemming from the object of interest, and the sensor modelling reduces to the design of a suitable likelihood function $\ell(z|x)$, describing the probability that the sensor will return observation z, conditioned on the state x of the object of interest.

Using batch 746 as a training set, an exponential distribution was fitted to the data residuals. The model agreed with the observations well, with a coefficient of determination of $R^2 = 0.9994$. This value is a measure of the correlation between the observed data and the predicted values, and a value so close to one is an indicator that the distribution can be accurately modelled as an exponential distribution. The fitted curve can be seen in Fig. 3, and the obtained equation for the likelihood is

$$\ell(z|x) \propto e^{-2.811.10^{-4}(0.5 \cdot c \cdot z - r)}, \tag{3}$$

where r is the range component of the target state x, in metres, and the observation z is in seconds. The factor $c/2$ is applied to convert from time to distance.

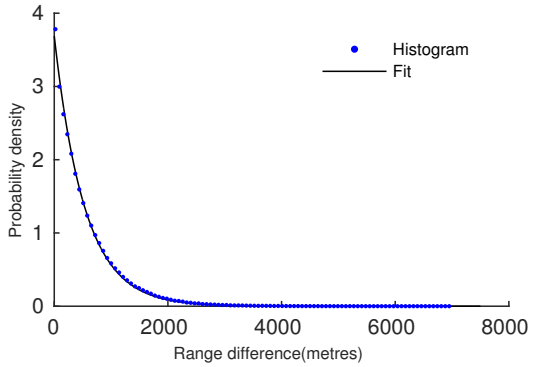

Fig. 3: A histogram of the data residuals of batch 746 using 100 bins, with corresponding exponential fit .

The likelihood function (3) shall be used for the sensor modelling for the remaining of the paper.

D. Filter design

Two approaches have been explored for the design of the filtering solutions: a Kalman filter [6], and a particle filter [7].

1) Kalman filter: The Kalman filter is a well-established filtering solution for single-target detection and tracking problems. Its main advantages lie in the simplicity of its implementation in a practical target tracking algorithm and in the reduced computation cost, though it requires strong modelling assumptions regarding the target motion model and the sensor model [6]. In particular, the Kalman filter assumes that the likelihood function $\ell(\cdot|x)$ follows a Gaussian distribution and is ill-adapted to the representation of heavily-skewed observation profiles such as the one designed for the SGF sensor in Eq. (3).

For the sake of illustration, a Gaussian-distributed likelihood was fit on the data distribution and the resulting Kalman filter was tested on batches 540 and 737. As expected and shown in Fig. 4, the filter assumes a data profile evenly distributed around the true target state and the estimated target trajectory is biased towards higher range values.

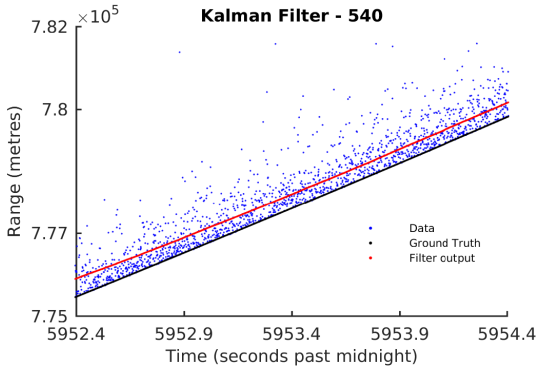

Fig. 4: Kalman filtering applied on batch 540. The ground truth is depicted with a black line, the estimated state with a red line, the data points are in blue.

2) Particle filter: Particle filtering methods impose little restrictions on the nature of the propagated probability distribution p_k, the targets' dynamical behaviour or the sensor observation process; as such, they are widely exploited in tracking problems involving non linear models [7].

In this paper a simple Sequential Importance Resampling (SIR) particle filter is exploited, where the new particles are sampled every time step from the prediction model (1), and reweighted using the likelihood function (3). That is, the posterior probability distribution p_k is approximated by a set of weighted particles $\{x_k^{(i)}, w_k^{(i)}\}_{i=1}^N$, i.e.

$$p_k(x) \simeq \sum_{i=1}^{N} w_k^{(i)} \delta_{x_k^{(i)}}(x), \tag{4}$$

where δ_x is the Dirac delta function centred around x, the number of particles N is a model parameter, and the updated particle set $\{x_k^i, w_k^i\}_{i=1}^N$ is computed from the posterior particle set $\{x_{k-1}^{(i)}, w_{k-1}^{(i)}\}_{i=1}^N$ through the equations

$$\begin{cases} x_k^{(i)} & = \begin{bmatrix} 1 & \Delta_k \\ 0 & 1 \end{bmatrix} x_{k-1}^{(i)} + n_k^{(i)}, \\ w_k^{(i)} & \propto \ell(z_k | x_k^{(i)}) w_{k-1}^{(i)}, \end{cases} \tag{5}$$

where $n_k^{(i)} \sim \mathcal{N}(\mathbf{0}, Q_k)$, $1 \leq i \leq N$. Resampling is done as in the classical bootstrap filter, where a set of particles is sampled from the original weighted set of particles with probability proportional to the original weight. All particles in the resampled set are assigned the same weight. The resulting particle set approximates the same distribution while focusing particles in areas with higher likelihood [16].

IV. Results

In this section, we present the obtained filtering distributions using both simulated data and the Herstmonceux datasets that were previously discussed. Since the Kalman filtering approach yielded biased distributions, we focus on the particle filtering method to present results.

A. Simulated Data

In addition to the data from Herstmonceux, we also simulated our own data where we specified a true trajectory and a noise distribution. This allowed us to test how the filter handles under different realisations. Exponential noise was simulated for 50 Monte Carlo runs, with the following equation:

$$l(x) \propto \begin{cases} e^{-0.0025x}, & x \in [100, 1000], \\ 0, & — \end{cases} . \tag{6}$$

Each Monte Carlo realisation was generated by adding noise sampled from this distribution, and added to the ground truth from dataset 540. The average Root Mean Squared Error (RMSE) can be seen in Fig. 5, alongside error bounds. Here it can be seen how the filter accurately locks into the trajectory after observing the object for a number of time steps.

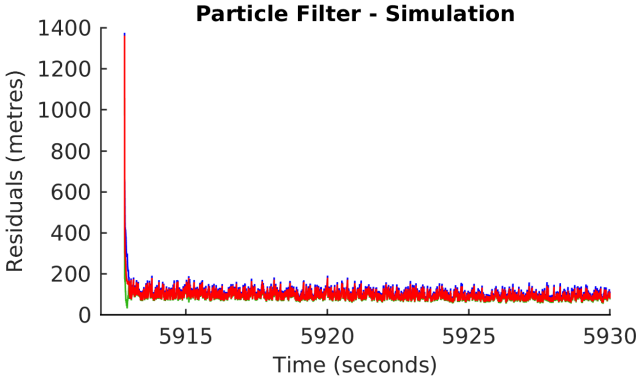

Fig. 5: Average RMSE for 30 simulated Monte Carlo realisations (black line), plus and minus one standard deviation (green and blue lines).

B. Herstmonceux Data

We applied the particle filter to the datasets generated by satellite passes 540 and 737. As it was said before, the training data to fit the exponential likelihood was that of pass 746. The two datasets analysed show different properties. Pass 540 has similar noise properties to the training set, while as it was said before, a temporary hardware issue caused pass 737 to have a more complicated noise structure.

The results of applying the filter on pass 540 can be seen in Fig. 6. It can be seen how the filtering distribution successfully mitigates the measurement noise in spite of the measurements being asymmetrically distributed around the expected range.

Fig. 7 shows the results of applying the filter to pass 737. As it was previously said, a temporary software fault caused the noise distribution to have range-dependent properties. In spite of this noise profile, the filter manages to track the range of the satellite with similar accuracy as in pass 540. In the zoomed-in view, it can be seen how the filtered distribution is robust to sudden changes in noise distribution.

V. Conclusion

We have developed a filtering solution to estimate the range of a satellite from SLR data. The proposed method is capable of handling the noise profiles usually find in SLR problems, which use gated single photon avalanche diodes. The particle filtering framework was exploited, as it allowed us to model the observation likelihood as an exponential

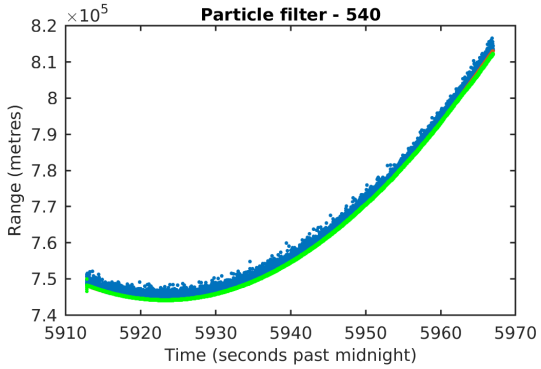

a) Maxima and minima of filtering distribution throughout the estimation (green), and data (blue)

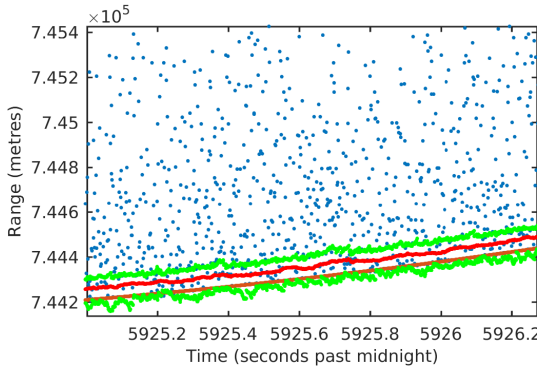

b) Zoomed-in view of the above. Data and extrema as before, ground truth is in orange, and estimate in red.

Fig. 6: Estimation results for pass 540

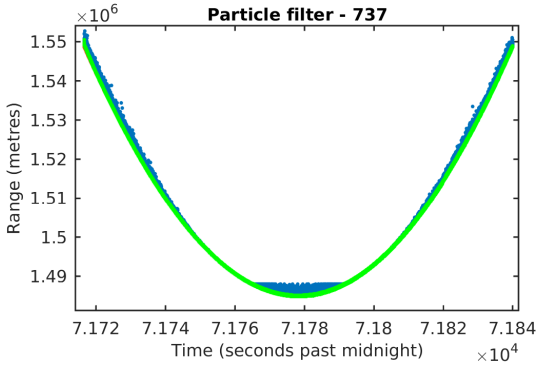

a) Maxima and minima of filtering distribution throughout the estimation (green), and data (blue)

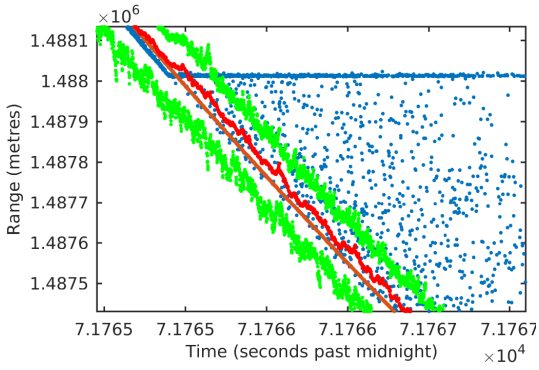

b) Zoomed-in view of the above. Data and extrema as before, ground truth is in orange, and estimate in red.

Fig. 7: Estimation results for pass 737

probability distribution function. The method was tested on both real and simulated data, and its resulting estimates are consistent with the orbital predictions obtained through numerical integration, with the added advantage of providing uncertainty information.

Acknowledgements

This work was supported by the Engineering and Physical Sciences Research Council (EPSRC) Grant number EP/K014277/1 and the MOD University Defence Research Collaboration in Signal Processing.

References

[1] A. Rossi, "The earth orbiting space debris," *Serbian Astronomical Journal*, vol. 170, pp. 1–12, 2005.

[2] E. D. Delande, C. Frueh, J. Houssineau, and D. E. Clark, "Multi-object filtering for space situational awareness," in *2015 AAS/AIAA Spaceflight Mechanics Meeting*, Jan. 2015, pp. AAS 15–406.

[3] A. Pak, D. E. Clark, J. Correa, M. Adams, E. D. Delande, J. Houssineau, J. Franco, and C. Frueh, "Joint Target Detection and Tracking Filter for Chilbolton Advanced Meteoreological Radar Data Processing," in *Advanced Maui Optical and Space Surveillance Technologies Conference*, Sep. 2016, submitted.

[4] O. Hagen, J. Houssineau, I. Schlangen, E. D. Delande, J. Franco, and D. E. Clark, "Joint Estimation of Telescope Drift and Space Object Tracking," in *2016 IEEE Aerospace Conference*, 2016, to appear.

[5] J. Franco, E. D. Delande, C. Frueh, J. Houssineau, and D. E. Clark, "A Spherical Co-ordinate Space Parameterisation for Orbit Estimation," in *IEEE 2016 Aerospace Conference*, 2016, to appear.

[6] R. E. Kalman, "A New Approach to Linear Filtering and Prediction Problems," *Journal of Basic Engineering*, vol. 82, no. 1, pp. 32–45, 1960.

[7] A. Doucet, N. de Freitas, and N. Gordon, *Sequential Monte Carlo Methods in Practice*, ser. Statistics for Engineering and Information Science. Springer, 2001.

[8] SLR Specifications (SGF website, http://sgf.rgo.ac.uk/sysspec/slr.html).

[9] M. Pearlman, J. Degnan, and J. Bosworth, "The international laser ranging service," *Advances in Space Research*, vol. 30, no. 2, pp. 135–143, 2002.

[10] L. Combrinck, "Satellite laser ranging," in *Sciences of Geodesy-I*. Springer, 2010, pp. 301–338.

[11] G. Seeber, *Satellite geodesy: foundations, methods, and applications*. Walter de Gruyter, 2003.

[12] Z. Altamimi, X. Collilieux, and L. Métivier, "Itrf2008: an improved solution of the international terrestrial reference frame," *Journal of Geodesy*, vol. 85, no. 8, pp. 457–473, 2011. [Online]. Available: http://dx.doi.org/10.1007/s00190-011-0444-4

[13] Z.-P. Zhang, F.-M. Yang, H.-F. Zhang, Z.-B. Wu, J.-P. Chen, P. Li, and W.-D. Meng, "The use of laser ranging to measure space debris," *Research in Astronomy and Astrophysics*, vol. 12, no. 2, p. 212, 2012. [Online]. Available: http://stacks.iop.org/1674-4527/12/i=2/a=009

[14] G. Kirchner, F. Koidl, F. Friederich, I. Buske, U. Vlker, and W. Riede, "Laser measurements to space debris from graz {SLR} station," *Advances in Space Research*, vol. 51, no. 1, pp. 21 – 24, 2013. [Online]. Available: http://www.sciencedirect.com/science/article/pii/S0273117712005492

[15] X. Li Rong and V. P. Jilkov, "A Survey of maneuvering Target Tracking. Part I: Dynamic Models," *Aerospace and Electronic Systems, IEEE Transactions on*, vol. 39, no. 4, pp. 1333–1364, Oct. 2003.

[16] N. J. Gordon, D. J. Salmond, and A. F. Smith, "Novel approach to nonlinear/non-gaussian bayesian state estimation," in *IEE Proceedings F (Radar and Signal Processing)*, vol. 140, no. 2. IET, 1993, pp. 107–113.

Cramer-Rao Bounds for Distributed System Size Estimation Using Consensus Algorithms

Sai Zhang, Cihan Tepedelenlioğlu, Jongmin Lee, Henry Braun and Andreas Spanias
SenSIP Center, School of ECEE, Arizona State University
Email: {szhang98, cihan, Jongmin.lee, hcbraun, spanias}@asu.edu

***Abstract*—System size estimation in distributed wireless sensor networks is important in various applications such as network management and maintenance. One popular method for system size estimation is to use distributed consensus algorithms with randomly generated initial values at nodes. In this paper, the performance of such methods is studied and Fisher information and Cramer-Rao bounds (CRBs) for different consensus algorithms are derived. Errors caused by communication noise and lack of convergence is also considered, and their effect on Fisher information and CRB is given. The results provide a lower bound on the variance of the estimator of system size. This in turn, provides guidelines on how to choose consensus algorithms and initial values at the nodes.**

***Index Terms*—System Size Estimation, Wireless Sensor Networks, Average Consensus, Max Consensus, Fisher Information, Cramer-Rao Bound, Communication Noise.**

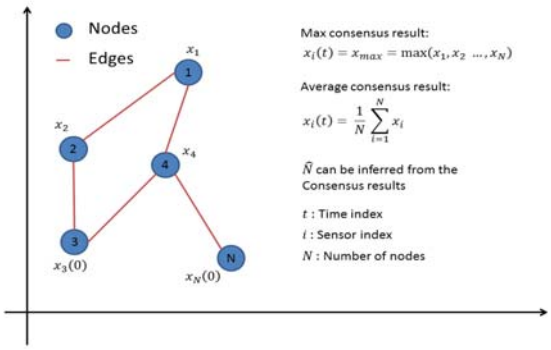

Fig. 1: Distributed network with N nodes.

I. Introduction

Distributed wireless sensor networks topologies are important in several research fields and applications [1] due to their robustness to link failures and low power.

System size estimation or counting the number of nodes in a distributed wireless network is essential in several applications. For example, some network maintenance protocols require the system size to incorporate a newly joined node in the system [2]. In [3], the soft-max based consensus method described requires the system size. On the other hand, in [4], the sum of the initial measurements is calculated using a consensus approach which exploits the system size. System size estimation is also important in military sensor network applications [1], [5]. In remote large-scale military sensor networks, sensor nodes are required to configure the network autonomously [5]. Estimating the system size enables the sensor network at any time to detect whether there are intrusions or whether there are new nodes attempting to join the network.

The problem of distributed system size estimation has been extensively studied in the literature [6]–[9]. A comparative study of distributed system size estimation algorithms is given in [6]. In [7]–[9], random walk algorithms are used to estimate the system size. More specifically, a selected sender transmits information and nodes pass the information to a selected neighbor and information propagates through the network in a "random walk" manner. Based on the average return time, an estimate of the system size can be obtained.

Another popular method for distributed system size estimation in wireless sensor networks uses consensus algorithms with randomly generated initial values at the nodes [10]–[14]. In [10], two algorithms for system size estimation are introduced. The first algorithm generates uniformly distributed initial measurements at nodes, and uses max consensus with an ML estimator (uniform + max consensus + ML). The second algorithm uses Gaussian + average consensus + ML. The consensus result is used to infer the system size. It is shown that result is the maximum likelihood estimator for N^{-1}, where N is the system size. In [11], a method based on average consensus with Bernoulli random initial values namely Bernoulli trail method is proposed. It is shown in [11] that the mean square error for the proposed method goes exponentially to zero as a design parameter increases. In [13], the nodes are assumed to be labeled and one node in the network holds an initial value of 1 and all other nodes are set to 0. The system size can be obtained from the average consensus result. A system size estimation algorithm in the presence of communication noise is proposed in [14]. The algorithm is based on average consensus and L_2 norm estimation. How the values of the initial measurements at nodes and the communication noise affect the performance of the algorithm are analyzed.

In this paper, we derive the Fisher information and Cramer-Rao bounds for consensus based system size estimators considering different noise conditions. It is shown that in the

978-1-5090-0326-6/16 /$31.00 ©2016 IEEE

absence of noise, the max consensus approach results in a lower CRB than the average consensus approach. In the presence of communication noise, we demonstrate how the SNR affects the Fisher information and CRBs. The results not only present the best estimation variance the algorithms can achieve, but also provide guidelines on how to choose consensus algorithms and initial values for system size estimation.

II. System Model

A distributed WSN is modeled as an undirected connected graph $\mathbb{G} = (\mathbb{N}, \mathbb{E})$ containing a set of nodes $\mathbb{N} = \{1, \ldots, N\}$ and a set of edges $\mathbb{E}$ as shown in Figure 1, where N is the total number nodes in the network, i.e., the system size. The set of neighbours of node i is denoted by $\mathbb{N}_i$. Two nodes can communicate with each other only if they are neighbours.

III. Review: System Size Estimation Using Consensus

In this section, we briefly review the max and average consensus algorithms, and then discuss how the results of consensus algorithms can be used to infer the system size.

A. System Size Estimation Using Max Consensus

By running max consensus, the states of nodes in the network converge to the maximum of the initial values. In [15], max consensus in the absence of communication noise is introduced. Let x_i be the initial value at node i and the state of node i at time t is denoted as $x_i(t)$. To compute the maximum of the initial measurements, the iterative max consensus algorithm can be expressed as

$$x_i(t+1) = \max\left\{x_i(t), \max_{j\in\mathbb{N}_i} x_j(t)\right\}. \tag{1}$$

In the absence of communication noise, by running the iterative algorithm of equation (1), states of nodes converge to the maximum of the initial values in finite time [15]. Note that in the presence of communication noise, the estimate may drift because of positive noise samples [3].

The max consensus result can be used to estimate the system size. In [10], the initial measurements are set to be uniformly distributed, $x_i \sim \mathcal{U}(0,1)$. The system size can be inferred from the max consensus result, $x_{\max} = \max\{x_1, x_2, \cdots, x_N\}$,

$$N = \frac{1}{\mathrm{E}[\ln x_{\max}]}. \tag{2}$$

In the algorithm, an estimate of the expected value $\mathrm{E}[\ln x_{\max}]$ is obtained by running the max consensus several times and taking a sample mean of the results.

B. System Size Estimation Using Average Consensus

Average consensus is also widely used and well studied [16]–[19]. By running the average consensus, the states of nodes converge to the average of the initial values. A simple linear average consensus in the absence of communication noise is introduced in [16]. The update of node i at time $t+1$ can be expressed as

$$x_i(t+1) = W_{ii}x_i(t) + \sum_{j\in\mathbb{N}_i} W_{ij}x_j(t), \tag{3}$$

where $W \in \mathbf{R}^{N\times N}$ is a doubly stochastic matrix named weight matrix, and its element in the ith row and jth column is denoted as W_{ij}. By running the iterative algorithm in equation (3), states of nodes converge to the average of the initial measurements [16], $\lim_{t\to\infty} x_i(t) = \bar{x} = \frac{1}{N}\sum_{i=1}^{N} x_i$.

In [17], distributed average consensus in the presence of communication noise is considered. The update of node i at time $t+1$ can be expressed as

$$x_i(t+1) = [1 - \alpha(t)d_i]\, x_i(t) + \alpha(t) \sum_{j\in\mathbb{N}_i} [x_j(t) + n_{ij}(t)], \tag{4}$$

where $n_{ij}(t)$ is the noise associated with the reception of $x_j(t)$ at node i, which is assumed to be independent across time and space with zero mean and variance σ_n^2. $\alpha(t)$ is a positive step and satisfies the persistence conditions [17], $\alpha(t) > 0,\ \sum_{t=0}^{\infty}\alpha(t) = \infty,\ \sum_{t=0}^{\infty}\alpha^2(t) < \infty$.

It is proved in [17] that by running the iterative algorithm as in equation (4), the states of nodes converge to a random variable θ, which is an unbiased estimate of the average of the initial values with bounded mean square error.

In [10], [11], [14], the average consensus result is used to infer the system size of the network. In [10], average consensus with standard normal distributed initial measurements, $x_i \sim \mathcal{N}(0,1)$ is used. The system size can be inferred from the average consensus result, $\bar{x} = \frac{1}{N}\sum_{i=1}^{N} x_i$,

$$N = \mathrm{E}\left[\bar{x}^2\right]. \tag{5}$$

In the algorithm, the expected value is obtained by running the average consensus multiple times and taking a sample mean of the results. In [11], the initial values at nodes are Bernoulli distributed and a lowest common multiple post-processing step is used to infer the system size. In [14], noisy conditions are considered and the effects of noise and initial values on estimation performance are discussed.

IV. CRB for System Size Estimation in the Absence of Noise

Consensus estimation is a powerful approach for parameter estimation in several sensor network applications [18]–[21].

Consensus algorithms can be used to estimate the system size in distributed wireless sensor networks. As mentioned above, different consensus algorithms and initial values can be used. In this section, we assume that the communications between nodes is perfect without any random noise, and consensus is reached. The Fisher information and CRB are calculated to compare between different approaches.

A. Max Consensus in the Absence of Noise

In this subsection, we assume that the max consensus as mentioned in Section III-A is used and consensus is perfectly reached, i.e. nodes converge to the maximum of the initial values. The following theorem characterizes the Fisher information and CRB result.

Theorem 1. *Assume the initial values at nodes x_i are i.i.d. with PDF $f(x)$ and CDF $F(x)$, and $f(x)$ is differentiable. When*

max consensus is used, the Fisher information for estimate of system size N is,

$$\mathcal{I}_{\max} = \frac{1}{N^2}. \tag{6}$$

The CRB is the inverse of the Fisher information, and a lower bound on the estimation variance can be expressed as

$$\mathrm{Var}\left[\hat{N}\right] \geq N^2. \tag{7}$$

The distribution of the initial values at nodes does not affect the Fisher information and CRB.

Proof: Assume max consensus is used and convergence is perfectly reached at time t. Let $y_i = x_i(t) = \max\{x_1, x_2, \cdots, x_N\}$ be the state at node i after convergence. Since x_i are i.i.d., the distribution of y_i can be calculated

$$\mathrm{CDF}: \{F(y)\}^N, \tag{8}$$

$$\mathrm{PDF}: N\{F(y)\}^{N-1} f(y). \tag{9}$$

Therefore, the Fisher information can be calculated from the definition, we have

$$\mathcal{I}_{\max} = \mathrm{E}\left[\left(\frac{\partial}{\partial N}\ln\left[N\{F(y)\}^{N-1} f(y)\right]\right)^2\right] \tag{10}$$

$$= \frac{1}{N^2} + \frac{2}{N}\mathrm{E}\left[\ln F(y)\right] + \mathrm{E}\left[\left(\ln F(y)\right)^2\right]. \tag{11}$$

Note that the system size estimation problem is formulated as a conventional parameter estimation problem, and N is estimated based on random values generated at nodes. Therefore, the estimate of the system size $\hat{N}$ can be non-integers and the differentiating respect to N in equation (10) make sense.

The term $\mathrm{E}\left[\ln F(y)\right]$ in equation (11) can be calculated by definition,

$$\mathrm{E}\left[\ln F(y)\right] = \int_{-\infty}^{\infty}\{\ln F(y)\} N\{F(y)\}^{N-1} f(y)dx = -\frac{1}{N}. \tag{12}$$

Similarly, term $\mathrm{E}\left[\left(\ln F(y)\right)^2\right] = \frac{2}{N^2}$ can be calculated Therefore, by substituting the calculated values into equation (11), the result in (6) can be obtained. ∎

Theorem 1 characterizes the best estimation variance that we can achieve if max consensus is used to estimate the system size. It is also shown that if max consensus is used and consensus is perfectly reached, the distribution of the initial values at nodes does not affect the Fisher information about system size estimation.

Note that the result in equation (7) is the best estimation variance in one consensus run. In real system size estimation applications, large sample statistics can be used to improve the performance. A more accurate $\hat{N}$ can be obtained by taking the sample mean of multiple consensus results.

B. Average Consensus in the Absence of Noise

In this subsection, we assume that the average consensus as mentioned in Section III-B is used and average consensus is perfectly reached at nodes. We also assume that the distribution of the initial values at nodes is i.i.d. with mean μ and variance σ^2, and the system size N is large. The following statement characterizes the Fisher information and CRB result.

Assume the initial values at nodes x_i are i.i.d. with mean μ and variance σ^2. Also assume that N is large. When average consensus is used, the Fisher information for estimate of system size N is

$$\mathcal{I}_{\mathrm{avg}} = \frac{1}{2N^2}. \tag{13}$$

The CRB is the inverse of the Fisher information, and an lower bound on the estimation variance can be expressed as

$$\mathrm{Var}\left[\hat{N}\right] \geq 2N^2. \tag{14}$$

Proof: Let $y_i = x_i(t) = \frac{1}{N}\sum_{i=1}^{N} x_i$ be the state at node i after nodes converge to the average. By using the central limit theorem, the convergence result y_i is Gaussian distributed, $y_i \sim \mathcal{N}\left(\mu, \frac{\sigma^2}{N}\right)$.

Therefore, the Fisher information can be calculated from the definition, we have

$$\mathcal{I}_{\mathrm{avg}} = \mathrm{E}\left[\left(\frac{\partial}{\partial N}\ln\left[\frac{\sqrt{N}}{\sqrt{2\pi\sigma^2}}\exp(\frac{-N(y-\mu)^2}{2\sigma^2})\right]\right)^2\right] \tag{15}$$

$$= \frac{1}{4N^2} - \frac{1}{2N\sigma^2}\mathrm{E}\left[(y-\mu)^2\right] + \frac{1}{4\sigma^2}\mathrm{E}\left[(y-\mu)^4\right]. \tag{16}$$

From the properties of Gaussian distribution, terms in equation (16) can be calculated, $\mathrm{E}\left[(y-\mu)^2\right] = \frac{\sigma^2}{N}$ and $\mathrm{E}\left[(y-\mu)^4\right] = \frac{3\sigma^2}{N^2}$. Therefore the Fisher information can be calculated as in equation (13). ∎

Note that the above proof is based on central limit theorem with N large (also holds for small N and $x_i \sim \mathcal{N}\left(\mu, \sigma^2\right)$). The distribution of the initial values does not affect the Fisher information when N large, which matches the result in [10] that scaling and translations of initial value distribution do not affect the performance of the optimal estimator. By comparing equation (14) with equation (7), we can see that system size estimation with max consensus has a lower CRB.

V. CRB for System Size Estimation in the Presence of Noise

Consensus in wireless sensor networks always suffers from different sources of error such as imperfect communication with noise and lack of convergence in finite time. In this section, error is considered and Fisher information and CRB for system size estimation are derived.

A. Max Consensus in the Presence of Noise

We model the final error at nodes to be Gaussian distributed $e \sim \mathcal{N}\left(0, \sigma_e^2\right)$. When max consensus is used for system size estimation, there is no closed form expression for the Fisher information and CRB. However, if we assume the distribution of the initial values has exponential tails and N is large, an upper bound on the Fisher Information can be obtained, the following statement characterizes the result.

Assume the initial values at nodes x_i have exponential tail and its tail PDF $\lambda e^{-\lambda x}$. The distribution of the max of the initial values can be approximated using Gumbel distribution. Assume that the final error at nodes is Gaussian distributed $e \sim \mathcal{N}\left(\mu_e, \sigma_e^2\right)$. The Fisher information for estimate of system size N is bounded by

$$\mathcal{I}_{\mathrm{nmax}} \leq \left(\frac{1}{N^2}\right)\left(\frac{\lambda^{-2}}{\sigma_e^2+\lambda^{-2}}\right). \tag{17}$$

The CRB is the inverse of the Fisher information, and a lower bound on the estimation variance can be expressed as

$$\mathrm{Var}\left[\hat{N}\right] \geq N^2\left(\sigma_e^2\lambda^2+1\right). \tag{18}$$

Proof: With the error term, node i in the network will converge to $z_i = \max\{x_1, x_2, \cdots, x_N\} + e$. Assume the initial values at nodes x_i have exponential tail and its tail PDF $\lambda e^{-\lambda x}$. The distribution of the maximum $y_i = \max\{x_1, x_2, \cdots, x_N\}$ can be approximated using Gumbel distribution [22],

$$\mathrm{CDF}: e^{-e^{-(y-\mu)/\beta}}, \ \ \mathrm{PDF}: \frac{1}{\beta}e^{-\left(\frac{y-\mu}{\beta}+e^{-\frac{y-\mu}{\beta}}\right)}, \tag{19}$$

where $\mu = (\ln N)/\lambda$ and $\beta = 1/\lambda$. Therefore we can write z_i as

$$z_i = \frac{\ln N}{\lambda} + \tilde{y}_i + e, \tag{20}$$

where $\tilde{y}_i$ has PDF: $\lambda e^{-\left(\lambda x + e^{-\lambda x}\right)}$. Note that the closed form expression for the distribution of $\tilde{y}_i + e$ (sum of Gumbel random variable and Gaussian random variable) cannot be obtained, therefore an upper bound on the Fisher information is derived herein.

The upper bound calculation can be expressed as three phases: i) Fisher information for random variable $\tilde{y}$ and e are calculated; ii) Fisher information inequality is applied; and iii) parameter transformation lemma in [23] is used. Details of the calculation are presented in the following.

Firstly, we introduce the Fisher information of a real random variable X whose density function $f(x)$ is independent of the estimated quantity N [23],

$$\mathcal{I}_X := \int \frac{1}{f(x)}\left(\frac{\partial f(x)}{\partial x}\right)^2 dx. \tag{21}$$

From the definition of Fisher information of a random variable, the Fisher information for $\tilde{y}_i$ and e can be calculated

$$\mathcal{I}_{\tilde{y}} = \lambda^2, \ \ \mathcal{I}_e = \frac{1}{\sigma_e^2}. \tag{22}$$

Secondly, Fisher information inequality is used to calculate the upper bound on Fisher information of $\tilde{y}_i + e$, we have

$$\mathcal{I}_{\tilde{y}+e} \leq \frac{\mathcal{I}_{\tilde{y}}\mathcal{I}_e}{\mathcal{I}_{\tilde{y}}+\mathcal{I}_e} = \frac{\lambda^2}{\sigma_e^2\lambda^2+1}. \tag{23}$$

Note that equality in equation (23) is achieved iff $\tilde{y}_i$ and e are both Gaussian distributed. Finally, the parameter transformation lemma (Lemma 4 in [23]) is used and the Fisher information about N can be calculated,

$$\mathcal{I}_{nmax} = \left(\frac{\partial\frac{\ln N}{\lambda}}{\partial N}\right)^2 \mathcal{I}_{\tilde{y}+e} \leq \frac{1}{N^2}\left(\frac{\lambda^{-2}}{\sigma_e^2+\lambda^{-2}}\right). \tag{24}$$

Therefore, equation (17) and (18) is obtained.

Note that here we assume that x_i to be exponentially distributed for simplicity purpose. Similar proof can be obtained if the distribution of the initial values has exponential tail, for example Gaussian distribution. Also note that there is no close form expression for the true distribution of the final error in this case. If the final error is not Gaussian distributed, the upper bound on the Fisher information can be expressed as: $\mathcal{I}_{nmax} \leq \left(\frac{1}{N^2}\right)\left(\frac{\lambda^{-2}}{1/\mathcal{I}_e+\lambda^{-2}}\right)$ from equation (23) and (24). ■

The SNR can be defined as $\mathrm{SNR} = \frac{\lambda^{-2}}{\sigma_e^2}$. From equation (17) and (18) we see that larger SNR causes a larger Fisher information and lower CRB. From equation (17), we also see that in the absence of error with $\sigma_e^2 = 0$, equation (17) is the same as the no error case in equation (6).

B. Average Consensus in the Presence of Noise

Assume average consensus is used and the final error at nodes is Gaussian distributed $e \sim \mathcal{N}\left(0, \sigma_e^2\right)$. Note that the error in the average consensus is usually caused by lack of convergence in finite time and communication noise. The noise is usually assumed to be Gaussian distributed [17] and the error caused by lack of convergence is approximately Gaussian distributed which is proved in [24]. Also assume that the distribution of the initial values at nodes is i.i.d. with mean μ and variance σ^2, and the system size N is large. The following statement characterizes the Fisher information and CRB result.

Assume the initial values at nodes x_i are i.i.d. with mean μ and variance σ^2, the final error at nodes is Gaussian distributed $e \sim \mathcal{N}\left(0, \sigma_e^2\right)$. Also assume that N is large. When average consensus is used, the Fisher information for estimate of system size N is

$$\mathcal{I}_{\mathrm{avg}} = \frac{1}{2N^4}\left(\frac{\sigma^4}{\left(\frac{\sigma^2}{N}+\sigma_e^2\right)^2}\right). \tag{25}$$

When N is large, equation (25) *can be approximated as*

$$\mathcal{I}_{\mathrm{avg}} \approx \frac{1}{2N^4}\left(\frac{\sigma^2}{\sigma_e^2}\right)^2 = \frac{1}{2N^4}(\mathrm{SNR})^2, \tag{26}$$

where SNR is defined as $\mathrm{SNR} = \frac{\sigma^2}{\sigma_e^2}$. The CRB is the inverse of the Fisher information, and an lower bound on the estimation variance can be expressed as

$$\mathrm{Var}\left[\hat{N}\right] \geq 2N^4\frac{\left(\frac{\sigma^2}{N}+\sigma_e^2\right)^2}{\sigma^4}. \tag{27}$$

Proof: The proof of is same as the proof of Theorem IV-B. ■

From equation (26) and (27) we see that larger SNR causes a larger Fisher information and lower CRB. From equation (25), we also see that in the absence of error with $\sigma_e^2 = 0$, equation (25) is the same as the no error case in equation (13).

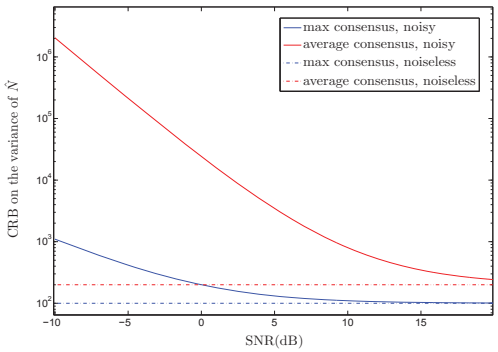

Fig. 2: CRB comparison with different SNR.

VI. Simulations

In Figure 2, we assume $N = 10$ and $\sigma_n^2 = 1$. The SNR is defined as $\mathrm{SNR} = \lambda^{-2}/\sigma_n^2$ in the case of max consensus with noise, and $\mathrm{SNR} = \sigma^2/\sigma_e^2$ in the case of average consensus with noise. The CRB results derived in Section IV and Section V are plotted. From the figure, we can see that the max consensus case has a lower CRB than the average consensus case and the CRBs in the presence of noise converge towards the CRBs in the absence of noise as SNR becomes large.

Note that the plot shows the estimation performance for one consensus run. In real system size estimation applications, each node locally generates M i.i.d. random initial values. Then, by taking a sample mean of the consensus results, the variance of the system size estimator scales by $1/M$.

VII. Conclusion

The problem of system size estimation using consensus algorithm is considered. The Fisher information and Cramer-Rao bounds of the system size estimate using different consensus algorithms and different initial value distributions are derived. It is shown that if max consensus is used, the distribution of the initial values does not affect the Fisher information and CRB results. We also see that the max consensus case has a lower CRB than the average consensus case. We also consider error caused by communication noise and lack of convergence, and the Fisher information and CRB in this case are also calculated. The analysis in this paper not only presents lower bounds results for system size estimation using consensus, but also provides guideline towards how to choose consensus algorithm and initial values to get a better estimation performance. In the absence of communication noise, max consensus should be used since the estimation variance will be smaller. In the presence of communication noise, large SNR results in better estimation performance, which is a trade-off in the problem.

Acknowledgment

The authors from Arizona State University are funded in part by the NSF award ECCS - 1307982 and the SenSIP Center, School of ECEE, Arizona State University.

References

[1] J. Yick, B. Mukherjee, and G. Dipak, "Wireless sensor network survey," *Computer Networks*, vol. 52, p. 22922330, Aug. 2008.

[2] A. Ganesh, A. Kermarrec, E. Merrer, and L. Massoulie, "Peer counting and sampling in overlay networks based on random walks," *Distributed Computing*, vol. 20, pp. 267 – 278, Jan. 2007.

[3] S. Zhang, C. Tepedelenlioglu, M. Banavar, and A. Spanias, "Max-consensus using the soft maximum," in *2013 Asilomar Conference on Signals, Systems and Computers*, Nov. 2013, pp. 433 – 437.

[4] M. Bawa, H. R Garcia-Molina, A. Gionis, and R. Motwani, "Estimating aggregates on a peer-to-peer network," Department of Computer Science, Stanford University, Tech. Rep., 2003.

[5] S. H. Lee, S. Lee, H. Song, and H. S. Lee, "Wireless sensor network design for tactical military applications : Remote large-scale environments," in *2009 IEEE MILCOM*, Oct. 2009, pp. 1 – 7.

[6] E. Le Merrer, A.-M. Kermarrec, and L. Massoulie, "Peer to peer size estimation in large and dynamic networks: A comparative study," in *2006 15th IEEE International Symposium on HDPC*, 2006, pp. 7 – 17.

[7] B. Ribeiro and D. Towsley, "Estimating and sampling graphs with multidimensional random walks," in *Proceedings of the 10th annual conference on Internet measurement*, Nov. 2010, pp. 390 – 403.

[8] C. Gkantsidis, M. Mihail, and A. Saberi, "Random walks in peer-to-peer networks: Algorithms and evaluation," *Performance Evaluation*, vol. 63, pp. 241 – 263, March 2006.

[9] R. Ali, S. Lor, and M. Rio, "Two algorithms for network size estimation for master/slave ad hoc networks," *arXiv:0908*, vol. 56, Oct. 2009.

[10] D. Varagnolo, G. Pillonetto, and L. Schenato, "Distributed statistical estimation of number of nodes in networks," in *49th IEEE Conference on Decision and Control*, Dec. 2010, pp. 1498 – 1503.

[11] ——, "Distributed cardinality estimation in anonymous networks," *IEEE Trans. on Automatic Control*, vol. 59, no. 3, pp. 645 – 659, March 2014.

[12] S. Kamath, D. Manjunath, and R. Mazumdar, "On distributed function computation in structure-free random wireless networks," *IEEE Transactions on Information Theory*, vol. 60, no. 1, pp. 432–442, Jan. 2014.

[13] M. Jelasity and A. Montresor, "Epidemic-style proactive aggregation in large overlay networks," in *2004. Proceedings. 24th International Conference on Distributed Computing Systems*, 2004, pp. 102 – 109.

[14] S. Zhang, C. Tepedelenlioglu, M. Banavar, and A. Spanias, "Distributed node counting in wireless sensor networks," in *49th Asilomar Conference on Signals Systems and Computers*, Nov. 2015.

[15] F. Iutzeler, P. Ciblat, and J. Jakubowicz, "Analysis of max-consensus algorithms in wireless channels," *IEEE Trans. SP*, vol. 60, pp. 6103 – 6107, Nov. 2012.

[16] L. Xiao and S. Boyd, "Fast linear iterations for distributed averaging," in *Proc. 42nd CDC*, vol. 5, Dec. 2003, pp. 4997 – 5002.

[17] S. Kar and J. Moura, "Distributed consensus algorithms in sensor networks with imperfect communication: Link failures and channel noise," *IEEE Trans. SP*, vol. 57, no. 1, pp. 355 –369, Jan. 2009.

[18] S. Dasarathan, C. Tepedelenlioglu, M. Banavar, and A. Spanias, "Nonlinear distributed average consensus using bounded transmissions," *IEEE Trans. SP*, vol. 61, pp. 6000 – 6009, Dec. 2013.

[19] ——, "Robust consensus in the presence of impulsive channel noise," *IEEE Trans. SP*, vol. 63, pp. 2118 – 2129, March 2015.

[20] J. Lee, C. Tepedelenlioglu, M. K. Banavar, and A. Spanias, "Nonlinear diffusion adaptation with bounded transmission over distributed networks," in *ICC*, June 2015, pp. 6707 – 6711.

[21] X. Zhang, M. K. Banavar, M. Willerton, A. Manikas, C. Tepedelenlioglu, A. Spanias, T. Thornton, E. Yeatman, and A. G. Constantinides, "Performance comparison of localization techniques for sequential WSN discovery," in *SSPD*, Sept. 2012, pp. 1 – 5.

[22] H. A. David and H. N. Nagaraja, *Order Statistics*. WILEY, 2003.

[23] R. Zamir, "A proof of the fisher information inequality via a data processing argument," *IEEE Transactions on Information Theory*, vol. 44, no. 1, pp. 1246 – 1250, May 1998.

[24] M. Huang and J. H. Manton, "Stochastic consensus seeking with measurement noise: Convergence and asymptotic normality," in *2008 American Control Conference*, June 2009, pp. 1337 – 1342.

Joint Array and Spatial Sparsity Based Optimisation for DoA Estimation

Mingyang Chen, Mark Barnard and Wenwu Wang
Centre for Vision Speech and Signal Processing
Department of Electronic Engineering
University of Surrey, Guildford GU2 7XH, United Kingdom
Emails: {m.chen; mark.barnard; w.wang}@surrey.ac.uk

***Abstract*—Traditional spatial sparse techniques for DoA estimation are implemented by full arrays. However in practice, it is desirable to use as few sensors as possible to reduce the cost for manufacturing the array or to counter against sensor failure. As a result, joint optimisation of sparse array and spatial sparsity becomes an ideal alternative. In most of existing methods, these two kinds of sparsity are studied separately. This paper proposes a joint model which achieves source detection in a subset of space using partial array sensors. The core idea is to use the weight coefficients obtained in sparse array optimisation to scale the model for the sparse reconstruction based DoA estimation. Compressive sensing based optimisation is used for both steps. The numerical results of DoA estimation for both stationary source and moving source are used to demonstrate the feasibility of this joint model.**

I. Introduction

An acoustic array system, which is a collection of acoustic transducers operating through array signal processing techniques, has been used in many areas, such as non-destructive evaluation, underwater detection and machine diagnosis. In these applications, Direction of Arrival (DoA) estimation from the array output is an important issue in source localisation and separation [1].

Classically, DoA estimation is addressed by methods, such as Capon beamformer, high-resolution and multiple signal classification (MUSIC) algorithm [2] [3] [4]. Recently, spatial sparsity motivated techniques, which aim at extracting meaningful lower-dimensional representations from high-dimensional data, have attracted wide interests in DoA estimation, since it drastically improves system performance on data storage and transmission [5]. Compressive sensing (CS) based sparse reconstruction [6], which is a popular solution to sparse representation, has been used for DoA estimation in [7], where the activity of source is assumed to be sparse and the sparsity is enforced by a constraint based on l_1 norm of a vector of the coefficients corresponding to the source activities in the spatial domain [7]. A sequential algorithm has been developed recently in [8] [9], where continuous DoA estimation is obtained from the array observation in an on-line manner, based on the least absolute shrinkage and selection operator (LASSO).

In the techniques discussed above, a full array is used and the adjacent sensor separation is often assumed to be no larger than half of the wavelength of the signal [10]. In practice, however it is desirable to use as few sensors as possible to reduce the cost for array design and manufacturing or to address the problem of sensor failure in the sense that the weight coefficients corresponding to the remaining working sensors can be re-configured with the sparse optimisation techniques. As a result, the idea of the sparse array was proposed as an alternative [11], where the CS techniques can also be used [12] by limiting the number of non-zero elements (l_0 norm) of the weighting parameters. Alternatively, the method can be more efficiently addressed as a minimisation of the l_1 norm of the weighting coefficients as in [13].

Spatial sparsity and array sparsity have been exploited separately in most existing methods discussed above. In [14], however, these two types of sparsity have been considered, where the direct data covariance (DDC) matrix is used to form a virtual array model with an extended aperture. Then two methods addressing the LASSO problem with this array model are presented. The DDC matrix instead of omni-directional steering vector is used to obtain the desired signal with the sparse array. However, the sparsity of the linear array was manually set in their experiments.

In this paper, we propose a new joint model to exploit sparsity in both array and source space where a CS based two-step iterative process is used. Through this joint model we are able to calculate the weight coefficients for each sensor, which are then used in a sequential sparse reconstruction algorithm to estimate the DoAs. Combining spatial sparsity and the sparse array optimisation enables DoA estimation in a lower-dimensional space and at the same time using as few sensors as possible.

This article is organised as follows. In Section II, the background about the sparse array and the spatial sparse representation is presented. The proposed algorithm is presented in Section III. In Section IV, numerical results on a stationary source, a moving source and noise added sources are presented. Finally, the conclusion is given in Section V.

II. Background

A. Array Model

We assume that a narrowband linear array is used, and each array element has an unitary sensitivity. In addition, source signals can only arrive in one half of the plane and the array is expected to have a perfect baffle, which means the arrival

978-1-5090-0326-6/16/$31.00 ©2016 IEEE

directions are from -90 degree to +90 degree along the plane of the array elements, and 0 degree is the normal to the line of the array.

As in [15], the observed sensor signal at each time step k is denoted as $\mathbf{y}_k = (y_{k1}, y_{k2}, \cdots, y_{kN})$, where N is the number of sensors. At each time step, there is a vector reflecting possible angles for the DoA $\mathbf{x}_k = (x_{k1}, x_{k2}, \cdots, x_{kM})$, where M is the number of potential source directions.

A matrix $\mathbf{A}$ is created by sampling all possible directions of arrivals (DoAs). The size of $\mathbf{A}$ is $N \times M$ where $N \ll M$. The nm-th element of $\mathbf{A}$ is defined by

$$\mathbf{A}_{nm} = \frac{1}{\sqrt{N}} exp\left[-j2\pi\mu_n \sin\theta_m\right] \tag{1}$$

where $\mu_n = \dfrac{d_n}{cT_s}$ with temporal sampling period T_s for $n = 1, 2, \cdots, N$, d_n denotes the distance between the n-th sensor and the middle sensor, c is the speed of wave propagation, and $\theta_m = \frac{\pi m}{M} - \pi/2$ is the DoA of the m-th hypothetical source to the n-th sensor in the array.

For each vector $\mathbf{x}_k$, there are M source directions corresponding to the columns of $\mathbf{A}$, leading to the array model

$$\mathbf{y}_k = \mathbf{A}\mathbf{x}_k + \mathbf{n}_k \tag{2}$$

where $\mathbf{n}_k$ is random noise. Here we consider isotropic noise in the assumed half plane as used in our experiments.

B. CS-Based Sparse Array

Following [13], the CS based sparse narrowband array problem can be formulated as a minimisation of the l_1 norm of the weight coefficients, as follows,

$$\begin{aligned} &\min \quad \|\mathbf{w}\|_1 \\ &subject \quad to \quad \|\mathbf{f} - \mathbf{w}^H\mathbf{A}\|_2 \leq \alpha \end{aligned} \tag{3}$$

where $\mathbf{w} \in \mathbb{C}^N$ is the coefficient vector of the array, $\mathbf{f} \in \mathbb{C}^M$ is the vector holding the desired beam response at the sampled angular points θ_m for the frequency of interest Ω, $m = 1, 2, \cdots, M$, $\alpha \in \Re^+$ is the constraint to define how much the designed response is similar to the desired response, $(\cdot)^H$ is a Hermitian operator, $\|\cdot\|_1$ and $\|\cdot\|_2$ are respectively the l_1 and l_2 norm of their arguments.

In detail, $\mathbf{f}$ is defined by

$$\mathbf{f} = [f(\Omega, \theta_1), f(\Omega, \theta_2), \cdots, f(\Omega, \theta_M)] \tag{4}$$

where $f(\Omega, \theta)$ is a desired response at the direction θ.

C. Spatial Sparse Reconstruction Using LASSO

Assuming a full array is used, the DoA estimation problem can be cast as a sparse reconstruction problem. This can be achieved by dividing the source space into multiple ranges of possible directions, with each range assigned a weight to indicate the activity of the source in that rangle. To find the DoA of the source, the weights corresponding to each range need to be found. This can be achieved by e.g. using a sequential Bayesian technique based on the LASSO function, as in [8], [9], assuming that the number of active sources is small as compared to the total number of ranges of possible directions.

For the signal $\mathbf{y}_k$ at time k and source activation vector $\mathbf{x}_k$, the cost function to be minimised is given as follows,

$$\underset{\mathbf{x}_k}{\operatorname{argmin}} \quad \|\mathbf{y}_k - \mathbf{A}\mathbf{x}_k\|_2^2 + \mu\|\mathbf{D}\mathbf{x}_k\|_1 \tag{5}$$

with

$$\mathbf{D} = \sigma^2\mathbf{V} \tag{6}$$

$$\mathbf{V} = diag(\mathbf{v}) \tag{7}$$

where $\mathbf{D}$ and $\mathbf{V}$ are matrices holding the coefficients vector $\mathbf{v} = (v_1, v_2, \ldots, v_{\mathrm{M}})^T$, which corresponds to the source activity in the source space, μ is a regularization parameter, and σ^2 is the noise variance.

As for sequential estimation, the result at the $(k+1)$-th time step should be calculated by the signal at the k-th time step. This is achieved based on the relationship between $v_m[k]$ and $v_m[k+1]$.

In the neighbourhood of an active source defined by a threshold l [9], the predicted weights $v_m[k+1]$ are calculated as below:

$$\left(v_m[k+1]\right)^2 = \left(\sum_{j=-l}^{l} \frac{\alpha_j}{\left(v_{m+j}[k]\right)^2}\right)^{-1} \tag{8}$$

with non-negative coefficients α_j, $\sum_j \alpha_j$ = 1 and the weights in $\mathbf{v}$ are bounded by 1. In practice, a small threshold e.g. 100×2^{-52} is used to prevent the value of $v_{m+j}[k]$ from approaching zero in order to avoid invalid division.

When the estimation is out of the neighbourhood of the active source, the weight prediction is replaced by:

$$v_m[k+1] = v_m[k] + cv_0 \tag{9}$$

where v_0 and c are defined empirically [9].

III. Joint Sparsity Based Method

The proposed method consists of two main steps. With the input of a given beam, the first step is to implement the CS-based sparse array algorithm through the cost function (3) to obtain a series of sparse sensor weight coefficients. The second step is to plug the estimated weight coefficients into the cost function (5), as a scaling factor for $\mathbf{y}_k$.

For the CS-based sparse array optimisation with the cost function (3), as the vector weight coefficients $\mathbf{w}$ are complex numbers, i.e. $\mathbf{w} = \mathbf{w}_R + \mathbf{w}_I i$, to achieve sparse solutions, the l_1 norm should be modified as

$$\begin{aligned} &\min \quad \|\mathbf{w}_R\|_1 + \|\mathbf{w}_I\|_1 \\ &subject \quad to \quad \|\mathbf{f} - (\mathbf{w}_R + \mathbf{w}_I i)^H \mathbf{A}\|_2 \leq \alpha \end{aligned} \tag{10}$$

where $\mathbf{f}$ is the input vector holding the desired beam response at source directions and α is a constraint controlling the fitting error [13].

After obtaining the estimated $\mathbf{w}$, the LASSO function (5) is then modified as

$$\underset{\mathbf{x}_k, v_m}{\text{argmin}} \quad \|\mathbf{W}\mathbf{y}_k - \mathbf{A}\mathbf{x}_k\|_2^2 + \mu\|\mathbf{D}\mathbf{x}_k\|_1 \tag{11}$$

where $\mathbf{W}$ is defined as

$$\mathbf{W} = \begin{pmatrix} |w_1| & & \\ & \cdots & \\ & & |w_N| \end{pmatrix} \tag{12}$$

Both cost functions (10) and (11) are optimised by the CVX toolbox in Matlab [16].

The above two steps are iterated in an alternating manner. The input beam response $\mathbf{f}$ can be initialised randomly. The joint model is able to estimate the correct DoA estimation after a few iterations as follows,

1. Set k = 1 and create an initial beam response as input $\mathbf{f}$ of (10), corresponding to a randomly selected direction.
2. Implement two-step optimisation and obtain the possible angles $\mathbf{x}_k$ by solving (11).
3. Replace $\mathbf{f}$ by $(\mathbf{A}\mathbf{x}_k)^H\mathbf{A}$, and set k = k+1.
4. Repeat stages 2 to 3 until k reaches the predefined maximum time step K.

IV. Numerical Results

In this section, the performance of the proposed method is investigated for narrowband DoA estimation through a sparse linear array. All the experiments are based on simulated data, including a stationary source at 40 degree and a moving source starting from 0 degree, turning to 48, -48.5, 57, 52, 57, -57.5, 57 degrees, ending at 13.5 degree. Here we assume the source angle is changing at a constant range, hence no Doppler shift is considered in this paper.

The underwater speed of sound used in this model is assumed to be 1500 m/s, and the frequency of the sources is 200 Hz. In the noisy case, the level of noise in terms of Signal to Noise Ratio (SNR) is 20 dB. A grid of 100 potential sensors are used.

For the stationary source estimation, the inter-sensor spacing is 0.1λ (λ is the wavelength) and the maximum running step is $K = 20$. For the moving source estimation, the inter-sensor spacing is 0.05λ and the maximum running step is $K = 100$. Experiments show that the sensor separation should be small enough with respect to the scale of the array and running time. It was observed that the number of steps chosen for the stationary and moving source cases was large enough for the proposed algorithm to converge. The constraint value of α used in (10) is 0.3, which controls how close the designed response is to the desired response.

In order to measure the accuracy of DoA estimation, we define the performance metrics of Mean Square Error (MSE) and Standard Error (SE) according to functions (10) and (11) as follows,

$$MSE = 20log_{10}\left(\frac{\|\mathbf{f} - \mathbf{w}^H\mathbf{A}\|_2^2}{M}\right) dB \tag{13}$$

$$SE = \sqrt{\left(\frac{\|\mathbf{y}_k^H\mathbf{A} - (\mathbf{A}\mathbf{x}_k)^H\mathbf{A}\|_2^2}{M}\right)} degree \tag{14}$$

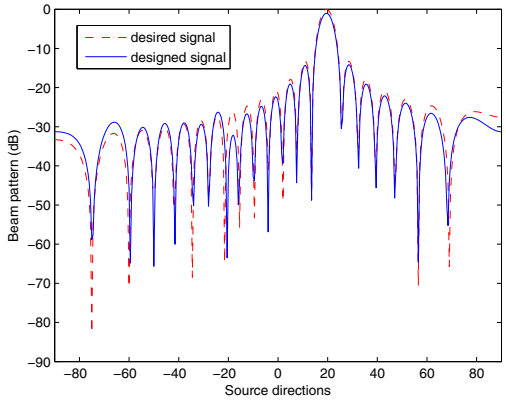

Fig. 1. The desired response $\mathbf{f}$ given in initialisation and the designed response $\mathbf{w}^H\mathbf{A}$ obtained by the first step of the proposed two-step method for the stationary source without noise.

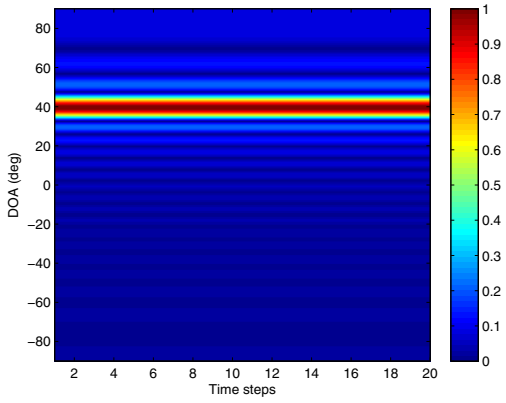

Fig. 2. DoAs estimated ($(\mathbf{A}\mathbf{x}_k)^H\mathbf{A}$) for the stationary source without noise, at 40 degree.

where M is the number of potential source directions. Both MSE and SE are calculated in each time step (the total time step is K) and the average values are calculated for each performance metric. We distinguish MSE in decibel and SE in degree because decibel is often used for presenting the difference in beam response while degree is used for measuring the DoA directions.

A. Stationary Source

The input beam response of the sparse array is initialised at 20 degree (intentionally set to be different from the ground truth of the source direction). It was observed in our experiments that 36 of 100 sensors become active in this case. The weight coefficients become stable after 20 time steps. Figure 1 illustrates the simulation between desired signal (the red dashed line) and designed signal (the blue line), where the desired response corresponds to $\mathbf{f}$ given in initialisation and designed response corresponds to $\mathbf{w}^H\mathbf{A}$ obtained by the first iteration of the proposed two-step method. The simulation shows the designed response matches well with the initial

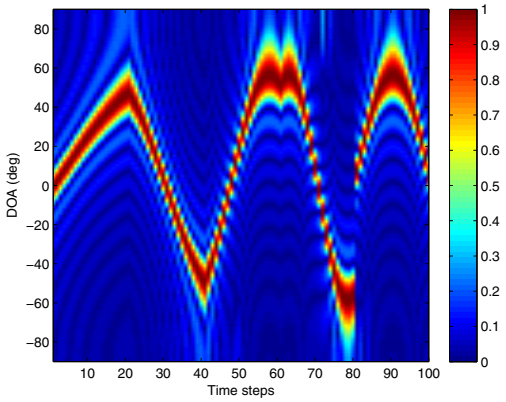

Fig. 3. DoAs estimated $((\mathbf{A}\mathbf{x}_k)^H\mathbf{A})$ for the moving source without noise.

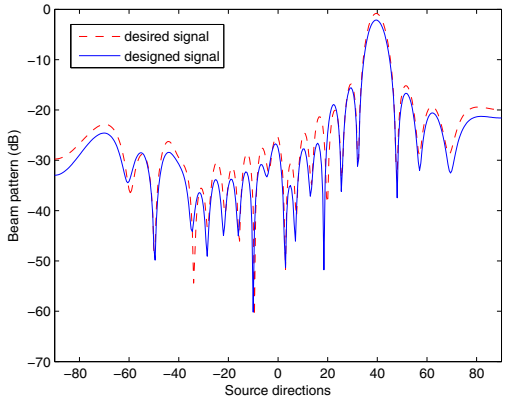

Fig. 4. The mean value of desired response $\mathbf{f}$ given in continuous k time steps and the mean value of designed response $\mathbf{w}^H\mathbf{A}$ obtained by the first step of the proposed two-step method for stationary source with noise (SNR = 20 dB).

desired response. The mean square error (MSE) defined by (13) between two responses is -66.7 dB.

With the result of the sparse array optimisation, the weight coefficients are then used to scale $\mathbf{y}_k$ in the LASSO problem (11), which is used to find spatial sparse representation $\mathbf{x}_k$.

In Figure 2, the source DoA at 40 degrees can be clearly observed through the beamforming of $((\mathbf{A}\mathbf{x}_k)^H\mathbf{A})$. The standard error (SE) defined by (14) between the estimated DoA $((\mathbf{A}\mathbf{x}_k)^H\mathbf{A})$ and the target DoA $(\mathbf{y}_k^H\mathbf{A})$ is 0.49 degrees, demonstrating a satisfatory performance of the joint method.

We should note that even though in the sparse array optimisation step, the sensors were selected based on the DoA initialised to an angle, e.g. 20 degree, which is different from the ground truth, the second step of the proposed algorithm is able to find the correct DoA based on the selected subset of the sensors. This is also the case observed in the moving source scenario, as discussed next.

B. Moving Source

For the moving source, the first input beam response of the sparse array is also initialised at 20 degree, then the source DoA estimated at time k is given as the input to the sparse array optimisation at time $k+1$. The optimised weight coefficients in sparse array changes in each time step. It was found that the average number of active sensors selected by the sparse array optimisation is 22 (note the total number of sensors is 100). The mean value of the MSE between the desired signal $\mathbf{f}$ and designed signal $\mathbf{w}^H\mathbf{A}$ is -70.6 dB for all the time steps.

Figure 3 shows the DoA estimates (in terms of $(\mathbf{A}\mathbf{x}_k)^H\mathbf{A}$) with respect to the time steps. The SE between the estimated DoA $((\mathbf{A}\mathbf{x}_k)^H\mathbf{A})$ and the target DoA $(\mathbf{y}_k^H\mathbf{A})$ is 0.27 degrees. Each turning point of the source can be seen clearly in this figure despite the existence of some estimation noise. We believe that the estimation noise can be further reduced with more time steps.

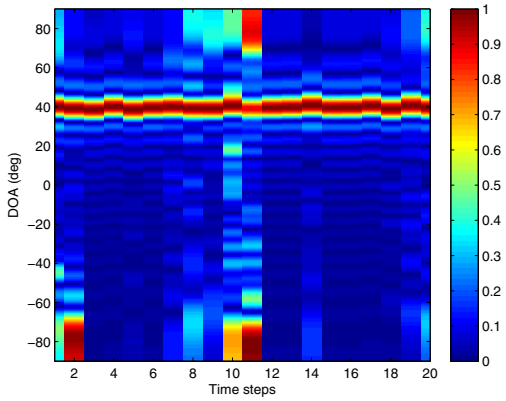

Fig. 5. DoAs estimated $((\mathbf{A}\mathbf{x}_k)^H\mathbf{A})$ for the stationary source with noise (SNR = 20 dB), at 40 degree.

N^{th}	Weights	N^{th}	Weights
6	3.1652	51	3.1769
7	0.9644	52	1.1229
16	0.2658	67	0.3500
17	0.4516	68	1.6212
18	0.8040	71	0.2090
29	0.2799	81	0.9776
33	2.2697	82	2.2576
34	0.3991	94	0.7304
40	0.3540	95	1.9352

TABLE I
WEIGHT COEFFICIENTS OF ARRAY FOR MOVING SOURCE WITH NOISE (SNR = 20 dB) AT TIME STEP OF 3.

C. Signals with Random Noise

This section evaluates how the algorithm performs when the observed signals are noisy. To this end, noise at the level of SNR = 20 dB, which is isotropic around the half space and follows the i.i.d Gaussian distribution with zero mean and unit variance, is added to the observed signals. The initial input beam response is set the same as previous sections. It was

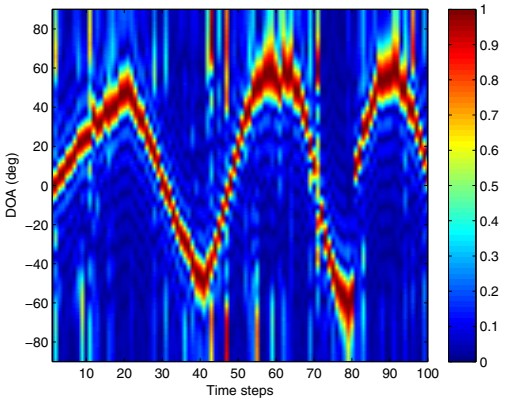

Fig. 6. DoAs estimated ($(\mathbf{A}\mathbf{x}_k)^H\mathbf{A}$) for the moving source with noise (SNR = 20 dB).

observed that, 22 active sensors were selected by the sparse array optimisation algorithm for the moving source, which was smaller than the 37 active sensors in the stationary case. The coefficients for optimised array change continuously due to the noise. Table I is an example of the weight coefficients for the active sensors at time step $k = 3$ for the moving source example.

For the stationary source with added noise, the comparison between the mean value of the desired response $\mathbf{f}$ given in continuous k time steps and the mean value of the designed response $\mathbf{w}^H\mathbf{A}$ obtained by the first step of the proposed two-step method is shown in Figure 4. The mean value is calculated because there are small fluctuations at each time step due to the existing noise. The MSE between two responses is -70.7 dB. For the moving source with noise, the mean value of MSE is -71.4 dB, which is similar to the MSE result of moving source without noise.

Figures 5 and 6 show the DoA results for the stationary source and the moving source respectively. It can be observed that in both cases, the sources are still well tracked. However, the estimates are more noisy, and the SE between the estimated DoA ($(\mathbf{A}\mathbf{x}_k)^H\mathbf{A}$) and the target DoA ($\mathbf{y}_k^H\mathbf{A}$) becomes 0.55 degrees for the stationary source case and 0.31 degrees for the moving source case respectively.

V. Conclusion

A new method has been presented to exploit the joint sparsity in array design and source localisation. The method is operated in a two-step iterative process, of which the first step is to find the sensors to be used from the array and the second step is to perform source localisation with the LASSO algorithm with the selected sensors. The two steps are iterated in an alternating manner. The algorithm can start with a random guess of the DoA of the source when performing the optimisation for the sparse array, but eventually find the DoA of the source with the sparse reconstruction algorithm. The results evaluated for both stationary source and moving source show good performance of the proposed method. For the future work, we will extend the array from the narrowband to the wideband, as well as to a large scale.

Acknowledgment

The authors would like to thank Christoph F. Mecklenbräuker from Vienna University of Technology for sharing the codes of [9] and Wei Liu from Sheffield University for the helpful discussions. This work was supported by the Engineering and Physical Sciences Research Council (EPSRC) Grant number EP/K014307/1 and the MOD University Defence Research Collaboration in Signal Processing.

References

[1] M. R. Bai, J.-G. Ih, and J. Benesty, *Acoustic Array Systems: Theory, Implementation, and Application*. John Wiley & Sons, 2013.

[2] P. Händel, P. Stoica, and T. Söderström, "Capon method for doa estimation: accuracy and robustness aspects," in *Proceedings of The IEEE Winter Workshop on Nonlinear Digital Signal Processing*. IEEE, 1993, pp. P–7.

[3] P. Totarong and A. El-Jaroudi, "A novel approach for robust high-resolution doa estimation," in *Proceedings of The IEEE Sixth SP Workshop on Statistical Signal and Array Processing*. IEEE, 1992, pp. 366–369.

[4] A. Hakam, R. M. Shubair, and E. Salahat, "Enhanced doa estimation algorithms using mvdr and music," in *2013 International Conference on Current Trends in Information Technology (CTIT)*. IEEE, 2013, pp. 172–176.

[5] P. Knee, "Sparse representations for radar with matlab® examples," *Synthesis Lectures on Algorithms and Software in Engineering*, vol. 4, no. 1, pp. 1–85, 2012.

[6] D. L. Donoho, "Compressed sensing," *IEEE Transactions on Information Theory*, vol. 52, no. 4, pp. 1289–1306, 2006.

[7] D. Malioutov, M. Çetin, and A. S. Willsky, "A sparse signal reconstruction perspective for source localization with sensor arrays," *IEEE Transactions on Signal Processing*, vol. 53, no. 8, pp. 3010–3022, 2005.

[8] C. F. Mecklenbrauker, P. Gerstoft, A. Panahi, and M. Viberg, "Sequential bayesian sparse signal reconstruction using array data," *IEEE Transactions on Signal Processing*, vol. 61, no. 24, pp. 6344–6354, 2013.

[9] E. Zochmann, P. Gerstoft, and C. F. Mecklenbrauker, "Density evolution of sparse source signals," in *2015 3rd International Workshop on Compressed Sensing Theory and its Applications to Radar, Sonar and Remote Sensing (CoSeRa)*. IEEE, 2015, pp. 124–128.

[10] L. Harry and V. Trees, "Optimum array processing part iv of detection, estimation, and modulation theory," *New York: John Wiler & Sons*, 2002.

[11] P. Jarske, T. Saramäki, S. K. Mitra, and Y. Neuvo, "On properties and design of nonuniformly spaced linear arrays [antennas]," *IEEE Transactions on Acoustics, Speech and Signal Processing*, vol. 36, no. 3, pp. 372–380, 1988.

[12] J. K. Schindler, "Compressive sensing for sparse arrays," in *2013 IEEE International Symposium on Phased Array Systems & Technology*. IEEE, 2013, pp. 240–245.

[13] M. B. Hawes and W. Liu, "Robust sparse antenna array design via compressive sensing," in *2013 18th International Conference on Digital Signal Processing (DSP)*. IEEE, 2013, pp. 1–5.

[14] N. Hu, Z. Ye, X. Xu, and M. Bao, "Doa estimation for sparse array via sparse signal reconstruction," *IEEE Transactions on Aerospace and Electronic Systems*, vol. 49, no. 2, pp. 760–773, 2013.

[15] M. Barnard and W. Wang, "Adaptive bayesian sparse representation for underwater acoustic signal de-noising," in *Proc. 2nd IET International Conference on Intelligent Signal Processing*, 2015.

[16] M. Grant, S. Boyd, and Y. Ye, "Cvx: Matlab software for disciplined convex programming," 2008.

Scanning Emitter TMA by Two Fixed Observers using Time of Interception

Zhang Yifei
Information Engineering Department
Rocket Force University of Engineering
Xi'an, P. R. China
littleblack7@126.com

Zhang Min and Guo Fucheng
College of Electronic Science and Engineering
National University of Defense Technology
Changsha, P. R. China
zhangmin1984@126.com and gfcly@21cn.com

***Abstract*—The target motion analysis (TMA) for a moving scanning emitter with known fixed scan rate by two fixed passive observers using the time of interception (TOI) measurements only is investigated in this paper. By transforming the TOI model into the direction difference of arrival (DDOA) model, an instrumental variable (IV) estimator is proposed to solve the scanning emitter tracking problem. It is a closed-form solution with no initial guess required. Simulations show that the proposed algorithm can provide estimation accuracy very close to the Cramer-Rao lower bound (CRLB) with significantly lower estimation bias at moderate noise levels compared to the conventional pseudo-linear least square (PLS) estimator.**

Keywords—target motion analysis; scanning emitter; time of interception; least squares

I. INTRODUCTION

Determining the position and velocity of a moving source by one or more observers, which is also referred as target motion analysis (TMA), is essential for many applications such as radar, sonar, reconnaissance, and wireless networks[1]-[3]. However, the traditional TMA methods[3]-[7] cannot be directly used for the scanning emitter[8], such as the mechanically scanning radar, from which only the measurements named as time of interception (TOI) can be obtained. The TOI is defined as the time instant when the peak location of the main-lobe of the scanning emitter reaches the observer.

To locate the scanning emitter, a geometric solution when there are only three observers available is proposed in [8], and it is extended to the scenario with more than three observers by using a nonlinear least square (NLS) estimator[8]. However, the NLS estimator, as well as the maximum likelihood (ML) estimator proposed in [9]-[12], needs an initial guess close enough to the true location of the emitter to guarantee the convergence, which may not be easily found in practice. By transforming the TOI measurements to the direction difference of arrival (DDOA), a pseudo-linear least square (PLS) estimator is proposed in [10]. However, the PLS estimator is well known for its bias caused by the correlations between the measurement matrix and the noises[4],[7]. Moreover, existing estimation methods all assumed that there are at least three observers and the emitter is stationary[8]-[12]. In order to improve the performances, more than three of stationary or moving observers are needed, which may not be satisfied in practice. In addition, these methods cannot be easily extended to the moving scanning emitter. For these reasons, the TOI-based tracking of a moving scanning emitter with known fixed scan rate by two fixed observers is investigated in this paper.

For two stationary observers, the state of the non-cooperative moving scanning emitter cannot be determined in one scan cycle. Measurements should be accumulated over multiple scans for parameter or state estimation. Accordingly, the multiple scan cycles TMA model is established by transforming the TOI to the DDOA. By introducing the first direction of arrival (DOA) as a nuisance parameter to be estimated, a PLS estimator by two observers is then proposed to obtain the initial position and velocity at the start of the target trajectory. To reduce the estimation bias caused by the correlations between the measurement matrix and noises in the PLS estimator, an instrumental variable (IV) estimator is finally proposed. Simulation results show that the IV estimator attains performance close to the Cramer-Rao lower bound (CRLB) at moderate noise levels.

The rest of this paper is organized as follows. Section 2 establishes the DDOA model for the scanning emitter TMA based on TOI measurements. Section 3 presents the closed-form PLS estimator as well as the IV estimator. Section 4 presents the simulation results to verify the proposed estimators. Section 5 draws the conclusions.

II. PROBLEM FORMULATION

Without the loss of generality, we considered the TMA problem in the two dimensional (2D) plane. As shown in Fig. 1, suppose an emitter is moving at a constant velocity $\dot{\mathbf{x}}=[\dot{x}_T \;\; \dot{y}_T]^T$. The antenna of the emitter is scanning with a known constant scan rate ω. Its main beam periodically sweeps across two fixed observers $\mathbf{s}_n=[x_{On} \;\; y_{On}]^T \;\; (n=1,2)$, which intercept the signals and record the interception time of the beam peaks[12]. Assuming that at time t_k, one of the observers $\mathbf{s}_n$ intercepts the main beam signal, which was

This study was co-supported by the Shanghai Aerospace Science and Technology Innovation Fund of China (No. SAST2015028) and the Equipment Prophecy Fund of China (No. 9140A21040115KG01001).

978-1-5090-0326-6/16/$31.00 ©2016 IEEE

transmitted by the emitter at $\mathbf{x}_k=[x_{Tk}\ \ y_{Tk}]^T$, where $k=1,2,\cdots,N$ and N is the total number of the interceptions.

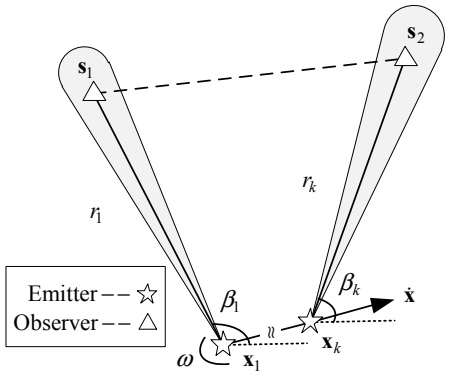

Fig. 1. Tracking a moving scanning emitter with two fixed observers.

According to Fig. 1, the TOI measurement of the scanning signal is

$$\hat{t}_k = t_k + \eta_k = (\beta_k - \beta_0)/\omega + \lfloor (k-1)/2 \rfloor T_p + r_k/c + t_0 + \eta_k \quad (1)$$

where c is the speed of light. $T_p = 2\pi/\omega$ is the scanning period, which is known because ω is known. $\lfloor \bullet \rfloor$ is the truncating operator, which rounds the element to the nearest integer smaller than or equal to itself. t_0 and β_0 are the initial signal transmission time and azimuth of the rotating antenna. $r_k = \sqrt{\mathbf{r}_k^{\mathrm{T}}\mathbf{r}_k}$ denotes the signal propagation range between observer $\mathbf{s}_n$ and the emitter, where $\mathbf{r}_k = \mathbf{s}_n - \mathbf{x}_k$ represents the vector from the emitter to the observer. $\beta_k = \arctan(y_k/x_k)$ is the angle between vector $\mathbf{r}_k$ and the x-axis anti-clockwise, where $x_k = x_{On} - x_{Tk}$ and $y_k = y_{On} - y_{Tk}$ are the relative coordinates of each axis. η_k is a zero mean Gaussian white noise with the covariance σ_k^2. For theoretical analysis, we assume that $\mathbf{s}_1$ intercepts the scanning signal for the first time. Afterward, the two observers intercept the scanning signal alternately without signal loss. Thus, the index of the observer is determined by $n = \mathrm{mod}(k+1,2)+1$, where $\mathrm{mod}(k,2)$ is the modulo operator, which returns the remainder after division of k by 2.

To eliminate the influence of t_0 and β_0, the time difference of interception (TDOI) between two TOI measurements is evaluated as

$$\hat{t}_{ij} = \hat{t}_i - \hat{t}_j = \beta_{ij}/\omega + \lfloor (i-j)/2 \rfloor T_p + (r_i - r_j)/c + \eta_{ij} \quad (2)$$

where $i \geq j$, $i, j = 1,2,\cdots,N$. $\beta_{ij} = \beta_i - \beta_j$ is the difference of the radiating angle between two intercepted signals, equaling to the DDOA. $\eta_{ij} = \eta_i - \eta_j$ is the measurement error.

For a distant emitter[8], it is reasonable to apply the approximation that $r_i \approx r_j$, which can eliminate the influence of the term $(r_i - r_j)/c$. The TDOI is then given by

$$\hat{t}_{ij} \approx \beta_{ij}/\omega + (i-j)T_p + \eta_{ij}. \quad (3)$$

After multiplying ω on both sides of (3), the measured DDOA becomes

$$\hat{\beta}_{ij} = \omega \hat{t}_{ij} - 2(i-j)\pi = \omega t_{ij} - 2(i-j)\pi + \varepsilon_{ij} \quad (4)$$

where t_{ij} is the true value of $\hat{t}_{ij}$ and $\varepsilon_{ij} = \omega(\eta_i - \eta_j)$ is the corresponding measurement error. In this way, the measured TOIs are converted to the DDOA measurements, approximately.

The DDOA between the k-th interception and the first one with respect to $\mathbf{u}_1 = [\mathbf{x}_1^T\ \ \dot{\mathbf{x}}^T]^T$ is

$$\beta_{k1}(\mathbf{u}_1) = \arccos\left[(\mathbf{s}_1 - \mathbf{x}_1)^T (\mathbf{s}_n - \mathbf{x}_k) \big/ (r_1 r_k) \right] \quad (5)$$

where $k = 2,3,\cdots,N$, $\mathbf{x}_1$ is the emitter position where its first intercepted signal is radiated, and

$$\mathbf{x}_k = \mathbf{x}_1 + t_{k1}\dot{\mathbf{x}} = \mathbf{x}_1 + \hat{t}_{k1}\dot{\mathbf{x}} - \eta_{k1}\dot{\mathbf{x}} \approx \mathbf{x}_1 + \hat{t}_{k1}\dot{\mathbf{x}}. \quad (6)$$

To facilitate the following theoretical and algorithm development[5],[7], we assume that the moving process of the scanning emitter is noiseless, and make $\mathbf{u}_1$ as the unknown to be estimated in this TMA problem. For simplicity, the index k is presumed to run from 2 to N in the sequel unless otherwise specified. The measurement of DDOA corrupted by the noise is written in terms of $\mathbf{u}_1$ as

$$\hat{\beta}_{k1} = \beta_{k1}(\mathbf{u}_1) + \varepsilon_{k1}. \quad (7)$$

According to the distribution of η_k, it can be deduced that ε_{k1} is zero mean and the covariance is

$$E\left\{ \begin{bmatrix} \varepsilon_{21} \\ \vdots \\ \varepsilon_{N1} \end{bmatrix} \begin{bmatrix} \varepsilon_{21} & \cdots & \varepsilon_{N1} \end{bmatrix} \right\} = \omega^2 \underbrace{\begin{bmatrix} \sigma_1^2 + \sigma_2^2 & \sigma_1^2 & \cdots & \sigma_1^2 \\ \sigma_1^2 & \sigma_1^2 + \sigma_3^2 & \cdots & \sigma_1^2 \\ \vdots & \vdots & \ddots & \vdots \\ \sigma_1^2 & \sigma_1^2 & \cdots & \sigma_1^2 + \sigma_N^2 \end{bmatrix}}_{\boldsymbol{\Sigma}} \quad (8)$$

The corresponding measurement errors are Gaussians and they follow $\mathcal{N}(\mathbf{0}, \omega^2\boldsymbol{\Sigma})$, where $\mathcal{N}(\mu, \Omega)$ denotes the Gaussian distribution with mean μ and covariance Ω.

Accordingly, the scanning emitter TMA problem can be transformed to an optimization problem, which is to estimate the initial state $\mathbf{u}_1$ from a batch of DDOA measurements given by (4) with (6) and (7) being the dynamic and observation models.

III. ESTIMATION ALGORITHMS

A. Pseudo-linear least square estimator

It is a strictly nonlinear problem to determine the location and the velocity of the moving scanning emitter. In order to find a closed-form solution, a pseudo-linear model can be obtained by introducing an extra parameter β_1 [10] and rewriting the cotangent of β_{k1} as

$$\cot\beta_{k1}=\cot\left(\beta_k-\beta_1\right)=\frac{1+\cot\beta_1\cot\beta_k}{\cot\beta_1-\cot\beta_k}=\frac{\cos\beta_{k1}}{\sin\beta_{k1}}. \quad (9)$$

After putting the definitions $x_k=x_{On}-x_{Tk}$ and $y_k=y_{On}-y_{Tk}$, (9) is recast into

$$z_k=\mathbf{h}_k\boldsymbol{\theta}_k \quad (10)$$

where $\mathbf{h}_k=\left[\sin\beta_{k1}\ -\cos\beta_{k1}\ 0\ 0\ y_{On}\cos\beta_{k1}-x_{On}\sin\beta_{k1}\right]$, $z_k=x_{On}\cos\beta_{k1}+y_{On}\sin\beta_{k1}$, $\boldsymbol{\theta}_k=\mathbf{R}_1[\mathbf{u}_k^T\ 1]^T$, $\mathbf{u}_k=[\mathbf{x}_k^T\ \dot{\mathbf{x}}^T]^T$ is the k-th state of the emitter, $\mathbf{R}_1=\left[\begin{array}{cc|c}\mathbf{R}_{\beta_1} & \mathbf{0} & \mathbf{0}\\ \mathbf{0} & \mathbf{R}_{\beta_1} & \\ \hline \multicolumn{2}{c|}{\mathbf{0}} & \cot\beta_1\end{array}\right]$ and $\mathbf{R}_{\beta_1}=\begin{bmatrix}\cot\beta_1 & 1\\ -1 & \cot\beta_1\end{bmatrix}$.

Substitute the noise corrupted DDOA measurements (7) into (10) yields the pseudo-measurement function as

$$\hat{z}_k=\hat{\mathbf{h}}_k\boldsymbol{\theta}_k+\nu_k \quad (11)$$

where $\hat{\mathbf{h}}_k=[\sin\hat{\beta}_{k1}\ -\cos\hat{\beta}_{k1}\ 0\ 0\ y_{On}\cos\hat{\beta}_{k1}-x_{On}\sin\hat{\beta}_{k1}]$, $\hat{z}_k=x_{On}\cos\hat{\beta}_{k1}+y_{On}\sin\hat{\beta}_{k1}$, and ν_k is the corresponding noise term. Substituting (6) into (11) yields

$$\hat{z}_k=\hat{\mathbf{h}}_k\boldsymbol{\Phi}_{k1}\boldsymbol{\theta}_1+\nu_k\approx\hat{\mathbf{h}}_k\hat{\boldsymbol{\Phi}}_{k1}\boldsymbol{\theta}_1+\nu_k \quad (12)$$

where $\hat{\boldsymbol{\Phi}}_{k1}=\boldsymbol{\Phi}_{k1}\big|_{t_{k1}=\hat{t}_{k1}}$. The approximation is due to t_{k1} in $\boldsymbol{\Phi}_{k1}$ being unavailable, so $\hat{t}_{k1}$ is used instead. Rewrite all the measurements in a compact form

$$\mathbf{z}=\mathbf{H}\boldsymbol{\theta}_1+\mathbf{v} \quad (13)$$

where $\mathbf{z}=[\hat{z}_2\ \hat{z}_3\ \cdots\ \hat{z}_N]^T$, $\mathbf{H}=[\hat{\mathbf{h}}_2^T\ \hat{\mathbf{h}}_3^T\ \cdots\ \hat{\mathbf{h}}_N^T]^T$ and $\mathbf{v}=[\nu_2\ \nu_3\ \cdots\ \nu_N]^T$. Thus, the problem of determining $\boldsymbol{\theta}_1$ has a pseudo-linear form. The PLS estimator of $\boldsymbol{\theta}_1$ is given by

$$\hat{\boldsymbol{\theta}}_{\mathrm{PLS}}=\left(\mathbf{H}^T\mathbf{H}\right)^{-1}\mathbf{H}^T\mathbf{z}. \quad (14)$$

When $\hat{\boldsymbol{\theta}}_{\mathrm{PLS}}$ is obtained, the initial state of the emitter can be determined as

$$\begin{cases}\hat{\beta}_1=\operatorname{arccot}\left(\hat{\boldsymbol{\theta}}_{(3)}\right)\\ \hat{\mathbf{x}}=\hat{\mathbf{R}}_{\beta_1}^T\hat{\boldsymbol{\theta}}_{(1:2)}\sin\hat{\beta}_1\end{cases} \quad (15)$$

where $\hat{\boldsymbol{\theta}}$=$\hat{\boldsymbol{\theta}}_{\mathrm{PLS}}$, $(\bullet)_{(i)}$ denotes the i-th element of a vector and $\hat{\mathbf{R}}_{\beta_1}$ is calculated when $\beta_1=\hat{\beta}_1$.

Although the PLS estimator is a closed-form solution, it is well known for suffering enormous bias, due to the correlations between the measurement matrix and the noises[13]-[16]. To overcome this difficulty, the bias compensation (BC) method [14],[17] and the instrumental variable (IV) method[15],[16] are always used to alleviate the bias. The BC method needs to estimate the bias, which is hard to evaluate accurately, caused by the PLS estimator and is difficult to reach the theoretical accuracy as the IV estimator does. Therefore, an IV estimator is proposed in the following to eliminate the bias.

B. Instrumental variable estimator

The normal equation for the PLS estimator is

$$\mathbf{H}^T\mathbf{H}\hat{\boldsymbol{\theta}}_{\mathrm{PLS}}=\mathbf{H}^T\mathbf{z}. \quad (16)$$

According to the IV theory[13], the correlations between the measurement matrix and the noise term can be asymptotically eliminated by modifying the normal equation to

$$\mathbf{G}^T\mathbf{H}\hat{\boldsymbol{\theta}}_{\mathrm{IV}}=\mathbf{G}^T\mathbf{z} \quad (17)$$

where $\mathbf{G}$ is the IV matrix. $\hat{\boldsymbol{\theta}}_{\mathrm{IV}}$ is the IV estimator, which is derived by

$$\hat{\boldsymbol{\theta}}_{\mathrm{IV}}=\left(\mathbf{G}^T\mathbf{H}\right)^{-1}\mathbf{G}^T\mathbf{z}. \quad (18)$$

The optimal choice of $\mathbf{G}$ is $\mathbf{H}$ calculated with the true value of the DDOA, but it is not available. A suboptimal choice is taken as follows. Firstly, the DDOA evaluated from the PLS estimator is given as

$$\hat{\beta}_{\mathrm{PLS},k1}=\beta_k\left(\hat{\mathbf{u}}_1\right)-\hat{\beta}_{\mathrm{PLS},1} \quad (19)$$

where $\hat{\beta}_{\mathrm{PLS},1}$ and $\hat{\mathbf{u}}_1$ are estimated from (15) when $\hat{\boldsymbol{\theta}}=\hat{\boldsymbol{\theta}}_{\mathrm{PLS}}$. $\beta_k(\hat{\mathbf{u}}_1)=\arctan[(y_{On}-\hat{y}_{Tk})/(x_{On}-\hat{x}_{Tk})]$, $\hat{x}_{Tk}$ and $\hat{y}_{Tk}$ are obtained from (6) by substituting $\mathbf{u}_1$ with $\hat{\mathbf{u}}_1$. Secondly, the TDOI is estimated by

$$\hat{t}_{\mathrm{PLS},k1}=\hat{\beta}_{\mathrm{PLS},k1}/\omega+\lfloor(k-1)/2\rfloor T_p. \tag{20}$$

Thirdly, replacing β_{k1} and t_{k1} with $\hat{\beta}_{\mathrm{PLS},k1}$ and $\hat{t}_{\mathrm{PLS},k1}$ in $\mathbf{H}$ gives the IV matrix as

$$\mathbf{G}=\mathbf{H}\big|_{t_{k1}=\hat{t}_{\mathrm{PLS},k1},\beta_{k1}=\hat{\beta}_{\mathrm{PLS},k1}}. \tag{21}$$

The estimated TOI $\hat{t}_{\mathrm{PLS},k1}$ is used to compensate the approximation made in (6) as well as in (12). Thus, on replacement of $\mathbf{H}$ and $\boldsymbol{\theta}$ with $\mathbf{G}$ and $\hat{\boldsymbol{\theta}}_{\mathrm{PLS}}$ respectively, (13) reduces to a consistent matrix equation with zero noise as

$$\mathbf{G}\hat{\boldsymbol{\theta}}_{\mathrm{PLS}}=\hat{\mathbf{z}} \tag{22}$$

where $\hat{\mathbf{z}}=\mathbf{z}\big|_{\beta_{k1}=\hat{\beta}_{\mathrm{PLS},k1}}$ is the equivalent measurement data vector. Since $\hat{\beta}_{\mathrm{PLS},k1}$ and $\hat{t}_{\mathrm{PLS},k1}$ are obtained from $\hat{\boldsymbol{\theta}}_{\mathrm{PLS}}$ uniquely, the matrix $\mathbf{G}$ is uncorrelated with $\mathbf{v}$ asymptotically[15]. Once $\hat{\boldsymbol{\theta}}_{\mathrm{IV}}$ is determined, the initial state of the emitter can be determined in the same way as given in (15), where $\hat{\boldsymbol{\theta}}=\hat{\boldsymbol{\theta}}_{\mathrm{IV}}$.

IV. Simulation Results

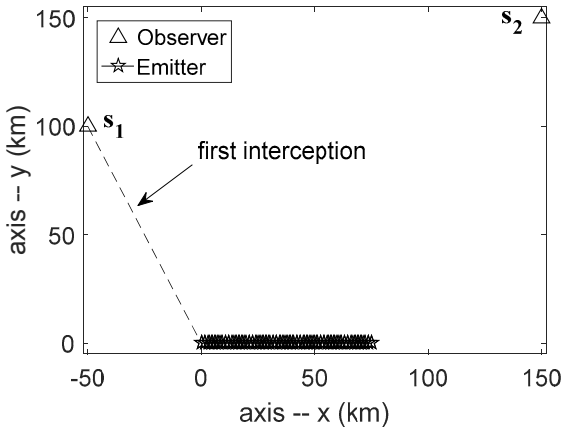

Fig. 2. The geometry of the moving scanning emitter tracking by two fixed observers in the 2D scenario.

The moving scanning emitter tracking geometry considered in the simulation is shown in Fig. 2. An emitter located at $[0\ 0]^T$ km moves at a constant velocity $[150\ 0]^T$ m/s. The scanning radar with 10s scan cycle is working clock-wisely. Two fixed observers are located at $\mathbf{s}_1=[-50\ 100]^T$ km and $\mathbf{s}_2=[150\ 150]^T$ km, respectively. The scanning signal is firstly intercepted at the beginning of the scenario by observer $\mathbf{s}_1$. The total scenario is about 500s, and produces 102 TOI measurements.

For performance comparison, the bias and the root mean squared error (RMSE) of every estimator are obtained after 1000 Monte-Carlo simulation runs. The bias is defined by $\left\|E\{\hat{\mathbf{g}}\}-\mathbf{g}\right\|_2$ and the RMSE by $[\mathrm{tr}(E\{(\hat{\mathbf{g}}-\mathbf{g})(\hat{\mathbf{g}}-\mathbf{g})^T\})]^{1/2}$, where $\mathrm{tr}(\bullet)$ is the trace of a matrix, and $\hat{\mathbf{g}}$ is an estimation of $\mathbf{g}\in\{\mathbf{x}_1,\dot{\mathbf{x}}\}$ from different estimators[18].

We first examine the performances of the PLS estimator, the IV estimator in different noise levels. The ML estimator[10], which is implemented using the Gauss-Newtown algorithm and is initialized to the true value, is also presented as a benchmark[18]. The RMSE of every estimator are compared with the CRLB[8]. The TOI measurement noise of each observer is independent identical distributed. Its standard variance ranges from 0 to 12ms with 2ms as the interval. The RMSE and bias of the initial state are calculated at the last interception of the scenario.

The simulation results in Fig. 3 and Fig. 4 show that all estimators perform the same trend in the RMSE and the bias of location and velocity estimations. The ML estimator is approximately unbiased and reaches the CRLB. The PLS estimator presents significant variance and bias. The IV estimator alleviates the bias caused by the PLS estimator, and is almost unbiased in the given situation. It is comparative to the ML estimator and asymptotically attains the CRLB in moderate measurement noises.

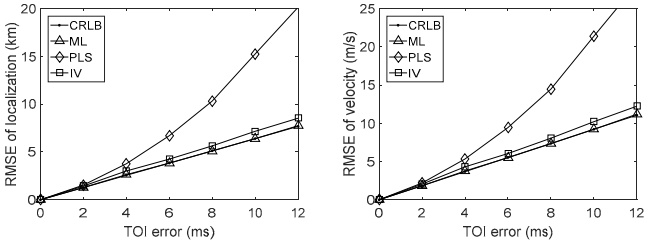

Fig. 3. RMSE of location and velocity estimations with different noise levels.

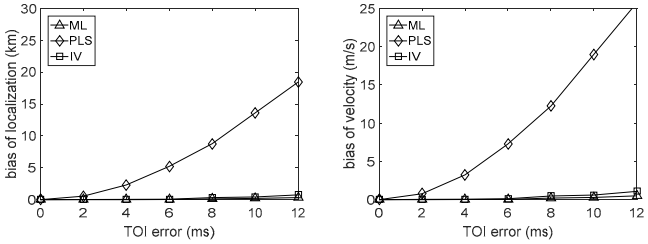

Fig. 4. Bias of location and velocity estimations with different noise levels.

We take the noise standard variance $\sigma=6$ms to examine the influence of different interception numbers N for the PLS estimator, the IV estimator and the ML estimator. The RMSE and the bias are also derived to evaluate the estimators.

The simulation results shown in Fig. 5 and Fig. 6 are presented with $N=[25,102]$. The RMSE and bias of every estimators decrease as N increase. The ML estimator always reaches the CRLB while the system is observable. When $N>60$, the IV estimator attains the CRLB. However, the PLS estimator cannot reaches the CRLB even at the end of the scenario. The bias of the ML estimator is the smallest, and when $N>30$, it is steadily unbiased. The bias of the IV estimator is asymptotically reaches 0 when $N>60$. The bias of the PLS estimator does not vanish as N increases.

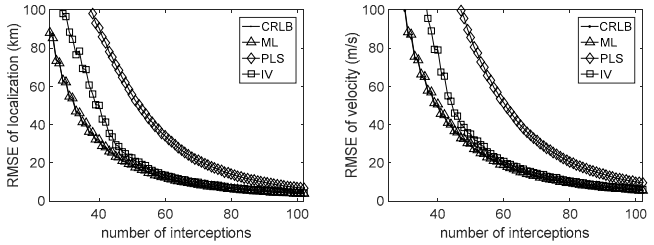

Fig. 5. RMSE of location and velocity estimations with different numbers of interceptions when $\sigma=6$ms.

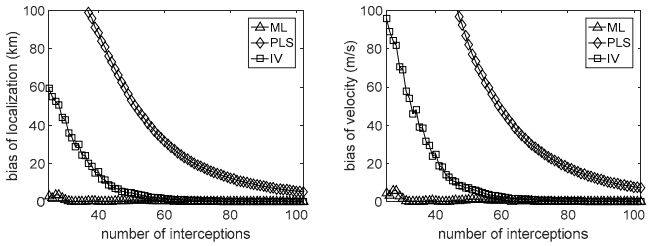

Fig. 6. Bias of location and velocity estimations with different numbers of interceptions when $\sigma=6$ms.

V. Conclusions

The moving scanning emitter TMA by two fixed observers has been discussed in this paper. The DDOA model is established based on the TOI measurements in multiple scan cycles. Simulations show that the proposed IV estimator reduces the bias and variance caused by the PLS estimator explicitly. The performance of the IV estimator is comparative to the ML estimator and reaches the CRLB at moderate TOI measurement errors.

Acknowledgment

The authors are grateful to the reviewers for providing valuable comments and constructive suggestions that have resulted in improving the quality of the manuscript.

References

[1] Z.K. Sun and M. Zhang, "Passive location and tracking using DOA and TOA measurements of single nonmanuvering observer," Proceedings of the IEEE 1988 National Aerospace and Electronics Conference; pp. 340-344, Dayton, OH, 1988.

[2] H.C. So, and K. W. Chan, "A generalized subspace approach for mobile positioning with time-of-arrival measurements," IEEE Transactions on signal processing, vol. 55, no. 10, p. 5103-7, Oct. 2007.

[3] R.L. Streit, and M.J. Walsh, "Bearing-only target motion analysis with acoustic propagation models of uncertain fidelity," IEEE Trans. Aero. Electron. Syst., vol. 38, no. 4, p. 1122-37, Oct. 2002.

[4] S.C. Nardone, A.G. Lindgren, and K.F. Gong, "Fundamental properties and performance of conventional bearing-only target motion analysis," IEEE Transactions on automatic control, vol. ac-29, no. 9, p.775-87, Sept. 1984.

[5] V.J. Aidala, "Kalman filter behavior in bearing-only tracking applications," IEEE Trans. Aero. Electron. Syst., vol. AES-15, p. 29-39, Jan. 1979.

[6] A.G. Lindgren, and K.F. Gong, "Position and velocity estimation via bearing observations," IEEE Trans. Aero. Electron. Syst., vol. AES-14, p. 564-77, Jul. 1978.

[7] K. Doğançay, "3D pseudolinear target motion analysis from angle measurements," IEEE Transactions on Signal Processing, vol. 63, p. 1570-80, Mar. 2015.

[8] H. Hmam, "Scan-based emitter passive localization," IEEE Trans. Aero. Electron. Syst., vol. 43, pp. 36-54, Jan. 2007.

[9] K. Doğançay, and P.D. Samuel, "Bias reduction for the scan-based least-squares emitter localization algorithm," 14th European Signal Processing Conference (EUSIPCO 2006), Florence, Italy, Sep. 2006.

[10] K. Doğançay, "A closed-form pseudolinear estimator for geolocation of scanning emitters," IEEE ICASSP, pp. 3546-3549, 2010.

[11] H. Hmam, and K. Doğançay, "Joint estimation of scan rate and emitter location in scan based passive localization systems," 15th European Signal Processing Conference (EUSIPCO 2007), Poznan, Poland, pp. 3-7, Sept. 2007.

[12] H. Hmam, and K. Doğançay, "Passive localization of scanning emitters," IEEE Trans. Aero. Electron. Syst., vol. 46, pp. 944-951, Apr. 2010.

[13] K.Y.Wong, and E. Polak, "Identification of linear discrete time systems using the instrumental variable method," IEEE Trans. Automatic Control. vol. ac-12, no. 6, pp.707-718, Dec. 1967.

[14] N.H. Nguyen, and K. Doğançay, "Single-platform passive emitter localization with bearing and Doppler-shift measurements using pseudolinear estimation techniques," Signal Processing (2016)

[15] K. Doğançay, "Passive emitter localization using weighted instrumental variables," Signal Processing, vol. 84, no. 3, pp. 487-497, Mar. 2004.

[16] M. Zhang, F.C. Guo, and Y.Y. Zhou, "A closed-form solution for moving source localization using LBI changing rate of phase difference only," Chinese Journal of Aerounautics, vol. 26, no. 2, pp.365-374, 2014.

[17] K. C. Ho, "Bias reduction for an explicit solution of source localization using TDOA," IEEE Trans. Signal Process, vol. 60, no. 5, pp.2101–2114, 2012.

[18] S.M. Kay, Fundamentals of statistical signal processing, estimation theory. Englewood Cliffs (NJ): Prentice Hall; 1993.

Enhanced-Range Intrusion Detection Using Pyroelectric Infrared Sensors

Sami A. Aldalahmeh[1,†], Amer M. Hamdan[1,†], Mounir Ghogho[2,3,‡] and Des McLernon[2,‡]
[1] Al-Zaytoonah University of Jordan, Jordan, [2] Leeds University, UK.
[3] International University of Rabbat, Morocco.
[†] {s.aldalahmeh, a.hamdan}@zuj.edu.jo, [‡] {m.ghogho, d.c.mclernon}@leeds.ac.uk.

***Abstract*—In this paper, the problem of intrusion detection using pyroelectric infrared (PIR) sensors is investigated. We study the output PIR signal in the light of the intruder's trajectory and the geometry of the sensor's field of view (FOV) and propose an inverse-square law that describes the relation of incident heat flux to the distance. The signal is modeled by a sum of exponentially modulated sinusoids. Consequently, the intrusion detection is formulated as a hypothesis testing problem and we propose an exponentially windowed periodogram (EWP) detector, which is also able to detect the direction of movement. The simulation results shows the superior performance of the EWP detector when compared to conventional detectors such as the traditional periodogram detector and the energy detector over large distances. Furthermore, results show nearly 100% correct detection of the direction of movement.**

I. Introduction

Intrusion detection is a vital field of research with significant practical impact. Several sensor modalities are used for intrusion detection, some of which are magnetic, acoustic, seismic, and thermal sensors [1]. However, pyroelectric infrared (PIR) sensors present themselves as an attractive option due to their low power requirement, low cost, and small form factor. PIR sensors are made from pyroelectric crystals that are intrinsically polarized [2]. When exposed to temperature change, the polarization is temporally disturbed producing a current proportional to the heat gradient. Thus, PIR sensors measure the change in temperature making them suitable for motion detection. Usually, two sensor elements are connected serially in reverse polarity, thus producing a positive voltage when motion occurs in the positive element field of view (FOV) and a negative voltage when motion occurs in the negative element's FOV. Hence, PIR sensors can be found in many indoor applications, such as [3]. Recently, PIR sensors were also used with wireless sensor networks (WSNs) in outdoor applications [4], due to the previously stated features. However, due to limited detection range the outdoor applications are limited. Therefore, advanced processing techniques are needed in order to increase the detection range of the PIR sensors

Several processing methods have been suggested in the literature. In [5], energy detection with adaptive noise threshold was proposed. Simple high-pass filtering was also used to improve the SNR. A combination of the Haar transform and support-vector-machine was used in [6] to detect intrusion in the presence of clutter. In [7], the authors proposed using a linear regression model in conjunction with hidden Markov models to detect and classify human walking movement. PIR sensors were used for tracking of direction and distance of motion in [8] via feature extraction methods. A set of two orthogonal PIR sensor pairs were used in [9] to detect the direction of movement.

In this paper we investigate increasing the detection range of PIR in outdoor environments using the statistical hypothesis testing framework leading to advanced signal processing methods, in contrast to the simplified processing adopted in [6]. Firstly, we show that the incident heat flux at the sensor obeys the inverse square law for an arbitrary source shape. Secondly, we model the incident heat flux time varying signal as a function of the intruders' trajectory parameters. Finally, we formulate the detection problem as multiple hypothesis testing.

This paper is organized as the following. Section II presents the system model. In Section III, the detection problem is formulated and the corresponding detection algorithms are proposed. Simulation results are provided in IV. Finally, the conclusions and future work are given in Section V.

II. Modeling of Intruder's Signature

In this section the time-varying heat flux signature generated by the intruder and the PIR sensor are formulated.

A. Intruder Heat Flux

We are interested in measuring the heat flux generated by a mobile intruder moving with constant speed and direction. The intruder is assumed to be in thermal equilibrium with its environment. The measured flux at the sensor mainly depends on the temperature, source geometry, and the spatial orientation of the intruder and the sensor with respect to (wrt) each other. Assuming a Lambertian grey body emitting uniformly in space, the heat flux at the sensor is [2]

$$\Phi = \frac{1}{\pi}\varepsilon k_B \omega_{i,s}\left(T_i^4 - T_e^4\right) A_i \tag{1}$$

where $0 < \varepsilon < 1$ is the intruder's emissivity, $k_B \approx 1.381 \times 10^{-23}\text{kg.m}^2/\text{s}^2\text{K}$ is the Steveman-Boltzmann constant, T_i is the intruder's absolute temperature, T_e is the environment's temperature, A_i is the intruder's surface area, and $\omega_{i,s}$ is the projected solid angle of the intruder onto the sensor. So the geometry of the source w.r.t. the sensor is given by

$$\omega_{i,s} = \frac{1}{A_s}\int_{A_i}\int_{A_s}\frac{\cos\beta_i \cos\beta_s}{R_{i,s}^2} dA_i dA_s \tag{2}$$

where A_s is the sensor's area, β_i and β_s are the angles of dA_i and dA_s wrt to the axis connecting them, and $R_{i,s}$ is the

978-1-5090-0326-6/16/$31.00 ©2016 IEEE

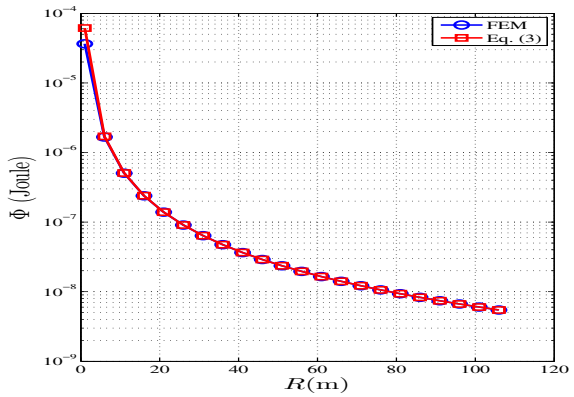

Fig. 1: Heat flux, Φ, as a function of distance R for the FEM and the approximation in (3). The human source is modeled by a rectangular head and body with dimensions of $0.22\text{m} \times 0.14\text{m}$ and $1.7\text{m} \times 0.4\text{m}$ respectively. The human temperature is $T_i = 37^o$ with emissivity $\varepsilon = 1$, environment temperature $T_i = 20^o$, sensor area $A_s = 20\mu\text{m}^2$, intruder area $A_i = 0.7\text{m}^2$.

distance separating the infinitesimal elements dA_i and dA_s. Consequently, the total heat flux is found by solving the double integration in (1) and substituting in (1).

For an arbitrary geometry, the incident heat flux is usually found by the finite element method (FEM), which is known to be cumbersome. Instead, we propose the following closed-form approximation

$$\Phi \approx \varepsilon k_B \left(T_i^4 - T_e^4\right) \frac{A_i A_s}{4R^2}. \tag{3}$$

which is simply an inverse square law relationship. The above approximation is compared with the FEM results in (1) for a human source at different distances. The results show excellent matching with our approximation for distances greater than 5 meters.

As the intruder passes in front of the PIR sensor, a Fresnel lens modulates the incident heat flux by partitioning the FOV into multiple segments[1] as shown in Fig. 2(a), where each segment concentrates the flux onto the PIR sensor. Consequently, the PIR sensor's signal depends on the intruder's trajectory through the FOVs. Take for example an intruder crossing the central FOV segment with constant speed v making an angle ψ_0 with the main sensor axis at distance R_0 as shown in Fig. 2(b). The squared distance between the intruder and the sensor is given by the cosine rule [6] as

$$R^2(t) = v^2 t^2 + \left(\frac{R_0 \sin\psi_0}{\sin\left(\psi_0 + \gamma\right)}\right)^2 + \frac{2vtR_0 \sin\psi_0}{\tan\left(\psi_0 + \gamma\right)}. \tag{4}$$

Therefore, the incident heat flux has the form

$$\Phi(t) = \frac{\tilde{\Phi}}{R^2(t)} \left[\Pi\left(\frac{t - t_0}{d_0^+/v}\right) - \Pi\left(\frac{t - t_0 - d_0^+/v}{d_0^-/v}\right)\right] \tag{5}$$

where $\tilde{\Phi} = \varepsilon k_B \left(T_i^4 - T_e^4\right) A_i A_s/4$, t_0 is the entry time, and $\Pi(t)$ is the unit rectangular function in the time interval

[1]In the context of intrusion detection, such an arrangement increases the probability of detection.

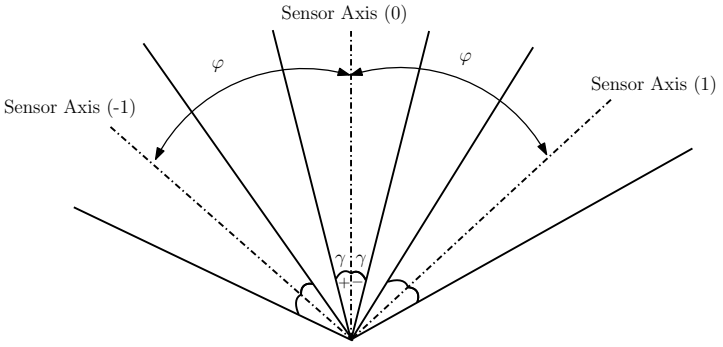

(a) Multiple-segment FOV Fresnel lens configuration. Each segment has a FOV with angle 2γ.

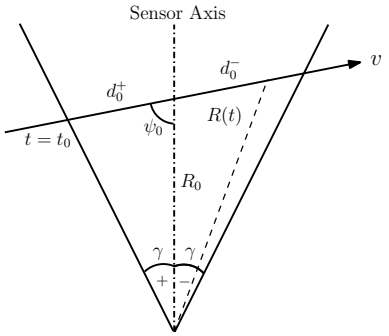

(b) Intruder crossing FOV.

Fig. 2: Intruder crossing the FOV of the Fresnel lens.

$[0, 1]$. In general, For $(2F + 1)$ FOV segments indexed by $j = -F, \cdots, F$, we have $\psi_j = \psi_0 - j\varphi$ for $j \neq 0$. Thus, the heat flux signature has the form

$$\Phi(t) = \frac{\Phi_0}{R^2(t)} \sum_{i=-F}^{F} \left[\Pi\left(\frac{t - t_j}{d_j^+/v}\right) - \Pi\left(\frac{t - t_j - d_j^+/v}{d_j^-/v}\right)\right] \tag{6}$$

where t_j is the jth segment entry time.

Figs. 3(a) and 3(b) show the heat flux signal for an intruder moving toward and away from the sensor.

B. PIR Signal

The PIR sensor converts the impinging heat flux into an electrical voltage. The responsivity, which is the ratio of the output voltage to the input heat flux, completely characterizes the sensor. The responsivity is actually a bandpass system [10] given by

$$H(s) = \frac{V(s)}{\Phi(s)} = \frac{Ks}{(1 + \tau_t s)(1 + \tau_e s)} \tag{7}$$

where K is the sensor's gain, τ_t is the thermal time constant of the sensor, and τ_e is the electrical time constant. Therefore, the output voltage signal is a filtered version of the heat flux in (6), i.e.,

$$s(t) \quad = \quad h(t) * \Phi(t) \tag{8}$$

where $h(t)$ is the sensor's time-domain responsivity and $*$ is the convolution operator. An example is given in Figs. 3(c) and 3(d).

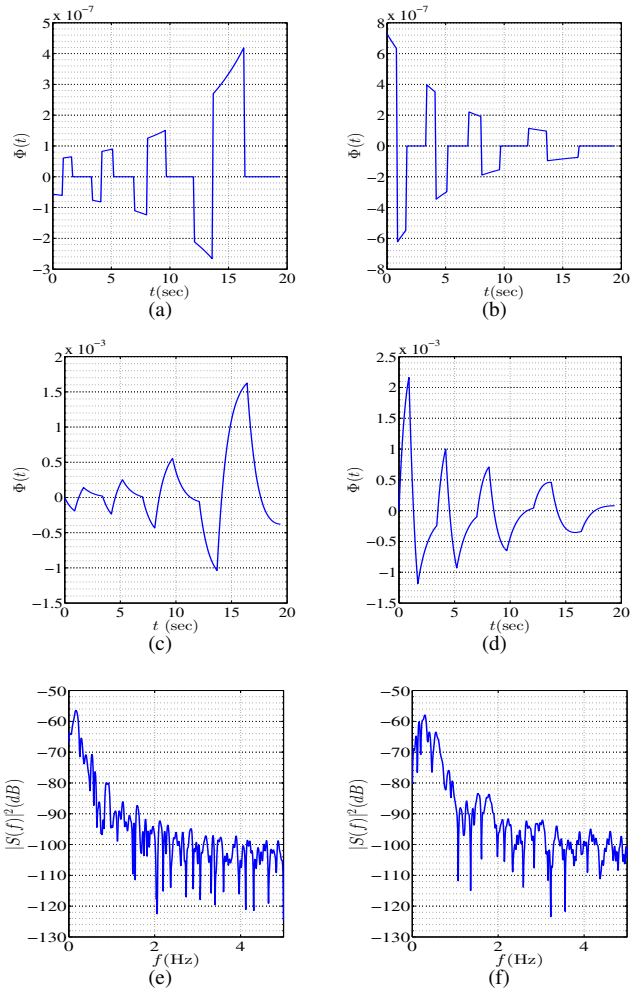

Fig. 3: The intruder at $R_0 = 50$m moving with speed of $v = 5$ kmph and $\psi = 50^0$. The sensor has $F = 4$ FOVs. Figs. (a) and (b) show the heat flux, Figs (c) and (d) show the sensor signal for $K = 6. \times 10^3$, $\tau_T = 4.2$ sec, and $\tau_E = 1$ sec. Figs. (e) and (f) show the periodograms of the sensor signal sampled with $F_s = 10$ Hz and a FFT length of 2048. The first column is for the intruder moving toward the sensor and the second column for it moving away.

The PIR sensor elements are usually followed by a JFET voltage buffer, which superimposes the sensor signal on a dc bias of the transistor. Also, the signal is corrupted by noise, which is dependent on the sensor and the environment background heat radiation. However, we assume that the voltage signal at the input of the analog to digital converter, $x(t)$, is appropriately conditioned to remove the dc bias and reduce the noise before being sampled at a sampling frequency of F_s. Hence, the raw available sensor is

$$x[n] = s[n] + w[n]$$

for $0 \leq n \leq N-1$ where $w[n]$ is assumed to be additive white Gaussian noise with zero mean and known variance, σ^2.

III. Intrusion Detection

For a given intruder's class (e.g. humans) the signal's energy is dependent on the separation distance, since the intruder's energy and the sensor's noise energy are fixed. Hence, we resort to statistical hypothesis testing methods to provide acceptable performance.The intrusion detection problem is formulated as the following hypothesis testing problem, i.e.,

$$\begin{aligned} \mathcal{H}_0 : x[n] &= w[n], \qquad 0 \leq n \leq N-1 \\ \mathcal{H}_1 : x[n] &= s[n] + w[n], 0 \leq n \leq N-1. \end{aligned} \tag{9}$$

One way to tackle this problem is to assume that $s[n]$ is completely unknown, and so the optimal detector in this case would be the energy detector (ED), with the following test statistics

$$T_{\text{ED}}(\mathbf{x}) = \frac{1}{\sigma^2} \sum_{n=0}^{N-1} x^2[n]. \tag{10}$$

Unfortunately, the energy detector has the worse performance among all detectors, since no prior information is used.

Interestingly, we can infer some valuable information from the shape of the PIR signal. Indeed, $s(t)$ in Fig 3(c) has a striking resemblance to an exponentially decaying sinusoid and to an exponentially increasing sinusoid in Fig. 3(d). This observation is also consolidated by (8). Furthermore, Figs 3(e) and 3(f) suggest having several dominant sinusoidal components. Hence, we propose the following approximation

$$\begin{aligned} s[n] &\approx \sum_{i=0}^{L-1} \alpha^n A_i \cos\left(2\pi f_i n + \phi_i\right) \\ &= \sum_{i=0}^{L-1} a_i \alpha^n \cos(2\pi f_i n) + b_i \alpha^n \sin(2\pi f_i n) \end{aligned} \tag{11}$$

where A_i, f_i, ϕ_i are the ith amplitude, frequency, and phase of the ith component respectively. Whereas $\alpha \geq 0$ is the exponential factor and the parameter vector, $a_i = A_i \cos(\phi_i)$ and $b_i = A_i \sin(\phi_i)$. The above can be compactly represented in vector format as

$$\mathbf{s} = \mathbf{G}(\boldsymbol{\theta})\mathbf{c} \tag{12}$$

$$\mathbf{c} = (a_0, \cdots, a_{L-1}, b_0, \cdots, b_{L-1})^T \tag{13}$$

$$\mathbf{G}(\boldsymbol{\theta}) = \Big(\mathbf{g}_c(\alpha, f_0) \cdots \mathbf{g}_c(\alpha, f_{L-1})\, \mathbf{g}_s(\alpha, f_0) \cdots \mathbf{g}_s(\alpha, f_{L-1})\Big) \tag{14}$$

where $\mathbf{s} = (s[0], \cdots, s[N-1])^T$, the signal parameters are lumped in $\boldsymbol{\theta} = (\alpha, f_0, \cdots, f_{L-1})^T$, and the columns of the matrix $\mathbf{G}(\boldsymbol{\theta})$ are

$$\mathbf{g}_c(\alpha, f_i) = \Big(1, \alpha\cos(2\pi f_i), \cdots, \alpha^{N-1}\cos(2\pi f_i(N-1))\Big)^T \tag{15}$$

$$\mathbf{g}_s(\alpha, f_i) = \Big(0, \alpha\sin(2\pi f_i), \cdots, \alpha^{N-1}\sin(2\pi f_i(N-1))\Big)^T \tag{16}$$

Consequently, the detection problem can be formulated as

$$\begin{aligned} \mathcal{H}_0 : \mathbf{x} &= \mathbf{w} \\ \mathcal{H}_1 : \mathbf{x} &= \mathbf{G}(\boldsymbol{\theta})\mathbf{c} + \mathbf{w} \end{aligned} \tag{17}$$

where $\mathbf{x} = (x[0], x[1], \cdots, x[N-1])^T$ and $\mathbf{w} = (w[0], w[1], \cdots, w[N-1])^T$. The above is a composite hypothesis testing, since $\boldsymbol{\theta}$ needs to be estimated. An asymptotically optimal detector is the generalized likelihood ratio

test (GLRT) [11]. It can be shown that the GLRT reduces to finding the best projection of $\mathbf{x}$ onto the space spanned by the columns of $\mathbf{G}(\boldsymbol{\theta})$, i.e.,

$$T_{\text{GLRT}}(\mathbf{x}) = \max_{\boldsymbol{\theta}} \|P_{\mathbf{G}}(\boldsymbol{\theta})\mathbf{x}\|^2 \tag{18}$$

where $P_{\mathbf{G}}(\boldsymbol{\theta}) = \left(\mathbf{G}^T(\boldsymbol{\theta})\mathbf{G}(\boldsymbol{\theta})\right)^{-1}\mathbf{G}(\boldsymbol{\theta})^T$ is the projection matrix on the space spanned by the columns of $\mathbf{G}(\boldsymbol{\theta})$.

Apparently, the GLRT is computationally demanding mainly due to the non-zero correlation between the columns of $\mathbf{G}(\boldsymbol{\theta})$. Consequently, we propose a sub-optimal detector in which we assume orthogonal columns in $\mathbf{G}(\boldsymbol{\theta})$. In other words,

$$\sum_{i=0}^{L-1}\sum_{j=0}^{L-1} \mathbf{g}_c^T(\alpha, f_i)\mathbf{g}_s(\alpha, f_j) = \begin{cases} N, \ i = j \\ 0, \ i \neq j \end{cases} \tag{19}$$

for all α and f_i's. Hence, the resulting detector in this case has the form

$$T(\mathbf{x}) = \max_{\alpha, f_0, \cdots, f_{L-1}} \frac{1}{N}\sum_{i=0}^{L-1} |\mathbf{x}^T\mathbf{g}_c(\alpha, f_i)|^2 + |\mathbf{x}^T\mathbf{g}_s(\alpha, f_i)|^2 \tag{20}$$

which for a given α is a separable maximization problem, i.e., it has L peaks at the optimal frequencies $(\widehat{f_i})$ values.

The detector in (20) can be further simplified by noting that the correlations $\mathbf{x}^T\mathbf{g}_c(\alpha, f_i)$ and $\mathbf{x}^T\mathbf{g}_s(\alpha, f_i)$ can be decomposed into two steps. First, multiply the data samples, $x[n]$, by the *window* function α^n for a given α and $0 \leq n \leq N-1$. Defined the windowed data $x_\alpha[n]$ and then the detector in (20) becomes

$$T_{\text{EWP}}(\mathbf{x}) = \max_{\alpha, f_0, \cdots, f_{L-1}} \frac{1}{N}\sum_{i=0}^{L-1} |X_\alpha(f_i)|^2 \tag{21}$$

which we will call the exponentially windowed periodogram (EWP) detector. $X_\alpha(f_i)$ in (21) is the widowed periodogram defined as

$$X_\alpha(f_i) = \sum_{n=0}^{N-1} x_\alpha[n]e^{(-j2\pi f_i)}. \tag{22}$$

Thus, the EWP detector chooses the window that gives the greatest L spectral peaks. It follows that the periodogram detector (PD) is a special case of the EWP detector when α is fixed at unity, giving

$$T_P(\mathbf{x}) = \max_{f_0, \cdots, f_{L-1}} \sum_{i=0}^{L-1} |X_1(f_i)|^2. \tag{23}$$

Interestingly, the optimal window, $\widehat{\alpha}$, found earlier gives an indication about the movement direction. If $\widehat{\alpha} < 1$ then the signal is decreasing with time implying that the intruder is moving away from the sensor. Oppositely, if $\widehat{\alpha} > 1$ the intruder is moving toward the sensor. Thus,

Decide intruder is moving away from sensor, $\widehat{\alpha} > 1$;

Decide intruder is moving toward from sensor, $\widehat{\alpha} < 1$.

IV. Simulation Results

In this section we have simulated a human intruder passing through the FOV of a PIR having $F = 4$ segments and $\gamma = 7.5^o$. The intruder moves with a constant speed of $v = 5$ kmph in a straight line making angle with the main PIR sensor axis of $\psi = 50^0$ away from the sensor. The intruder's temperature is $T_i = 37^o$ with emissivity $\varepsilon = 1$, environment temperature $T_i = 20^o$, sensor area $A_s = 20\mu\text{m}^2$ and intruder area $A_i = 0.7\text{m}^2$. The PIR sensor has $K = 6. \times 10^3$, $\tau_t = 4.2$ sec, and $\tau_e = 1$ sec. The noise in the system is zero-mean AWGN with standard deviation of $50\,\mu$V.

We compare the detection performance via ROC graphs showing the probability of detection (P_D) against the probability of false alarm (P_{FA}) of the ED in (10), the EWD in (21), and the PD in (23) (both use $L = 3$ sinusoidal components) in a Monte Carlo simulation with 10^5 iterations. Two sets of simulations are run, one with the intruder moving away from the sensor and the second when the intruder is moving toward the sensor. Figs. 4-8 depict the ROC for different R_0 values when the intruder is moving away from the sensor, whereas Figs. 9-13 show the ROC when the intruder is moving toward the sensor. In general, for a relatively small distance, both the EWP and the PD achieve a similar performance as shown in Figs. 4,5,9, and 10, while still performing better than the ED. On the other hand, the rest of the figures show the superior performance of the EWD over large distances. Finally, the direction of movement is estimated by the EWD algorithm, by testing the $\widehat{\alpha}$ as mentioned before. The EWD achieves almost 100% correct direction estimation for all different distances as shown in Table I.

TABLE I: Direction Estimation

R_0	10m	30m	50m	70m	90m
Intruder moving away	100%	100%	100%	100%	100%
Intruder moving toward	100%	100%	100%	100%	99.89%

V. Conclusions and Future Work

We have investigated the problem of long range intrusion detection using PIR sensors. An inverse square-law relation is established for the incident heat flux and the separation distance. Then, the PIR sensor output signal is modeled by the sum of exponentially modulated sinusoids. Accordingly, an exponentially windowed periodogram detector is proposed showing very good detection performance for long distance cases when compared to both the conventional periodogram detector and the energy detector. In future work, we intend to investigate the use of sensor arrays for intrusion detection.

Acknowledgment

Research presented in this paper was funded by Al-Zaytoonah University of Jordan grant (8/12/2014). The authors gratefully acknowledge this support.

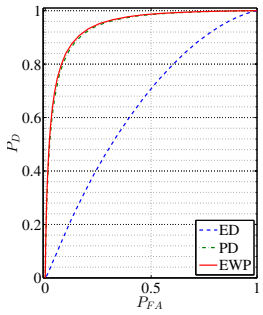

Fig. 4: ROC for $R_0 = 10$m and inruder moving away from sensor.

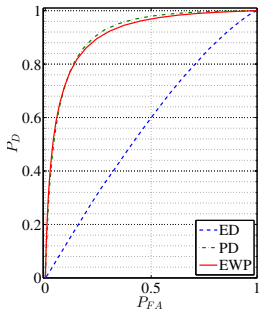

Fig. 5: ROC for $R_0 = 30$m and inruder moving away from sensor.

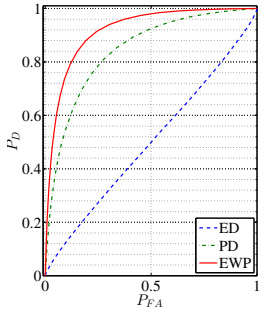

Fig. 6: ROC for $R_0 = 50$m and inruder moving away from sensor.

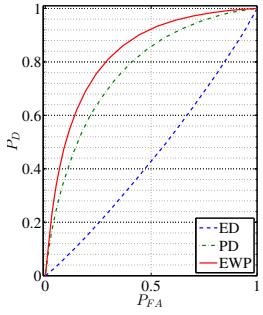

Fig. 7: ROC for $R_0 = 70$m and inruder moving away from sensor.

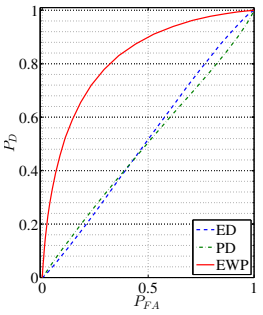

Fig. 8: ROC for $R_0 = 90$m and inruder moving away from sensor.

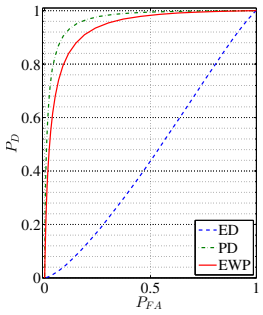

Fig. 9: ROC for $R_0 = 10$m and inruder moving toward from sensor.

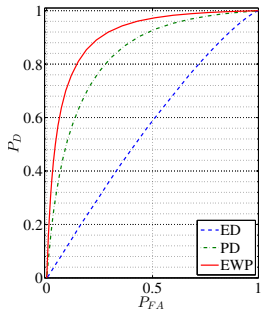

Fig. 10: ROC for $R_0 = 30$m and inruder moving toward from sensor.

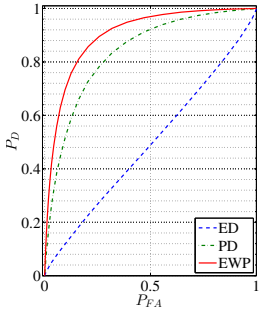

Fig. 11: ROC for $R_0 = 50$m and inruder moving toward from sensor.

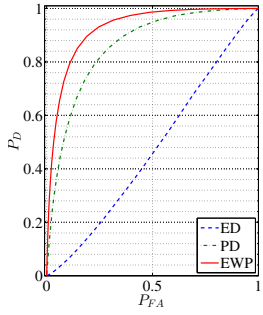

Fig. 12: ROC for $R_0 = 70$m and inruder moving toward from sensor.

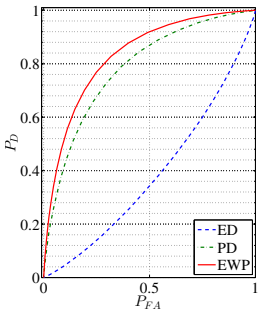

Fig. 13: ROC for $R_0 = 90$m and inruder moving toward from sensor.

REFERENCES

[1] A. Arora, P. Dutta, S. Bapat, V. Kulathumani, H. Zhang, V. Naik, V. Mittal, H. Cao, M. Demirbas, M. Gouda *et al.*, "A line in the sand: a wireless sensor network for target detection, classification, and tracking," *Computer Networks*, vol. 46, no. 5, pp. 605–634, 2004.

[2] H. Budzier, *Thermal infrared sensors theory, optimization, and practice*. Chichester, West Sussex, U.K. Hoboken, N.J: Wiley, 2011.

[3] R.-S. Hsiao, D.-B. Lin, H.-P. Lin, S.-C. Cheng, and C.-H. Chung, "Indoor target detection and localization in pyroelectric infrared sensor networks," *IEEE VTS APWCS. Singapore City: IEEE*, pp. 115–119, 2011.

[4] S. Akbas, M. A. Efe, and S. Ozdemir, "Performance evaluation of pir sensor deployment in critical area surveillance networks," in *Distributed Computing in Sensor Systems (DCOSS), 2014 IEEE International Conference on*. IEEE, 2014, pp. 327–332.

[5] L. Gu, D. Jia, P. Vicaire, T. Yan, L. Luo, A. Tirumala, Q. Cao, T. He, J. A. Stankovic, T. Abdelzaher *et al.*, "Lightweight detection and classification for wireless sensor networks in realistic environments," in *Proceedings of the 3rd international conference on Embedded networked sensor systems*. ACM, 2005, pp. 205–217.

[6] R. Abu Sajana, R. Subramanian, P. V. Kumar, S. Krishnan, B. Amrutur, J. Sebastian, M. Hegde, and S. Anand, "A low-complexity algorithm for intrusion detection in a pir-based wireless sensor network," in *Intelligent Sensors, Sensor Networks and Information Processing (ISSNIP), 2009 5th International Conference on*. IEEE, 2009, pp. 337–342.

[7] Q. Hao, J.-S. Fang, D. J. Brady, and B. D. Guenther, "Real-time walker recognition using pyroelectric sensors," *IEEE Sensors Journal, submitted*, 2006.

[8] P. Zappi, E. Farella, and L. Benini, "Tracking motion direction and distance with pyroelectric ir sensors," *Sensors Journal, IEEE*, vol. 10, no. 9, pp. 1486–1494, 2010.

[9] J. Yun and M.-H. Song, "Detecting direction of movement using pyroelectric infrared sensors," *Sensors Journal, IEEE*, vol. 14, no. 5, pp. 1482–1489, 2014.

[10] A. Odon, "Modelling and simulation of the pyroelectric detector using matlab/simulink," *Measurement Science Review*, vol. 10, no. 6, pp. 195–199, 2010.

[11] S. M. Kay, *Fundamentals of Statistical Signal Processing, Volume 2: Detection Theory*. Prentice Hall, 1998.

Knowledge-aided Adaptive Detection with Multipath Exploitation Radar

Utku Kumbul
Department of Electrical and
Computer Engineering
TOBB University of Economics and Technology
Ankara,Turkey
Email: ukumbul@etu.edu.tr

Harun Taha Hayvaci
Department of Electrical and
Computer Engineering
TOBB University of Economics and Technology
Ankara,Turkey
Email: hhayvaci@etu.edu.tr

***Abstract*—The adaptive detection of point-like targets in the presence of multipath is considered in this article. Target return signal is modeled as the sum of direct path return and reflected path return signals under the assumption of a zero-mean complex circular Gaussian noise with an unknown covariance matrix. A new approach to exploit multipath returns in target detection with an adaptive regime is studied. The novelty of this approach is that the multipath returns are exploited with a *priori* knowledge of the reflecting environment, so that we have the knowledge of the reflected steering vector for a known actual direct path steering vector. As a case study, we analyze a radar-target scenario over a flat conducting surface.**

I. Introduction

The adaptive detection of radar signals in a Gaussian noise with an unknown covariance matrix has been an active research topic for decades. It is well known that a uniformly most powerful (UMP) test does not exist in the sense of the Neyman-Pearson criteria due to unknown target and noise parameters, i.e. return signal strength and the covariance matrix of the noise environment. Thus, various methods have been studied. Among these, two well known are Kelly's detector [1] and Adaptive Matched Filter (AMF) [2], where both suggest Generalized Likelihood Ratio Test (GLRT) and present constant false alarm rate (CFAR) property. The AMF and Kelly's detector assume steering vector is perfectly aligned with the nominal one. In [3]–[5], steering vector mismatch is studied and it is shown that performance of the detection suffers from loss when there is a mismatch between actual steering vector and the nominal one. Several mismatched conditions and their solutions are addressed in [5]–[11].

In addition, the multipath exploitation radar has been challenging and yet promising topic in modern radar problems. It can provide additional degrees of freedom, and better detection and estimation performance by incorporating a *priori* information about radar-target environment [12]–[14]. Interestingly, in [15] an adaptive detector able to exploit multipath returns without assumptions on its structure, i.e. the knowledge of its steering vector, is devised. In this article, the adaptive detection of point-like targets with a knowledge-aided multipath exploitation radar is studied. It is assumed that we have the knowledge of reflected steering vector for a known actual direct path steering vector.

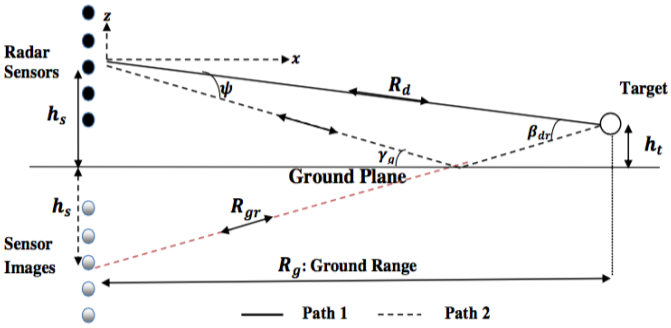

Fig. 1: Geometry of the problem: Radar-Target over a Ground Plane

In this study, multipath exploitation on adaptive radar detection for point-like target is considered. We model the target return signal as the sum of direct and reflected path returns under the assumption of zero-mean complex circular Gaussian noise with unknown covariance matrix. We propose a new detector to exploit multipath returns in order to enhance adaptive radar target detection performance. The advantage of the proposed approach is that multipath returns are exploited with a *priori* knowledge of the reflecting environment. Herein we have the knowledge of the reflected steering vector for a known actual direct path steering vector.

The rest of the paper is organized as follows. Section II is about the formulation of the detection problem. Section III gives the detector design, while Section IV provides performance assessment. Section V includes some concluding remarks.

II. Formulation of the Detection Problem

In this section, we formulate the detection problem with the assumption of N sensors receiving the target return signal. We have the $\boldsymbol{r} \in \mathbb{C}^{N\times 1}$ as a received vector of the primary data and presume the $\boldsymbol{r}_k$, $k = 1,\ldots,K$ $(K \geq N)$ as the secondary data set that shares the same noise environment with the primary data. It is important to note that the sample covariance matrix of the secondary data is full rank with $K \geq N$. Radar-target geometry along with the reflecting boundary is

978-1-5090-0326-6/16/$31.00 ©2016 IEEE

given in Figure 1. Thus, the corresponding detection problem is formulated with the following binary hypothesis testing.

$$H_0: \begin{cases} \boldsymbol{r} = \boldsymbol{n} \\ \boldsymbol{r}_k = \boldsymbol{n}_k, \;\; k = 1, \ldots, K \end{cases}$$
$$H_1: \begin{cases} \boldsymbol{r} = \alpha_1 \boldsymbol{p} + \alpha_2 \boldsymbol{s} + \boldsymbol{n} \\ \boldsymbol{r}_k = \boldsymbol{n}_k, \;\; k = 1, \ldots, K \end{cases} \tag{1}$$

where

- $\boldsymbol{p} \in \mathbb{C}^{N\times 1}$, $\|\boldsymbol{p}\|^2 = 1$, is the target steering vector associated with the direct path return.
- $\boldsymbol{s} \in \mathbb{C}^{N\times 1}$, $\|\boldsymbol{s}\|^2 = 1$, is the reflected path target steering vector.
- α_1 and $\alpha_2 \in \mathbb{C}^{N\times 1}$ are the unknown deterministic parameters for attenuation in propagation associated with the direct path and reflected path, respectively;
- $\boldsymbol{n}$ and $\boldsymbol{n}_k \in \mathbb{C}^{N\times 1}$, $k = 1, \ldots, K$, denote the noise contributions which are assumed to be independent and identically distributed (iid), complex normal random vectors with zero-mean and covariance matrix $\boldsymbol{C} \succ \boldsymbol{0}$. Thus, primary data and secondary data set are assumed to have the same covariance matrix, i.e. $E[\boldsymbol{n}\boldsymbol{n}^\dagger] = \mathbb{E}[\boldsymbol{n}_k \boldsymbol{n}_k^\dagger] = \boldsymbol{C}$.

III. Detector Design

In this section, we design a new adaptive detector based on the hypothesis testing given in (1). Based on the Neyman Pearson criteria, the resulting optimum test is known as the Likelihood Ratio Test (LRT) for a given probability of false alarm (P_{fa}) constraint [16]. However, no UMP test exists with unknown signal and noise parameters [16], [17]. Thus, as a common approach, we adopt GLRT in an adaptive regime. Resulting likelihood ratio test is

$$\frac{\max\limits_{\alpha_1,\alpha_2\in\mathbb{C},\boldsymbol{C}} \; p_1(\boldsymbol{r};\alpha_1,\alpha_2,\boldsymbol{C})}{\max\limits_{\boldsymbol{C}} \; p_0(\boldsymbol{r};\boldsymbol{C})} \underset{H_0}{\overset{H_1}{\gtrless}} \eta_1, \tag{2}$$

where $\boldsymbol{C} \succ \boldsymbol{0}$ specifies the overall covariance matrix of the primary data, η_1 is the threshold for a given P_{fa}, p_0 is the probability density function (PDF) of the primary data under H_0 given by

$$p_0(\boldsymbol{r};\boldsymbol{C}) = \frac{1}{\det(\pi \boldsymbol{C})} \exp\left\{-\boldsymbol{r}^\dagger \boldsymbol{C}^{-1} \boldsymbol{r}\right\} \tag{3}$$

and p_1 is the PDF of the primary data under H_1 given by

$$p_1(\boldsymbol{r};\alpha_1,\alpha_2,\boldsymbol{C}) = \frac{1}{\det(\pi \boldsymbol{C})} \exp\left\{-\bar{\boldsymbol{r}}^\dagger \boldsymbol{C}^{-1} \bar{\boldsymbol{r}}\right\} \tag{4}$$

where $\bar{\boldsymbol{r}} = \boldsymbol{r} - \alpha_1 \boldsymbol{p} - \alpha_2 \boldsymbol{s}$. The AMF detector proposes a two-step GLRT by neglecting $\alpha_2 \boldsymbol{s}$ term which is due to multipath. Here in this article, α_2 is assumed unknown but $\boldsymbol{s}$ is a known reflected-path steering vector once we have the prior knowledge on radar-target geometry and the direct-path steering vector. Thus, our GLRT first finds maximum likelihood estimates (MLE) of unknown deterministic parameters for attenuation in propagation associated with the direct path and reflected path, α_1 and α_2 simultaneously, then estimates the unknown covariance matrix based on secondary data and replace it with the primary covariance matrix $\boldsymbol{C}$. We assume that primary and secondary data sets share the same covariance matrix.

Taking the natural logarithm of the likelihood ratio in (2) yields the log-likelihood ratio as

$$\max_{\alpha_1,\alpha_2\in\mathbb{C},\boldsymbol{C}=\boldsymbol{S}} \left(-\bar{\boldsymbol{r}}^\dagger \boldsymbol{C}^{-1} \bar{\boldsymbol{r}} + \boldsymbol{r}^\dagger \boldsymbol{C}^{-1} \boldsymbol{r}\right) \underset{H_0}{\overset{H_1}{\gtrless}} \eta_2, \tag{5}$$

MLE of α_1 and α_2 can be found by maximizing the likelihood function p_1 with respect to α_1 and α_2 [18], and solving the linear equations

$$\alpha_1 \boldsymbol{p}^\dagger \boldsymbol{C}^{-1} \boldsymbol{p} + \alpha_2 \boldsymbol{p}^\dagger \boldsymbol{C}^{-1} \boldsymbol{s} = \boldsymbol{p}^\dagger \boldsymbol{C}^{-1} \boldsymbol{r}$$
$$\alpha_1 \boldsymbol{s}^\dagger \boldsymbol{C}^{-1} \boldsymbol{p} + \alpha_2 \boldsymbol{s}^\dagger \boldsymbol{C}^{-1} \boldsymbol{s} = \boldsymbol{s}^\dagger \boldsymbol{C}^{-1} \boldsymbol{r}$$

yield

$$\hat{\alpha}_1 = \frac{\boldsymbol{p}^\dagger \boldsymbol{C}^{-1} \boldsymbol{r} - \dfrac{\boldsymbol{p}^\dagger \boldsymbol{C}^{-1} \boldsymbol{s}}{\boldsymbol{s}^\dagger \boldsymbol{C}^{-1} \boldsymbol{s}} \; \boldsymbol{s}^\dagger \boldsymbol{C}^{-1} \boldsymbol{r}}{\boldsymbol{p}^\dagger \boldsymbol{C}^{-1} \boldsymbol{p} - \dfrac{\boldsymbol{p}^\dagger \boldsymbol{C}^{-1} \boldsymbol{s}}{\boldsymbol{s}^\dagger \boldsymbol{C}^{-1} \boldsymbol{s}} \; \boldsymbol{s}^\dagger \boldsymbol{C}^{-1} \boldsymbol{p}} \tag{6}$$

$$\hat{\alpha}_2 = \frac{\boldsymbol{s}^\dagger \boldsymbol{C}^{-1} \boldsymbol{r} - \boldsymbol{p}^\dagger \boldsymbol{C}^{-1} \boldsymbol{r} \; \dfrac{\boldsymbol{s}^\dagger \boldsymbol{C}^{-1} \boldsymbol{p}}{\boldsymbol{p}^\dagger \boldsymbol{C}^{-1} \boldsymbol{p}}}{\boldsymbol{s}^\dagger \boldsymbol{C}^{-1} \boldsymbol{s} - \boldsymbol{p}^\dagger \boldsymbol{C}^{-1} \boldsymbol{s} \; \dfrac{\boldsymbol{s}^\dagger \boldsymbol{C}^{-1} \boldsymbol{p}}{\boldsymbol{p}^\dagger \boldsymbol{C}^{-1} \boldsymbol{p}}} \tag{7}$$

Inserting MLEs of α_1 and α_2, given in (6) and (7), respectively, and the estimated covariance matrix into the log-likelihood ratio, we have

$$\frac{\dfrac{\left|\boldsymbol{p}^\dagger \boldsymbol{S}^{-1} \boldsymbol{r}\right|^2}{\boldsymbol{p}^\dagger \boldsymbol{S}^{-1} \boldsymbol{p}} + \dfrac{\left|\boldsymbol{s}^\dagger \boldsymbol{S}^{-1} \boldsymbol{r}\right|^2}{\boldsymbol{s}^\dagger \boldsymbol{S}^{-1} \boldsymbol{s}} - 2\Re\left\{\dfrac{\left(\boldsymbol{p}^\dagger \boldsymbol{S}^{-1} \boldsymbol{r}\right)\left(\boldsymbol{r}^\dagger \boldsymbol{S}^{-1} \boldsymbol{s}\right)}{\boldsymbol{p}^\dagger \boldsymbol{S}^{-1} \boldsymbol{s}}\right\} \cos^2\theta}{1 - \cos^2\theta}$$

where θ is the angle between direct-path and reflected-path steering vectors in the whitened observation space [19], so that we have

$$\cos^2\theta = \frac{\left|\boldsymbol{s}^\dagger \boldsymbol{S}^{-1} \boldsymbol{p}\right|^2}{\left(\boldsymbol{p}^\dagger \boldsymbol{S}^{-1} \boldsymbol{p}\right)\left(\boldsymbol{s}^\dagger \boldsymbol{S}^{-1} \boldsymbol{s}\right)}$$

$\boldsymbol{S}$ is the estimated covariance matrix and computed as the sample covariance matrix of the secondary data.

$$\boldsymbol{S} = \frac{1}{K} \sum_{k=1}^{K} \boldsymbol{r}_k \boldsymbol{r}_k^\dagger \tag{8}$$

The decision test in (2) can be written as

$$\frac{|y_1|^2}{p_1} + \frac{|y_2|^2}{s_1} - 2\Re\left\{\frac{y_1 y_2^*}{y_3^*}\right\} \cos^2\theta \underset{H_0}{\overset{H_1}{\gtrless}} \eta_3 \tag{9}$$

where $y_1 = \boldsymbol{p}^\dagger \boldsymbol{C}^{-1} \boldsymbol{r}$, $y_2 = \boldsymbol{s}^\dagger \boldsymbol{C}^{-1} \boldsymbol{r}$, $y_3 = \boldsymbol{s}^\dagger \boldsymbol{C}^{-1} \boldsymbol{p}$, $p_1 = \boldsymbol{p}^\dagger \boldsymbol{C}^{-1} \boldsymbol{p}$, $s_1 = \boldsymbol{s}^\dagger \boldsymbol{C}^{-1} \boldsymbol{s}$. and η_3 is the detection threshold set with a desired probability of false alarm.

IV. Performance Assessment

In this section, we assess the performance of the proposed detector, which we call Multipath Adaptive Matched Filter (MP-AMF), by comparing Kelly's detector and the AMF. We compare MP-AMF, AMF and Kelly's GLRT in terms of probability of detection (P_d). Both Kelly's detector and AMF neglect the existence of $\alpha_2 \boldsymbol{s}$ term. In [1], Kelly's detector is given as

$$\frac{|\boldsymbol{p}^\dagger \boldsymbol{S}^{-1}\boldsymbol{r}|^2}{(\boldsymbol{p}^\dagger \boldsymbol{S}^{-1}\boldsymbol{p})\left(1+\frac{1}{K}\boldsymbol{r}^\dagger \boldsymbol{S}^{-1}\boldsymbol{r}\right)} \underset{H_0}{\overset{H_1}{\gtrless}} \eta_4, \tag{10}$$

and, in [2], AMF detector is given as

$$\frac{|\boldsymbol{p}^\dagger \boldsymbol{S}^{-1}\boldsymbol{r}|^2}{\boldsymbol{p}^\dagger \boldsymbol{S}^{-1}\boldsymbol{p}} \underset{H_0}{\overset{H_1}{\gtrless}} \eta_5. \tag{11}$$

where η_4 and η_5 are the thresholds for Kelly's detector and the AMF, respectively, and are set according to the desired level of P_{fa}.

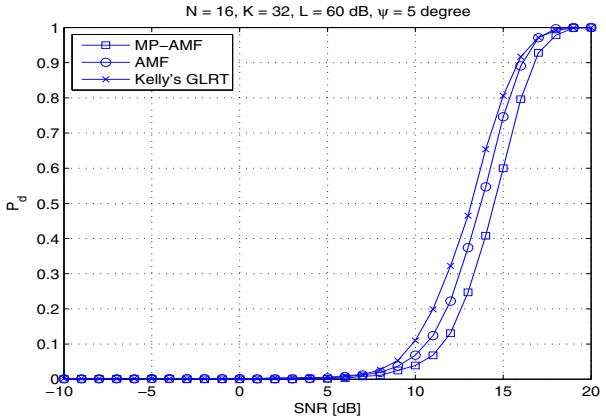

Fig. 2: P_d versus SNR for the MP-AMF, the AMF, and Kelly's GLRT; No Multipath exists, $L = 60$ dB, $N = 16$, $K = 32$, $\psi = 5°$, $P_{fa} = 10^{-4}$.

First, we evaluate performance results when there is no multipath, i.e. α_2 is set to be 60 dB below α_1, so that the reflected steering vector is useless. In other words, we have the loss associated with reflected path relative to direct path $L = 60$ dB, where $|\alpha_2| = |\alpha_1|/\sqrt{L}$. The difference between angles of arrival of direct and reflected path returns is set to $\psi = 5°$. In Figure 2, it is shown that MP-AMF detector has slight performance degradation compared to the AMF and Kelly's detector. However, this is well expected since MP-AMF estimates a second unknown parameter, i.e. reflected path signal strength, which requires a certain level of SNR [12].

In Figure 3, performance results are presented for the case where multipath return has sufficient power to be exploited, i.e. $L = 10$ dB, and $\psi = 5°$. It is shown that MP-AMF detector quite outperforms both the AMF and Kelly's detector by exploiting known multipath return. It is observed that MP-AMF has a noteworthy ~ 5 dB SNR gain compared to the AMF and Kelly's detector, particularly at higher P_d rates. It is also notable that AMF performance is more robust than Kelly's detector in this scenario.

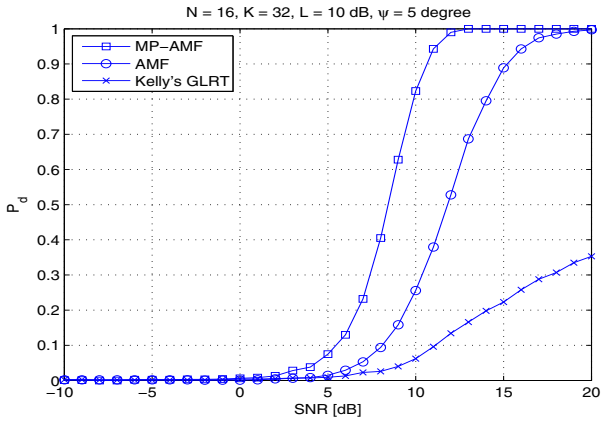

Fig. 3: P_d versus SNR for the MP-AMF, the AMF, and Kelly's GLRT; Multipath exists, $L = 10$ dB, $N = 16$, $K = 32$, $\psi = 5°$; $P_{fa} = 10^{-4}$.

In Figure 4, we consider the scenario where multipath returns are highly clumped, i.e. $\psi = 1°$ and yet reflected path has 10 dB loss with respect to direct path return. It is observed that MP-AMF has a ~ 3 dB performance degradation with respect to the AMF and Kelly's detector at the higher rates of probability of detection. This performance degradation is due to highly clumped multipath structure where multipath returns are not sufficiently distinguishable to be exploited.

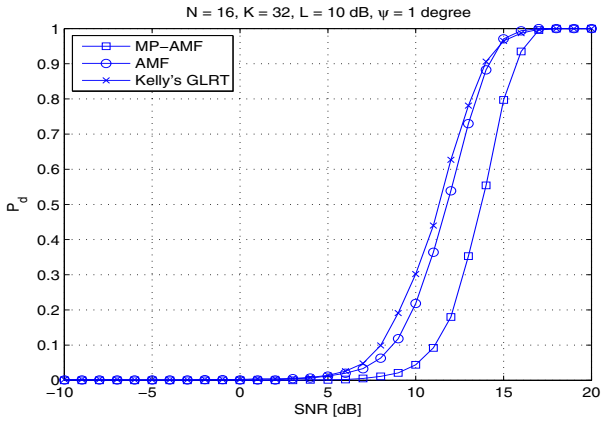

Fig. 4: P_d versus SNR for the MP-AMF, the AMF, and Kelly's GLRT; Multipath exists, $L = 10$ dB, $N = 16$, $K = 32$, $\psi = 1°$; $P_{fa} = 10^{-4}$.

In Figure 5, we have the scenario where the reflected path has 3 dB loss relative to direct path, i.e. $L = 3$ dB and $\psi = 5°$. It is observed that the MP-AMF outperforms both the AMF and Kelly's detector with a ~ 10 dB SNR gain at $P_d = 0.9$. Both in Figure 3 and Figure 5, it is shown that exploiting

multipath return provides remarkable performance increase. However, in Figure 4, it is deduced that this performance increase depends on whether multipath returns are highly clumped or not.

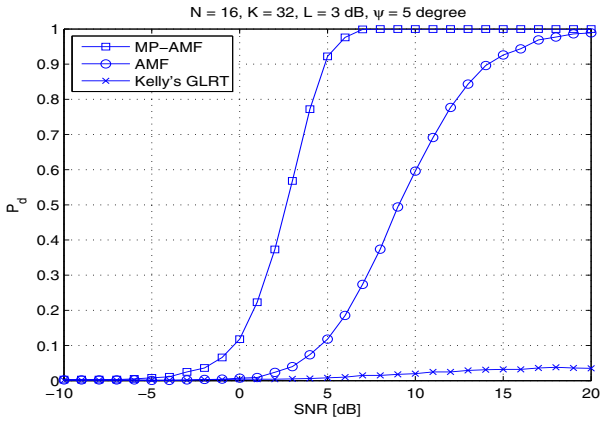

Fig. 5: P_d versus SNR for the MP-AMF, the AMF, and Kelly's GLRT; Multipath exists, $L = 3$ dB, $N = 16$, $K = 32$, $\psi = 5°$; $P_{fa} = 10^{-4}$.

V. Conclusion

In this paper, we have considered multipath exploitation on adaptive radar detection for point-like target. We have modeled the target return signal as the sum of direct path and reflected path returns under the assumption of zero-mean complex circular Gaussian noise with unknown covariance matrix. We have introduced a new adaptive detector, namely MP-AMF, to exploit multipath returns in target detection.

The performance assessments have been provided for variety of practical scenarios. It has been shown that when there is significant multipath returns which are distinguishable, the MP-AMF detector outperforms the AMF and Kelly's detector with a significant SNR gain at higher P_d rates. However, at highly clumped multipath structures and very low power reflected path returns, MP-AMF has slight performance degradation with respect to the AMF and Kelly's detector. This is expected since the MP-AMF estimates a second unknown parameter, i.e. reflected path signal strength, which requires a certain level of SNR and partially distinguishable multipath structure.

For future research track, authors will study extended, distributed, target model in the content of multipath exploitation radar with adaptive regime. Moreover, structured interference [4], [20]–[22], as well as oversampling data in range [23] would be interesting for future work.

References

[1] E. J. Kelly, "An Adaptive Detection Algorithm," *IEEE Trans. on Aerospace and Electronic Systems*, vol. 22, no. 1, pp. 115-127, March 1986.

[2] F. C. Robey, D. R. Fuhrmann, E. J. Kelly, and R. Nitzberg, "A CFAR Adaptive Matched Filter Detector," *IEEE Trans. on Aerospace and Electronic Systems*, vol. 28, no. 1, pp. 208-216, January 1992.

[3] S. Z. Kalson, "An adaptive array detector with mismatched signal rejection," *IEEE Trans. on Aerospace and Electronic Systems*, vol. 28, no. 1, pp. 195-207, January 1992.

[4] S. Bose and A. O. Steinhardt, "A Maximal Invariant Framework for Adaptive Detection with Structured and Unstructured Covariance Matrices," *IEEE Trans. on Signal Processing*, vol. 43, no. 3, pp. 2164-2175, September 1995.

[5] S. Kraut, L. L. Scharf, and L. T. McWhorter, "Adaptive Subspace Detectors," *IEEE Trans. on Signal Processing*, vol. 49, no. 1, pp. 1-16, January 2001.

[6] A. De Maio, "Robust adaptive radar detection in the presence of steering vector mismatches," *IEEE Trans. on Aerospace and Electronic Systems*, vol. 41, no. 4, pp. 1322-1337, October 2005.

[7] F. Bandiera, A. De Maio and G. Ricci, "Adaptive CFAR Radar Detection With Conic Rejection," *IEEE Trans. on Signal Processing*, vol. 55, no. 6, pp. 2533-2541, June 2007.

[8] A. De Maio, S. De Nicola, Y. Huang, S. Zhang and A. Farina, "Adaptive Detection and Estimation in the Presence of Useful Signal and Interference Mismatches," *IEEE Trans. on Signal Processing*, vol. 57, no. 2, pp. 436-450, February 2009.

[9] A. Aubry, A. De Maio, D. Orlando and M. Piezzo, "Adaptive Detection of Point-Like Targets in the Presence of Homogeneous Clutter and Subspace Interference," *IEEE Signal Processing Letters*, vol. 21, no. 7, pp. 848-852, July 2014.

[10] A. De. Maio and M. S. Greco, *Modern Radar Detection Theory*, New Jersey: SciTech, 2016.

[11] A. De Maio and D. Orlando, "Adaptive Radar Detection of a Subspace Signal Embedded in Subspace Structured Plus Gaussian Interference Via Invariance," *IEEE Trans. on Signal Processing*, vol. 64, no. 8, pp. 2156-2167, April 2016.

[12] H. T. Hayvaci, A. De Maio, and D. Erricolo, "Improved Detection Probability of a Radar Target in the Presence of Multipath with Prior Knowledge of the Environment," *IET Radar, Sonar & Navigation*, vol. 7, no. 1, pp. 36-46, January 2013.

[13] H. T. Hayvaci, P. Setlur, N. Devroye and D. Erricolo, "Maximum likelihood time delay estimation and Cramér-Rao bounds for multipath exploitation," *2012 IEEE Radar Conference*, Atlanta, GA, 2012, pp. 0764-0768.

[14] H. T. Hayvaci and D. Erricolo, "Improved radar target time-delay estimation with multipath exploitation," *2013 International Conference on Electromagnetics in Advanced Applications (ICEAA)*, Torino, 2013, pp. 1232-1235.

[15] A. Aubry, A. De Maio, G. Foglia and D. Orlando, "Diffuse Multipath Exploitation for Adaptive Radar Detection," *IEEE Trans. on Signal Processing*, vol. 63, no. 5, pp. 1268-1281, March 2015.

[16] H. L. Van Trees, *Detection, Estimation and Modulation Theory*, vol 1. New York: John Wiley & Sons, 2001.

[17] Steven M. Kay, *Fundamentals of Statistical Signal Processing, Detection Theory*, vol 2. New Jersey: Prentice Hall, 1998.

[18] Steven M. Kay, *Fundamentals of Statistical Signal Processing, Estimation Theory*, vol 1. New Jersey: Prentice Hall, 1993.

[19] F. Bandiera, D. Orlando, and G. Ricci, "Advanced Radar Detection Schemes under Mismatched Signal Models," *Synthesis Lectures on Signal Processing*, No. 8, Morgan & Claypool Publishers, 2009.

[20] A. Aubry, A. De Maio, L. Pallotta and A. Farina, "Maximum Likelihood Estimation of a Structured Covariance Matrix With a Condition Number Constraint," *IEEE Trans. on Signal Processing*, vol. 60, no. 6, pp. 3004-3021, June 2012.

[21] A. Aubry, A. De Maio and V. Carotenuto, "Optimality Claims for the FML Covariance Estimator with respect to Two Matrix Norms," *IEEE Trans. on Aerospace and Electronic Systems*, vol. 49, no. 3, pp. 2055-2057, July 2013.

[22] A. De Maio and D. Orlando, "An Invariant Approach to Adaptive Radar Detection Under Covariance Persymmetry," *IEEE Trans. on Signal Processing*, vol. 63, no. 5, pp. 1297-1309, March 2015.

[23] A. Aubry, A. D. Maio, G. Foglia, C. Hao and D. Orlando, "Radar detection and range estimation using oversampled data," *IEEE Trans. on Aerospace and Electronic Systems*, vol. 51, no. 2, pp. 1039-1052, April 2015.

Author Index

Q

R

S

T

U

V

W

X

Y

Z

SSPD 2017

Sensor Signal Processing for Defence Conference

6 - 7 December, 2017

Savoy Place, London

WC2R 0BL

Important Dates:

Submission of Papers: 22nd June 2017

Notification of Paper Acceptance: 22nd August 2017

Final version of Paper Due: 30th September 2017

The Sensor Signal Processing for Defence Conference is organised by the University Defence Research Collaboration (UDRC) in Signal Processing. SSPD 2017 aims to bring together researchers from academia, industry and government organisations interested in Signal Processing for Defence.

Call for papers: www.sspdconference.org

Papers are solicited from the following areas:-

- Array Signal Processing
- Image Processing
- Radar, Sonar and Acoustic
- Multimodal Signal Processing
- Multi-Target Tracking
- Signal Acquisition and Sensor Management
- Multiple-input and multiple-output (MIMO)
- Data Fusion
- Source Separation
- Anomaly Detection
- Distributed Signal Processing
- Low Size Weight & Power Solutions
- Target Detection and Identification
- Electro-Optic Sensing

All submitted papers will be peer reviewed. Accepted papers will be published in conference proceedings which will be archived in IEEE Xplore. Sponsored by Dstl and EPSRC.

Expressions of interest – email janet.forbes@ed.ac.uk

UDRC [dstl] SSPD Conference EPSRC Engineering and Physical Sciences Research Council AESS tm

Technical Co-Sponsor

IEEE Signal Processing Society